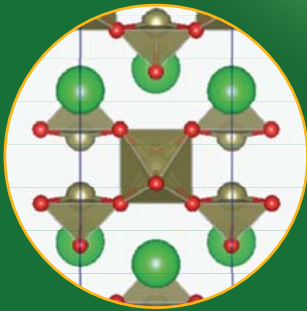
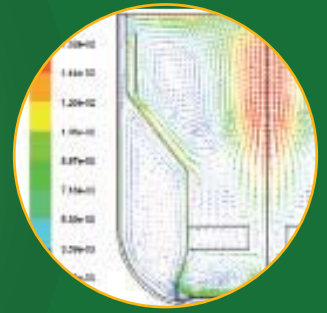
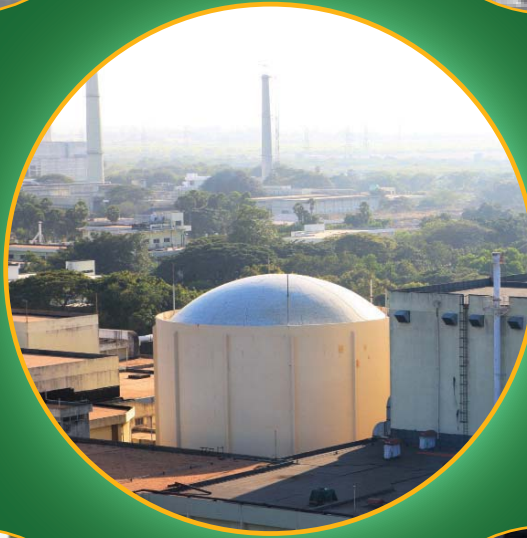
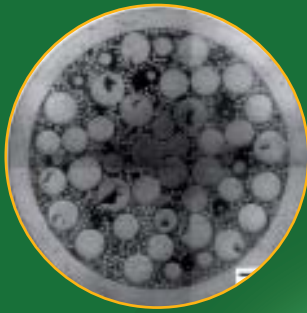




Indira Gandhi Centre for Atomic Research

Annual Report 2016



सत्यमेव जयते

Government of India
Department of Atomic Energy
Indira Gandhi Centre for Atomic Research
Kalpakkam - 603 102

IGCAR

INDIRA GANDHI CENTRE
FOR ATOMIC RESEARCH

Annual Report - 2016



Government of India
Department of Atomic Energy
Indira Gandhi Centre for Atomic Research
Kalpakkam 603 102

Apex Editorial Committee

Chairman

Dr. M. Sai Baba

Members

Dr. N. V. Chandra Shekar

Dr. Saroja Saibaba

Dr. Vidya Sundararajan

Editorial Committee

Shri B. Babu

Shri G. V. Kishore

Dr. T. S. Lakshmi Narasimhan

Dr. C. Mallika

Dr. B. K. Nashine

Shri K. Natesan

Dr. R. Sandhya

Dr. C. V. Srinivas

Shri S. Varatharajan

Publication Team

Shri K. Varathan

Shri G. Pentaiah

Shri K. Ganesan

Shri V. Rajendran

Address for Correspondence

Dr. M. Sai Baba

Chairman, Apex Editorial Committee

Director, Resources Management Group

Indira Gandhi Centre for Atomic Research

Kalpakkam - 603 102

Phone : +91-44-27480115

Fax : +91-44-27480060

Email : msb@igcar.gov.in

Website : www.igcar.gov.in

CONTENTS

Foreword

Editorial

I. Fast Breeder Test Reactor 1

II. Prototype Fast Breeder Reactor 11

III. R&D for Fast Breeder Reactors 39

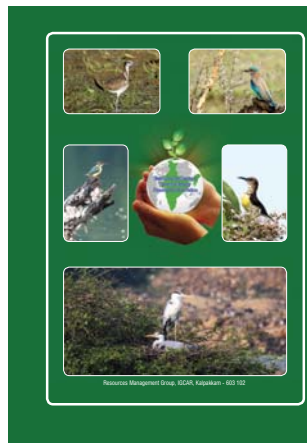
IV. Fuel Cycle 71

V. Directed Basic Research and
Infrastructure Facilities 103

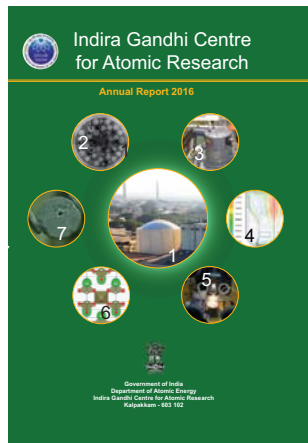
VI. Basic Research 131

VII. Awards/Publications/
News & Events/Organisation 171

Back Cover



Front Cover



Front Cover

1. Fast Breeder Test Reactor
2. Photomicrographs of sphere-pac fuel pin section
3. PSGIS device installed on the steam generator of PFBR
4. Velocity vectors (m/s) at steady state temperature of 328 K
5. The plutonium nitrate preparation in the glove box
6. Orthorhombic unit cell of BaTe₂O₆
7. The electro-reduced thorium metal

Back Cover

Flora and Fauna at Kalpakkam

Published by

Resources Management Group

Indira Gandhi Centre for Atomic Research, Kalpakkam - 603 102

Foreword



It is my pleasure to forward the Annual Report from IGCAR for 2016. Some of the achievements of this Centre towards realizing the mission oriented programmes on Fast Reactor and associated closed fuel cycle technologies through innovations and breakthroughs in science and technology in the year 2016 are listed in the report.

Fast Breeder Test Reactor, the flagship of our Centre, is in the 24th irradiation campaign and it is heartening to note that it was operated at its highest power level of 26.1MWt producing 5.2 MWe. A new test reactor facility (FBTR-2) for continuing the material irradiation programmes beyond the life of present FBTR using metal fuel is being planned under the Vision programme. Site for the proposed 100 MWt FBTR-2 reactor, has been identified and preliminary design is being prepared in line with the experience from PFBR.

KAMINI continues to provide excellent services in testing pyro-devices for all space launches of ISRO. Facilities for post-irradiation examination of advanced fuels and structural materials have been augmented. Recent performance evaluation of MOX sphere-pac fuel pins and ferro-boron shielding material irradiated in FBTR have provided valuable insights into their irradiation behaviour.

The commissioning of PFBR has made immense progress and we continue to extend our technical expertise and support towards obtaining

necessary regulatory and safety clearances. We have also evolved a new methodology based on glancing angle ultrasonic imaging for mapping the sub-assembly heads in PFBR. It was indeed a major achievement to complete the required pre-service tube inspection of all the eight PFBR Steam Generators using the state-of-the-art in-house developed robotic device, the PFBR Steam Generator Inspection System (PSGIS).

We have made significant progress in the design of 600 MWe future FBRs, which will be deployed as twin unit reactors, incorporating the latest design standards with a view to totally eliminate accidents. In parallel, state-of-the-art design safety criteria for MOX fuelled future FBRs is being finalized in collaboration with AERB, invoking post-Fukushima and Gen-IV safety standards. A processor based CPU card has been indigenously designed and developed for diversified real time computer systems for future FBRs in collaboration with ANURAG, DRDO. A unique experimental facility has been developed in-house, to assess the effect of stress fluctuations on creep behavior of reactor structural materials.

CORAL continues to operate and reprocess the spent fuel of FBTR, completing fourteen campaigns as per its design specifications. One of the significant achievements has been in the in-situ replacement of degraded radiation shielding window, which has been carried out for the first time with minimum man-REM

expenditure. The construction activities are nearing completion at DFRP. Successful demonstration of pyrochemical reprocessing of U-Zr fuel (100 gram) in a hot cell facility is indeed a significant milestone. Construction of the Fast Reactor Fuel Cycle Facility (FRFCF) and fabrication of major components have gained momentum during the year. FRFCF would continue to be a project of priority to the Centre

A significant number of experimental facilities have also been commissioned during the current year, notably the large scale (5/8th) water-model test facility at Engineering Hall-IV, facility based on travelling heater method, 1.7 MV Tandatron accelerator etc. A new Sodium Facility for Component Testing, with state-of-the-art features is in an advanced stage of commissioning. An indigenous fully automated Waste Assay Computed Tomography (WACT) nested modeling system, atmospheric dispersion studies and a decision support system for nuclear emergencies have been developed. Multi-purpose high-performance parallel computing cluster with 180 teraflops has also been commissioned.

A significant milestone was achieved when the BARC Training School at IGCAR successfully

completed its tenth year and young qualified scientists and engineers were placed in various Units of DAE. Training School and Homi Bhabha National Institute are providing robust manpower for conducting the mission programmes. Collaborations have been furthered with eminent institutions. The service groups have worked towards providing better amenities, infrastructure, safety, medical facilities and better environment. Programmes aimed towards development of neighbourhood and creating awareness about our activities are progressing well.

I would like to compliment the Editorial team for bringing out this document with the traditional flavor and invigorating with modern design. I also appreciate colleagues from Resources Management Group for their contributions and efforts.

As always, we would be happy to receive your comments and suggestions to enable us to move further.



(Arun Kumar Bhaduri)

Director, IGCAR

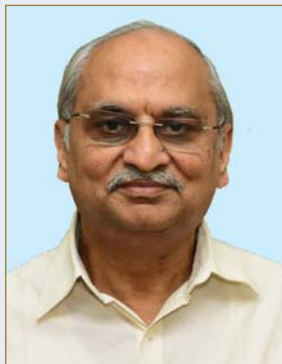
Mission of IGCAR

- « *To conduct a broad based multidisciplinary programme of scientific research and advanced engineering development, directed towards the establishment of the technology of Sodium cooled Fast Breeder Reactors (FBR) and associated fuel cycle facilities in the Country*
- « *The development and applications of new and improved materials, techniques, equipment and systems for FBRs and*
- « *To pursue basic research to achieve breakthroughs in fast reactor technology*

Vision

To be a Global Leader in Sodium cooled Fast Breeder Reactor and associated Fuel Cycle Technologies by 2020

Editorial



I am happy to forward the Annual Report of Indira Gandhi Centre for Atomic Research for the year 2016 as the Chairman of the Editorial Committee. Over the years, the annual report has continued to evolve into a complete document, highlighting the multi-disciplinary activities of the Centre, even while completing the mission oriented targets.

The layout of the Annual Report is segregated in seven chapters, as in the previous issues. The articles reflecting the themes have been specially chosen to bring out the excellence and leadership achieved by the Centre towards pursuing "Science based Technologies". It has been a constant endeavour of the editorial team to ensure relevance, accuracy and readability in the information provided. I take this opportunity to thank the editorial committee, for their dedicated efforts in bringing out the magazine, enhancing the flavor and quality year after year.

The articles are segregated into chapters to highlight the achievements with respect to Chapter-I: Fast Breeder Test Reactor, our Flagship Reactor; Chapter-II: Prototype Fast Breeder Reactor, in advanced stages of commissioning with the R&D support from our Centre; Chapter-III: R&D for FBRs, our pursuits for the future; Chapter-IV: Fuel Cycle, mission oriented programme towards setting of India's first ever Fast Reactor Fuel Cycle Facility; Chapter-V: Directed Basic Research and Infrastructure Facilities, a new dimension in our research and for rendering the support towards pursuing the programmes; Chapter-VI: Basic Research, innovations and breakthroughs in the year that passed and Chapter-VII: Diary of important events, awards, honours received etc.

Fast Breeder Test Reactor, has continued to operate successfully and has served as a test bed for irradiation of fuels and materials and for qualifying some of the equipment. The details of Highlights of 25th Irradiation Campaign, Identification of Leaky Steam Generator Module, Performance Evaluation of Tin Oxide Based Sensor and Characterization of

Neutron Spectrum of KAMINI Reactor are some of the interesting articles in the first Chapter.

Our Centre has successfully delivered all the systems for PFBR and continued to support towards obtaining mandatory safety and regulatory clearances for commissioning. Some of the efforts undertaken are highlighted in Chapter-II. Chapter-III deals with R&D towards future reactors including metal fuelled fast reactors. Topics covered include the design of reactor core and components for future reactors with emphasis on improved economics and safety. In line with the Department's emphasis on closing of the fuel cycle, a number of programmes are being pursued in the back end of the fast reactor fuel cycle and these are presented in Chapter-IV. Chapter-V showcases some of our successes in the new focus towards directed R&D and basic research activities and activities undertaken towards infrastructural development. Chapter VI contains an array of articles in basic research in the domains of science and engineering, most of them having direct applications to the mission programmes of the Centre. Chapter-VII provides list of significant events including seminars, workshops and eminent and popular lectures/ colloquia and awards/honors received in recognition of our achievements.

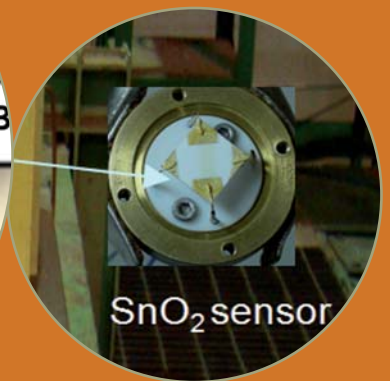
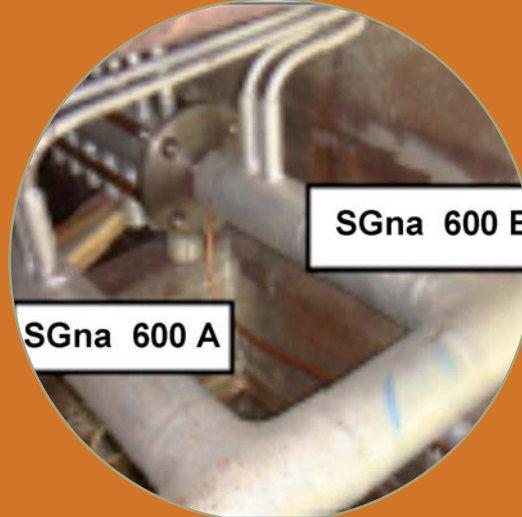
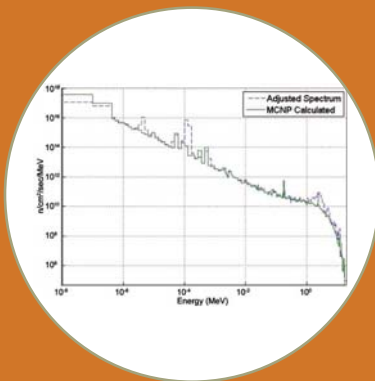
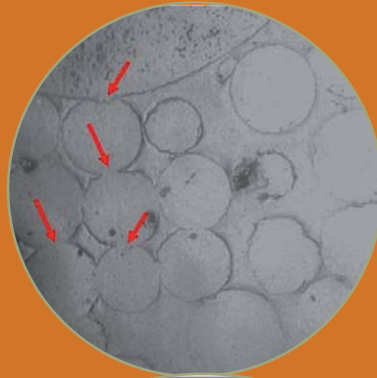
The Editorial Committee acknowledges the contribution of the groups and authors in providing interesting articles highlighting the achievements. The Editorial Committee is grateful to, Dr. A. K. Bhaduri, Director, IGCAR, for his encouragement, guidance and support towards bringing out the publication in its present form.

We look forward to your comments and suggestions, for further enhancement in the next issue.

M. Sai Baba

(M Sai Baba)

Chairman, Editorial Committee
Director, Resources Management Group



CHAPTER I

Fast Breeder Test Reactor

1.1 Highlights of 25th Irradiation Campaign

At the end of 24th irradiation campaign, the Mark-I fuel sub-assembly at 03/12 and two Mark-II fuel sub-assemblies at the locations 04/03 & 04/07 attained the target burn-up of 155 & 100 GWd/t respectively and were shifted to periphery for in-pile cooling. Four Mark-I fuel sub-assemblies (3 for replacement for burnt and one additional sub-assembly for reactivity) were loaded in the core. Fuel handling was carried out in two steps to keep core reactivity estimation uncertainty within the limits and also to measure the worth of MOX fuel sub-assembly in the 5th ring.

The core had 53 fuel sub-assemblies (39 Mark-I + 5 Mark-II + 8 MOX + one IFZ100 at central location). The reactor power when the peak rated 1st ring (01/02) Mark-I fuel sub-assembly operates at 400 W/cm is 27.3 MWt. Total duration of the irradiation campaign was expected to be 75 days at 27.3 MWt. The campaign ends when the experimental sub-assembly at “00/00” location will attain the burn-up limit of 97.3 GWd/t.

Following are the objectives of the campaign:

- Continuing irradiation of the sodium bonded metallic fuel pins at two locations in the first ring
- Continuing long term irradiation of structural materials in the fifth ring
- Irradiation of grid plate material for reassessing its residual ductility

The 25th irradiation campaign was started on July 01, 2016. Reactor attained criticality when control rod-E was at 287mm with other rods banked at 233.1 mm. The deviation during criticality was observed to be -22 pcm which is well within the technical specification limit of ± 150 pcm. Calibration of control rods and temperature co-efficient measurement were carried out and the total control rod worth was found to be 9127 pcm. The shutdown margin for the 25th campaign was found to be 5691 pcm. The average value of isothermal temperature and power coefficients of reactivity were found to be -4.26 pcm/°C and -7.22 pcm/MWt respectively. Off-line calibration of steam generator leak detection system (SGLDS) was carried out at sodium temperature of 400°C. Steam generator was valved in and reactor power was gradually increased in steps to 21 MWt. Turbo generator was rolled and connected to grid, when the reactor was operating at 21 MWt. Reactor power was raised to target power of 27.3 MWt and alternator power was increased to 5.8 MWe. The campaign came to an end temporarily after the steam generator water leak in to sodium incident on October 18, 2016.

Table 1: 25th irradiation campaign process parameters

Process parameter	Value
Reactor power/turbo-generator power	27.3 MWt/ 5.75 MWe
Reactor inlet/outlet sodium temperature	380°C/480°C
Central sub-assembly outlet temperature	520°C
Primary flow	938 m ³ /h
Secondary loop flow	245 m ³ /h
SG inlet/outlet temperature	471°C/294°C
Feed water flow	42.5 m ³ /h
Feed water/steam temperature	190°C/440°C
Steam pressure	120 kg/cm ²
Cumulative operating time of reactor	53600 hours
Thermal energy produced	109712 GWd
Cumulative operating time of turbo-generator	2112 hours
Electrical energy produced	10.73 MU

On August 31, 2016, a leak was observed at the bend portion of the feed water line downstream to steam generator (Figure 1). Leaky portion was cut and a new piece was welded after shutting down the reactor. The weld was qualified by hydro testing at a pressure of 196 kg/cm² by running main boiler feed pump.

On July 2, 2016 at 14:22 hours, when control rod calibration was in progress at 25 kWt, control rod drive mechanism-F (CRDM-F) became inoperable. After confirmation, the reactor was shut down by manual SCRAM. Investigations revealed the deterioration of insulation between the pins of the circular connector plug in the power supply circuit of drive motor of CRDM-F. Plug and socket of a circular connector through which motor power supply of E & F mechanisms is fed was replaced. This problem resurfaced again on August 14, 2016 when the reactor was operating at 27.3 MWt. Voltage surges were generated during repeated inching operation of CRDM-F due to the time lag between the application of voltage to the motor and the build up of sufficient direct current voltage in the brake circuit. The time taken for direct current voltage build up of power supplies of CRDM-F & CRDM-C was more

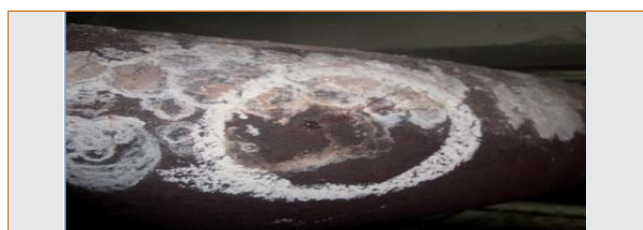


Fig. 1 The bend portion of the feed water line downstream to steam generator

than that of other CRDMs. Because of this, when the time duration between two inching operations is less, the motor gets operated with brake engaged (locked rotor). Measurements indicated that voltage surges peaking to more than 3 kV were generated during inching operation. The high voltage surge caused flashover across the pins in the connector, leading to failure of insulation and shorting. The incident was due to the deterioration of the characteristics of brake power supply unit of CRDM-F combined with consecutive inching operation done on CRDM.

On October 7, 2016, at 14:50:15 hours, “west loop hydrogen level high” alarm appeared and was persisting in the control room when reactor was operating at 27.3 MWt and turbo-generator connected to the grid generating 5.8 MWe. All the three SGLDS signals (sputter ion pump current which is a function of H₂ concentration in sodium at SG outlet) of west loop were showing increasing trend. At 14:51:55 hours, reactor underwent LOR on “steam generator leak”, as west SGLDS signals Fhr 621B and Fhr 621C crossed their LOR thresholds simultaneously viz. the absolute threshold and the rate of rise threshold respectively. The channel Fhr 621A signal also showed increasing trend. Following the LOR, West steam generator safe configuration took place on auto and nitrogen injection to steam generator tubes, as per design intent. Decay heat was removed with available east loop and subsequently by natural convection by opening steam generator trap doors. Both the electro chemical hydrogen meters (ECHM) did not show any increase in signal during the incident (Figure 2).

Hydrogen and nitrogen content in the expansion tank cover gas sample were analyzed and found to be 5 & 6 % respectively after two hours of reactor trip. Plugging temperature of secondary west loop sodium was measured to be 112°C after 2.5 hours. Thus, all the investigations ascertained the genuine leak in west steam generator. Helium leak test carried out at 5 bar pressure in tube side showed 272 ppm of helium on shell side, which confirmed the tube leak. SGna 600 B

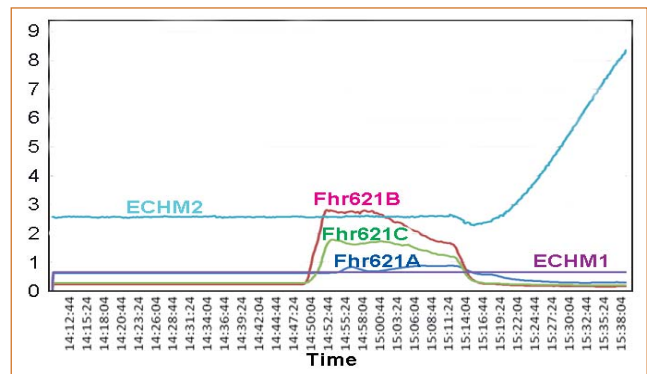


Fig. 2 Steam generator leak detection system data

was identified as the defective module by trace gas technique. At a pressure of 40 bar on the tube side, helium content of 1300 ppm was observed on the shell side when module SGna 600B tube side was pressurized with helium and module SGna 600A tube side was pressurized with argon. This test indicated that the steam generator module SGna 600B was leaky. The test was repeated with SGna 600A filled with helium and SGna 600B filled with argon and no increase in helium concentration was noticed on the shell side, assuring the leak in SGna 600B. At present the replacement of defective tube with a spare new one is in progress.

An estimation of the total duration of steam/water leak into sodium side based on transportation time, leak detection time and steam generator depressurization time was found to be around 6 minutes. Estimated quantity of water/steam leak in the sodium based on the measured hydrogen concentration in cover gas and in the dumped sodium was 492 grams.

Increase in west cover gas pressure was not observed during the period of water/steam leak into sodium side. As there was no increase in west steam generator sodium outlet temperature and tube outlet temperatures, it is concluded that there is no appreciable energy release due to sodium-water reaction during the period of water/steam leaking into sodium side.

I.2 Identification of Leaky Steam Generator Module and Qualification of Spare Steam Generator Module

FBTR steam generator (SG) modules are of *once through*, counter flow type with hot sodium entering the shell side from top and water entering the tube side from bottom. Each loop has two steam generator modules. Each module has seven water tubes. Out of the seven tubes, three tubes in each steam generator module were blanked to attain the system temperature closer to the design temperature with the current constraints on core size and reactor power. Any leak

of water/ steam from the tube side to the sodium in the shell side of the steam generator is detected by highly sensitive triplicated steam generator leak detection system (SGLDS) by detecting the presence of H₂. When reactor was operating at 27.3 MWt with turbo generator generating 5.8 MWe in the 25th irradiation campaign, the reactor underwent loss of reactivity due to high SGLDS signals, which indicated steam generator tube leak. To confirm the tube leak after reactor shutdown,

helium leak test was carried out by pressurizing the steam generator tube side with helium up to 5 bar and presence of helium was noticed in the steam generator shell, which confirmed the tube leak. As provision of localization of failed module is not available in the design, gas tracing technique was employed to identify the leaky module. In this method, two different gases namely helium and argon were injected at 40 bar in the tube side of either modules (Injected at the bottom of the steam generator with slight purge flow through top to prevent mixing of gases) and steam generator shell cover gas was sampled at regular intervals to check the presence of helium. When module SGNa 600 B tube side was pressurized with helium and module SGNa 600 A tube side was pressurised with argon, helium content in the steam generator shell was found raising with respect to time and pressure. Similarly, when SGNa 600 A tube side was pressurised with helium and SGNa 600 B filled with argon, no increase in helium concentration was noticed in the shell side, which confirmed SGNa 600 B as the leaky module.

For reconfirming the failure in SGNa 600B, water and steam header of SGNa 600 B were cut open and suitable leak tight plugs were provided. SGNa 600 B alone was pressurized with helium to 40 bar and steam generator shell cover gas was sampled periodically. Helium concentration was found to be 1012 ppm at the end of six hours. The same test was repeated for checking the integrity of SGNa 600A also and was found to be healthy.

Work is in progress to replace the defective steam generator module (SGNa 600B) with a qualified spare. After removing the failed module from the system, it will be erected on a tilting structure. In-situ cleaning work will be carried out for removing the residual sodium in the shell side as per the standard procedure, after identifying the leak location in the tube. Once the location is identified, shell side of steam generator near the leak location will be cut open for carrying out metallographic examination of the failed tube to find out the root cause for failure. In case damage is minor and adjacent tubes are not affected, possibility of reusing will be explored after consulting with the designer.

The spare steam generator module (2.25Cr-1Mo steel) is stored in the steam generator building of FBTR on an anchored tilting type support structure. The shell outer surface of the module has been painted with high temperature aluminum paint and wrapped in black polythene sheet. The shell side and the tube side openings were blanked and kept in inert atmosphere with helium under positive pressure. In order to use spare module for replacing the failed module SGNa 600B in the secondary sodium west loop of FBTR, three tubes need to be cut and blanked, similar to the modification done in the existing modules in the system. Also, the bayonet

type locked orifice assemblies provided at the inlet of the tubes in the feed water header have to be replaced with welded orifice assemblies. Before undertaking the modification, the module was subjected to helium leak testing to check its integrity and found to be alright.

The blanking of the three alternate tubes was done after confirming that the tube layout arrangement in the spare module is as per the drawing. This confirmation was required since there were mismatches among the actual arrangement of tubes in the existing steam generator modules with respect to the layout in the drawing which got revealed during blanking of tubes of the modules in the system. For this purpose, radiography of the steam and water headers at the portion where the tubes emerge out the shell was done at 45° angle. Interpretation and cross checking of the radiographic testing images with the layout drawing indicated that the order of arrangement of the seven tubes in water/steam headers is as per the drawing. This was further confirmed by cutting one tube at the steam header and pouring hot de-mineralised water through it. The tubes at the water header were scanned by using an infrared camera, which indicated high temperature in the corresponding tube. After cutting the tube at the bottom, correspondence was reconfirmed by pouring de-mineralised water from the top end and checking for its emergence from the bottom end. Same way, reconfirmation of the other two tubes was done. After blanking of the three tubes on both ends and modification of orifice assemblies, radiographic testing of the tube side and header side blanked weld joints was done before carrying out post weld heat treatment. After post weld heat treatment, liquid penetrant inspection and radiographic testing were carried out for these weld joints again. For the orifice assemblies which were assembled to the tube ends by fillet weld, liquid penetrant inspection was done. The bosses in the feed water header were cut for the orifice assembly modification work. The weld joints were qualified by root and final liquid penetrant inspection. These joints were subsequently ultrasonically tested. The modified spare module was subjected to helium leak testing under vacuum once again and no helium leak was observed from the weld joints. Now the spare steam generator module has been qualified for replacing the defective steam generator (Figure 1).

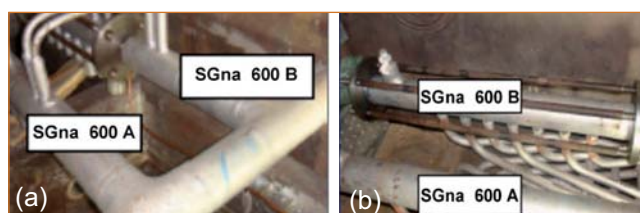


Fig. 1 Set-up for carrying out helium leak test of SGNa 600 B after cutting (a) blanking the water inlet header and (b) steam outlet header

I.3 Evaluation of Mark-1 Fuel Performance at 400 W/cm Peak Linear Heat Rating and 400°C Reactor Inlet Temperature

The peak burn-up attained by the Mark-1 carbide fuel of FBTR was as high as 165 GWd/t. This could be achieved due to moderate linear heat rating, lower inlet temperature of operation and also based on the constant feedback from the post irradiation examination carried out at various burn-up intervals. In order to operate FBTR nearer to its target ratings, it is desired to raise the operating parameters such as inlet temperature and the peak linear heat rating of the Mark-1 fuel to 400°C and 400 W/cm respectively. This warrants the estimation of allowable burn-up to be prescribed. For determining the burn-up limit, it is required to know the various life limiting (burn-up) phenomena for the FBTR Mark-1 fuel. These aspects have been analysed in a detailed way and the burn-up limit is determined.

The burn-up limit of the fuel sub-assembly is restricted from the factors like wrapper dilation, wrapper residual ductility, fission gas pressure and fuel clad mechanical interaction (FCMI) induced stress on pin, clad strains, clad residual ductility, clad cumulative damage fraction (CDF) and sub-assembly flow reduction.

For this estimation, the overall pin performance is arrived at after integrating the results at five axial locations. The fission gas pressure in the pin increases with burn-up and is a function of local burn-up and temperature distribution of various pellets in the pin. A typical fission gas release from Mark-1 carbide fuel and the corresponding pin pressure as a function of burn-up is shown in Figure 1.

The results of the analysis with respect to various burn-up limits are listed in Table 1. It can be observed that the burn-up limit is more dictated by the creep damage of the clad under hotspot conditions.

Creep damage of the clad arises due to fission gas pressure and FCMI in excess of fission gas pressure estimated. The lowest burn-up limit, 85 GWd/t, comes from CDF consideration under hotspot temperature conditions. However, the actual burn-up potential of the fuel is likely to be much higher at nominal conditions as evidenced from the analysis. It is clear that the influence of temperature on the

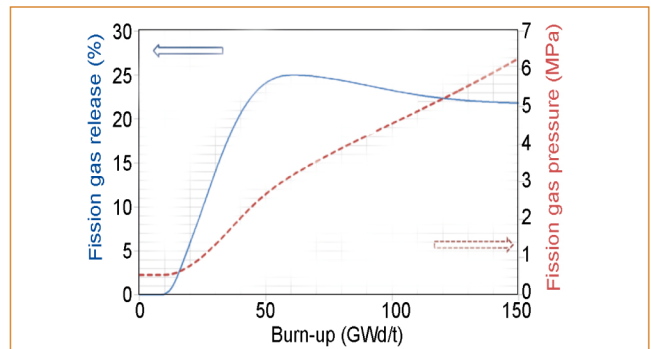


Fig. 1 Average fission gas release and pin pressure

creep rupture life of the clad (CDF limit) is quite substantial. The possible burn-up for the normal operation under nominal temperature condition from CDF (0.25) consideration is far greater than 150 GWd/t. Hence, under nominal conditions, it is possible that Mark-1 fuel has the potential to achieve burn-up beyond 85 GWd/t.

The next burn-up limit comes at 103 GWd/t. This limit is dictated by the wrapper dilation, where sufficient ductility would still be available. Corresponding to this burn-up level, various performance parameters were computed and listed in Table 2. From the table, it is observed that the maximum FCMI peaks out at 70 GWd/t burn-up and subsequently seems to relax. Similar is the case with the hoop stress on the clad which peaks out at 70 GWd/t and relaxes thereafter. The ductility limits mentioned in the Table 1 are arrived at by extrapolating the ductility as a function of void swelling from the post-irradiation examination data.

To increase the FBTR power, core is constantly expanded towards its maximum level. The minimum burn-up limit of 85 GWd/t is arrived at in a conservative manner for a Mark-1 fuel pin operating at constant linear heat rating of 400 W/cm and 400°C right from beginning-of-life based on clad hotspot temperatures. This is important in establishing the safety margin. However, It is seen that the Mark-1 fuel pin has the capability to achieve a burn-up of 103 GWd/t based on nominal clad temperature and wrapper dilation considerations.

Table 1: Burn-up limit on Mark -1 fuel from different parameters at 400 W/cm linear heat rating and 400°C inlet temperature

Parameter	Allowable burn-up value, GWd/t
Wrapper dilation	103
Wrapper residual ductility	141
Fission gas pressure and FCMI stress	Far greater than 150
Clad residual ductility	140
CDF – hotspot	85
CDF – nominal	Far greater than 150

Table 2: Performance parameters at the target burn-up of 103 GWd/t

Parameter	Peak value
Fission gas release	23.3% at 103 GWd/t
Fission gas pressure	4.7 MPa
Fuel clad mechanical interaction	15 MPa (peaks at 70 GWd/t burn-up and at 240 mm from core bottom)
Hoop stress (primary + secondary)	98 MPa (peaks at 70 GWd/t burn-up)
Clad inelastic strain	2.8% at core mid
Clad volumetric swelling	4.5% at core mid
Flow reduction	2.1%

I.4 Beginning-of-life Performance Evaluation of MOX Sphere-pac Fuel Pins

Sol-gel process is being considered as an alternate to the conventional “powder-pellet” route for the fabrication of ceramic nuclear fuels. It minimizes the problems of radioactive aerosols and is amenable for automated fuel fabrication involving the highly radiotoxic element, plutonium. In this method, fuel in the form of sintered microspheres is vibro-compacted in the cladding to the required smear density.

Two sphere-pac fuel pins and one reference pellet pin with a composition of $(U_{0.56}Pu_{0.44})O_2$ were irradiated in FBTR in an experimental sub-assembly. MOX fuel microspheres of 780 μm size, prepared at BARC and natural UO_2 microspheres of 115 μm size, prepared at IGCAR were used in the ratio $\sim 3:1$ to fabricate fuel pins of $\sim 78\%$ smear density. The capsule containing the sphere-pac and pellet pins were irradiated at a linear heat rating of 205 W/cm for the first 200 hours followed by 260 W/cm for the next 100 hours. The objective of this test irradiation was to assess the beginning-of-life (BOL) irradiation performance of the sphere-pac fuel pins.

Post irradiation examination (PIE) of sphere-pac fuel pins was carried out in the hot cells of Radio Metallurgy Laboratory after attaining a burn-up of 1626 MWd/t. Neutron radiography, gamma scanning and metallography were employed to evaluate the irradiated fuel behavior such as restructuring of the fuel column, axial distribution of fission products and change in fuel stack length.

The pre-irradiation neutron radiographs (NR) of the sphere-pac pin indicated uniform filling of microspheres. Figure 1 shows the NR of irradiated sphere-pac fuel pin. NR of the irradiated sphere-pac pins did not indicate any gross changes like restructuring or formation of central hole in the sphere-pac fuel pins. The individual microspheres could be discerned clearly in the neutron radiographs after processing the raw image. Gamma scanning indicated marginal reduction in the count rate at the peak power location in both the sphere-pac fuel pins. Stack lengths measured from the radiographs and gamma scanning did not indicate any significant change from the pre-irradiation values in both sphere-pac and reference pellet pins.

Metallography of the fuel pin cross-sections was carried out to confirm the observations from non-destructive tests regarding the re-structuring behaviour. The fuel column in the pins was filled with liquid epoxy resin by a newly developed vacuum impregnation technique for immobilizing the microspheres/pellets before cutting

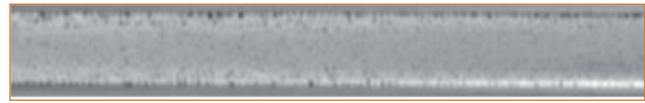


Fig. 1 Raw neutron radiograph image of as fabricated sphere-pac fuel pin

the fuel column. After impregnation the specimens were extracted from three different axial locations and subjected to sequential grinding and polishing to enable metallographic examination.

Figure 2a shows the photomicrograph of the sphere-pac fuel pin cross-section at the peak power location. It indicates that no major restructuring has occurred, confirming the observations from NR. However, necking and coalescence of microspheres at the central region indicated initiation of restructuring, as shown in Figure 2b.

Within the central region of the fuel pin cross-section, necking has initiated in regions where-ever packing density of microspheres is higher. Porosities could be observed in the larger MOX microspheres, which would have formed by the merger of adjoining microspheres through necking and coalescence accommodating gaps during the process. The porosities were found to have migrated to the MOX microspheres located in the centre of the fuel cross-section, since local temperatures are higher at that location due to higher fission density as compared to smaller UO_2 microspheres.

Pellet cross-section also did not indicate any evidence of densification or columnar grain growth formation. Absence of any significant restructuring in sphere-pac and pellet fuel pins could be due to the lower linear heat rating undergone by them. PIE of the sphere-pac and MOX fuel pins has thus given valuable feedback on the beginning-of-life behavior of the sphere-pac fuel pins irradiated in FBTR.

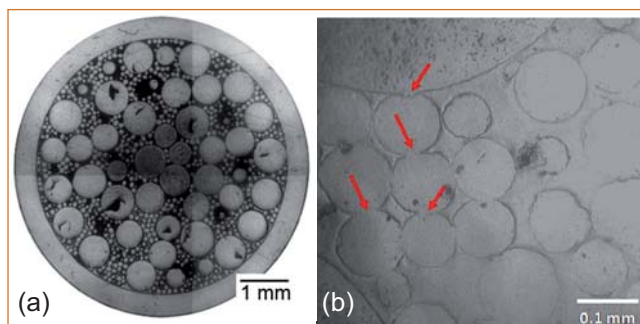


Fig. 2 Photomicrographs of (a) sphere-pac fuel pin section and (b) necking of microspheres

I.5 Design of SCRAM Logic for Reactor Protection System of FBTR

FBTR is a 40 MWt (13 MWe) loop type, sodium cooled fast reactor that uses mixed uranium and plutonium carbide fuel. In order to protect the reactor from any postulated events, FBTR is provided with a reactor protection system. Reactor protection system receives trip signals to process and initiate control rod accelerated movement (SCRAM) parameters from neutron flux monitoring (power, period and reactivity), core temperature monitoring, coolant flow monitoring and delayed neutron detection systems.

Reactor protection system consists of signal processing electronics (for SCRAM parameters), SCRAM logic and control rod drive mechanism. Six control rods with B₄C (90% enriched in ¹⁰B) material, which is an excellent neutron absorber is used for both power regulation and shutdown functions. Stand-alone fine impulse test system for online testing of SCRAM logic for diagnosing and annunciating safe and un-safe faults in the system is provided.

Each control rod is held by an electromagnetic coil in control rod drive mechanism. In case of occurrence of any postulated event, it is required to drop all the six control rods into the core by simultaneously de-energizing all the six electromagnetic coils and allowing all the six control rods to drop under gravity into the reactor core, which is termed as SCRAM.

The existing SCRAM logic for reactor protection system of FBTR was commissioned in early eighties and is operational as on today. However, due to the non availability of various spare parts and in order to overcome various maintenance issues with this ageing system, it has been decided to refurbish the existing system with a new hardwired system.

SCRAM logic receives signal trips, good operation trip and auto inhibition signals from the signal processing electronics as logic type of signals. It also receives core temperature parameters from central data processing system as potential free contact type signals. Manual inhibition signals for delayed neutron detector SCRAM parameters and manual SCRAM are received from the control room as potential free contact type signals. SCRAM logic performs 2/3 voting logic for triplicated parameters and 1/1 logic for single channel parameters. If all the SCRAM parameters are in healthy state, it energizes the electromagnetic coils of control rod drive mechanism by passing the required current. A SCRAM signal persisting for more than 40 ms duration is treated

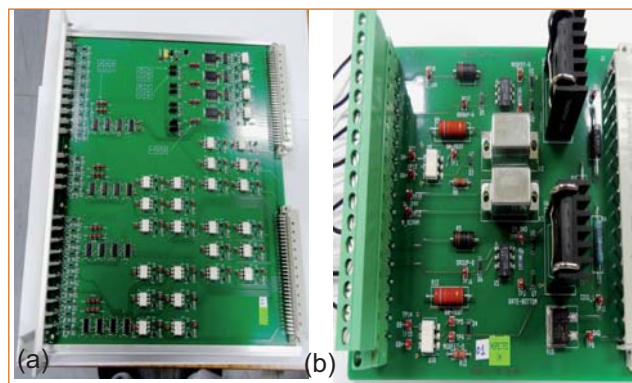


Fig. 1 Prototype hardware modules of (a) 2/3 logic and (b) electromagnetic coil board

as genuine signal and the safety action is latched to ensure that electromagnetic coils are de-energized to get control rods dropped into the core.

To make the new system highly reliable and easily maintainable, the operating experience of the existing SCRAM logic system was taken into account for the new design. The following are the salient features of the new SCRAM logic system:

- For better reliability, segregation between safety critical versus non-safety critical functionality was carried out.
- To enhance the reliability of the overall system and minimize physical wiring across the hardware modules, a custom backplane methodology was adopted.
- Modular design concept was followed for ease in maintenance.
- Enhanced indications for critical signals were provided for ease of troubleshooting during the planned maintenance activities.
- Better electromagnetic compatibility was achieved by using logic devices with high noise margin and quiet operation as compared to other logic families.
- Augmenting of these logic devices from multiple manufacturers with pin compatibility for easy replacement.
- Non-safety critical functionality and heat dissipating items were moved out of the 19" sub-rack, which will be housing safety critical hardware modules.

Prototype fabrication of some of the critical hardware modules was carried out. Figures 1a and 1b show the photographs of the prototype hardware modules.

I.6 Commissioning of Process Disturbance Analyzer for FBTR

In FBTR, for the analysis of incidents like fuel clad failure, fast variation in important signals from the reactor is to be recorded. The present system is inadequate in handling the volume of this data. This has necessitated the development of a standalone process disturbance analyzer (PDA) system, to monitor 58 numbers of important plant signals with a scanning interval of 100 ms continuously. The architecture of three tier based system and a trend view is shown in Figure 1a and 1b. It consists of an embedded system from ADLINK and an UBUNTU based data server connected to the CDPS LAN, which is not a part of campus network for security reasons. All PCs in CDPS are in intranet with client mode.

The analog signals, including signals from neutronic system, fuel sub-assembly temperature, primary and secondary flow, IHX inlet and outlet temperatures, feed water flow, steam temperature etc. are connected to the system through signal conditioners. The embedded system is based on intel Core 2 duo@2.2 GHz processor with 4 GB memory.

The embedded system, with linux kernel, was programmed to scan the analog signals in every 100 milli second interval and send the data packet every second through Ethernet. Each data packet consists of 10 samples of each signal with time. An UBUNTU based server receives the data, does engineering unit conversion and stores them in MYSQL data base. A Web based GUI was developed using JSP, which can be used by authorized user on the intranet of CDPS.

The features of the PDA system are

- Display instantaneously the values of all the fifty eight signals on demand with print facility



Fig. 2 Commissioned system process disturbance analyzer

- To present the history of maximum of ten numbers of selected signals, for one hour interval, in table form
- Graphical trend of four signals can be viewed with provision for printing and downloading in PDF form
- Dumping of group of signals for a period of half an hour in Excel format on demand
- At any instant of time the system will hold the history data of all the signals at 100 ms interval for the previous 5 days.

The system as shown in Figure 2, has been commissioned and is working satisfactorily. The system being browser based does not require any client application to be installed on the GUI system. The GUI application runs on Google chrome or Firefox. The system has provision for future addition of signals.

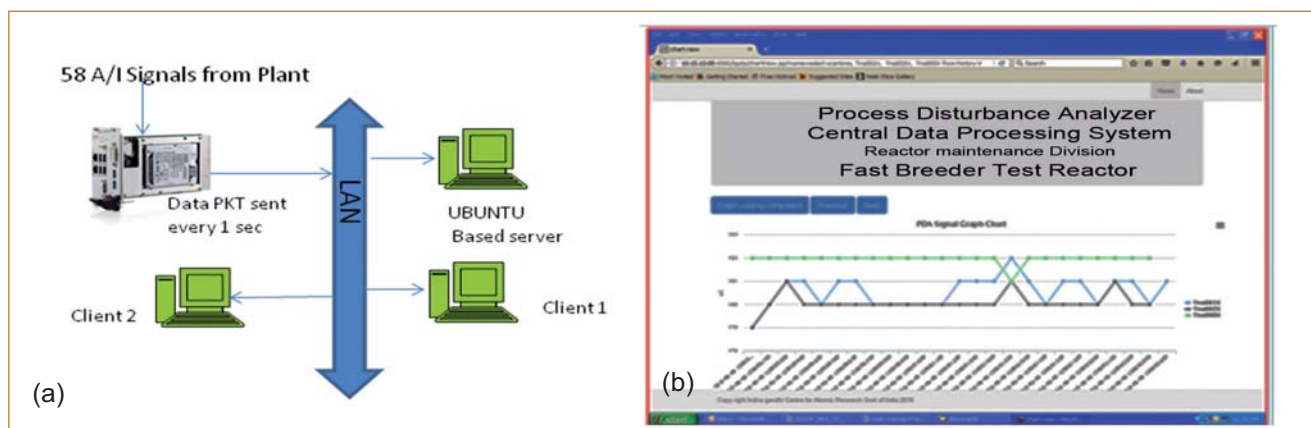


Fig. 1 (a) Architecture of three tier based system and (b) a trend view of the system

I.7 Performance Evaluation of Tin Oxide Based Sensor for Monitoring Trace Levels of H₂ in Argon Cover Gas Plenum

A compact tin oxide sensor was developed in order to monitor trace levels of hydrogen in argon cover gas over sodium systems. This sensor works on the principle of change in surface conductivity on interaction with hydrogen and the relative change directly provides the concentration of hydrogen. This sensor was integrated at the downstream of the thermal conductivity detector (TCD) based sensor system. Electronic modules for sensor signal output measurement and control-cum-measurement of sensor temperature were designed and developed in-house. The heater control circuit ensures the temperature to be maintained at 623 K across the heater without deploying a separate temperature sensor. The temperature accuracy was found to be ± 0.25 K. The mean background hydrogen concentration in the argon cover gas was monitored for about six months and it was found to be less than 1 ppm. The minimum detection (3σ) and quantification (10σ) limit shown by SnO₂ sensor towards H₂ were 1 and 9 ppm respectively. The photograph of the installed sensor in FBTR is shown in Figure 1.

Performance of the sensor system by hydrogen injections in the argon cover gas over sodium during shutdown condition of the reactor (sodium temperature 453 K) was evaluated.

Calibration experiments were conducted by admitting 10, 25, 50 and 100 ppm of H₂ in the argon cover gas of FBTR. Figure 2 shows the typical response behavior towards 10 ppm of H₂ in argon cover gas. It took about 7 minutes from the time of admitting hydrogen to the cover gas, to realize a change in the sensor output. To

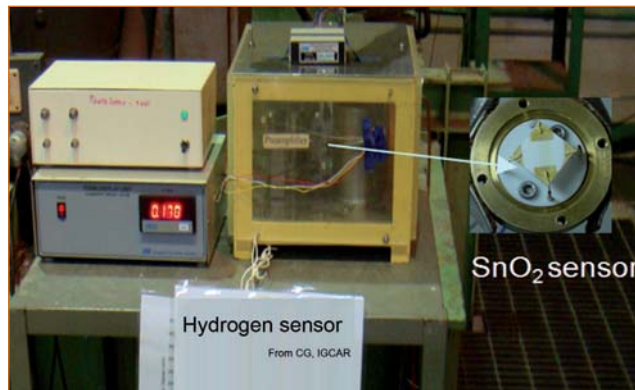


Fig. 1 Photograph showing the installation of SnO₂ sensor at the thermal conductivity detector outlet in the secondary sodium circuit (west) of FBTR

check the retrace behavior of the sensor, pure argon was introduced directly into the sensor chamber by bypassing hydrogen containing argon line from thermal conductivity detector. It took about 20 minutes to attain 90% recovery, which corresponded to a baseline hydrogen concentration of less than 1 ppm. The present experimental studies and the results demonstrate the usefulness of tin oxide based sensor for monitoring low levels of hydrogen in argon cover gas over sodium system when sodium temperature is maintained at 453 K (shutdown conditions). The sensor responded to down to 10 ppm level of hydrogen in argon and is possible to detect up to 100 ppm reliably. These studies show when the tin oxide based sensor is used in conjunction with the thermal conductivity detector, the lower detection limit for hydrogen in argon cover gas over sodium system can be about 10 ppm.

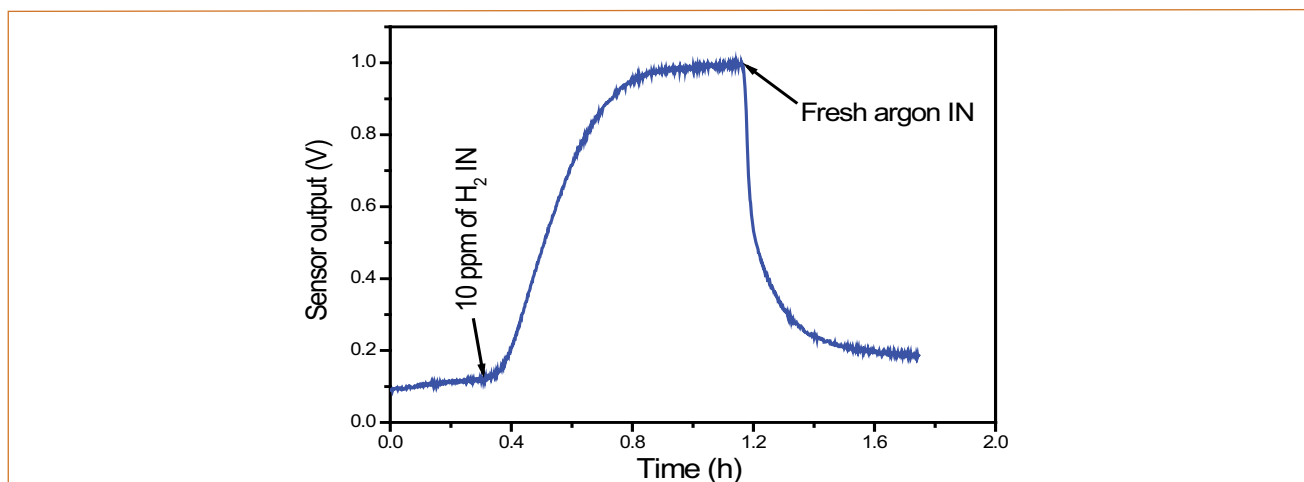


Fig. 2 Response shown by SnO₂ sensor during the introduction of 10 ppm of H₂ in argon cover gas of FBTR

I.8 Characterization of Neutron Spectrum of KAMINI Reactor

Neutron spectrum characterization of a neutron source is essential to evaluate nuclear reactions involving the irradiation of materials. The neutron energy spectrum can be characterized by studying the nuclear reaction rates of identically irradiated activation foils. These reaction rates with their threshold energies are generally unfolded using various codes like SAND-II, SANDBP and SPECTRA. KAMINI is a 30 kW, ²³³U fuelled, light water moderated and cooled research reactor with a neutron flux of 10¹² n/cm²/s at the core centre. A pneumatically operated fast sample transfer system (PFTS) in KAMINI is used for irradiation of samples. A brief report on the evaluation of the neutron spectrum at PFTS of KAMINI reactor is presented here. All the activation samples viz., Au (0.1 mm), Ti (0.125 mm), Ni (0.1 mm), In (0.125 mm), Mo (0.1 mm), Fe (0.125 mm), Co (0.125 mm) and Al (0.03 mm) foils and Y₂O₃ powder of purity > 99.9 % sealed in polythene bags that were in turn placed in polypropylene containers were irradiated in PFTS. After allowing them to cool sufficiently, they were assayed using HPGe detector. The reaction rates and saturated activities were determined for different nuclear reactions of the irradiated activation samples using the equation,

$$\text{Reaction Rate } (\sigma\phi) = \frac{\text{cps}}{a_{\gamma} * \epsilon * SDC * N}$$

where, *cps*, *a_γ*, *ε*, *S*, *D*, *C* and *N* are net count rate (counts/s), gamma-ray abundance, absolute detection efficiency, saturation factor, decay factor, decay during counting correction factor and number of target atoms respectively. The reaction rates obtained were

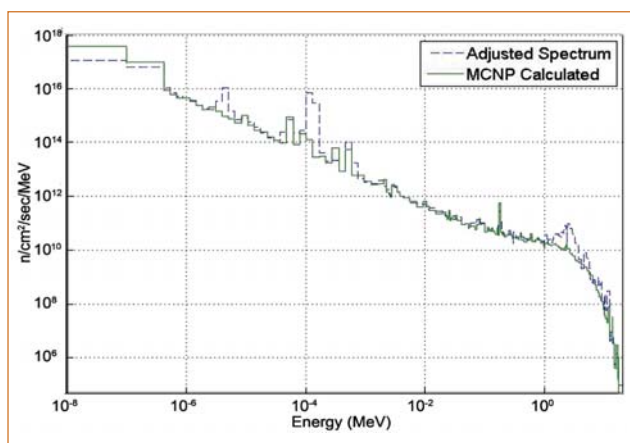


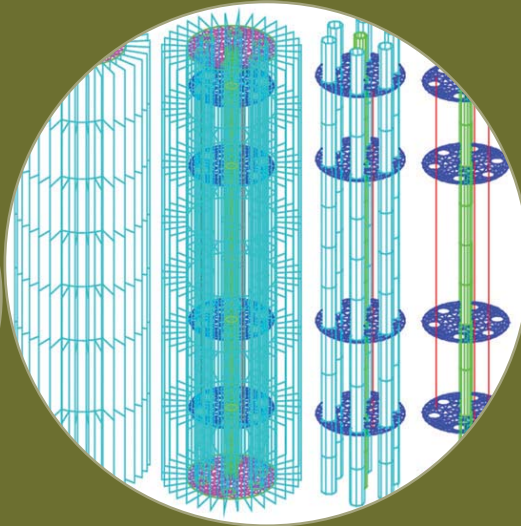
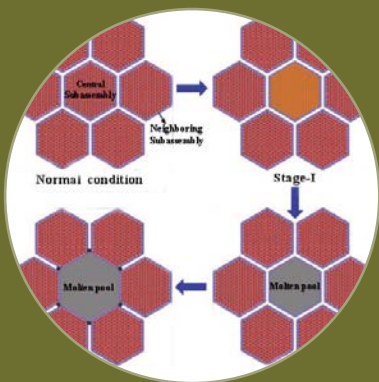
Fig. 1 Neutron spectrum at pneumatically operated fast sample transfer system of KAMINI reactor

compared with the adjusted and guess spectra as shown in Table 1. The guess spectrum calculation presented in this work was carried out using Monte Carlo neutral particle (MCNP) code for the core configuration. Acceptable solution was arrived by using minimization of constraint function. The spectrum unfolding was based on least square minimization approach. The adjustment procedure makes use of multi-parametric function minimization algorithm based on steepest descent method “*fminunc of octave*”. The adjusted and MCNP calculated spectra for the PFTS position of KAMINI reactor are shown in Figure 1.

Neutron spectrum has been characterized using foil irradiation method. Estimated spectrum was arrived using theoretical model of the reactor with Monte Carlo neutral particle. The deviations associated with the reaction rates were well within the experimental tolerances.

Table 1: Relevant data and neutron activation characteristics of the activation samples

Activation reaction	Threshold energy (MeV)	Measured gamma energy (keV)	Measured reaction rate	Deviation from measured reaction rates	
				MCNP spectrum (%)	Adjusted spectrum (%)
²⁷ Al(n,p) ²⁷ Mg	4.4	843.8	4.7 x 10 ⁻¹⁶	-50.6806	4.2760
⁴⁸ Ti(n,p) ⁴⁸ Sc	7.6	1037.5	4.82 x 10 ⁻¹⁷	-61.6144	-3.5190
⁵⁴ Fe(n,p) ⁵⁴ Mn	3.1	834.8	1.37 x 10 ⁻¹⁴	-69.9747	-8.6656
⁵⁸ Fe(n,γ) ⁵⁸ Fe	Thermal	1099.2	3.33 x 10 ⁻¹⁴	89.9633	1.8023
⁵⁹ Co(n,γ) ⁵⁹ Co	Thermal	1332.5	1.53 x 10 ⁻¹¹	-92.9543	-3.0522
⁵⁸ Ni(n,p) ⁵⁸ Co	2.8	810.8	1.68 x 10 ⁻¹⁴	-67.8614	0.7529
⁹⁸ Mo(n,γ) ⁹⁸ Mo	Thermal	739.5	1.23 x 10 ⁻¹³	-37.2020	-0.0465
¹¹⁵ In(n,n') ^{115m} In	1.2	336.3	3.41 x 10 ⁻¹⁴	-72.7174	3.1989
¹⁹⁷ Au(n,γ) ¹⁹⁷ Au	Thermal	411.8	7.12 x 10 ⁻¹¹	-81.8508	0.0732
⁸⁹ Y(n,2n) ⁸⁸ Y	11.6	1836.05	2.4 x 10 ⁻¹⁷	-18.1018	0.0996



CHAPTER II

Prototype Fast Breeder Reactor

II.1 Commissioning Status of PFBR

Prototype Fast Breeder Reactor (PFBR) is a 500 MWe (1250 MWt) sodium cooled pool type reactor using mixed oxide of uranium and plutonium as fuel (Figure 1). Activities related to commissioning of all the systems are in progress and preparation for preheating of primary and secondary systems are in an advanced stage. The major activities that have been completed during the year 2016 are as follows:

A committee consisting of experts from IGCAR and NPCIL reviewed the actions taken for integral leak rate test of reactor containment building and the feasibility to adopt suitable measures for further improvement of leak-tightness. After completion of micro-pressure grouting at observed leak paths, the Integrated Leak Rate Test (ILRT) of reactor containment building (RCB) was repeated and reduction in leak rate was achieved. Cold pool area of the reactor assembly was inspected and the surfaces were cleaned. Visual examination was carried out remotely in the annular inter-space between main vessel and safety vessel and the space was cleaned using a specially devised vacuum method (Figure 2).

Pressure hold test for reactor assembly was carried out, leak paths were identified and corrective actions were undertaken. Pressure run down test for inflatable seals in large and small rotatable plugs was completed to check their leak-tightness. Two numbers of extended electrode leak detector (EELD) in safety vessel-main vessel inter-space were mounted in position. Insertability of startup neutron detector handling mechanism (SNDHM) in central canal plug was ensured by physical insertion of SNDHM.



Fig. 1 Overall view of PFBR

In fuel handling system, three uninterrupted cycles of operations of handling the sub-assemblies from in-vessel transfer port (IVTP) to ex-vessel transfer port (EVTP) and vice versa were done from handling control room (HCR). Two cycles of bowed sub-assembly handling movement, viz. one from IVTP to an empty position in inner core and another from IVTP to an empty position in outer core and vice versa were completed. Subsequently, two cycles of normal sub-assembly handling from IVTP to EVTP and vice versa using inclined fuel transfer machine were completed. Top view of the reactor is shown in Figure 3. Towards commissioning the shutdown system, all three diverse safety rod drive mechanisms (DSRDM) were operated and frictional force was measured. Commissioning of DSRDM in air at room temperature was completed. Response time of electromagnet and drop time for all nine control safety rod drive



Fig. 2 Vacuum cleaning of cold pool zone of the main vessel

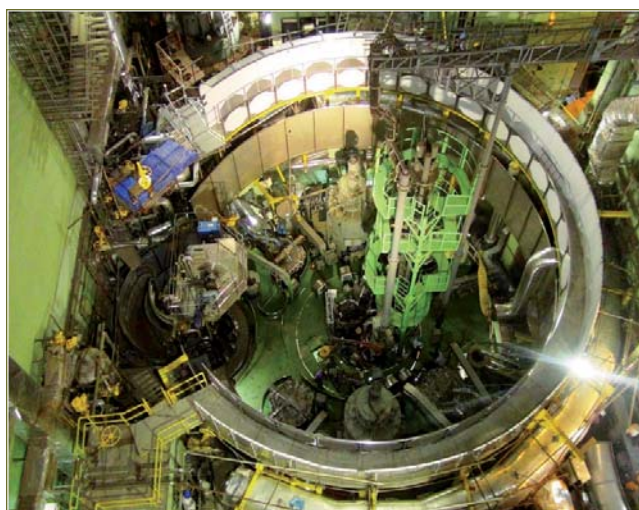


Fig. 3 Top view of the reactor

mechanisms (CSRDM) along with control rods were measured. Further, frictional force and motor characteristics data were generated for all nine CSRDMs. Core flow monitoring mechanism and thermowells above core top are shown in Figure 4.

Performance and pressure hold tests of primary sodium pump – intermediate heat exchanger (PI) flask (35 metre tall and 140 tonne weight) was completed (Figure 5). Handling of PI flask using RCB crane from storage location to pump location and lifting of one primary sodium pump from its position with the PI flask were demonstrated.

Manufacturing and inspection of multipurpose flask for handling in-vessel transfer port plug, Observation port plug and under sodium ultrasonic scanner was completed. As part of multi-purpose flask commissioning, load testing of connecting pieces of under sodium ultrasonic scanner, in-vessel transfer port shield plug and observation port plugs were completed.

Towards commencement of integrated pre-heating, segmental trial pre-heating of all sodium pipes in secondary system were completed. Further, augmentation of heaters in the secondary pipe segments for ensuring adequacy of heating based on the observations of steady state temperatures attained in different pipe segments, is in progress.

With respect to steam water system, pressure hold test (tube side) of all the four steam generators in SGB-2 was completed. In-service inspection vehicle of steam generators was qualified in the full scale mock-up facility and the vehicle was deployed in the steam generators. Pre-service inspection (PSI) data of 10% of tubes in seven steam generators and 100% of 547 tubes in eighth steam generator were collected.

In-service inspection vehicle (DISHA) for inspection of dissimilar weld of roof slab was developed for visual and ultrasonic examinations. The mock up facility for qualification of DISHA vehicle at room temperature and operating temperature is being established.

Emergency mode transfer (EMTR-1 and EMTR-2) panel was connected with various field equipment like 6.6 kV buses, motor control centre, power control centre, heater control centre, diesel generator, main control room panels and is ready for commissioning. Commissioning of digital distributed control system (DDCS) network was completed in control building, steam generator building, rad waste building, reactor containment building and fuel building.

The pre-commissioning works of sea water system have been completed. Condensate cooling water pump of 49,000 m³/h capacity was operated through condenser by charging the tunnel and fore-bay.



Fig. 4 Core flow monitoring mechanism and thermowells above core top

Integrated preheating of primary and secondary heat transport systems will be started after ensuring inertness of the systems with nitrogen. After filling sodium and completing the initial test programme, fuel loading will commence towards approaching first criticality.

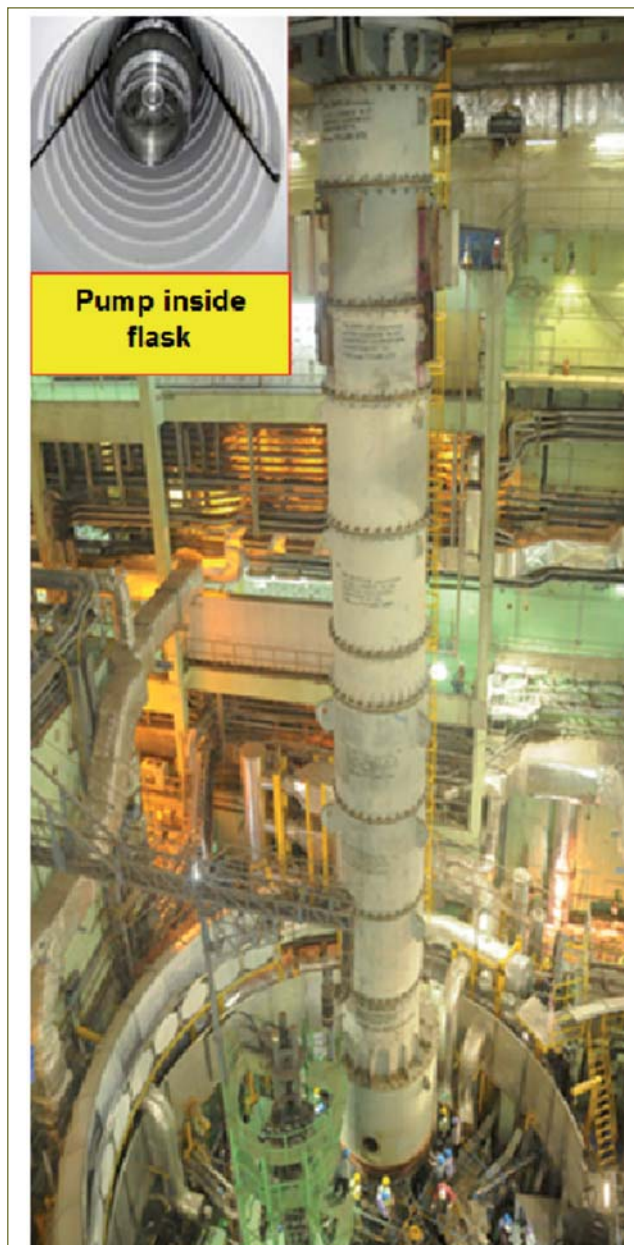


Fig. 5 Sodium pump inside the flask over the reactor top

II.2 Steam Generator Tube Inspection of PFBR at BHAVINI with Indigenously Developed PFBR Steam Generator Inspection System

Prototype Fast Breeder Reactor (PFBR) has eight steam generators (SG) in the two secondary loops. Each SG has 547 tubes running through about 23 metre from top header to the bottom header. Figure 1 shows the sketch of PFBR Steam Generator. The tubes have expansion bends in the middle to accommodate for the thermal expansion. The PFBR steam generator inspection system (PSGIS) has been designed and developed for inspection of steam generator tubes using remote field eddy current (RFEC) testing probe for full length of the tube. Tube inspection of the steam generators is important to qualify the steam generators for their safe operation. The PSGIS has been deployed for moving the probe inside the steam generator tubes at constant inspection speed. The device has seven modules for various functions. The device is designed in a modular way for easy assembly and dismantling. PSGIS is mounted on the steam generator manhole and various modules are operated to perform the tube inspection.

Following are the seven modules of PSGIS device:

1. Device deployment module (DDM)
2. Tube locator module (TLM)
3. Cable pusher module (CPM)
4. Cable dispenser module (CDM)
5. Comprehensive control system (CCM)
6. Inspection system module (ISM) containing
 - a) Eddy current probe and analysis system
 - b) Vision probe and analysis system (VPAS)
7. Cable take up module (CTM)

For the inspection, the prime requirement is to deploy the device from the manhole flange into the top header, then to orient the TLM to enable inspection of any of the 547 tubes and push the probe with cable to 23 metre down the steam generator till the bottom spigot weld and to obtain the remote field eddy current signals.

Figure 2 shows the CAD model of the PSGIS device along with the control units. The PSGIS device gets mounted on the steam generator manhole flange and fills the manhole completely. It also forms a tight rigid coupling with the steam generator in order to reach all the tubes with high precision referencing from the top manhole flange.

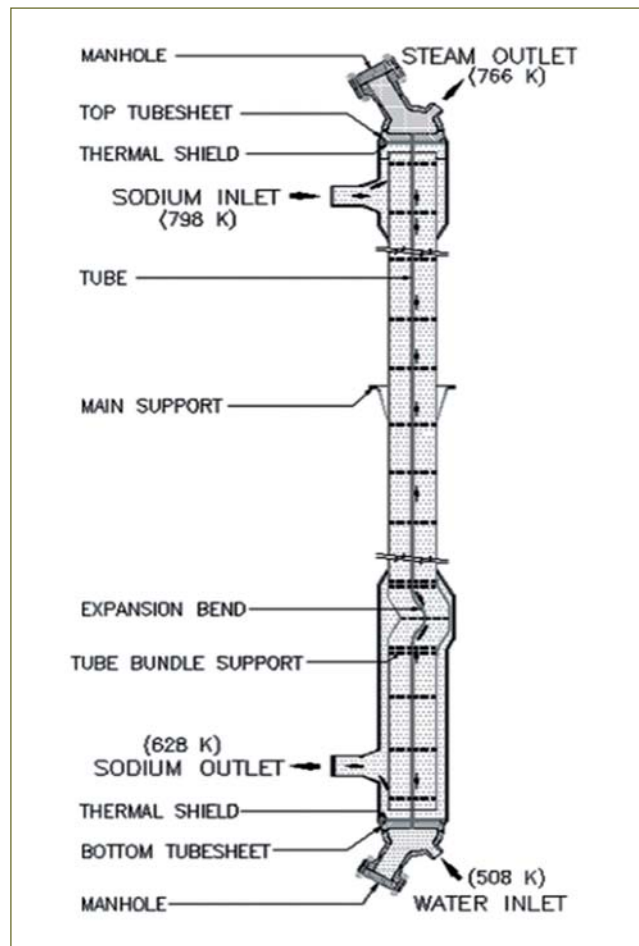


Fig. 1 PFBR steam generator

The deployment module, DDM is used to deploy the robotic arm, TLM into the top header of the Steam

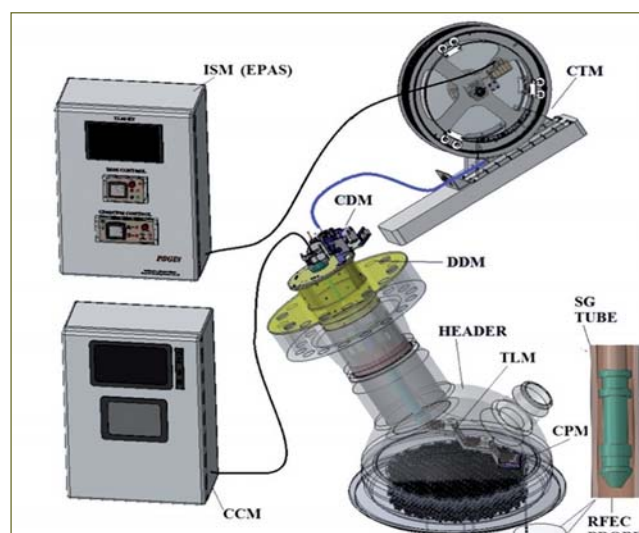


Fig. 2 Various modules in PSGIS device

Generator. This is a single axis servo drive system with top and bottom limit switches for the operational boundaries. The total stroke is about 450 mm.

TLM is a precision automatic robotic arm which works on the kinematic motion to reach all the 547 tubes of the steam generator. TLM uses AC servo actuator for precise arm motion.

The cable pusher module and cable dispenser module help to push the cable from the top header to the bottom making inspection probe travel 23 metre down. Synchronous servo motion is applied on 4 motors to achieve this pushing.

Remote field eddy current testing data acquiring and analysis system is used to acquire the tube inspection data from all the tubes.

The PSGIS device installed on a steam generator is shown in Figure 3.

The broad functions of PSGIS device involve the following:

- a) Device deployment operation
- b) Tube location operation
- c) Cable pushing operation

Tube location operation is an important one. The TLM module has two axis robotic arm operated by shoulder and elbow actuator which are AC Servo motors. The actuators have a gear reduction of 50% to have self locking and increased output torques.

The tube location operation will have the following four classifications:

- a) Homing operation
- b) Kinematic operation
- c) Parking operation
- d) Free jogging operation

The kinematic operation is briefly given here.

After the homing operation, the arms are ready for the kinematic move to reach any tube in the 547 tubes array. The tube number and row number in the tube array is translated to its actual tube coordinates as Cartesian values. An advanced inverse kinematic algorithm programmed into the system now converts this Cartesian coordinates to axis coordinates i.e. motor encoder counts. Synchronous operation of both shoulder and elbow motors is performed to move the cable pusher with the probe to the designated tube for inspection. The TLM is operated by the tube number and row number only. Since the start position and end target tube position vary in each operation, a pre-tabulated value on the motor encoder counts as a lookup table cannot be used. In such a case it demands in-numerous solution steps. Hence, the kinematic solution is solved by the motion

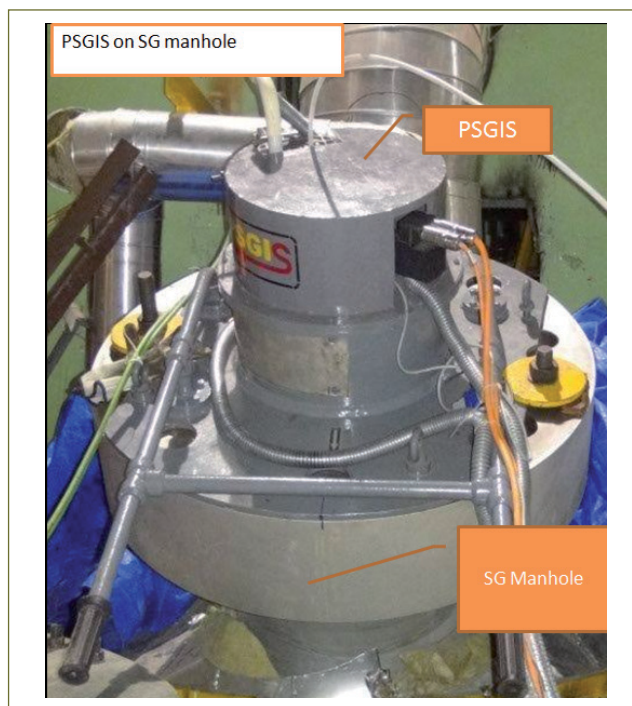


Fig. 3 PSGIS device installed on the steam generator

controller on the fly and it then provides the joint axis values in terms of encoder counts to run the actuators. The servo motors are run on velocity and position feedback controls using these counts. This typical two axes synchronous operation to reach inspection position or calibration point tube is called as kinematic operation. Calibration is performed prior to installing the PSGIS device in the manhole of any steam generator and after completion of baseline data collection in the specified tubes. Calibration was found to be intact during the baseline data generation. Off-line analysis of the stored baseline data revealed that none of the tubes contain indications in straight, expansion bend, and spigot weld regions with peak phase change values comparable and higher than 50% peak phase change of Flaw-D in the calibration tube. Figure 4 shows a baseline RFEC data of the steam generator tube.

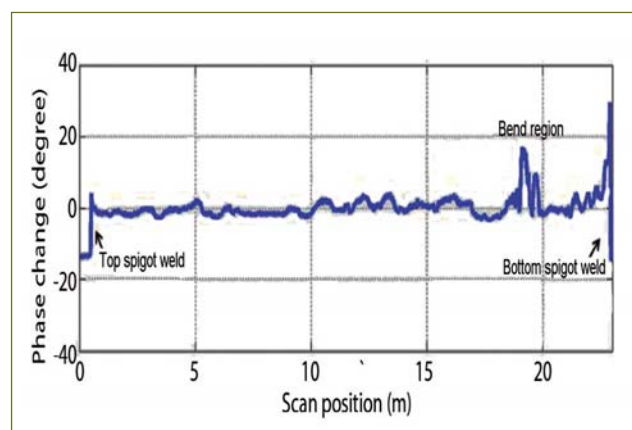


Fig. 4 Baseline RFEC data of a steam generator tube

II.3 Interaction of PFBR - AHX Tubes under Seismic Excitation: Experimental and Computational Investigations

Sodium - air heat exchanger transfers decay heat from safety grade decay heat removal (SGDHR) loop to air. It is a cross flow type heat exchanger with finned tubes. Sodium flows inside the tubes and air flows across the finned tubes. Structural integrity of air heat exchanger under all loading conditions is to be ensured for safe decay heat removal. Several experimental and theoretical studies have been carried out towards safety demonstration of safety grade decay heat removal system. Schematic of the air heat exchanger type – A is shown in Figure 1.

Computational and experimental investigations of seismic response behavior of the air heat exchanger of Prototype Fast Breeder Reactor (PFBR) were carried out for operating basis earthquake, safe shutdown earthquake (SSE) and beyond design basis earthquake conditions. For the numerical study, a finite element model consisting of air heat exchanger header and connecting tubes as shown in Figure 2 was developed using the general purpose finite element code CAST3M. Air heat exchanger is installed at an elevation of sixty metre on the top of steam generator building. Spectrum Compatible time histories were generated and time history analyses were performed for all the three earthquake loading conditions. To confirm the analyses findings, shake table experiments were performed using 100 ton multi axial shake table. The test set up consisted of five air heat exchanger tubes along with fins arranged in triangular pitch with tube to tube spacing same as in the reactor is shown in Figure 3.

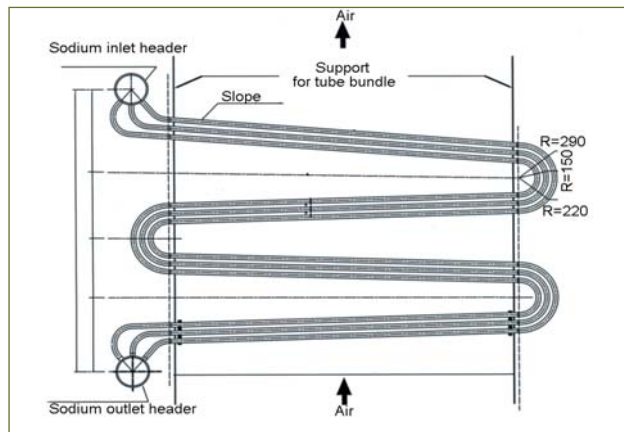


Fig. 1 Schematic sketch of air heat exchanger type –A

To simulate the effect of fluid inside the tubes under dynamic conditions, tubes were filled with water and pressurized to simulate operating conditions in the plant. Responses were captured using accelerometers, strain gauges and non contact type displacement sensors.

Tube to tube interactions at fin locations were observed under SSE and beyond SSE conditions as evidenced from the response spikes in accelerometer; strain gauge readings and from the relative displacements measured using non contact type displacement sensors. However, the structural integrity of tube bundle is demonstrated by repeating the experiments many times for SSE and beyond SSE conditions. From these experiments it is confirmed that the local impacts at the fin locations are not a concern for the structural integrity of air heat exchanger.

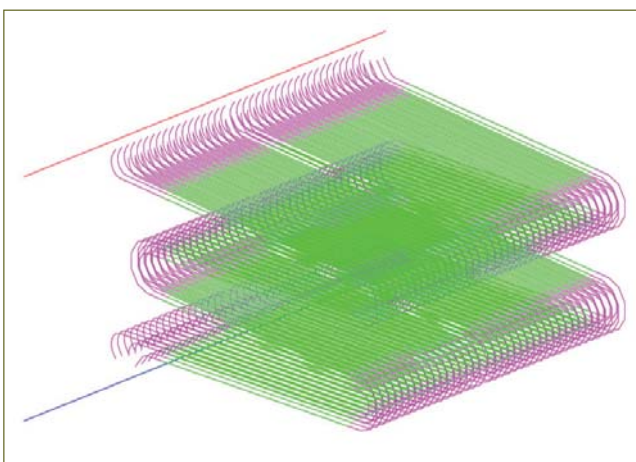


Fig. 2 Finite element model of air heat exchanger type-A



Fig. 3 Experimental test set up of air heat exchanger tubes mounted on shake table

II.4 Development of Improved Sealing Arrangement in Transfer Arm of PFBR

Based on the experience gained during performance testing of transfer arm in sodium, it was seen that after few cycles of testing, rotary lip seals provided between guide tube and oval shield plug are prone to leak both in static and dynamic conditions. Hence, design and development of improved sealing arrangement was taken up and a test assembly was designed and manufactured along with the sealing arrangement.

Additional sealing arrangement consists of seal housing, rubber bellows and universal joint is shown in Figure 1a. Bore of the seal housing consists of two raised faces called guides at both the ends and two O-rings located inside the grooves provided between the guides. Clearance, as in the full scale machine, is provided between seal housing and guide tube. Seal housing is made to rest on the oval shield plug through the universal joint. This joint will allow the seal housing to get positioned and oriented with the guide tube and hence remains concentric to it. This ensures a better leak tightness during both static and dynamic conditions. Bellows is provided between oval shield plug and guide tube and acts as a flexible leak tight barrier. Bellows is made up of neoprene rubber with nylon reinforcement. The seal housing was designed to permit assembly within the constraints existing in the present transfer arm.

In the test setup shown in Figure 1b, required operating conditions as in the reactor like cover gas pressure, speed of operation, rotation angle and total distance of travel can be simulated. Test setup consists of model oval shield plug and model guide tube. Their lateral dimensions are identical to the oval shield plug and guide tube but their heights are reduced. Rotational motion of the model guide tube is achieved through rotational drive mechanism and linear motion through screw nut mechanism. In the test setup, provisions are also made to test the seal arrangement for misaligned conditions of model guide tube with respect to model oval shield plug. Bottom end of the test setup is provided with argon chamber and a pressure transducer for monitoring the chamber pressure. Rotation, raising and lowering of the model guide tube is done through manual operation.

After manufacturing, test setup was assembled at Engineering Hall – III along with the sealing arrangement. During initial cycles of testing, with rotation of model guide tube, a high torque was observed. Modifications were carried out in the seal housing and model guide

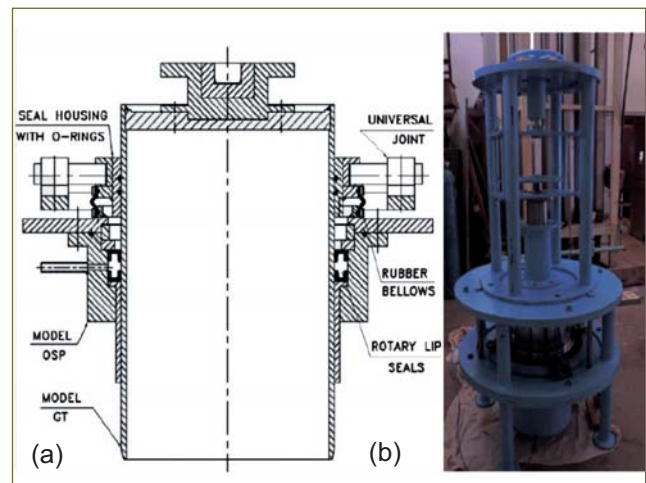


Fig. 1 (a) Schematic of sealing arrangement and (b) test setup assembly

tube and then testing was resumed. Further testing was found to be trouble free. A total of 50 cycles were carried out, viz. 30 cycles in aligned condition and 20 cycles in misaligned condition. In misaligned condition, 2 mm offset was maintained between the axes of model guide tube and model oval shield plug. For both aligned and misaligned conditions, torque values of 5 N-m required for raising and lowering. Measured torque values for rotation during aligned condition were between 45 to 60 N-m and for misaligned condition were between 55 to 75 N-m. Torque values for linear motion were well within the limits. During 2 mm misaligned condition testing, movements in the universal joints were measured through two dial gauges. During testing, system was pressurized for 38 to 40 mbar (g) for dynamic condition and around 130 mbar (g) for static conditions (the corresponding values in the reactor are 10 and 100 mbar(g) respectively). No pressure decay was observed during dynamic conditions. After every 10 cycles, 24 hour leak test was carried out at static condition. No pressure decay was observed when static leak test was carried out in aligned condition. However, 6 mbar reduction (for 24 hours) was observed when static leak test was carried out in misaligned condition which corresponds to leak rate of 0.192 std cc/min.

Over all performance of the additional sealing arrangement is satisfactory. In future, testing will also be carried out for stuffing box type seals instead of O-ring seals.

II.5 Development of Automatic Gamma - Neutron Monitoring System for PFBR Fuel Sub-assemblies at Interim Fuel Storage Building

Health physics surveillance during PFBR fuel pin assembling operation at interim fuel storage building (IFSB) mandates measurement of individual fuel sub-assemblies and fuel magazines at three different levels, i.e., top, middle and the bottom using teletector in order to find out the maximum gamma dose rate. Throughout the process, the health physicist involved in the operation must hold the telepole survey meter at a constant distance from the sub-assembly and simultaneously make a note of dose rate values displayed. This practice might lead to the occupational exposures and also may induce human errors. To make this process more simple and effortless, an automatic gamma neutron monitoring system is designed and developed to measure, store and visualize instantaneous gamma and neutron dose rate of PFBR fuel sub-assembly. The system uses ADVANTEC APAX series of modular add-on cards and APAX 6572 controller. The system uses Geiger Mueller (GM) detectors for gamma measurements and neutron monitor with pulse output facility for neutron dose rate measurements. The photograph of the automatic gamma neutron monitoring system is shown in Figure 1.

A user-friendly graphical user interface tailored to suit the application requirement is developed, which operates with minimum operator intervention and effortless style. Functionalities of the system like radiation level data acquisition, supplementation of sensitivity factors, real time data visualization, data storage, file archiving and management are controlled by application software developed in VB.Net platform using VS 2008.

The dynamic response of GM detectors were checked

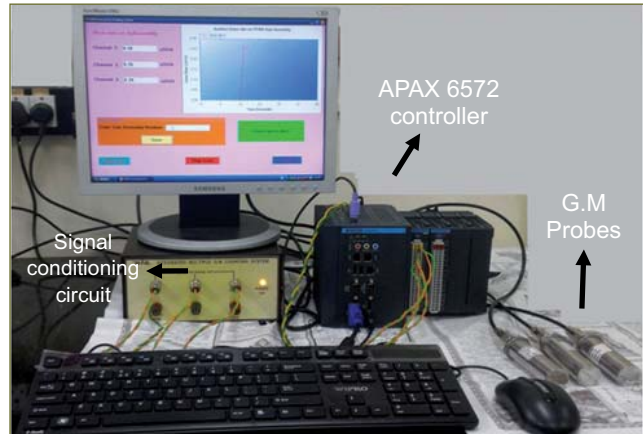


Fig. 1 Automatic gamma neutron monitoring system

individually using standard Cs-137 (0.9859 Ci) source. The values showed linear response from 0.5 $\mu\text{Sv/h}$ to 10 mSv/h. Response graph of GM probes are shown in Figure 2. The sensitivity factors for individual GM probes (cps/ $\mu\text{Sv/h}$) are calculated and applied to the system. The observed maximum error in the measured dose rates is approximately $\pm 10\%$ for all the three GM probes up to 10 mSv/h. System performance was assessed by acquiring gamma and neutron profile of PFBR fresh fuel sub-assembly using the automatic gamma neutron monitoring system. The gamma dose rate profile at 1 cm, projected on-contact gamma and neutron dose rate of PFBR un-irradiated sub-assembly acquired by system is shown in Figure 3.

This method is an improvement over the conventional method of dose rate measurement using Teletector and it standardizes the dose rate measurements by avoiding human errors.

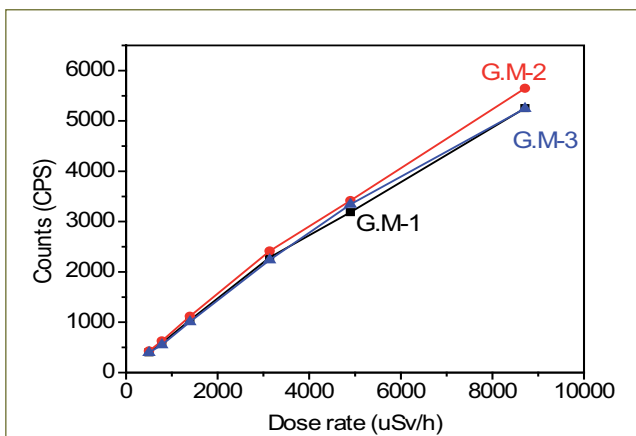


Fig. 2 Response curves for GM probes

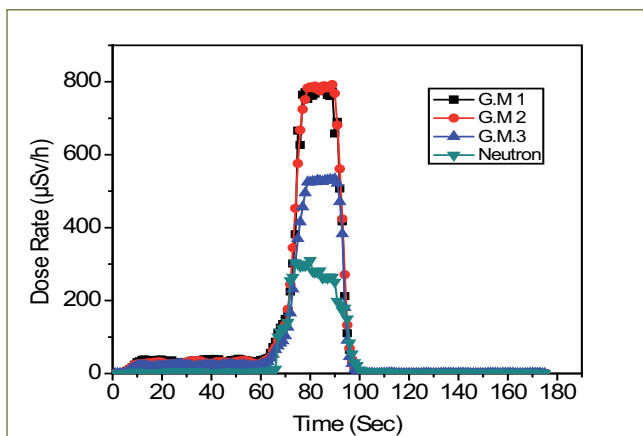


Fig. 3 Dose rate profile of fuel sub-assembly

II.6 Development of Ultrasonic Glancing Angle Imaging Methodology for Mapping of Fuel Sub-assembly Heads

The PFBR core is immersed in a pool of sodium. The in-vessel transfer machine handles fuel and other core sub-assemblies (SAs) for fuel handling operation. The non-protrusion of any SA beyond a permissible level has to be ascertained before starting any fuel handling operation. An under sodium ultrasonic scanner (USUSS) is used to ensure this by using side viewing transducers.

USUSS can also be used for core mapping using downward viewing transducers that can provide the extent of growth and bowing of core SAs. For core mapping, the USUSS is placed in the observation port in the small rotating plug (SRP). However, due to the rotational constraints of the large rotating plug (LRP) and SRP in PFBR, mapping of all core FSAs is not possible using the downward viewing transducers placed on USUSS. The imaging of the inaccessible locations in the core can be performed using a specifically developed sweep arm scanner (SAS). As an alternative to SAS, an ultrasonic glancing angle imaging methodology has been developed for mapping of the SA heads at locations inaccessible with downward viewing transducers.

In the glancing angle methodology, the transducer is aligned at a very small angle ($\sim 5^\circ$) with respect to the horizontal axis, as shown in Figure 1a. The glancing angle allows to obtain reflected signals simultaneously from a large number of SAs due to the divergence of the ultrasonic beam. The experimental setup consists of an ultrasonic C-scan system with a 5-axis scanner. In order to study the effect of the orientation of the SAs on mapping using glancing angle, 19 SAs of 150 mm height were arranged inside the immersion tank to form a honeycomb arrangement and filled with water. For convenience, SAs in the honeycomb arrangement were

nomenclated. The placement of ultrasonic transducer (x and z in Figure 1a) with respect to the SA head and the glancing angle (θ) were optimized based on the detailed experimental investigations. The transducer was swept about Z-axis by 90° to scan the entire honeycomb arrangement. A specific software was developed in LabVIEW for analyzing the data and visualizing the SA heads.

After optimizing the parameters, imaging of the honeycomb arrangement was performed for various extents of protrusions of different SAs. Figure 1b(i) shows the glancing angle ultrasonic map for the SAs without any protrusion. Figures 1b(ii) and 1b(iii) clearly show the increase in the amplitude of reflected signals corresponding to the SAs (#4 and #5, respectively) protruded by 16 mm above the general level of SAs. This clearly demonstrates that glancing angle based methodology can be used for mapping the SA heads and for detection of their protrusion, if any. The extent of protrusion can be quantified by measuring the time of flight of the reflected signals from the corresponding SA (Figure 2). It can be seen in Figure 2 that the time of flight values decrease with increasing extent of protrusion, irrespective of the orientation of the SA. This is in line with the theoretically calculated time of flight values for a cylindrical geometry. The marginal variations in the absolute change in the time of flight values for different orientations (0, 10, 20 and 30°) of the SA are attributed to the complex geometry of the SA head with 6 fold symmetry.

Thus, ultrasonic glancing angle imaging methodology can be used for mapping of sub-assembly heads and to detect their protrusion, without the need of placing an ultrasonic transducer right above the sub-assembly.

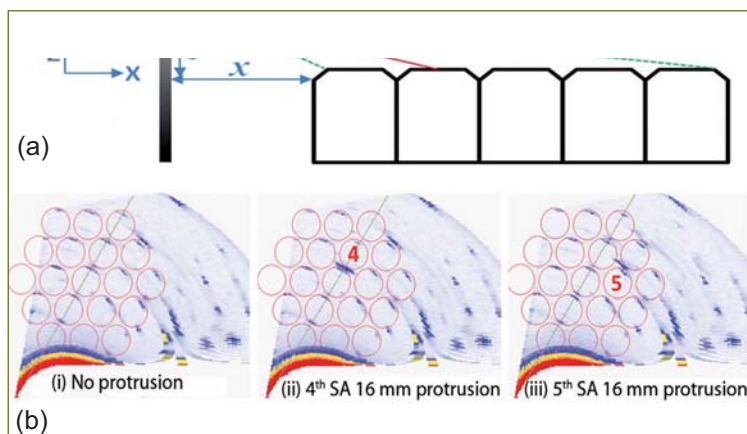


Fig. 1 (a) Schematic and (b) Imaging of sub-assembly heads of the glancing angle methodology

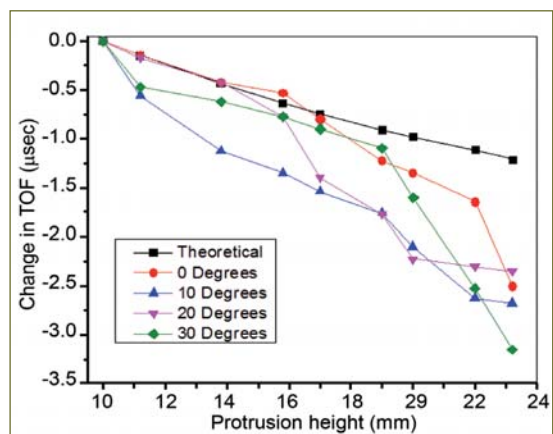


Fig. 2 Variation in time of flight with protrusion height

II.7 Investigation of Total Instantaneous Blockage in a Fuel Sub-assembly of PFBR

A local blockage in fuel sub-assembly reduces the coolant flow causing rise in the coolant outlet temperature. Such blockages grow gradually and the core monitoring thermocouples located at the outlets of every sub-assembly are capable of detecting them at their infancy. But, large size blockages will not be detected by the thermocouple due to low sodium velocity, leading to sub-assembly damage till reactor trips. The speed and extent of damage progression depends up on the size and type of blockage. But, total instantaneous blockage (TIB) at sub-assembly inlet is generally considered as an envelope of all blockages. During initial stage of a TIB event, coolant boiling takes place, followed by clad and fuel melting. During these transient phenomena, there is heat transfer from the blocked sub-assembly to neighboring sub-assembly. Monitoring sodium outlet temperature of the neighboring sub-assembly and initiating safety actions, once the measured thermocouple reading exceeds the threshold value is one of the means to detect blockage. During a TIB event, the sequence of damages taking place within the blocked sub-assembly, results in progressive change in the geometric configuration of the blocked sub-assembly. Further a fuel pool is formed attacking the neighboring six sub-assembly hexcan walls. These are complex thermal hydraulic phenomena involving moving solid-liquid interfaces, phase change heat transfer and natural convection in fuel pool. During such an event, it is required to determine the rate of damage propagation in the core, the number of sub-assemblies that are likely to get damaged before reactor trips and the usefulness of neighboring sub-assembly thermocouples in detecting this event. Towards this, an enthalpy based transient thermal model has been developed which considers actual power distribution in fuel pins and transient natural convection in the fuel pool.

The mathematical model considers the event to progress in three stages as depicted in Figure 1.

In stage - I, the model represents blocked sub-assembly, inter-wrapper sodium, and neighboring sub-assembly hexcan in axis-symmetric geometry. First a nominal steady state temperature field is obtained by solving steady state form of governing equations. Subsequently, flow to the blocked sub-assembly is brought to zero, leading to total instantaneous blockage. During transient, various components of the sub-assembly undergo temperature/phase changes.

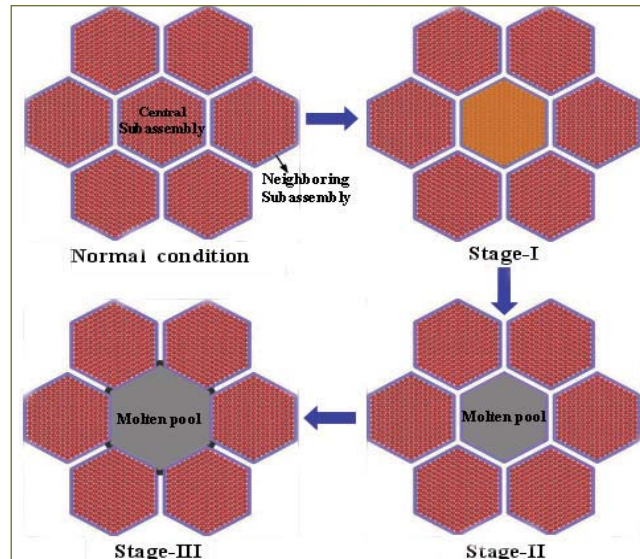


Fig. 1 Various stages of total instantaneous blockage event progression

Clad melting and liquid steel draining down during stage-I results in formation of steel blockage at the bottom of active region. Further melting of fuel pellets leads to formation of a molten fuel pool in the blocked sub-assembly and attacking its hexcan. The objective of stage-II is to examine the thermal transients in blocked sub-assembly hexcan, inter-wrapper sodium and neighboring sub-assembly hexcan during molten fuel attacking blocked sub-assembly hexcan. Further, it also provides an estimate of the time taken for complete melting of blocked sub-assembly hexcan and corresponding temperature rise in the neighboring sub-assembly sodium. The major heat loss from fuel pool is in radial direction to six sides of hexcan, which are externally cooled by inter-wrapper sodium flow. During this phase, large temperature difference develops between the central and peripheral zones of the pool and as a consequence of this, natural convection sets-in within the pool, which augments the heat transfer from the pool to neighboring sub-assembly. Meanwhile, molten pool also damages the hexcan. The rate and extent of damage propagation depend strongly on the time dependent radial heat flux emerging during natural convection that takes place within the fuel pool. Establishment of fully developed natural convection within the pool takes a finite time. Also assuming a fully established convection leads to unrealistic damage propagation. Hence, transient natural convection in molten pool is considered along with hexcan melting.

After the failure of blocked sub-assembly hexcan due to molten fuel attack during stage-II, the melt front advances radially towards the neighboring sub-assembly. The molten steel resulting from the hexcan melting enters the inter-wrapper region and blocks the inter-wrapper gap which prevents the escape of molten fuel through inter-wrapper gap. As a consequence of this, a confined fuel pool is formed which is surrounded by six neighboring sub-assemblies. The molten fuel attacks the neighboring sub-assembly hexcan walls. In this stage, transient natural convection in the pool and evolution of hexcan thickness are predicted.

The sequence and time of occurrence of principal events during total instantaneous blockage in PFBR fuel sub-assembly predicted by the model are presented in Table 1.

Results of total instantaneous blockage analysis reported for prototype fuel sub-assemblies of CEFR (Chinese Experimental Fast Reactor) and French PHENIX reactor are also presented in the same table. It is clear that the present results compare well with the reported data, generated using the advanced SIMMER code. The results of Scarabee experiments reported in open literature are also presented in Table 1.

Onset of various events in blocked sub-assembly having impact on reactor neutronics is depicted in Figure 2. It is seen that fuel melting is completed within about 16 seconds after the total instantaneous blockage, as boiling heat transfer was found to take place. Hence, detection of this event before the damage propagates to neighboring sub-assembly is not possible. Hence, eventually a molten fuel pool is formed which is held by the frozen steel mass at the bottom and hexcan walls of six neighboring sub-assembly. Vigorous natural convection was observed within the fuel pool that leads to enhanced

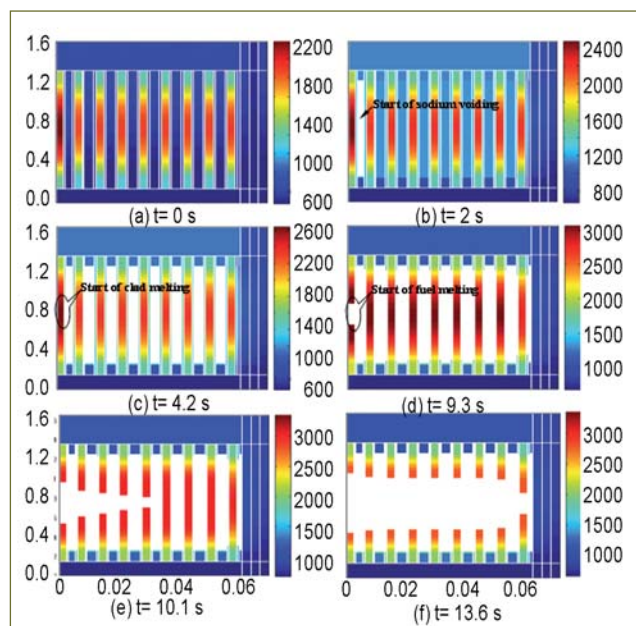


Fig. 2 Temperature distribution in blocked sub-assembly during stage-I: (a) normal operation, (b) onset of sodium voiding, (c) onset of clad melting, (d) onset of fuel melting, (e) incoherent melting of fuel pins and (f) onset of fuel melting in peripheral row

heat transfer to the neighboring sub-assembly in stage-III. The rate of melting of neighboring sub-assembly hexcan is slow initially and it reaches a peak value of 0.17 mm/s due to the onset of vigorous natural convection. This rate reduces gradually to zero at ~ 60 s due to continuous reduction in hexcan wall thickness. The reactor trips at 37 seconds based on signal from core monitoring thermocouples. The residual thickness of hexcan at this instant is 51%, which is quite significant. Thus, damage during total instantaneous blockage event is limited to blocked sub-assembly and one row of surrounding sub-assembly limiting the thermal load to core catcher to seven sub-assembly melt debris.

Table 1: Instants of occurrence of various events during a total instantaneous blockage

Process	Time (seconds)					
	Numerical study			Experimental study: Scarabee test		
	PFBR	PHENIX	CEFR	BE+1	BE+2	BE+1
Start of total instantaneous blockage	0	0	0	0	0	0
Start of sodium boiling	0.5	0.5	1	3	2	-
End of sodium boiling	4.0	5	2.5	-	3	-
Start of clad melting	4.3	6	2.5	6	5.5	-
End of clad melting	8.5	9.2	6	-	-	-
End of fuel melting	16.0	-	15	-	-	-
End of blocked hexagon melting	18.0	18.5	16.6	-	-	21

II.8 An Integrated Thermo-Mechanical Analysis of PFBR – IHX to Finalize Preheating Scheme

Preheating of primary circuit is an important operation carried out in the commissioning stage of PFBR during which hot nitrogen gas is passed into the reactor assembly within the main vessel to heat the components to a temperature of 150 (+30, -0) °C. It is essential to assess that preheating is carried out such that the temperature difference between components in the primary circuit do not cross their allowable limits. Intermediate heat exchanger is a critical component to be analysed, because it has many thick structures like tube sheets as well as thin structures like tubes. As a result, there is a risk of non-uniform thermal expansion of intermediate heat exchanger structures thereby resulting in thermal stresses. To understand this a detailed thermal hydraulic and structural analysis of IHX during preheating operation has been carried out for two cases of nitrogen temperature increase, namely, 5 and 10 K/day.

Steady state flow distribution of nitrogen within the IHX tube bundle is first obtained using 3-D computational fluid dynamics calculations. This flow distribution forms the basic input for the transient thermal analysis of intermediate heat exchanger structures including tube sheets, thermal shields, tubes, down-comer, shells etc. 30° sector of the tube bundle has been considered for flow analysis as depicted in Figure 1. The total size of the mesh is 6.54 lakh hexahedral elements. The resistance of anti-vibration belts is modeled using porous body approach.

Domain considered for thermal analysis consists of intermediate heat exchanger tubes, nitrogen in between tubes, tube-sheets, inner and outer shells and the down comer. Nodalisation scheme in bottom window region is shown in Figure 2. Discrete control volumes are considered in the axial direction and the temperature field

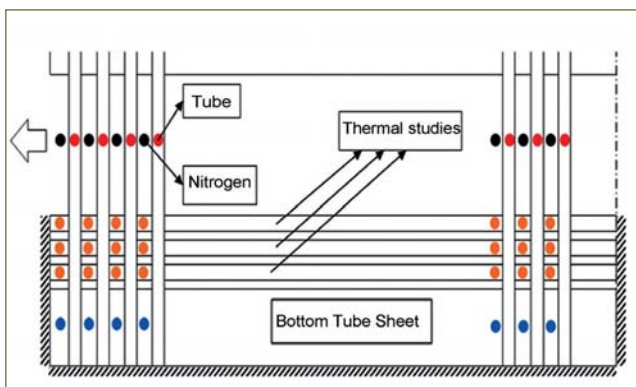


Fig. 2 Nodalisation scheme for top and bottom windows

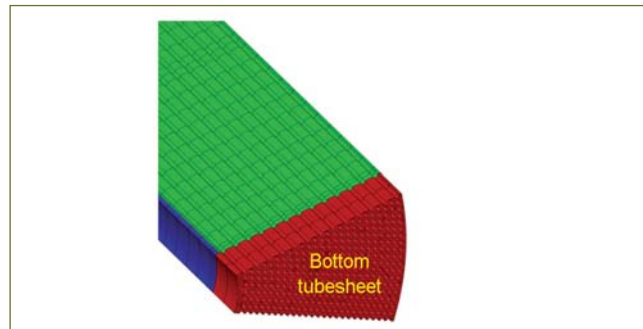


Fig. 1 Computational mesh for 3-D Finite difference method analysis of nitrogen flow in intermediate heat exchanger

is determined adopting a lumped parameter approach for heat balance among the nodes. Finite difference method is used to solve the resulting governing equations. Anisotropic effective thermal conductivity approach is used to model the presence of tubes in the porous tube sheets and thermal shields. Appropriate correlations for Nusselt number specific to different geometries are used to compute the convective heat transfer coefficient from nitrogen to intermediate heat exchanger structures. The predicted velocity distribution of nitrogen in a vertical plane through the tube bundle is shown in Figure 3. The velocity distribution along the rows is nearly uniform in the tube bundle region except the top and bottom window region. It is noted that nitrogen is able to penetrate up to the inner rows of tubes. The total pressure drop computed by computational fluid dynamics analysis is 4.53 Pa which is in good agreement with that obtained from

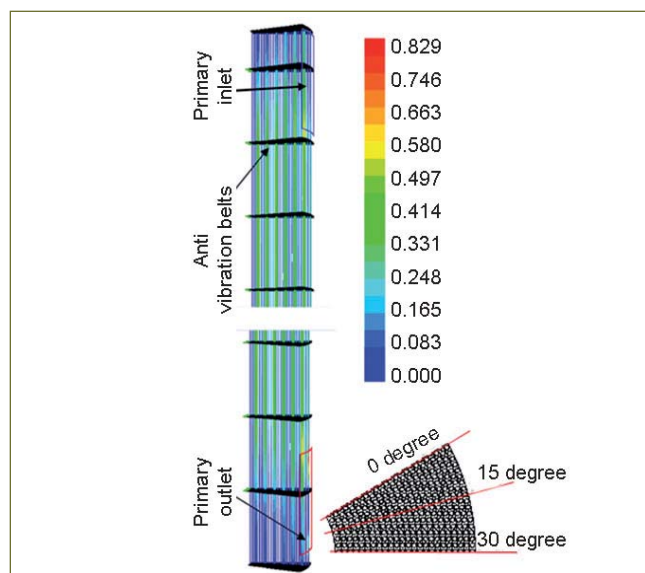


Fig. 3 Nitrogen velocity (m/s) in tube bundle at 15° plane

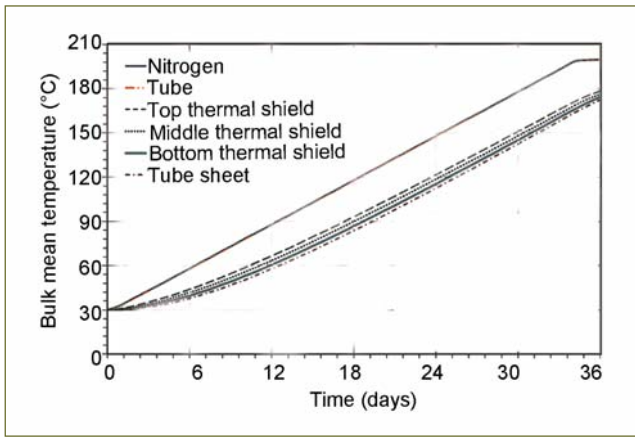


Fig. 4 Evolution of bottom tube sheet temperature at 5 K/day heating rate

1D simulation. During the transient phase it is seen that the tubes closely follow the nitrogen temperature due to small thermal inertia (tube thickness being only 0.8 mm) and large surface area of the tubes. On the other hand, the thermal inertia of tube sheets is large due to their large thickness (150 mm). Hence, they lag behind the nitrogen temperature by 15 – 70 K as given in Table 1.

At the end of preheating, the temperature of top tube sheet reaches close to 190 °C and that of bottom tube sheet reaches close to 170 °C (Figure 4). Hence, there is no risk of non heating of the tube sheet during the operation. The maximum radial temperature difference in the tube sheets are less than 3 °C at both heating rates. This thermal gradient is very small and is acceptable.

In the tube bundle, the outer row of tubes gets heated faster than the inner row of tubes followed by the down comer as shown in Figure 5. The down comer which is not in direct contact with hot nitrogen gets heated without much delay and its temperature is only about 2 °C less than that of inner row tubes. Two parameters that are important during preheating are, ΔT_b (the maximum average temperature difference between tube bundle

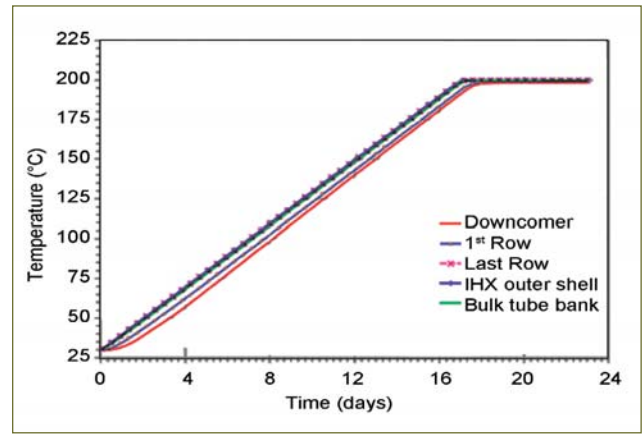


Fig. 5 Evolution of average tube bundle region temperatures at 10 K/day

and the hottest tube) and ΔT_p (the maximum average temperature difference between tube bundle and the coldest tube). ΔT_b and ΔT_p induce buckling and pullout stresses in the intermediate heat exchanger tubes respectively. It is seen that these values predicted during both preheating rates are less than those that prevail during full power operating condition of the reactor and hence are acceptable (Table 2).

It is observed from Table 1 that a maximum temperature difference of 70°C is obtained between the tube and the tube-sheet during preheating. The thermal stresses induced in the tubes adjacent to the tube-sheet due to this thermal gradient, are analyzed by finite element method. The resulting stress distributions are shown in Figure 6. It is observed that a maximum stress of 5 MPa is generated in the tube. The preheating operation being once in a life time event for the reactor and also, the stress generated is secondary in nature. Thus, the effects of these stresses are insignificant for fatigue and ratcheting. The possibility of thermal buckling is also ruled out as the stress is very small. Therefore, the thermal gradient of 70 °C between tube and tubesheet is acceptable.

Table 1: Maximum temperature difference between tubes and tube sheets		
Heating rate of nitrogen	Maximum temperature difference (°C)	
	Tubes	
	Top tube sheet	bottom tube sheet
5 K/day	15	40
10 K/day	30	70

Table 2: ΔT_b and ΔT_p values at different rates of preheating		
	ΔT_b (°C)	ΔT_p (°C)
Normal operating condition	11	22
Preheating at 5K/day	1	4
Preheating at 10K/day	1	7

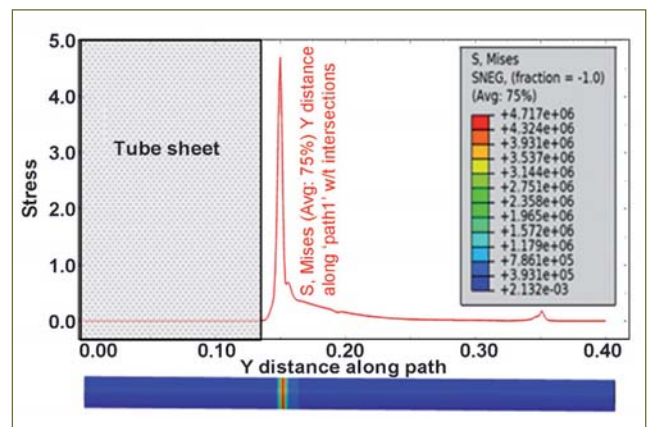


Fig. 6 Stress distribution along the intermediate heat exchanger tube

II.9 Impact Analysis of Fresh Fuel Transport Cask

Fresh fuel transport cask (FFTC) shown in Figure 1 is used to transport fresh fuel sub-assembly, from the manufacturing plant to the PFBR site. The cask with a weight of ~12000 kg is loaded to a low bed trailer and is tied to the trailer with the help of four slings provided in the cask. The cask has six fuel sub-assemblies placed vertically in a circular plate. The cask is designed for normal conditions of transport as per AERB guideline. Accidental falling of FFTC from the trailer is an event, which is to be considered for possible damage to the fuel sub-assemblies. As per AERB guideline, a fall height of 0.6 metre has to be considered in the design. Hence, a detailed structural mechanical analysis is to be performed to check the strain damage of fuel sub-assembly, by inelastic analysis. An elastic perfectly plastic model has been selected for the inelastic analysis of the cask. The design check has been performed for the allowable strain as per RCC - MR design rules.

FFTC is a vertical cylindrical shell with an outer diameter of 875 mm and 10 mm thick. The shell has a height of 4.7 metre and the middle portion of the shell with a height of 1.8 metre, is surrounded with shielding rings of 110 mm thick, 32 numbers of stiffeners of 10 mm thick running vertically from top to bottom are welded around the shell to minimize impact damage to the fuel sub-assemblies. It is covered at the bottom by a base plate bolted to the flange of the shell and at the top by a top closure plate bolted to the top flange of the shell. Sub-assemblies are restrained at the top by the top plug attached to the top closure plate and supported at the bottom by a sleeve attached to the base plate. They are guided at four locations in-between by centering plate, upper shielding plate, lower shielding plate and support plate which are connected to the center axle (hollow pipe). This axle is connected to the top closure plate and to the base plate. The centering plate and the support plate are tied down by tie rods. The whole arrangement can be lifted with a lifting attachment connected to the lugs of the shell and can be loaded on the trailer. This tie down arrangement helps to keep the fuel cask in position in the trailer, when tied to the trailer.

At interim fuel storage building (IFSB), the cask is not handled and is tied to the trailer. Hence, only fall of cask by 0.6 metre during its transport needs to be considered. The floor where the cask falls is assumed as an unyielding surface as per AERB guideline.

As per RCC – MR, a maximum plastic strain of 5% is allowed. The tensile stress-strain curve for SS 304L at 20°C (4S material) is taken from A3.4S.45. The stress

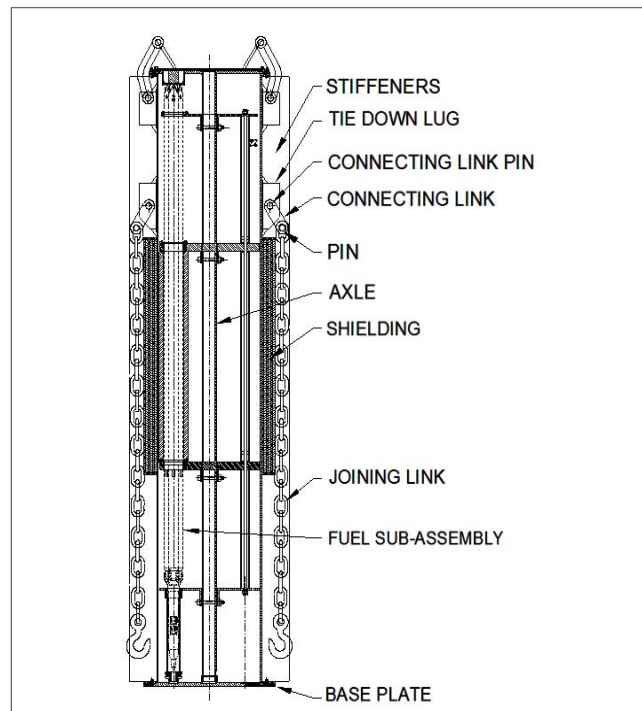


Fig. 1 General arrangement of fresh fuel transport cask

strain curve for SS 304L is extrapolated for elastic perfectly plastic material.

The geometry is analysed with CAST3M code. The analytical geometry is discretised with shell and beam elements. View of finite element model of Fresh fuel transport cask is shown in Figure 2. All major parts of FFTC are made of SS 304L

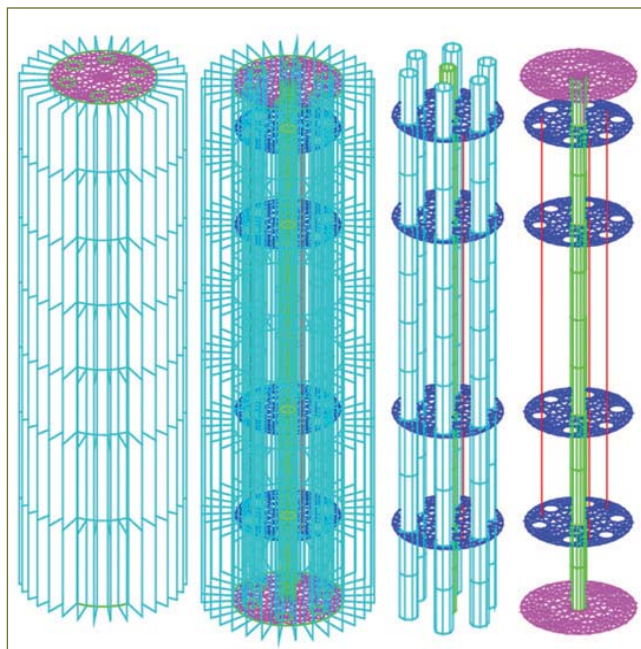


Fig. 2 FEM model of FFTC and its parts

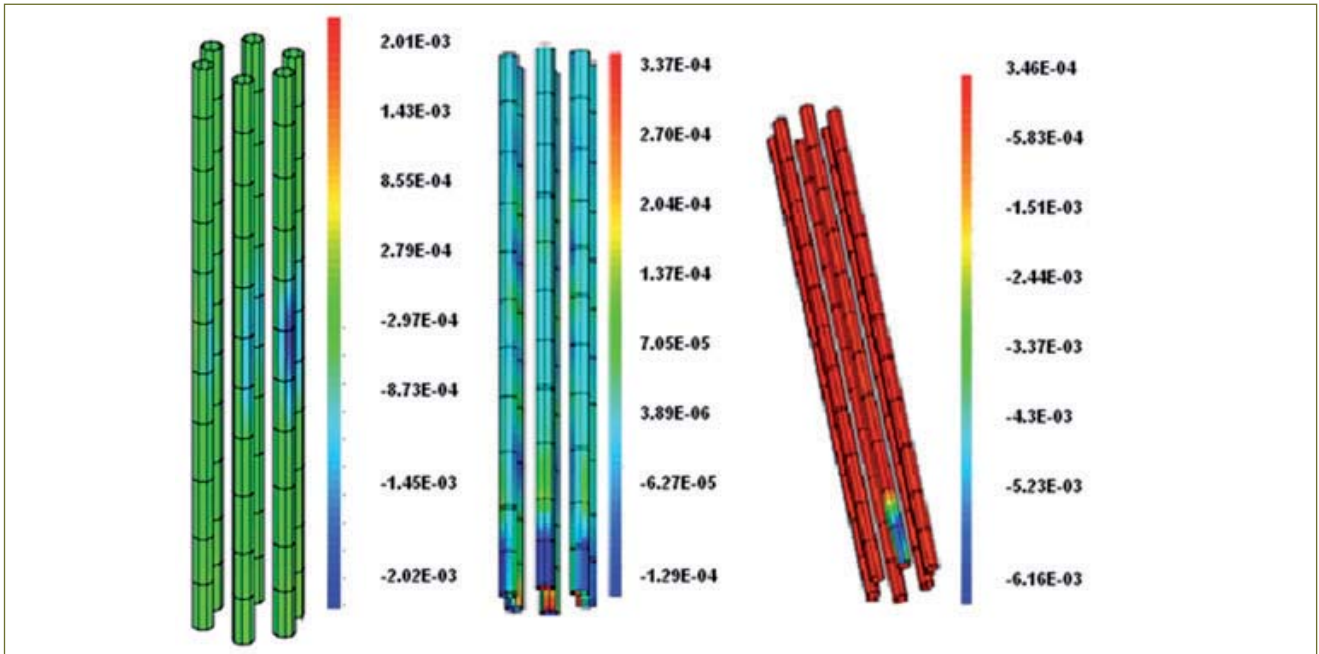


Fig. 3 Strain in fuel sub-assembly of fresh fuel transport cask

except shielding rings, which are of IS 2062. For 0.6 metre vertical fall, the centre of the base plate has been fixed, so that the entire geometry deforms in downward direction due to gravity. For 0.6 metre horizontal fall, the centre part of the stiffener is fixed. For the 0.6 metre oblique fall, the end part of the stiffener and base plate is fixed. Masses of tie down arrangement, lifting levers, connecting links and spacer pipe have been lumped at the respective locations of the shell.

Strain values and deformations in the cask and fuel sub-assembly for different time periods have been extracted for 0.6 metre impact. Some prominent strain and deformation distributions are depicted in Figures 3 to 5. The maximum strain in the fuel

sub-assembly is 0.0062. The maximum deformation for the horizontal impact in fuel sub-assembly is 55 mm. The corresponding values for vertical impact and oblique impact are 23.2 and 21.6 mm respectively. There is no interaction among the fuel sub-assembly as well as between the fuel sub-assembly and the shell, thus ensuring no risk of criticality. The bolts connecting the base plate with the shell and connecting pins connecting the shielding, centering, support plates with axle are also checked and found to meet the possible impact loads.

Thus, structural integrity of fuel sub-assemblies during an accidental fall of fresh fuel transport cask has been demonstrated by finite element analysis.

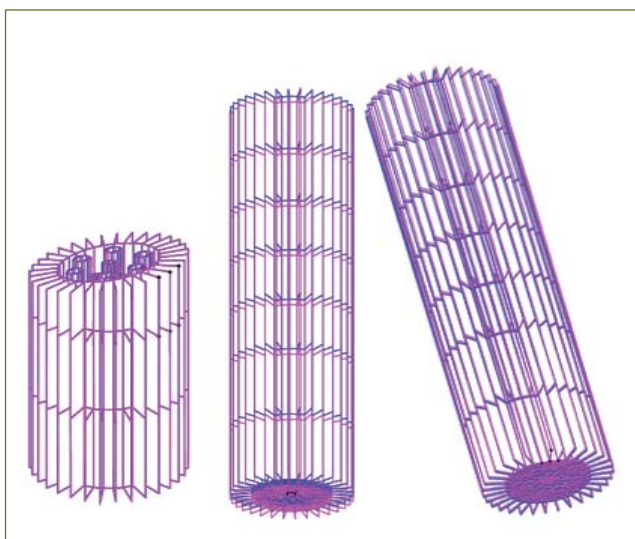


Fig. 4 Deformation in fresh fuel transport cask

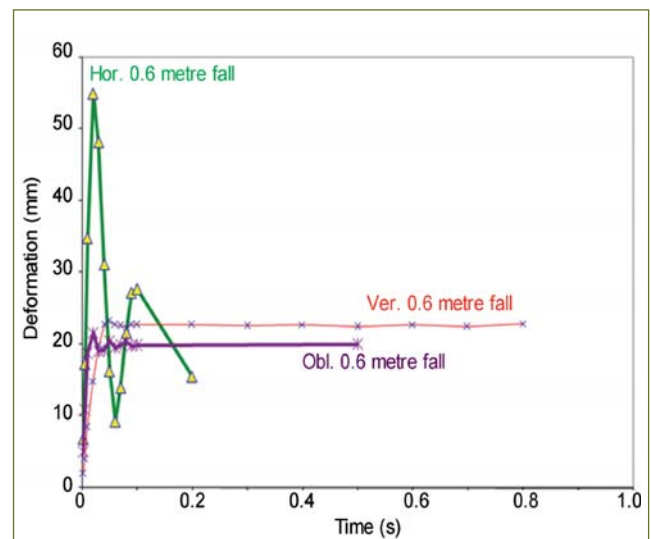


Fig. 5 Deformation plot in fresh fuel transport cask under 0.6 m fall

II.10 Seismic Qualification of Long Extended Stem Valves for PFBR

Below sealed globe valves are used in primary sodium purification circuits (PSPC) inside reactor containment building for regulation and isolation purpose in sodium purification circuits. These valves have long extended stems that penetrate through cell walls containing them. The stem length ranges from 5 to 10 metre with complex routing involving gear boxes and joints (Figure 1). Therefore operability, functionality and integrity of the valve have to be ensured under seismic conditions. Towards this, specially designed support structure that simulates the multi-support effect between valves and the extended stem has been designed and fabricated. Acceleration reading extracted at different elevation ensured simulation of multi-support effect on valve assembly. Seismic qualification experiments were performed for the valves using 100 tonne shake table facility. Tests were performed by mounting the valves along with the long stem of around 12 metre length and manual/electic actuators on a specially designed mounting structure.

The structure is designed to simulate the valve-extended stem assembly layout in the reactor, and for closely reproducing the seismic excitations transmitted to the assembly during the event of an earthquake (Figure 2). Experiments were performed for operating basis earthquake (OBE) as well as safe shutdown earthquake (SSE) conditions. The valve responses such as acceleration (Figure 3) and dynamic strain were acquired using dedicated multi-channel data acquisition system.

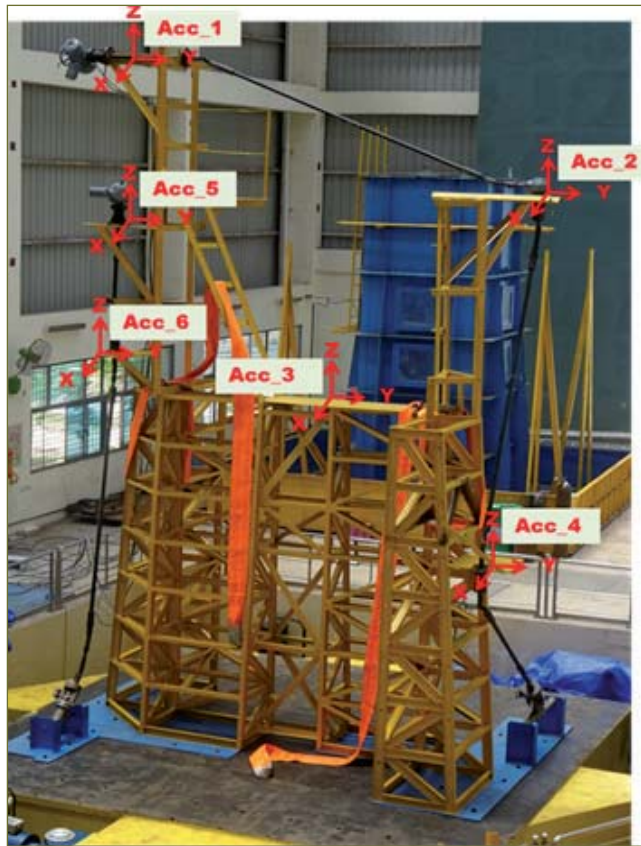


Fig. 1 Support structure for seismic qualification of large extended stem valves

The satisfactory operation of valves before and after the tests, demonstrates the seismic qualification of these valves.

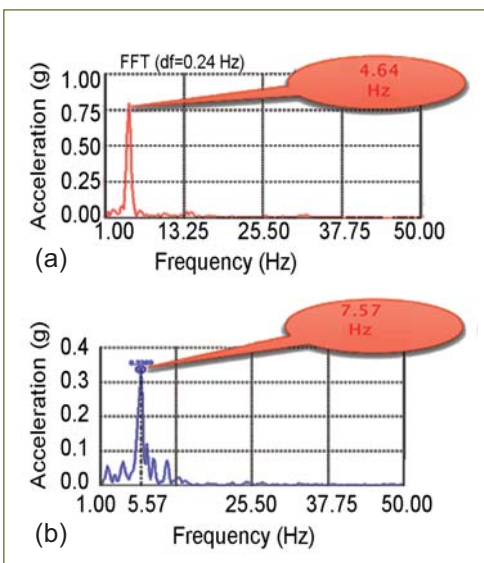


Fig. 2 Two distinct fundamental modes of support structure: (a) E-W direction and (b) N-S direction

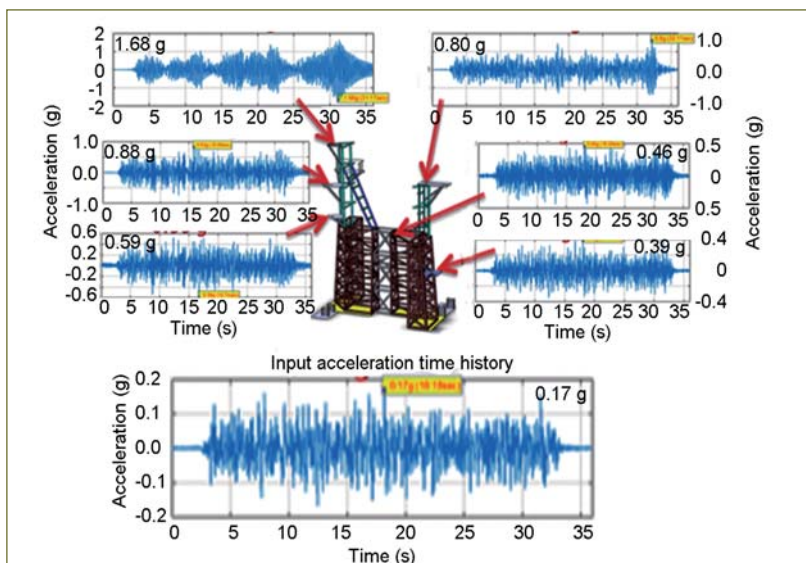


Fig. 3 Accelerations at various locations for operating basis earthquake

II.11 Qualification of Eddy Current Flow Meter of Primary Sodium Pump of PFBR against Seismic Loadings

In PFBR, eddy current flow meter (ECFM) probe, attached to primary sodium pump (PSP) measures the sodium flow through the core. The eddy current flow meter passage is a 9.3 metre long (1/4"sch10) tube with ECFM sensor of about 450mm at the bottom. ECFM probe consists of two ECFM sensors. Each sensor has one primary and two secondary coils. This probe is inserted into the inner guide tube of primary sodium pump. Inner guide of ECFM is supported at roof slab at the top and inner guide tube support at the bottom and at five additional supports at different elevations.

The natural frequency analysis of the primary pump shows predominant mode at 9 Hz frequency. Single axis test for the seismic qualification was proposed as the primary sodium pump is symmetric and no cross coupling exists. A specially designed support structure to simulate the primary sodium pump shell was fabricated with exciter locations corresponding to the roof slab at the top and spherical header at the bottom. Seismic excitations for the two support locations were extracted from the seismic analysis of reactor assembly.

The flow meter requires qualification for the two types of earthquake events namely operational base earthquake (OBE) and safe shutdown earthquake (SSE). Demonstration of structural integrity and functionality of ECFM after OBE is to ensure that, it will not call for its replacement after OBE, while test for SSE is to ensure its structural integrity.

Seismic testing was carried out at Advanced Seismic Testing and Research Laboratory (ASTaR Lab) of Structural Engineering Research Centre (SERC), CSIR, Taramani, Chennai. This facility has a 14 metre high concrete reaction wall with through holes for supporting the test structure. Two actuators with maximum displacement of ± 50 mm and maximum capacity of 5 tonnes were used for this testing. Figure 1 shows the ECFM test section along with support structure in assembled condition at SERC, Chennai.

ECFM structure (~13 metre length) was supported on an independent uni-axial linear ball bearing mounted on a rigid support structures fixed to the reaction walls. To measure response of the inner guide tube due to Seismic excitation, accelerometers and strain gauges were fixed on all support locations and on inner guide tube.

Die penetration test on ECFM probe and inner guide tube were carried out before commencement of experiment and no defects were found. Insulation resistance values and coil resistance values of sensors were recorded and



Fig. 1 ECFM test section along with support structure

found healthy. Experiments were carried out for five OBEs and one SSE. Typical accelerometer and strain gauge readings recorded during OBE is shown in Figure 2a and 2b. Test result shows that acceleration at different locations are within the range and match well with the analysis results. Stresses at all locations were found to be insignificant (maximum 15 micro strain) and within permissible level. Insertion and removal of the ECFM was also checked after each OBE by lifting the ECFM probe from inner guide tube and found satisfactory. No degradation of coil resistance and insulation resistance values were noticed after tests.

Test results have given confidence for satisfactory performance of eddy current flow meter along with inner guide during seismic conditions.

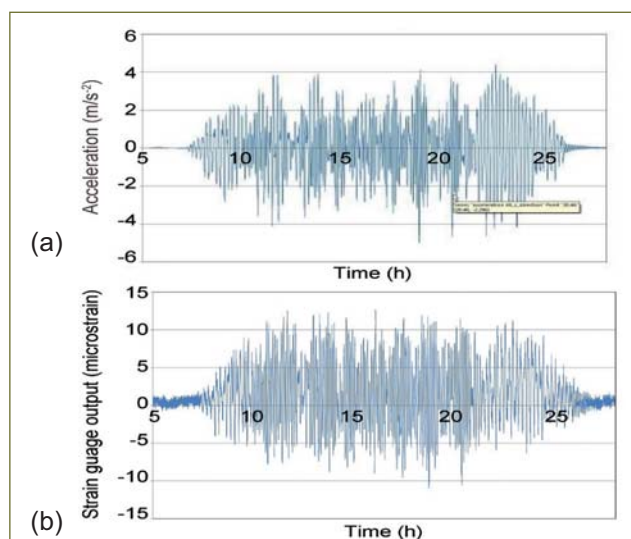


Fig. 2 (a) Accelerometer and (b) strain gauge output during OBE condition

II.12 Endurance Testing of In-house Developed Ultrasonic Transducer In Sodium

Under sodium ultrasonic scanner (USUSS) is developed for scanning the internal components of PFBR, viz., sub-assembly heads, control & safety rod and diverse safety rod, etc, during reactor shutdown period. It uses in-house developed ultrasonic transducers of 1 and 5 MHz to view horizontally, for side viewing and vertically for down ward viewing respectively. These transducers are designed to work in sodium at 180°C. To study the performance of the ultrasonic transducers at high temperature for a long period, endurance tests were carried out for 5 MHz ultrasonic transducers in sodium at 180°C.

The photograph of the 5 MHz transducer is shown in Figure 1. It consists of nickel housing with 0.6 mm thick diaphragm. The lead zirconate titanate crystal (curie temperature of 380°C) is bonded to the diaphragm by soldering, using high temperature solder alloy (96.5% Sn – 3.5% Ag) having a melting temperature of 220°C. The endurance test is conducted in the dedicated sodium vessel as shown in Figure 2.

Sodium was filled in vessel and closed with knife edge flanges. Sodium was heated to 180°C and maintained at $180 \pm 3^\circ\text{C}$ continuously and the echo was monitored and recorded periodically for 120 days. Throughout the test period there was no change in echo amplitude.



Fig. 1 Ultrasonic transducer

In order to test the transducer at elevated temperature, sodium temperature was raised to 200°C. After stabilizing the temperature, a pulse echo was recorded. The sodium temperature was maintained at $200 \pm 3^\circ\text{C}$ continuously and the echo was monitored and recorded periodically for 45 days. Throughout the test period there was no change in echo amplitude. Pulse echo output at various stages of experiment is shown Figures 3a and 3b.

Hence, it is emphasized that the in-house developed ultrasonic transducers used in the under sodium ultrasonic scanner of PFBR would work safely for five years (ie. For eight fuel handling campaigns) at a sodium temperature of $180 \pm 10^\circ\text{C}$.

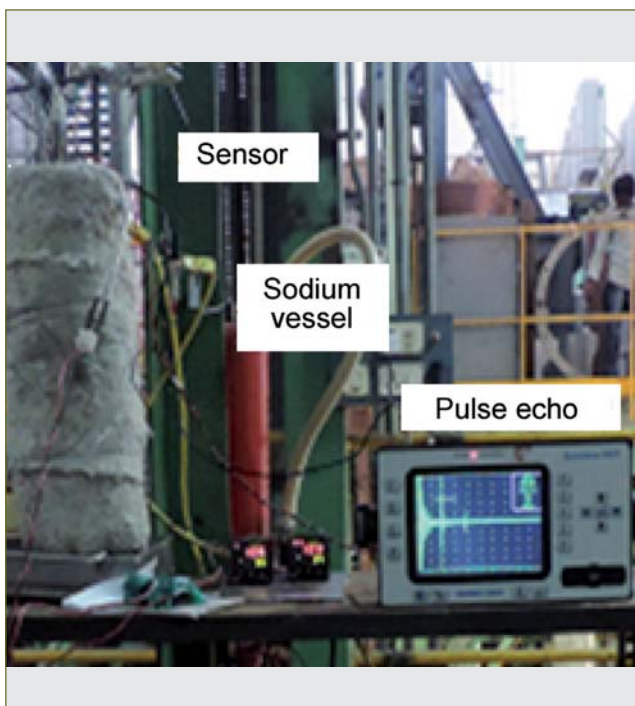


Fig. 2 Test setup

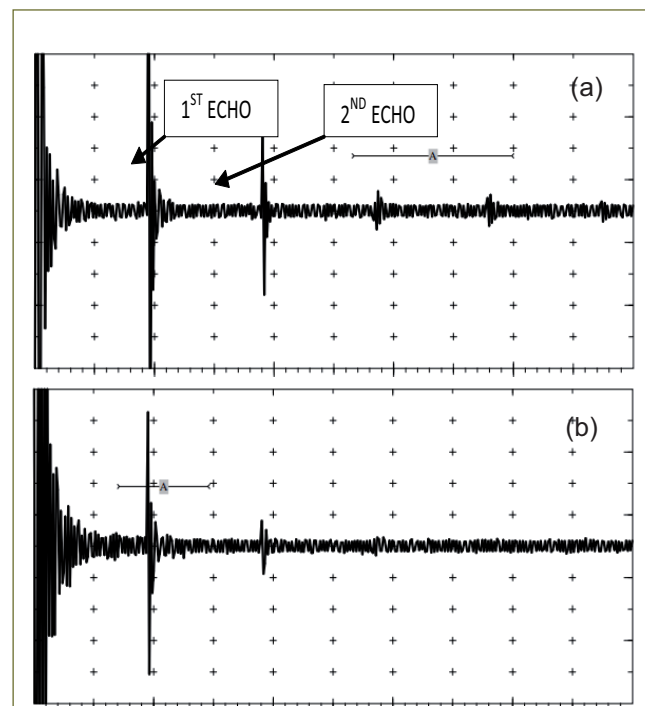


Fig. 3 Target echo at (a) room temperature in water and (b) 200°C in sodium (gain: 45 dB)

II.13 Performance Testing of Gate Valve and Shield Plug of IFTM under Reactor Simulated Conditions

Inclined fuel transfer machine (IFTM) is used for ex-vessel transfer of the core sub-assemblies in PFBR. Gate valve and shield plug of IFTM will be in an environment of sodium aerosols during reactor operating condition. The effect of the sodium aerosols on the performance of these components during subsequent fuel handling operation need to be ascertained by testing under simulated conditions. Testing of gate valve for 620 cycles and shield plug for 10 cycles was carried out successfully on test vessel-2 (TV-2) of LCTR.

Gate valve and shield plug were leak tested individually and assembled in Hall-III. The assembly was handled and erected on primary ramp liner of TV-2 simulating the orientations as in reactor conditions. Figure 1 gives the gate valve and shield plug assembly on primary ramp liner of TV-2. The torque required and number of rotations for open and close for gate valve and shield plug in air at room temperature was measured and recorded. Leak testing of the assembly with TV-2 was completed. Heaters, thermocouples fixing and connection of argon communication line to LCTR was carried out. After purging with argon and preheating, the hot argon testing (for 10 cycles of gate valve and one cycle of shield plug) was carried out. The torque values and leak tightness of gate valve were measured and recorded.

Sodium was filled in TV-2 at 200°C followed by testing for 10 cycles of gate valve and one cycle of shield plug. Sodium temperature was then raised to 550°C for 110 hours (first dwell period). After reducing the temperature back to 200°C, performance testing for first campaign was carried out for 300 cycles of gate valve and 4 cycles of shield plug. After completion of every 75 cycles of gate valve operation, one (manual) cycle of shield plug was carried out. Sodium temperature was raised to 550°C for second dwell period of 100 hours. Temperature was reduced back to 200°C, performance testing for second campaign was repeated.

The parameters observed during performance testing were recorded. During testing, it was observed that the torque values measured in hot argon and sodium testing are comparable to those at room temperature. The increase in torque values in sodium testing compared to the hot argon testing is relatively less. However, the operation of the gate valve and shield plug are smooth during the above testing.



Fig. 1 Gate valve and shield plug on test vessel-2

Individual leak testing of gate valve revealed leak due to failure of the O-ring in the gate valve. The O-ring used was a jointed one and already subjected to large number of cycles including testing at supplier's works.

It was decided to repeat the performance testing of gate valve and shield plug to check the healthiness of gate valve seat during testing and also to observe for any deposition of sodium aerosols over the bottom side of the shield plug disc and its effect on leak tightness of the shield plug, after exposure to sodium at 550°C for more than 100 hours. The failed O-ring in gate valve was replaced with a new moulded O-ring of Viton rubber. After replacement of O ring, seat leak testing of the gate valve alone was carried out and leak tightness confirmed up to 150 mbar.

Gate valve was assembled in TV-2 on ramp extension piece and seat leak testing of gate valve was repeated once again. This repeat campaign of performance testing was carried out similar to the first campaign, but after every 50 cycles of gate valve operation, seat leak testing of the gate valve was carried out. No seat leak is observed even after 600 cycles of gate valve operation. The torque values of both gate valve and shield plug during repeat campaign are similar to those in the previous campaign. During this repeat campaign, one more additional dwell period at 550°C was carried out to examine visually for any sodium at the bottom of the shield plug during removal of shield plug from TV-2 and the same was not found. Operation of gate valve and shield plug during both campaigns was smooth. It was observed that the presence of sodium aerosols does not affect the overall performance of gate valve and shield plug.

II.14 Effect of Crash Cooling on Reactor Components of PFBR during SCRAM

The rate of cooling of hot pool sodium during reactor shutdown, which in turn results in thermal shock in the components has been studied. In PFBR, when there is a reactor SCRAM, the temperature change takes place in two phases. In the first phase, the hot pool sodium is rapidly cooled from 820 to 623 K within 25 minutes during which main condensers of the plant will be in operation. Second phase is to cool down the sodium systems from 623 to 453 K at a controlled rate of 20 K/hr by deploying the operating grade decay heat removal system (OGDHR). During this controlled cooling phase, the pumps incorporated in the OGDHR system operate under high suction pressure of the order of 170 bars which varies up to 15 bars. The high and varying operating mode of suction pressure of the pump makes the pump design complex, mainly from the point of view of sealing arrangement. In view of this, the requirement of controlled cooling from 623 to 453 K has been relooked for future FBR and it is proposed to deploy the operating grade decay heat removal system only after reaching cold shutdown condition.

Reactor components in the hot pool

During crash cooling, the sudden change in the hot and cold pool sodium temperatures induce stresses in the reactor components like control plug (CP), inner vessel (IV) and intermediate heat exchanger (IHX), which are immersed in the primary sodium. This results in creep and fatigue damage of the components. Hence, detailed investigation of the hot pool components has been carried out to estimate the damage. The critical region in control plug, inner vessel and intermediate heat exchanger is the sodium free level because of the continuous change in the sodium level and sodium temperature.

Loading conditions

Following SCRAM, the sodium temperature is brought down by operating the main condensers. With a decrease in sodium temperature, the density of sodium increases and thereby the volume decreases, resulting in continuous fall in sodium level with drop in sodium temperature.

The initial sodium level (at 820 K) is at 27400 mm. During the first phase, when the sodium is cooled to 623 K in 25 minutes, the sodium level reaches to 27000 mm. Thus, the average rate of change in the sodium level is 16 mm/min.

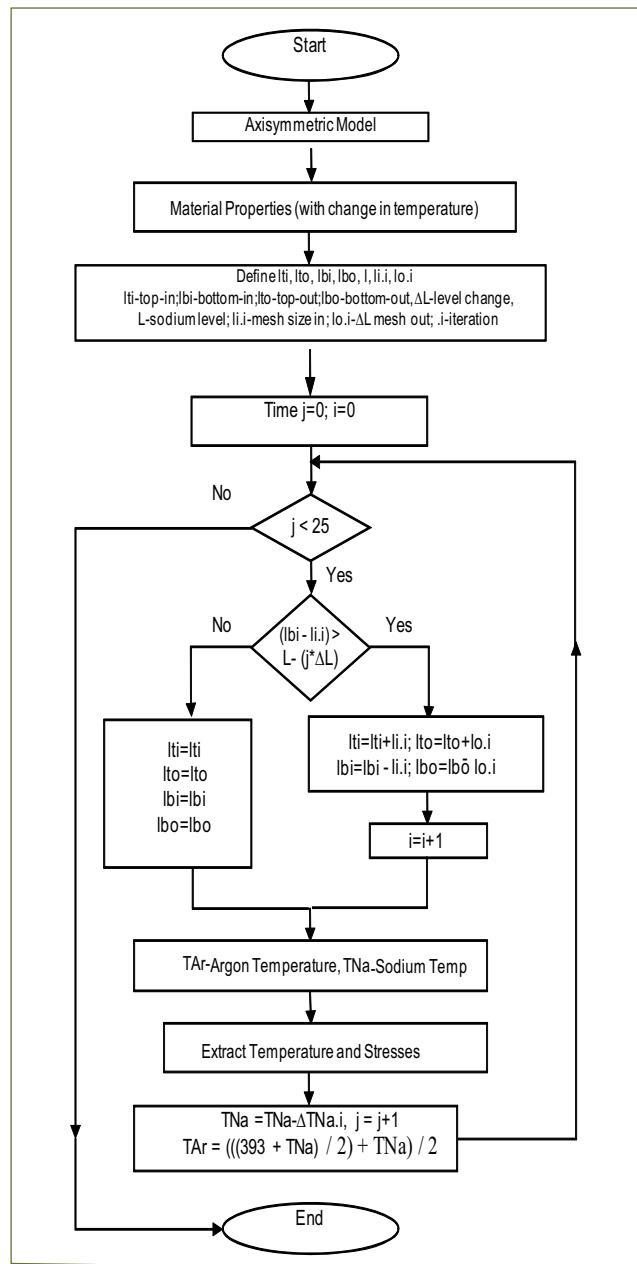


Fig. 1 Flow chart for developing a finite element program to simulate the change in length and temperature of sodium

During the second phase when the sodium at hot shutdown condition (623 K) is cooled to the cold shutdown condition (453 K), the sodium level falls from 27000 to 26700 mm at an average rate of 3 mm/min.

Flow chart for developing FE program

In order to simulate the complex loading conditions at the free surface, a numerical model has been developed using CASTEM code. In Figure 1, the

generalized approach followed to obtain the stresses and temperature at every minute has been indicated.

The maximum fatigue and creep damages for intermediate heat exchanger, control plug and inner vessel are estimated (Table 1).

In the future FBR, the requirement of controlled cooling rate from 623 to 453 K has been relooked to avoid various complexities and it is proposed to deploy the operating grade decay heat removal system only after reaching cold shutdown condition. Hence, the main condenser is used to cool down the hot pool sodium from 820 to 623 K (I-phase) at an average rate of 400 K/hr and from 623 to 453 K (II-phase) at the rate of 100 K/hr. Thermo-mechanical analysis of control plug, inner vessel and intermediate heat exchangers has been carried out for the shutdown involving two phases and the combined creep-fatigue damage in each component has been estimated. It is found that the creep and fatigue

Table 1: Creep fatigue damage values		
Component	Fatigue damage	Creep damage
Intermediate heat exchanger	7.58×10^{-4}	1.01×10^{-3}
Control plug	1.17×10^{-7}	6.0×10^{-4}
Inner vessel	5.7×10^{-3}	19×10^{-4}

damages are negligible. Hence, the simplified scheme of deploying operating grade decay heat removal system after reaching a sodium temperature of 453 K is recommended for future FBR. Temperature evolution in IHX during I-phase shutdown is shown in Figure 2.

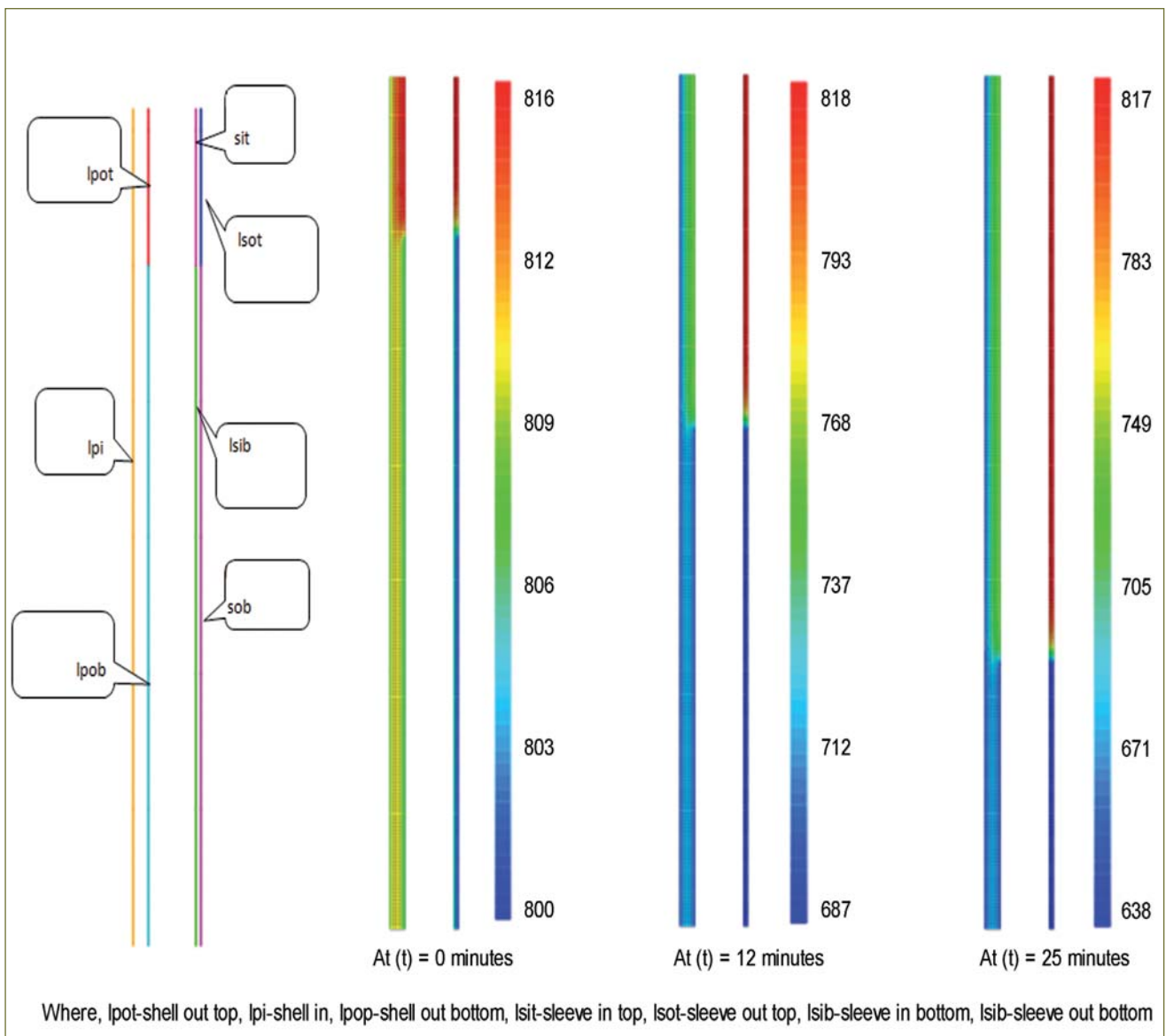
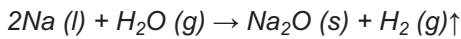
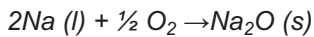


Fig. 2 Temperature evolution in IHX during I-phase shutdown

II.15 Computational Modeling of Hydrogen Evolution in PFBR Top Shield Following A CDA

In the event of a Core Disruptive Accident (CDA), 350 kg of sodium is expected to be released into the enclosure between Top Shield and Working Platform (Figure 1). Based on the signal from the gamma monitors and duct monitors, ventilation system will get isolated. The sodium reacts with the oxygen and moisture present in the air releasing heat. Reaction of sodium with moisture is accompanied by release of hydrogen. A detailed modeling is carried out and various parameters in the enclosure, viz., pressure, temperature, density and concentration of hydrogen are estimated. Parametric study is carried out considering relative humidity (RH) inside Reactor Containment Building (RCB) as a parameter, to understand its effect on the thermal hydraulic parameters and hydrogen concentration during burning period.

The sodium reacts with oxygen and moisture present in the enclosure. The heat liberated by combustion increases the temperature of the internals and air present in the enclosure. The combustion of sodium is governed by the following equations



This reaction of sodium is accompanied with 9460 kJ/kg of energy. The relative amounts of sodium reacting with moisture and oxygen are calculated based on their availability in the enclosure and the stoichiometry of reactions. The burning rate of sodium (in kg/s) is given by

$$\frac{dNa}{dt} = \frac{40 A_{pool}}{3600} \left(r \frac{y_{H_2O}}{y_{H_2O,amb}} + (1-r) \frac{y_{O_2}}{y_{O_2,amb}} \right)$$

where A_{pool} : pool area of sodium burning, y_{H_2O} : instantaneous moisture concentration (by mass) in the enclosure, y_{O_2} : instantaneous oxygen concentration (by mass) in the enclosure, $y_{H_2O,amb}$ and $y_{O_2,amb}$: moisture and oxygen concentration (by mass) in the enclosure at the time $t=0$, r : relative amount of moisture burnt

The heat generation rate (in Watt) is given by:

$$\dot{H}_R = \frac{dNa}{dt} \times 9460 \times 10^3$$

Heat released during combustion is absorbed by the air and structural components in the enclosure. Heat transfer to structural materials is through radiation. A part of the heat is transported out with the outlet flow.

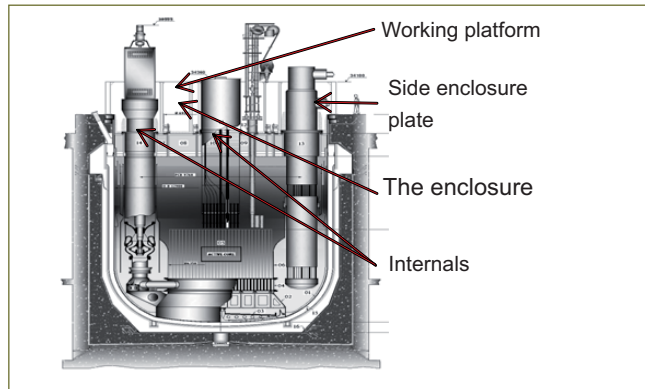


Fig. 1 Vertical section of reactor assembly

The rise in temperature of air is calculated by solving energy balance equation as:

$$\frac{\partial}{\partial t} (\rho V c T) = \dot{m}_{in} c T_{in} - \dot{m}_{out} c T + \dot{H}_R - A_{int} h (T - T_{int})$$

Where, ρ : density of air in the enclosure (kg/m^3), V : volume of enclosure (m^3), c : specific heat of air ($J/kg/K$), T : Temperature of air in the enclosure (K), \dot{m}_{in} : inlet flow rate of air (kg/s), T_{in} : temperature of intake air (K), \dot{m}_{out} : outlet flow rate of air (kg/s), A_{int} : surface area of internals participating in the heat exchange (m^2), h : convective heat transfer coefficient between air and internals (W/m^2K), T_{int} : temperature of internals in the enclosure (K), ϵ : emissivity, σ : Stefan-Boltzman constant, T_f : sodium flame temperature.

The rise in temperature of components is calculated by solving energy equation similar to as mentioned above.

During the burning of sodium, high temperature exists inside the enclosure which generates buoyancy head. Air flows into the enclosure by natural circulation due to the buoyancy head. The actual air flow into the enclosure is determined by the net effect of buoyancy head and pressure difference between the enclosure and RCB using the following equation:

$$M \frac{dv_{in}}{dt} = \frac{\Delta \rho g H A_{en}}{2} - (P_{RCB} - P_{en}) A_{in} - \frac{k}{2\beta} A_{in} \rho v_i$$

Where M : mass of air inside enclosure (kg), v_{in} : velocity of incoming air into the enclosure (m/s), H : height of enclosure (m), A_{en} : cross-sectional area of enclosure (m^2), P_{RCB} : pressure in RCB (Pa), P_{en} : enclosure pressure (Pa), A_{in} : inlet area of enclosure (m^2)

The outlet flow rate of hot air from the enclosure is calculated similar to that of inlet flow rate.

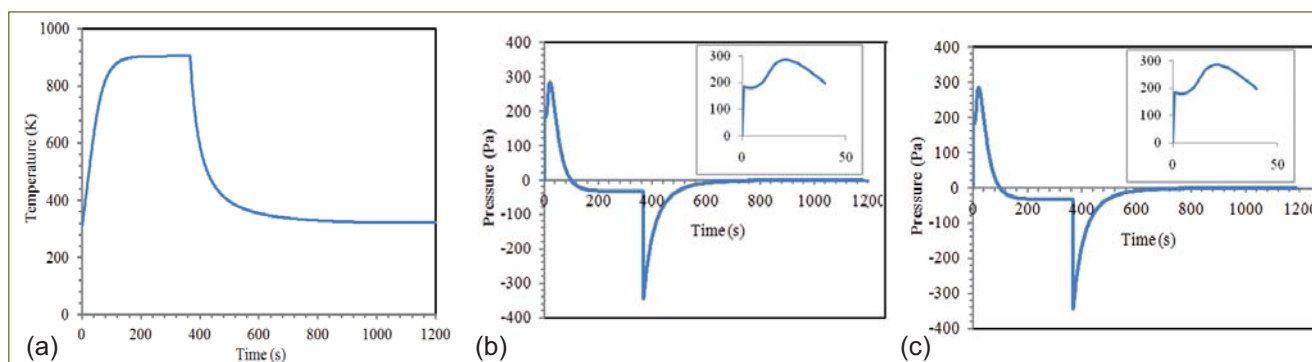


Fig. 2 Evolution of (a) air temperature, (b) pressure and (c) hydrogen concentration inside the enclosure

Mass inside the enclosure at any time is calculated by solving continuity equation. During the reaction hydrogen is generated while oxygen and water vapor are consumed. Based on this generation and consumption rate, continuity equation is formulated. Density of air inside the enclosure at any time is calculated based on the mass of gaseous substances inside the enclosure.

The rate of generation of hydrogen inside the enclosure depends on the rate of reaction and molecular mass ratio of hydrogen to sodium. With the increase in concentration of hydrogen in the enclosure, a part of it comes out with the outlet flow. Thus hydrogen concentration in the enclosure is estimated based on generation rate and transport of hydrogen out of the enclosure.

Oxygen and water vapor react with sodium and form solid sodium oxide. Hence, these two are considered to be consumed during the reaction and the consumption rate is calculated based on rate of reaction and molecular mass ratio of these components to that of sodium.

Pressure inside the enclosure is calculated using ideal gas equation. All the governing equations are solved by a finite difference method using explicit scheme.

From the analysis, it is found that 350 kg of sodium is burnt in 368 s. Evolution of air temperature inside the enclosure is depicted in Figure 2a. The maximum temperature of air during the burning is found to be 905 K, which prevails only for a short duration of ~5 minute. The temperature reaches the maximum value in 120 seconds, after which it remains nearly constant for rest of the burning period. The temperature reaches the maximum value in 120 seconds, after which it remains nearly constant for rest of the burning period.

Pressure (gauge) evolution inside the enclosure is shown in Figure 2b. Initially the pressure increases rapidly due to sudden rise in temperature associated with sodium burning. The maximum pressure is found to be 280 Pa. Thereafter the pressure decreases due to fall in density inside the enclosure. This low density develops buoyancy head which establishes natural circulation of air. After completion of burning, the pressure falls drastically as depicted in the figure as a sudden dip.

Evolution of hydrogen concentration (volumetric) is

shown in Figure 2c. Its maximum value is found to be 0.35%. As the reaction starts, hydrogen concentration increases, remains fairly constant during stable burning period and falls to zero after the reaction is completed. The hydrogen generated during reaction comes out of the enclosure along with outlet flow. There is no chance of accumulation of hydrogen in the enclosure.

A parametric study is carried out taking relative humidity (RH) of incoming air as a parameter. The various RH values considered for the analysis are 27 and 33.3% (20.4 gm/kg specific humidity). Concentration of hydrogen for various RH values is given in Figure 3. It is found that a maximum 0.7% hydrogen concentration is reached during sodium burning for 33.3% RH, which is double of the hydrogen concentration at 27% RH. This increase is due to increase in specific humidity of air.

The phenomenon of sodium burning in the space between top shield and working platform during CDA has been mathematically studied. Evolution of various parameters, viz., temperature, pressure, density and hydrogen concentration etc. are estimated. The maximum hydrogen concentration in the enclosure is found to be 0.35%, which is much less than the deflagration limit of 4 %. This study also suggests that hydrogen concentration in the enclosure remains in limits for all possible RH values.

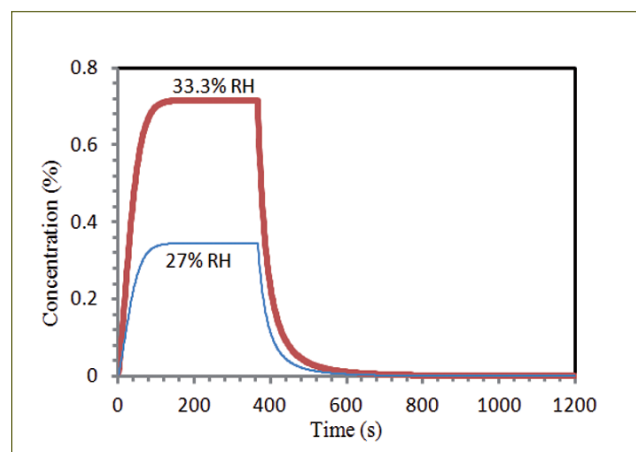


Fig. 3 Effect of relative humidity on hydrogen concentration of air inside enclosure

II.16 Modeling and Simulation of CSRDM/DSRDM for PFBR Operator Training Simulator

Modeling and simulation of control safety rod drive mechanism (CSRDM) and diverse safety rod drive mechanism (DSRDM) is a part of development of PFBR full scope replica operator Training simulator. The operator needs to be trained to operate the CSRDM & DSRDM drives using the controls provided in control room. This work involves the development of logic and 3D models of various drive mechanisms, integration and testing with simulator. 3D models will aid the operator in better understanding of CSRDM & DSRDM operations that need to be carried out in a nuclear plant.

The controls and interlocks were modeled using standard libraries and in-house developed application specific functional blocks. The logic models were processed as per the set-points and thresholds available in the requirement document. The output signals of logic models were used for controlling and providing interlocks. CSRDM & DSRDM modeling involves discrete event simulation where various interlocks of the system are considered as events.

Development of 3D models of CSRDM consists of creating design drawings and general assembly drawings of various components like gripper finger, mobile assembly, dash pot, electromagnet etc in computer aided three-dimensional interactive application tool. Similarly, for DSRDM, various components such as electromagnet, support rods, mobile assembly etc have been modelled. These modeled components were imported into the Open Inventor software to assemble them such that animation like rotation, translation etc can be coded using C++ and be attached to each component. The 3D

simulation application outline includes C++ headers and 3D part models. A WinSock application was written in VC++ on windows platform. A user datagram protocol socket was created and binded with port address of simulator server, which executes in UNIX platform. Send and receive functions were incorporated at either end and successful communication was established and tested. The C++ code developed was then integrated with the associated process and control logic models of the various CSRDM and DSRDM components developed using simulator tool (Figure 1).

Integration of developed logic models with the FORTRAN based Neutronics model and testing of 3D and its animation sequence was also carried out. The sequence of operations that were modeled for CSRDM & DSRDM are:

- (i) Rod disengagement and engagement sequence for fuel handling and reactor start-up respectively
- (ii) Rod raising and lowering for reactor power control (Figure 2)
- (iii) Separation of electromagnet and dropping of all rods at reactor SCRAM
- (iv) Bulk rod movement at reactor power set back operation
- (v) Rod exercising operation with two rod movement in the opposite directions. Integrated testing of 3D models with logics and neutronic models in simulator environment in sync with control actions has been demonstrated and verified.



Fig. 1 DSRDM models in closer view

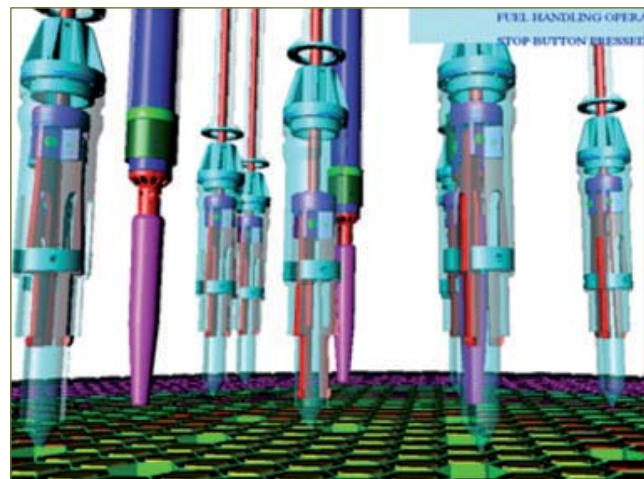


Fig. 2 CSRDM & DSRDM 3D models

II.17 Augmentation of EMI/EMC Qualification Facility

Qualification of electronic systems for electromagnetic interference (EMI) and electromagnetic compatibility (EMC) requirements is mandatory for Indian Nuclear Reactors as per AERB safety guidelines.

A test facility for EMI/EMC qualification of instrumentation and control systems has been established. This laboratory is augmented with (i) electro static discharge (IEC 61000-4-2), electrical fast transients (IEC 61000-4-4), Surge (IEC 61000-4-5), conducted RF (IEC 61000-4-6), power frequency magnetic field (IEC 61000-4-8), pulse magnetic field (IEC 61000-4-9), voltage dips & interruptions (IEC 61000-4-11) and conducted emission (CISPR 11) test facilities for various systems have been qualified with these facilities. Further to augment the laboratory with additional facilities, the following EMI/EMC qualification test facilities were added.

Ring wave

This test relates to the immunity requirements and test methods for electrical and electronic equipment, under operational conditions, to non-repetitive damped oscillatory transients (ring waves) occurring in low voltage power, control and signal lines supplied by public and non public networks. The ring wave is a typical oscillatory transient induced in low voltage cables due to the switching of electrical networks, reactive loads, faults and insulation breakdown of power supply circuits or lightning.

Distortion of power supply harmonicity

The objective of this test is to establish a common reference for evaluating the functional immunity of electrical and electronic equipment when subjected to harmonics, inter-harmonics and mains signaling frequencies. The test level is the harmonic voltage specified as a percentage of the fundamental voltage. It is essential that the root mean square voltage of the resultant waveforms remain at the normal value during the application of these tests by adjusting the voltage values of fundamental and harmonics according to the percentages indicated in the standard.

Voltage fluctuation immunity test

The objective of this test is to demonstrate the immunity of electric and electronic equipment when subjected to positive and negative low amplitude voltage fluctuations. This test may apply to all equipment intended for connection to public networks, industrial networks and electricity plants that are likely to be sensitive to voltage fluctuations.

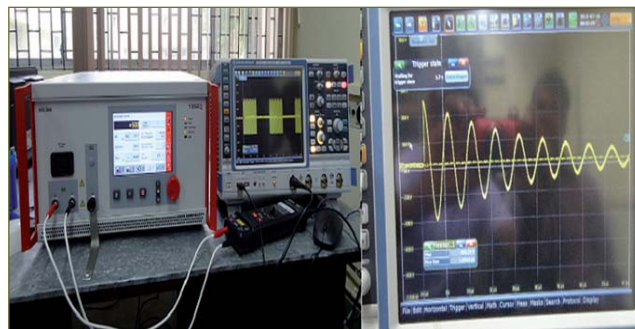


Fig. 1 Verification of damped oscillatory wave from generator

Damped oscillatory wave

The objective of this test is to establish the immunity requirements for evaluation of the performance of electrical and electronic equipment intended for residential, commercial and industrial applications as well as equipment intended for power station and substations. The slow damped oscillatory wave represents the switching of disconnections in HV/MV open air substations and in particular the switching of HV bus bars as well as to the background disturbance in industrial plants. The preferential test levels are 0.5, 1 and 2 kV for common mode and 0.25, 0.5 and 1 kV for differential mode. The generator is a single shot damped oscillatory wave generator with 75 ns \pm 20% voltage rise time for the first peak and decayed by 50% of the peak value between the third and sixth periods. The oscillation frequency is 100 kHz and 1 MHz \pm 10%. The repetition rate is at least 40/s for 100 kHz and 400/s for 1 MHz and the burst duration is not less than 2 seconds (Figure 1).

Harmonic current emission

This test deals with the limitation of harmonic currents injected into the public supply system. It specifies the limits of harmonic components of the input current which may be produced by equipment, tested under specified condition. For the purpose of harmonic current limitation, equipment are classified as Class A, B, C and D depending on the nature of the equipment. The power frequency current harmonics emission from the equipment under test is measured up to 40th harmonics.

Voltage fluctuation and flicker emission

This test deals with the limitation of voltage fluctuations and flicker impressed on the public low voltage system. It specifies limits of voltage changes which may be produced by equipment tested under specified conditions and gives guidance on methods of assessment.

II.18 Design and Development of Indigenous Processor based CPU Card for CPCI Backplane based I&C System

One of the biggest challenges the Fast Reactor I & C community faces is the short life cycle of the electronic components when compared with the reactor life time. One of the ways of overcoming this problem of component obsolescence is the complete ownership of digital IPs, erstwhile used as hardware chips in the form of hardware description language source code so that at any point of time depending on requirement it can be ported to a hardware programmable device or be converted to an application specific integrated circuit. The design and development of ABACUS SoC v1.2 (developed by ANURAG, DRDO) based central processing unit card for cPCI platform was taken up to demonstrate the feasibility of building a high integrity instrumentation and control platform around an indigenously developed processor and building a system on chip around it for future FBR applications.

The major reasons for choosing ABACUS are as follows:

- Well proven in defence applications
- Availability of complete source code making it amenable to verification
- Proven GCC based tool-chain
- Presence of inbuilt floating point arithmetic unit
- Simple RISC processor with classic five stage pipelined architecture
- MMU for OS porting

Simplified ABACUS architecture and manufactured prototype are shown in Figures 1a and 1b. The ABACUS processor performance was evaluated at the lowest possible frequency to check whether it is meeting the timing requirements for the most demanding of fast reactor applications. Also infrared thermography was carried out to measure the surface temperature of the chip at different frequencies (Figure 2a). The peak surface package temperature (55 °C) was observed at a core frequency of 150 MHz, which was well within the acceptable limits.

The core specifications of the board are as follows:

- ABACUS SoC v1.2 working @175-225 MHZ
- 32 MB EDAC protected SRAM
- 32 MB NOR flash for application and boot loader
- 128KB SPI EEPROM for configuration data storage / look up table
- 1MB MRAM for run time configuration data.
- PCI 2.3 host controller and PCI-PCI bridge

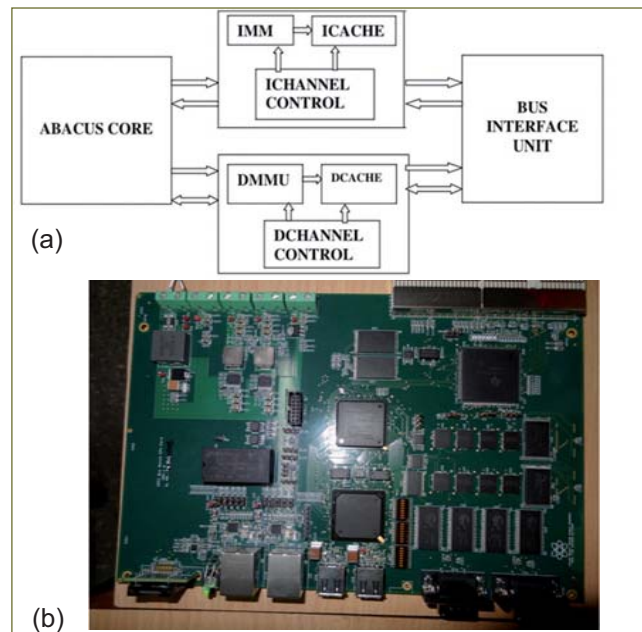


Fig. 1 (a) Simplified ABACUS architecture and (b) manufactured prototype

- Dual 10/100 ethernet
- Dual USB 2.0 host
- Dual UART
- I2C based temperature sensor and real time clock

An eight layer stackup was used for PCB fabrication to accommodate the multiple nets and to meet the timing requirements for the memory interface. Various quality assurance measures like ball grid array (BGA) joint X-ray was performed to ensure the working of the board (Figure 2b).

A custom monitor to test the board was written using assembly language where in power on self test, interrupt handler and exception handlers were written and tested. Using the monitor key specifications like interrupt latency, memory fault tolerance were checked and quantified.

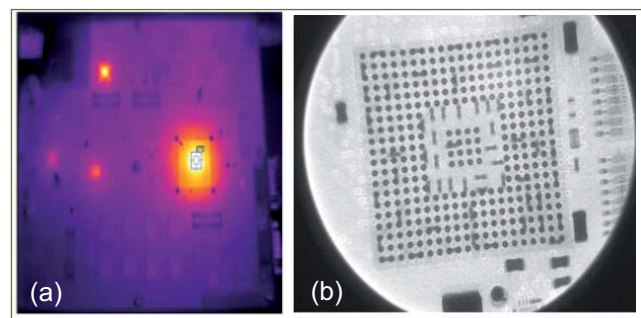


Fig. 2 (a) Infrared thermograph image of evaluation platform showing hot spots and (b) BGA joint X-ray report of ABACUS

II.19 Design and Development of Galvanically Isolated Dual Output Current to Voltage Converter Signal Conditioning Module

Safety Class-2 systems in PFBR implement dual redundant system architecture, where a single sensor input has to be isolated, converted to voltage, duplicated and provided as an input to next stage. The module designed acts as an interface module with 3- port isolation between the single 4-20 mA input and each of the dual voltage output compatible with the next stage voltage input. This module is a potential case for single point failure for SC-2 system as failure here leads to system downtime as both the systems are affected. The architecture for this SCM is rationalized keeping in mind the stringent dependability requirement from this module and is designed with a target MTBF one order of magnitude greater than the next level components. The major specifications and capabilities of the board are as follows:

- Accepts 4-20 mA inputs from both loop powered and non loop powered process transmitters to facilitate interoperability (Figure 1a)
- Supplies isolated power to loop powered transmitters, hence reduces the need for extra power supplies
- Worst case accuracy of 0.1% @55 degree celsius
- Two independent channels to feed dual redundant system at next level

- 5-pole Bessel filter with 3Hz cut off
- High common mode rejection ratio
- 24V/50 mA power supply requirements
- Transient voltage, reverse voltage, 230V continuous protection on power lines
- 500V galvanic isolation between input and output
- Field wire break detection
- Output transient protection against EFT and ESD
- Active over current limitation circuit and EFT protection at the input side

3D-modelling of the board was performed so that the printed circuit board fits seamlessly into the standard off the shelf electronic housing (Figures 1b and 1c).

A six layer stackup was used for layout as per IPC guidelines to meet the low noise and isolation requirements (Figure 2a).

Testing was done with both two wire and four wire transmitters and an accuracy of 0.05% was achieved at room temperature. A 168 hour burn in test was performed and the graphical result is presented in Figure 2b.

Future work would involve the environmental and EMI/EMC qualification of this SCM module before incorporating in a nuclear reactor.

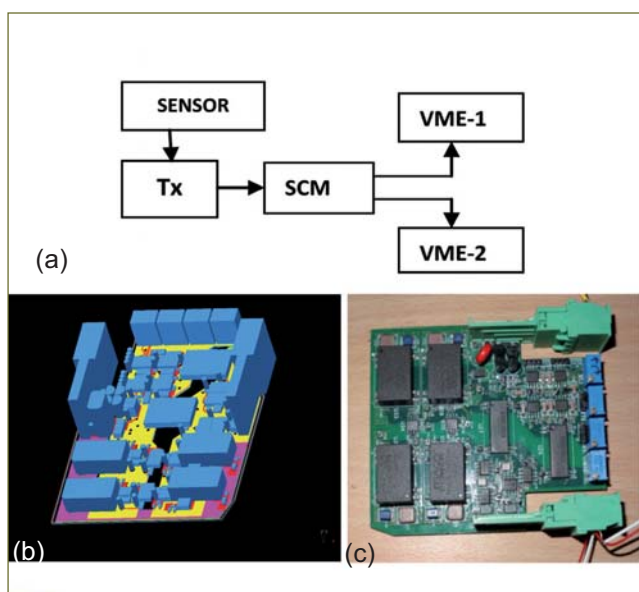


Fig. 1 (a) Tx=4-20 mA current transmitter, (b) 3D model of the board and (c) printed circuit board

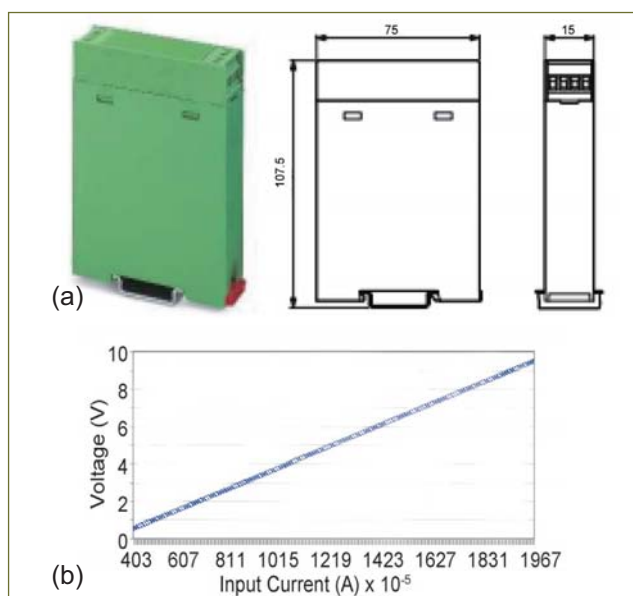


Fig. 2 (a) Actual picture of the fabricated board and phoenix contact electronic housing and (b) burn in test results (0.5 to 9.5 V conversion)

II.20 Development of Differential Pressure based Flow Meter for Low Flow Application

Precise measurement of low flow rates (~5 lpm) of gaseous fluids is needed in process applications in nuclear industry. An attempt was made to develop an in house differential pressure based flow meter. An independent calibration approach was also evolved for calibration of this instrument.

The sensor uses an orifice where the pressure difference between the upstream and downstream of the flow line is measured using an in house proven differential pressure sensor, developed for PFBR. Pulsating technique, offering high resolution, was used for measuring the differential pressure. The differential pressure between the upstream and downstream of the orifice is proportional to the square of the flow rate, that needs to be measured.

Mechanical assembly comprises of two parts, viz. orifice flow meter and calibration setup. Figure 1 shows the experimental setup using orifice flow meter through which compressed argon gas from a gas cylinder is passed through the system. Orifice flow meter consists of

- (i) Argon cylinder with constant displacement air pump for regulated flow
- (ii) Variable area flow meter of flow rate 0-5 lpm (rotameter) as a reference for calibration and operation
- (iii) Pipe test section (a perspex tube of 20 mm diameter and 2 metre length), where the orifice plate was mounted in-between two flanges via upstream flange and downstream flange.

Flow sensor and the air trap are connected using a normally closed electrically operated three-way solenoid valve whose electrical actuation was controlled through a personal computer. One way of the valve was connected to the air trap and the other way was let open to atmosphere. The calibrator was connected to the normally closed port of the solenoid valve. Orifice plate, flange connectors and the flange pressure tapings are machined as per the respective IS standards.

Calibration setup consists of air trap, electrically operated three way solenoid valve and a U-tube for sensing pressure inside the vacuum trap. Air trap is an expandable type air collection tank that consists of two cylindrical vessels with one end open in both. Bottom vessel contains a low volatile oil filled to its half. Top vessel is inverted and inserted inside the bottom vessel such that atmospheric air is trapped in-between the top vessel and the oil. A stainless steel tube runs through

the centre of the bottom vessel with one end of the tube open to the chamber of the air trap. Gas coming out from the orifice plate is connected to the other end of the stainless steel tube with a flexible tube and proper connector via a three way solenoid valve. A pressurised argon cylinder was used for gaseous flow.

Experimentation was done simultaneously for the flow meter and its calibration. For calibration of the flow meter, quick closing valve technique was adopted to collect the flowing liquid for a fixed time duration from which flow rate was calculated.

Argon coming out of the orifice plate was collected in the air trap for three seconds. For different flow rates, argon was collected in the air trap to arrive at actual volumetric flow rate. A relation between pulse frequency obtained from the differential pressure sensor (a function of pressure difference) and volumetric flow rate obtained from the calibrator was correlated to arrive at the measured flow rate.

An in-house developed calibration facility was designed and deployed for independent calibration of the pulsating sensor based flow meter. Relation between frequency and flow rate was obtained. The sensitivity of measurement is 320 Hz/lpm. From the results, it was observed that average shift in frequency for 0.5 lpm is 160 Hz. The precision in frequency measurement is within 5 Hz in the entire measurement range. Taking three times of standard deviation, it was found that the resolution in measurement is about 0.05 lpm.

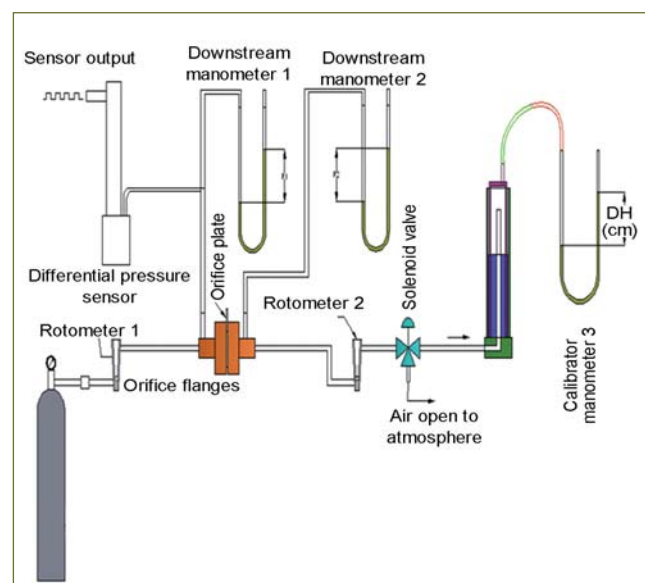
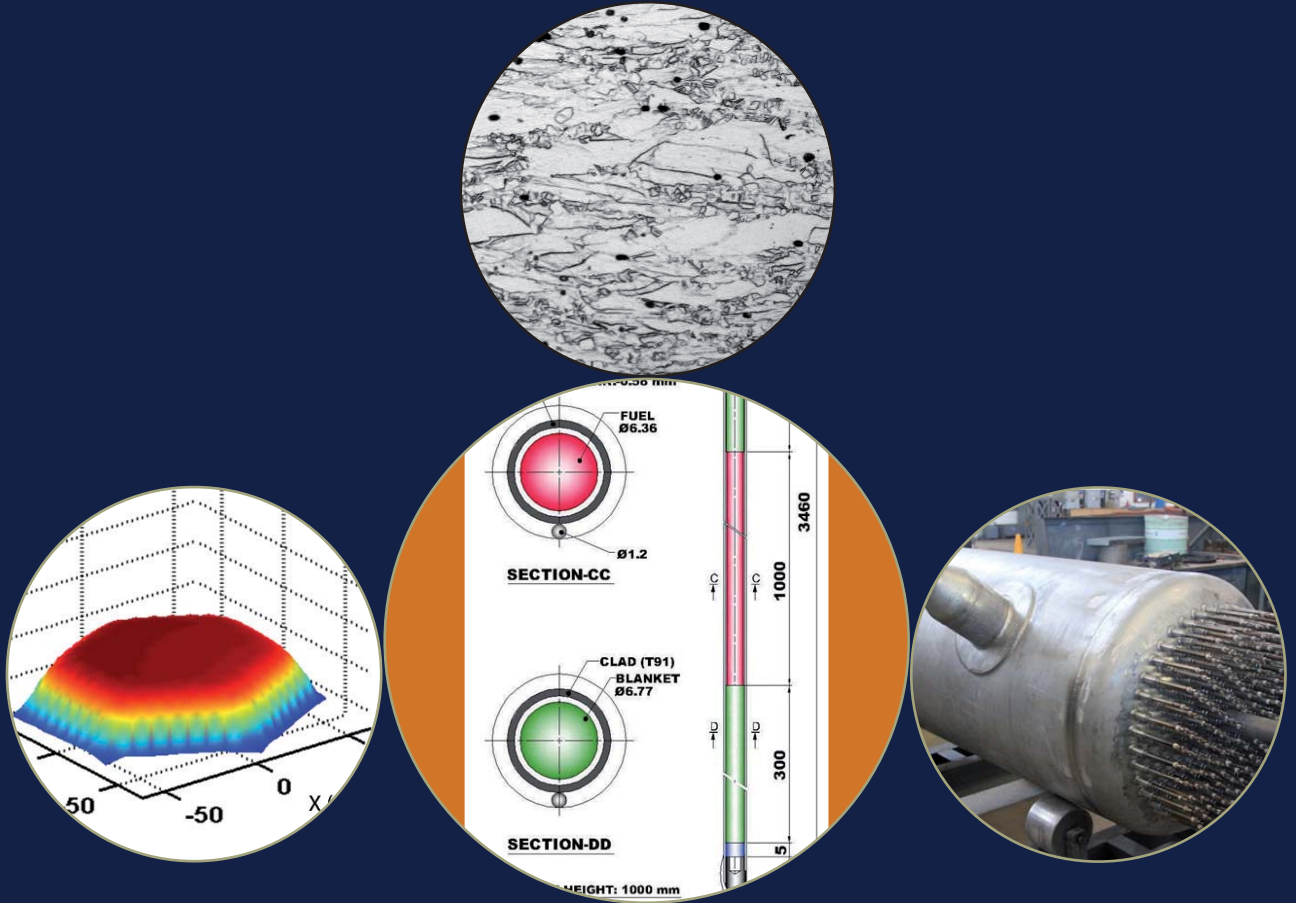


Fig. 1 Schematic diagram of the experimental setup



CHAPTER III

R&D for Fast Breeder Reactor

III.1 Height Optimization of Cylindrical Fuel Sub-assembly for Protrusion Detection

The under sodium ultrasonic scanner experiments for protrusion detection using direct and indirect imaging technique have been successfully carried out using hexagonal fuel sub-assembly. In future FBRs, it is planned to weld cylindrical attachment over the top of the hexagonal fuel sub-assembly head to facilitate protrusion detection in a simpler way using ultrasonic technique. Hence studies are required to determine the optimum height of the cylindrical attachment over hexagonal fuel sub-assembly.

For this purpose, experiments are carried out using 0.6 MHz transducer in 5 metre diameter water tank simulating the beam divergence effect in water equivalent as that of sodium. The cylindrical attachment was fabricated with step arrangement so that it seats above the hexagonal sub-assembly. The cylindrical target of height varying from 20 to 70 mm in steps of 5 mm was fabricated. The sub-assembly with cylindrical attachment was kept at a maximum distance of 3.8 metres in water and differential growth was simulated from 20 to 70 mm. Figure 1 shows the schematic of water setup with dimensional details.

The detection of protrusion was carried out using direct imaging technique and C-Scan images are shown in Figure 2 for 45 and 50 mm protrusion. Ultrasonic data was collected from 20 to 70 mm protrusion in steps of 5 mm. The collected data was analysed for constructing

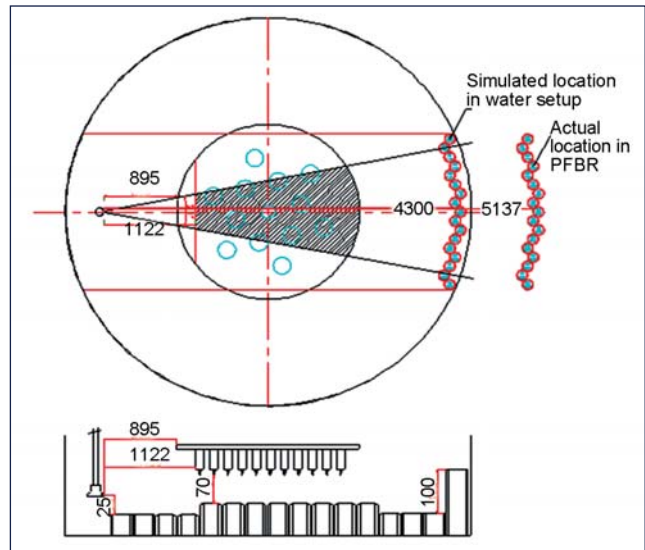


Fig. 1 Schematic showing sector-1 in water setup

the C-Scan image. It was found that, below 45 mm protrusion, signal strength is not sufficient enough to construct the image. At 45 mm protrusion the signal strength is less. At 50 mm protrusion, the signal strength is good enough for easy detection. Hence, 50 mm differential growth is considered as optimum height for protrusion detection.

The cylindrical attachment of height 50 mm is selected for protrusion detection using ultrasonic direct imaging technique.

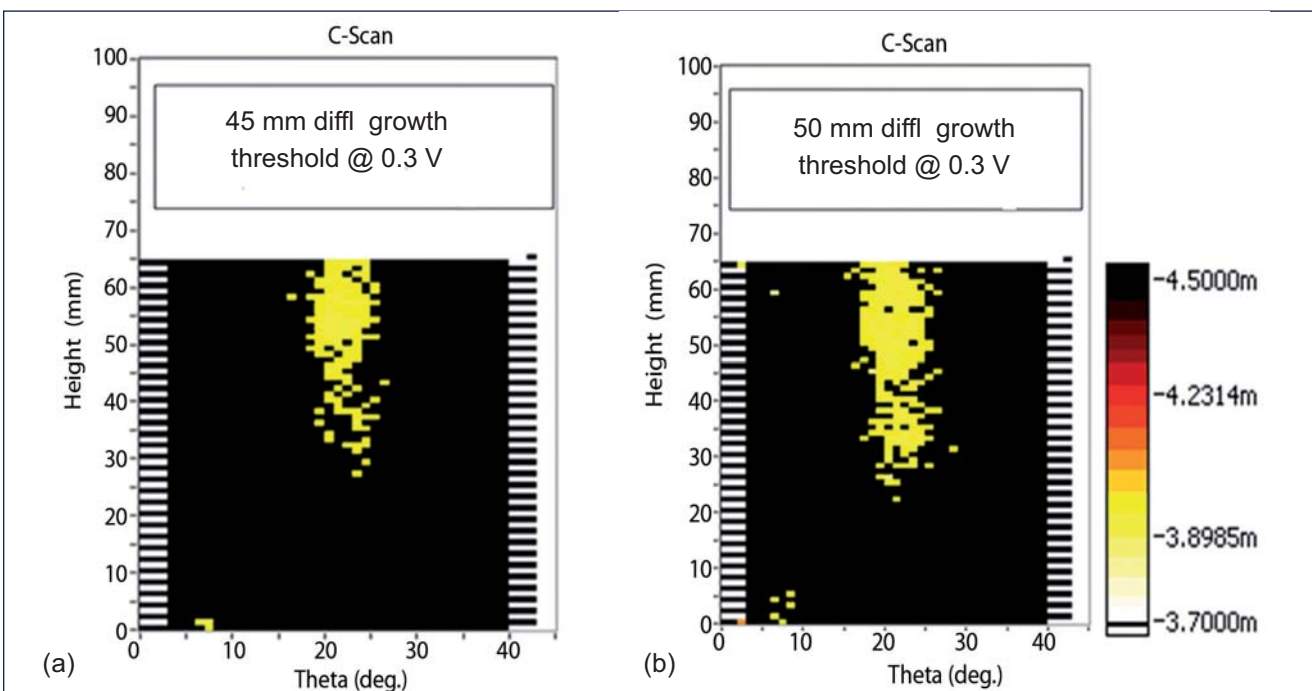


Fig. 2 C-Scan image for (a) 45 mm and (b) 50 mm protrusion

III.2 Development and Testing of Electromagnetic and Probe Type Sodium Flow Meters

Permanent magnet flowmeters (PMFMs) are used in FBR for sodium flow measurement, due to its simple construction and absence of requirement of power supply. However they are slightly bulky and have limitations in operation for high temperatures. Flow measurement at failed fuel location module demands operation at high temperature and compactness due to space constraints. Keeping this in mind development of an electromagnetic flowmeter was conceptualized. New design comprises of a stainless steel pipe and a magnetic core made up of soft iron and mineral insulated cable. Mineral insulated cable, which can withstand 550 °C, is wound on the soft iron magnetic core and is connected to a constant current DC supply to produce constant magnetic flux in magnetic core. Magnetic core is suitably mounted to produce transverse magnetic field perpendicular to flow of sodium. Stainless steel electrodes are mounted (welded) outside the stainless steel pipe in diametrically opposite positions and perpendicular to the direction of both magnetic field and flow. The potential difference developed across the electrodes due to motion of liquid sodium in steady magnetic field is measured to obtain the flow of sodium in pipe. Photograph of flow meter and support arrangement of electromagnetic flowmeter (EMFM) are shown in Figures 1 and 2 respectively. Sensitivity evaluation for EMFM was done in Thermal Shock Test Facility (TSTF) located in Engineering Hall-3 at 250, 350, 450 and 550°C at different flow rates.

Sensitivity evaluation was done using constant volume method. Fixed volume of sodium (0.505 m³) was drained through EMFM pipe. Total millivolt seconds (mV.s) and the quantity of sodium drained was equated to obtain sensitivity of EMFM. Figure 3a shows a typical EMFM output for flow rate of 1.4 m³/h. Sensitivity of EMFM at

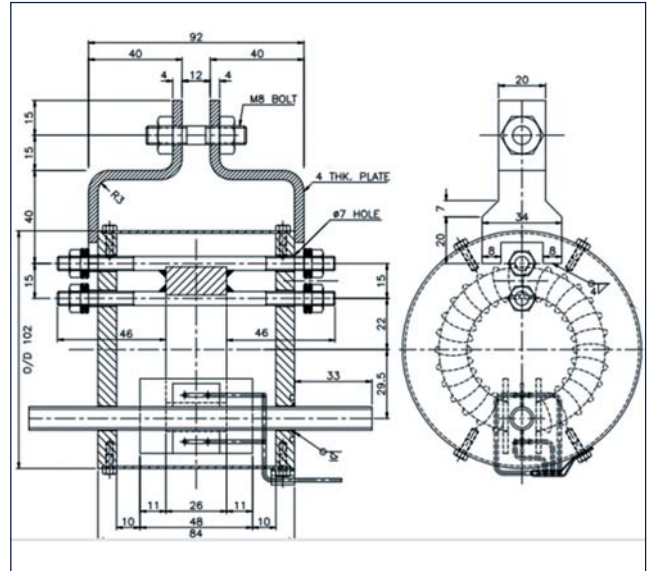


Fig. 2 Supporting arrangement of electromagnetic flowmeter

different temperatures is shown in Figure 3b. It can be seen from Figure, that EMFM is having sensitivity of 7.1 mV/m³/h.

Probe-type permanent magnet flow sensor (PMFS) offer an alternative for measuring the flow in large diameter pipes as conventional PMFM requires magnets in proportion to the pipe size. Probe-type PMFS mainly consists of a disk shaped permanent magnet, one pair of electrodes and an outer stainless steel sheath.

Figure 4 shows the cross sectional view of probe type PMFS. The disk shaped magnets are magnetized such that the magnetic field lines are perpendicular to sodium flow. The magnetic field extending into annular space induces voltage which is linear with flow velocity over a wide range. ALNICO-8 magnet has been chosen due to its excellent magnetic properties. To measure the electrical potential generated in sodium a pair of

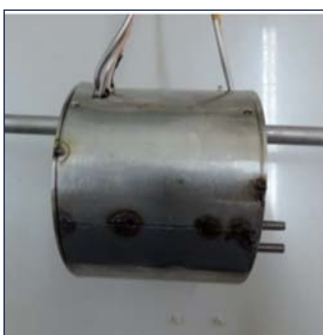


Fig. 1 Photograph of EMFM

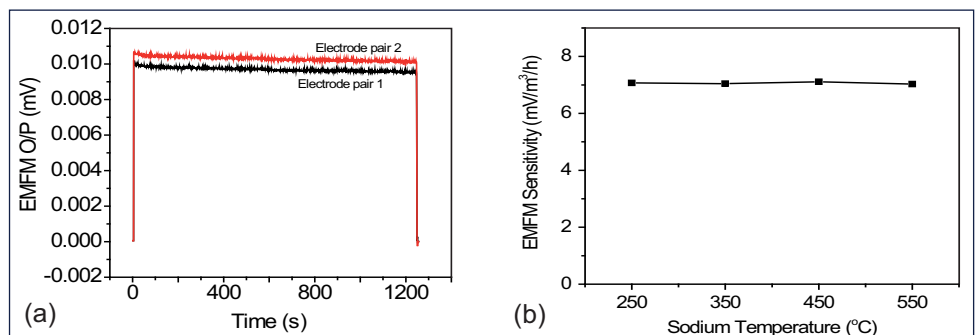


Fig. 3 (a) Typical EMFM output and (b) sensitivity of EMFM versus temperature

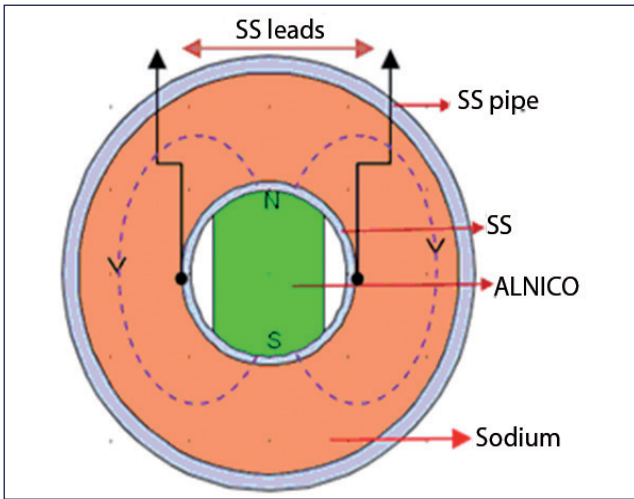


Fig. 4 Cross sectional view of the pipe with PMFS

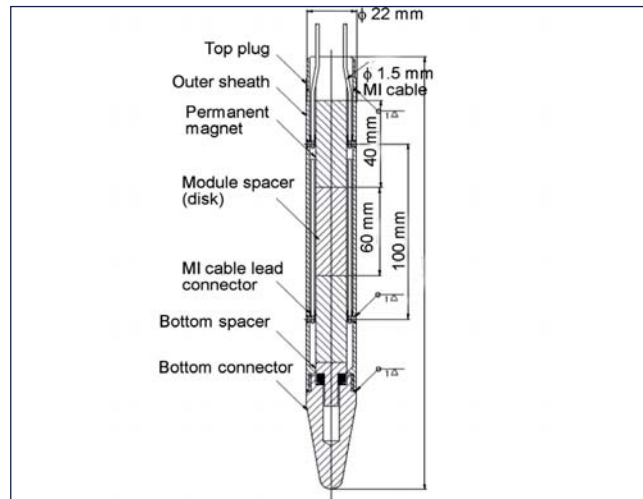


Fig. 5 Schematic of probe type PMFS

electrodes were welded with outer stainless steel sheath. The electrodes are made up of MgO insulated stainless steel sheathed cable with stainless steel conductor. Figure 5 shows the schematic of probe type PMFS.

Fabricated probe has two sensors separated by a stainless steel spacer. Each magnet with one pair of electrodes acts as a flow sensor. The probe with two flow sensors separated by a known distance helped us to determine the velocity of flowing sodium by transit time measurement. The major advantage of this method is that the calculated velocity is independent of magnetic strength. The other reason for having two flow sensors in a single probe is redundancy and for sensitivity comparison.

Probe type PMFS was calibrated in SGTF sodium system. During this calibration, flow through the sensor was varied from 10 to 35 m³/h in steps of 5 m³/h and the temperature of sodium was varied from 250 to 400°C in steps of 25°C. The output of the flow sensors were calibrated with reference to a PMFM located in the loop. A detailed data analysis was carried on PMFS output in order to study the effect of flow on sensor output, effect of flow on sensitivity, effect of temperature on sensor

output and effect of temperature on sensitivity. Stable performance of the sensor at all temperatures justifies the selection of permanent magnetic material. The corresponding results are discussed below.

It was observed that as the flow through the sensor increases the output of both PMFS 1 & 2 and outputs are increasing linearly with respect to sodium flow. Figure 6 shows PMFS output with respect to flow for various temperatures.

It was observed that as the flow through the sensor increases the sensitivity of PMFS 1&2 were decreasing. Maximum non-linearity of sensitivity with respect to flow is found to be 5.06%.

It was observed that the mV output generated from both the sensors is stable at all temperatures (250 - 400°C). Sensitivity of the PMFS 1 & 2 was measured to be 0.303 and 0.306 mV/m³/h (Figure 7). The major advantage of this probe is that, the output is linear with respect to the flow i.e. 10 to 35 m³/hr and mV output generated by both the PMFS is stable at all temperatures i.e. 250 - 400 °C. Sodium flow can be measured without any temperature compensation and complex electronics.

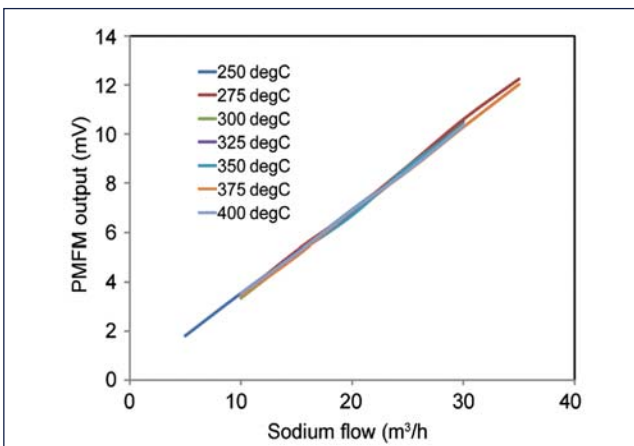


Fig. 6 PMFS output versus sodium flow for different temperatures

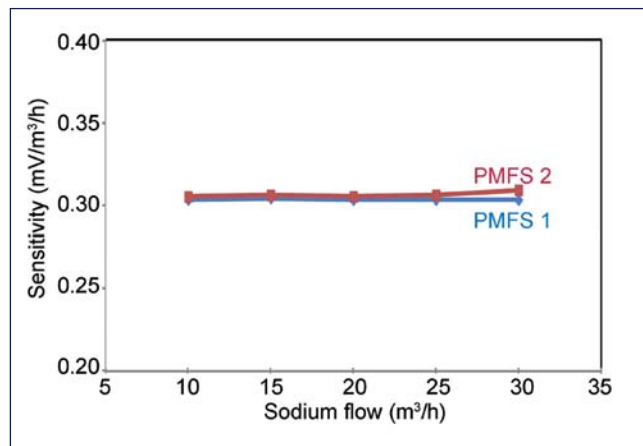


Fig. 7 PMFS sensitivity versus sodium flow for different temperatures

III.3 Indigenous Development of 450NB Sodium Frozen Seal Valve

Butterfly type valves are provided in Indian Fast Breeder Reactors (FBR) to isolate the steam generator during situations which demand steam generator isolation. The size of sodium supply line to steam generator in 600MWe FBRs is arrived as 450NB. After closing these isolation valves at the upstream and downstream of steam generator, sodium in the steam generator will be drained and the thermal insulation around the sodium piping nearby the valve will be removed to enhance the heat transfer from sodium to atmosphere. The slowly leaked sodium at the steam generator side of the valve will freeze gradually and form a frozen seal in the pipe line. In these valves, a sodium frozen seal will also be formed in the gap between the valve stem and the bonnet and the sodium leak from the valve body through the annular gap between stem and bonnet will be arrested.

For the usage in PFBR, steam generator isolation valves were manufactured and supplied by M/s Babcock Power Espana, Spain. For future FBRs, these valves are indigenously developed. Schematic of the newly developed butterfly valve is shown in Figure 1. Sodium will rise from the main pipe through the 1mm annular radial gap between valve bonnet and stem and is made to freeze. The heat conducted through the valve bonnet, valve stem and through the sodium inside the annular gap will be lost to the atmosphere by natural/mixed convection from the external surface of the valve bonnet. External fins are provided on the outer surface of the bonnet to enhance the heat transfer from sodium to atmosphere and thus to form a stable and sound sodium frozen seal inside the radial gap. Welded type fin configuration is adopted in the present valve design to reduce the cost of manufacturing. The material of construction of the valve in FBR system is SS316LN and the material of construction of the butterfly valve for qualification is chosen as SS 316L. The design basis operating temperature and pressure of the valve are 550°C and 55 bar respectively. The design life of the valve is 60 years with a load factor of 75%.

As part of the development of the valve, numerical studies have been conducted for the design optimization of the fins and the bonnet geometry for freezing the sodium in the annular gap between the fixed bonnet and rotatable stem at as a minimum level as possible under external environmental conditions at the vicinity of the valve. Studies are also conducted to confirm the frozen seal with 20°C more temperature than the design

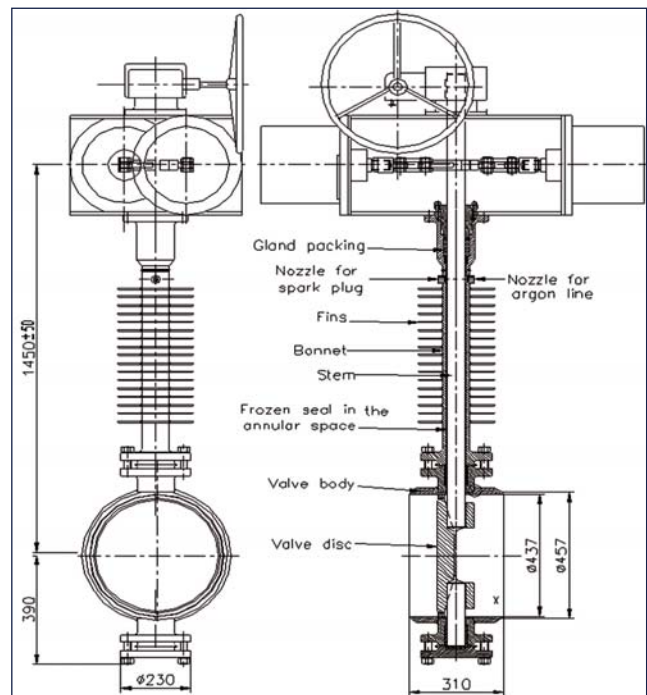


Fig. 1 Schematic of the 450 NB butterfly valve

basis ambient temperature of 60°C. With the final fin configuration, sodium frozen seal has been observed to be formed near to 6th and 7th fins which is around 55% of the bonnet height at design basis temperatures. Figure 2 shows the temperature contours in symmetrical plane of sodium and metal portion of the geometry and the variation of temperature of sodium in the annular region for various ambient conditions. In the case with an ambient temperature of 80°C, the frozen seal is observed to be formed at around 70% of the bonnet height. The valve with this bonnet configuration is under fabrication at M/s Instrumentation Ltd, Palakkad. Finally, this valve will be tested in SFCT facility of Engineering Hall-1 to confirm the operation at intended service conditions.

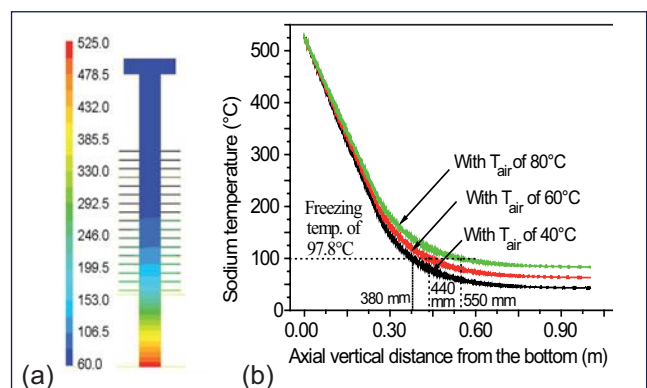


Fig. 2 (a) Temperature contours in the symmetric plane of valve and (b) temperature profiles of sodium in annular space for various T_{air}

III.4 Development and Performance Testing of Electromagnetic Pumps in Sodium

Electromagnetic pumps are used for pumping liquid sodium in auxiliary circuits of fast reactors and in experimental sodium facilities. This article deals with development and testing of electromagnetic pumps meant for low flow applications.

An alternating current conduction pump of flow rate 2 m³/h and 2 kg/cm² head was designed using magnetic circuit approach and analyzed with FEM code. Subsequently, the pump was manufactured with support of Indian industry. Various components such as stainless steel duct, primary windings, secondary windings for alternating current conduction of the pump were tested at manufacturer's site. Electrical tests such as high voltage test, insulation tests and no load test were conducted satisfactorily. Sodium testing of the alternating current conduction pump will be carried out shortly. Figure 1a depicts the photograph of the manufactured alternating current conduction pump. Alternating current conduction pump has the advantage of using a standard single phase alternating current power supply and occupies less space.

Along with the development of alternating current conduction pump, design, development and manufacturing of an annular linear induction pump of flow rate 1.5 m³/h and head 2 kg/cm² was also carried out for meeting low sodium flow requirements. After manufacturing, the pump was tested in a sodium loop, to verify the design by obtaining the head versus flow characteristics of the pump experimentally. Endurance test for 1000 hours was also carried out to assess the performance of the pump. Figure 1b depicts the annular linear induction pump installed in a sodium loop. Experimentally obtained head versus

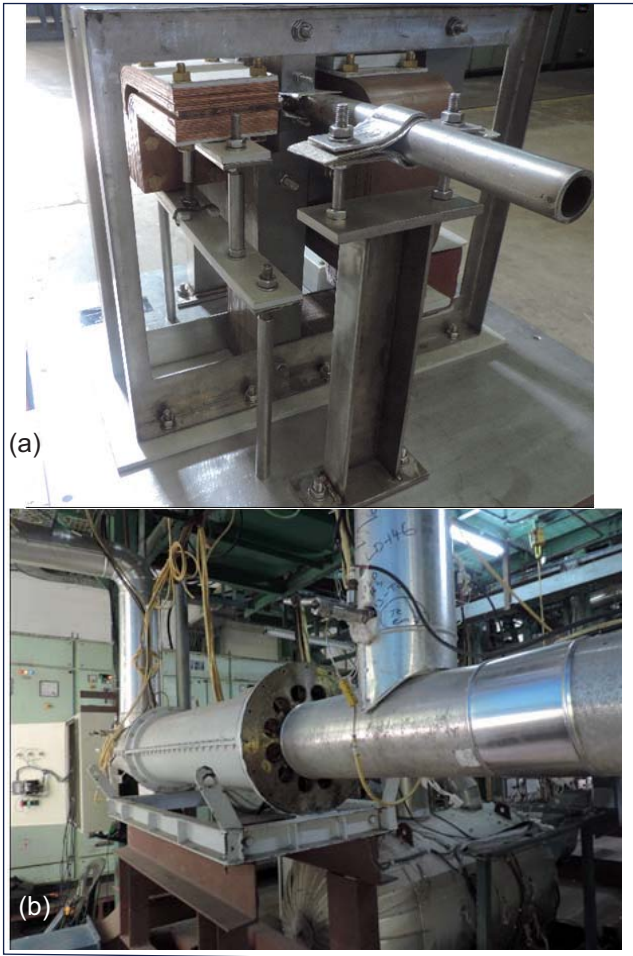


Fig. 1 (a) Manufactured alternating current conduction pump (b) 1.5 m³/h annular linear induction pump during sodium testing

flow and efficiency versus flow characteristics of 1.5 m³/h annular linear induction pump are shown in Figures 2 and 3 respectively.

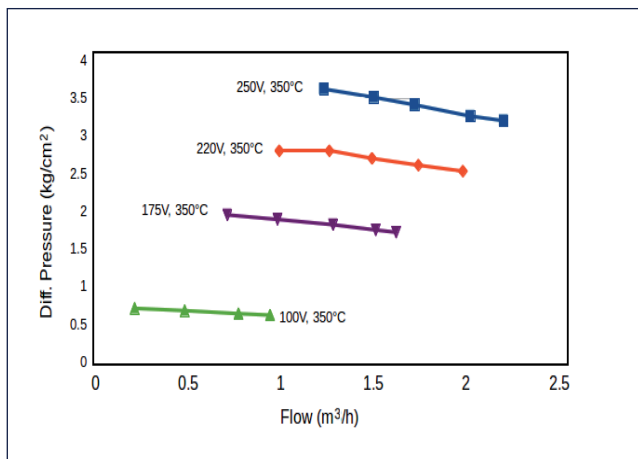


Fig. 2 Experimentally obtained head versus flow characteristics of annular linear induction pump

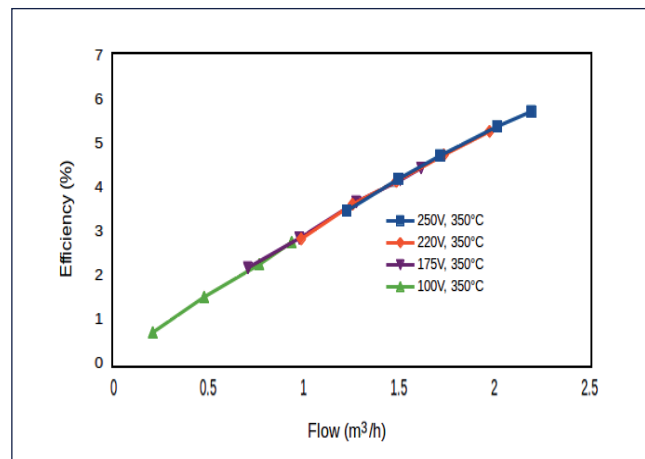


Fig. 3 Efficiency versus flow characteristics of annular linear induction pump

III.5 Modelling Atmospheric Dispersion of Sodium Aerosols for Consequence Analysis during Accidental Leaks

In a sodium cooled fast reactor any leakage of sodium in the secondary heat transfer loop may result in the production of large amount of aerosols. A mixture of sodium combustion aerosols (Na_2O , Na_2O_2) are generated in the case of sodium fires. They react with humidity to form sodium hydroxide (NaOH) which is corrosive, toxic and causes inhalation hazard for humans when the concentration exceeds 2 mg/m^3 . The NaOH aerosols transform to less toxic sodium carbonate and sodium bicarbonate aerosols by reaction with CO_2 and moisture prevailing in the atmosphere. In case of sodium fire scenarios, atmospheric dispersion of aerosols needs to be computed in distance ranges of few kilometers for assessing the environmental impact interns of inhalation hazard to the populations around the site as per regulatory requirements.

A kinetic model developed by CEA, France is coupled to a Lagrangian Particle Dispersion Model FLEXPART for representing the rate of conversion of NaOH to sodium carbonate (Na_2CO_3) during the transport and dispersion of aerosols in a range of few kilometers. The kinetic model is based on the CO_2 reactive absorption and the two-film theory and the physical state of NaOH aerosols at various RH conditions considering the CO_2 absorption at the particle external surface. To couple the kinetic model with the atmospheric dispersion model the variation in sodium hydroxide conversion rate (X_B) is expressed as a function of reaction time by a polynomial regression equation with six parameters A, A', B', A'', B'', C.

$$X_B = A \cdot \ln(1+t) \cdot [A' \cdot t B' + A'' \cdot t B''] + C \quad (1)$$

Equation (1) expresses the X_B as a function of time (t) uniquely for various RH and temperature conditions which may vary during an actual sodium fire scenario. As an example Figure 1 shows the polynomial fit [$A=-1.43$, $A'=0.869$, $B'=-0.617$, $A''=0.869$, $B''=-0.617$ and $C=1.22$] for initial particle size (R_0) of $2 \mu\text{m}$, $T = 33^\circ\text{C}$ and $\text{RH}=60\%$ typical of environmental conditions at Kalpakkam site.

In FLEXPART the pollutants are tracked as they move in the atmosphere and the motion of the parcels is treated as a random walk process. The turbulent diffusion is estimated from Lagrangian time scales estimated using the boundary layer parameters predicted by a mesoscale atmospheric model or observations. The aerosol concentration is obtained by computing the statistics of the trajectories of a large number of the

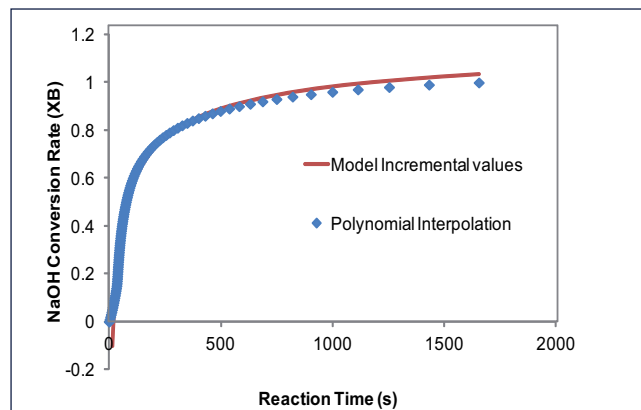


Fig. 1 Polynomial interpolation of the kinetic model for $R_0=2 \mu\text{m}$, $T = 33^\circ\text{C}$ and $\text{RH}=60\%$

parcels. The chemical conversion is incorporated in FLEXPART using particle mass, travel time of each particle and the polynomial interpolation equation (1) appropriate to each temperature and RH value.

The dispersion model with chemical kinetics is tested for the open sodium fire - atmospheric dispersion experiment conducted at Edaiyur, Kalpakkam site. The average meteorological parameters during the experiment were wind speed 5.3 m/s , wind direction $\sim 160^\circ \text{ N}$ and relative humidity 90% . The nature of aerosols during fire scenario is considered as pure NaOH with a MMAD of $4 \mu\text{m}$, density of 2.13 g/cm^3 and release rate of 8.2 g/s . Simulated aerosol concentrations at different sampling points along the plume centerline up to 400 metres compare well with measurements (Figure 2). The model concentrations at 90 metres are 0.8846 , 0.3962 and 0.4884 mg/m^3 for total aerosol, NaOH and Na_2CO_3 respectively against the actual measured total concentration of 0.6187 mg/m^3 .

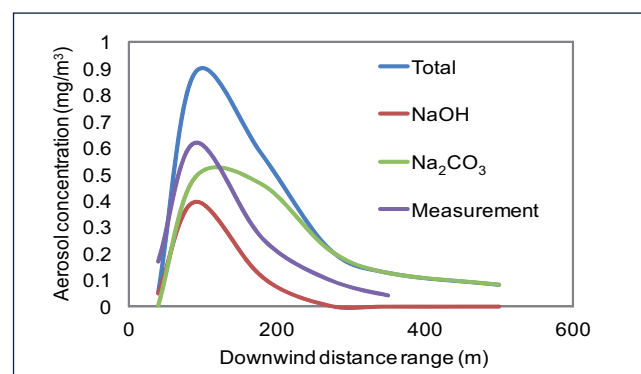


Fig. 2 Ground level aerosol concentrations simulated with FLEXPART

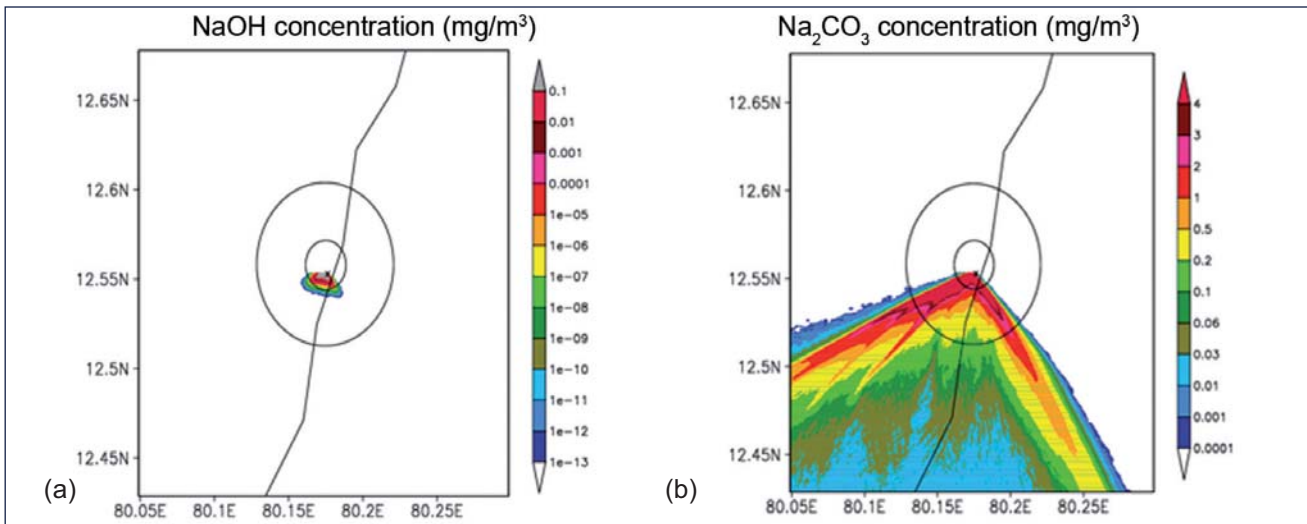


Fig. 3 Simulated aerosol concentrations (mg/m^3) (a) NaOH and (b) Na_2CO_3 in a domain of 12.5 km x 12.5 km for a twenty four hours release scenario for a stable atmospheric flow at Kalpakkam

The minute concentration of NaOH at 300 metres distance relative to that of Na_2CO_3 indicates almost complete conversion of NaOH to Na_2CO_3 at 300 metres. A simulation study is conducted using the coupled model to analyse the aerosol transport, dispersion and concentration distribution pattern for a postulated leak event in the Steam Generator Building (SGB) of Prototype Fast Breeder Reactor (PFBR). Simulations are conducted for typical days in different seasons representing the variability in the environmental parameters such as winds, atmospheric stability and atmospheric humidity at the site. A release rate of 163 g/s is assumed in FLEXPART for a typical sodium fire scenario of 140 t sodium leak in SGB. Figures 3a and 3b show the ground level concentration distribution for each aerosol species assuming a continuous release on a typical day 3 Jan 2013 with northeasterly stable flow. This indicates a spatially complex dispersion pattern under diurnally varying meteorological conditions at the site. The maximum concentrations of $0.4 \text{ mg}/\text{m}^3$ for NaOH

and $4.3 \text{ mg}/\text{m}^3$ for Na_2CO_3 are found at a distance of 0.5 km from the release location under stable conditions during winter season at the site. The concentrations are much smaller in all other meteorological conditions during other seasons. It is found that NaOH practically reduces to negligible concentrations ($<0.025 \text{ mg}/\text{m}^3$) beyond 800 metres due to rapid conversion to Na_2CO_3 which has significant concentrations of $0.5 \text{ mg}/\text{m}^3$ up to 12 km from the release location. These Na_2CO_3 concentrations are below the threshold limit ($10 \text{ mg}/\text{m}^3$) for inhalation hazard. Downwind concentration of sodium aerosols from the release are shown in Figures 4a and 4b. The dispersion modelling study with aerosol chemical kinetics shows the transport and dispersion of aerosols generated under postulated accidental sodium leaks in sodium cooled Fast Reactor does not cause environmental impact due to low environmental concentrations resulting from rapid conversion to Na_2CO_3 in the actual atmospheric conditions.

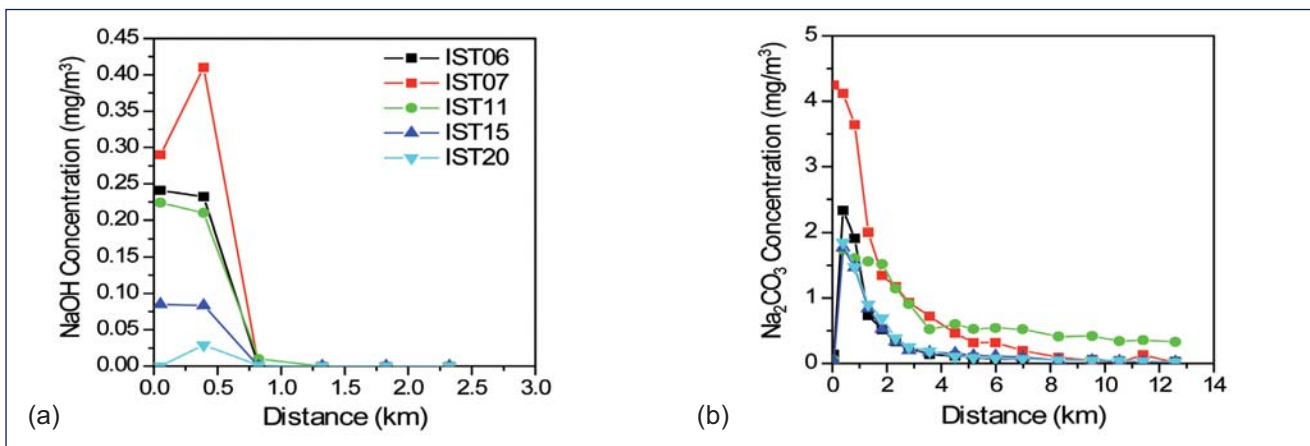


Fig. 4 Downwind concentration of sodium aerosols (mg/m^3) (a) NaOH and (b) Na_2CO_3 from the release location at 06, 07, 11, 15 and 20 IST on 3 Jan'13

III.6 Manufacture of Heater Vessel for 500kW Sodium Test Loop

A sodium heater vessel with 106 numbers of U type electrical heaters of 5.5 kW each was manufactured for heating sodium in the 500 kW sodium test loop. The overall size of the sodium heater vessel is 766 mm (OD) and 2315 mm in height. It was manufactured from AISI 316L material. The sodium heater vessel is required to handle high temperature sodium and hence requires high degree of leak tightness in the order of 1×10^{-8} Pa m³/s. Control of distortion due to welding 106 numbers of U-type electrical heaters with very close pitch under poor accessibility conditions was a challenging task.

The sodium heater vessel consists of cylindrical shell, tori-spherical dished end at both ends, lug supports, heater support plates, sleeves, inlet, outlet, cover gas and level probe nozzles. The tori-spherical dished ends are welded with cylindrical shell at both ends. The thickness ratio of dish end and outer sheath of U-Type heater is large, The sleeves are introduced between the dish end and the outer sheath of heater. The two hundred and twelve sleeves are welded with top dished end for welding with 106 U-type heaters as shown in Figure 1. The heaters are inserted through the sleeves, assembled and welded. The lug support pad plates are welded with cylindrical shell.

The cylindrical shell of size outer diameter 766 mm, inner diameter 750 mm, thickness 8 mm and height 1500 mm was formed using plate bending machine. Circularity of the shell was achieved using mechanical fixtures and spiders.

Long seam weld joint was carried out using gas tungsten arc welding process. The dished ends were cold formed by progressive forming technique, circularity and squareness was achieved by mechanical fixtures and machining. The dish ends were stress relieved at 1050 °C. The nozzles and sleeve locations were marked on the top dished end and holes were drilled. The two hundred twelve and sleeves of size outer diameter 19.5 mm, inner diameter 13.5 mm, thickness 3 mm and length 100 mm were machined with close dimensional tolerances. The machined sleeves were welded with top dished end. The sleeve with top dished end joint is a full penetration weld joint. Due to very close pith distance of sleeves on the top dish end, for better accessibility, all the 106 sleeves were first welded with the dish end. The weld joints were tested by ultrasonic testing method. The top dish end welded with sleeves was positioned on a suitable flat form at a height of 700 mm to facilitate easy access for welding. The heaters were assembled



Fig. 1 Manufactured sodium heater vessel

and the outer sheath of heaters and SS sleeves were seal welded on both the sides of sleeves. Sleeves with heaters at top side of dish end were welded in flat position (2F) and bottom sides of dish end were welded in over head position (4F). The heaters were welded sequentially from the centre to outer periphery to control distortion. The welding of large number of thin walled heaters in close pitch distance with top dished end, in an inaccessible location is a challenging task and have been welded successfully. The circular seam welding of bottom dish end, top dish end with heater assembly, nozzles, lug support plates etc. welded with the shell and the fabrication of sodium heater vessel was completed.

The machined sleeves, nozzles, shell, dish ends were subjected to dimensional inspection. The weld joints of sleeves with top dished end were subjected to all pass liquid penetrant examination. The long seam and circumferential seam welding of cylindrical shell and dished ends were subjected to 100% radiography. The heater insulation resistance was measured before and after welding with sleeve. The fabricated heater vessel was subjected to soap bubble test at 1 bar (g) and pneumatic test at 8 bars (g) using Nitrogen gas. Also, the heater vessel was subjected to helium leak test under vacuum and the leak rate was achieved $< 1 \times 10^{-8}$ Pa m³/s. Finally, it was subjected to pickling and passivation. The sodium heater was successfully manufactured meeting the specifications as given in Table 1.

Table 1: Specification	
Fluid handled	Sodium
Material of construction	AISI 316L
Design pressure	4 Bars (g)
Design temperature	600°C
Pneumatic test pressure	8 Bars (g)
Helium leak test	$< 1 \times 10^{-8}$ Pa m ³ /s

III.7 Thermal Hydraulic Simulation Rapid Voiding Under Severe Accident Condition in SFR

Understanding the dynamics of a nuclear power plant during various anticipated undesirable events that can occur during its lifetime is essential for establishing safety of the plant. Dynamics of a plant can be understood by computer simulation using plant dynamics codes. DYANA-P is a 1-D plant dynamics code for simulating dynamics in typical medium sized pool type Sodium cooled Fast Reactors (SFRs). Currently, it has single phase thermal hydraulic modules for simulating different systems of the plant from core to steam generators. However, coolant boiling may occur in the reactor core during Unprotected loss of flow accidents (ULOFA). To handle such scenarios, a model has been developed and incorporated in the DYANA-P code. Flow boiling phenomenon in liquid metals is different from that of water. Only a few experiments have been carried out around the world in this area and these data are used for the development of the model.

Neutronics, primary hydraulics and core thermal modules of DYANA-P code were modified to incorporate the boiling model. In neutronics module, it is assumed that the power generated in the core is assumed to be separable in space and time. The spatial variation of power is assumed to be unchanged during any operating condition as well as during transients. The time variation of power is calculated by solving the space averaged one energy group kinetics equation. Reactivity feedbacks are evaluated from temperature-reactivity coefficients (which in turn are obtained from material reactivity worth data) and Doppler constants as data. Numerical solution of the kinetic equations is obtained by prompt jump approximation for neutronic power and by simple finite difference in time for the equations of precursor concentrations. The total reactivity at any time is calculated by combining the external reactivity addition due to control rod movements along with various feedback reactivities due to fuel expansion, clad expansion, coolant expansion, Doppler effect, grid plate expansion, differential expansion between the main vessel and control rod support mechanisms and voiding of core.

The primary hydraulics module computes the steady state and transient hydraulics in the primary coolant circuit i.e. various flows, pool levels and pump speeds in the circuit. The solution of this model is decoupled from the solution of thermal model since hydraulics at any instant is not a strong function of temperature variation during the time step of integration. Buoyancy

head in the model equations are estimated from the most recently updated temperature distributions to make a good estimation of natural convection effects. The governing equations are obtained by making mass, momentum and torque balances of the components in the circuit. The pressure losses in the core flow channels are calculated by combining losses due to friction, gravity and acceleration of coolant. Appropriate correlations from literature are used to calculate various pressure losses during boiling. The flow regimes and heat transfer regimes used in the analysis are shown in Table 1.

Void fraction (α) is calculated with the expression shown below.

$$\alpha = 1 - \frac{1}{\phi_l}; \quad \phi_l^2 = 1 + \frac{20}{X_{LM}} + \frac{1}{X_{LM}^2}$$

Where ϕ_l is two phase friction pressure drop multiplier based on liquid flow and X_{LM} is Lockhart-Martinelli parameter. The core thermal module computes the temperature distribution in the fuel and blanket sub-assemblies of the core with power generation data and flow rate data for the sub-assemblies as input. One representative sub-assembly for each of the ten core neutronic zones is modeled in this module. Each such sub-assembly is axially meshed into different elements. Governing equations are obtained through the application of energy balance at each axial location. For coolant alone, energy balance is written in terms of enthalpy rather than temperature because the variable for coolant temperature becomes non-differentiable when there is phase change. The governing equations are discretized by finite difference method (FDM) and the resulting set of simultaneous linear equations is solved by the method of elimination.

Boiling is presumed to start at a control volume once the temperature of the coolant control volume reaches saturation temperature at that pressure. Thus single phase liquid heat transfer laws are used till this point.

Table 1: Flow regimes and heat transfer regimes

Void fraction (α)	Flow regime	Heat transfer regime
$\alpha = 0$	Single phase liquid regime	Single phase liquid regime
$0 < \alpha \leq 0.957$	Pre dryout regime	Pre dryout regime
$0.957 < \alpha < 1$	Post dryout regime	Post dryout regime
$\alpha = 1$		Single phase vapor regime

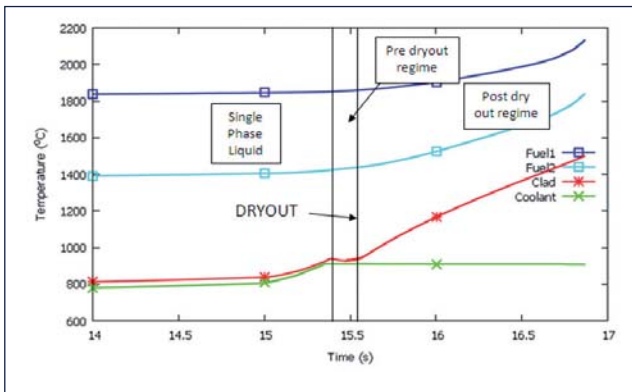


Fig. 1 Evolution of core temperatures at critical location

Coolant quality (x) is then obtained based on the enthalpy of the fluid based on the thermodynamic equilibrium quality relation.

Hydrostatic pressure head at each location is calculated at the end of each time step based on homogeneous density. Regime dependant heat transfer coefficients are used in this study to calculate the heat flux from coolant to clad. Dryout is assumed to occur when void fraction exceeds 0.957, as per the literature data.

The event of Station Blackout with failure of all shut down systems is chosen for simulation with PFBR design data as reference. The event is simulated by making the drive torque for the pumps to be zero. Then the pumps coast down by spending the energy stored in its flywheel to impeller and friction work. During the transient, boiling starts at about 15 seconds in the top of the fifth neutronic zone representative sub-assembly and propagates towards the middle of the core. The simulation is stopped when the peak clad temperature reaches the melting point at the middle of active core in this sub-assembly. This location is termed as “critical location” henceforth in discussion. From Figure 1, it is observed that clad temperature at the critical location increases rapidly after dryout is reached and reaches melting point of 1500°C within ~2 seconds from dryout. Figure 2 shows the axial temperature distribution in the sub-assembly at the end of the simulation.

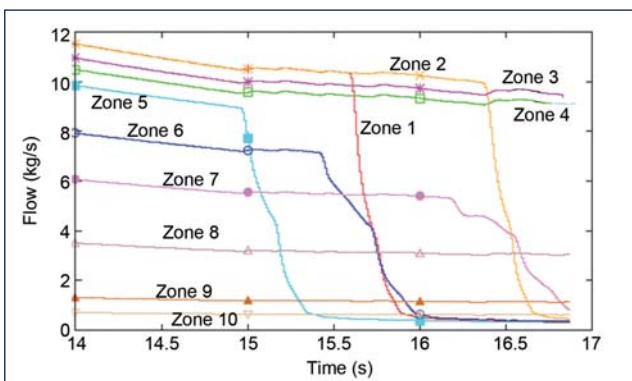


Fig. 3 Evolution of flow rates in various radial zones

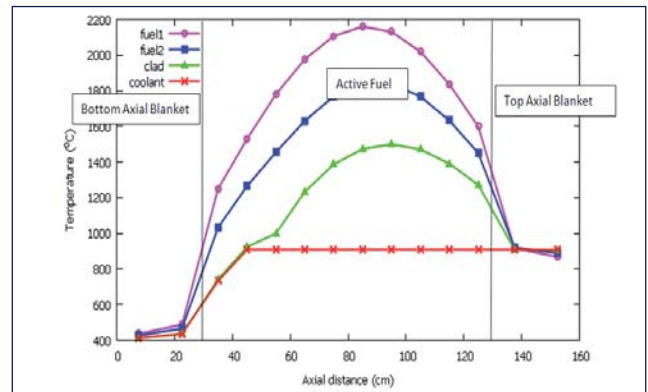


Fig. 2 Axial temperature distribution in critical sub-assembly at the end of simulation

From Figure 3, it is observed that the flow reduces drastically once boiling starts in a particular sub-assembly due to drastic increase in the two phase flow resistance. During simulation, boiling has started in all the fuel sub-assemblies.

From Figure 4, it is seen that after boiling initiation, the total reactivity increases drastically mainly due to the contribution from sodium void feedback coefficient. The total reactivity is about 250 pcm at the end of simulation. As a result, the reactor core power increases drastically and it is about 3.3 times of the nominal core power at the end of simulation.

During station blackout event with failure of both shutdown systems, it is seen that boiling starts at the top of the sub-assembly at about 15 seconds and the void propagates from top to center of the core in all the boiling channels rapidly. Within a few seconds of boiling initiation in the core (~2 seconds), clad failure in the middle of the core is predicted. The power of the reactor at this point is ~3.3 times that of nominal value. The current simulation is stopped when there is clad failure. Melting models would be required to continue the simulation further. It is expected that there would be a Core Disruptive Accident following this postulated event. In future, the model for severe accident propagation after clad failure will be developed to know the consequences in detail. This would in turn be useful for enhanced safety analysis of future SFRs.

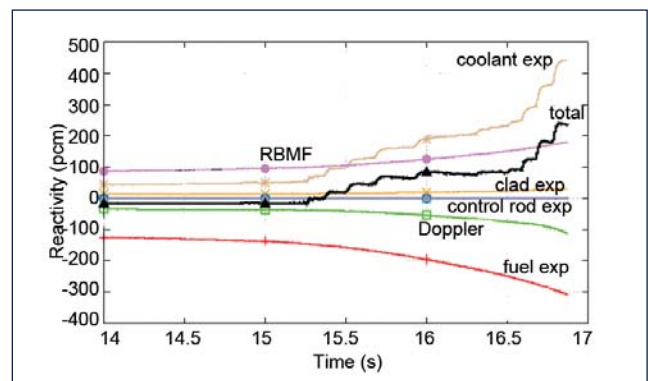


Fig. 4 Evolution of components of core reactivity

III.8 Thermal Hydraulic Investigations on Porous Blockage in a PFBR Fuel Pin Bundle

In a typical medium size sodium cooled Fast Reactor, each fuel sub-assembly has 217 pins, with 487 flow subchannels. Further, each fuel pin is wound with helical wire. Typical hydraulic diameter of the subchannel is ~3 mm. Large number of tiny subchannels combined with helical wire wrap enhances the possibility of blockages in fuel sub-assemblies. Any blockage would have adverse impact on availability and safety of the reactor. To understand the thermal hydraulic consequence of such blockages in 217 pin bundle, detailed computational fluid dynamic simulations have been carried out with the aid of parallel computing facility. The computational fluid dynamic model has been validated against benchmark blockage experiment reported in literature. A blockage within the pin bundle can possibly take wide ranges for blockage radius, porosity, and mean particle diameter. Critical length of blockage that would result in local sodium boiling as a function of aforementioned blockage parameters has been estimated and the parametric zone posing risk of sodium boiling has been identified.

Geometric features

Nominal dimensions of PFBR fuel pin bundle considered are: pin diameter = 6.6 mm, wire diameter = 1.65 mm and helical wire pitch = 200 mm. The number of axial pitches considered is 7, consisting of two pitches of axial blanket (one at the bottom and one at the top) and five pitches of fuel region. Wire surface and hexcan wall are adiabatic. A non uniform heat flux which is a function of

axial distance obtained from neutronic calculations for 217 pin bundle is applied over all the pins. Detailed grid independence study was carried out and expanded view of mesh around fuel pins in the 217 pin bundle is shown in Figures 1a and 1b.

Sub-assembly flow reduction due to blockage

As the pressure drop available with the coolant pump is fixed, the excess resistance due to blockage will result in sub-assembly flow reduction. This reduction in flow is calculated with available in-house experimental data on pressure drop and flow rate for various components along the length of the sub-assembly. The maximum pressure drop due to blockage (0.13 bar in the case of 4-row blockage) is small compared to the total pressure drop (5.15 bar). It is found that for most of the blockage cases studied, the flow reduction due to blockage is <1% and the associated bulk coolant temperature increase at the sub-assembly exit is < 2 K. The maximum flow reduction occurs for 4-row blockage, which is < 2.5%.

Critical length of blockage

For any blockage configuration (i.e., porosity, radial extent, particle diameter), the maximum clad temperature within the domain will increase with increase in axial length of the blockage. At critical axial length of the blockage, the maximum clad temperature will reach saturation temperature of sodium. In this study, the

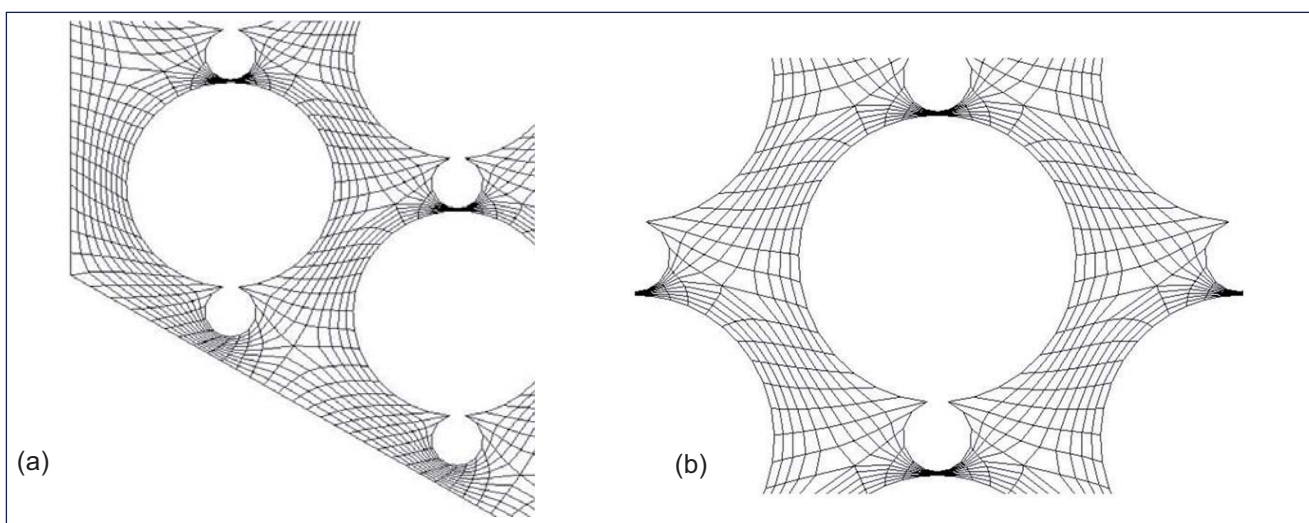


Fig. 1 Computational fluid dynamic mesh in (a) corner, peripheral and (b) central subchannels

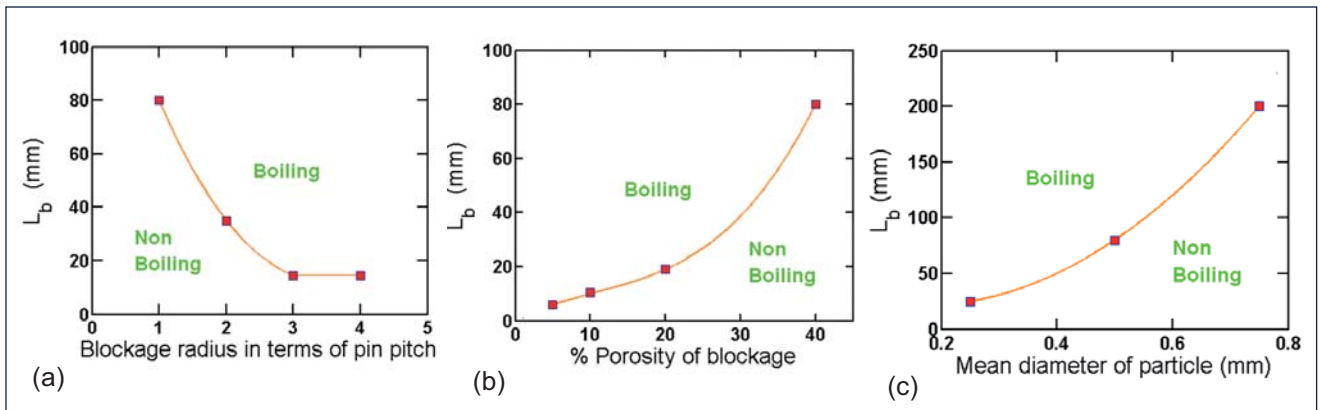


Fig. 2 Critical length as a function of (a) blockage radius ($\max T_{cp}=1186\pm 32$ K) (b) blockage porosity ($\max T_{cp}=1194\pm 35$ K) and (c) particle diameter ($\max T_{cp}=1166\pm 7$ K)

critical length of blockage for various configurations has been estimated and are depicted in Figures 2a to 2c.

Detectability of blockage

In a typical sodium cooled Fast Reactor, the temperature of sodium exiting from every fuel sub-assembly is continuously monitored. A 10 K rise in the sodium temperature leads to reactor trip, while a 5 K rise actuates an alarm. From heat balance, these global rises in outlet sodium temperature correspond to flow reduction of 6 % and 3 % respectively. It is found that the maximum reduction in flow among the various cases analyzed is <2.5 %. Thus, presence of internal porous blockages cannot be detected by global sub-assembly outlet temperature monitoring, before the onset of boiling.

Temperature non-uniformity at pin bundle outlet

Figures 3a to 3c show sodium temperature profile at the exit of unblocked and blocked pin bundles. It could be

seen that for an unblocked case the temperature profile is almost uniform throughout the section, whereas large peak in sodium temperature occurs in the cases with internal blockages. Larger the radial extent of blockage, higher is the magnitude of the peak temperature. The peak outlet temperature in a four row blockage is 160 K higher than that in unblocked case (Figure 3c). This local peak in sodium temperature could be used as a source for early detection of the blockage with sophisticated instrumentation.

Thermal hydraulics of PFBR fuel sub-assembly with internal porous flow blockages have been investigated by a special purpose computational fluid dynamics tool. It is seen that for all blockages that can lead to local sodium boiling, the total flow reduction is < 2.5%. This suggests, that global bulk sodium temperature monitoring at the outlet of the sub-assembly is unlikely to detect slow growing internal porous blockages.

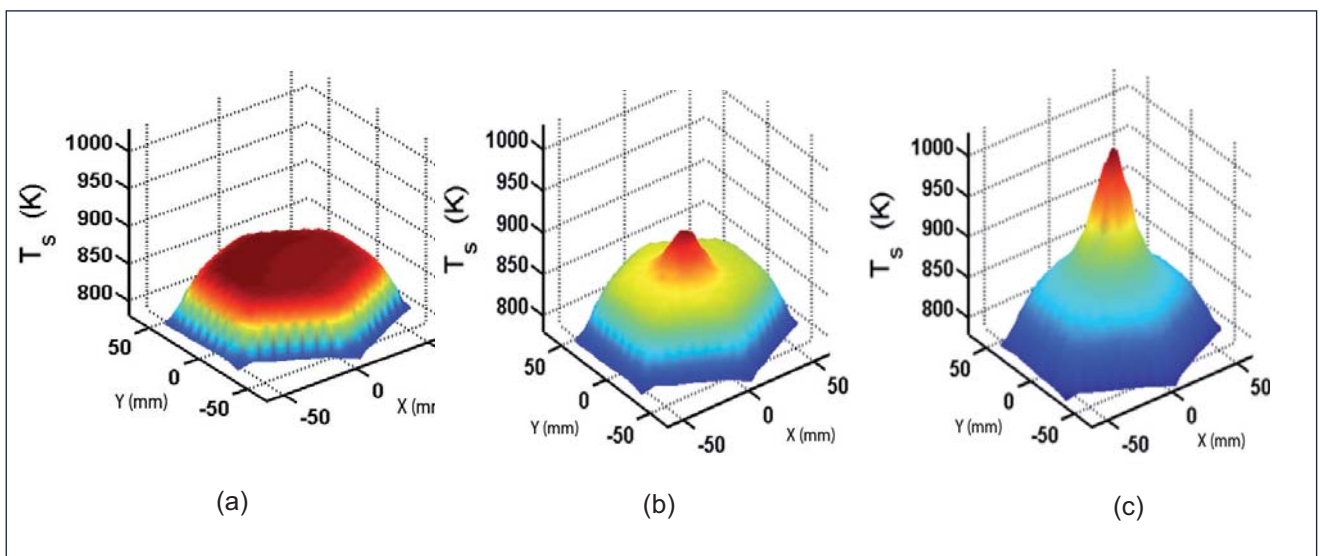


Fig. 3 Temperature profile at bundle exit in (a) unblocked sub-assembly, (b) sub-assembly with 2-row blockage and (c) sub-assembly with 24-row blockage

III.9 Secondary Side Flow Zoning in IHX of Future FBR: A Coupled Thermal Hydraulic Investigation

Future fast reactors could be of 1500 MWt capacity and of pool type design. In these type of reactors, there could be four intermediate heat exchangers (IHX) dipped in primary sodium pool. IHX is a shell and tube, counter current vertical heat exchanger having 3900 straight tubes arranged in 25 rows (Figures 1 and 2). The primary sodium enters into the IHX radially, takes a downward turn, flows vertically down and leaves IHX radially. Due to the radial entry/exit of primary sodium in the shell side of IHX and counter current flow of secondary sodium in the tube side, the straight tubes are subjected to uneven temperatures. Due to possible unequal thermal expansion of the tubes between the top and bottom sheets, the tubes are subjected to buckling or pull out loads. Hence, it is essential to determine the possible secondary side flow zoning options, which will reduce the differential temperature load on the IHX tubes and also the variation in secondary outlet temperature. Towards this, a hybrid 1-D network model and a coupled 2-D porous body based computational fluid dynamics model have been developed. Using these models, the required flow zoning has been finalized.

For the 1-D network model, primary sodium flow field is assumed, considering 25 radial rows and uniform axial velocity beyond the window zones. Cross flow is considered only in the inlet/outlet windows. Velocity weighted effective heat transfer coefficient is considered in the cross flow region. Temperature field in primary and secondary sodium are solved as a coupled problem. This 1-D network model was found to be computationally less intensive and hence was used for parametric studies.

To assess the accuracy of the network model a 2-D axi-symmetric computational fluid dynamics model of the IHX has been developed. Because of the computational difficulties associated with meshing and velocity field resolution through large number of tubes and compact arrangement of bundle, a porous body formulation has been adopted and the pressure drop encountered due to the presence of the tubes is specified as additional resistance in the momentum equations. The flow and temperature distributions of intermediate sodium in the tubes and primary sodium on the shell side have been solved as a conjugate problem using commercial CFD code FLUENT.

The primary sodium temperature distribution within the IHX predicted by computational fluid dynamics model is depicted in Figure 3 for the case of uniform secondary

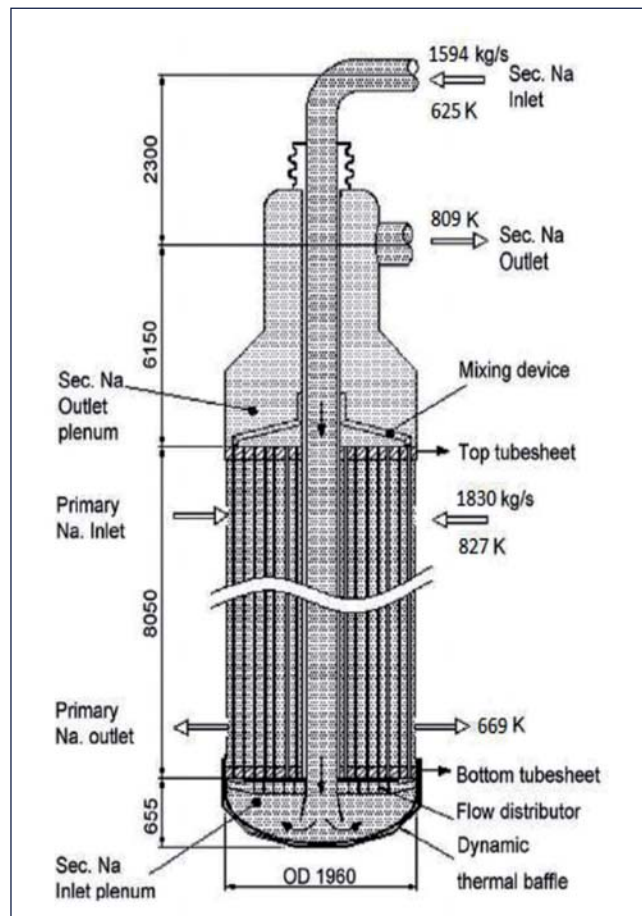


Fig. 1 Schematic of IHX

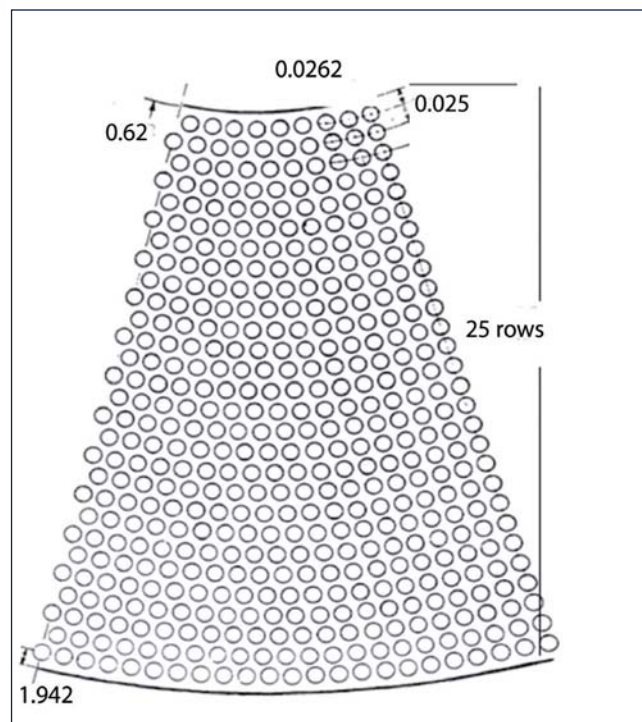


Fig. 2 IHX tube array – top view

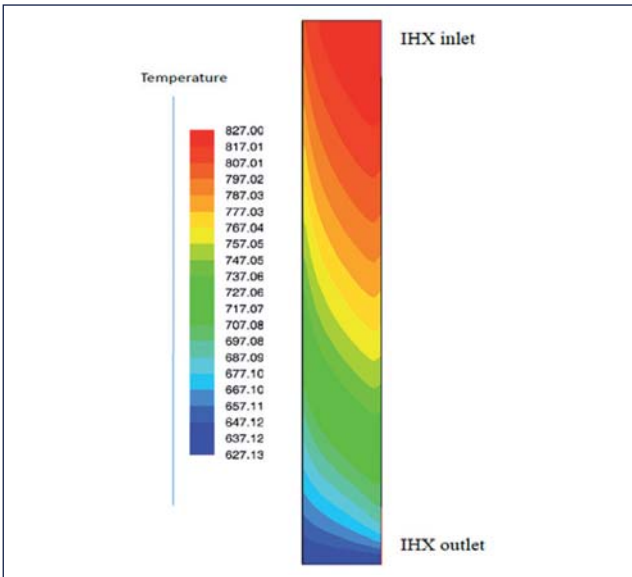


Fig. 3 Primary sodium temperature (K) in intermediate heat exchanger tube bundle for uniform flow

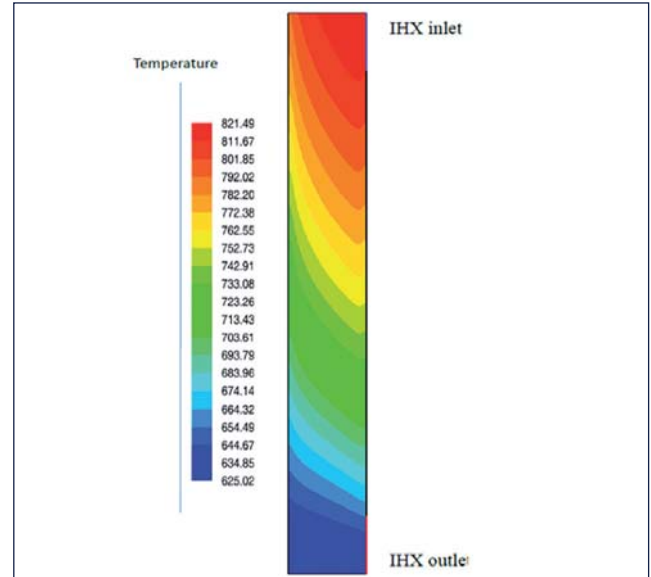


Fig. 4 Secondary sodium temperature (K) in intermediate heat exchanger tube bundle for uniform flow

flow in the tubes. The corresponding secondary sodium temperature field is depicted in Figure 4. For uniform secondary sodium flow through the tubes, the inner rows of tubes experience lower temperature of primary sodium and outer rows experience hot sodium. Hence, in this case the secondary sodium outlet ΔT between the outer and inner rows of the tube bundle is found to be 38 °C which is very high.

To obtain a nearly uniform temperature distribution at the outlet of secondary sodium, it requires more sodium flow in those rows which experience hot primary sodium to avoid the sharp temperature gradient at the secondary side outlet. Therefore, a detailed parametric study has been performed to find out the best flow zoning option to reduce the temperature gradient to a minimum acceptable value. Two flow zoning options investigated and the corresponding secondary sodium

outlet temperatures are shown in Figures 5 and 6 respectively. It was also seen that the predictions by the network based 1-D model are very close to that of the computational fluid dynamics model.

Coupled thermal hydraulic models have been developed for investigation of flow and temperature fields in intermediate heat exchangers of future FBR. Using the network model, an optimum secondary side flow zoning has been arrived at. The findings of the network model have been validated using the porous body based computational fluid dynamics model. It is found that there is a large temperature difference in the tube temperature between the inner and outer rows. The ΔT between inner to outer rows of tubes and the bulk of the tube bundle is 31°C when the secondary sodium flow through the tubes is uniform. This value reduced to 6°C with an optimum secondary side flow zoning.

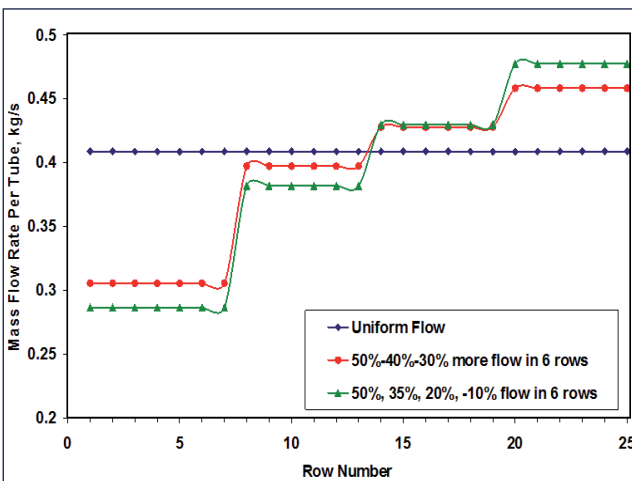


Fig. 5 Secondary sodium mass flow zoning determined by network model

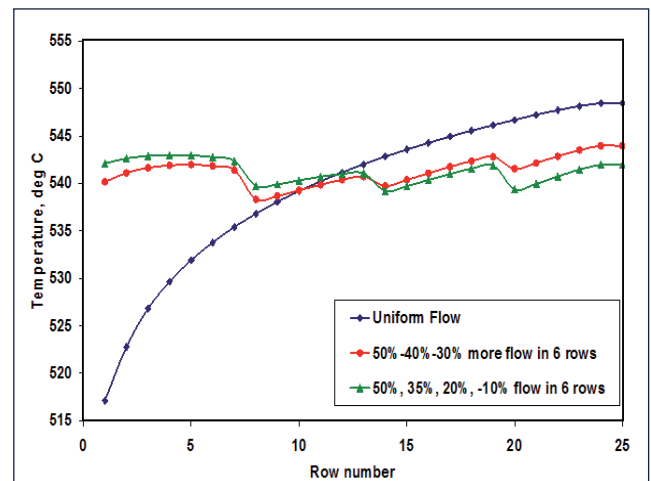


Fig. 6 Secondary sodium outlet temperature distribution using computational fluid dynamics model

III.10 Study of Reactor Hot Pool Velocity Pattern using 5/8 Scale Water Model

Thermal hydraulic studies for primary circuit of Sodium cooled Fast Reactor (SFR) plays an important role towards generating a safe and economic design. Argon entrainment into the sodium pool of the reactor is one such important hydraulic issue in the reactor design which needs attention from safety as well as operational point of view. Free surface flow pattern and the magnitude of velocity influence the gas entrainment from free surface. The free surface flow pattern can be mapped using scaled down water model studies. The present study has been carried out in a 5/8 scale model of FBR primary circuit using water as simulant.

The experiment has been carried out by maintaining Froude (Fr) number similitude which is the dominant non dimensional number to be respected for hydraulic studies with large free surface. The distortion in Reynolds number is neglected owing to the turbulent flow regime in the hot pool. The flow rate estimated in the model is 2200 m³/h. The photograph of the 5/8 scale model has been shown in Figure 1.

The free surface velocity is measured by two different types of instruments. These instruments are ultrasonic velocity profiler and propeller anemometer which use different principles for measurement of velocity. The resultant velocity is calculated from these velocity components. It is found that the measured velocity values by these instruments are comparable. A vector plot of the velocity vector measured by propeller anemometer across the hot pool is shown in Figure 2.



Fig. 1 5/8 scale water model

It can be seen from this figure that the flow at free surface takes place from inner vessel towards the control plug. A contour plot of resultant velocity magnitude at the free surface generated from the linearly interpolated measured velocity data by ultrasonic velocity profiler is shown in Figure 3. The maximum free surface velocity in the model is found to be around 1 m/s. The extrapolated value of maximum free surface velocity from the experimental result for the reactor is estimated as 1.24 m/s. This value is comparable with PFBR results whose maximum free surface velocity was found to be 1.16 m/s which was estimated from 1/4 scale SAMRAT model experiments.

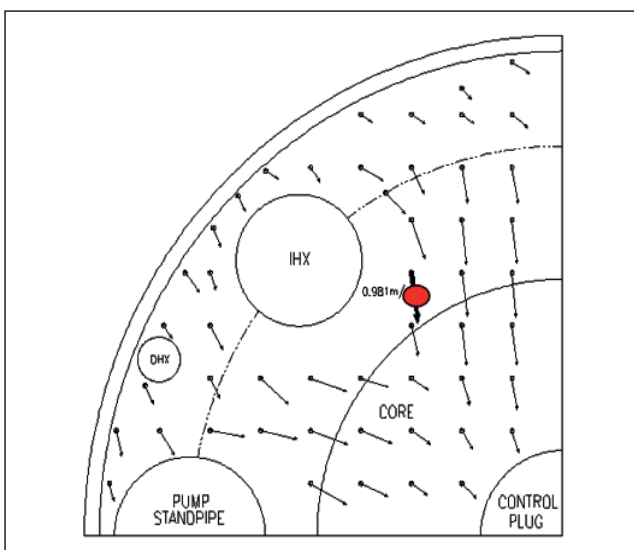


Fig. 2 Vector plot for the hot pool velocity

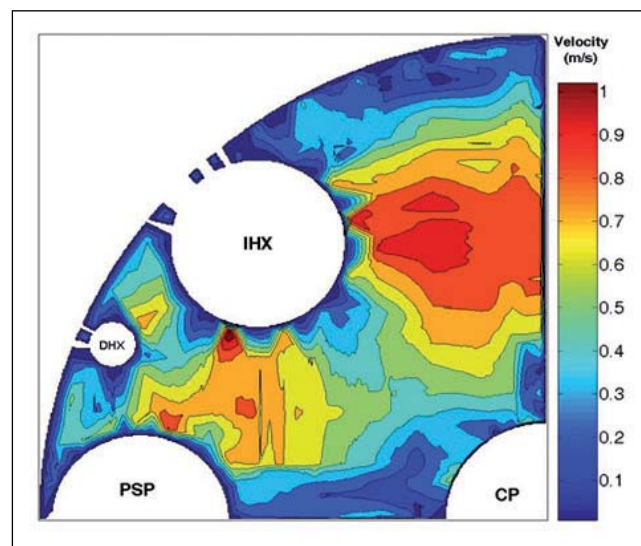


Fig. 3 Contour plot of velocity magnitude at free surface

III.11 Numerical Study on Impurity Precipitation in Cold Trap and its Validation by Experiment using Surrogate Solution

Cold traps are used for online purification of sodium in FBRs. Cold trap works on the principle of crystallization and precipitation of oxides and hydrides of sodium in a wire mesh of cold trap. A numerical model is developed in order to predict the precipitation pattern over the wire mesh of a cold trap under any given conditions of flow, temperature, dissolved impurity levels and mesh design. Numerical thermal hydraulic studies are carried out to evaluate the flow and temperature distribution of sodium in wire mesh using a commercially available computational fluid dynamics tool. With a given inlet impurity, numerically derived velocity and temperature distribution, the impurity precipitation in a wire mesh packed cold trap is quantified with a numerical simulation code.

Mass transfer equation and empirical correlations were used for the development of the numerical model. These correlations will impart uncertainties in the prediction of precipitation pattern. This suggests that predictive capability of the model for impurity precipitation in wire mesh packed cold trap should be validated under controlled experiments. These experiments were conducted with surrogate fluid in wire mesh packed unidirectional flow system instead of liquid sodium. Sodium and its impurities trapped in wire mesh being highly reactive to air, will oxidize when exposed to atmospheric conditions and leads to safety issue and wrong quantification of impurities deposited. Potassium chlorate is selected as a surrogate fluid to perform the experiments. The point of consideration while selecting a surrogate fluid is mainly the variation of relative solubility with respect to base temperature.

An experimental cold trap packed with ten equal segments of wire mesh is designed to study the precipitation of potassium chlorate on wire mesh packing. A photograph of the experimental setup is shown in Figure 1. Saturated solution of KClO_3 at required saturation concentration was passed through wire mesh of the cold trap and cooled to a temperature less than saturation temperature using external jacket forced circulation water. When the solution reaches saturation temperature KClO_3 starts depositing over the wire mesh. Flow through the cold trap was maintained till appreciable reduction in the flow was obtained. The cold trap was then dismantled and each segment of wire mesh was analyzed.



Fig. 1 Experimental setup

It was observed that deposition is increasing logarithmically along the length and it is maximum at the end of the cold trap. Outer radial region of the wire mesh have more deposition compared to inner region. This trend of precipitation pattern is observed both in the experimental and theoretical analysis. Graphical representation of comparison of experimental and theoretical results is shown in Figure 2. Percentage deviation between experimental and theoretical data was estimated and it was observed that 79% of data falls between deviation of -20% and +20%, 35% of data falls between deviation of -10% and +10%. So, the experimental results of precipitation pattern are fairly in good agreement with the theoretical prediction of precipitation pattern over the wire mesh. Thus, the numerical code for predicting the impurity precipitation pattern is validated by experiments with $\text{KClO}_3\text{-H}_2\text{O}$ solution and hence the numerical code can be used in future to predict impurity precipitation pattern in a cold trap with good accuracy.

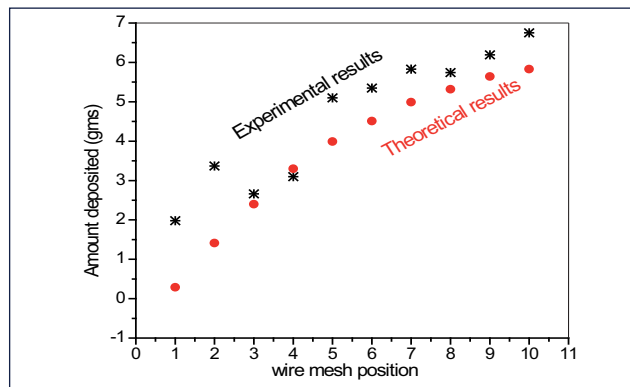


Fig. 2 Comparison of experimental and theoretical results

III.12 Performance Assessment of the Full Scale Integrated Cold Trap Model in Sodium

To avoid the transport of radioactive sodium outside the reactor vessel, in-vessel sodium purification is planned for future fast breeder reactors and thus enhancing the safety. The total purification system will be immersed in the hot sodium pool of the reactor and this leads to advantage in radiological, safety and economical aspects. The challenging part of the design is the achievement of sodium cold point temperature in the order of 110°C inside the hot pool sodium with temperature of 547°C within a short radial gap of 300 mm.

The conceptual design of integrated cold trap (ICT) is shown in Figure 1. ICT contains an integral assembly of cold trap wire mesh, economizer, annular linear induction pump and a permanent magnet flow meter (PMFM). Annular linear induction pump takes sodium from the hot sodium pool and passes to the tube side of economizer through the flow meter. After transferring heat in the tube side, sodium will be further cooled by external jacketed nitrogen circuit and cold sodium flows through the wire mesh region of cold trap. The impurities will be precipitated over wire mesh and the purified sodium returns back to the hot sodium pool through the shell side of economizer.

A full scale model of ICT was manufactured to carryout performance assessment in sodium before implementing the design in the reactor. The testing was performed in the test vessel - 3 of large component test rig (LCTR) in Engineering Hall – III which simulates the reactor hot sodium pool. Experiments were conducted in ICT to assess the heat transfer performance, mass transfer performance and the behavior of the system under various transient conditions.

The sodium in the loop was heated by immersion heaters provided in heater vessel and circulated through test vessel which simulates reactor hot pool. After filling sodium at 200°C in the test vessel, sodium flow rate at $2\text{ m}^3/\text{h}$ was circulated through ICT. The cold point temperature of the cold trap was maintained around 120°C during the operation. After achieving the steady state conditions, the sodium pool temperature was gradually raised upto 547°C in steps. At each sodium pool temperature, the cold point of 120°C was achieved and heat transfer performance of ICT was studied. At 547°C , 0.322 kg/s nitrogen flow rate was required to achieve cold point of 120°C inside the cold trap. The nitrogen temperature was increased

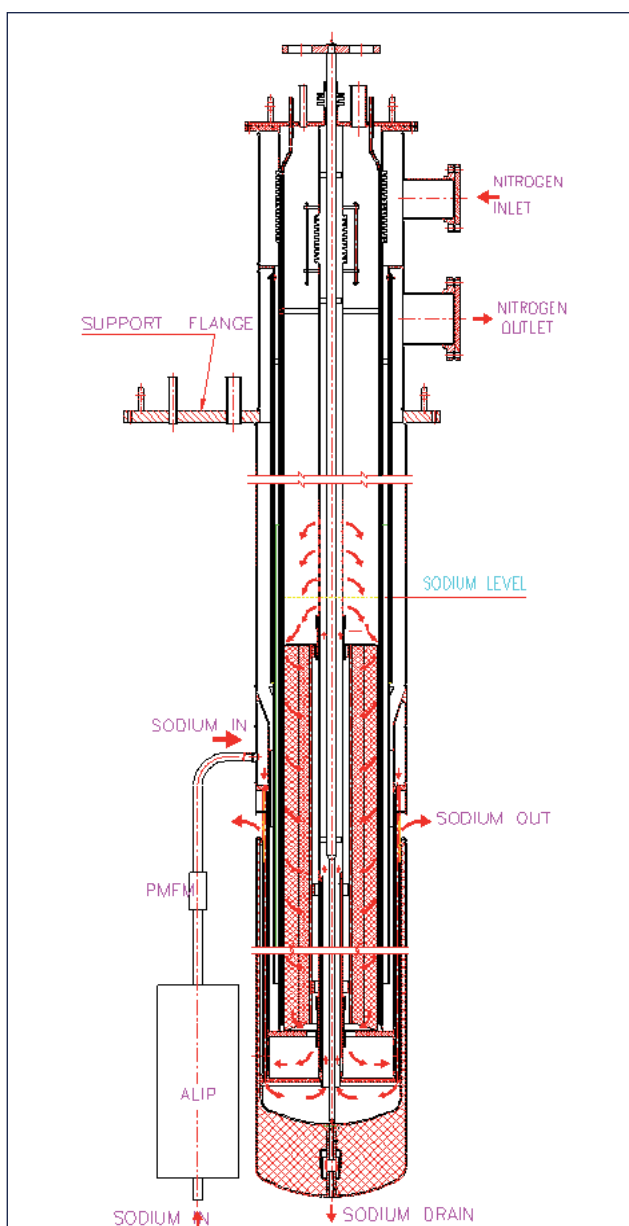


Fig. 1 Schematic configuration of integrated cold trap

from 54 to 235°C during the process. The total heat removed from sodium in ICT was 60 kW . Thus the establishment of cold point in the order of 120°C in the sodium pool temperature in the range of 200 to 547°C was demonstrated. Design calculations with operating conditions show a heat transfer from sodium to nitrogen as 72 kW . The difference between experimental and design calculation is mainly due to the uncertainties in heat transfer correlation and material properties like thermal conductivity of insulation used for these calculations.



Fig. 2 Integrated cold trap

The behavior of the system during transient conditions due to specific incidents on design basis events was studied. The effect of inadvertent tripping of sodium pump was studied. The sodium pump was tripped from normal operating conditions when the sodium pool temperature and cold point temperature was 547 and 120 °C respectively. Nitrogen flow rate was controlled to maintain the required cold point temperature of ICT. During this study, the stability of cold point with nitrogen cooling and without sodium pump in operation was confirmed.

The response of ICT on failure of sodium pump as well as nitrogen blower was also studied. The sodium pump and nitrogen blower was simultaneously tripped from the normal operating conditions. Then the heating of wire mesh region was continuously monitored. The

time taken for rise in cold point from 120 to 160 °C was around 50 minutes and 120 to 400 °C was 7 hours. In the event of shutdown of ICT resulting heating rates are lower hence several hours would be available to examine the situation and take the necessary steps. After conducting this study, sodium pump and nitrogen blower was started simultaneously when static sodium inside ICT was around 420 °C. Initially sodium flow rate was maintained around 0.15 kg/s and gradually raised to 0.5 kg/s. The nitrogen flow was adjusted to maintain the cold point temperature. During this startup studies from trip condition, the time taken to reduce the cold point from 420 to 120 °C was around 4 hours.

After completing the steady state and transient heat transfer studies of ICT, the impurity removal performance was studied by experiments. Loading of sodium oxide and hydride impurities in ICT was carried out in batches. The impurities were imparted to the 16,000 kgs of flowing sodium from the existing cold trap in LCTR. This was achieved by circulating sodium at required temperatures for sufficiently less time to get a saturated solution corresponding to circulating sodium temperature. The dissolved impurities were trapped in ICT. There were 10 batches of experiments conducted and the total quantity of impurities trapped in ICT was 5.289 kg (1.917 kg of hydride and 3.372 kg of oxide). The impurity loading capacity of ICT (volume ratio of impurities and wire mesh) was reached around 1.78%.

After loading of impurities in ICT, dissolution studies were carried out. During this study, sodium pump was stopped after reaching normal operating condition. The cold point temperature was continuously monitored and was allowed to rise from 120 to 450 °C in seven days by controlled nitrogen flow. At 120 °C cold point temperature, the dissolution rate was almost negligible. At cold point temperature of 450 °C in ICT, the dissolution of sodium oxide and sodium hydride from ICT to the sodium pool was estimated as 1.445 mg/s and 0.898 mg/s respectively.

The experimental observation shows that the performance of full scale model of ICT is in line with the design expectations (Figure 2). The cold point temperature of ICT in the order of 120 °C was established in the sodium pool temperature is in the range of 200 to 547 °C. The behavior of the system during transient conditions due to specific incidents on design basis events like failure of sodium pump and safety actions was studied. The purification of 16,000 kgs of sodium was experimentally demonstrated. The overall performance of newly developed ICT was satisfactory.

III.13 Investigation of Natural Convection during Post Accident Scenario

In case of a hypothetical core disruptive accident (CDA) or whole core meltdown in a Fast Breeder Reactor (FBR), the molten core and structural material (corium) will come in contact with the cold pool sodium leading to molten fuel coolant interaction, fragmentation of debris and settlement of debris as a bed on the core catcher provided at the bottom of main vessel. Heat removal from this debris is very crucial to avoid re-melting of the debris, which may lead to formation of critical fuel mass and breach the main vessel. Hence, assurance of post accident heat removal towards maintaining coolable geometry needs to be demonstrated. A facility for post accident thermal hydraulics (PATH) has been setup, to investigate continuous heat removal capability of core catcher through natural convection with scaled reactor internals simulating the heat source and heat sink using water as coolant. Photograph of post accident thermal hydraulics facility is shown in Figure 1. The facility has been commissioned with all internals and integrated with model decay heat exchangers and cooling loop. Numerical model is developed to study the natural circulation pattern during post accident phase. Experiment has been carried out and the results have been validated with numerical predictions.

The setup consists of a test vessel which is 1:4 geometrically scaled model of PFBR main vessel with internals like inner vessel, core support structure and grid plate. The inner vessel was made in split type assembly for ease of handling and erection in the main vessel. A monorail assembly of two tonnes capacity was also fabricated and erected for handling the internals. Six heater modules in sectors, each of 16 kW capacity were mounted on the core catcher plate. Two 1:4 scale model decay heat exchangers were also erected on the top of the main vessel to simulate decay heat removal. The basic governing equations of unsteady turbulent fluid flow include the transient form of RANS equations for mass, momentum and energy conservation and the equations for turbulent kinetic energy (k) and its dissipation rate (ϵ). A 2-D axi-symmetric model of the 1:4 scaled geometry of the reactor with reactor internals is developed for simulating the turbulent natural convection phenomenon in the pool. Since the external cooling of the safety vessel is not considered, outer surface of the main vessel is insulated with glass wool. A gap depicting the core meltdown has been modelled in the grid plate



Fig. 1 Photograph of the experimental facility

to provide a path for heat transfer from lower pool to the upper pool. Symmetric boundary conditions were imposed on the vertical axis. No slip boundary conditions were used for the entire solid-fluid interface.

The numerical predictions of the thermal fields have been verified with the experimentally obtained data for similar heat source conditions. Heat flux of 18 kW was given at the heat shield plate. The temperature of the pool was initially at 304.5 K. Convective boundary conditions were given at the top wall of the vessel and the outer wall of the solid insulation. A heat transfer coefficient of $h=5 \text{ W/m}^2\text{K}$ and the ambient temperature of 307 K was taken.

Experimental validation of the developed numerical methodology has been carried out and the detailed agreement with experimental data is shown in Figure 2. These figures show the temperature variation along the central axis for the experimental core catcher assembly, where experimental temperature data points after one and two hours are plotted along with the numerically obtained curve for purpose of comparison. As observed here, the experimentally achievable transient temperatures slightly differ from that predicted by the computational studies, but the overall trend matches well within the limit taking the source temperature difference into consideration. Temperature distribution and maximum flow velocities

in the pool predicted numerically at steady state are depicted in Figures 3a and 3b.

For a typical case of isothermal boundary condition on heat shield plate (HSP) at 328 K, it is found that initially the maximum temperature is on HSP and the rest of the pool remains almost isothermal at initial conditions. With time, the heat starts diffusing into the pool and a variation in the pool temperature is observed. After 60 hours, the temperature at sink is 319 K (ΔT between source and sink being 9 K). After 180 hours, the temperature at sink is 323 K (ΔT between source and sink being 5K). Very slow change in temperature was observed beyond 180 hours. The steady state is declared at 360 hours where no significant changes are observed in the axial temperature. The difference in source and sink temperature at steady state is found to be ~ 4 K.

Post accident thermal hydraulics facility has been setup to investigate continuous heat removal capability of core catcher with scaled reactor internals simulating the heat source and heat sink using water as coolant. The facility has been commissioned with all internals and integrated with model decay heat exchangers. Numerical model is also developed to study the natural circulation pattern during post-accident phase. Experiments have been completed and the results are validated with numerical predictions and found to be satisfactory. Temperature

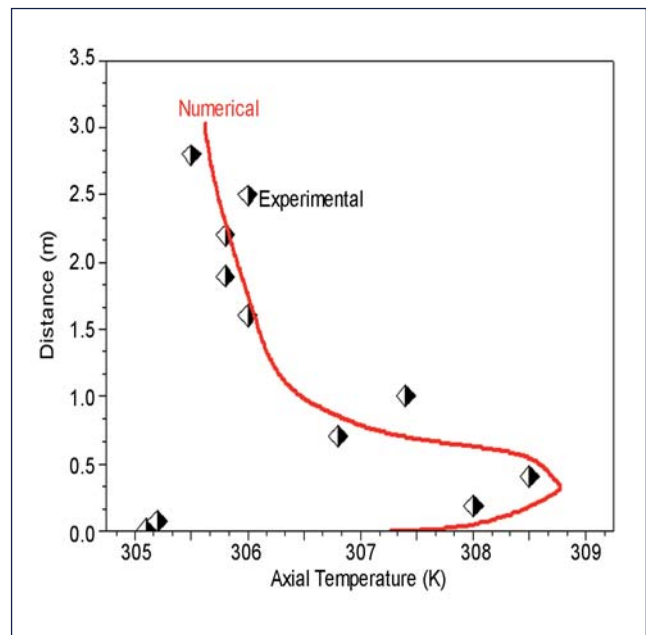


Fig. 2 Transient temperature after two hours

distribution and maximum flow velocities in the pool are observed at regular time intervals. Initially, flow instabilities are observed in the chimney region. The maximum fluid velocity decreased by 35% at steady state as compared to initial hours. However, significant amount of heat is transferred to the upper region of the pool rather accumulating near the triple point. These data helped in identifying the critical stagnant locations in the pool, which can lead to possible design modifications in core catcher assembly.

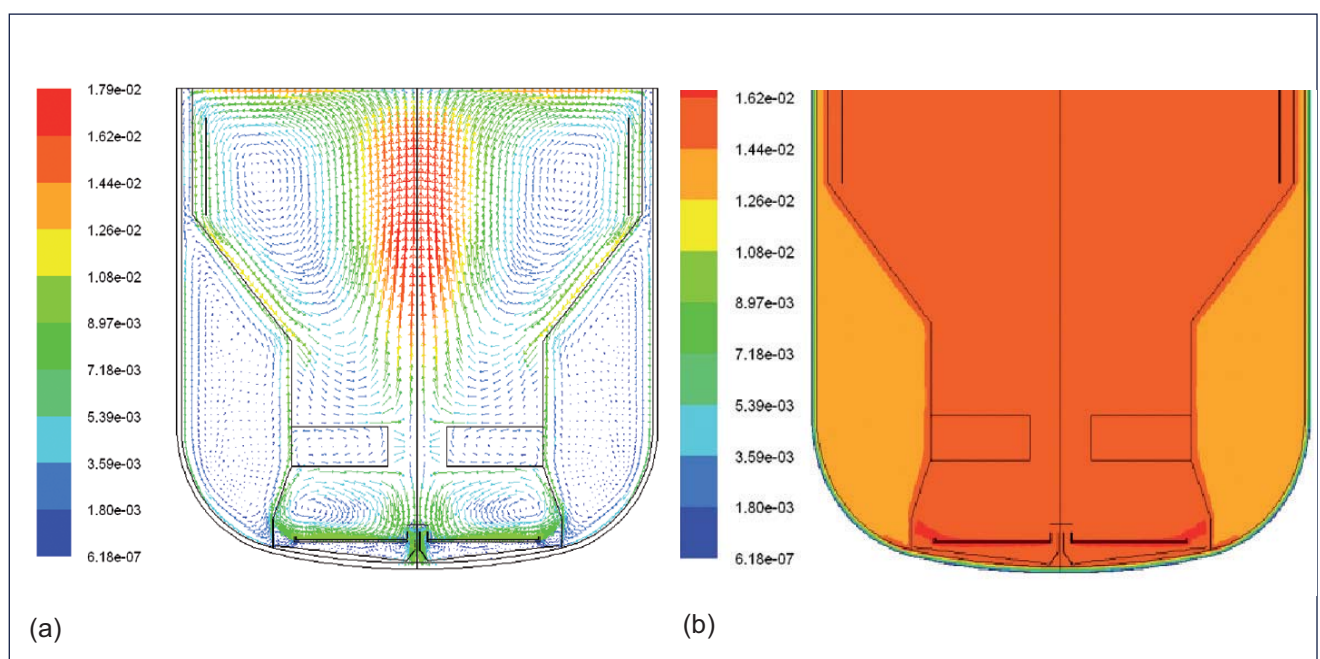


Fig. 3 (a) Velocity vectors (m/s) and (b) isotherm at steady state temperature of 328 K

III.14 Impingement Wastage Experiments with High Steam Leak Rates

In sodium heated steam generator, if a defect develops on one of the heat transfer tubes, steam/water leaks into sodium causing sodium-water reaction. This exothermic reaction damages the steam generator tube. If the leak is between 100 mg/s and 10 g/s (known as small leak), it damages an adjacent tube, which is called impingement wastage. Ultimately, it punctures the adjacent tube causing a larger steam leak which could result in hydrogen pressure build up, overheating and failure propagation to other adjacent tubes. Experimental studies are going on in Sodium Water Reaction Test Facility (SOWART), to understand the damage mechanism of wastage. In the first phase, steam injection experiments with a maximum leak rate of 1 g/s were performed. Once the methodology to conduct sodium-water reaction experiment safely was proven with lower steam leaks, it was planned to conduct steam injection experiments with leak rates higher than 1 g/s, which is the second phase of SOWART program. Three experiments with leak rates < 5 g/s but more than 1 g/s were carried out in SOWART, after obtaining necessary safety clearances.

Experiments were carried out in impingement wastage test section (Figure 1) which houses a leaking tube/leak simulator and an adjacent tube (target tube). Sodium flows from top to bottom inside impingement wastage test section in the same way as in the steam generator. Sodium water reaction will be instantaneously detected by acoustic detectors provided around the test section, and it will be further confirmed by the hydrogen meters installed in the meter section. During experiment, target tube was pressurized to 4 kg/cm² with argon. All of the three experiments were carried out with nickel leak tubes having mechanically drilled holes. Experiment 1 produced 0.54 mm deep wastage when duration of injection was only for 53 seconds. During experiment 2,

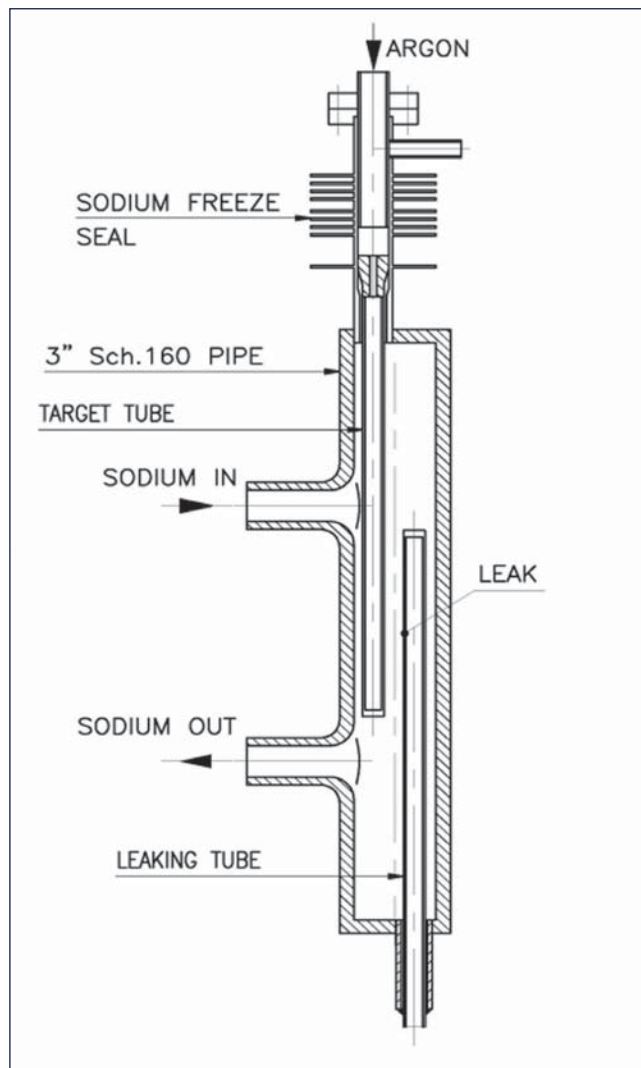


Fig. 1 Impingement wastage test section

no damage was observed in the adjacent tube, this may be attributed to low rate of hydrogen evolution, indicating partial blockage of the pin hole. During experiment 3, target tube was punctured (Figure 2). Observations of all the three experiments are indicated in Table 1.

Table 1: Observations of the three experiments				
Exp no	Hole size mm	Leak rate	Time of injection	Wastage observed
1	0.31	3 g/s	53 seconds	0.54 mm
2	0.25	Hole blocked	150 seconds	Nil
3	0.27	2.3 g/s	900 seconds	2.3 mm



Fig. 2 Punctured target tube after experiment 3

III.15 Analysis of Strain Rate Sensitivity of a Nitrogen Enhanced 316LN Stainless Steel

The response of a material to imposed deformation varies with the rate at which it is deformed. This variation is represented by a parameter called strain-rate sensitivity. Strain-rate sensitivity is used to characterize the plastic deformation behavior of a material and hence to identify the optimized workability domains for different materials. It is considered as an intrinsic characteristic of the material which alters with compositional changes and heat treatment etc. Therefore, in this context it becomes utmost important to understand the strain-rate sensitivity of all the key materials developed for in-core structural application in Fast Reactors.

Recently, it has been demonstrated that among the high nitrogen grade 316LN steels with various nitrogen content, 0.11-0.22 wt.%, the steel with 0.14 wt% N content (composition given in Table 1) shows optimum mechanical properties. Therefore, this material is being considered for the application in future generation fast reactors. Considering intended application, this investigation aims to understand the response of the steel at different strain rates in hot working domain. The experimental data have been generated by performing the uni-axial compression tests in the temperature ranges of 1073-1423 K (in steps of 50 K) at constant true strain rates of 0.001, 0.01, 0.1, 1 and 10 s⁻¹ as per the standard. The effect of strain rate on the flow stress at a constant strain is shown in Figure 1. Slope of stress versus strain rate plot represents SRS of the material. The figure indicates that depending on the slope between the flow stress and strain rate, the entire regime could be divided into three domains viz. D₁ (bounded by 1073-1223 K and 0.001-0.1 s⁻¹), D₂ (bounded by 1073-1223 K and 0.1-10 s⁻¹) and D₃ (bounded by 1223-1423 K and 0.001-10 s⁻¹). From these domains, it can be seen that the material exhibits two slope behavior at low temperatures, i.e ≤ 1223 K.

To substantiate this behavior microstructural investigation was carried out. A set of microstructures determined at 1223 K is given in Figure 2. From this figure, it can be seen that the microstructure corresponding to 0.1s⁻¹ shows a stage of deformation, where the dynamic

C	N	Mn	Cr	Mo	Ni	Fe
0.025	0.14	1.74	17.6	2.53	12.15	balance

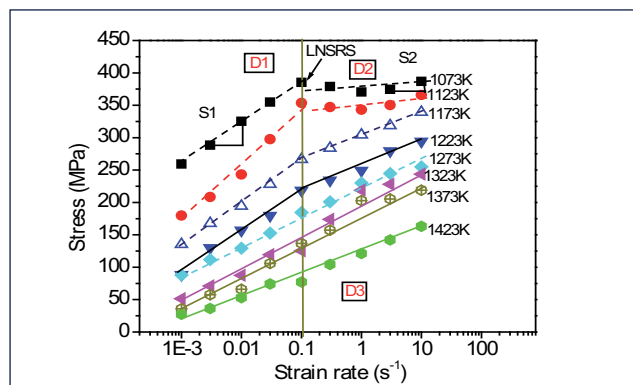


Fig. 1 Variation of stress with strain rate at different temperatures at 0.65 strain

recrystallization has not been initiated, whereas the microstructures corresponding to a lower strain rate (i.e 0.001 s⁻¹) and a higher strain rate (i.e. 10 s⁻¹) shows relatively advanced stage of dynamic recrystallization. This clearly shows a discontinuity in the evolution, which is not witnessed at high temperatures. Based on the microstructural and flow behavior analysis, the regime below 1223 K is divided into two different domains with 0.1 s⁻¹ as the boundary. The higher stress witnessed at the strain rate at 0.1 s⁻¹ may be correlated to delay in plastic strain and dynamic recrystallization commencement stage. As the temperature increases, the difference between the slopes disappears and σ increases linearly with logarithms of strain rate. This discontinuity in the response of the material and microstructural evolution at the transition strain rate (i.e) 0.1 s⁻¹ below 1223 K is not favorable for plastic deformation of the material as the processing in this domain may lead to inhomogeneity in microstructure and consequent poor mechanical property. On the basis of analysis of strain rate sensitivity, the temperature domain above 1223 K is recommended for the plastic deformation of 316L stainless steel with 0.14 wt% N content.

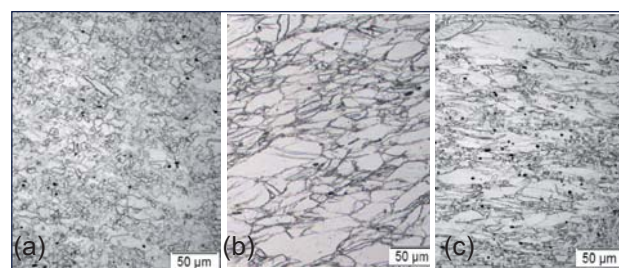


Fig. 2 Microstructure of the specimens tested at 1223K with strain rate of (a) 0.001 (b) 0.1 and (c) 10 s⁻¹

III.16 Low Cycle Fatigue-High Cycle Fatigue Interaction in 316LN Stainless Steel

Most of the current investigations pertaining to the fatigue behavior of structural materials in PFBR are primarily based on low cycle fatigue (LCF). This imposes serious concern in the design of components which feature unavoidable combinations of both LCF and high cycle fatigue (HCF). Such a situation arises in the inner vessel owing to fluctuations in the sodium free-level which imparts HCF damage on the component. The impingement of sodium from the fuel and blanket sub-assemblies onto the core cover plate of the control plug also inflicts HCF damage. The LCF damage that results from thermal cycling during the start-up and shutdown operation of the reactor gets superimposed on the above mentioned HCF damage, leading to strong LCF-HCF interactions.

The present investigation was undertaken to simulate such cumulative damage accumulation occurring under reactor operating conditions, in the laboratory. Towards this, experiments were carried out at 923 K on 316LN SS through a two-step loading sequence of LCF cycling under strain control for different life-fractions, followed by HCF cycling under stress control. Remnant HCF life was found to decrease drastically with increase in prior fatigue exposure as a result of strong LCF-HCF interactions. The rate of decrease in the remnant HCF life varies widely with prior LCF exposure as well as applied strain amplitude which were brought out clearly by plotting the difference (drop) in remnant HCF life between two consecutive levels of prior LCF exposure as a function of the degree of prior LCF exposure (Figure 1). A *threshold damage* in terms of prior LCF life-fraction was found, below which no significant LCF-HCF interaction takes place. Similarly, a *critical damage* marking the maximum rate of damage accumulation or strongest LCF-HCF interaction was found to exist at some specific pre-LCF damage depending on the strain amplitude employed. Thus, the window for effective LCF-HCF interaction was found to be a strong function of both the prior exposure and the applied strain amplitude under LCF, shifting towards higher LCF pre-exposure with a decrease in the strain amplitude.

The critical damage can be linked to both the fracture surface observations and microstructural features through appearance of striation pockets and microtwins respectively. Under LCF-HCF interaction, the formation of a small stage-II crack can be looked upon as 'effective crack initiation' at which difference in remnant HCF life with consecutive levels of fatigue exposure is the highest, or in other words, LCF-HCF interaction is

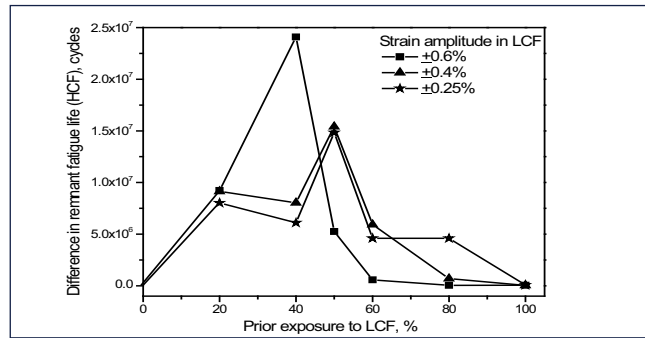


Fig. 1 Variation of difference in remnant fatigue lives (rate of fatigue damage) between different levels of prior LCF exposure as a function of degree of prior LCF exposure and strain amplitude

the strongest (Figure 1) (*critical damage*). However, lack of coalescence of such Stage-II cracks during the subsequent HCF cycling has allowed them to remain as isolated pockets of striations with different orientations and sizes compared to that of striations pertaining to the primary crack. Similarly, microtwins are also found to appear extensively through transformation of stacking faults. Extensive twinning does not appear under pure HCF in the present case, since the critical shear stress for the same is not expected to be attained at the low stresses employed under HCF. However, after cycling under pre-LCF upto *critical damage* when at least one stage-II crack has formed, the local shear stress in the adjacent region of the crack which is already pre-deformed may reach the critical value even at a lower HCF stress to cause twinning during subsequent HCF cycling. Hence, striation pockets or microtwins appear only in a particular window of strain amplitude and prior LCF exposure where the LCF-HCF interaction is most prominent or critical damage (marked through X in Figure 2) is reached.

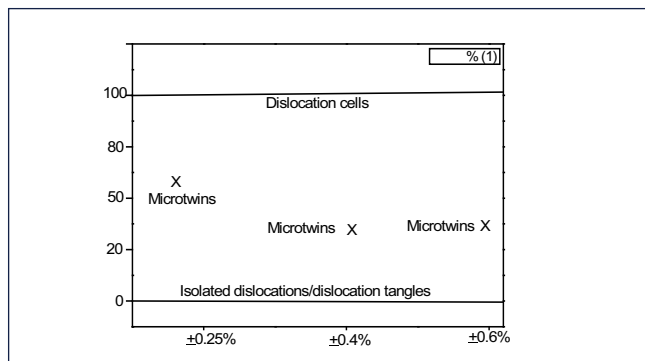


Fig. 2 Plot showing the occurrence of microtwinning and striation pockets (as a prominent feature of LCF-HCF interaction) as a function of prior LCF exposure as well as applied $\Delta\epsilon_r/2$

III.17 Development of Out-of-Pile Version of Instrumented Capsule for Online Determination of Uniaxial Creep Behaviour in Structural Specimens

Materials used for fuel cladding and structural components in fast reactors can undergo significant dimensional and physical changes due to exposure to high energy neutrons. At high temperatures in nuclear environment, material undergoes considerable deformation due to thermal and irradiation creep. Out-of-pile version of the instrumented irradiation capsule (Figure 1) for online determination of creep deformation has been developed and tested in the furnace by raising the temperature gradually up to a typical value of 550°C.

The out-of-pile version of instrumented capsule has various zones located one over the other. In the bottom zone of the capsule, there is a gas filling arrangement in which argon gas has been filled and sealed at high pressure to enable applying load on the tensile specimen of dimensions 40 mm length x 8 mm shoulder width x 1 mm thick through a set (2 numbers) of bellows.

Two numbers of stainless steel bellows are arranged back to back by circumferential welding along with the central tube passing through the center of the bellows. In the top zone, LVDT is connected with the data acquisition system to record the data. The deformation of the tensile specimen is transferred to the core of LVDT through a ceramic rod which passes through the central tube. Load is applied on the specimen by the expansion of bottom bellow using the pressurized argon gas. Pressurization of the bottom bellow has been carried out at room temperature and the filled pressure is 6 MPa. At the test temperature of 550°C in the electrical furnace, this pressure increases to 16 MPa.

The out-of-pile version of instrumented capsule was fabricated and tested in electrical furnace (Figure 2),



Fig. 2 Out-of-pile experimental set up arrangement with capsule loaded in electric furnace

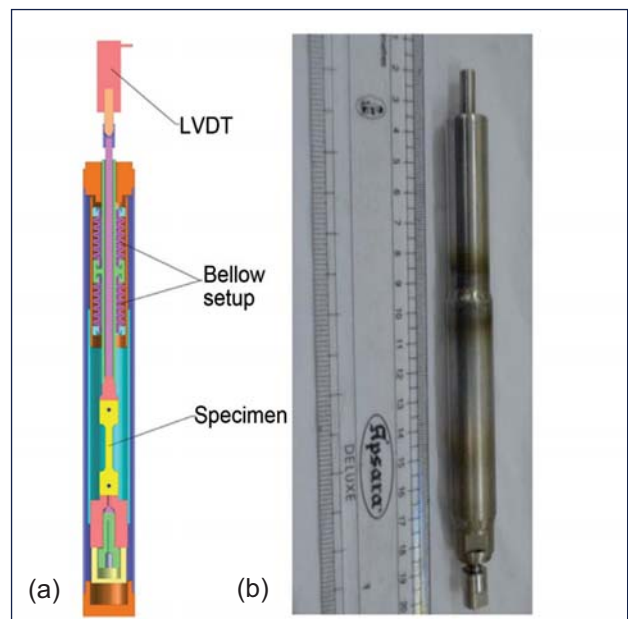


Fig. 1 Out-of-pile version of instrumented capsule
(a) schematic view and (b) actual capsule

to verify its capability for inducing creep elongation in creep/ tensile specimen and to test the integrity of high pressure gas-filled bellows at high temperatures.

The experiment has been carried out at three different temperatures and corresponding three different stresses (269 MPa at 450°C, 287 MPa at 500°C and 306 MPa at 550°C). The results showing the elongation of the tensile specimen (as indicated by LVDT) with respect to time are shown in Figure 3. The overall diameter of this instrumented capsule is 20 mm which matches with the diameter of the irradiation location available in FBTR.

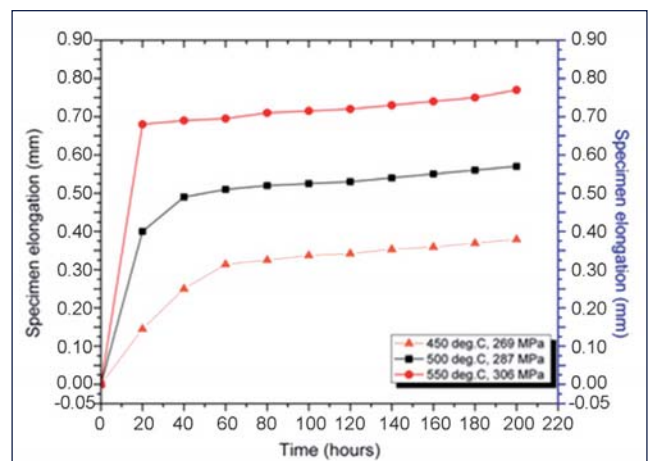


Fig. 3 Elongation of the specimen with respect to time at 450, 500 and 550°C

III.18 Internal-state-variable based Constitutive Modeling of Creep Deformation Behaviour of Tempered Martensitic 9Cr-1Mo Steel

Creep deformation is characterised by a decrease in creep rate in the primary or transient creep region followed by a minimum or a steady state creep rate in secondary creep and an increase in creep rate during tertiary creep leading to failure. Modeling creep deformation behaviour becomes essential for long-term creep life prediction, safe-life design and remnant life assessment of high temperature structural components and for the development of new materials for applications at high temperatures. Generally, most of the investigations on creep have been devoted towards understanding the secondary creep deformation behaviour of materials. Often, design engineers require the parameters associated with creep equations for the prediction of long-term creep behaviour in the primary and secondary creep regimes. In view of this, an attempt has been made to develop the constitutive model based on microscopic internal-variable, i.e., mean internal stress (σ_i) defined as the local internal stress acting against the dislocation motion. The concept of stress dependent activation volume and average dislocation segment length based on Friedel statistics has been incorporated into the kinetic creep law. The internal stress formulation proposed by Estrin and Mecking has been coupled with kinetic creep law in order to get a better description of the deformation behaviour. The applicability of the model has been demonstrated by describing primary and secondary creep behaviour of 9Cr-1Mo steel in two heat treated conditions, (quenched and tempered, Q+T and simulated post weld heat treated, SPWHT) for wide range of stresses

and temperatures. The parameters associated with the present formulation have been obtained based on error minimization algorithm using experimental and predicted creep strain-time data. Further, the predictability of the model has been demonstrated by predicting steady state creep rate and its comparison with experimentally measured values in 9Cr-1Mo steel. The coupled evolution of creep rate and internal stress with time has been given as:

$$\dot{\epsilon} = \frac{\rho_m b^2 v_D \sigma_e (\sigma_i^2 \sigma_e)^{-1/3}}{M^2} \exp\left(\frac{-Q}{RT}\right) \sinh\left(\frac{\sigma_e}{MkT} b^3 \left[\frac{G}{(\sigma_i^2 \sigma_e)^{1/3}}\right]\right)$$

$$\frac{d\sigma_i}{dt} = \frac{1}{\sigma_i \epsilon_s} (\sigma_s^2 - \sigma_i^2) \dot{\epsilon}$$

At all test conditions, the present model provided appropriate description of primary and steady state creep behaviour of 9Cr-1Mo steel. The accuracy of prediction is shown in terms of creep rate-time at 873 K for SPWHT condition in Figure 1. According to the present model, the application of an external applied stress produces plastic flow and consequently the strain hardening during primary creep deformation, thereby causing continual increase in internal stress with strain. The decrease of creep rate with strain/time results from a decrease in effective stress and increase in internal stress. Good match between the predicted and experimental steady state creep rates has been observed (Figure 2). This implies that the model appropriately describes the primary and secondary deformation behaviour of the steel.

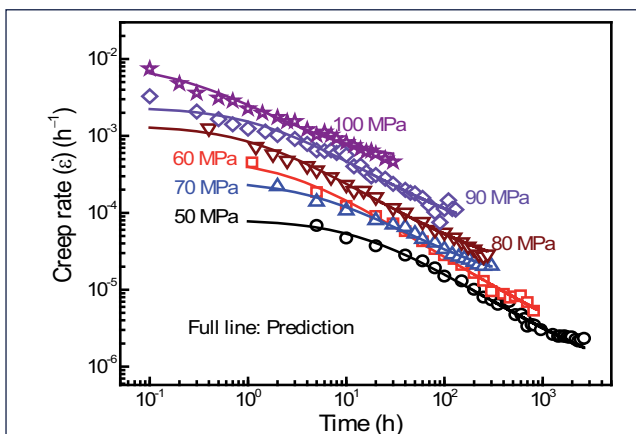


Fig. 1 Variations in creep rate with time for different stress conditions at 873 K (9Cr-1Mo steel (SPWHT))

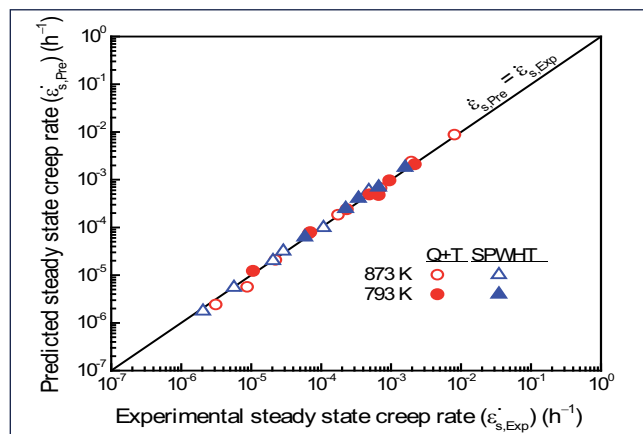


Fig. 2 Predicted versus experimental creep rate at 793 and 873 K for Q+T and SPWHT conditions (9Cr-1Mo steel)

III.19 Effect of Stress Fluctuation on Creep Behavior of Modified 9Cr-1Mo Steel

Modified 9Cr-1Mo steel is the material used to fabricate the steam generator in PFBR. Design is based on constant nominal stress and temperature creep, the results of which are far from reality. Under normal operating condition, the steam generator is subjected to cycle stress and temperature variation around the mean values. Such variations may have considerable effect on the creep deformation and rupture behaviour of the steel. The effect of cyclic loading can either accelerate or retard creep deformation depending on the material structure, temperature and stress conditions. In the case of static creep, the response of the material is simple as a static state. However, in the case of cyclic creep, it is complex because of the dynamic nature of the loading and furthermore, its behavior has been rarely reported. It is thus important to understand whether the cyclic creep leads to an acceleration or retardation in the evaluation of creep strain leading to the static creep. A unique experimental facility is needed to conduct creep test under controlled stress and temperature fluctuation around the mean values. Such studies have the potential to relook the design of high temperature pressure vessel components more realistically.

An innovative creep testing machine, having capability of providing stress variation about the mean value in a controlled way during creep deformation, has been designed and established. It is an electro-mechanical loading type machine and operates by closed loop control system through pre-planned program. It has capacity of 50 KN tensile-tensile loading and the creep elongation measurement is carried out by using conventional extensometer along with digital dial indicator. Tension-tension cyclic loadings that have been

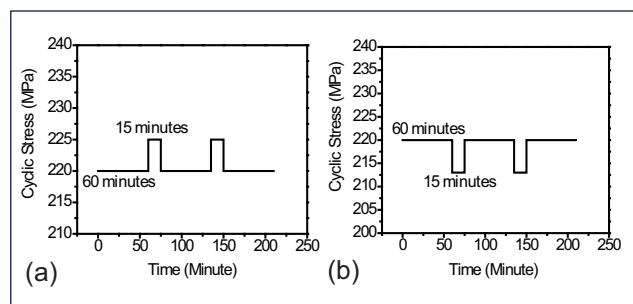


Fig. 1 Cyclic creep loading pattern (a) positive and (b) negative variation

applied to the specimen in the present investigation is shown in Figures 1a and 1b.

Creep tests at 220 MPa and 873 K with periodic stress changes of ± 5 , ± 10 , ± 15 and ± 20 % over 220 MPa (as illustrated in Figure 1) have been carried out using the indigenously designed and developed creep machine. The cyclic creep curve of the modified 9Cr-1Mo steel at 220+10%, 873 K is shown in Figure 2 along with the static creep curve at 220 MPa, 873 K. A magnified view of the portion of cyclic creep curve showing accumulation of cyclic strain is inserted in Figure 2. Under cyclic creep condition, the increase in creep deformation rate associated with decrease in rupture life is observed. Comparison of the creep rupture life of the steel with time averaged mean stress under cyclic creep condition and uniaxial creep condition are shown in a double logarithmic plot in Figure 3. Under both positive and negative stress variations the creep rupture life of the modified 9Cr-1Mo steel decreases over that of static loading. The decrease in rupture life was more both at higher positive and negative stress variations.

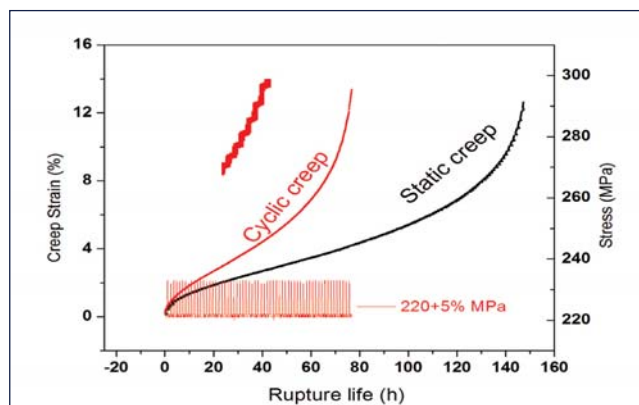


Fig. 2 Static and cyclic creep curve of modified 9Cr-1Mo steel at 220+10% MPa at 873 K (P91)

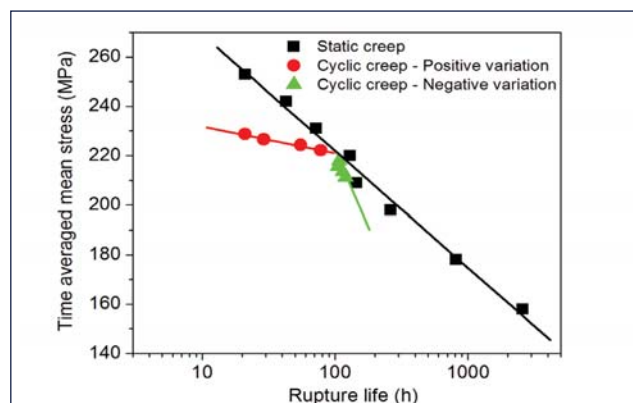


Fig. 3 Comparisons of creep rupture life of the modified 9Cr-1Mo steel under static and cyclic creep at 873 K

III.20 Numerical Simulation of Fluid Flow during A-TIG Welding of 10 mm Thick 316LN Stainless Steel

A-TIG welding has been reported to enhance the depth of penetration by 300% during autogenous welding. One of the proposed mechanisms for enhancing the depth of penetration is due to reversal of Marangoni flow in the weld pool caused by the change in coefficient of surface tension from negative to positive by the addition of surface active element oxygen through activated flux. To simulate the convective fluid flow during A-TIG welding of 316LN stainless steel commercial software ANSYS fluent is used to generate a 2-D model. Numerical models based on CFD were developed to infer the weld bead profile and the weld pool characteristics based on the heat input and the measured oxygen content. Figure 1 compares the fluid flow in TIG and A-TIG welding. Figure 2a compares the predicted and measured depth of penetration. Figure 2b shows the predicted weld bead profile, velocity vectors and the temperature distribution obtained in simulation for various activated flux compositions. Full penetration of 10 mm could be achieved only with particular flux compositions. Figure 2c compares the simulated weld bead profile with that of the experimentally obtained weld bead profile. There is good agreement between

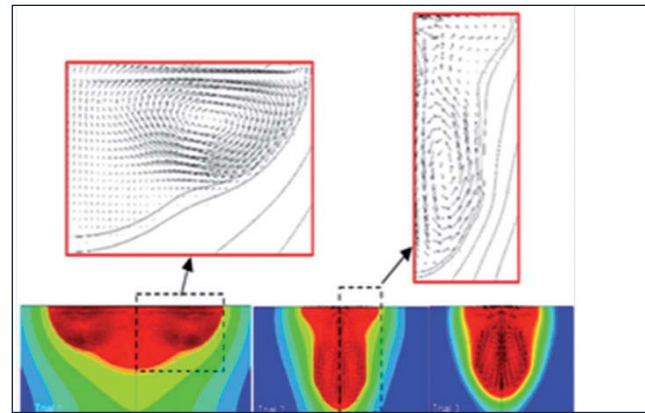


Fig. 1 Comparison of fluid flow in TIG and A-TIG welding

the two profiles implying that the fluid flow model could predict the flow behavior well. Figure 2d compares the measured and predicted weld bead depth as a function of oxygen content. The depth of penetration increased with oxygen content and remained same with further increase in oxygen content beyond 300 ppm. Therefore, minimum oxygen content required in the weld pool to produce 10 mm depth of penetration is determined as 300 ppm for 316LN stainless steel.

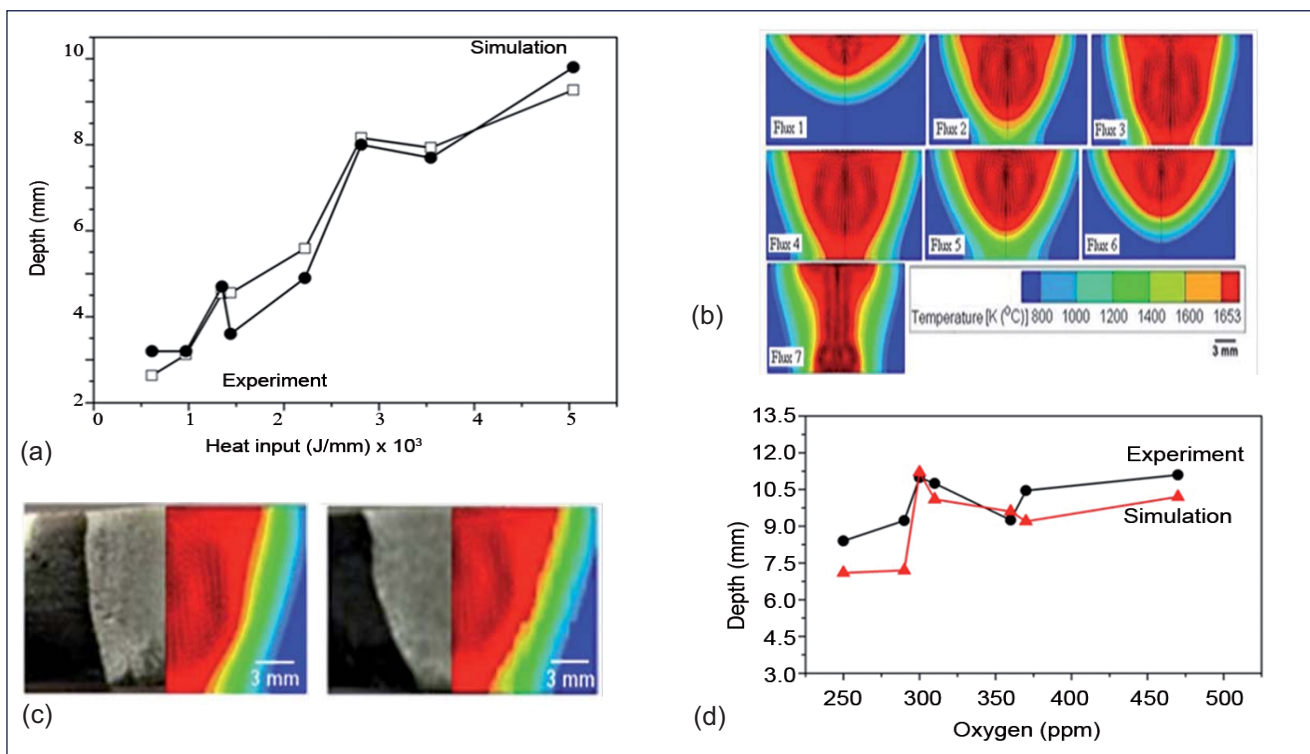


Fig. 2 (a) Validation of predicted and measured depth of penetration as a function of heat input, (b) simulated weld bead profiles for various dissolved oxygen contents in the weld pool, (c) comparison of actual weld bead profile with simulated weld bead profile and (d) validation of depth of penetration as a function of oxygen content in the weld pool

III.21 Development and Implementation of Customized SCADA based Control System for Sodium Facility for Component Testing

A new dynamic sodium loop termed as ‘Sodium Facility for Component Testing’ is constructed for sodium testing of FBR components and to conduct various sodium experiments for future FBRs. This facility consists of various types of equipment, piping, pumps and instruments at different elevations. A customized data acquisition and control system has been developed and commissioned in sodium facility for component testing .

The data acquisition and control system consists of remote input/output based architecture. The sensor data acquired at remote input/output is transmitted to data acquisition and control system through ethernet. The supervisory control and data acquisition (SCADA) acts as a client. The client requests the controller and displays the data on the screen.

The SCADA system enables the operator to know the state of sodium system and different actions are taken up by the operator based on the temperature data of the loop components.

The development of customized SCADA includes the design of mimic pages, trends, graphs, data logging, and shift wise reports. Operator query pages required for the system is developed to display the real time field data.

The main mimic page consists of multiple selections list from which operator can select any one of the process parameters to be viewed. The operator has the privilege to open multiple windows to view multiple process parameters.

The SCADA has been customized for monitoring and control of various parameters like temperature, argon pressure, valve control, level display etc., The safety related systems of sodium facility for component testing are hard wired. All pneumatically operated sodium dump valves are hard wired control with essential interlocks provided in control room. Figure 1 shows the main mimic screen of sodium facility for component testing.

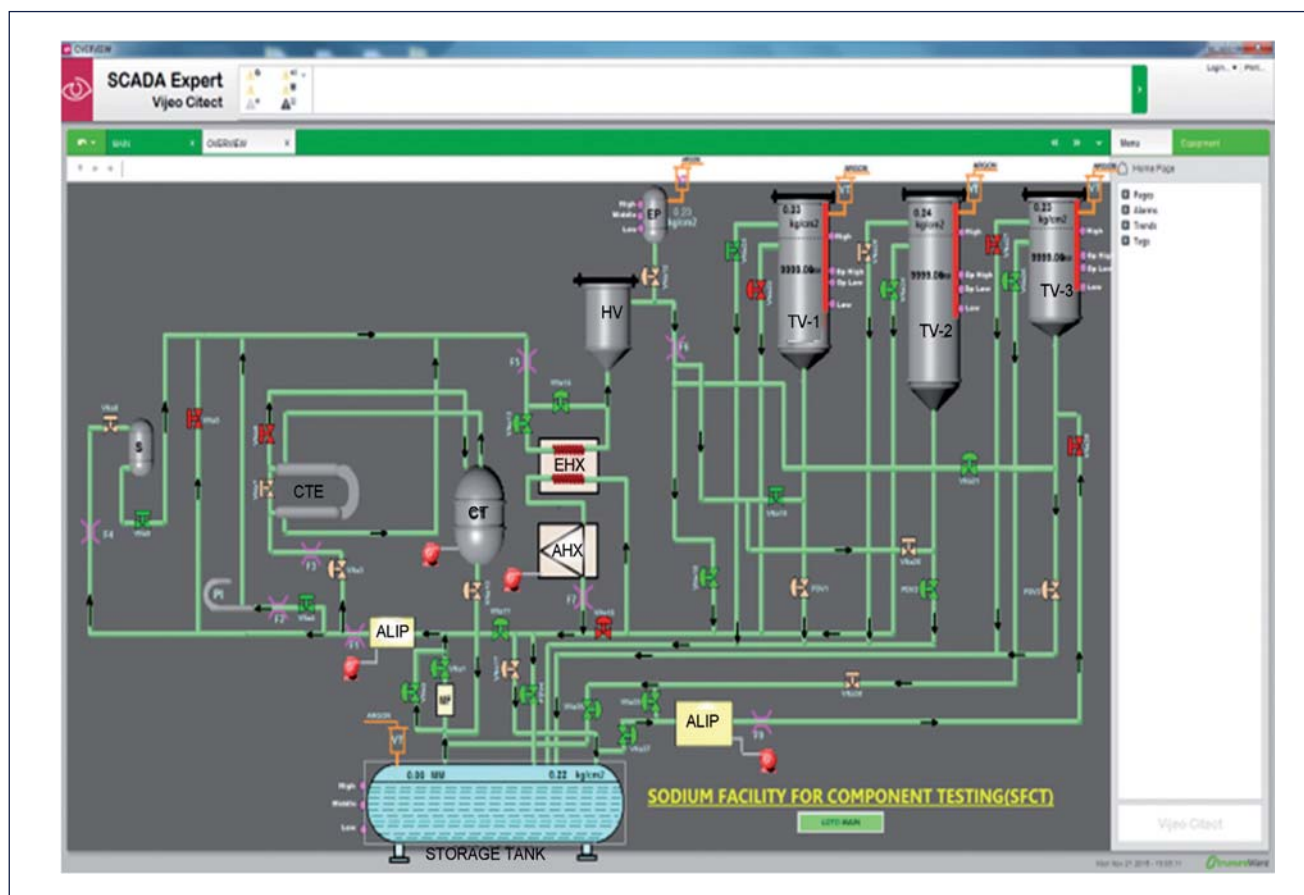


Fig. 1 Main mimic screen of sodium facility for component testing

III.22 Modeling and Testing of Instrument Setup for Calibration of Void Fraction Studies

Void fraction (VF) needs to be monitored and kept under strict control in different pipe line flows particularly in power plants and chemical process industries. Innovative void fraction sensor was designed for basic studies and its operation was successfully demonstrated at various facilities in BARC and Jadavpur University.

The calibration technique involves inserting non-conducting beads for simulating voids. Volume of void and that of fluid passing through the sensing probe (electrodes) per unit time (discharge) and volume of the sensing zone were found out from experimental investigations. Ring type electrodes are chosen for better sensitivity.

Void fraction relation for ring type conductivity electrode is the ratio of the volume occupied by the voids (beads) in the sensing zone to the volume of the sensing zone. Since the sensor output is frequency, the change in frequency obtained for beads of various sizes by passing through the electrodes, is correlated to the calculated void fraction, attributed by the corresponding beads, to obtain the void fraction. Thus a relation between void fraction and conductance (change in frequency) is established. The condition of relative velocity between the void and fluid is simulated by keeping the fluid stationary and making the beads to move at a fixed speed, which will give the same effect of voids moving in a flowing liquid.

Experimental facility (Figure 1) consisting of U-tube assembly and a bead drive assembly was setup at ISS/SISD, in order to facilitate the movement of beads in predetermined path inside a pipe line, filled with water. Movement of beads inside the U-tube at controlled speeds and specified paths are integrated along with the U-tube system.

The U-tube assembly, is a set of straight tubes, designed with provisions for assembling and removing sensing

electrodes. The bead drive assembly consists of an array of various sized beads, tied at predetermined distances along a 0.4 mm diameter rope, and a stepper motor with pulley assembly, to drive the beads. Beads are passed through the electrodes using a bead drive assembly. Electrodes form part of pulsating sensor that provide variable resistance with the flow of voids in water medium. Depending upon the percentage of voids flowing in the water medium, resistance offered by the medium varies, which causes a proportional change in frequency of the output pulses. A single channel rapid counter unit with front end software was used to process frequency output from void fraction sensor.

Water of known conductivity was filled in the U-tube assembly. Beads of various sizes were allowed to pass through the test section and the corresponding frequency plot was recorded and analysed to calculate (1) frequency variation due to different volume of voids, (2) active sensing zone, (3) relation between VF% and frequency. Prior to the actual determination of void fraction, sensing zone was computed. Volume of sensing zone is the volume in between the two positions of beads, where the conductance changes from minimum to maximum. This was calculated to be 8831.25 vmm³. Void fraction for individual beads is given in Table 1.

The smallest bead of 6 mm diameter created a void fraction of 1.2% and the largest bead of 19 mm diameter created a void fraction of 40%. Change in frequency due to different sizes of beads which correspond to particular void fraction is shown in Figure 2. Based on the correlation made between void fraction and change in frequency for each bead, it is found that, for unit percentage change in void fraction, the change in frequency is 82 Hz. Thus the sensitivity of the sensor is found to be 0.1%. Pool void fraction studies are in an advanced stage of completion.

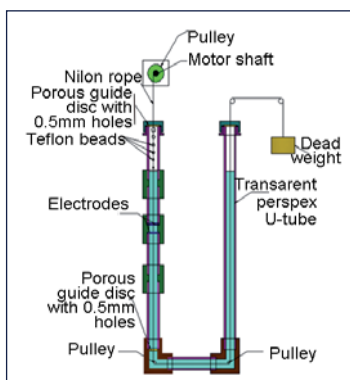


Fig. 1 Experimental setup of the facility

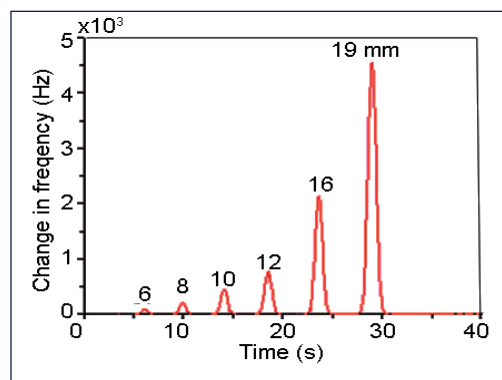


Fig. 2 Time versus conductance plot in terms of change in frequency

Table 1: Percentage void fraction of conductance based sensor			
S.No	Beed size (mm)	Volume of beed (mm ²)	Void fraction
1	6	113.097	1.281
2	8	268.083	3.036
3	10	523.599	5.929
4	12	904.799	10.245
5	16	2144.661	24.285
6	19	3591.364	40.667

III.23 Design of a High Availability Fault Tolerant Controller for Control Applications in FBRs

In PFBR, for high-availability control applications, dual VME bus based systems are used in hot-standby configuration. Each VME bus based system had a CPU card, analog input cards and analog/digital output cards. For future FBRs, a stand-alone PID (proportional, integral, derivative) controller has been designed for high availability control applications involving process variables such as temperature, pressure etc. It is capable of performing PID control as well as ON/OFF control with the set points / coefficients / hysteresis configurable by the user. Care has been taken in the design to ensure that single failure criterion is met (i.e.) even if one component / power supply fails, the system can continue to work without interruption. This will help in reducing the need for using redundancy at system level. For this, adequate redundancy and voting has been made part of the controller design.

For conceptualization of the fault tolerant design, initially, various architectures were considered and analyzed. At the end of this phase, it was decided to design the system with triple modular redundant (TMR) architecture. The hardware was decomposed into the following modules interconnected using a custom backplane.

1. Power supply module
2. Analog input module (AIM)
3. CPU module (CPUM)
4. Relay output module (ROPM)
5. Analog output module (AOM)
6. Configuration / communication module (CCM)

The detailed design for the various modules was carried out in the next phase. The power supply module was

Control types	PID control, ON/OFF control
Process variables	Two numbers
Types of inputs	T/C, RTD, 4-20 mA current loop and 0-10 V
Types of outputs	Relay output (for ON/OFF control) and current loop (for PID control)
Configuration	Stand-alone (with keypad and digital display) and through PC software (over ethernet)
Communication	Modbus/TCP, Modbus/RTU, Modbus/ASCII
Communication ports	Ethernet, RS485

designed to provide three isolated power supplies for the three channels of the TMR architecture. The CPUM has three independent channels (A, B & C), that communicate with each other via isolated serial buses and execute the control algorithm. Each module of AIM contains sensor specific signal processing circuits. AIM, ROPM, and AOM have three independent channels that communicate with the respective CPUM channels via mutually isolated backplane buses. There is no inter-channel communication in any module other than CPUM. The CCM communicates with the three independent CPUM channels via the mutually isolated backplane buses. It provides the external interface for the controller. A dedicated voting module is employed for routing the control output from AOM/ROPM to the actuating devices. Block diagram of high availability fault tolerant controller is shown in Figure 1. The salient features of the system are given in Table 1.

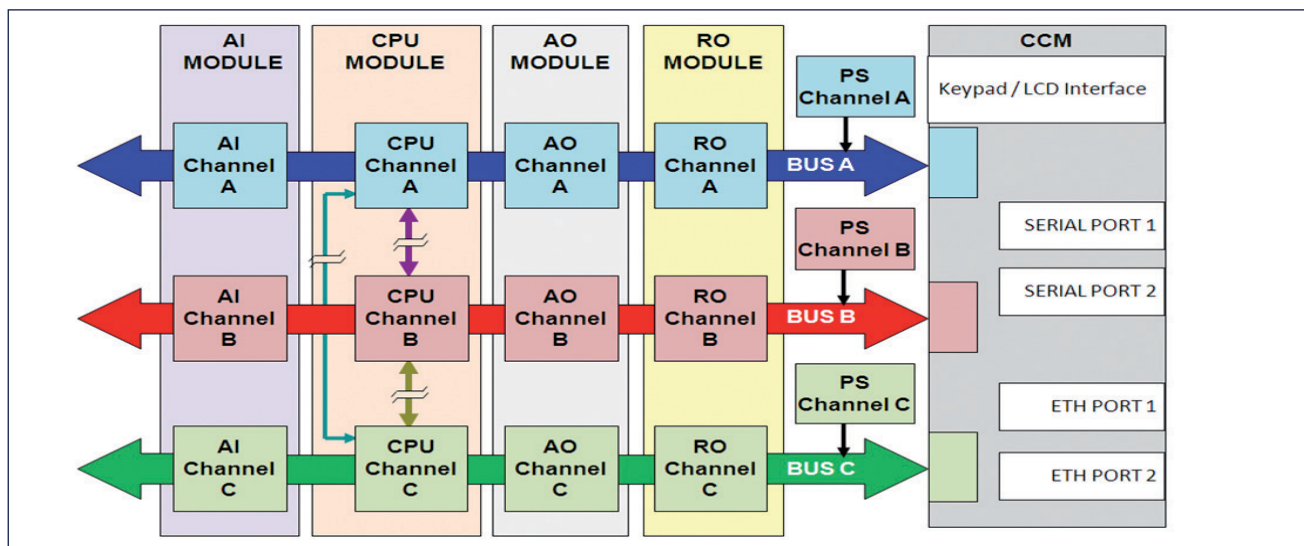


Fig. 1 Block diagram of high availability fault tolerant controller

III.24 Conceptual Design of Sodium Bonded Metal Fuel Pin for 100 MWt Test Reactor

Before the commercial deployment of 1000 MWe Metal fuelled Fast Reactors, a test reactor of about 100 MWt is envisaged. To understand the fuel performance and its behaviour at the power reactor ratings. Since the life of the presently operating Fast Breeder Test Reactor (FBTR) with carbide fuel is expected up to 2028, an alternate to FBTR is being sought. Thus, a test reactor with metal fuel would fit the requirement for a fast spectrum test reactor. With the proposed test reactor with metal fuel, it is possible to demonstrate safe and high performance of metal fuel FBR in closed fuel cycle. More importantly, the fuel performance, from the point of view of achievable peak LHR, core inlet & outlet temperatures and active fuel column length, etc., envisaged for a commercial power reactor will be simulated in this core. The test reactor with metal fuel is at present termed as FBTR-II.

Design criteria

1. The center-line temperature of fuel at 115% peak power under hotspot conditions shall not exceed its melting point.
2. The clad inside surface hotspot temperature shall not exceed 923 K under normal operating conditions for fuel pin to avoid fuel-clad eutectic formation.
3. Cumulative damage fraction (CDF) under normal operation shall be ≤ 0.25 to preserve clad integrity.

Reactor core parameters

The reactor core consists of 44 fuel sub-assemblies (SA) surrounded by reflector and blanket SA with provisions for three experimental SA. The fuel column height is 1000 mm and the peak linear heat rating (LHR) is 430 W/cm. Target burn-up is presently fixed at 100 GWd/t and could be enhanced after studying its performance in post irradiation examination.

Description of sodium bonded metal fuel pin

Sodium bonded metal fuel pin with a smear density of 75% is selected to accommodate the high volumetric swelling nature of metal fuel. The clad is made of modified 9Cr-1Mo (T91) material which is having a very high swelling resistance but moderate creep strength. Ternary alloy of composition U-23w%Pu-6w%Zr is chosen as the fuel material. Based on the physics studies, the fuel pin diameter is selected as 8.5 mm (as it is close to the typical power reactor pin) with a clad thickness of 0.58 mm with total number of fuel pins

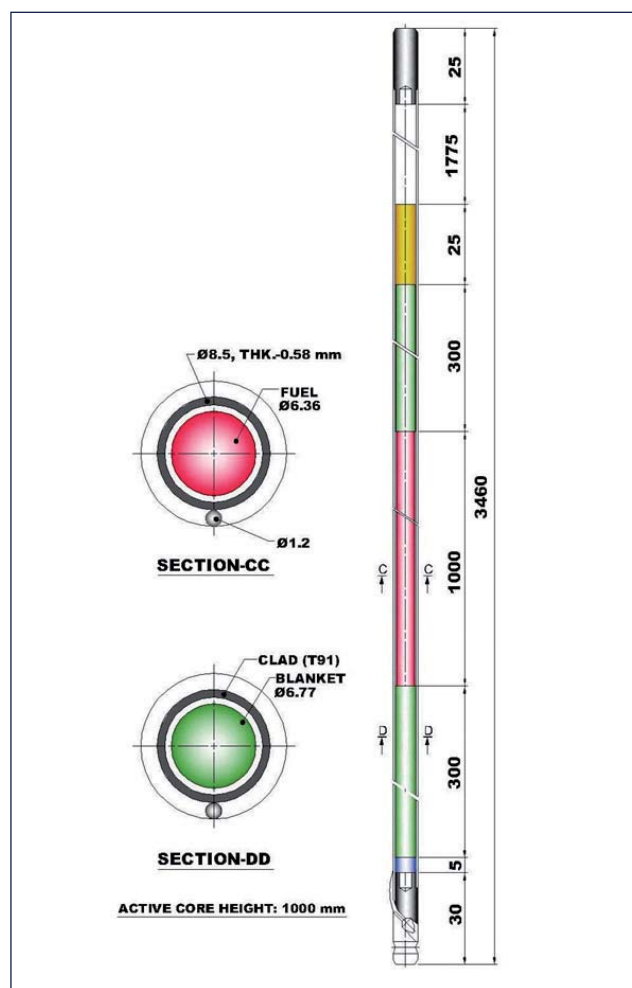
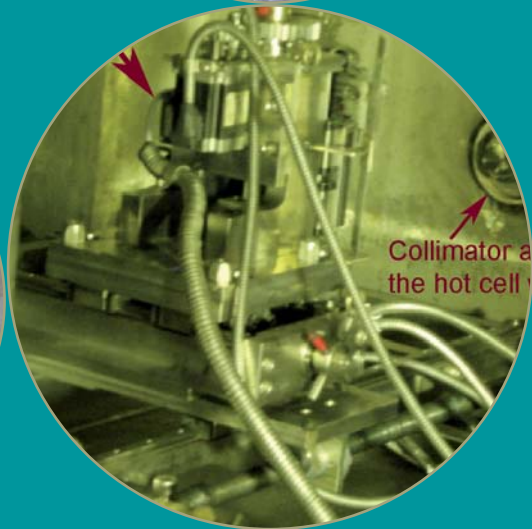
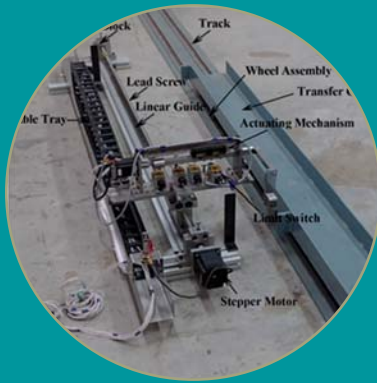


Fig. 1 Metal fuel pin

per SA as 91. The fuel diameter works out to 6.36 mm for 75% smear density. The spacer wire diameter is 1.2 mm. The fuel pin consists of 1000 mm of fuel column, 300 mm each of upper and lower blanket column (Figure 1) and the entire column of fuel and blanket is bonded by sodium

Pin design

Analysis of CDF of fuel pin was carried out for the metallic fuel pin in the central fuel SA. From the analysis, the fission gas plenum length required at the fuel pin top is arrived at as 1390 mm for a target peak burn-up of 100 GWd/t. Accommodating for axial fuel swelling and for the sodium expulsion in the plenum region, the total plenum required is arrived at as 1775 mm. Free sodium level of 25 mm is provided above the fuel column just to take care of thermal change in fuel and blanket column lengths during operation. Thus, the total pin length is arrived at as 3460 mm.



CHAPTER IV Fuel Cycle

IV.1 Fast Reactor Fuel Cycle Facility - Current Status

The construction activities of Fast Reactor Fuel Cycle Facility (FRFCF), are in full swing. The construction of facilities such as the administrative building, training centre, central control room etc, is nearing completion (Figures 1a and 1b). In the nuclear island, where the plant buildings foundation are made on hard rock, to meet the seismic qualification requirements. Deep excavation works including controlled blasting, geotechnical investigation, geo mapping and grouting works have been completed. The civil construction works of the major process plants such as the Waste Management Plant, Fuel Fabrication Plant, Core Sub-assembly Plant and Reprocessed Uranium Oxide Plant have already commenced, with the first pour of RCC carried out on April 25, 2016 (Figures 1c to 1e).

Civil tenders for the construction of the Fuel Reprocessing Plant are in an advanced stage of processing and work orders will be issued shortly. On the housing front, construction of 600 units is in progress. Regulatory consent for construction of FRFCF was successfully obtained from AERB, after meeting all the stipulated norms. Construction works are being carried out with a good safety records and about 8.7 million man hours of work have been achieved so far, without any untoward incident.

Procurement has been initiated for raw materials and major long delivery items. Raw materials such as stainless steel plates of varying thickness from

3 to 48 mm, required for the fabrication of various equipments have been delivered to site and action initiated for fabrication of process tanks for high level waste, intermediate level waste and low level waste large capacity storage tanks. Lead ingots for various requirements have been procured. Manufacture of lead bricks for master slave manipulators (MSM) liner and window liner is under progress. Other long delivery items such as glove boxes and fume hoods have been received. Fuel fabrication process equipments such as attritors, hydraulic compaction press, jaw crushers and rotary press have also been received. Orders have been placed for the procurement of other long delivery items and manufacture is under progress for different versions of master slave manipulators such as extended reach MSMs, articulated MSMs, three piece MSMs and for optical quality glass slabs for radiation shielding windows for the hot cells.

Design validation and mockup testing for equipment like fuel pin chopper and intercell transfer system has been completed and is under progress for centerless grinder machine along with automation system, fully automatic wire wrapping machine, spool making system, linear mass measurement system, pin tray storage, retrieval automation system etc.

About two hundred and twenty posts have been sanctioned for FRFCF and recruitment has been initiated.



Fig. 1 (a) Waste management plant, (b) fuel fabrication plant, (c) core sub assembly plant, (d) administrative building and (e) training centre

IV.2 3D Modeling and Animation of Plutonium Processing Section of Fuel Reprocessing Plant of Fast Reactor Fuel Cycle Facility

Fast Reactor Fuel Cycle Facility comprises of five plants operating at various stages of the reprocessing cycle. Fuel Reprocessing Plant is designated for recovering uranium dioxide and plutonium dioxide from the spent fuel. Block-4 of Fuel Reprocessing Plant houses the Plutonium Processing Section. Spent fuel comes to Plutonium Processing Section in powder form in truck mounted, shielded bunkers. Electrical overhead trolley cranes in the truck entry corridor are used to unload the bunkers from the trucks onto ground based guided vehicles, which move them to various process cells.

Plutonium processing section consists of eight concrete shielded process cells. Each of these cells houses annular stainless steel tanks for storing process solution and related high dense piping. Electrical overhead trolley cranes are used for equipment and material movement within the process cells. This block also houses off-gas filter area, exhaust fan rooms, service areas, transmitter gallery, off-gas fan room, etc.

3D modeling and workflow animation of this facility has been taken up for design review and analysis. The Civil structure and process equipment have been modeled and assembled using 3D modeling software. 3D models of process piping has also been imported and incorporated into the final assembly. Process-workflow has been animated using a software which includes removal of off-gas filters from the filter area using electrical overhead trolley cranes and ground based guided vehicles to the truck entry area, where it is kept on a truck to be taken out to Waste Management Plant. During visualization, lights were introduced into the scene to provide suitable illumination to the models.

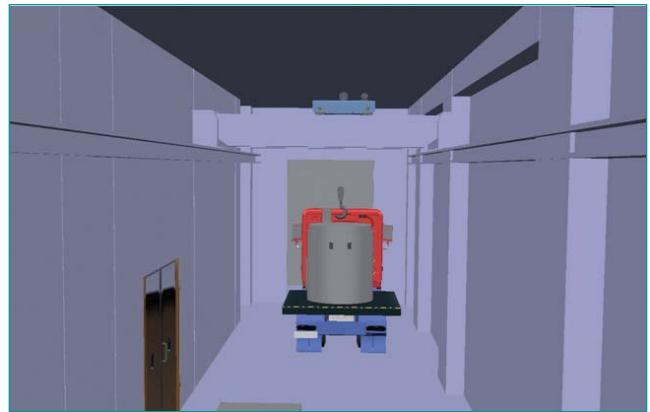


Fig. 1 Truck entry corridor

The animations were captured from desirable viewpoints by setting up cameras and controlling their timing and behavior using scripts. Transparency was created by changing material properties and cut view was generated by modifying the clipping planes of cameras. This has rendered visibility to the required internal details of the model during the animation sequence. Particle systems were introduced to create special effects such as liquid flow and gas flow. Rope animations were simulated using scaling operations coupled with controlled rendering.

A text document describing the functions of each system, the operation sequence was prepared and developed into an audio narration. This audio narration runs in synchronization with the animation in visualization software. This enhances the depth of the visualization by providing a better understanding of the system.

The completed visualization has been ported to the advanced visualization center for viewing in 3D environment (Figures 1 to 3).

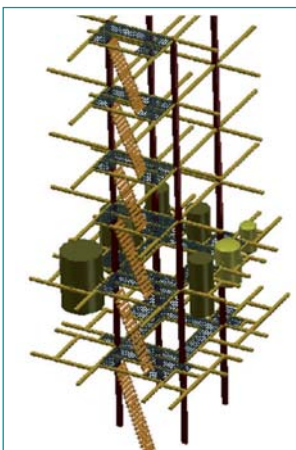


Fig. 2 Process cell

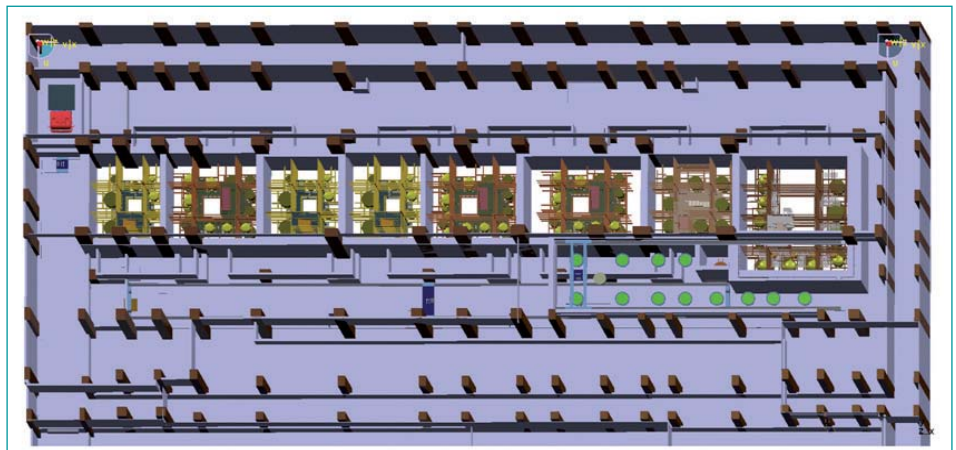


Fig. 3 Block 4 top view

IV.3 Design of PFBR Sub-assembly Tilting System for Storage Cell of FRP-FRFCF

Fuel sub-assemblies (FSA) and radial sub-assemblies (blanket sub-assemblies, RSA) were received in horizontal position and they have to be tilted vertically for positioning and storing the sub-assembly in the cavities of storage cells of FRP/FRFCF. A sub-assembly tilting system (SATS) has been designed for this purpose. The various challenges in design are, component shall be of modular design for remote maintenance, tilting of 4.5 metres sub-assembly, special locking arrangement to prevent fall of sub-assembly and selection of suitable materials amenable for radioactive environment. A conceptual design is made and a detailed engineering drawing is prepared for mockup qualification.

The important components of sub-assembly tilting system are transfer carriage, rope, rope drum, sheaves, tilting table consisting of hinges (fulcrum), clamps, stopper, end rope fixing assembly and necessary instrumentation. A transfer carriage loaded with FSA or RSA keeps on the track by means of six wheels which are amenable for remote maintenance and replacement. During tilting, transfer carriage motion is at rest. A stopper is provided at the receiving end of sub-assembly which prevents fall of sub-assembly during tilting of table and also restricts the movement of transfer carriage while sub-assembly tilting system is loaded. Also, three clamps are provided to prevent the fall of sub-assembly while tilting vertically and vice-versa. Clamps are designed to accommodate sub-assembly with maximum 50 mm bowing. Hinge

(fulcrum) is mounted on the opposite ends of stopper on tilting table and the other end is connected with rope and drum mechanism as shown in Figure 1. The hinges are amenable for remote maintenance. Drum is driven by motorized gear unit. Tilting table consists of hinges at one end and removable support at the other end.

The material for the construction of all the parts are chosen from strength as well as corrosion point of view. The parts which require high strength as well as, those which undergo wear and tear due to movements, are to be manufactured with martensitic steel with hard chrome plating and other parts are of SS304L/SS304 depending on welding requirement.

Clamps and stopper lock with the help of master-slave manipulator, when fuel sub-assembly or radial sub-assembly is placed on transfer carriage. In order to avoid load on collapsible support, the tilting table has to be lifted slightly with the help of rope and drum mechanism. Collapsible support has to be rotated in horizontal plane with the help of manipulator. After removing the collapsible support, rope drum starts to rotate in clockwise direction, subsequently tilting table rotates about its fulcrum due to self weight. Rotation speed of tilting table is controlled by rope drum drive. Instrumentation has been provided for sending signal to motor when it reaches the vertical position. After removing sub-assembly from tilting table, the drum is rotated in anti-clock wise direction to make the tilting table horizontal.

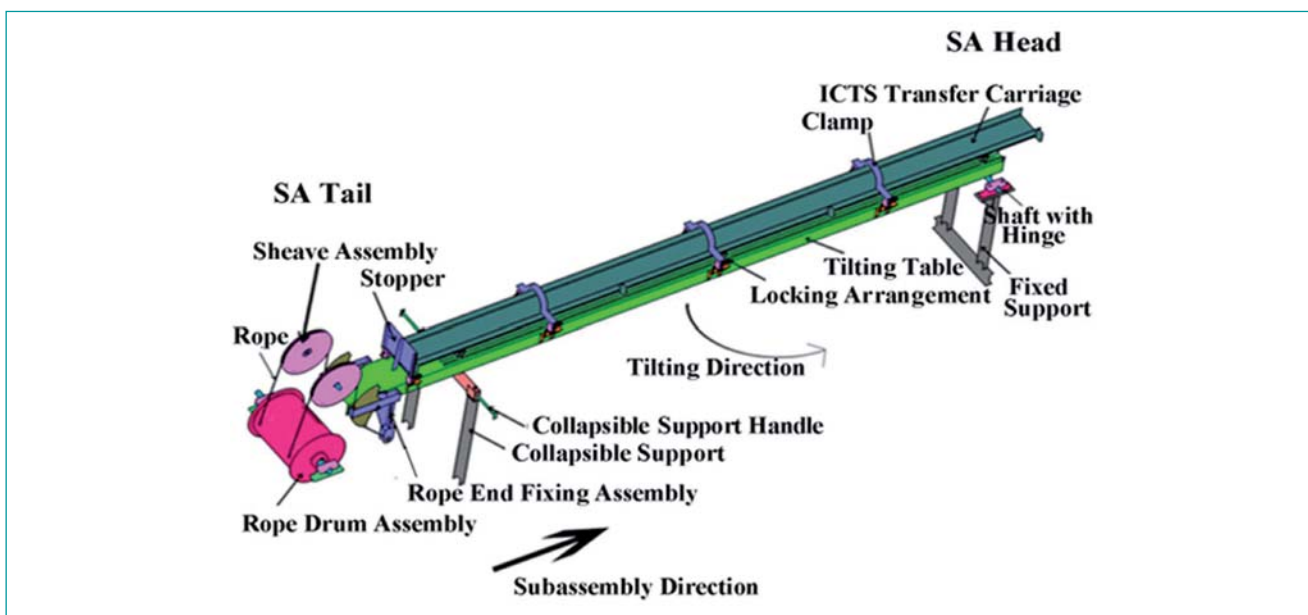


Fig. 1 3D model of sub-assembly tilting system

IV.4 Design and Development of Multi Pin Chopper for Fuel Pins of PFBR Fuel Sub-assembly

A special and unique shearing machine (chopper) which is first-of-its-kind has been designed to shear fuel pins of fuel sub-assemblies of PFBR (Figure 1). It is a vertical shearing machine provided with multi-fuel pin chopping to meet the capacity requirement of FRP/FRFCF. Design consideration has been made for its modular construction and the parts which can undergo wear and tear are designed for remote operation & maintenance.

The challenges are:

- High burn-up, high plutonium content and acidic environment - demands robust remote operation & maintenance
- Limitations of the remote handling equipment, viewing systems and radiation hardened electronics
- The interference of spacer wire during chopping
- Literature data not available, hence, need for indigenous design
- Optimization of various features result in complex and intricate profile of critical components, demanding special machining process

The important mechanical components of the chopper (Figure 2) are magazine, gripper block, stationary block and multiple pin cutter.

The magazine is designed to hold ten pins at a time and it is optimized based on the limitations on size and weight of the magazine and cutting tool from remote handling perspective as well as the throughput requirements. Length of the magazine has been arrived, considering the elongation of the pin after irradiation.

Fuel pins slide on stationary block up to 32 mm projected length of the pin and then it is gripped by gripper block with the help of pneumatic cylinder.

Table 1: Cutting tool details	
Shear force on tool (estimated)	2500 kgf
Shear force on tool (measured)	2000-2400 kgf
Maximum stress on the cutting tool	128 MPa (allowable: 800 MPa)
Tool life	>10 ⁶ cycles (as per fatigue life)
	≈10 ⁵ cycles (due to wear and tear)
Cutting speed	16 mm/s

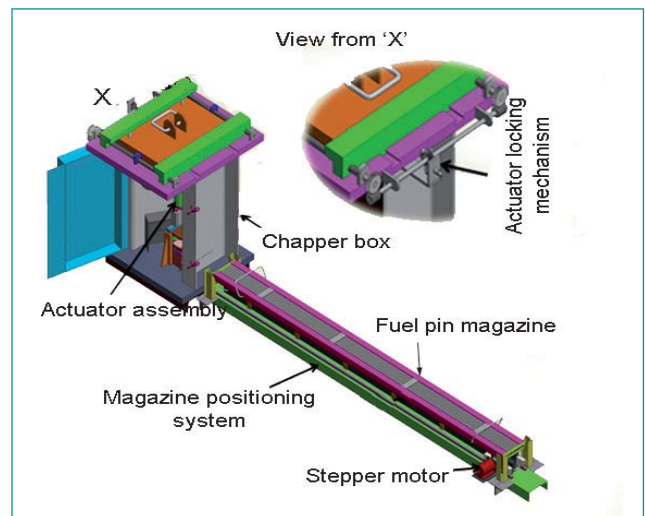


Fig. 1 3D drawing of special shearing machine

The shear force required for cutting two pins at a time has been calculated to be 2500 kgf. Material of cutting tool is chosen based on the requirements such as hardness, toughness, corrosion resistance and wear resistance.

Prototype of the chopper was manufactured and mock up trials were carried out for feeding, gripping and shearing systems. Tests were carried out on dummy fuel pins and also on pins with different materials to demonstrate the shearing performance of the equipment.

Finite element analysis was carried out to estimate the stresses on the cutting tool and design life of cutting tool was calculated based on failure modes such as Blunting of the tool and high-cycle fatigue.

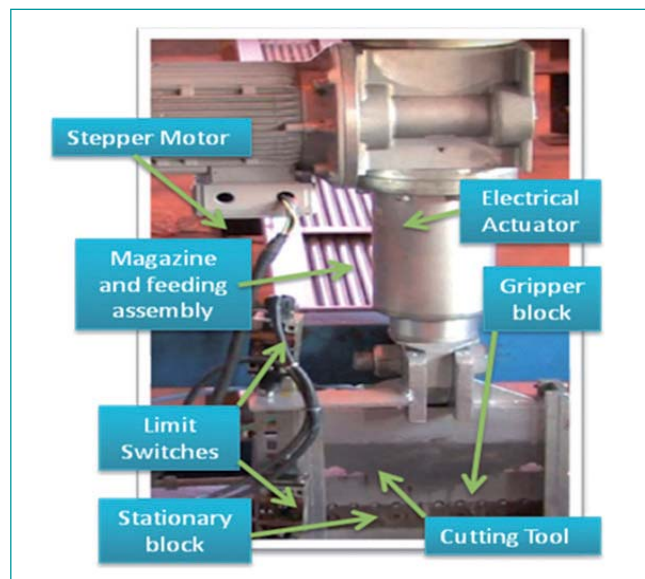


Fig. 2 Multi pin chopper

Cutting tool performed well for aluminum rod, stainless steel rods and dummy fuel pins of PFBR FSA pin (Table 1). Dummy fuel pins along with spacer wire were chopped and performance in chopping of pins was satisfactory. Actual photograph of cutting, gripping and feeding mechanism and chopped pieces are shown in Figures 3a and 3b respectively.

With the validation of the design several improvements are being implemented in the engineering drawing for the fabrication of chopper for deployment in the plant.

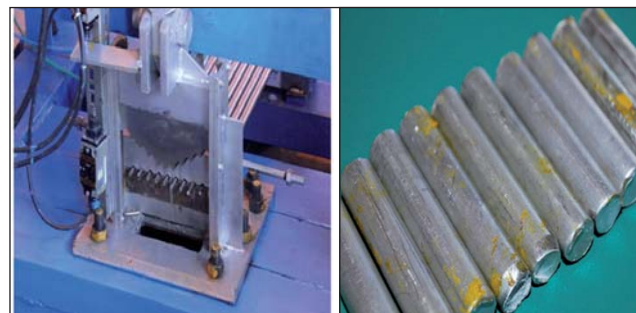


Fig. 3 (a) Photograph of cutting, gripping and feeding mechanism and (b) chopped pieces

IV.5 Design and Validation of Inter Cell Transfer System for Storage Cell of FRP-FRFCF

Inter cell transfer system (ICTS) is required to horizontally transfer spent fuel sub-assemblies (FSA) and radial sub-assemblies (blanket sub-assemblies, RSA) between storage and dismantling cells of FRP/FRFCF. To facilitate the operation, a system has been designed, a mock up model manufactured, and design is validated. The various challenges are, component need to be modular design for remote maintenance, travel length to be 11 metre from storage cell to dismantling cell and achieving alignment of the guide plate for such a long distance travel, development of customized drive mechanism and selection of materials amenable for radioactive environment.

The important components of inter cell transfer system are transfer carriage, track and actuating mechanism with necessary instrumentation. A transfer carriage carrying fuel and radial sub-assemblies moves on the track and it consists of six wheels which are amenable for maintenance and replacement. The movement of transfer carriage is provided by electrical actuator as shown in Figure 1. Transfer carriage has been attached to the electrical actuator by an actuating mechanism to the actuator engagement plate at different locations as shown in Figure 1. The actuating mechanism is designed in such a way that the stroke length required is less, which results into compact mechanism. Actuation of this mechanism is done by electrical actuator.

Once FSA/RSA is placed on the transfer carriage of inter cell transfer system, actuating mechanism pushes the carriage along longitudinal direction with the help

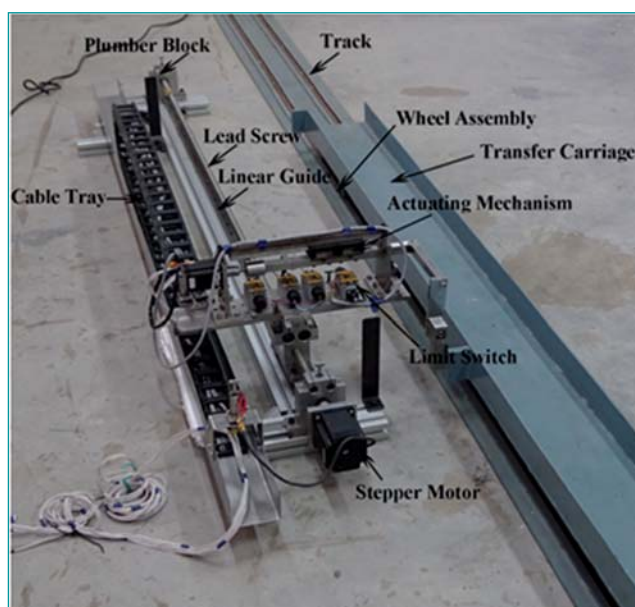


Fig. 1 Prototype model of inter cell transfer system

of engagement plate of transfer carriage. The complete stroke of transfer carriage is pushed repeatedly by actuating mechanism. This necessitates the actuator mechanism to make to and fro motion to push the transfer carriage completely into the inter cell transfer port. A double door mechanism is employed to close the inter cell transfer port to prevent any radioactive contamination between cells. The carriage is pulled by the same actuating mechanism placed on the other side from the transfer port.

A mock up of inter cell transfer system was fabricated, trials were conducted and design has been validated.

IV.6 Thermal Fatigue Analysis of Tube to Tubesheet Joint of FRP Thermosyphon Evaporator and its Fatigue Damage Assessment

The aqueous wastes arising out of various cycles of solvent extraction process in the spent fuel reprocessing are reduced in volume by evaporating these large quantities in a controlled manner. Evaporation is also employed to concentrate the uranyl nitrate solution. Thermosyphon evaporators (TSEs) are used for this purpose.

A thermosyphon evaporator is a liquid reboiler in which natural circulation of the boiling liquid is obtained by buoyancy. Low-pressure steam is used as heating medium in the evaporators. Thermosyphon evaporator consists of a reboiler section/heat exchanger (HX), vapor drum for vapor-liquid separation and a down comer. The reboiler is a shell and tube heat exchanger. Steam is admitted at the shell side at 130°C and process liquid in tube side at 30°C. The concentrated process liquid is discharged from the bottom and the overhead vapors are also condensed and collected at bottom. A typical TSE is shown in Figure 1.

Experience from Indian reprocessing plants indicate that failures of TSEs occur at the tube to tubesheet joint in the heat exchanger part of TSEs. One of the possible reasons for the failure of TSEs at tube to tubesheet joint is due to crevice corrosion combined with thermal fatigue. To avoid the crevice corrosion, it is suggested to attain good strength by adopting radiography qualified butt joint, spigot type tube to tubesheet joint and a detailed fatigue analysis of TSEs is performed to assess the fatigue damage.

There are five types of evaporators based on the capacity used in plant. Based on the geometric configuration and aspect ratio, small size heat exchanger having highest

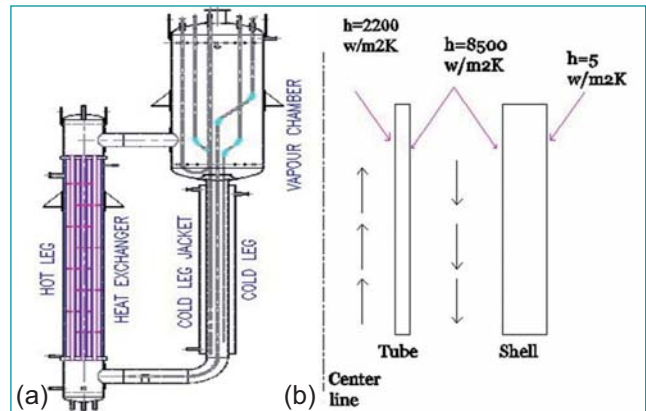


Fig. 1 (a) Thermosyphon evaporator and (b) schematic of demonstrator tube and shell HX with fluid flow

stiffness is chosen as representative model for analysis. If the selected representative TSE's HX qualifies, then the remaining TSE's HX are treated as qualified.

Since the transient analysis of global model require high computing facility as well as consumes more time resources, it was planned to evaluate the critical operating loading condition by performing the simulation analysis on one demonstrator tube associated with HX shell. The schematic sketch of demonstrator tube and shell with boundary condition and fluid flow is shown in Figure 1b. The transient analysis carried out on the demonstrator tube and shell and the corresponding temperatures are plotted in Figures 2 and 3 as function of time.

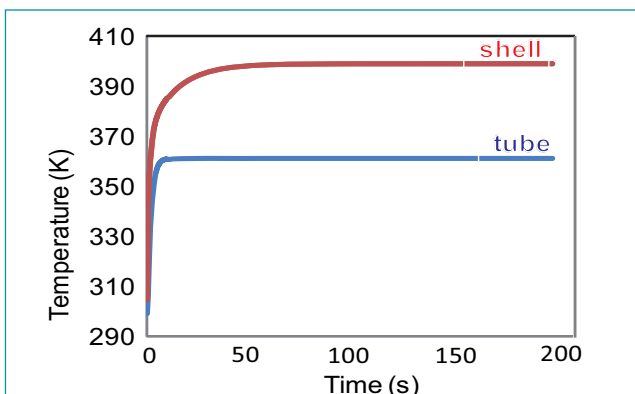


Fig. 2 Variation of temperature in the demonstrator tube and shell

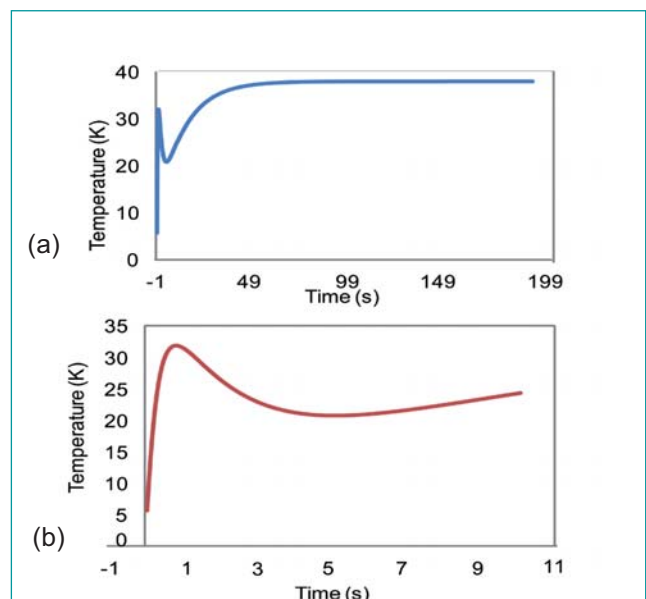


Fig. 3 Variation of temperature difference, ΔK in the demonstrator (a) tube and (b) shell

Initially the inner area of shell and tube were at the same temperatures i.e., ΔT is zero. With increase in time, temperature of the area in contact with the hot fluid increases quickly. Due to thermal resistance, variation of temperature of inner tube surface is less. From Figure 4a it is very clearly seen that, up to about a second ΔT increases rapidly and with time, temperature of inner surface of shell also increases, hence the rate of heat transfer decreases thereby decreasing the rate of temperature rise. Simultaneously when the temperature of tube raises quickly, ΔT is less due to less heat transfer to the process fluid. After heat transfer for five seconds the process fluid becomes significant causing slow rate of increase of tube temperature, hence ΔT increases. After 6-8 seconds tube attains steady state temperature of 360 K. Shell steady state temperature 398 K is achieved after 40-45 seconds. Max ΔT is found out to be 38 K.

The maximum temperature difference (ΔT) was observed to exist in steady state condition. Maximum temperature difference (ΔT) causes the maximum stress range; hence maximum stress range (ΔT) will be obtained in steady state condition. On the basis of demonstrator transient analysis, it is concluded that for the global and local analysis of TTS junction of thermosyphon evaporator, steady state analysis needs

to be performed to obtain maximum stress range.

To avoid the crevice regions and attain good strength at tube to tubesheet joint, spigot joint of tube to tubesheet with suitable fillet radius was worked out, which facilitated 100% radiography qualified butt weld. The global finite element modelling of thermosyphon evaporator carried out using mapped meshing for better results, required a number of iterations and meticulous planning in attaining the mesh due to its intricate shape. The local finite element modelling of thermosyphon evaporator with fillet radius was also developed to account for the stress concentration factor. Actual stress and stress range calculation were carried out with number of iterations in order to avoiding the singular points (Figures 4b and 4c).

Under the sustained thermal loads on the thermosyphon evaporator, the maximum allowable reversals obtained was more than 106 cycles. Stress and number of cycles by global and local analysis were in good agreement. Maximum number of cycles required for thermosyphon evaporator type 2 is 33120. As representative thermosyphon evaporator, the stiffest evaporator has been taken up for analysis which was found to be safe and hence, the design analysis report is valid and safe for all the remaining thermosyphon evaporators.

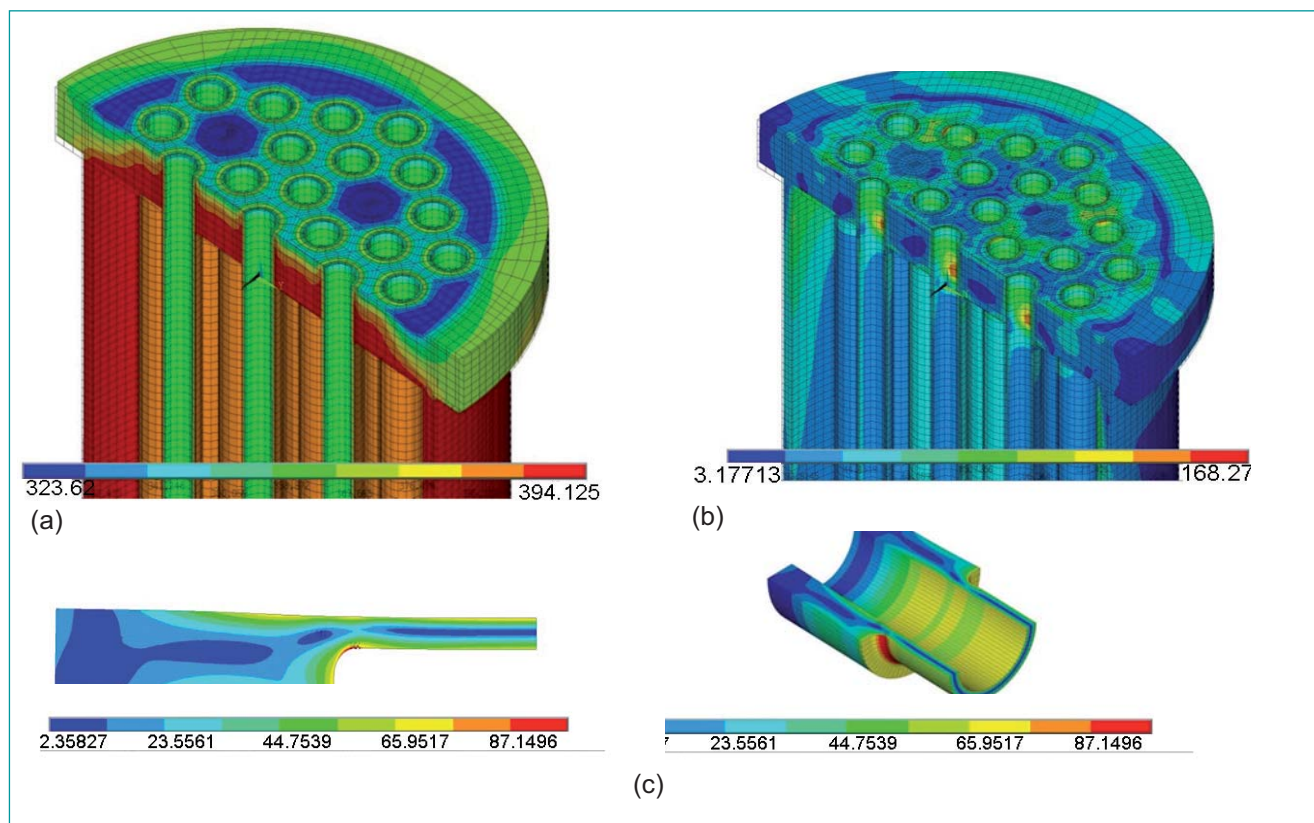


Fig. 4 (a) Temperature distribution in TTS junction of TSE, (b) stress distribution in TTS junction of TSE and (c) stress distribution in local model analysis of TTS junction of thermosyphon evaporators. (plane and 1800 expanded view of TTS joint)

IV.7 Hydraulic Analysis of Ballast Tank Operation of High Level Liquid Waste Storage Tank in FRP of FRFCF

High Level Liquid Waste (HLLW) which contains about 99.9% of fission products is generated during the separation of uranium and plutonium from the spent fuel by solvent extraction. This waste is stored in horizontal cylindrical stainless steel storage tanks in Waste Tank Farm (WTF) of Fuel Reprocessing Plant (FRP) of Fast Reactor Fuel Cycle Facility (FRFCF). Total volume of each HLLW storage tank is 212 m³ with an inside diameter of 4.7 metres and a cylindrical length of 11 metres. During its storage, solids containing fission products may settle at the bottom, which also generates decay heat. This may lead to formation of local hot spot, since heat removal will not be effective. This local increase in temperature may give rise to bumping of liquids and may enhance the corrosion rate. Ballast tanks are provided in each HLLW tank to keep the solids in suspension. Ballast tanks are small vertical tanks with a nozzle at the bottom. It is used to unsettle the solids which settle at the bottom of the tank. Compressed air is admitted into the top of the ballast tanks for a certain period, and the liquid is jetted through the bottom nozzle, thereby unsettling the solids. Figure 1 shows the schematic of ballast tanks in HLLW tank. Each HLLW tank consists of eight ballast tanks. Liquid jet velocity and jetting time are the major design parameters of ballast tank. Ballast tank is made from 400 NB pipe with 3.6 metres height and 25 NB SCH 40 bottom nozzle.

Computational fluid dynamic investigation was carried out to study the jet flow development near the bottom surface of the tank during impingement of liquid jet with a velocity of 15 and 20 m/s. A symmetric model was created and the fundamental governing equations such as continuity, momentum (Navier-Stokes) and energy

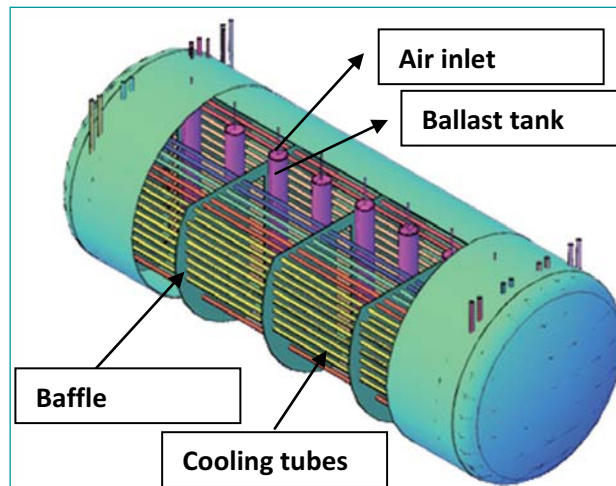


Fig. 1 Schematic of ballast tanks in HLLW tank

balance equations along with the equations for modeling the turbulence were used.

It is assumed that flow is incompressible, Newtonian, constant fluid properties without any buoyancy effects and negligible viscous dissipation. k-ε turbulence model was used since it is accurate near wall region and is successful for jet flows. The intensity of turbulence (I) at the inlet of nozzle was taken as 5% and nitric acid was used as the working fluid. Appropriate boundary condition and convergence criterion were considered. The study is carried out for the uniform liquid jet velocity (15 and 20 m/s) from the nozzle. Figure 2 shows the schematic of planes and points used for data reduction.

Figure 3 shows axial velocity variation along the jet axis plotted against distance along O - O' (refer Figure 2). Velocity is zero near the wall due to no-slip wall boundary condition. Further away from the wall, fluid velocity

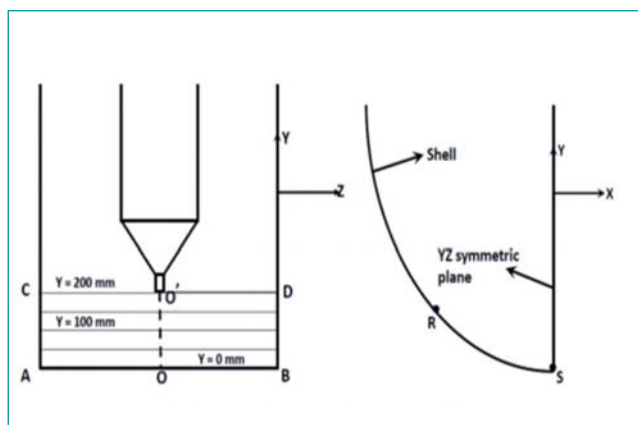


Fig. 2 Schematic of planes and points used for data reduction

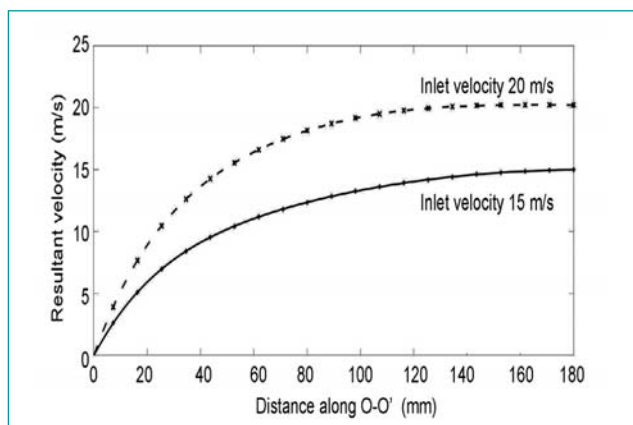


Fig. 3 Velocity variation along axis of jet plotted along O - O'

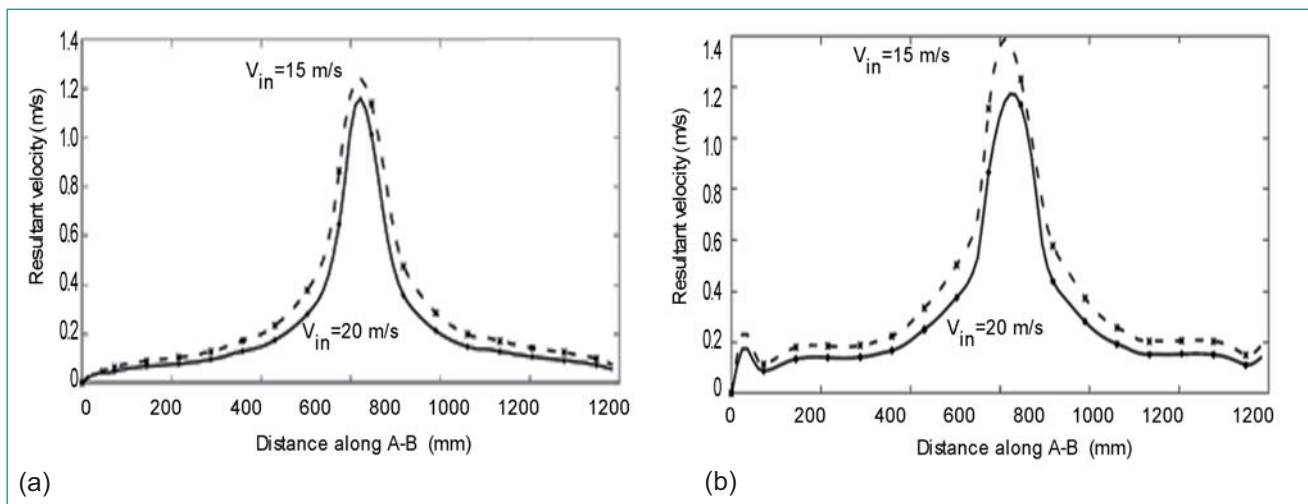


Fig. 4 Velocity variation along line A-B at various Y. (a) Y = 0 and (b) Y = 50 mm

gradually increases till a height of approximately 40-45% of jet axis from wall and then becomes nearly constant. Absolute velocity is plotted at various horizontal planes (i.e. at different y, refer Figure 2) parallel to AB below jet nozzle, as shown in Figure 4. It was observed that flow was predominant along the jet axis and loses its momentum and energy away from the nozzle. Velocity decreased below 1.5 m/s near the baffle region, which is evident from Figure 4. The parabolic behavior of flow depicts the jet penetration phenomenon inside the tank. Figure 5 represents velocity variation along curved peripheral plane near the tank's bottom surface, i.e. along S - R (refer Figure 2). It is evident that velocity was higher in the region near to jet axis and drastically

decreased to 1.5 to 2 m/s in the region 0.1 m away from jet axis towards tank periphery. Velocity near jet axis was 8 and 13 m/s for 15 and 20 m/s conditions respectively, as shown in Figure 5.

From the study it is concluded that Jet impingement induces flow mixing near the tank wall and it was also observed that near the wall and below the jet, fluid velocity ranges from 1 to 2.5 m/s, when inlet liquid jet velocity was in the range from 15 to 20 m/s. Away from the jet, the flow velocity near the wall was approximately 0.1 m/s. It is also concluded that number of ballast tanks provided and the chosen jet velocity are adequate and able to create disturbance without any dead zones in the tank.

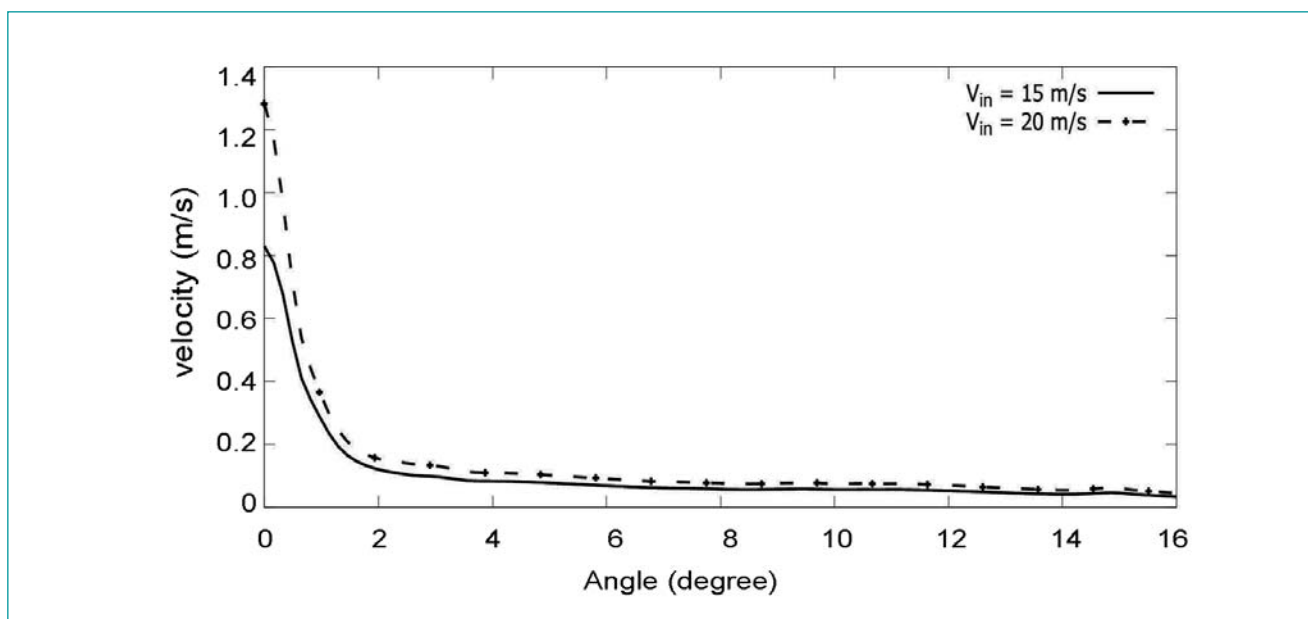


Fig. 5 Velocity variation along S-R, on periphery of cylindrical tank (Angle 0° at S and increased along S - R)

IV.8 Detector Transfer System for Hull Monitoring in DFRP

Chop-leach process is adopted in fuel reprocessing, where the spent fuel pins are cut into pieces and subjected to dissolution. After dissolution, the fuel pin clad is disposed as solid waste, called hulls. This hull waste needs to be assayed for fissile material content, before disposal. For assaying the fissile material content of the hull inside a hot cell on engineering scale, a system was designed and developed for DFRP. This system for fissile material assaying of hulls is referred to as “hull monitoring system”.

The hull monitoring system comprises two sub systems, viz. a detector transfer system and a hull holding station. The detector transfer system comprises various sub-assemblies such as motorized boom and supporting structure. Hull holding station consists of hull basket guiding chute, modular interlocking shield assembly, movable lead door, leak tight tunnel etc.

The controlled movement necessary for the HPGe detector assembly is provided by the detector transfer system (Figure 1). The detector and its accessories are rigidly fixed at the front end of a cantilever boom. This boom is made of 16 mm thick SS304L plate and is 3 metres long. Carriage with boom is moved through a leak tight tunnel using a lead screw-nut mechanism up to hull holding station, located 3 metres inside the dissolver cell. Stepper motor in the detector transfer system is controlled using a Human machine interface (HMI). Electrical limit switches as well as mechanical stoppers are also provided to stop overrun of boom. The tunnel acts as a primary barrier between the cell and operating area and it also provides a leak tight containment.

Hull holding station serves the purpose of holding the hull basket during monitoring. A modular shield assembly provides required shielding to the hull basket to minimize the background gamma radiation. This modular shielding consists of six interlocking lead rings. Hull basket is

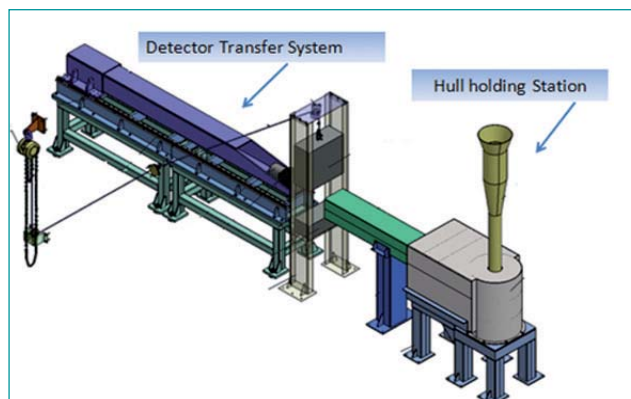


Fig. 1 Detector transfer system

inserted into hull holding station through a chute from the top and fissile material assaying is carried out using detector transfer system.

the complete system has been manufactured and assembled at site with perfect alignment using optical instruments. The movement of the boom with carriage was found to be smooth without any vibration. The system has been tested and commissioned successfully (Figure 2).



Fig. 2 Assembled detector transfer system at DFRP

IV.9 Fast Reactor Fuel Reprocessing Plants

CORAL (COmpact Reprocessing of Advanced fuels in Lead Cell) has continued to process spent fuel from FBTR successfully. One of the degraded radiation shielding windows (RSW) has been replaced successfully in-situ, after obtaining clearance from

AERB, with minimum man-rem expenditure. This was a first-of-its-kind activity to be carried out. This replacement of RSW has restored the visibility and has aided the successful maintenance and rectification of feed clarification system viz. centrifuge, which has

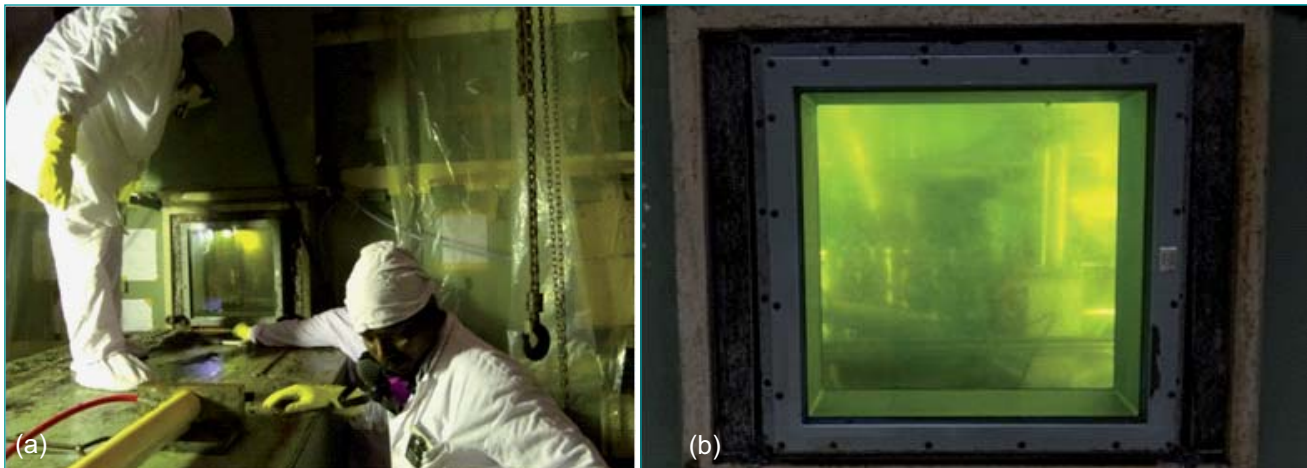


Fig. 1 (a) RSW replacement under progress and (b) RSW after replacement

performed well in the recent runs, has solved many of the plant problems (Figure 1). Subsequent to these improvements, further campaigns have been completed. Third phase formation during solvent extraction with high plutonium bearing solution has safety implications and hence, a methodology of detection of third phase in solvent system by using electrical conductivity method is successfully demonstrated for the first time. Other important work carried out are the design improvement of criticality alarm system (CAS) for enhancing the reliability and preventing spurious alarms.

Considerable physical progress has been achieved in Demonstration Fast Reactor Fuel Reprocessing Plant (DFRP) and construction activities are about to be completed. All the major equipments such as chopper, dissolver, centrifuges, centrifugal extractor banks, evaporators, tanks etc., have been erected at site, tested and piping completed. Many important and first-of-its-kind equipment like robotic sampling system, hull monitoring system etc., have been tested at site. Commissioning activities have started and water runs are under progress. As part of water runs, calibration of tanks, checking of transfer systems, spargers etc., have been completed. Necessary preparations are underway

for taking up the next phase of commissioning namely the Acid-TBP runs. Plant services namely the compressed air system, steam system, process cooling water system, electrical system etc. have been commissioned and are operating. Process instrumentation has been completed and majority of the radiation monitoring and physical protection instrumentation are in place.

One of the critical equipments, a novel handling system for the dissolver cell has been designed and developed to cater to the remote operation and maintenance of various in-cell systems like fuel transfer system, chopper, dissolver, hull transfer mechanisms etc., is employed in the dissolver cell of DFRP. As, the dissolver cell is of square size requiring high long travel, innovative designs consisting of lead screw with floating nut are incorporated to get a very compact system providing maximum handling reach. Special mechanisms were formulated in order to bring all the wear and tear components requiring periodic maintenance such as drive motors, gear boxes and limit switch systems out of the hot cell and to keep in an alpha tight drive box for contact maintenance. The main control room and special in-cell crane for dissolver cell of DFRP are shown in Figure 2.



Fig. 2 (a) View of main control room and (b) and (c) special in-cell crane for dissolver cell of DFRP

IV.10 Dissolution Studies on Simulated (U, Ce) MOX Fuel in Nitric Acid

In a spent nuclear fuel reprocessing plant, dissolution is one of the sluggish processes which decide the overall throughput of the plant, specially for the FBR MOX spent fuel which is rich in plutonium. Designing this process for continuous mode operation would go a long way in increasing the plant throughput apart from offering many other advantages. Determination of the dissolution kinetics of the spent nuclear fuel is one of the essential input data for designing a continuous spent fuel dissolution system. Hence, it was decided to study the kinetics of dissolution of a simulated MOX fuel using Ce as a surrogate material for Pu before studying the U, Pu MOX fuel. For this purpose four different compositions of (U, Ce) MOX, viz, 15, 22, 28 and 35 atom percent Ce were chosen. These pellets were prepared by combustion synthesis using citric acid as the combustion fuel and sintered at 1600°C.

Experiments were conducted under typical PUREX process conditions to study the effect of Ce composition and mixing intensity on the dissolution kinetics of the simulated MOX fuel in a cylindrical glass reactor which has provisions for mechanical mixing, temperature control and off-gas treatment. It was found that addition of Ce to the MOX gradually decreased the overall dissolution rate which establishes the sluggish dissolution behaviour of ceria. It was also found that higher the mixing intensity, lower is the dissolution rate. This is due to the autocatalytic effect of nitrous acid on the oxidative dissolution of urania-ceria. At higher speed of mixing, the nitrous acid produced at the solid surface is dispersed into the bulk liquid which makes it relatively unavailable for the dissolution reaction. Effect of Ce composition and mixing intensity on the dissolution

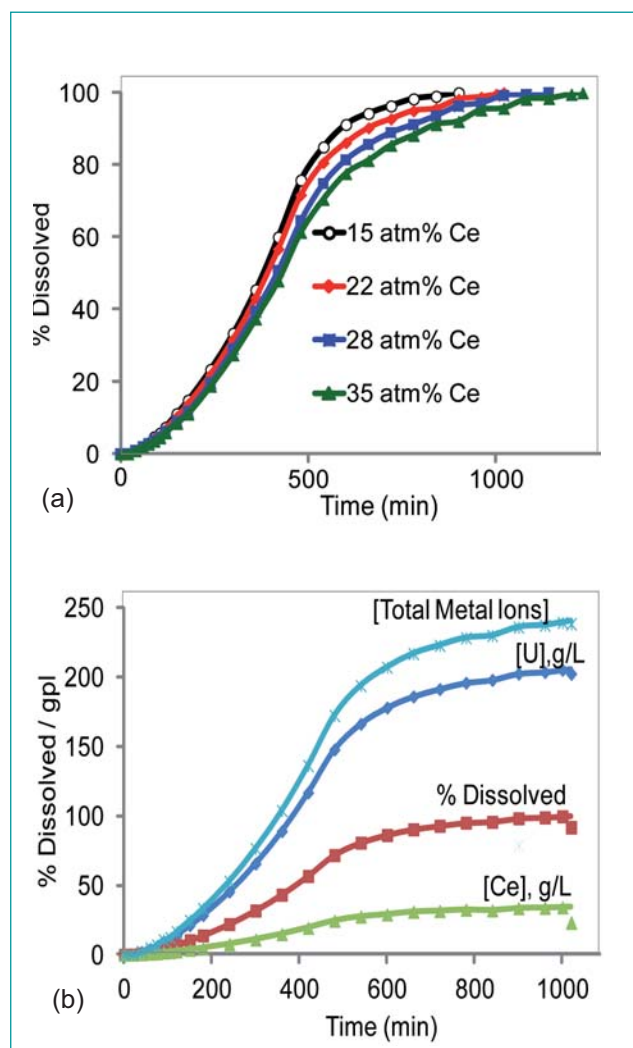


Fig. 1 Effect of Ce composition and mixing intensity on the dissolution kinetics of simulated MOX fuel in nitric acid

kinetics of simulated MOX in nitric acid is shown in Figures 1a and 1b.

IV.11 Long-Term Corrosion Testing of Advanced Dissolver Materials in Zircaloy Mock-Up Dissolver

Reprocessing plants for the aqueous processing of Pu-rich spent fuels of FBRs are characterized by high concentrations (11.5 M) of boiling nitric acid, high radiation field and highly oxidizing fission and corrosion products. To meet the demand of zero failure concept during the service life of reprocessing plants zirconium,

titanium and their alloys are considered for the fabrication of dissolver vessel for FBR fuel reprocessing. A mock-up Zircaloy (Zr-4) dissolver vessel was fabricated and commissioned in collaboration with NFC. To qualify and to assess the service life of the Zr-4 dissolver, long-term corrosion testing of the mock-up dissolver using

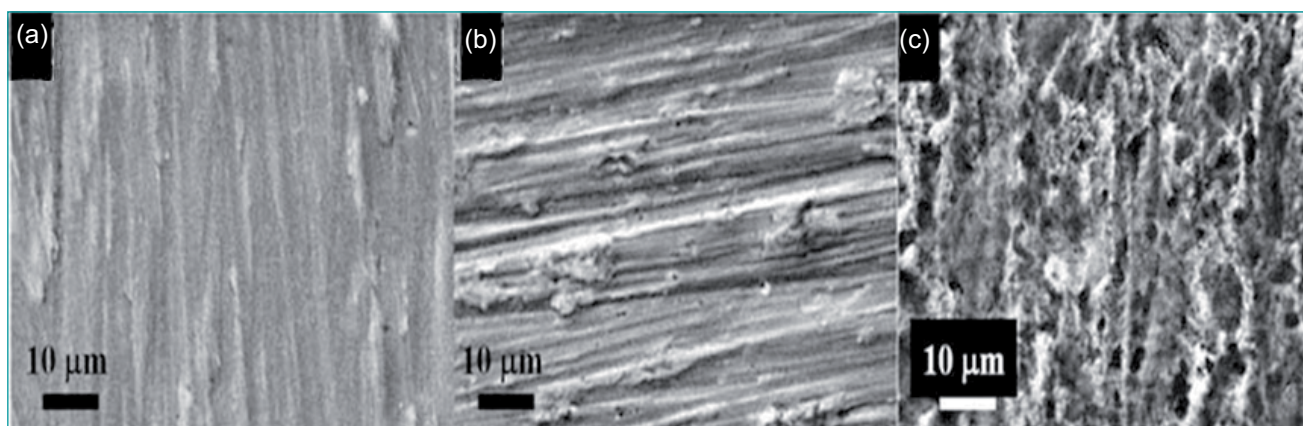


Fig. 1 SEM images of samples exposed to SDS for 5000 hours (a) CP-Ti in liquid phase, (b) Zr-4 in liquid phase and (c) Ti to vapor phase

simulated dissolver solution (SDS) at boiling condition was aimed at. Calculated quantities of metal oxides or nitrates corresponding to the composition of fission and corrosion products envisaged in the mixed carbide fuel, which had undergone a burn-up of 150 GWd/t and after a cooling period of one year were dissolved in 11.5 M nitric acid and used to simulate the dissolver solution. Several candidate materials based on zirconium and titanium (commercially pure Ti (CP-Ti), CP-Ti weld, Ti-5Ta-1.8Nb, zirconium-702 (Zr-702), Zr-702 weld, Zr-4, Zr-4 weld and autoclaved Zr-4 coupons) were also subjected to corrosion testing in the simulated dissolver solution.

The dissolver was maintained at the boiling temperature (110°C) of the simulated dissolver solution. A PTFE sample holder assembly, designed in such a way that the samples are exposed to both the vapor (85 °C) and the boiling liquid phase of SDS was fabricated for holding the corrosion test coupons inside the vertical limb of the dissolver. As the dissolver is connected to SS304L feed conditioning tank using SS304L pipes in the plant, corrosion rates of the explosively welded Zr-4/SS304L and CP-Ti/SS304L samples were also evaluated. Several campaigns of 100, 250, 500, 1000, 2500 and 5000 hours of operation were carried out, and the average corrosion rates were calculated based on the weight loss.

After completion of 5000 hours of campaign, no corrosion attack was observed at the outer surface and at the weld joints of the Zr-4 dissolver vessel operated in boiling SDS. Zr-702, Zr-702 weld, Zr-4, Zr-4 weld and autoclaved Zr-4 exhibited low corrosion rates of 0.21, 0.24, 0.23, 0.26 and 0.1 µm/y, respectively and CP-Ti, CP-Ti weld and Ti-Ta-Nb showed corrosion rates of 0.19, 0.29 and 0.22 µm/y, respectively in the boiling liquid phase of SDS. In the vapor phase of SDS, CP-Ti, CP-Ti weld and Ti-Ta-Nb showed marginally higher corrosion rates of 0.64, 1.57 and 1.61 µm/y, respectively.

The surface of the samples after exposure to the vapour and boiling liquid phases of the simulated dissolver solution was characterized by scanning electron microscope (SEM) and LASER Raman Spectroscopy (LRS). SEM investigations (Figures 1a and 1b) of Zr and Ti samples exposed to boiling liquid phase revealed smooth and un-attacked surface morphology. However, the SEM image for Ti alloy (Figure 1c) exposed to the vapor phase indicated corroded surface with rough morphology. The corrosion rates for CP-Ti/SS304L dissimilar welds were as high as 6.3 and 5.3 mm/y, respectively in the vapor and liquid phase of simulated dissolver solution, when the exposure period was 500 hours. Similarly, high corrosion rate of 6.9 mm/y and interface failure were observed for Zr-4/SS304L dissimilar weld, when exposed to boiling liquid phase of SDS for 1000 hours. The SS 304L side of the welds had undergone severe dissolution. Nevertheless, their counterpart (Zr-4 and CP-Ti) side was un-affected. Thus, for the safe operation of the dissolver, the nitric acid solution should be transferred through the dissimilar weld joints only at low temperatures and not at boiling conditions. Further, to minimize the vapor phase attack, the dissimilar welds should be placed far away from the dissolver vessel. The surfaces of Zr and Ti samples exposed to boiling liquid, and vapor phases of SDS were investigated by LRS to understand the passivation behavior. LRS analysis confirmed the presence of anatase and rutile mixed phases in the passive films of CP-Ti samples exposed to boiling SDS and for the zirconium samples the film was composed of tetragonal zirconia in addition to monoclinic ZrO₂ as the major phase.

Long term corrosion testing under the simulated condition is in progress and the corrosion rates obtained after 10000 hours campaign would be used to model and predict the life expectancy of Zr-4 dissolver vessel.

IV.12 Identification of Diluent Degradation Products in Irradiated PUREX Solvent

For the aqueous reprocessing of nuclear spent fuels by plutonium uranium extraction (PUREX) process, tri-n-butyl phosphate (TBP) in n-dodecane (DD) is employed as the solvent. During the extraction stage in the reprocessing of fast reactor spent fuels, the solvent comes in contact with intense ionizing radiation as well as with nitric acid, resulting in the formation of various degraded products. Alkali wash of the degraded solvent removes the TBP degradation products, whereas diluent degradation products (DDP) get accumulated in the solvent and disrupt the extraction process. Though a vast literature data is available on the identification and quantification of the degradation products of TBP either in single phase or in biphasic system, data on the characterization of diluent degraded products are scanty and hypothetical. Hence, in the present study efforts were made to separate and identify the DDPs formed in the radiolyzed solvent.

A 1.1 M solution of TBP in n-DD after equilibration with 4 M HNO₃ was subjected to radiolysis up to 100 MRad absorbed dose using a ⁶⁰Co gamma chamber that gave the dose rate of 3.58 kGy/h. The degraded solvent was washed with 1:1 (v/v) alkali to remove the acidic degradation products of TBP. The washed solvent was fractionally distilled at reduced pressure. The FT-IR spectra of the collected fractions were compared with that of the residual solution (Figure 1). The fractions collected were observed to be rich in diluent and the final residue was rich in TBP based compound along with the DDP. The GC spectra of the residue confirmed this observation (Figure 2). Since the residual solution was enriched in DDP, it was subjected to column chromatographic separation (silica gel; 100-200 mesh) using ethyl acetate/hexane gradient mixture as eluent. The separated fractions were analyzed by gas chromatography (GC) and fractions with identical GC profiles were combined and concentrated (F1-F5).

GC profiles obtained for the five sets revealed that the first set, F1 contained only dodecane, whereas the last set, F5 contained only TBP. The remaining sets, F2, F3 and F4 comprised the radiolytic degraded products, and F3 was a mixture of F2 and F4. The characterization of the degradation products of the diluent was carried out using GC-MS and ¹³C NMR techniques for the set F2 since the compounds were well resolved in a capillary column.

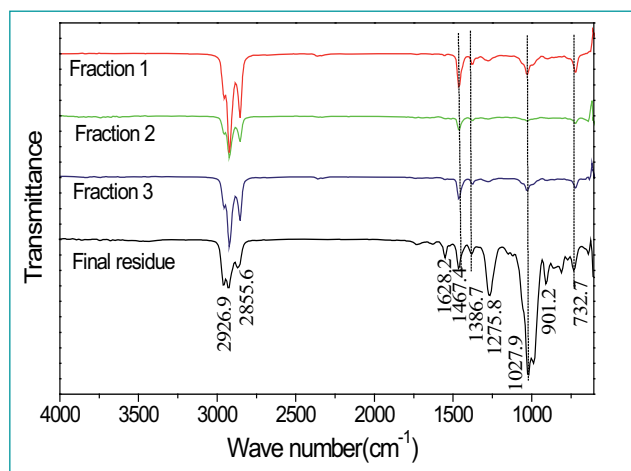


Fig. 1 IR spectra of collected fractions of DDPs, during fractional distillation

The mass fragmentation corresponding to the three product peaks for F2 were analyzed and were identified to be three dodecanol isomers: dodecan-3-ol, dodecan-4-ol and dodecan-5-ol in the ratio 6:2:1. During degradation in presence of nitric acid, the acid serves as a source for the formation and regeneration of radical like molecule of NO₂, which in combination with diluent may form diluent radical and subsequently alkyl nitrite. The alkyl nitrite on hydrolysis gives alcohol. Formation of the three alcohols was confirmed from the ¹³C NMR spectrum of set F2. The three carbon signals in the region 72-74 ppm appeared in the NMR spectrum, corresponding to the -CHOH group present in the alcohols.

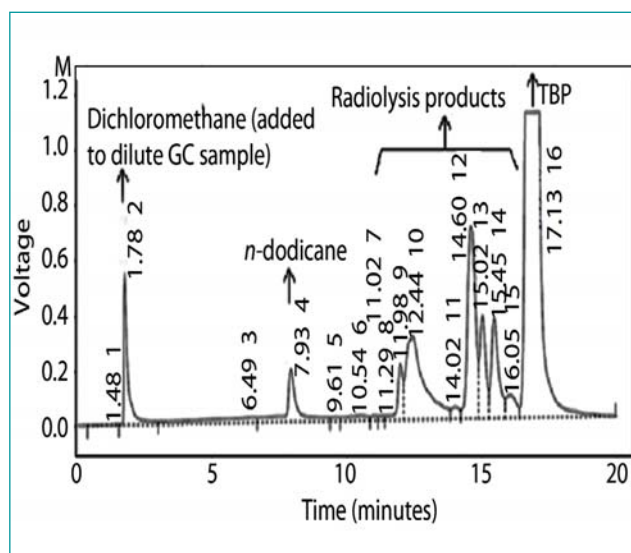


Fig. 2 Gas chromatography profile of final residue

IV.13 Distribution Behavior of Ruthenium with TiAP/ Dodecane System

The experience gained in the spent nuclear fuel reprocessing revealed that Tri-n-butyl phosphate (TBP) has some limitations such as third phase formation with tetravalent metal ions, high aqueous solubility which can lead to "red oil formation," chemical degradation, radiation degradation, etc. Tri-iso-amyl Phosphate (TiAP) has been proposed as an alternate extractant to TBP to overcome these limitations. Ruthenium is a troublesome fission product in the aqueous reprocessing of nuclear fuels contributing 75-90% of the beta and gamma activity. The fission yield of ruthenium is about 5%. Around 20% of the total activity is due to ^{106}Ru in a typical 28% Pu containing MOX fuel discharged from Fast Breeder Reactors (FBRs) with an average burn up of around 81 GWd/t and cooled for six months. As TiAP is proposed as a promising alternative solvent to TBP, the distribution behaviour of ruthenium with TiAP/dodecane (DD) system needs to be established. The distribution behavior of ruthenium with TBP/DD system is reported in the literature, however, data on the distribution of ruthenium with TiAP/DD system is not available.

Distribution of ruthenium with 1.1M TBP/DD and 1.1M TiAP/DD in nitric acid system was studied as a function of time over a period of twenty four hours in 2M HNO_3 . The results indicated that K_d of Ru increased initially and attained equilibrium after four hours. The effect of nitric acid concentration on K_d of Ru using 1.1M TBP/DD and 1.1M TiAP/DD was evaluated. The data obtained are given in Figure 1. It was observed that K_d of Ru increased with increase in acidity up to a concentration of 1.5 M and then decreased. The initial increase in K_d with acidity could be due to the increase in free organic concentration as well as highly extractable ruthenium nitrosyl trinitrato complexes and further decrease in K_d with increase in acidity is due to predominant decrease in free organic concentration compared to the increase in the highly extractable ruthenium nitrosyl trinitrato complexes. From Figure 1 it is clear that at all acidities, lower K_d values of Ru is observed with TiAP/DD than with TBP/DD system. This is attributed to the difficulty in complexation of nitrosyl ruthenium complexes with TiAP as compared to TBP due to bulkier iso amyl groups. Distribution of ruthenium with 1.1M TBP/DD and 1.1M TiAP/DD at 0.25 M HNO_3 was studied as a function of nitrate ion concentration between 0.25 to 6M. The results obtained are shown in Figure 2. It indicates that K_d of Ru increases with increase in nitrate ion concentration and is lower with 1.1M TiAP/DD

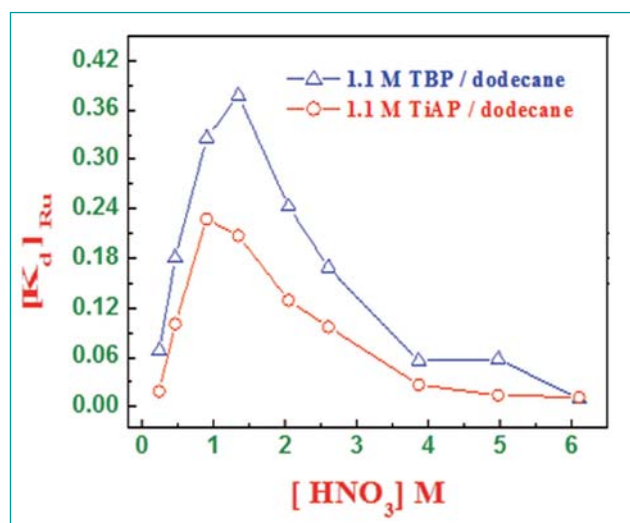


Fig. 1 Distribution of Ru as a function of nitric acid concentration

system compared to 1.1M TBP/DD system at all nitrate ion concentrations. The increase in K_d of Ru with nitrate ion concentration is due to the increase in highly extractable ruthenium nitrosyl trinitrato complex.

Distribution of ruthenium with TBP/DD and TiAP/DD as a function of ruthenium, organic phase concentration and temperature were also investigated. In all the above experiments lower K_d of Ru was observed with TiAP/DD than with TBP/DD system under various experimental conditions. It is concluded that using TiAP/DD as a solvent better decontamination may be achieved with respect to ruthenium than with TBP/DD system.

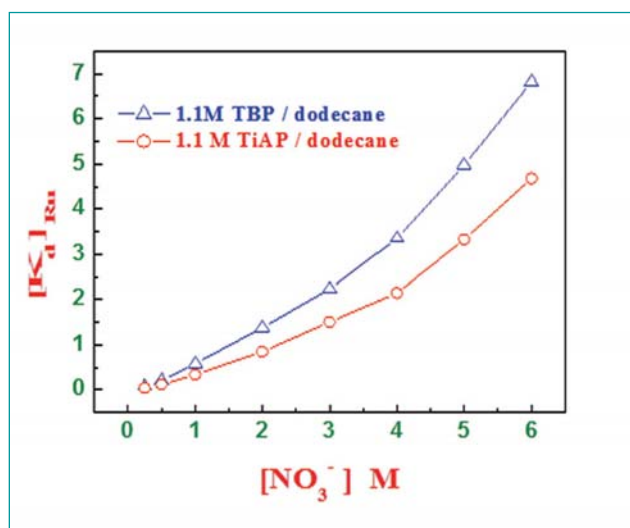


Fig. 2 Distribution of Ru as a function of nitrate ion concentration

IV.14 Investigation on Aggregation Behaviour of Metal Loaded Solvents using Small Angle Neutron Scattering

Tri-n-butyl phosphate (TBP) is the most widely used extractant in nuclear technology. However, some limitations of TBP such as third phase formation, aqueous solubility, degradation and poor U/Th separation pose problems during solvent extraction. Our earlier studies revealed that trisec-butyl phosphate (TsBP) exhibits higher U/Th separation factor with less tendency for third phase formation compared to its isomers TBP and tri-iso-butyl phosphate (TiBP). Hence, TsBP is considered as a suitable extractant for U/Th separation. Limiting organic concentrations (LOC, maximum amount of metal that could be accommodated by the organic phase at the threshold of third phase formation) have been measured for several trialkyl phosphates (TalP)-metal nitrate systems as a function of various parameters. The LOC was found to increase with the following: (i) increase in the chain length of alkyl groups of extractant, (ii) decrease in the diluent chain length and (iii) increase in temperature. Tetravalent metal ions viz., Zr(IV), Th(IV) and Pu(IV) are more likely to form the third phase with TalPs as compared to UO_2^{2+} .

Aggregation of extracted species resulting in the formation of reverse micelles leads to third phase formation. Small angle neutron scattering (SANS) is a powerful tool to probe the aggregation behaviour of such systems. SANS experiments were undertaken in collaboration with Solid State Physics Division (BARC), in order to get insights into the aggregation behaviour of metal loaded solvents in the extraction of Th(IV) and U(VI) from 1M HNO_3 by 1.1M solutions of TalP in deuterated dodecane ($n-C_{12}D_{26}$). Organic phases containing known concentration of Th(IV) and U(VI) in 1.1M TalP/ $n-C_{12}D_{26}$ were used for SANS measurements. TalPs having the general formula $(RO)_3P=O$ with n-butyl groups in TBP, iso-butyl groups in TiBP, sec-butyl groups in TsBP and sec-amyl groups in TsAP were investigated.

Scattering experiments were carried out using the small angle neutron scattering facility (Dhruva reactor, BARC).

$$Q = \frac{4\pi\sin\theta}{\lambda}$$

The differential scattering cross-section per unit volume ($d\Sigma/d\Omega$) was measured as a function of scattering vector (Q), where θ is the half-scattering angle and λ is the mean wavelength of the incident neutrons used.

$$\frac{d\Sigma}{d\Omega}(Q) = N_p V_p^2 (\rho_p - \rho_s)^2 P(Q) S(Q)$$

The samples taken in a quartz cell (thickness : 2 mm) were scanned in the Q range from 0.017 to 0.35 \AA^{-1} . The scattering intensity from a collection of particles depends on the form factor $P(Q)$, structure factor $S(Q)$, number density of particles (N_p), square of volume of particles (V_p) and scattering contrast $(\rho_p \rho_s)^2$ between the particles (reverse micelles) and the medium (diluent). Using Baxter's sticky hard-sphere model, the stickiness parameter (τ^{-1}), diameter of micelle (σ), width of square-well potential (Δ), depth of square-well potential (U_0) which is the potential energy of attraction and temperature (T) can be co-related as:

$$\tau = \frac{\sigma + \Delta}{12\Delta} \exp\left(\frac{U_0}{k_B T}\right)$$

In general, higher $d\Sigma/d\Omega$, τ^{-1} and U_0 imply higher aggregation behaviour and hence, higher third phase formation tendency. The effect of extractant structure on scattering intensity (Figure 1a) indicates that aggregation behaviour of TBP system is higher than the other three extractants. The effect of nature of metal ion on aggregation behaviour (Figure 1b) also supports higher third phase formation tendency of Th(IV) system. Other parameters (metal loading and temperature) also indicate that there is a clear correlation between scattering intensity, aggregation behaviour and tendency to form the third phase.

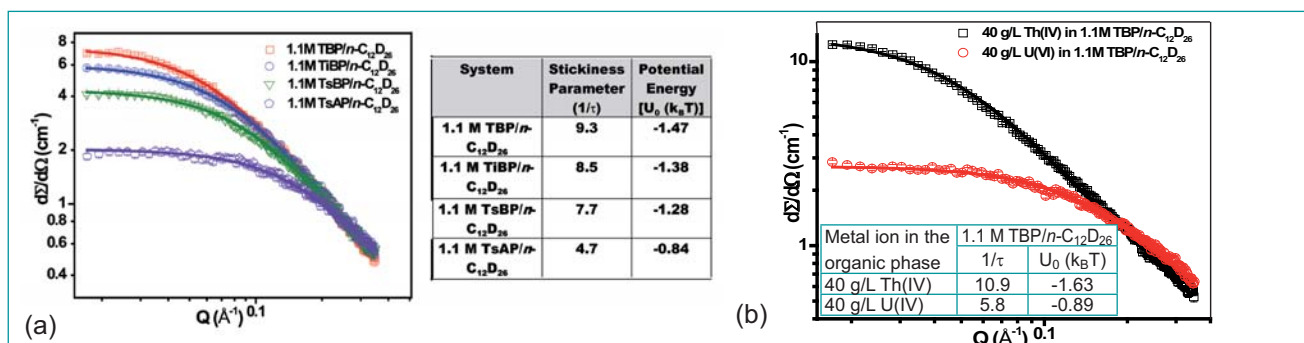


Fig. 1 Small angle neutron scattering data of (a) 1.1 M TalP/ $n-C_{12}D_{26}$ - 30 g/L $Th(NO_3)_4$ - 303K and (b) 1.1 M TBP/ $n-C_{12}D_{26}$ - metal nitrate - 308 K systems

IV.15 Preparation of Cubic (Metastable) Nanocrystalline HfO₂ through Nitrate Fusion Synthesis

All the stable isotopes of Hf have a high neutron absorption cross section. Hence, compounds of Hafnium (HfO₂ and HfB₂) can be used in the fabrication of control rods, for use in the fission nuclear reactors. Further, owing to its chemical inertness, HfO₂ could be used as a candidate material for holding reactive metals including molten uranium. The monoclinic form of this oxide is thermodynamically stable at room temperature, while its cubic analogue is stable at temperatures above 2873 K. In the application warranting the use of crucibles made out of hafnia, phase transitions are undesirable. Hence, the cubic phase is stabilized at room temperature by the addition of an aliovalent cation viz., Y³⁺. Thus the yttria stabilized hafnia is pertinent to such applications. Since hafnia is thermodynamically compatible with molten uranium at temperatures above 1300 K, crucibles made out of hafnia would be useful for applications involving containment of molten uranium. However, investigations on the synthesis of fine grained nanocrystalline c-HfO₂ are rather limited. Hence, experiments pertaining to scaled-up synthesis of nanocrystalline (nc) c-HfO₂ have gained prominence. In view of the above an experimental procedure was devised to produce (about 30 grams per batch) c-HfO₂ powder with crystallite size ranging from 6 to 21 nm using nitrate fusion technique. This is a “first-of-its-kind” experiment.

The specific surface area of the hafnia powder showed a strong dependence on the composition of the melt. Size distribution of particles in the “as prepared” nanocrystalline hafnia powder was found to be unimodal and comprised particles with a mean size of 10 nm. Nanocrystalline c-HfO₂ powders were calcined in air at different temperatures in order to find out the temperature at which the equilibrium phase is restored as well as coarsening of the grains. X-ray diffraction pattern of the

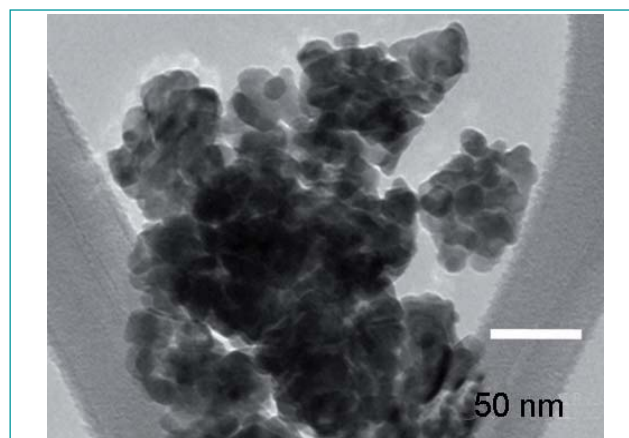


Fig. 1 Dark field image revealing nano grains

powders that were heated in air at various temperatures revealed that both grain coarsening and phase reversal to the thermodynamically stable monoclinic phase takes place at around 1473 K. The c-HfO₂ possesses minimum residual lattice strain, which does not seem to vary significantly with the calcination temperature.

Thermal analysis revealed that the nitrate fusion reaction takes place close to the eutectic temperature (457 K). This was further reaffirmed by evolved gas analysis (NO, NO₂, Cl₂, O₂ and HCl) and the weight loss observed in the thermogravimetric investigation. The addition of nitrite to the nitrate fusion mixture brings about a reduction in the oxygen potential of the melt which in turn controls the reaction kinetics as well as the characteristics of the product. Nanocrystalline c-HfO₂ powders prepared in this study did not show any Raman active mode in the spectrum.

Microstructural investigation of c-HfO₂ ascertained the presence of grains with uni-modal distribution of sizes (Figures 1 and 2) with a maxima at around 10 nm. High magnification image revealed that it comprised of faceted cubic crystals (Figure 3).

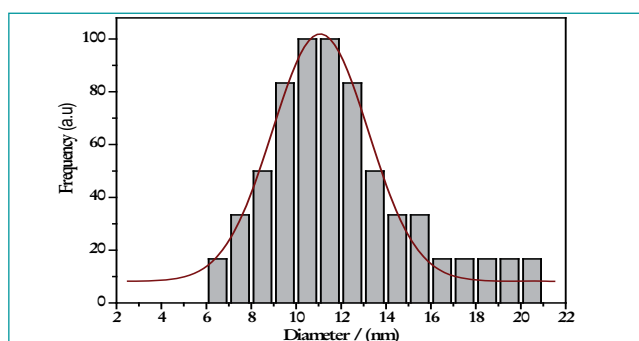


Fig. 2 Grain size distribution of c-HfO₂

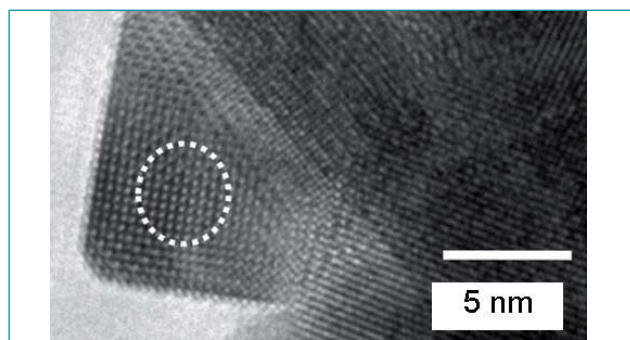


Fig. 3 HRTEM image

IV.16 Development of High Temperature Electro-Refiner

Molten salt electrorefining is the core process step in pyroprocess technology. In this step separation of actinides from fission products takes place. Lab scale electrorefining studies on plutonium bearing alloys and engineering scale studies on alloys of natural uranium up to 1 kg per batch scale have been carried out. An engineering scale facility named as Pyro Process R&D Facility-1 (PPRDF-1) is being setup for demonstrating two major process steps of the pyroprocess flowsheet, viz. electrorefining and cathode processing. Ten kilograms of natural uranium alloy containing gadolinium (simulating plutonium) and non-radioactive isotopes of important fission products will be processed per batch, in this facility. The electrorefining will be carried out in the fabricated high temperature electro-refiner (HTER) system.

The input to this system will be chopped pieces of simulated spent fuel rods. The output will be in the form of uranium dendrites occluded with salt in solid cathode and uranium and gadolinium in cadmium ingot in another cathode. The system consists of four major subsystems viz. electrorefining station, electrodes attaching-detaching station, scrapping station and tilting station.

These subsystems are housed inside a large argon atmosphere containment box to prevent oxidation of uranium metal and to avoid absorption of moisture by the salt used in the electrorefining vessel. The system has an integrated electrical and control system for all the stations which is housed inside the control room of the facility.

The electro-refining station consists of a rectangular leak tight process vessel located in a furnace well which is hanging from the floor of containment box. The process vessel is of size 1.8 m (L) x 1.1 m (B) x 1.4 m (H) and is made of 9Cr-1Mo steel in which 900 kg of molten LiCl-KCl, containing about 5 wt% UCl_3 , will be maintained at 773 K.

The simulated spent fuel loaded in a basket and dipped in the salt, acts as the anode. The uranium deposit takes place on solid rod and U-Gd deposit inside a crucible containing cadmium. The other three stations will perform specific mechanical operations



Fig. 1 (a) Electrodes attaching-detaching station and (b) scrapping station

supporting the electrorefining process. The electrodes are attached to electrode sub-assemblies which are mounted on the cover plate of the process vessel. With number of penetrations in the cover plate for electrode sub-assemblies, level probes, cadmium vapor traps, etc., achieving leak tightness was a challenging task.

Electrodes attaching-detaching station (Figure 1a) performs the function of attaching or detaching of anode basket, solid cathode and cadmium cathode with the respective sub-assemblies. The electrodes are removed from the sub-assemblies for ease in handling during loading of uranium alloy pellets and cadmium in the respective electrodes/baskets. Precision machining of the various mechanisms of this station ensured smooth functioning as observed during testing.

At the scrapping station (Figure 1b), dendritic uranium deposit on the solid cathode is scraped and collected. Two cutting tools are provided 180° opposite. The scraped uranium falls in a collection vessel placed below the cathode.

The anode sub-assembly after electrorefining is taken to electrodes attaching-detaching station where the anode is detached from the sub-assembly and taken to tilting station. Here, the anode is mounted on the tilting platform, inverted upside down and is heated to about 400°C. The remains in the basket which have not been electro-refined, fall from the anode basket into the collection vessel below. Removal of cadmium ingot (containing uranium and gadolinium) from the crucible of cadmium cathode is also carried out at this station.

IV.17 Electrochemical Behaviour of Zirconium(IV) in Ionic Liquid Medium for Metal Fuel Reprocessing

Zirconium is a constituent of the metal alloy fuel U-Pu-Zr and in this alloy Zr is generally present to the extent of 10 wt.%. Pyrochemical electrorefining method has been proposed for reprocessing of spent metallic fuels. The method involves the anodic dissolution of actinides present in the spent fuel in high-temperature molten salt medium composed of LiCl–KCl eutectic mixtures and the dissolved actinides are recovered at cathode by electrodeposition. In contrast to high-temperature molten salts, room temperature ionic liquids (RTILs) are organic salts molten at temperatures lower than 373 K. Employing such organic salts (or RTILs) in place of inorganic chloride media facilitates the operation of entire process at near ambient conditions. The wide electrochemical window, usually more than 6 V, and extended cathodic stability make RTILs, promising candidate for non-aqueous reprocessing and nuclear fuel cycle applications. In view of this, as well as towards the development of ionic liquids for metallic fuel reprocessing, the electrochemical behaviour of Zr(IV) in 1-butyl-3-methyl imidazolium bis (trifluoromethylsulfonyl) imide ($C_4mimNTf_2$) ionic liquid medium was studied.

The cyclic voltammogram (CV) of $C_4mimNTf_2$, recorded at glassy carbon (GC) working electrode indicated that $C_4mimNTf_2$ offers an electrochemical window of about 4.7 V, as shown in Figure 1. The CV of Zr(IV) recorded at glassy carbon working electrode at the scan rate of 100 mV/s at 353 K consisted of a minute cathodic wave occurring at the peak potential of +0.2 V (Vs Pd). This

could be due to the reduction of Zr(IV) to Zr(II), and a prominent cathodic wave occurring at the onset of -1.3 V (Vs Pd) is attributed to the reduction of Zr(II) to Zr(0). The reduction at -1.3 V (Vs Pd) is accompanied by a nucleation loop at -1.6 V during scan reversal at -2.0 V. The voltammogram also showed the oxidation waves at -0.6 V (Vs Pd) and at +0.5 V (Vs Pd) due to oxidation of Zr(0) to Zr(II) and Zr(II) to Zr(IV), respectively. The oxidation of Cl^- to Cl_2 occurred at the onset of +0.8 V (Vs Pd). The voltammogram thus showed that Zr(IV) in $C_4mimNTf_2$ medium had undergone a two-step two-electron transfer reduction to zirconium metal at the working electrode.

Electrodeposition of Zr metal from $C_4mimNTf_2$ was carried out for about one hour at glassy carbon working electrode at -1.7 V (Vs Pd). The deposit was characterized to be metallic zirconium by SEM–EDX analysis and XRD technique. This study revealed that zirconium can dissolve in ionic liquid or molten salt medium to a significant extent during anodic dissolution of uranium and plutonium from the spent metallic fuel. Owing to the low negative potential needed for the electrodeposition of zirconium as compared to uranium and plutonium deposition, zirconium is predominantly reduced to metallic form along with actinides during the recovery. The study indicated the requirement of optimization of anodic potentials for dissolution of actinides to minimize the dissolution of zirconium and contamination of zirconium in the actinide deposit.

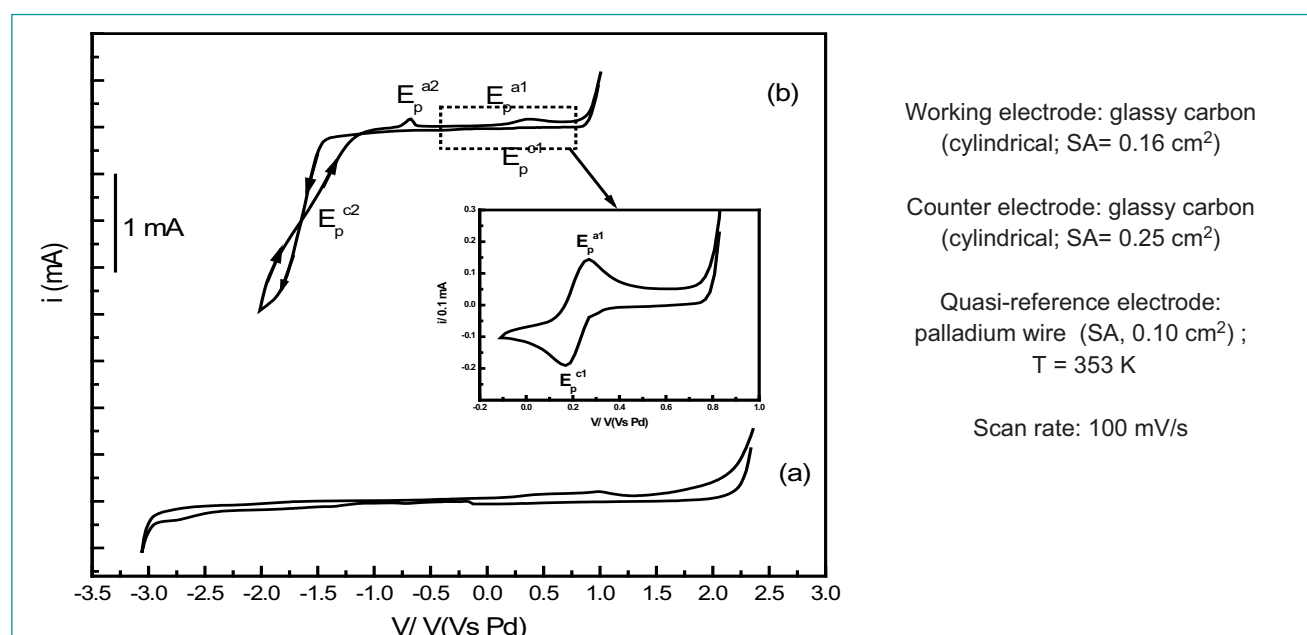


Fig. 1 Cyclic voltammograms of : (a) $C_4mimNTf_2$ and (b) solution of Zr(IV) in $C_4mimNTf_2$ from -2.0 V to +0.8 V

IV.18 Development of Exchange Current Density Database for Actinides and Fission Products in LiCl-KCl Eutectic

The flowsheet for pyrochemical reprocessing of spent metallic fuels is being developed in our laboratory. The separation of actinides from spent U-Pu-Zr alloy in pyroprocessing is carried out using molten salt electrorefining that employs LiCl-KCl eutectic operated at 773 K. Investigation of this separation process involves the knowledge of thermodynamic and electrochemical properties of actinides and fission products in LiCl-KCl eutectic. Electrode kinetics of these species at both solid steel cathode and liquid cadmium cathode also require an investigation since it can provide valuable inputs to large scale electrorefiners in addressing issues like limiting current density, polarization etc. One of the important parameters in electrode kinetics is exchange current density, which is defined as the current density at equilibrium potential. Development of exchange current density database for LiCl-KCl eutectic was taken up in our laboratory.

Anodic polarization experiments were carried out with Na-bonded U-Zr alloy, U-Gd-Zr alloy, Gd metal and the data were compared with our previous study on U, Zr and U-Zr alloy. Data on cathodic polarization of UCl_3 , ZrCl_4 and GdCl_3 at liquid cadmium cathode were subsequently added and compared with those at the solid inert cathode. DC amperometry is the conventional method for generating current versus potential profile. This profile was subjected to Tafel and Allen-Hickling

analysis for estimating exchange current density of the various systems.

A comparison of cyclic voltammograms at inert and liquid cadmium electrode showed that U^{3+} , Zr^{2+} and Gd^{3+} underpotentially deposited in cadmium, forming liquid alloys. The respective equilibrium potentials were used in deducing the Tafel slopes. Anodic dissolution of U-Gd-Zr alloy considered to simulate the electrorefining behaviour of U-Pu-Zr alloy, showed that the equilibrium potentials were depending on the presence of UCl_3 in the electrolyte. The equilibrium potential of U-Gd-Zr alloy was -1.56 V in blank LiCl-KCl eutectic and it was -1.34 V in LiCl-KCl- UCl_3 electrolyte (Figure 1). Dissolution of zirconium was similar, irrespective of the presence of UCl_3 . The dissolution potential of uranium was similar to those reported earlier for Na-bonded U-Zr alloy (-1.46 V).

The Tafel plots of the systems studied in LiCl-KCl eutectic at 773 K are shown in Figure 2. It was observed that the exchange current density of zirconium was the lowest among U^{3+} , Zr^{2+} and Gd^{3+} . The exchange current density at cadmium was lower than that at inert cathode. The exchange current density of Na-bonded U-Zr alloy varied in the range 40-46 mA/cm^2 , whereas it varied from 17 to 25 mA/cm^2 for U-Gd-Zr alloy. These data will be useful in calculating activation over potentials during electrorefining. These data will also be compared with the polarization data of U-Pu-Zr alloy.

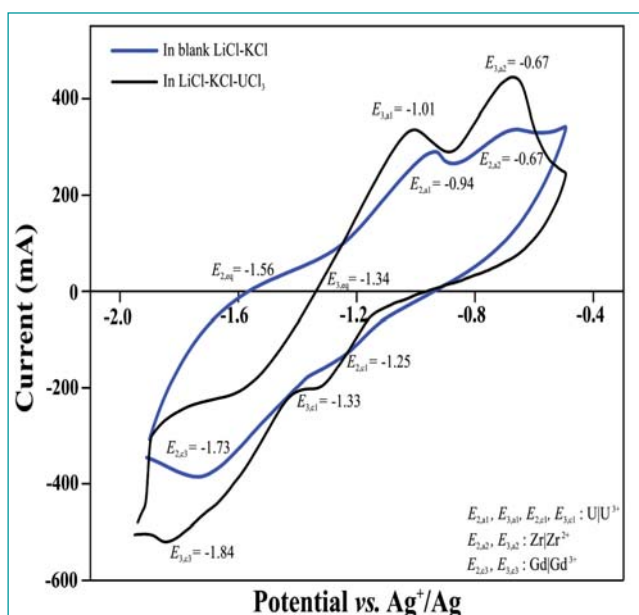


Fig. 1 Cyclic voltammograms of U-Gd-Zr alloy in LiCl-KCl eutectic at 773 K

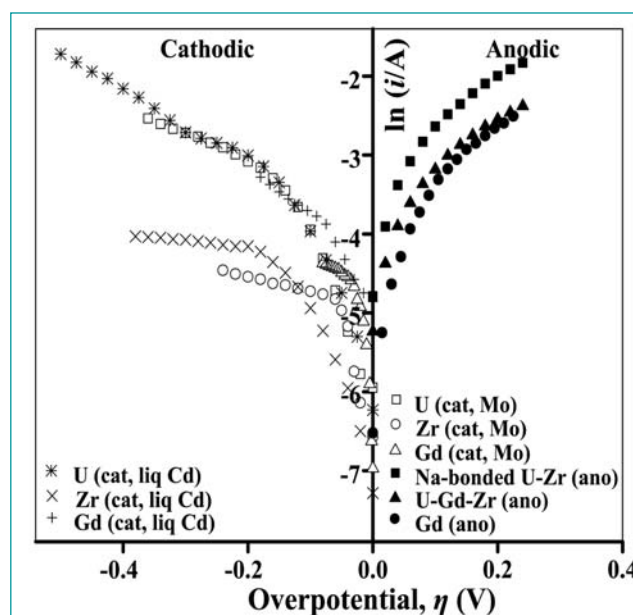


Fig. 2 Tafel plots of various systems in LiCl-KCl eutectic at 773 K

IV.19 Demonstration of Electrorefining of Unirradiated U-Zr Alloy in Hot Cells

For the demonstration of pyrochemical reprocessing of irradiated U-Zr fuel capsules (in FBTR), a laboratory scale (100 g) hot cell facility is being developed. The work involved detailed design and fabrication of special equipment like electrorefining cell (Figure 1) with electrode handling systems, radial hoist for remotely positioning components, surveillance systems, cathode processor etc. These equipment are designed to be compact for easy handling using manipulators. Various equipment, both mechanical and electrical for remote handling of electrochemical cell assembly and its accessories were installed and commissioned inside the hot cell. The mechanical equipment installed included (i) radial hoist positioning system (for loading and unloading of electrodes), (ii) device for scrapping of electrode deposit, (iii) furnace assembly for heating the outer vessel, (iv) curved railing for retrieval of furnace from a remote location below the containment box in hot cell, (v) inner vessel with electrode assembly consisting of a lifting arrangement (Figure 2) and (vi) parking station for parking of electrodes. The electrical equipment installed were (i) slip rings for DC power supply, (ii) surveillance systems including pan-tilt-zoom (PTZ) camera, (iii) power and control wiring, (iv) reverse bayonet leak tight connectors and (v) gold coated push pull connectors. All the equipment were independently operated and demonstrated. The oxygen and moisture meters for analyzing the argon gas of the hot cell were also commissioned. Complete leak testing under positive and negative pressure was also carried out.

Since the viewing window of hotcell had some problems, all operations during electrorefining were carried out by viewing PTZ cameras positioned inside the hotcell. The oxygen and moisture levels inside the cell before electrorefining were in the range of 200-300 ppm and -30 to -35 °C dew point, respectively. Argon gas was re-circulated through purification towers during the course of electrorefining. About 2.8 kg of LiCl-KCl eutectic containing 5 wt.% UCl_3 was prepared. 100 grams of un-irradiated U-Zr alloy rods were also loaded in the perforated anode basket. A 10 mm diameter SS-430 rod was used as cathode. The reference electrode used was Ag/AgCl in a perforated SS-430 thermowell to avoid damage during the experiments. Electrorefining of U-Zr alloy was carried out at 773 K using constant current and constant potential modes. In potentiostatic mode, applied potential varied from -1.65 to -1.8 V, whereas in constant current mode, current varied in the range of 1-2.2 A. Electrorefining was carried out under rotation of both anode and cathode. The electrodes were also equipped with slip rings through which current was passed. A total of 55781 coulomb of charge was passed, which corresponded to a total of 15.49 ampere-hour of current. A hard compact uranium deposit (~ 35 mm diameter, ~ 35 mm height) was obtained. The anode basket and cathode rod were lifted above the salt surface and the furnace was cooled to room temperature. The cathode rod containing the deposit was then slowly guided into the vessel inside a scrapping furnace (Figure 3). The furnace was heated to 973 K for softening the electrodeposit and subsequent scrapping.



Fig. 1 Electrorefining cell with electrodes installed in hot cells

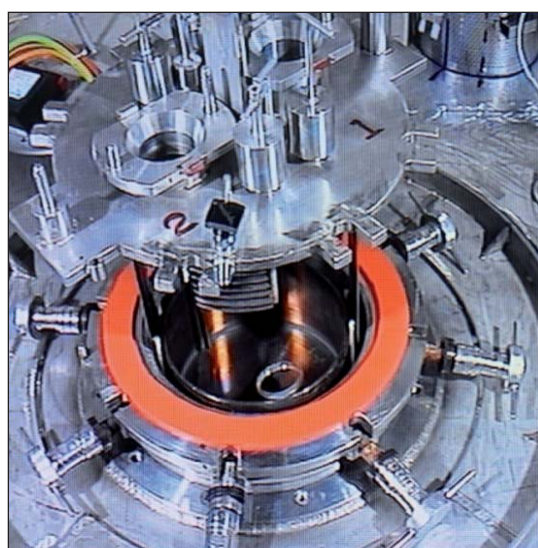


Fig. 2 Loading of top flange onto the inner vessel



Fig.3 Uranium electrodeposit

IV.20 A Glove Box Facility for Gelation Studies of Plutonium Containing Solutions

Sol-gel facility is being set-up for the fabrication of $(U,Pu)O_2$ and $(U,Pu,Am)O_2$ microspheres. For the fabrication of these samples, plutonium nitrate solution is required. Plutonium nitrate is prepared by dissolution of PuO_2 in nitric acid with HF as a catalyst. Gelation studies on mixed oxide by measuring the dynamic change in viscosity of the Broth as a function of temperature is required to determine equilibrium gelation temperature, which data for different compositions of the Broth are in turn, required to generate gelation field diagram. For carrying out both these activities in a glove box facility, a double module glove box was commissioned. The glove box was partitioned in to two equal halves with a sliding window in-between. One part of the glove box is used for the dissolution of plutonium (Figure 1) and the other part is used for weighing, Broth preparation and viscosity measurements (Figure 2). The glove box after providing the necessary accessories (electrical/signal feedthrough, water and gas lines), was leak tested and was found to be less than 0.05% of box volume per hour. Both the inlet and outlet HEPA filters were tested for their efficiency and was found to be greater than 99.97%. The equipment required for carrying out these experiments, namely (i) stainless steel tripod stand for holding platinum bowl, (ii) double walled cooling vessel for cooling plutonium and uranyl nitrate solutions, HMTA:urea solution and sample vessel, (iii) stainless steel stand for positioning the IR lamp heating source and (iv) stainless steel - NO_x getter assembly was fabricated in-house and commissioned. Pipelines required for maintaining and controlling the negative atmosphere in the glove box were laid and leak tested.

Plutonium nitrate solution (1 M) was prepared by dissolution of PuO_2 in concentrated nitric acid with HF as catalyst and heated under IR lamp to remove excess nitric acid. The plutonium nitrate crystals formed were dissolved in 0.5 M nitric acid and made up using standard flask to the required concentration. Acid deficient uranyl nitrate solution (ADUN) and HMTA:urea (HU) (gelating agent) were prepared in the fume hood and transferred in to the glove box using bag-in port. Appropriate quantities of ADUN, HU and plutonium nitrate solution were taken and cooled using the cooling vessel. These solutions were mixed to form a Broth. The Broth was introduced in to the pre-cooled sample vessel and the change in the viscosity of the Broth as a function of temperature was determined. Viscosity measurements were carried out by isothermal as well as dynamic methods. In the isothermal method, the change in the viscosity was measured by a double walled sample holder, which in turn was cooled by a water circulator. Initially, the temperature of the water bath was maintained at 273 K and once the sample was introduced in to the sample vessel, the temperature of the bath was raised to 313 K at a heating rate of 0.3 K min^{-1} and the temperature was maintained a constant at 313 K for 3 hours. In the second method, after the sample was introduced into the pre-cooled sample vessel, the measurement of viscosity was carried out from 273 to 363 K using a temperature programmable furnace at a heating rate of 3.6 K min^{-1} . The gelation temperature, which is indicated by an abrupt large change in the viscosity was observed at 313 K after 2 hours in the isothermal method and at 348 K in the dynamic mode.

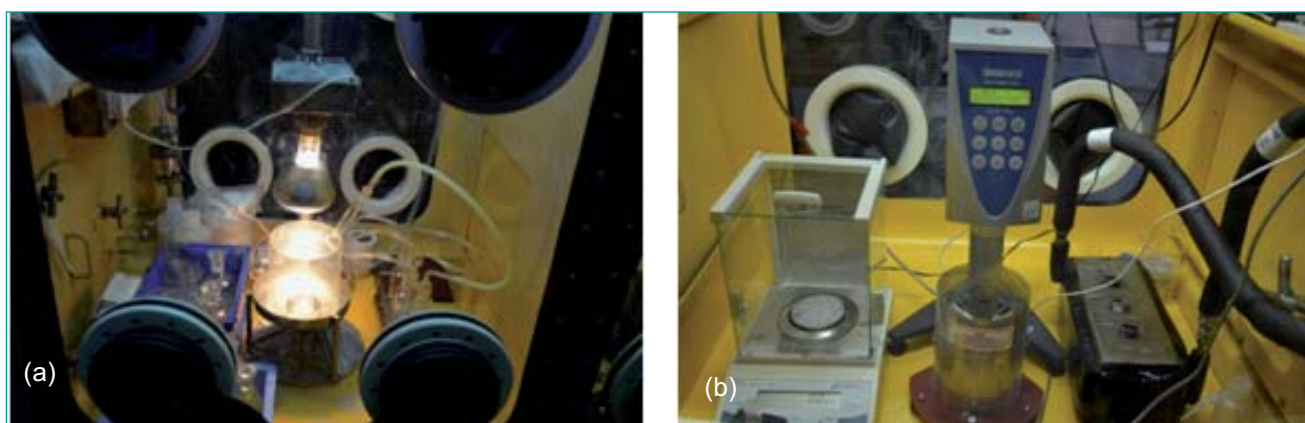


Fig. 1 (a) Plutonium nitrate preparation in the glove box and (b) Broth preparation and viscosity measurement in the glove box

IV.21 Application of Digital Industrial Radiography for Qualification of Weld Joints of Rolled & Welded Austenitic Stainless Steel Pipes

During the material procurement for Fast Reactor Fuel Cycle Facility (FRFCF), rolled and welded pipes are to be fabricated from austenitic stainless steel plates of controlled chemistry with supplementary requirement of Inter Granular Corrosion test as per ASTM A262 Practice C. Outer diameter (OD) of pipes vary from 200 to 762 mm and thickness vary from 4.0 to 8.0 mm. All pipes are 5-7 meters in length. Due to the non standard sizes, pipes are fabricated by rolling stainless steel plates in circular form as shown in Figure 1a, followed by Plasma Arc Welding (PAW) with or without filler metal. Circular profile formation of plate is done in multiple stages.

Efficient and effective Quality Assurance Plan (QAP) coupled with standardized and well proven quality assurance practices are followed during the fabrication and inspection activities. Liquid Penetrant Examination was prescribed as surface NDE and Radiographic Examination was prescribed as volumetric NDE. Conventional radiography involves the usage of films and chemical processing of the same. It consumes more time for setting up the films and processing the films and more over it will affect the delivery schedule. Considering the above facts, it has been decided to use Digital Industrial Radiography (DIR), instead of conventional radiography.

Digital Industrial Radiography is a form of X-ray imaging, where digital X-ray sensors are used instead of photographic film. Flat panel detectors are used as digital X-ray sensors. This flat panel detector uses an amorphous selenium-coated thin-film-transistor (TFT) array to capture and convert X-ray energy directly into digital signals. Also, less radiation can be used to produce an image of similar contrast compared to conventional radiography. DIR requires shorter test and process time. No chemical waste is involved in the DIR process as compared to the conventional radiographic film processing.

All the personnel who perform the DIR have been qualified and certified as Level I/II. The radiographic images are reviewed and interpreted by Level II/III personnel qualified and certified as per SNT-TC-1A or IS 13805.

An X-ray generating system with 40 to 320 KV capacity with dual focus (0.4 & 1.0 mm) has been used for the DIR. A flat panel detector of 205 × 205 mm in size with a pixel size of 0.2 mm has been used as an image conversion system. A 510 mm size TFT monitor with a resolution of 1280 × 1024 pixel has been used as display monitor. Double Wall Single Viewing technique has been used for welded pipes up to 456.0 mm outer diameter and Single Wall Single Viewing technique has been used for pipes including and above 456.0 mm outer diameter. Duplex penetrameter has been used to assess the effectiveness of spatial resolution. Duplex penetrameter is placed below the weld at 5° inclination at the first segment of each pipe as shown in Figure 1b. ASME standard wire type penetrameter is used to assess the sensitivity. ASME standard wire type penetrameter is placed at both ends and additionally at two middle locations in between to ensure the sensitivity.

Geometric un-sharpness on weld surface was limited to 0.5 mm as per ASME B&PV code section V article 2. DIR System was calibrated for contrast and sensitivity. A detailed procedure including the shooting sketch has been prepared and approved by the competent authority. Performance of the DIR is evaluated by taking radiography of the stainless steel welded pipes as per ASME B&PV Code Section V article 2 and approved procedure. Radiography of welded pipes was done in auto mode and images were reviewed by online monitoring. All the images were preserved in digital format for the future reference. A proper identification methodology has been followed for the identification

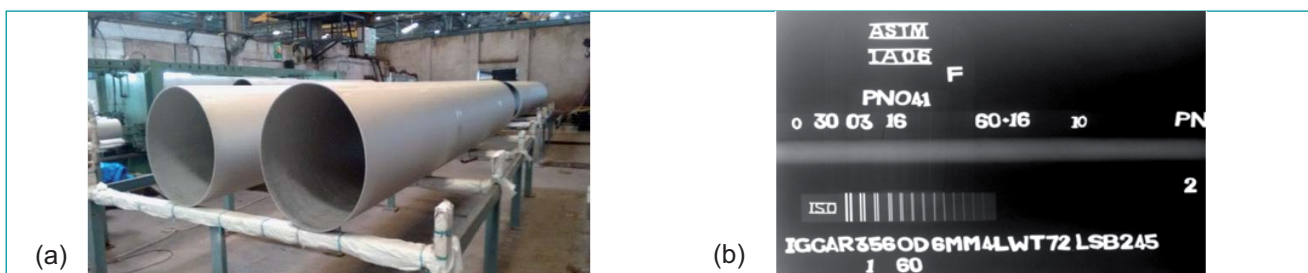


Fig. 1 (a) Rolled and welded stainless steel and (b) DIR image of pipe segment

of images with respect to segment and welded pipe identification.

Total time consumed for the radiography of the entire lot was significantly reduced by the implementation of DIR without any dip or deviation from the quality requirement. Retaining films for a period of about

10 years is a major concern due to limited shelf life. DIR has allowed us to overcome this problem. Application of Digital Industrial Radiography instead of conventional film based radiography played a vital role in realizing the procurement of stainless steel welded pipes well within the stipulated time period.

IV.22 Enhancing Post Irradiation Examination Capabilities in an Operating Alpha-Beta-Gamma Hot-Cell

Recent augmentation in the hot cells include a radial gamma scanning and an optical microscopy system. The conceptualization, installation and successful operation / maintenance of such sensitive equipment in an operating hot cell pose enormous challenges like constraints of space, new provisions for remote operation and maintenance, need for modifying and retrofitting the existing hot cell facilities, extensive mock-up trials, mandatory safety clearances and safe implementation without any spread of contamination.

Migration of fission products during irradiation influences fuel pin performance and hence, its study is of immense interest. As many fission products are gamma active, their radial and axial migration behavior can be evaluated by gamma scanning of irradiated fuel pin. The high alpha/beta/gamma activity of irradiated fuels makes such studies challenging. An existing system facilitates axial gamma scanning along the length of the fuel pin to evaluate the distribution of fission products.

A new system has been established recently in the hot cell for radial gamma scanning. It comprises

- (a) a collimator assembly, established by modifying an existing blank service plug in the hot cell wall
- (b) a four-axis gamma scanning bench for precise positioning of a sample, prepared from transverse cross section of fuel pin
- (c) HPGe detector, positioned outside the hot cell.

The collimator with an aperture of 0.3×0.3 mm was integrated by assembling four cylindrical stainless steel blocks, and aligning them coaxially with high precision inside a sleeve, designed to fit into the service plug.

The four-axis radial gamma scanning bench incorporates stepper motors, lead screw and precision linear motion guides. This has been installed in the hot cell (Figure 1) and was aligned with the collimator assembly in the cell wall and the HPGe detector in the operating area to facilitate gamma spectroscopy.

A new optical microscopy system has been installed in the hot cell, which permits direct viewing of polished and etched metallographic specimens.

This is a custom-built modular system comprising of individual modules such as fibre-optic illumination system, digital camera for imaging, reflected light illuminator, motorized turret and specimen positioning system and radiation resistant objective lenses. The sample positioning mechanism consists of a four axis mechanical stage with micro-stepping stepper motor drives that allow precise positioning of the sample.

To facilitate maintenance of the sensitive optical microscope and other in-cell equipment in this cell, the sealing door on the rear side of the hot cell has been modified. Hands-on maintenance is made possible by providing glove ports and radiation resistant viewing ports. An alpha tight transfer system has also been incorporated into this sealing door for transfer of low active materials from/to the hot cell. This innovatively modified cell-sealing door permits hands-on maintenance of in-cell equipment similar to that in a glove-box, but under conditions that are permitted by the safety committee.

The retrofitting of the above systems into the operating hot cells has greatly enhanced the capabilities of the hot cells and it is a typical demonstration of the maturity attained in upgrading and maintaining alpha-beta-gamma hot cells.

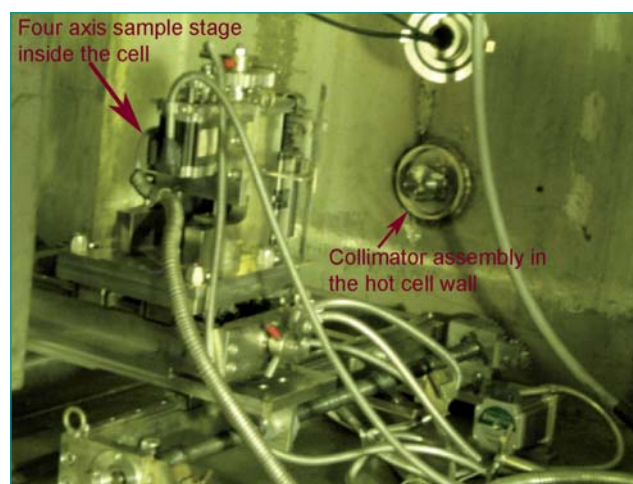


Fig. 1 Radial gamma scanning system

IV.23 Development of Inline Static Mixer based Pulse Column for Reprocessing Applications

Solvent extraction unit is widely employed in many chemical industries to separate valuable materials from liquid mixtures and it is one of the major unit operations in nuclear reprocessing plants to separate uranium and plutonium from spent nuclear fuel. Different types of solvent extraction equipment are available in the market and they are widely classified into stage-wise contactor and differential contactor. Sieve plate column, disc and doughnut column, packed column, spray column, etc. come under differential contactor. Sieve plate pulse column (23% free area) is in use in nuclear reprocessing plants for more than six decades. The main advantages of sieve plate pulse column are reliable performance and zero maintenance and its disadvantages are the requirement of tall shielded cell to accommodate approximately 15 metre high columns and it cannot handle liquid with solid particle, which may choke sieve plates. To overcome the above disadvantages a novel static mixer based pulse column was developed and it consists of static mixer internals (Figure 1, greater than 95% free area). This static mixer is used for mixing of two viscous fluids in concurrent mode.

Mass transfer performance of any pulse column is determined by the number of transfer units (NTU) or length of the column required to produce the given degree of separation. Variables controlling mass transfer performance are (i) system properties and (ii) rates of inter-phase mass transfer. Inter-phase mass transfer can be enhanced by increasing interfacial area available for mass transfer and it depends upon energy input (pulsing velocity = amplitude (A) x frequency (f)), ratio between aqueous and organic flow rate and total throughput. To



Fig. 1 Static mixer internals

validate the static mixture based pulse column, mass transfer experiments were conducted using 30% TBP and nitric acid system.

During extraction experiment, 4N nitric acid was used as aqueous phase and acid free 30% TBP as organic phase at constant organic to aqueous phase flow ratio of 4 and the total throughput was maintained constant at 100 mL/min. In this experiment, variation of NTU with respect to pulsing velocity was calculated based on McCabe-Thiele method and height of transfer unit (HTU) was back calculated from NTU. Graphical construction of NTU for extraction run is shown in Figure 2. Extraction results showed that, NTU for a given pulse column increased from 0.69 to 4.16 with increasing pulsing velocity from 0 to 4.78 cm/s and the plot of NTU against pulsating velocity is shown in Figure 3a.

Similarly, stripping experiments were conducted with 0.01 N nitric acid as aqueous phase and acid loaded 30% TBP as organic phase at constant organic to aqueous phase flow ratio of 4 and pulsing velocity was maintained around 3.2 to 3.7 cm/sec. In this experiment, variation of NTU with respect to total throughput was calculated. Stripping results showed that NTU for the given pulse column increased from 1.1 to 3.8 with increase in total throughput from 25 to 100 mL/min.

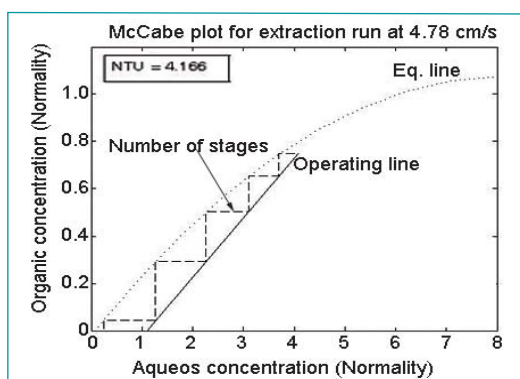


Fig. 2 McCabe plot for extraction run at $Af = 4.78$ cm/s

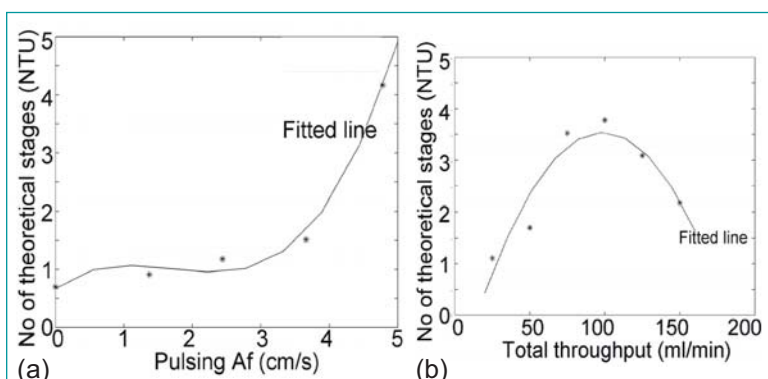


Fig. 3 Number of transfer units vs (a) pulsing velocity (Af) at constant total throughput of 100 mL/min and (b) total throughput at the pulsing velocity of 3.2 to 3.7 cm/sec

The NTU subsequently decreased from 3.8 to 2.1 with increase in total throughput from 100 to 150 mL/min and the results are shown in Figure 3b.

Maximum NTU from extraction experiment for above novel static mixer column was 4.16 and its corresponding HTU was 24 cm. The maximum NTU

from stripping experiment for the above column was 3.8 and its corresponding HTU was 26 cm. The HTU value for conventional pulse column is approx. 40-50 cm, whereas HTU value for novel static mixer pulse column is much lower than the conventional pulse column and it can handle liquids with solid particles also.

IV.24 Development and Performance Evaluation of RFD based Fluidic Pump for High Discharge Head Application

Diversification of liquid transfer systems in reprocessing plants provides an alternative to the concept of standby thus reducing the dependability of a particular system and improving the availability of the transfer systems. Transfer systems for radioactive liquids in nuclear fuel reprocessing plants require pumps which are maintenance-free, highly reliable, simple, easy to fabricate and operate and should have no moving parts .

For the potential application of radioactive liquid transfer, RFD based prototype fluidic pumps of chamber volume one and seven litre and nozzle diameter of 6 mm were developed as an alternative to air-lift or steam jet operated liquid transfer systems. These pumps offer the advantage of no dilution or heating of process liquid streams as in steam jet transfer systems, devoid of entrainment as in the case of liquid transfer by air lift and thus, no formation of radioactive aerosol, thereby decreasing the load on ventilation filtration system. Since no replacement of failed components (which are in contact with the radioactive liquids) is required for the entire service life, reliability of plant operation is much higher

as compared to its mechanical equivalents. Studies on fluidic pumps have been reported in literature. In this work, the results obtained from the experiments carried out with a RFD based fluidic pump of chamber volume seven litre is discussed.

The compact RFD based fluidic pumps operate in three phases called suction, drive and vent phase. These three phases are cyclically controlled by cyclic actuation and deactuation of respective solenoid valves. Pumping and refilling of the pump chamber is achieved by pressurization and depressurization respectively. A view of the experimental set-up is shown in Figure 1. The pump with chamber volume of seven litre was tested with water as test fluid up to a discharge head of twenty two metre. During the performance study, a discharge flow rate of 165 lph for a cycle time of about 120 second was observed at the discharge head of 20 metre. Characteristic plots were generated for different motive air pressures as shown in Figure 2. A decreasing trend of flow rate with increasing discharge head was observed, following the trend of rotodynamic pumps as against the trend of positive displacement pumps.



Fig. 1 A view of the experimental setup for testing of the RFD based fluidic pump

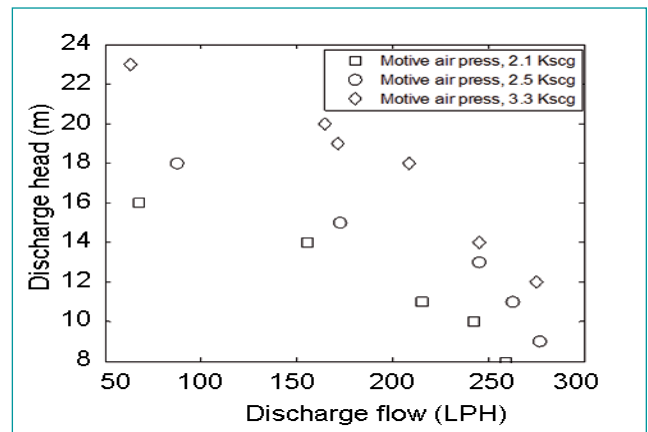


Fig. 2 Pump discharge flow rate (lph) versus discharge head (m of WC)

IV.25 Evolution of Robotic Sampling and Analytical System for FBR Fuel Reprocessing Plants

Automated robotic sampling and analysis play an important role in the reprocessing of fast reactor spent fuel. The process solution of fast reactor spent fuel is highly radioactive as compared to that of thermal reactor spent fuel and there is a need for precise, fast and reliable control of the process parameters. In this direction, a comprehensive R&D programme was initiated to design and develop robotic sampling and analytical system. Prototype sampling and analytical robotic devices have been fabricated for the CORAL facility, and the expertise and experience gained have been utilized for the development of the sampling and analytical robotic system for DFRP.

The sampling and analysis of process solution will be carried out in two different hot cells in DFRP using Sample Handling Robot (SHR) and Analytical robotic system. To meet this requirement, dedicated remote sampling and analytical robotic systems have been designed and fabricated. Both the systems have undergone extensive pre-commissioning tests and trials in the mock-up sampling cell in DFRP.

The robotic sampling and analytical systems are modularly designed to facilitate remote maintenance and replacement of components that are prone to failure, using Master Slave Manipulator (MSM) and in-cell cranes remotely. One of the salient features of the design of this system is the standardization of each module of the system namely, motors, limit switches, push-pull cable connectors, and drive train, with interchangeability among the respective modules, to achieve complete remote assembly/disassembly and good remote maintenance.

Sample Handling Robot (Figure 1) is designed to collect process samples ranging from 5 to 10 ml from 60 sampling points provided in the sampling cell. The SHR is a Cartesian robot (X, Y and Z) to cover the workspace of 6000 x 700 x 400 mm. The Z-axis carries two redundant Y-axes with grippers placed diametrically opposite to each other to provide extended reach to the end-effectors/grippers along Y-axis as well as precise motion to reach the target for grasping the sample bottle. In addition, a rotational axis (θ) is provided about the Z-axis to flip the redundant Y-axis as per the requirement. The 6000 mm long X-axis rail and the moving carriage are the critical components of the SHR and they can be remotely assembled / disassembled using in-cell crane and MSM with a set of anti-topple tapper roller lock. Counterweights are provided to offset the cantilever effects of Y-axis translation stage with two grippers and a payload capacity of 50 N. The SHR collects empty sample bottle from the user-selectable location in the sample bottle storage rack inside the cell and transports the empty sample bottle to the pre-defined sampling point, collects the samples and places it in the user-selectable storage location in the filled bottle storage rack. The filled sample bottle is subsequently transported to the analytical cell (lower cell) using the in-cell crane. The filled sample bottle received from the sampling cell is taken for analysis in the analytical cell by the analytical robotic system.

Analytical robotic system is placed at a lower elevation in the sampling cell. It consists of Analytical Rack (AR), Cap Handling Module (CHM), Cap Stand, and Pipette Robot (PR) to carry out the operations of de-capping,



Fig. 1 Sample handling robot

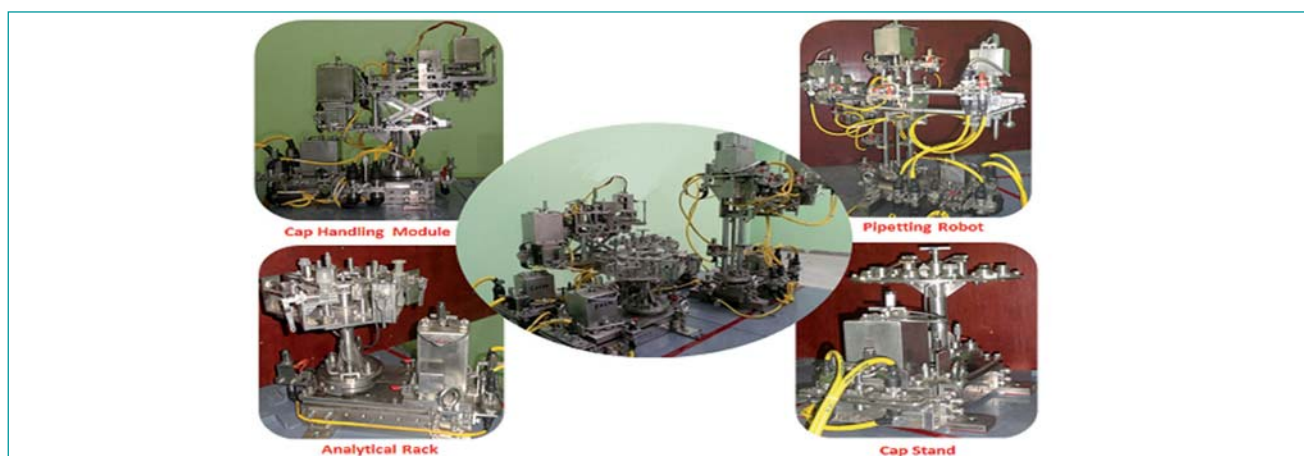


Fig. 2 Analytical robotic system

pipette tip collection, pipetting, dispensing, tip ejection and capping of sample bottles (Figure 2). The sampling and analytical systems are interconnected through a server PC, which in turn controls both systems.

The pipette robot can draw and dispense 50 -1500 μl of process liquid with a precision of <1%. The positional accuracy, of the X-axis is 0.5 mm with repeatability ≤ 0.3 mm. The positional accuracy of other translational axes is better than 100 μm with repeatability ≤ 50 μm . The positional accuracy of rotational axis is 20 arc-min with repeatability ≤ 10 arc-min.

Application software has been developed and tested successfully for the various operations of the system. Software interlocks are provided to restrict the illegal operations and the operations and status monitoring can be performed from both the pendant and PC. It has administrative controls viz. setting of operator privilege, motor configurations, monitoring of various in-cell operations, event alarm logging, and tracking of sample bottles. Provisions are made in the application software for teaching of robots, jogging, calibrations of robots, and homing of robots. Hard coded programs are

embedded in the software for 12 auto sequences which were identified to be used during the entire analytical operations with a maximum cycle time of 10 minutes. Provisions have been made in the software for the operator acknowledgment after the execution of each instruction and for online correction in case of a shift in the target position, and the corrected new position can be stored permanently as per the requirement.

The software for the SHR is provided with hard coded program for 60 sampling points and user can choose any one out of 60 points and same can be executed. Provisions are made in the software to generate unique ID for each sample bottle on successful completion of sampling, and in case of unsuccessful sampling operation, the reason for failure is logged in the database during the sample collection. Both the SHR and analytical robotic system are being utilized by the user group as part of trials of the equipment and for operator training. The SHR and Analytical robotic systems would serve as a benchmark, based on which similar sampling and analytical robotic systems with necessary modifications can be made to suit FRFCF sampling and analytical cells.

IV.26 Corrosion Behavior of Metal Waste Form Alloy in Simulated Geological Repository Environment

The solid metallic waste generated during the electro-refining step of pyrochemical reprocessing of spent metallic fuels comprises the hull (9Cr-1Mo steel), noble metal fission products (NMFPs), Tc, Nb, actinides and zirconium metal from the metallic alloy fuel. Metal waste form (MWF) alloy based on 9Cr-1Mo steel with Zr is proposed for consolidating the solid waste for its disposal in deep geological repositories. Development of Fe-9Cr-1Mo-Zr based metal waste form alloys and the

influence of NMFPs on the microstructure and corrosion behavior in simulated ground water media are presented in this report.

Ingots of 9Cr-1Mo steel-12Zr based metal waste form alloys with the concentrations (in wt.%) of noble metal fission products represented as 1-NMFP (Ru: 0.46, Rh: 0.16 and Pd: 0.31), 2.5-NMFP (Ru: 1.3, Rh: 0.47 and Pd: 0.8) and 4-NMFP (Ru: 2.0, Rh: 0.7 and Pd: 1.2) were cast by arc melting. A typical as-cast ingot (100 g)

is shown in Figure 1a. The SEM-BSE images of the as-cast alloys revealed two different contrasts of bright and dark lamellar structure, as shown for the 2.5-NMFP alloy in Figure 1b. Addition of Zr to 9Cr-1Mo steel resulted in the formation of intermetallic phases, as Zr has a very low solubility in Fe. Simultaneous formation of α -Fe and Fe-Zr intermetallic phases resulted in a layered eutectic microstructure. The dark and the bright contrast regions (Figure 1b) correspond to Fe based solid solution and Zr enriched phase, respectively. Phase identification by X-ray diffraction analysis revealed the presence of α -Fe, Fe_2Zr and $\text{Fe}_{23}\text{Zr}_6$ stable phases. The noble metal fission products were also present in the solid solution. The relative intensity of the intermetallic peaks increased with the increase in noble metal fission products. FeRu , Fe_3Rh_7 and FePd_3 phases were also observed along with Fe-Zr intermetallics in the 2.5- and 4-NMFP MWF alloys. Only FeRu phase was observed along with Fe_2Zr , in the 1-NMFP MWF alloy.

The higher corrosion potentials measured for 2.5-NMFP and 4-NMFP MWF alloys than for 1-NMFP alloy in both Rajasthan ground water (RGW) and Kalpakkam ground water (KGW) media are attributed to the formation of more stable passive films with increase in the noble metal concentration of the alloy. Higher breakdown potential observed for the alloys in RGW (~1000 mV) than in KGW (~400 mV) was due to the higher Cl^- ion concentration in KGW that had led to an easy breakdown of the passive film.

Electrochemical impedance spectroscopic (EIS) measurements were carried out on 9Cr-1Mo steel-12Zr-NMFP MWF alloys in RGW and KGW media under open circuit potential conditions. The Nyquist plots shown in Figures 2a and 2b respectively revealed that the impedance arc diameter increased with increase in noble metal fission product concentration of the metal waste form alloys. The polarization resistance was found to be better for 2.5- and 4-NMFP MWF than for 1-NMFP MWF alloy in

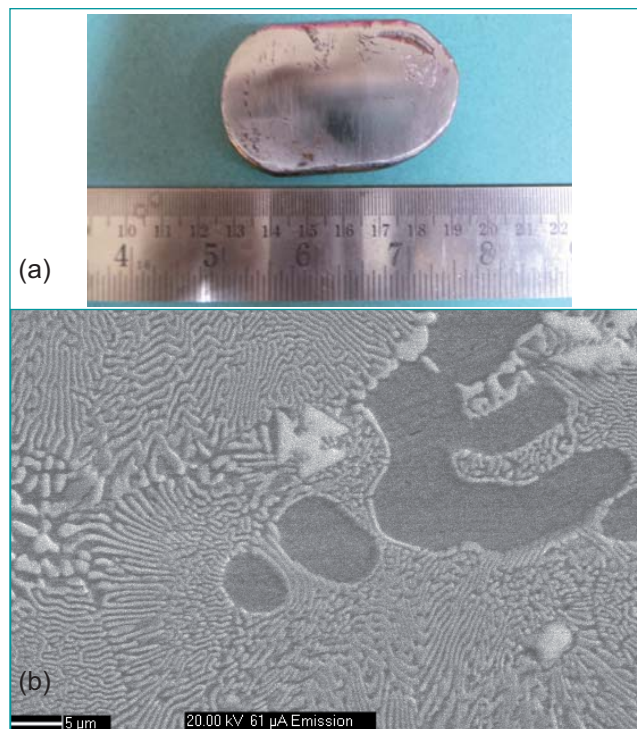


Fig. 1 (a) As-cast ingot of 1-NMFP MWF alloy and (b) SEM-BSE image of 2.5-NMFP MWF alloy

RGW, indicating that the passive film stability was higher in RGW than in KGW medium. An order of increase in the magnitude of polarization resistance in RGW than in KGW is attributed to the the lower concentration of Cl^- ions in RGW, which favored the formation of the hydrated passive film especially the insoluble $(\text{Ca},\text{Mg})\text{SO}_4$ layer. The formation of intermetallic phases and the stability of the passive films of the metal waste form alloys were found to be largely influenced by the presence of noble metal fission product concentrations, which in turn, enhanced the corrosion resistance of the metal waste form alloys. Thus, 2.5-NMFP and 4-NMFP MWF alloys exhibited better corrosion resistance in the tested geological repository media.

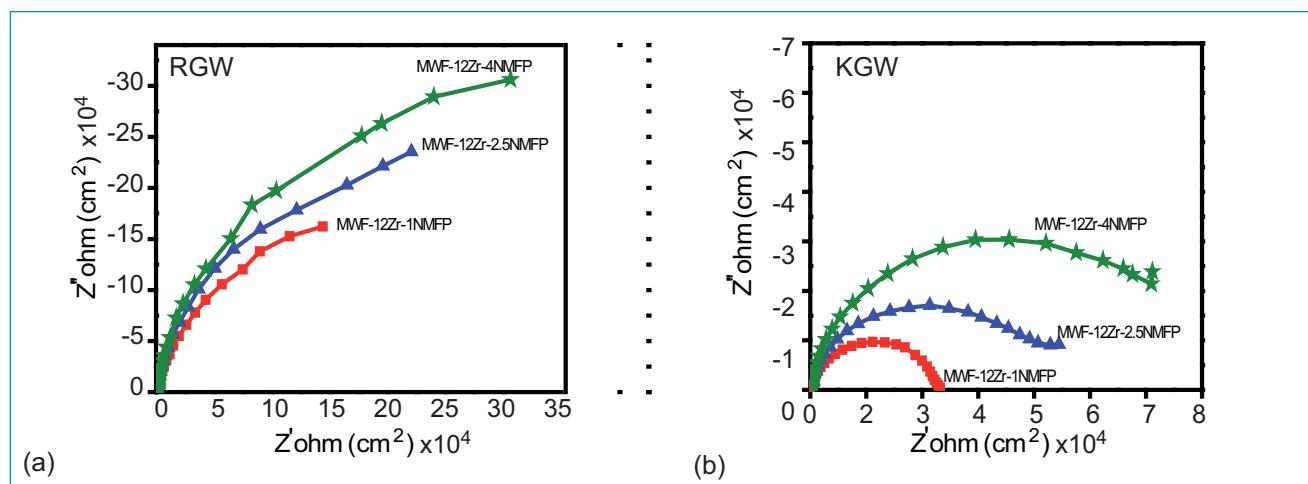


Fig. 2 EIS-Nyquist plots for Fe-9Cr-1Mo-Zr-NMFP MWF alloys in simulated ground water media

IV.27 Synthesis and Characterisation of Simulated Pyrochemical Waste Loaded Chloroapatite with Different Types of Glass Bonding

Pyrochemical reprocessing of metallic fuel by molten salt electro-refining leads to highly radioactive chloride salt waste. Apatites, $M_{10}(PO_4)_6X_2$, ($M = Ca, Sr, Ba, X = OH, Cl, F$) are naturally occurring minerals which can immobilize chloride wastes. Generally, chloroapatite encapsulated in borosilicate glass (BSG) is used. However, to see the efficacy of various other glass compositions, studies were carried out on Sr-chloroapatite (SrApCl), $Sr_{10}(PO_4)_6Cl_2$, glass-ceramics with different glasses such as aluminoborosilicate glass (AIBSG), barium borosilicate glass (BaBSG) and lead borosilicate glass (PbBSG). The synthesis, characterization and thermophysical properties of these glass-ceramics are presented in this report.

Glass-bonded SrApCl simulated waste forms were prepared by mixing 70 wt% strontium chloroapatite + 10 wt% simulated chloride waste + 20 wt% glass (Sr10W20BSG, Sr10W20AIBSG, Sr10W20BaBSG and Sr10W20PbBSG) and heated at 1023 K for 5 hour in air. The products were characterized by XRD. The thermal expansion and of less transition temperature (T_g) of these composites were measured using a home-built quartz push-rod dilatometer. Heat capacities were measured by drop calorimetry.

Formation of SrApCl was evident from the powder XRD patterns as shown in Figure 1 for various glass bonded composites.

The percentage bulk thermal expansion of these composites is shown in Figure 2. Coefficient of thermal expansion were found to be 14.5, 15.1, 16.2 and $16.4 \times 10^{-6} K^{-1}$ for SrApCl with AIBSG, BSG, BaBSG

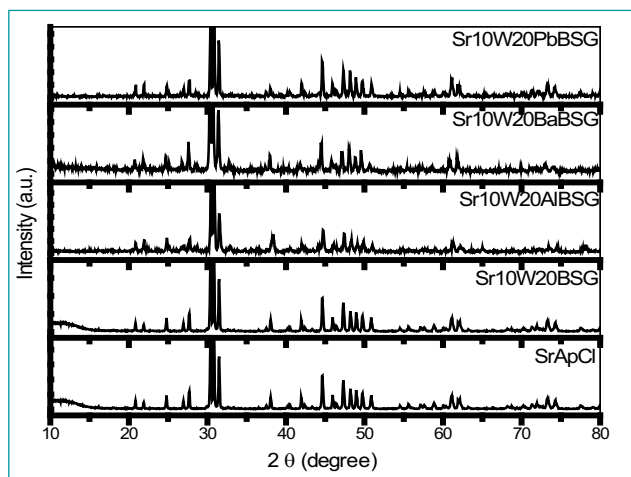


Fig. 1 XRD patterns of the chloroapatite glass-ceramic composites

and PbBSG respectively. It was observed that waste loaded strontium chloroapatite with aluminosilicate glass bonding exhibited the lowest thermal expansion. This may be attributed to the relatively strong bonding in SrApCl-AIBSG compared to other compositions.

The T_g values derived from dilatometry experiment are 710, 702, 673 and 680 K for SrApCl with AIBSG, BSG, BaBSG and PbBSG respectively.

The heat capacities (C_p) of the composites are shown in Figure 3. The C_p of AIBSG was found to be higher than BaBSG and PbBSG.

AIBSG shows better thermal properties for use as glass bonding for chloroapatite waste form. However, further studies like chemical durability and radiation stability need to be carried out on these glass-ceramics.

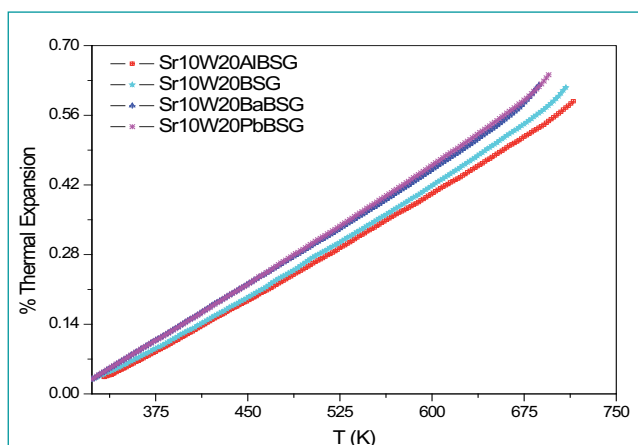


Fig. 2 Percent linear thermal expansion of glass-bonded Sr-chloroapatites

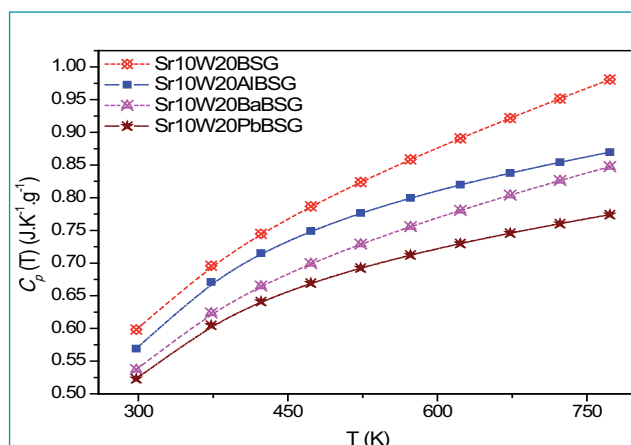


Fig. 3 Heat capacity, C_p of the glass-bonded Sr-chloroapatites by drop calorimetry

IV.28 Sequential Estimation of Plutonium and Uranium in Urine

Estimation of actinides at mBq levels in urine provides an indirect assessment of internal dose received by radiation workers due to its intake in nuclear facilities. Conventional anion exchange method for the estimation of plutonium in urine involves co-precipitation of plutonium along with other actinides from wet oxidized urine matrix by $\text{Ca}_3(\text{PO}_4)_2$ and subsequently separating Pu from other elements using anion exchange resin in 8-10 M HNO_3 medium. Similar conventional method can be used for the estimation of uranium in urine using anion exchange resin in 8-10 M HCl medium for separation. Finally, the eluates containing plutonium and uranium are evaporated, electrodeposited and counted for their alpha activity using alpha-spectrometer. It is proposed to develop a sequential method for the separation of plutonium and uranium from wet oxidized urine matrix either by $\text{Ca}_3(\text{PO}_4)_2$ or HTiO precipitants and subsequent anion exchange separation in 8-10 M HCl medium.

Conventional eluents for U from anion exchange column are diluted HNO_3 and diluted HCl . These eluents will co-elute plutonium and Fe sorbed along with uranium in the anion exchange column. In our previous study, it was found that uranium in the anion exchange column is selectively eluted using the eluent 5M HCl -3M HClO_4 . A known amount of ^{242}Pu and ^{232}U at mBq level were spiked in each 1000 ml simulated urine samples containing a varying amounts of Ca, Mg and Fe. Plutonium and uranium were co-precipitated with $\text{Ca}_3(\text{PO}_4)_2$ and the precipitate was separated from the urine matrix and dry ashed with HNO_3 . The residue was dissolved in HCl and evaporated to dryness. The content of the beaker was dissolved in 10 M HCl solution and passed onto Dowex 1 x 8 anion exchange column, conditioned in 10 M HCl solution. Figure 1 shows the setup for ion-exchange of plutonium and uranium. During this ion exchange step, Pu^{4+} and Fe^{3+} ions would have sorbed along with uranyl ions as anionic complexes. Therefore, uranyl ion was selectively eluted from the anion exchange column using the in-house developed eluent 5M HCl – 3M HClO_4 solution. The column was washed with 8-9 M HNO_3 to remove acid impurities and Pu was selectively eluted with 1.5M $\text{NH}_2\text{OH.HCl}$ in 1M HCl . The eluates were evaporated to dryness and the intended radionuclides in the eluates were electrodeposited in ammonium oxalate medium conditioned in the pH range from 2 to 2.5 for 3 hour at a current of 0.6A. The plutonium and uranium electrodeposited planchettes were counted in an alpha



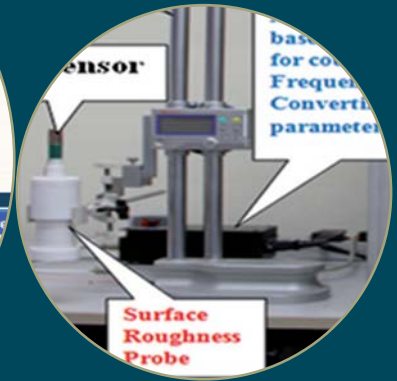
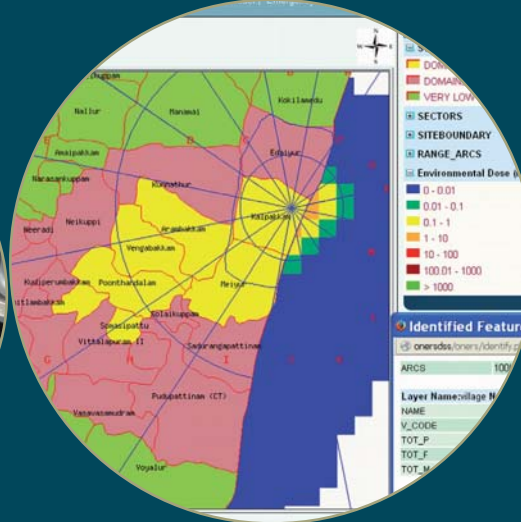
Fig. 1 Ion exchange of uranium and plutonium

spectrometer for their plutonium activity. Average percent recovery of 10 samples for plutonium was 86% and that for uranium was 92%. The analysis time is estimated for plutonium and uranium, by using this method takes six days.

Co-precipitation of actinides with $\text{Ca}_3(\text{PO}_4)_2$ results in macro amount of Ca and Mg in the precipitate. This is due to the variable amount of Ca (100-300 mg) and Mg (100-200 mg) that are normally present in 24-hour human urine samples. This results in time consuming ion-exchange step for the removal of Ca and Mg from the anion exchange column. In an attempt to co-precipitate plutonium with HTiO precipitant from wet oxidized urine matrix, interference of Ti ions during ion exchange separation of plutonium and uranium was studied up to 2000 mg Ti (Table 1) at different pH. Each sample contained 100 mg Ti^+ ions and mBq level of ^{242}Pu . Co-precipitation behaviour of uranium at different pH of the aqueous sample is being studied.

Table 1: Co-precipitation behaviour of plutonium

Sl.No	pH of aqueous sample	Percent recovery of plutonium
1	3 ± 0.3	76
2	5 ± 0.3	80
3	6 ± 0.3	78
4	7 ± 0.3	78
5	8 ± 0.3	96
6	9 ± 0.3	94



CHAPTER V

Directed Basic Research and Infrastructure Facilities

V.1 Development of Contact Angle Measurement System for Molten Metals

Wetting behaviour of sodium at low temperature is of considerable significance in the context of under sodium viewing with under sodium ultrasonic scanner (USUSS). Contact angle of sodium at the interface of substrate is the experimental parameter that can be measured for studying the wetting of sodium on the substrate. A contact angle measurement system with provision for substrate heating was standardised for measurement in open atmosphere and modified for adaptation in high purity argon glove box. High purity argon glove box was commissioned and the contact angle measurement system was incorporated into the glove box. Heater was specially designed for heating the sodium delivery syringe and fixed to the contact angle measurement system.

Sodium was sampled into a glass syringe in the glove box. It was ensured the needle and glass body of the syringe were well introduced into the heater. The needle and glass body of the syringe were simultaneously heated to required temperature. The optimal power for sodium melting was arrived prior to the experiment. After melting the sodium in the syringe, liquid sodium drop was formed at the tip of the needle by careful movement of the stem of the syringe. The drop was collected on the heated substrates (SS316LN) by moving substrate attached to XYZ table with a heater provision. The substrates samples were ground, polished and used for the study.

Contact angle was immediately measured by analysing image taken using high speed camera. Figure 1 shows the photograph of the experimental facility and Figure 2 shows the image of sodium sessile drop on stainless steel substrate. Contact angle measurements were



Fig. 1 Experimental set-up for sodium contact angle measurement

carried out as a function of temperature and Figure 3 shows the variation of sodium contact angle as a function of temperature.

A contact angle measurement system for liquid metals has been successfully commissioned and contact angle of sodium on SS316LN has been measured for the first time. Table 1 shows the temperature and contact angle details of liquid sodium on SS316LN samples.

Table 1: Contact angle of liquid sodium on SS316LN samples

Sl.No	Temperature (K)	Contact angle (°)
1	473	136.3
2	523	121.8
3	573	107.8
4	623	94.3

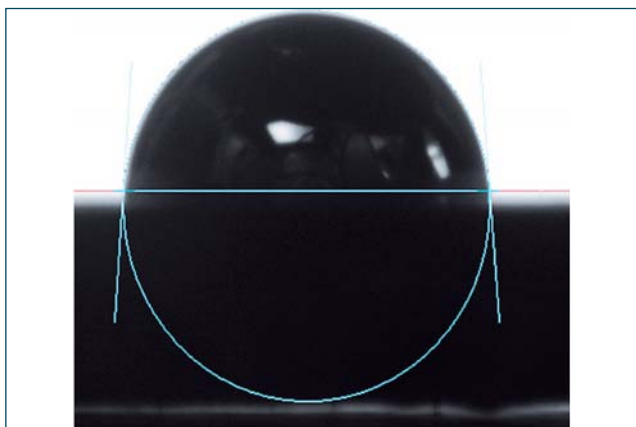


Fig. 2 Liquid sodium sessile drop image on stainless steel substrate at 623 K

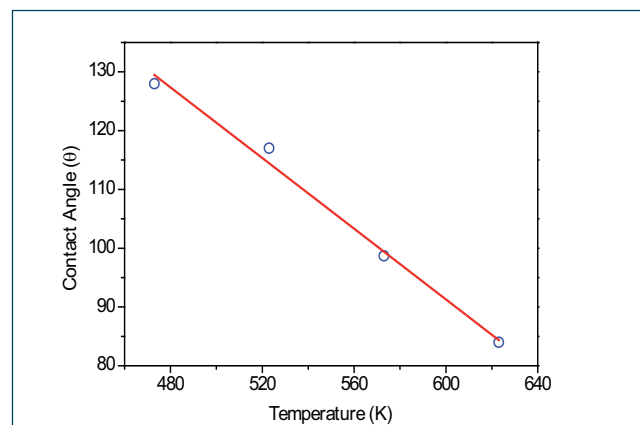


Fig. 3 Contact angle of liquid sodium on SS316L samples as a function of temperature

V.2 Development of Yttria Coating on Inner Surface of Quartz Mould for Injection Casting of Metal Fuel Slug

U-Pu-Zr alloy, a candidate material for metallic fuel reactor is produced by vacuum induction melting technique. The injection casting process is proven to be a good choice for fabrication of metallic fuel slug as it is very simple, safe and amicable for remote operation inside hot cells with good dimensional tolerance. As a prelude, casting of U-Zr alloy slugs is being carried out at Demonstration Facility for Metallic Fuel Fabrication. Quartz tube is chosen as mould material because the metal fuel slugs can be easily recovered by demoulding after casting. However, during casting of fuel slugs using quartz moulds, there is a possibility of migration of silica into metal when quartz tubes are in direct contact with molten metal alloy. In order to overcome this interaction, a ceramic coating barrier is required which should withstand high temperature (1723 K) and be inert in nature with quartz and metal alloy. Yttrium (Y_2O_3) oxide is chosen as the ceramic coating pigment as it satisfies the above requirement.

The procedure for standardizing Y_2O_3 coating on the inner surface of the quartz mould is developed. Y_2O_3 is used as coating pigment and sodium carboxymethyl cellulose (CMC) as a binder. GradeV214 fused quartz tubes of length 500 mm, ID 5 mm and OD 7 mm were used for producing fuel slugs of required dimensional tolerances.

The coating setup is shown in Figure 1. Slurry of Y_2O_3 powder and CMC were prepared. Cleaned quartz tube with both ends open is dipped into coating slurry present in a container. The slurry is siphoned into the quartz mould up to a length of 470 mm at a suction pressure of 200 to 300 mm of water column and at a rate of 460 mm/min. The coating solution is held in the tube for < 45 s and then drained by passing compressed air at a pressure of 10 to 15 mm of water column. Y_2O_3 coated quartz tube is dried at room temperature for 16 to 20 hours. Then it is initially dried at 533 K for 1 hour and at 1373 K for 1 hour to sinter the pigment on quartz surface. One end of the coated tube is fused and this is further used as mould for casting the metallic slugs. The process flow sheet for coating is shown in Figure 2.

Experiments were carried out to optimize the particle size of Y_2O_3 and amount of CMC. Lower the particle size of Y_2O_3 , better is the adherence on quartz tube. Higher percentage of CMC results in excess thickness of the coating. From the experiments, it is optimized



Fig. 1 Experimental set up for Y_2O_3 (a) before and (b) after coating

35 wt% of Y_2O_3 , < 5 μm particle size with 0.25 wt% CMC in water produce required uniform 40 μm thickness coating with good adherence. Y_2O_3 coated quartz tubes were used for the injection casting of U-Zr metal alloy slugs. After several runs of the injection casting of slugs and demoulding, there was no transfer of Y_2O_3 particle from quartz tube to fuel slugs. Silica contamination on fuel slugs is within the acceptable limits. Good and uniform adherence of Y_2O_3 coating on inner side of quartz tube was demonstrated adopting this procedure.

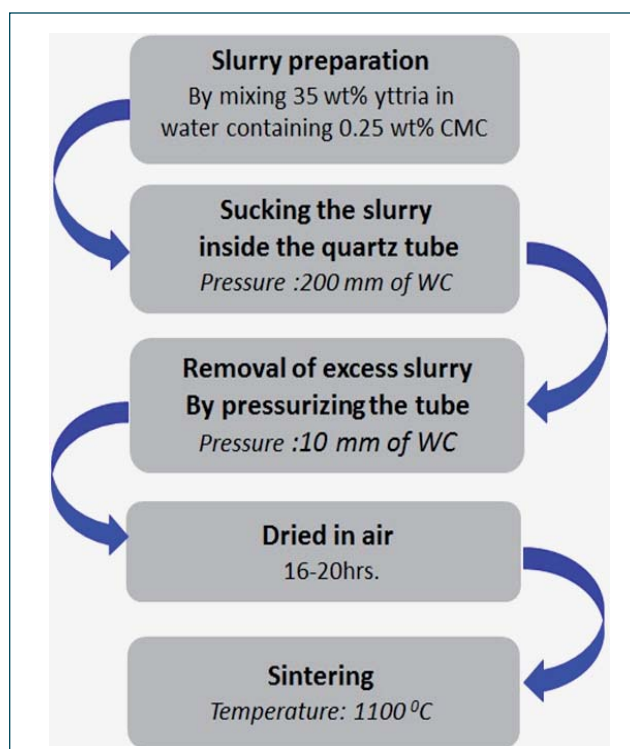


Fig. 2 Process flow sheet for Y_2O_3 coating on inner surface of quartz tube

V.3 Comparative Assessment of Creep Rupture behaviour of RAFM/316LN Dissimilar EB Weld Joint in the as-welded and Post Weld Heat Treated Conditions

The reduced activation ferritic martensitic (RAFM) steel is a candidate structural material which would be used in the fabrication of test blanket module (TBM) which will be tested in the experimental fusion reactor, ITER. The elements in the steels have been optimised to avoid induced radioactivity. Assembly of various components into TBM is carried out by welding. As some of the components are made of 316LN stainless steels, dissimilar weld joints are unavoidable. Materials in the TBM are subjected to intense radiation which can result in embrittlement. The fusion zone and Heat Affected Zone (HAZ) are more prone to embrittlement when compared to base metal. Therefore, conventional welding techniques which utilize higher heat input and produce wider fusion zone and HAZ are not preferred for fabricating TBM components. As an alternative, high energy density welding processes like Electron Beam (EB) Welding, Laser Welding and Narrow Gap welding are being envisaged. Towards this perspective, the influence of post weld heat treatment (PWHT) on the creep properties of RAFM/ 316 LN dissimilar weld joints fabricated by EB welding is being studied.

PWHT is carried out on welded joints to temper the martensite formed in the fusion zone. Microstructural investigations before testing showed that in the RAFM side, HAZ consisted of coarse grained, fine grained and intercritical region as in weld joints fabricated by conventional welding techniques. The difference was however in the width of these three regions. Since EB welding was carried out with relatively lower heat input, the width of all the three constituent regions was relatively smaller. There was considerable variation in the hardness values taken across the weld joint in the as-welded and tempered condition. In the as-welded

condition, the formation of martensite in the fusion zone increased the hardness in this region considerably. The hardness values of the fusion zone adjoining the RAFM/fusion zone interface were highest. This is due to the formation of high carbon martensite in this region as a result of carbon diffusion from the RAFM steel side to the fusion zone during welding. PWHT reduced the hardness of the fusion zone appreciably. There was considerable dip in hardness of the fusion zone especially near the RAFM/fusion zone interface. This could be possible due to the formation of coarse $M_{23}C_6$ carbides in this already carbon enriched region.

Creep tests were carried out on both as-welded and post weld heat treated condition at 823 K at stress levels in the range of 140-225 MPa. The rupture life of the steel after PWHT was considerably higher than the steel in the as-welded condition (Figure 1). The rupture life of the joints with PWHT increased upto ten times for a reduction of applied stress from 180 to 160 MPa.

At higher stress levels the failure location of the joints both with and without PWHT was in the ferritic side adjacent to the HAZ. Significant elongation was observed in the grains adjacent to the failure location which resulted in a higher area of reduction. With decrease in stress level, the reduction in area of the joints decreased significantly in both the conditions. The failure location of the joint at lower stress levels in the as weld condition was in the ferritic side far from the HAZ. For PWHT joint tested at 160 MPa, type IV failure characterized by cavities in the intercritical region was evident (Figure 2). Though the width of the intercritical region was quite small, the constraint caused by the adjoining stronger regions resulted in cavitation damage leading to ultimate failure.

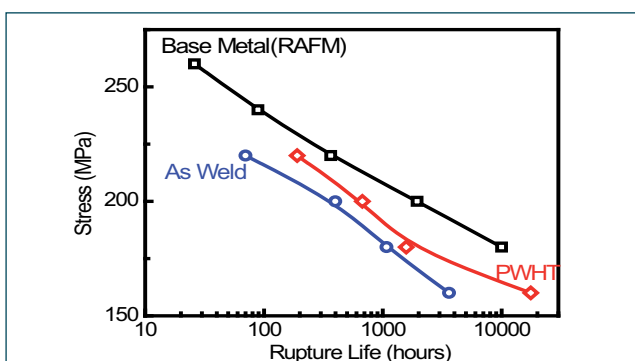


Fig. 1 Comparison of creep rupture life of RAFM/316LN dissimilar joint with and without PWHT

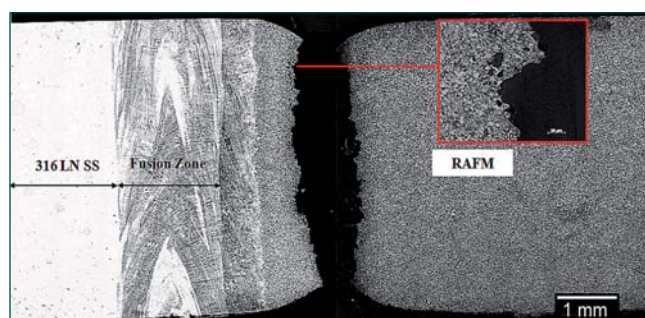


Fig. 2 Figure showing the failure location of the weld joint tested at 160 MPa (rupture life 17,600 hours), the insert shows cavities formed in the intercritical region

V.4 Microstructural Evolution in the Weldment of 9Cr RAFM Steel with Varying Tungsten Content

As a part of the long term R&D efforts to support the fusion program in India, the India-Specific RAFM (INRAFM) steel with 1.4 wt% W and 0.06 wt% Ta was developed. Although the principal carbide in this steel is $M_{23}C_6$, small amounts of very stable carbo-nitrides of V and Ta also form during tempering. With prolonged thermal exposure, the tempered martensite structure undergoes continuous evolution both in sub-structure as well as in the secondary phases. In the present study, impression creep (IC) test is used to compare the creep properties of RAFM steels with two different tungsten (1 and 1.4 wt %) contents. The change in property is corroborated with microstructural evolution predicted by 'JMatPro' and validated by experimental characterization. Since welding is an inevitable fabrication process, study on structural and mechanical properties of the welded joints of 9Cr-RAFM steels is considered as a thrust area of research. In fusion welding, the weldment would possess a highly heterogeneous microstructure leading to variations in response to post weld heat treatment and to long-term service exposures – this aspect is also covered in the study.

1W and INRAFM steels in the normalized and tempered (n&t) condition possess a tempered martensitic structure, with an average prior austenite grain size of ~14 and 10 μm respectively, and an average hardness in the range 220-230VHN. TEM analysis revealed the retention of lath structure (Figure 1) of size ranging ~500-600 nm with characteristic high dislocation density. Precipitates of various sizes and morphologies (Figure 1) decorate the prior austenite and lath boundaries. XEDS analysis showed $M_{23}C_6$ to be Cr rich (~58wt %) with W content as high as 11wt%. However, MX carbides were found to be rich either in V or Ta. Size distribution of $M_{23}C_6$ carbides showed a Gaussian distribution with an average size range of 70-100 nm. In contrast, MX carbides were few and of very fine size (10-15 nm). Computation by 'JMatPro' predicted equilibrium phases to comprise of $M_{23}C_6$, MX, ferrite and austenite in the temperature range of interest (1000-1253 K). Dissolution temperature of $M_{23}C_6$ is predicted to be higher in IN-RAFM as compared to 1W steel, due to the higher amount of W in the carbide. It also predicted $M_{23}C_6$ with few MX carbides after one hour of tempering at 1033 K, which is in agreement with experimental results. Computed concentration of major alloying elements, in $M_{23}C_6$ and MX carbides (both 1W and INRAFM) also agreed with the values obtained by XEDS analysis.

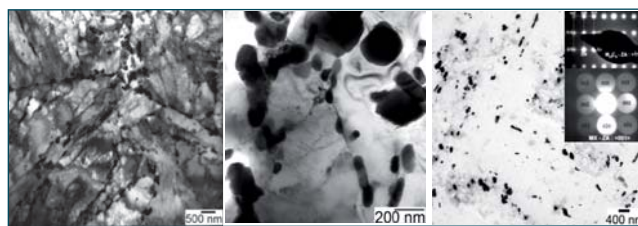


Fig. 1 TEM images showing substructure and distribution of precipitates

IC test was carried out at 823 K on n&t and aged IN-RAFM steels under a punching stress of 787 MPa. Figure 2 shows the plot of creep rate versus time for both the steels. Testing of the n&t steel showed a negligible primary creep compared to aged steels, which has undergone substructure changes. In the primary creep region, resistance to deformation increases due to work hardening giving rise to a decreasing creep rate. Though the secondary creep rates obtained from impression tests are higher than the conventional tests, it is evident that creep rate reduces to nearly half the value with an increase of 0.4% W in INRAFM steel. It is known that W strikingly reduces the rate of self diffusion of Fe thereby limiting dislocation climb which is the major deformation mechanism in creep. INRAFM steel aged at 823 K for 5000 hours showed the lowest creep rate or highest creep strength among all the aged steel despite the higher substructure changes expected on exposure to higher temperature. This is clearly ascribed to the existence of the fine intermetallic Laves phase (Fe_2W) that formed at 823 K as seen in Figure 3.

Coarsening and a progressive increase in the Cr content in $M_{23}C_6$ (evolution of metastable $M_{23}C_6$ phase towards stable $M_{23}C_6$) were observed as the tempering time is increased. Laves phase was found to have nucleated around or near the coarse carbides in lath/grain boundaries.

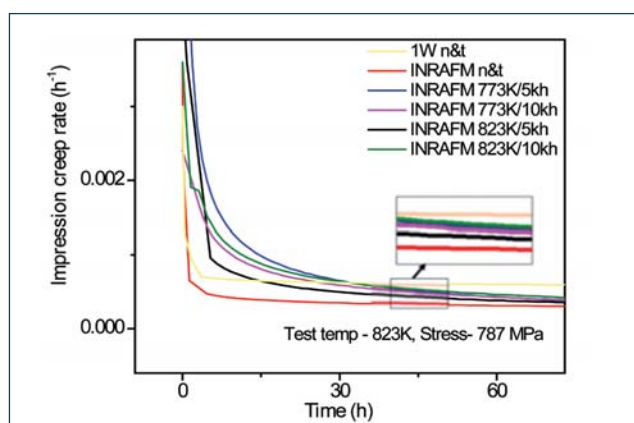


Fig. 2 Impression creep rate for 1W and IN-RAFM steels

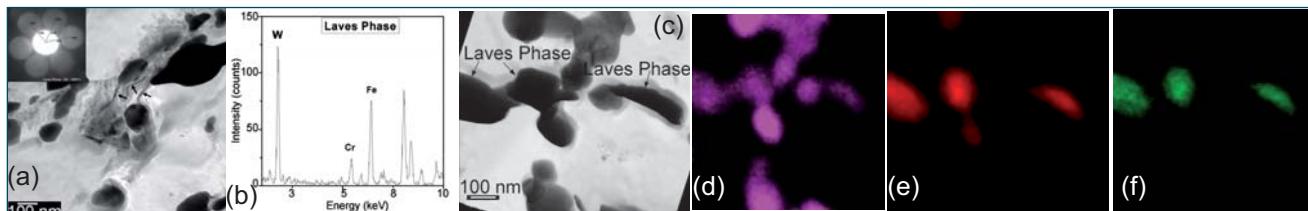


Fig. 3 TEM images of INRAFM steel after ageing (a) 823K/5kh-fine Laves, (b) EDS from Laves, (c) 823K/10kh- coarse Laves and (d-f) X-ray map depicting the distribution of Cr, Fe and W in the precipitates

Coarsening of carbide consumes large amount of Cr and C, leaving the surrounding matrix depleted in Cr. This results in localized increase in W concentration favoring the nucleation of Laves phase, in presence of the thermodynamic driving force for its formation. However, an increase in ageing time (10000 hours) at 823 K increased the creep rate, which could be due to discontinuous network of coarse brittle Laves phase. Even though 'JMatPro' computations indicated the formation of low amounts of Laves phase in both the steels after 1000h of aging at 823K, no experimental evidence was obtained for its presence in 1W steel, due to lower W content in the matrix.

The weldments of RAFM steel showed a heterogeneous microstructure (Figure 4a). While weld metal showed columnar grains, heat affected zone (HAZ) showed coarse (CGHAZ) and fine (FGHAZ) prior austenite size grains depending upon the thermal cycles experienced in the region, but complete martensitic structure. A region with mixed (α' + α) microstructure (Figure 4b) known as intercritical heat affected zone (ICHAZ) also could be identified.

Ageing of weld metal resulted in two types of $M_{23}C_6$ carbides with distinct size, shape and chemistry. The fine needle shaped (circled in Figure 5a) were found to be aligned in two perpendicular directions parallel to [111] direction of the matrix and having higher Cr contents of about 80 wt.% as compared to other coarse carbides, which had only 60-65wt (Figure 5b). %Cr. It is known that the Fe rich ($M_{23}C_6$, Epsilon- ϵ) carbides

and Cr rich M_2X (hcp) form in 9Cr steels in the early stages of tempering or lower temperatures, subsequently transform to Cr rich $M_{23}C_6$ as tempering proceeds. Laves phase could be identified in the weld metal after 823K/10 kh. The delay in appearance of Laves phase in the weld metal as compared to the base metal is attributed to the initial carbide free martensite structure and the slow consumption of carbon as tempering/ ageing proceeds at temperatures lower than the peak tempering temperature. Precipitation behavior of CGHAZ followed a similar trend as the weld metal.

The Laves phase formed in FGHAZ after ageing at 823K/5kh is found to be fine with an average size of 40 nm, whereas it was found to be coarse (~100 nm) after 10000 hours (Figures 5 c and 5d). On comparing the size of Laves phase that formed in the base metal and FGHAZ at 823K/5kh, it can be deduced that Laves phase formed first at FGHAZ. It is well known that the coarsening of carbides and formation of Laves phase is detrimental to fracture toughness. Hence, it can be concluded that during thermal exposures at temperatures ≥ 823 K, FGHAZ is the weakest region in the weldment from microstructural point of view, which is in accordance with the reported creep failures in the HAZ region of similar steels. No experimental evidence could be obtained for Laves phase in any region of 1W steel after ageing at 823K. The formation of Laves phase early in the HAZ of INRAFM steel during high temperature exposures is attributed to the higher W content in the steel as well as abundant precipitation of carbide which in turn increases the availability of W in the matrix.

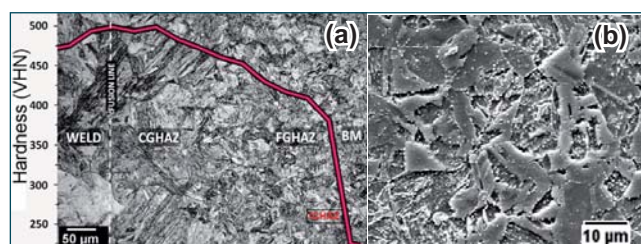


Fig. 4 (a) Micrograph showing the weld, CGHAZ, FGHAZ and base metal regions of the weldment of 1W steel, with hardness plot superimposed (b) ICHAZ showing a mixed microstructure consisting of martensite and ferrite

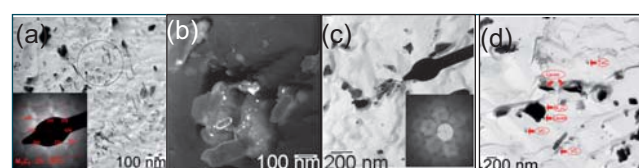


Fig. 5 Microstructure of (a & b) weld metal and FGHAZ (c & d) of INRAFM steel, (a) presence of fine needle type precipitates, after ageing at 773K/5kh (b) dark field image of Laves phase surrounding coarse carbide, after ageing at 833K/5kh (c) fine precipitates of Laves phase after ageing at 823K/5kh and (d) coarse Laves phase after ageing at 823K/10kh

V.5 Ageing Induced Degradation of Fracture Resistance of Alloy 617

Alloy 617 is a class of Ni based superalloy, developed for use in advanced ultra-supercritical (AUSC) coal-fired power plants in India. Alloy 617 has attracted the attention of researchers and is nowadays under active considerations as the piping and ducting material for high temperature applications in both the thermal and nuclear power plants, likely to be used in a temperature regime of 973 to 1033 K at high pressures of 35 MPa. The high nickel and chromium content offers the alloy a very high resistance to variety of reducing and oxidizing environments. The presence of aluminum, in conjunction with the chromium, provides oxidation resistance at elevated temperatures. Solid-solution strengthening is imparted by the cobalt and molybdenum. The major alloying elements present in Alloy 617 are shown in Table 1.

To evaluate the ageing induced degradation of fracture resistance, the Alloy 617 has been subjected to fracture tests under impact and quasi-static loading after ageing at 1023 K for different durations up to 20 kh. Figure 1a shows the Charpy impact energy, as obtained at room temperature up to 20 kh. The as-received specimen shows the highest value with average energy of 285 J. One kh ageing shows a significant drop in the energy (~ 157 J). The subsequent ageing for 5 kh and 10 kh has shown a steady decrease, with a loss of 80% in the overall fracture energy after 20 kh. Towards the fracture resistance evaluation under quasi-static loading condition, the J-R curves have been established for the as-received material and after ageing treatment, as mentioned above. A comparison of the J-R curves for the as received condition and after 20 kh ageing treatment is shown in Figure 1b. The J values at 2 mm crack extension are found to be ~ 1000 and 200 kJ/m^2 for as-received and 20 kh aged material respectively. The degradation of fracture toughness due to ageing is found to be 85%. It can be observed that the ageing induced degradation of fracture resistance of the Alloy 617 follows a similar trend for the impact (80%) and the quasi-static loading conditions (85%). This indicates that similar fracture mechanisms, are operating in terms of crack initiation and growth in the aged specimens for the impact and quasi-static loading

Table 1: The major alloying elements present in Alloy 617

	Ni	Cr	Al	Co	Mo	Ti	Fe
Min	49.0	21.0	0.8	11.0	8.0	0.3	-
Max	Bal	23.0	1.3	13.0	10.0	0.5	1.5

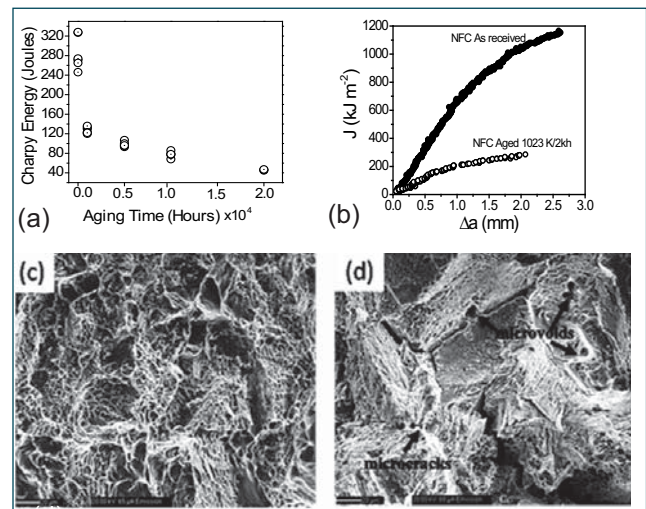


Fig. 1 Fracture resistance of alloy 617 (a) Charpy energy, (b) J-R curve, (c) fracture surface of as-received sample and (d) fracture surface of 10kh sample

conditions. To this end, a detailed investigation based on SEM based fractography and TEM based microscopy has been carried out.

Figures 1c and 1d represents the SEM photographs of the fractured surfaces after room-temperature Charpy impact test of as-received and 10kh aged samples at 1023 K respectively. Fractographic analysis shows the presence of large dimples in as-received material indicating ductile nature of fracture. Contrary to this, the 10 kh aged specimen shows dominating intergranular fracture indicating grain boundary embrittlement. This aging induced embrittlement has been attributed to the aging induced loss of fracture resistance for the Alloy 617.

In the TEM studies, 10 kh aged specimen shows precipitates of γ' $\text{Ni}_3(\text{Ti}, \text{Al})$, as compared to the as received one. Where the γ' can be attributed to matrix hardening, the grain boundary embrittlement has been attributed to the formation and ageing induced coarsening of M_{23}C_6 (M: Cr, Co) precipitates, at the grain boundaries (Figure 2).

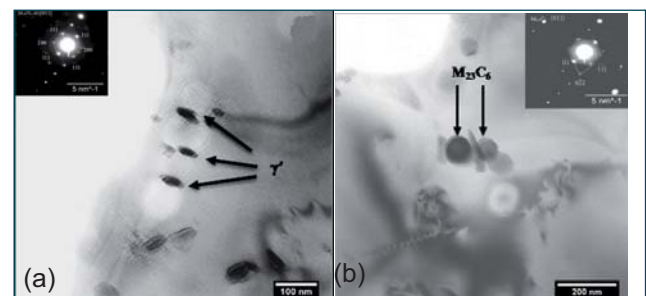


Fig. 2 TEM micrographs after 10 kh ageing: (a) γ' precipitates and (b) M_{23}C_6 (M: Cr, Co) precipitates

V.6 Narrow-Gap Hot Wire TIG Welding of Thick Sections for Indian Advanced Ultra Super Critical Thermal Power Plant

Narrow-Gap TIG welding is an advancement in TIG welding process used for joining of thick sections in nuclear and thermal power plants. Narrow-Gap TIG (NG-TIG) welding is carried out using specially designed TIG torch on a narrow-groove joint preparation. NG-TIG welding in conjunction with hot-wire technique increases the productivity. In-house NG-TIG welding facility has been established to develop the welding procedure for joining of thick components for fission and fusion reactor programs, and Advanced Ultra Super Critical (AUSC) coal-fired power plant. Alloy 617M and 10%Cr ferritic-martensitic steel are candidate rotor materials under consideration for steam turbine of India AUSC plant. There is a dissimilar metal welding between 10% Cr steel rotor parts to Alloy 617M rotor parts. In this article, the welding procedure developed for joining of thick welds of 304 SS, Alloy 617M, and dissimilar metal welding of 10Cr steel to Alloy 617M using in-house NG-TIG facility is presented.

Figure 1 shows hot wire NG-TIG welding machine at IGCAR with column and boom arrangement to manipulate the TIG torch for linear welding of plate, and circular welding of pipe using tilt table Positioner-Rotator. To develop the welding procedure for plate welding, 304 SS plate of 40 mm thickness was welded using ER308L filler wire (\varnothing 0.8 mm) with hot-wire mode. The weld joint passed liquid penetrant examination (LPT) and X-ray radiography. Figure 2a shows the photograph of the metallography sample revealing a very narrow weld bead of 10 mm width. Weld joint passed in X-ray radiography met the tensile properties and side-bend test (Figure 2b) requirement as per ASME Section IX.

Prior to dissimilar metal welding of 10Cr steel to Alloy

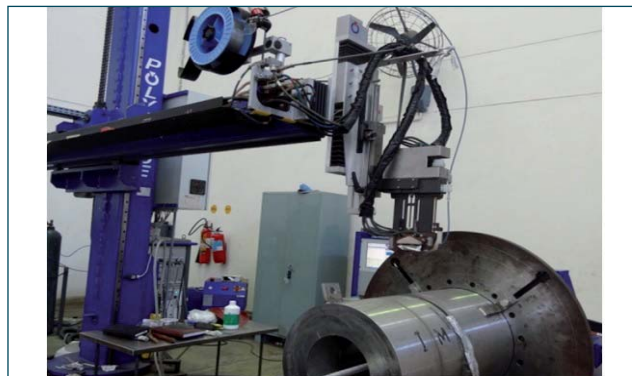


Fig. 1 NG-TIG welding machine at IGCAR

617M hollow circular forgings, welding trials were carried out on 304 SS thick pipes with narrow-gap edge preparation with included groove angle of 5° . Welding parameters and shielding gas requirement has been optimized on circular welding of 304 SS pipes up to 120 mm wall thickness. The dissimilar metal welding of 10Cr steel to Alloy 617M is planned to be demonstrated by two methodologies. The first method is direct welding between 10Cr steel and Alloy 617M using Alloy 617 filler metal (ERNiCrCoMo-1) followed by post weld heat treatment. The second method is by buttering/overlaying of 10Cr steel using ERNiCrCoMo-1 followed by post weld heat treatment and subsequent welding of overlay deposit with Alloy 617M part. A mock-up welding trial carried out for direct welding between 10Cr steel and Alloy 617M hollow circular forgings of 200 mm diameter and 50 mm weld thickness passed LPT and showed no noticeable defects in gamma radiography (Figure 3). The buttering of 10Cr steel forging using ERNiCrCoMo-1 has been successfully carried out and deposited to the required height of 27.5 mm (Figure 4).



Fig. 2 (a) Weld bead cross section, and (b) side-bend test specimens

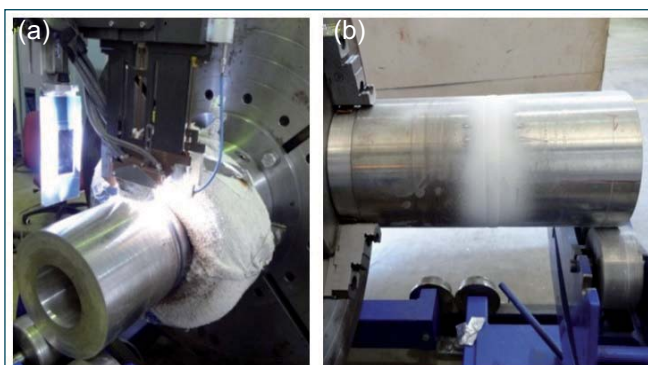


Fig. 3 10Cr steel/Alloy 617M DMW: (a) NG-TIG welding in progress, and (b) LPT after final weld pass

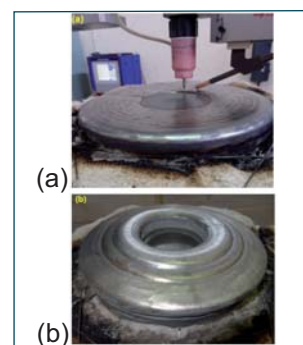


Fig. 4 Weld overlaying/buttering of 10Cr steel: (a) after 1st layer and (b) completion of buttering

V.7 Characterization and Performance of MgO Coated 316 SS

Magnesium oxide (MgO) is a ceramic having high refractoriness, high melting temperature and good corrosion resistance, which makes it a candidate for high temperature applications. MgO has the highest thermal expansion coefficient among the ceramics, that makes it ideal for the application of metal ceramic coating. Also, the thermal coefficient of MgO best matches with that of stainless steel than any other ceramic coating. MgO films are also considered for their use as insulation coatings.

The present work deals with the development of MgO coatings on SS316L using pulsed laser deposition technique. KrF excimer LASER ($\lambda=248$ nm) was used to synthesize these coatings. In order to tailor the microstructure and ensure the uniformity of these coatings to achieve desired properties, the process parameters such as oxygen partial pressure and substrate temperature were varied to get uniform coatings. XRD has been carried out to check for the phase purity and the strain associated with the coating. SEM studies reveal the microstructural integrity and morphology of the coatings in addition to establishing the chemistry of coatings. Sodium compatibility of the coatings has been tested to evaluate the performance of the coatings under sodium fire.

MgO coatings deposited on SS316L substrates at RT and 600°C in oxygen partial pressure of 10^{-2} mbar showed poor adhesion to the steel substrate. In order to improve the adhesion of MgO on steel, an intermediate metallic coating of Zr has been deposited on the steel substrate using Pulsed DC Magnetron Sputtering. The process parameters have been set based on the process optimization with respect to the microstructure. MgO coatings have been deposited on Zr coated SS316L substrate by varying the substrate temperature and oxygen partial pressure respectively. Substrate temperature was varied in the range of RT to 600°C by keeping oxygen partial pressure constant at 2×10^{-2} mbar and oxygen partial pressure was varied in the range of 2×10^{-2} mbar to 2×10^{-5} mbar by keeping substrate temperature constant at 600°C. Based on the XRD and SEM analysis, it was found that coating deposited on substrate heated to 600°C and with an oxygen partial pressure of 2×10^{-2} mbar exhibited uniform microstructure. Further, the lattice parameter and crystallite size of the film was better and the former matched with that of the standard value (ICDD Database JCPDS PDF card number MgO 00-004-0829).

In order to check the compatibility of the coatings with liquid sodium, in particular under incineration conditions, coupons of MgO coated SS316L were exposed in the incineration tank where sodium was burnt by exposure to atmosphere. The temperature profile of the liquid sodium measured using thermocouple at five minute intervals was found to be 700°C. XRD pattern and SEM micrographs of the samples before and after exposure are shown in Figure 1 which indicates that there is no phase other than MgO present on the substrate.

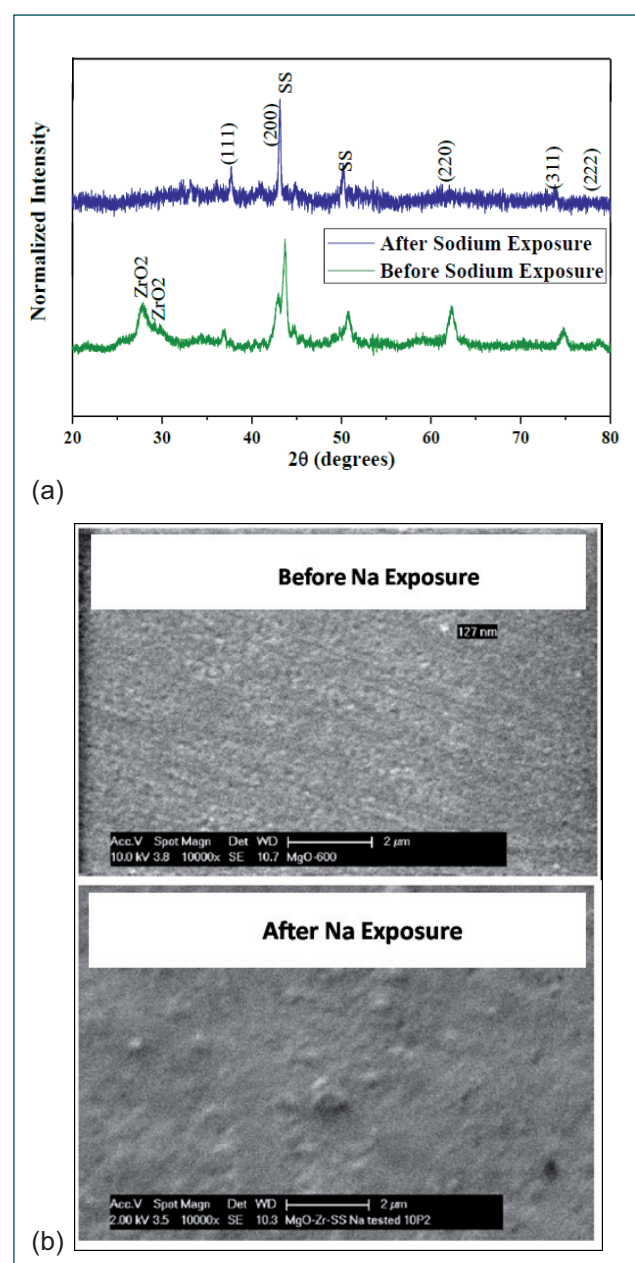


Fig. 1 (a) XRD pattern and (b) SEM micrograph of MgO coated SS 316 L before and after sodium exposure

V.8 Preliminary Studies on the Direct Electrochemical Reduction of ThO₂ to Th Metal in CaCl₂ Melt

Thorium metal is produced by calciothermic reduction of ThO₂ and by chemical reduction of thorium halides by sodium, magnesium or calcium. A new metal production process was reported in the recent past to convert solid metal oxides directly to metals by molten salt electrolysis. The feasibility of reduction of ThO₂ in the new method was studied for the first time.

In the electrochemical reduction method, the metal oxide in the form of powder compacted and sintered pellet is configured as the cathode against graphite anode in molten calcium chloride containing small amounts of calcium oxide at ~900°C (Figure 1). Calcium metal is electro-generated at the cathode and it chemically reduces the metal oxide to metal.

ThO₂ powder was prepared by precipitating Th(C₂O₄)₂·6H₂O from an aqueous solution of Th(NO₃)₄·5H₂O by oxalic acid followed by thermal decomposition in moist air. The powder was pressed to get green pellets (12.5 mm dia., 2.5 mm thick and weighing ~1.5g), which were sintered at 1200°C for 2.5 hours in air to obtain mechanically stable and porous ThO₂ pellets. The pellet was tied with a tantalum wire and used as cathode in the electro-reduction cell against a graphite rod anode. Calcium chloride containing 0.5 wt.% CaO was used as electrolyte. Experiments were carried out in leak tight stainless steel reactor under argon gas purging. Figure 1 shows schematic of the electrolytic cell assembly.

The electro-reduction was carried out by holding the oxide cathode at -0.3 V versus Ca/Ca²⁺ reference electrode i.e. at a potential sufficient to generate calcium metal at the oxide cathode.

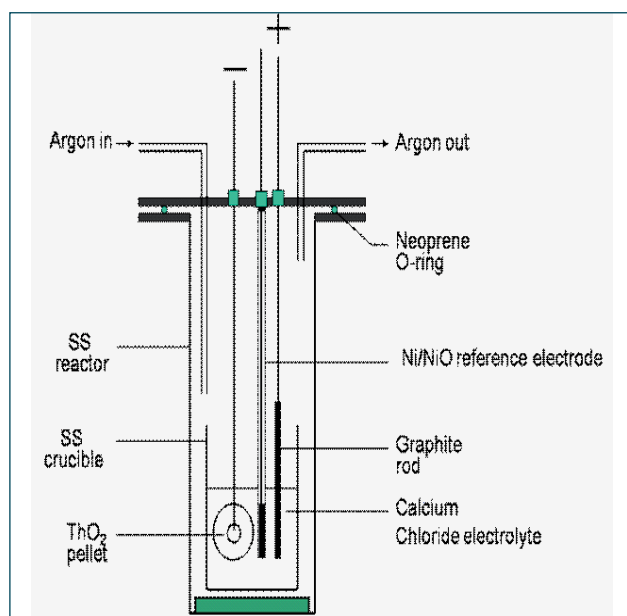


Fig. 1 Schematic of the electrolytic cell assembly

The pellet, after electrolysis, was found completely reduced and electrically conducting. The X-ray diffraction analysis showed that the original ThO₂ was reduced to Th metal. A nodular morphology, typical of an electro-reduced metal, was evident in the scanning electron microscope image of the fractured surface of the reduced pellet. Photograph, X-ray diffraction pattern and SEM image of the electro-reduced thorium metal are shown in Figures 2a to 2c. The experimental results showed that, unlike in the case of many metal oxides, Ca-Th-O intermediate compounds are not formed during electrolysis and the reduction of ThO₂ to Th probably occurred by transfer of four electrons in a single step, i.e. Th⁴⁺→Th.

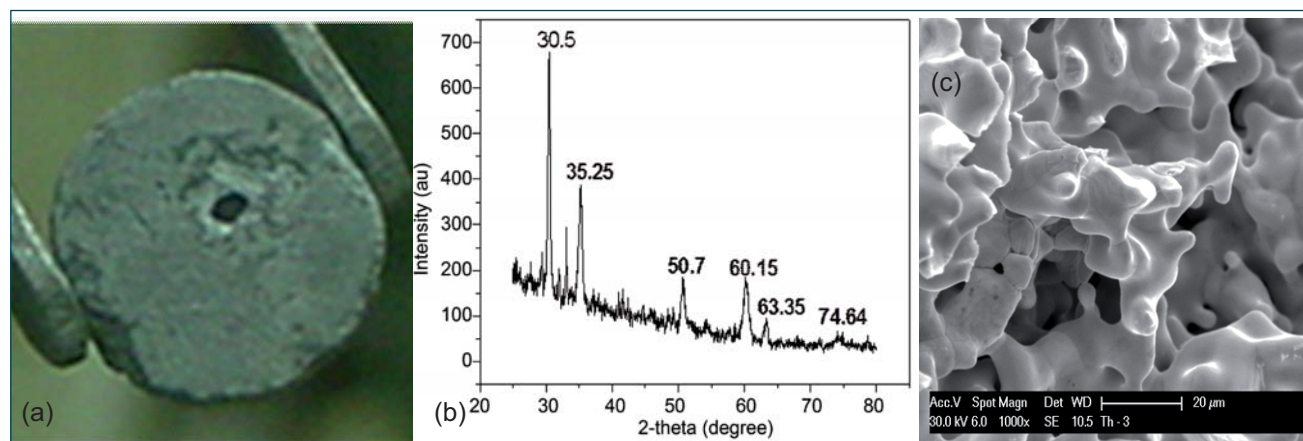


Fig. 2 (a) Photograph, (b) XRD pattern and (c) SEM image (1000X magnification) of the electro-reduced thorium metal

V.9 Innovative Design for Precise Temperature Control in a Confined Radioactive area

A Laser Raman Spectrometer was procured for R&D studies on radioactive samples and was planned to be installed in one of the existing radioactive lab. The confined area in the lab where the instrument was planned to be located requires precise control of temperature of $21 \pm 1^\circ\text{C}$ to operate efficiently and effectively. An innovative method was designed to enhance cooling in the confined space of existing radioactive facility without major revamping or replacement and with all safety interlocks.

In the multizone ventilation system of RCL building, various laboratories are connected to the supply and exhaust blowers through large sized ducts. The atmospheric air is drawn through pre-filter, HEPA filter and passed through a cooling coil, water eliminator and the conditioned air is supplied to the various laboratories by supply blowers. To avoid the spread of contamination the radioactive exhaust air is filtered through HEPA filter before release into atmosphere through stack. The ventilation system in the laboratory supplies fresh filtered and conditioned air to working areas like low level active laboratories, high level active laboratories, High bay areas, glove boxes and hot cells.

The instrument was planned to be installed in a laboratory which receives conditioned air from High level supply system. The area of the laboratory is around 255 square metres. The conditioned air supply to the laboratory is $7000 \text{ m}^3/\text{hr}$ and the exhaust air is about $7700 \text{ m}^3/\text{hr}$ from the laboratory. This is exhausted by high level exhaust blower. The main challenge was to maintain $25 \pm 1^\circ\text{C}$ in the laboratory for human comfort and to maintain $21 \pm 1^\circ\text{C}$ for the instrument in confined space without affecting the radioactive ventilation air flow pattern.

As it is not economical to enhance cooling in the entire laboratory, an aluminum cubicle for housing the instrument was proposed in a confined area based on the air conditioning duct layout without affecting the



Fig. 1 Fan coil unit with ducting/piping

air flow pattern. This was done by providing necessary louvers in the aluminum cubicle, so that the exhaust air can flow through the louvers; pass through the nearby fume hood, maintaining the necessary air changes per hour and air flow pattern. A booster fan coil unit was specially designed with chilled water cooling system and installed in the supply duct. Figure 1 gives the fan coil unit with ducting/piping.

Addition of the booster fan coil unit can pressurize the cubicle when exhaust blower trips. Hence, an interlock to trip the fan coil unit was also installed to avoid pressurization of the confined space. The pressure switch was tuned such that, the fan coil unit trips when the pressure in the duct is lower than the set value. By this way, it is ensured that, the cubicle would not pressurize and air flow pattern would be maintained. The photograph of the arrangement is shown in Figure 2.

The temperature control in the room was achieved by installing a thermostat in the cubicle with a feedback signal to three way mixing valve to regulate the chilled water flow. The performance of the system was examined for a period of 15 days and trend variation in the room temperature plotted in the graph shows temperature of $21 \pm 1^\circ\text{C}$. Figure 3 shows the trend variation in room temperature.



Fig. 2 Pressure tapping and pressure switch

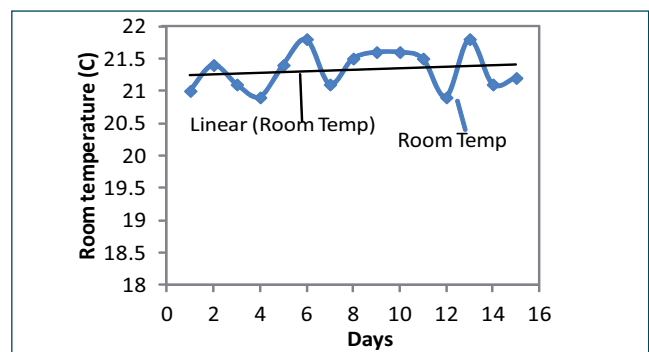


Fig. 3 Trend variation in room temperature

V.10 Development of Embedded Control System with Digital PID Current Control for Discharge Test of Class-I Power Supplies

Class-I power supplies in power plants have to be tested periodically to monitor their healthiness. Discharge test is the only test recommended by IEEE to determine the actual capacity of the battery. An automated battery discharge testing system has been developed for the discharge test of batteries to reduce the human errors during manual testing.

The automated discharge test involves measurement of the discharge current and controlling the current through the load in a closed loop. The system logs the time, voltage, discharge current and the capacity of the battery (Ah) during the testing. The system has provision for displaying the parameters being monitored on front panel LCD and an alarm annunciation, in case the discharge is terminated. Figure 1 explains overall block diagram of the control system.

A PIC microcontroller based constant current discharge system with digital PID algorithm has been developed for the closed loop control. The current is measured using Allegro ACS-709 Hall effect current transducer and the error voltage is used for generating the PWM control output. The control output from microcontroller is amplified using a high current MOSFET that is fed to the load circuit. Figure 2a shows the controller card for

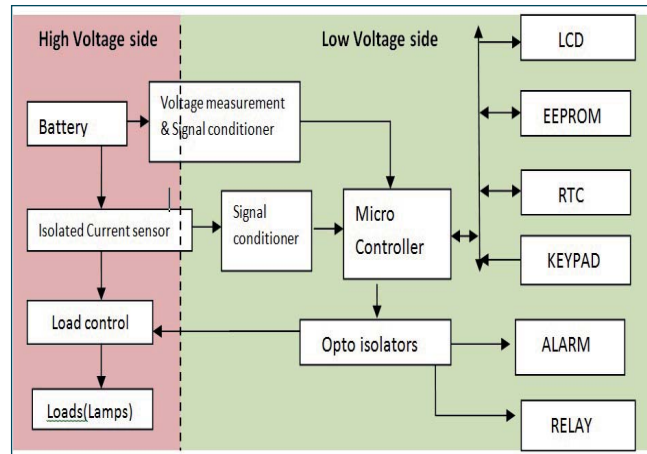


Fig. 1 Control block diagram

current measurement and control. Programmable load is designed using automotive lamps for testing 24, 30 and 48 V batteries, with maximum current up to 20 A. The loads are connected in two banks with series and parallel combinations for testing batteries of different ranges. Figure 2b shows the front panel of the control system. Selector switches are provided in the front panel for selecting the respective load. The battery is discharged at 10% of its rated capacity for 10 hours. The discharge test will be terminated if the battery voltage falls below threshold voltage, or if the total discharge time exceeds ten hours.

After completion of the test, the battery parameters are transferred to PC via USB port for plotting and further processing. The designed system has been tested on 24V/180Ah lead acid battery at C10 rate for ten hours and the discharge curve is shown in Figure 3. Automated testing has been performed on sub-station and DG batteries of RML and system has been commissioned successfully.

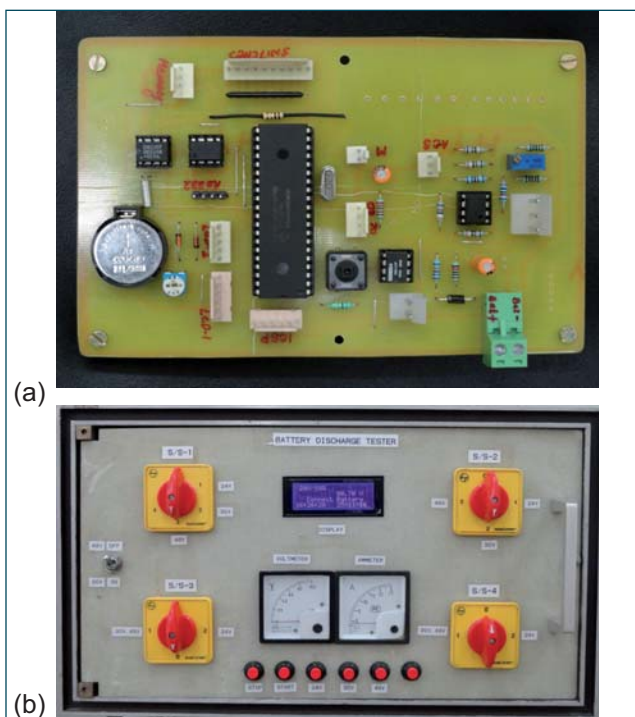


Fig. 2 (a) PIC controller card for current measurement and control and (b) control panel for testing batteries

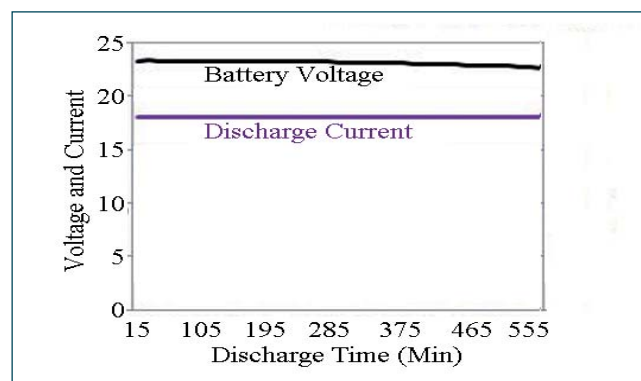


Fig. 3 Discharge curve of 24 V battery at 18 A

V.11 Sodium Testing of Level Sensor made of Indigenous Mineral Insulated Cable

The stainless steel sheathed mineral insulated (MI) cables are widely used in reactor for various types of sensors developed to measure temperature, flow and level. Presently the cables are being imported from reputed manufacturers like M/s Thermocoax, France. As part of indigenisation, an Indian manufacturer M/s Techno Instruments, Gujarat was identified and sample cable was procured to qualify for sodium applications.

Mutual inductance type level probes (MILP) are used for monitoring sodium level in sodium tanks and vessels. 1 mm diameter stainless steel sheathed MgO insulated mineral cable of 0.33 mm diameter copper conductor is used for making the probe.

A mutual inductance level probe of 1000 mm active length, 1000 mm non active length with 28 mm diameter bobbin wound with Indian make mineral insulated cable in bifilar winding was fabricated and tested in sodium. The mutual inductance type level probe is shown in Figure 1. The functionality was evaluated by calibrating it in sodium, obtaining sensitivity and operating frequency which is comparable with level probe made out of imported cable.

After winding the coils the free leads are cold end sealed and the insulation resistance was maintained at 20 GΩ.

After mounting the probe inside the Test Pot-2 in Thermal Shock Test Facility the insulation resistance and winding resistance were measured. Experiment was carried out to find the sensitivity (S) of the probe, optimum frequency and external temperatures compensation resistor. Table 1 gives the probe comparison data between Indian and imported mineral insulated cable. Figure 2 gives the variation of insulation resistance of primary and secondary coil at various temperature in the range 200



Fig. 1 Mutual inductance type continuous level probe

to 550°C. It is clear from the graph that the insulation resistance value improved after endurance test. After calibration, the probe was kept in sodium at 550 °C around 1000 hours for endurance test.

After 1000 hours the probe's secondary output was noted for full level and zero level at 200 and 550 °C. It was found that there is only a small variation in secondary millivolt which may be attributed to change in process conditions.

Table 1: Comparison between Indian and imported mineral insulated cable probe data		
Parameters	Imported	Indian
External resistor	203 Ω	89 Ω
Optimum frequency	2.50 kHz	2.50 kHz
Primary resistance	4.82 Ω	2.42 Ω
Secondary resistance	4.82 Ω	2.43 Ω
Sensitivity (S)	4.50	4.65
% S	18.20	18.61

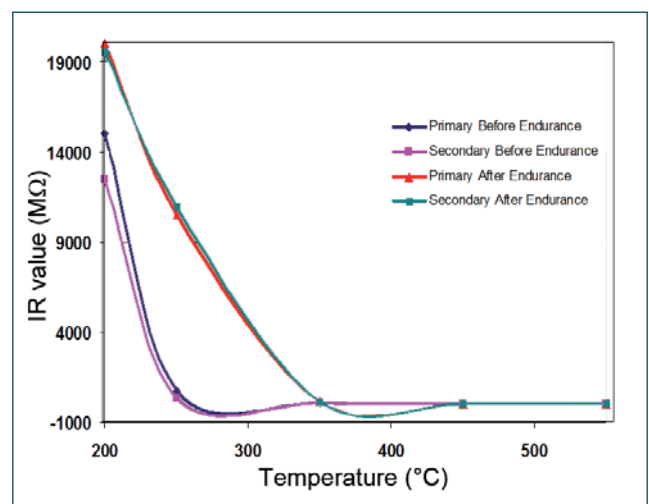


Fig. 2 Variation of insulation resistance value before and after endurance test

V.12 Infrared Thermography based Magnetic Hyperthermia Facility

In recent years, magnetic fluid hyperthermia (MFH) has become a rapidly developing alternate methodology for treatment of cancerous cells. Superparamagnetic Fe_3O_4 and $\gamma\text{-Fe}_2\text{O}_3$ are the most widely used magnetic system for hyperthermia applications because of their superior bio-compatibility (metabolization through heme oxygenase-1 to form blood hemoglobin), ease of synthesis and long term stability. To make MFH as a standard therapeutic procedure, further systematic studies on the safety and efficacy of magnetic nanoparticles inside tumour cells are required. Towards practical applications of MFH, biocompatible and stable nanofluids are required. Here, we investigate the MFH of water based phosphate coated Fe_3O_4 nanoparticles (biocompatible fluid) which are synthesized in our laboratory using a single step co-precipitation method. The specific absorption rate values are experimentally measured at a fixed frequency of 126 kHz and at low field magnitudes. We find a very high value of heating efficiency with an extremely low value of magnetic field and frequency product ($H.f$), which is found to be ideal for practical applications in cancer treatment. The effect of particle concentration on SAR is also studied to probe the role of dipolar interactions.

The phosphate coated magnetic nanoparticles were synthesized by co-precipitation technique using a 1:1 aqueous solution of $0.2\text{M FeCl}_3 \cdot 6\text{H}_2\text{O}$ and $0.1\text{M FeSO}_4 \cdot 7\text{H}_2\text{O}$. The samples are characterized using powder X-ray diffraction (XRD), cryogen free vibrating sample magnetometer, Zeta nanosizer, Transmission electron microscopy (TEM), Thermo Gravimetric Analysis - Differential Scanning Calorimetry and Infrared spectroscopy.

The hyperthermia measurements were carried out using a high frequency induction heating system with water cooled electrolytic copper heating coils of 50 mm diameter and 6 number of turns. The phosphate coated iron oxide nanoparticles were dispersed in water at six different concentrations. Hyperthermia experiments were carried out at a frequency of 126 kHz for five different field magnitudes. The temperature of the magnetic fluid was recorded using a radio frequency immune fiber optic temperature sensor with an accuracy of $\pm 1^\circ\text{C}$. Time dependent temperature rise curves were recorded for each sample and specific absorption rate values were determined from these curves in the non-adiabatic limit. Figure 1a shows the photograph of the magnetic hyperthermia experimental set up.

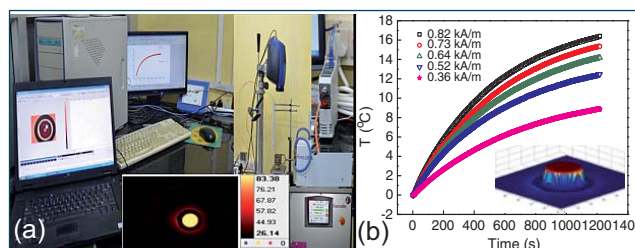


Fig. 1 (a) Photograph of the magnetic hyperthermia set up (b) temperature increase as a function of time for the phosphate coated iron oxide nanoparticles at 6 wt%

The procedures to evaluate specific absorption rate from time dependence temperature curves under radio frequency (RF) excitation are established. The specific absorption rate values are measured at a fixed frequency of 126 kHz and at extremely low field amplitude values. The SAR values are determined from the initial rate of temperature rise curves under non-adiabatic conditions. It is observed that the SAR initially increases with sample concentration, attains a maximum at an optimum concentration beyond which SAR decreases. The decrease in SAR values at higher concentration is attributed to the enhancement of dipolar interaction and agglomeration of particles. The system independent intrinsic loss power (ILP) values, obtained by normalizing the SAR values with respect to field amplitude and frequency, are ranging between $158\text{-}125 \text{ nHm}^2\text{kg}^{-1}$, which are the highest values reported in the biologically safe experimental limit of $1.03\text{-}0.92 \times 10^8 \text{ Am}^{-1}\text{s}^{-1}$. The very high value of ILP observed in the bio-compatible phosphate coated iron oxide nanofluids may find practical applications in hyperthermia treatment.

Figure 1b shows the temperature increase as a function of time for the phosphate coated iron oxide nanoparticles at 6 wt%. In the presence of an alternating magnetic field, the magnetic nanoparticle gets heated up due to Neel and Brownian relaxation. In the case of Neel relaxation, the Zeeman energy (due to relaxation of the magnetic moments from forced rotation) gets dissipated in the surrounding medium. On the other hand, heating is achieved by viscous shear force due to physical rotation of the particles in Brownian relaxation. Both the relaxation mechanisms ultimately lead to an enhancement of sample temperature which depends directly on the external parameters like amplitude of the applied field, frequency and sample concentration.

V.13 Ivy Cluster: The New Supercomputing Facility of IGCAR

As part of addressing the large-scale computational requirement of the Centre, a multi-purpose parallel high-performance computing cluster delivering a sustained numerical performance of 180 Teraflops has been installed and commissioned. With the commissioning of the supercomputing cluster which is named as 'Ivy Cluster', the cumulative high performance computing power at our Centre crosses the 200 Teraflops mark.

Ivy Cluster consists of two master/login nodes and four hundred compute nodes, along with two additional compute nodes with graphics processing unit accelerators and two nodes with multicore coprocessors (Intel Xeon Phi). The compute nodes offer a total of 9600 processor cores and 52 Terabytes of primary memory. The system is powered with low-latency high-bandwidth 56 Gbps InfiniBand interconnect network and 500 TB of usable storage. The details of the configuration and salient features of the system are given below.

The master node is the head node of the cluster, which is used for cluster administration and also provides user interface for job submission and management. The compute nodes are highly optimized to execute the parallel codes of the users. Each compute node has dual, 12-core 64-bit Intel Xeon Ivy-bridge processors and 128 Gigabytes of primary memory.

The cluster system has three interconnecting networks. The primary network meant for inter-process communication is based on the InfiniBand architecture. It provides very high bandwidth and low latency for communication and better scalability. The other two networks are based on gigabit ethernet and are meant for administration and hardware remote management respectively.

The storage system of Ivy Cluster is configured using a parallel and distributed file system called Luster and provides 500 TB of usable storage. The Luster storage architecture consists of two metadata servers (MDS) which manage the names and directories in the file system and four object storage servers (OSS) which provide file input/output (I/O) service. This configuration provides redundancy without extra overhead that improves file system performance, enhances file system recoverability and availability.

The nodes of Ivy Cluster run on open source, 64-bit Linux operating system and installed with latest version



Fig. 1 Front side view of Ivy cluster

of Intel C/C++ and FORTRAN compilers. For cluster management and job scheduling, an open source, fault-tolerant and highly scalable software tool named Slurm has been installed. Several scientific and mathematical libraries and special-purpose engineering applications have been installed in the Ivy Cluster.

The whole system is housed in fourteen, standard height (42U) server racks which are arranged in two rows, each with seven racks. The front side view of the cluster system is given in Figure 1. The industrial leading cooling concept named rear door heat exchanger (RDHx), that uses chilled water to provide cooling for individual racks, is installed. The electrical requirement of Ivy Cluster is estimated as 200KVA. Uninterrupted power supplies (UPS) and diesel generator backup are provided to some of the critical components of the cluster. The facility has equipped intelligent smoke and heat detectors with dual optical and heat sensors.

At present, the Ivy Cluster is one of the fastest supercomputing cluster available in the Department. Highly compute-intensive scientific applications in the areas of computational molecular dynamics, material design with desirable properties, reactor core calculations, multi-scale modeling of radiation damage, quantum monte carlo investigation of materials, computational modeling and simulations of plutonium recovery, weather modeling and engineering applications in the area of finite element analysis, computational fluid dynamics can effectively make use of the cluster to vastly reduce their run times.

V.14 Commissioning of Server Cooling System for High Performance Computing and Data Communicating Facility at Computer Centre

High performance supercomputing cluster servers with a numerical performance of 180 teraflops is designed and installed to meet the large scale numerical computing requirements in the area of computational fluid dynamics, finite element analysis, reactor core calculations, material design, etc. During the computing process enormous amount of heat is generated continuously in the servers, hence in order to remove the heat and maintain the required temperature and humidity, a chilled water based server cooling system (shown in Figure 1) consisting of rear door heat exchangers (RDHx), coolant distribution units (CDU) and primary and secondary loops was designed, installed and commissioned successfully.

Design basis

- Heat load-400 kW
- Server temperature- $22 \pm 1^\circ\text{C}$
- Humidity- 40 to 50%
- Dew point temperature - 14°C

This server rack cooling system consists of CDU (two numbers) of 200 kW capacity each with all accessories like rear door heat exchanger (sixteen numbers) of 20 kW each, inter linking piping, control and instrumentation as shown in Figure 2. The CDU consists of plate type heat exchanger with primary and secondary loops. Chilled water at 9 to 11°C is supplied to the primary loop of heat exchanger mounted inside the CDU at 3.5 kg/cm^2 and near de-mineralised water is circulated in the secondary loop at controlled temperatures above 14°C (dew point temperature of the air in the server room). Temperature, dew point and relative humidity sensors are provided in front and rear sides of the server cabinets to give feedback for maintaining precise set conditions in the servers. The water flow in the primary and secondary loops is modulated by micro processor based controller according to server loads using variable frequency driven pumps. Heat rejected to the secondary cooling loop from the servers is transferred to the chilled water (primary loop) which in turn rejects heat to atmosphere through cooling towers.

The following are the special features of the server cooling system

- The rear door heat exchangers are directly mounted behind the server cabinets to remove the heat at source itself



Fig. 1 Server cabinet with rear door heat exchangers

- It is a passive cooling system. Air velocity in the server is between 0.5 to 1 m/s , hence less noise
- Secondary loop with SS 304 piping and near de-mineralised water is used to minimize corrosion rate
- Intelligent capacity control system which varies the speed of the secondary pump and modulates the two way flow regulating valve in primary side
- The chilled water inlet temperature to rear door heat exchangers are maintained above the dew point temperatures of the air to prevent condensation in the server
- Water leak detecting sensors are provided in the SS drip tray which will give alarm if there is any water leakage present in the rear door heat exchangers
- Air handling units are provided to control the server room temperature and humidity

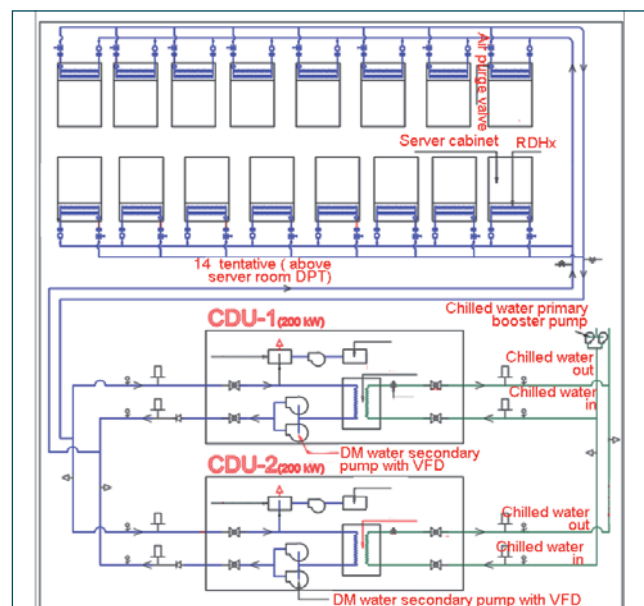


Fig. 2 Schematic of server cooling system

V.15 Application of Decision Support System ONERS for Off-site Emergency Exercise at Kalpakkam

A nuclear emergency situation can arise anytime during an unlikely event of accidents in nuclear facilities where large quantities of radioactivity are released to the environment. Emergency response in such situation calls for quick estimation of likely radiation doses to the public, environmental monitoring and dose projection on spatial maps for adopting suitable mitigation measures in the public domain. Off-site Emergency Exercise (OSEE) is conducted at DAE site Kalpakkam, once in two-years as part of emergency preparedness programme. The main aim of the OSEE is to prepare the official machinery as well as public in the emergency planning zone (EPZ) and keep them informed about the actions to be adopted in case of any potential accident leading to radiation leak in the environment from the nuclear power reactors situated at Kalpakkam nuclear complex. The Madras Atomic Power Station in association with other DAE units and district administration conducted OSEE in the EPZ around the Kalpakkam site. Our Centre has prepared the event chronology by performing all necessary calculations using the 'Online Nuclear Emergency Response' (ONERS) Decision Support System (DSS) as well in coordinating the DSS-operations during the exercise from the emergency control centre.

The ONERS is an Online Geographical Information System (GIS) based DSS developed by IGCAR in collaboration with NRSC, ISRO. This system features

- (i) Weather and Dispersion model predictions for a range of 100 km around the site
- (ii) Real-time meteorological observations of the site
- (iii) Source term estimation module using real-time environmental gamma dose measurements around the site and
- (iv) a GIS for projection and spatial query of the dose in association with many parameters.

The DSS is equipped with many spatial data base such as administrative boundaries (districts/tehsils/villages), transport routes, land-cover, demographic details, safety shelters and hospitals which are required at the time of emergency for planning. The DSS provides the concentration and dose profiles for a given source term based on real-time as well forecast meteorological parameters. The DSS can be used to make spatial queries with all the above parameters to obtain advance information on the areas that are

affected or likely to be affected and for identification of severity domains (sheltering, Iodine prophylaxis, evacuation) for guidance to mitigate the impact.

Simulations with decision support system for off-site emergency exercise

The ONERS DSS was adopted to plan the chronology of events and actions for implementation during the OSEE. For this, the end fitting failure scenario of MAPS-PHWR was considered as an accident leading to off-site emergency. Fission Product Noble gas (FPNG) and Iodine-131 were considered as released substances during the accident from ground and a 100 m stack of MAPS. The source term of FPNG was gradually varied in the calculations from $4.9\text{E}+09$ Bq/s to $9.82\text{E}+12$ Bq/s to represent the gradual progression of radiological events (site emergency, Off-site emergency Grade-I, II and III). A typical meteorological condition of East-North-Easterly winds (67.5°N) with wind speed 1.5 m/s associated with D-category atmospheric stability was assumed for calculations. A hindcast (simulation) for a past date which has the same meteorological scenario as used in the postulated case was also made using the WRF-FLEXPART prognostic modeling system of DSS. This provided information on time-varying radiation plume projections corresponding to the meteorological scenario on the day of OSEE. Calculations were performed using two dispersion models (FLEXPART, SPEEDI). Spatial query tools in ONERS were used to obtain information on the areas likely to be affected, emergency domains and suggested counter measures like sheltering, Iodine prophylaxis and evacuation.

The sixteen kilometre region up to Nerumbur/Perumbakkam falling in the G-sector from MAPS was simulated as radiological emergency domain. The dose values at different villages (Site Boundary; Nathamedu, Vengambakkam, Merkandai/Kottaimedu, Lattur, Sooradimangalam, Nerumbur, Perumbakkam at a distance of 1.5, 4.0, 6.0, 8.0, 9.0, 10.0, 12.0 kilometre respectively from MAPS) were estimated for each source term (in the increasing order during event progression). The critical exposure dose rates of 1 mR/h at site boundary was considered site emergency, 1, 3 and 10 mR/h at Merkandai village (~9 km away from MAPS) were considered for time attainment of Grade-I, II and III Off-Site Emergency events respectively in the public domain. Table 1 shows the DSS prepared

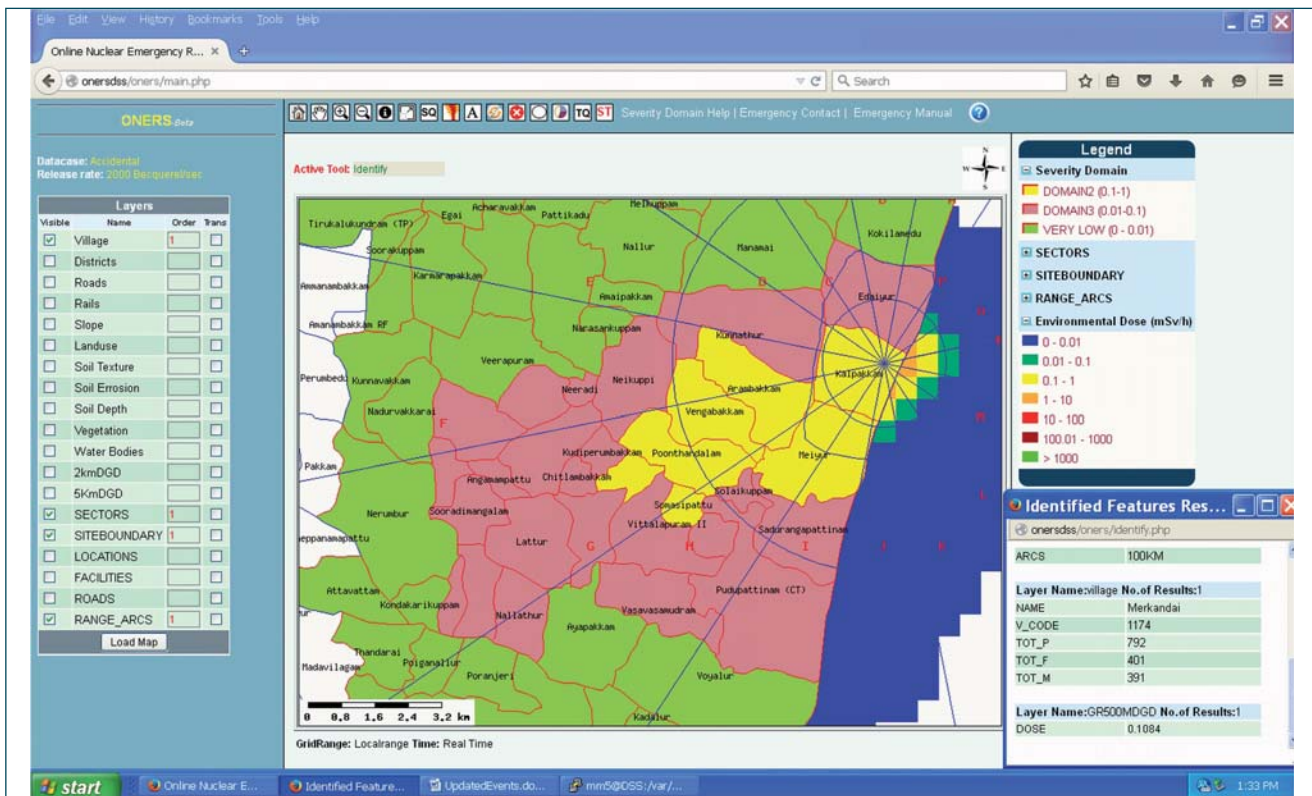


Fig. 1 Spatial projection of exposure dose (mR/h) using decision support system corresponding to Grade-III off-site emergency in the EPZ at 10:45 hours

chronology of events.

Figure 1 shows the DSS projected exposure doses overlaid on the village map corresponding to different events. The utility of DSS is seen in the depiction of the computed emergency domain in color shades overlaid on village boundaries, wind sectors and distance range-arcs.

An intercomparison was made between the estimates given by DSS-SPEEDI and EDPUFF used at Environmental Survey Laboratory (ESL), Kalpakkam for a wind speed of 1.5 m/s, stability category-D and source term of $4.91E+09$ Bq/s for FPNG with effective energy 0.7 Mev and $2.78E+07$ Bq/s for I-131. The

predicted I-131 concentrations and cloud exposure dose values are found to be in reasonable agreement with EDPUFF used by ESL is shown in Figure 2.

The DSS was used in MAPS Emergency Control Centre, at ESL for necessary guidance during the complete exercise involving field operations.

Using DSS the radiological impact could be spatially visualized on various maps in terms of emergency domains. Secondly, the information on likely dose in various villages could be generated using query tools and safe areas could be identified for evacuation. The utility of the DSS in the OSEE-2015 demonstrates its potential application in radiological

Table 1: DSS prepared chronology of events			
Time	Event	Dose at site boundary (mR/h)	Dose at Merkandai (mR/h)
06:30	Site emergency	1.275	0.118
07:55	Grade-I	10.0	1.01
09:30	Grade-II	35.7	3.33
10:45	Grade-III	102.0	10.84
11:55	Control measures	25.5	2.04
12:55	Normal	0.051	0.0047

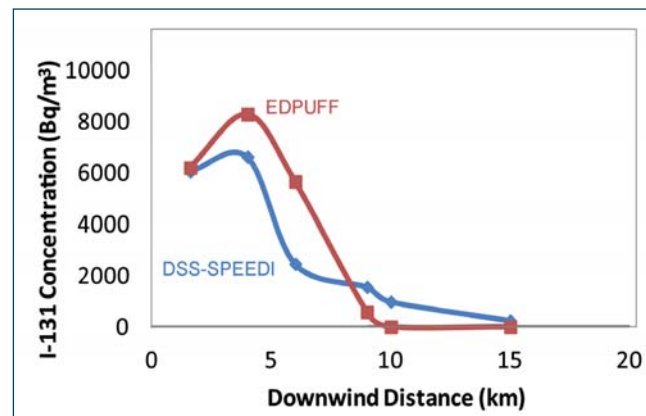


Fig. 2 Variation of I-131 concentration (Bq/m^3) with downwind distance by DSS-SPEEDI and EDPUFF

V.16 Design of a Laboratory Model Surface Profilometer

Surface profilometer is used to quantify the surface roughness or finish of any machined surface. In the various mechanisms used in fast reactors, surface finish plays a crucial role from structural integrity, leak tightness and smooth operation considerations. Redundant checks using surface profilometer during machining process, help in achieving smooth surface finish as per ASME B46.1-1995 and ASTM D4417-B.

A pulsating sensor based instrument has been developed for examining surface roughness. It consists of mechanical assembly of the tracer and inductance coil assembly as shown in Figure 1. Tracer assembly consists of a reference base plate with respect to which the stylus tip traces, the peaks & valleys of the surface to be measured. Reference base plate is threaded to the intermediate housing called as stylus guide housing. The inductance coil serves as the timing inductor of an oscillator circuit which is driven by a dc supply. With all other factors remaining unchanged, the digital pulse frequency at the output is governed by the change in inductance of the coil. The pulse frequency changes sensitively with the change in inductance and, hence, the reduction in measured pulse frequency with respect to the stylus position of tracer on object gives surface roughness.

The embedded system comprises of an optical isolator circuit, microcontroller based counter card. Pulses generated by the LGO are optically isolated to avoid ground interference with the power supply provided to the interfacing counter card. Single channel digital pulse counter card samples the pulse output from the LGO in desired gate time, so as to record the change in pulse frequency due to displacement of the ferrite core inside the induction coil of surface profilometer probe.

Counter card calculates the frequency and communicates the data with PC through serial port interface. Application specific Graphical User Interface software developed using Visual Basic, runs in PC which receives the data from the single channel rapid counter interfacing card through its serial port. GUI plots the frequency value in real time online and records for offline analysis. Options are provided in the front end, to set the desired gate time, recording time, parameter display, calibration coefficients and path for the data logging file.

Sensor calibration is done using a micrometer height gauge which has a resolution of 0.001mm. Surface profilometer is mounted on the sliding measuring jaw of the height gauge. A plain flat mirror finished surface

is fixed to the base of the height gauge for mark zero reference for calibration of the profilometer.

Since the maximum movement of the stylus after assembling in the setup is restricted to 5 mm, sensor calibration is done for the same length of movement. Calibration is done for an interval of 0.5 mm and the corresponding frequency change of the logic gate oscillator is noted. Relation between position of stylus and frequency is obtained.

Laboratory made surface profilometer is shown in Figure 2. Performance evaluation of the surface profilometer is done by moving the profilometer over two different surfaces.

Results of the above experiments are calculated in terms of Surface roughness (R_a) and RMS (R_q). Surface roughness (R_a) of wooden surface $330\mu\text{m}$ and RMS (R_q) value is $365\mu\text{m}$. Surface roughness of card board is $537\mu\text{m}$ and RMS value is $540\mu\text{m}$. It is observed that the developed gauge can measure with a sensitivity of 4000 Hz/mm , i.e. a resolution of $0.2\mu\text{m}$ can be achieved.

First-of-its-kind, innovative surface profile monitoring device using inductance based pulsating sensor is developed. Significant changes in the profiles were observed with surfaces of different surface roughness. Very smooth surfaces can be monitored with reduced stylus tip radius.

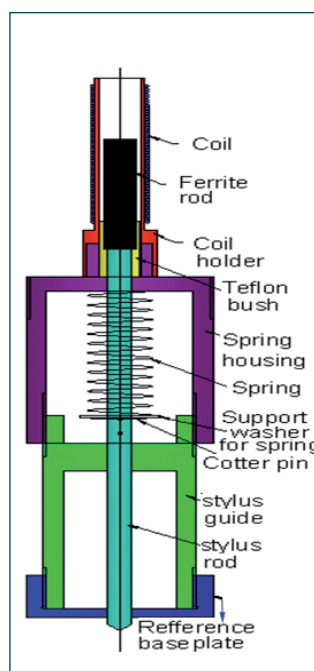


Fig 1 Mechanical assembly of sensor

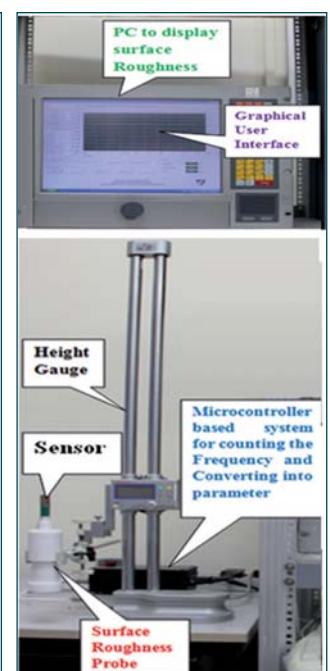


Fig. 2 Laboratory made surface profilometer

V.17 Manufacture of Large Size Containment Box for Pyro Reprocessing of Spent Metallic Fuel

Development of pyro-reprocessing technology for spent metallic fuel requires a leak tight argon atmosphere large containment box of 500 cum volume [size: 20(L) x 4.6(W) x 6(H) metres] for housing the process equipments, electrode refiner, cathode processor and metal casting furnace. The containment box is made of SS 304L grade austenitic stainless steel plates of 6 mm thickness at all five sides and bottom side is made of 10 mm thick plate to accommodate process equipment. The containment box is designed with seventeen numbers of lighting windows at the top, 27 numbers of viewing windows and 54 numbers of sealing blocks at the sides for fixing manipulators. All these windows and sealing blocks are leak paths, hence, achieving leak tightness in the containment box is a challenging task. The windows and sealing blocks are designed with two concentric 'O-rings' with inter seal arrangement for continuous monitoring and healthiness of O-rings. These windows have a larger rectangular opening of size 1256 mm x 956 mm and the sealing blocks are of size 300 mm diameter and 36 mm thickness and are made of austenitic stainless steel plates. Welding of thin section to thick sections (structural member with rectangular window frame) results in more weld distortion and difficulty in achieving the flatness of the windows. Hence, the fabrication procedures were planned and executed in such a way that welding process is minimized after machining of window frames and geometrical tolerance is achieved.

The weight of the containment box is about 60 metric ton. Hence, it is planned to pre-fabricate as multiple panel modules and shift to PPRD facility site, assemble the pre-fabricated modules of containment box at ground floor level, ensure the dimensions and geometrical tolerances such as flatness and perpendicularity. These assembled modules subsequently were erected at 4.5 metres elevation.

The leak tightness and inter seals are the important aspects to be achieved in the containment box viewing and lighting windows for operation point of view.

The individual window frames were pre-fabricated from 4000 x 1300 x 36 mm SS 304L plate. Various layout planning options were carried out for optimum material usage and minimum material wastage using 3D software. The individual window frames were cut using CNC plasma cutting machine by converting the

layout plan into DXF file format. The cut profile plates were assembled on the layout and welded. The side and top panel plate of 6 mm thickness of required size, rectangular and circular opening were cut with CNC plasma cutting machine.

During plasma cutting, the plate had got distorted and it was rectified by mechanical means. The window frames were assembled and fabricated. The weld distortion was rectified and semi-machined to the required dimensions. An inter-seal argon gas supply tube was fabricated to the required profile, welded with the window frame and subsequently welded with the panel plate. Carbon steel 150 mm square section structure was been pre-fabricated and welded with the side plate. The machining of O ring grooves and tapped holes on the window frames were machined in single setting using CNC Plano milling machine to achieve dimensional and geometrical tolerances.

The pre-fabricated panel modules were shifted to the PPRD site assembly and welding was carried out in the ground floor. All the weld joints were subjected to liquid penetrant inspection.

The fabricated and assembled modules were erected at 4.5 meter elevation using EOT crane. The intermediate panels were assembled between the erected modules and connected with panel plate by welding. The support brackets for EOT crane inside the containment box were assembled, leveled and welded with containment box side structures. The perpendicularity of containment box was checked using plumb bob. The containment box erected at PPRD facility is shown in Figure 1.



Fig. 1 Erected containment box

V.18 Sodium Technology Complex

Sodium Technology Complex (STC) is a large scale experimental facility being constructed in the northern area of IGCAR. The sodium and air testing facilities planned to be setup at STC (Hall-5) will be used for development, optimization, testing of reactor components and mechanisms for future FBRs. The overall size of the building is of 40 metres in length, 21 metres wide and 43 metres in height.

The civil construction activities for the building are in full swing. The building has reached the elevation of 37.5 metres. The building for the substation has been completed and is located on the south side of STC. The layouts of the trenches for the electrical cables from the substation to STC have been finalized and the civil works have been completed. Figures 1 and 2 show east and south side view of STC building respectively.

The three floors in the north and south sides of the high bay of STC consisting of the rooms for utilities, control room, electrical panel, instrumentation room, offices, air handling unit, etc. have been constructed. The plastering and internal civil finishing works are in progress. The internal electrification works in these rooms are also in progress.

The requirement for the ventilation system in the high bay area, exhaust fan locations and sizing have been finalized. The sliding doors for the east and west side entrances to the high bay area have been fabricated and brought to the site. The erection and installation of the east side high bay door is in progress.

The industrial safety at the construction site is continuously monitored. Safety personnel are present at site to ensure that the construction workers follow the safe working procedures, wear the appropriate personal protective equipment, have undergone training in safety and are qualified for performing works at heights. AERB regulatory inspection of the STC facility has been carried

out in August 2016. The requirements stipulated by AERB with regard to the industrial and fire safety aspects are being continuously monitored and their recommendations have been implemented. Fire emergency exercise has been carried out at the site in March & November 2016 and the emergency services have been familiarized with the site location.

The civil contractor has installed a tower crane at the south side of the STC building for safely and effectively carrying out the material handling works for this high rise construction. Ready mix concrete plants also have been commissioned by the civil contractor in the south side of the side for efficiently meeting the concreting requirements.

Construction of the dump pit for housing two numbers of 50 tonne capacity vertical sodium storage tanks (SST) has been completed on the east side of the building. The size of the dump pit is 13 metres in length, 7.8 metres width and 7 metres deep from the floor level. A dyke wall of 0.45 metres has been provided all around the dump pit. The bolts for erecting the sodium storage tanks have been anchored on to the floor of the dump pit and covered with a loose concrete layer for protection from damage.

The material storage area on the west side of the high bay area has been completed and the internal finishing works are in progress.

The mechanical fabrication of the top floor roof support structure such as trusses, cross members is in progress. The footings for the bases of the steel structure have been completed in the high bay. Design reports for sodium disposal, cleaning, loop support structure have been completed. Procurement for the fabrication of sodium loop components, stainless steel piping, plates, rounds, filler wires and bellow sealed valves have been initiated. The specifications of electrical panels have been finalized for the procurement.



Fig. 1 East side view of STC building



Fig. 2 South side view of STC building

V.19 Establishment of Fecal Bioassay Facility

Occupational radiation workers employed in reprocessing of spent fuel and fuel fabrication facilities may encounter internal contamination via inhalation, ingestion and injection/absorption through skin. As a result they are periodically monitored for internal contamination either by (i) direct methods (lung counting, thyroid monitoring, etc.) and/or (ii) indirect methods (urine/fecal assay). ICRP classified fuel compounds based on the nature of absorption by circulating blood as Type F, M and S, corresponding to Fast, Moderate and Slow absorption. In general, urinalysis is preferred for moderately absorbing (Type M – nitrates and oxalates of Plutonium) compounds, while analysis of fecal samples is preferred for slow absorption (Type S – Oxides and carbides of Plutonium) compounds. However, both techniques are complimentary to each other.

The predicted clearance of (ICRP 78) Type S and Type M compounds deposited in respiratory tract via fecal is about three to five orders higher than urinary excretion. Intake and committed effective dose for a radiation worker are estimated by measuring the amount of radionuclide excreted through urine/feces and interpreting the results using these models. By considering the practical difficulties involved in collection and processing, analysis of feces is not recommended on routine basis. However, analysis of feces is very important in case of an inhalation incident and also for determination of Pu/Am activity ratio of the inhaled aerosols.

In view of this, a facility for ashing fecal samples and standardization of procedures for analysis of fecal ash for estimating activity was established. The ashing facility comprises of

- (i) Muffle furnace
- (ii) Fume hood
- (iii) Dry and wet scrubbers connected in series to high power motor for complete removal of gases generated during ashing of the samples.

A photograph of the setup taken at the site is shown in Figure 1. After ensuring the leak tightness of the ashing facility using synthetic fecal samples, ashing of actual fecal samples were carried out. Fecal samples received from healthy, un-exposed individuals were ashed using the above facility. The ash was spiked with known activity of plutonium (Pu-239 as Plutonium nitrate, 33.3 mBq) and treated successively with nitric and hydrochloric acids. The leachates obtained were pooled



Fig. 1 Furnace, fume hood and scrubbers

together and the residue was treated with hydrofluoric acid to release traces of plutonium, if any, bound to the residue. Plutonium present in the leachate was co-precipitated along with calcium phosphate, separated via ion-exchange technique, electrodeposited and quantified by counting for a period of 20,000 seconds in an alpha spectrometer. The comprehensive analysis of a fecal sample requires 6-7 working days.

About 12 fecal samples have been analyzed so far and the recoveries were found to be in the range of 70- 80%. Alpha spectrum of a sample processed is shown in Figure 2. In order to reduce the time of analysis, application of polymer ligand films loaded with specific ligands that extracts plutonium in presence of other metal ions is being explored.

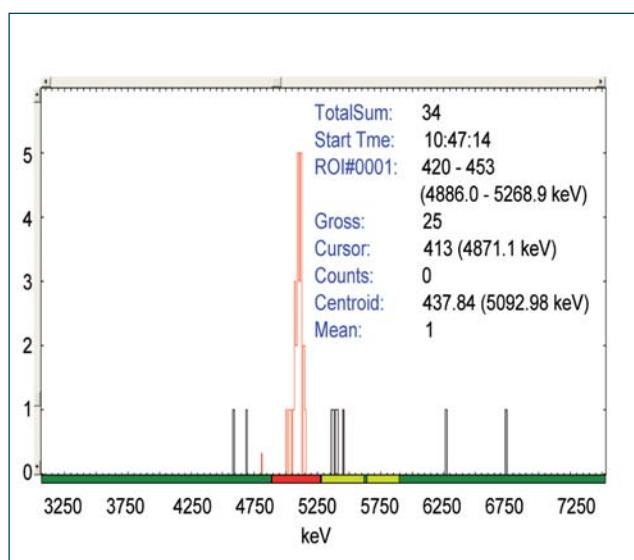


Fig. 2 α -spectrum of a fecal sample processed

V.20 Removal of Uranium from the Contaminated Wastewater by Unicellular Cyanobacterium

Biosorption has emerged as one of the most promising, economic and environmental friendly alternative to chemical adsorbents for the removal of uranyl ions. In a recent investigation uranium was found to be in the range of 0.48-6.13 $\mu\text{g/g}$ in the zooplankton tissues in the near shore marine environment. At times it increases by several times that of the limit for protection of aquatic life under chronic exposure (15 ppb). Invertebrates, particularly, cyanobacteria are efficient in accumulating U to several magnitudes of their body size and are versatile, cost effective and eco-friendly. Here the interactions of uranium with two marine cyanobacteria, *Chroococcus minor* BDU 91342 (CM) and *Synechococcus elongatus* BDU 75042 (SE) and their removal efficiency are investigated. It was observed that at pH 7.8 CM and SE could remove 92 and 90% of uranium respectively, at 20 mg L⁻¹ dose. Adsorption takes place within initial 30 minutes of exposure and EDXRF spectroscopy confirmed the association of uranium with the cells. Uranium was found to be associated with the surface active ligands of extracellular polysaccharides (EPS). FTIR analysis of uranium loaded cells showed shifts in peak positions of carboxylic groups. Deprotonated carboxylic groups on cyanobacterial cell surface was likely to be involved in uranyl adsorption. The results demonstrate noteworthy potential of those organisms for remediating uranium from the wastewater.

Cyanobacteria strains were grown in BG 11 culture media at pH 7.5 under continuous shaking (120 rpm) and illumination (30 $\mu\text{Em}^{-2}\text{s}^{-1}$) at 25°C. Uranyl nitrate, $\text{UO}_2(\text{NO}_3)_2$ was added to the experimental flask and pH was adjusted to 7.8. Mid-exponential growth cells of SE and CM were collected, washed with distilled water, resuspended at a density of 5 μg chlorophyll-a mL⁻¹ and incubated under shaking and illumination. Timed samples were collected to separate the supernatants and pellets. The supernatant fractions were acidified with 0.2 % HNO_3 acid to prevent precipitation. The uranium loaded cell pellets were acid digested. Both the mineralized fractions were assayed for uranium content by Inductively Coupled Plasma-Mass Spectrometry (Perkin Elmer, Siex, Elon 250).

Nearly 91.8% of dosed uranium (18.4 ppm) was bound to the cells of CM and SE during 6h of exposure time resulting in a loading of 7.75 and 8.9 g/kg dry weight of SE and CM respectively. A five day long experiment showed that the uranium binding efficiency of both the

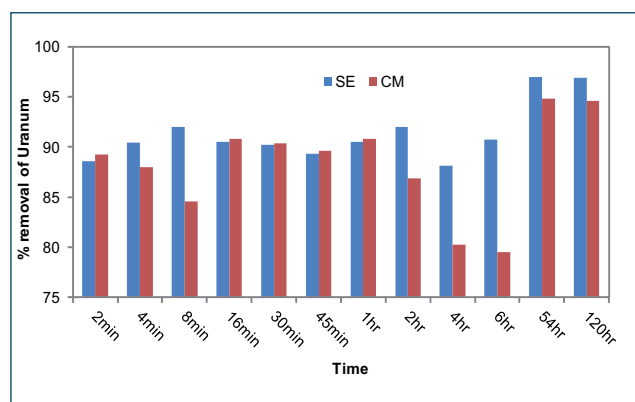


Fig. 1 Uranium removal by *chroococcus minor* and *synechococcus elongatus* in simulated experimental conditions supplemented with 20 ppm of U in form of $[\text{UO}_2(\text{NO}_3)_2]$

strains reached up to 97% (Figure 1). CM and SE cells were exposed to different doses of uranium resulting in a loading of up to 8.9 mg U g⁻¹ dry wt. Such U loaded cells exhibited black deposits around the cell margins as compared to control untreated cells. Treatment of U loaded cells with HCl showed loss of black deposits from the cell surface along with ~80% U desorption. EDXRF of uranium loaded biomass revealed the association of uranium with the cells. Further, studies revealed that the uranium was predominantly associated with the EPS and the FTIR results confirmed that the carboxyl and amide groups harboured within the EPS were found to be involved in uranyl binding. The uranyl binding efficiency of the EPS was similar to that of live cells, corroborating their extracellular localization. In the control spectra the sharp peaks between 1400 and 1500 cm^{-1} are due to the presence of carboxyl groups. Following U sorption, the spectra changed in peak positions which indicates the role of carboxyl groups in uranium binding.

The present study demonstrates superior efficiency of the biomass of two marine unicellular cyanobacteria CM and SE for U(VI) removal exhibiting its sustainability over a long duration in a larger scale. Experiments with different doses of uranium in form of $\text{UO}_2(\text{NO}_3)_2$, indicated that SE is efficient enough to remove 97% of dissolved uranium whereas, CM could remove 95%. EDXRF spectroscopy of uranium loaded biomass confirmed the association of uranium with the cells. These strains can further be used to recover Uranium from the nuclear fuel recycling wastes, and fuel fabricating processes.

V.21 Design of Power Efficient Wireless Sensor Node

Wireless sensor networks (WSN) offer a powerful combination of distributed sensing, computing and communication. They lend themselves to countless applications and, at the same time, offer numerous challenges due to their peculiarities, primarily in the issues related with energy. In the outdoor deployments where AC power is not available, nodes are powered by batteries. The restricted energy associated with batteries is a major limitation for the life time of wireless sensor network nodes. To extend the lifetime and to overcome the holdup, two different methods are explored. The power consumption of the existing wireless sensor network node has been reduced and energy harvesting technique is adapted.

Power consumption in sensor nodes is mainly attributed to data processing and communication. In the initial design of wireless sensor network nodes, ARM7 based microcontroller and XBee transceiver were used with linear regulators.

A thorough study on the power consumption of various microcontrollers were made and identified that Cortex M0+ based microcontroller as highly power efficient. It consumes 4mA when active and 3.8 uA when in sleep; which is much lower compared to ARM7 with 11 mA. Radio transceiver is the most energy intensive subsystem in a WSN node. Regulated operation of radio unit can lead to significant reduction in total power consumption. Instead of XBee transceiver that consumes 205 mA, the power efficient RF233 based SOC, which consumes 20 mA, is selected.

Generally the radio unit can be operated in three different modes: transmit, receive, and sleep. The power consumed in transmit and receive mode is much higher compared to the power consumed in Sleep mode. Hence, the sensor node radio has been configured to sleep if there is no data to transmit. Moreover, efficient routing protocol based on Zigbee standard has been developed in-house. It provides high control over functionality of the nodes, which in turn helps to manage the power budget of the nodes efficiently.

Voltage regulation is another major area where power wastage was significant. Earlier versions of wireless sensor network nodes used linear regulators that dissipate excess voltage as heat. On the other hand switching regulators, which toggles between open and saturation region, providing high efficiency voltage conversion were chosen.

With all these modifications, the prototype power efficient wireless sensor network nodes were designed,

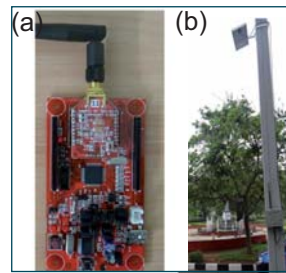


Fig. 1 Prototype power efficient WSN (a) node and (b) router with solar panel

Design (11.1V 1150 mAh Battery)	Sensor node (duty cycle 1%)	Router node (duty cycle 100%)
Initial	21 days	1 day
Power efficient	122 days	7 days

developed and tested (Figure 1a). Table 1 gives the comparison made between the initial design and power efficient design of wireless sensor network nodes.

Energy harvesting technique is an effective option as an alternate energy source for wireless sensor network nodes. Nodes can renew their power from various alternate energy sources like solar, indoor lighting, thermal, vibration and RF. Solar energy provides maximum harvested power among these methods. Solar based wireless sensor network nodes were designed, developed and utilized in outdoor wireless sensor networks deployments as shown in Figure 1b.

Ambient radio waves are universally present over an ever-increasing range of frequencies and power levels; research is going on to harvest this energy to power the wireless sensor network nodes. As an initial step, dedicated power transmitters were used for RF energy harvesting to convert this predictable RF energy into DC power. Feasibility study has been conducted using the 4W RF transmitter and power that could be generated at various distances from the transmitter is presented in Table 2. The harvested power levels decrease as the distance from the transmitter is increased. With improved RF sensitivity of the receiver, power harvesting can be optimised.

The enhanced design of wireless sensor nodes coupled with any type of energy harvesting technique can offer service as full functional devices for permanent deployment of wireless networks without the need of conventional AC power.

S. No	Energy harvesting sources	Power generated (in mW)			
		Tube light	Office lighting	Studio lighting	Sunlight
1	18V solar panel	21.6	45	160.2	11700
2	4W wireless power transmitter	Receiver at 1 m	Receiver at 2m	Receiver at 3m	Receiver at 4m
		25.1	2.2	1.4	1

V.22 Online Work Permit System for FBTR

In FBTR, the purpose of protection code is to provide protection for plant personnel when working on reactor and plant auxiliary systems equipment and to ensure that after a maintenance job, the equipment is taken back into service in an orderly manner without damage to equipment.

The protection guarantee by way of deficiency report cum work permit gives authority for specified work on specified apparatus and guarantees that certain conditions viz., status of the valves, power supplies, breakers or fuses etc. will be maintained as indicated in the permit while the work is being carried out, as long as the permit is in force. Any maintenance work on any equipment under the operator's jurisdiction shall be done only with work permit approved by senior shift engineer or junior shift engineer.

The deficiency report cum work permit system has five stages namely, deficiency report (raising normally done by operation or maintenance), work permit applying (done by concerned maintenance), work permit issuing (done by operation), work permit surrendering (done by maintenance) and work permit clearing (done by operation). The entire process involves ten steps, each of which is to be completed by the concerned official before the permit passes to the next step, through paper format.

The entire work flow has been automated now, with the commissioning of computer based Work permit management system (WPMS) in FBTR. The system is developed using JAVA with MYSQL as backend data base. The architecture of the WPMS is shown in Figure 1. It has a main server with network attached storage (NAS) attached for data archival and an offline backup server. The client software being web browser-based, can be used by any user on the FBTR LAN having valid username and password. To one of the client systems kept in control room, printers are connected to enable the operator for printing the danger tag and jumper tag respectively through the WPMS. The danger tag / red tags designate danger to personnel or equipment. It signifies about a circuit breaker not to be closed or a valve not to be opened or equipment not to be operated. The pink color Jumper tag is used for the permits, which needs some jumpering of relay contacts, limit switches or change in settings of the parameters. To highlight, this tag will be placed on the panel at which the jumpering was done.

The main features of work permit management system are online / paperless, web based – works with google

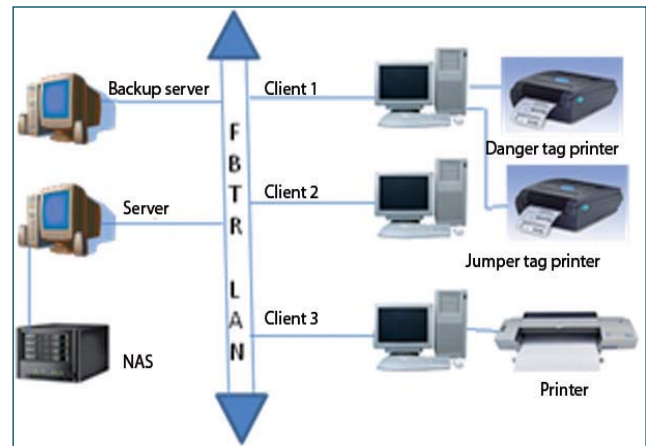


Fig. 1 Architecture of the work permit management system

chrome / fire fox etc, all ten steps of WPMS are available with authorization, jumper permits, isolation through order to operate (OTO), manage OTO, cutting & welding permits, industrial safety permits, radiological permits, notifications and email, view active permits for editing (with filters for, created by, permit number, created date range, agency, equipment number, suspended), suspend permits at 8th step due to test fail or 6th step, revert back to step 1 from step 4 by shift engineer only, transfer permits at 6th step to other maintenance agencies, temporarily surrender permit at 6th step, cancel permit before issue stage, classified reports (system wise, equipment wise, work permit number wise and date wise) for pending permits, permits at every stage and re-issue suspended permits by shift engineer only.

The system has the security features of

- Login user name / password
- Access control group wise
- Password lock on 4 consecutive error attempts
- Authorization is required for each step and will be set by administrator only
- System logs
- Event logs
- User logs
- Ip address based protection for permit issue
- Completed step is not allowed for re-edit
- Issued permits cannot be cancelled
- NAS server with automatic periodic backup of data base
- Backup server to improve availability
- Virus entry is restricted due to the use of Ubuntu operating system
- The server is kept under lock and key to avoid tampering.

V.23 Development and Deployment of Knowledge Management Portals for Fast Breeder Reactors

The enabled nuclear knowledge management system is designed as a generic, customizable framework and developed in-house fully using open-source platform and APIs in our Centre. Knowledge management portals with advanced content management and search features were developed and deployed for acquisition, preservation and utilization of records of Prototype Fast Breeder Reactor (PFBR) and Fast Breeder Test Reactor (FBTR) (Figure 1). The knowledge repository has been created with the explicit knowledge available in the form of drawings, control notes, design notes, operation notes, experiments notes, specifications, project reports, commissioning procedures, operating procedures, system manuals, training manuals, flow sheets, test procedures and various other reports. The number of reports hosted in PFBR and FBTR knowledge management portal are given in Table 1.

The portal provides a scientific search platform for navigation, efficient retrieval and sharing of knowledge assets acquired and stored in the repository in different forms and in different file formats with required security features. Also it enables administrators to carry out tasks associated with content management, user management and rights management.

An online print request facility has been provided to create request for taking hardcopy of records with required approvals and enable further processing by the record section. Analytic reporting module produces detailed analysis of knowledge assets from different

Knowledge assets	PFBR	FBTR
Reports/ manuals	5200	2000
Drawings	20000	4800

dimensions and generates various textual/graphical reports dynamically. The periodic statistical reports can be generated based on different parameters like users, sections, divisions, groups.

In addition, the following customized modules have been developed for automating the processes associated with FBTR Records management.

Control room panel alarm module to display the details of an alarm with associated test procedures and alarm drawings.

- (1) Engineer change notice module to upload/view engineer change notices raised, associated status reports and technical bulletins.
- (2) System modification proposal module to automate the overall activities related to system modification proposal system.
- (3) Engineer shift log module to upload/view the daily plant operation shift logs.
- (4) SORC module to preserve and securely view the minutes of safety review meetings.

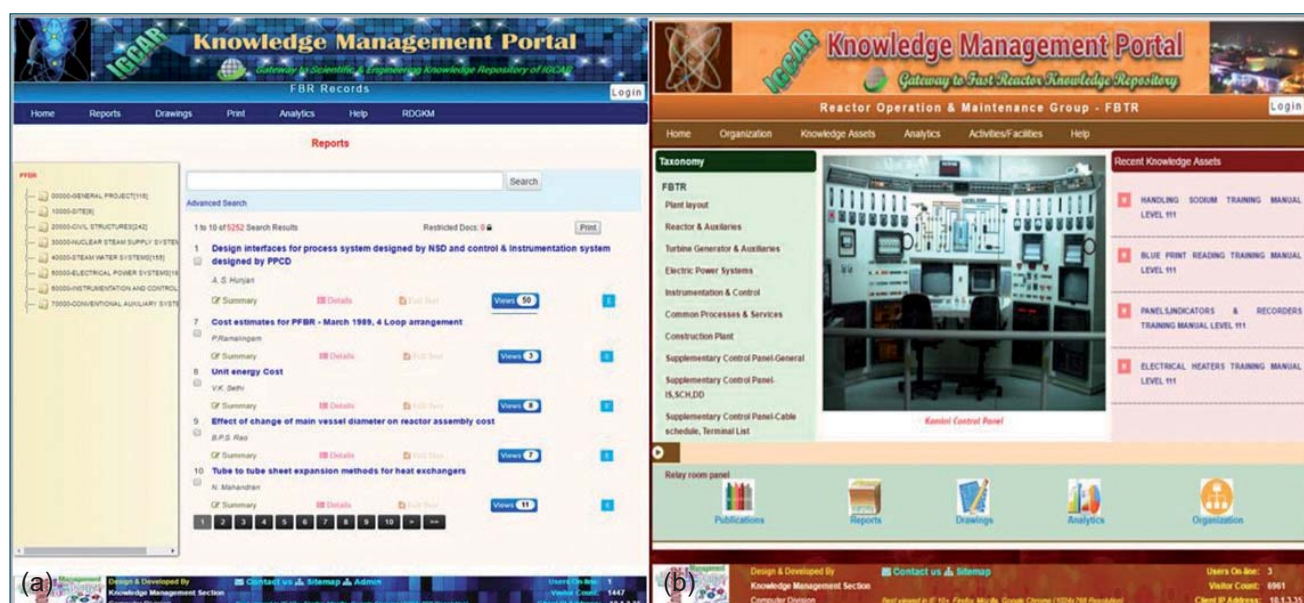


Fig. 1 Knowledge management portal (a) PFBR and (b) FBTR

V.24 Enhanced Information Access

Implementation of the state-of-the-art technology for efficient and enhanced dissemination of information services to the user community, has been one of the important mandates of our Centre. Taking into consideration, the diverse and changing needs of a researcher, the collection of e-resources is being upgraded constantly. Necessary value additions to these resources by creating Metadata, Resource access portals, Usage statistics etc. are augmented. The Digital Library infrastructure is upgraded constantly to support the value added information services.

Integrated e-books portal

In our effort to continuously enrich the resources, more e-Books have been added to the existing collection. The ease of access to these e-books is facilitated by means of a web portal. Screenshot of the portal is as shown in Figure 1.

This portal is developed in-house using PHP and MySQL. The e-Book collections are predominantly from the publishers like Elsevier, ebrary, Cambridge University Press, Springer, Wiley-IEEE Press etc. The metadata of the e-books are loaded into the database and appropriate links are given for access to the users.

Enrichment of e-resources

During this year, the major e-resources including Springer e-books, Elsevier e-books, BIS Standards, ASM Alloy database, Nature archive etc. have been added to the collection.

RFID based entry system

Smart access entry control systems based on RFID technology has been commissioned. This system



Fig. 2 RFID based entry readers

authenticates the user through his identity card with the employee master database available within this system. The database is updated periodically for new membership and change in user profiles, if any, from all the Units at Kalpakkam. This system can generate various reports such as visiting pattern of users, Unit wise reports etc (Figure 2).

User logging system

A user logging system is designed and developed in-house to monitor the entry of users other than employees for accessing the scientific resources available at the Centre. The user enters important information like type of user, purpose of visit etc. into this system while checking-in and his feedback while checking out. The system registers the time stamp at the time of check-in and check-out along with the basic profile of the user.

The various reports that can be generated from this system are categorized into daily reports, history and trends.

The above system is developed using ASP.Net, VB.Net, Javascript and MS SQL.

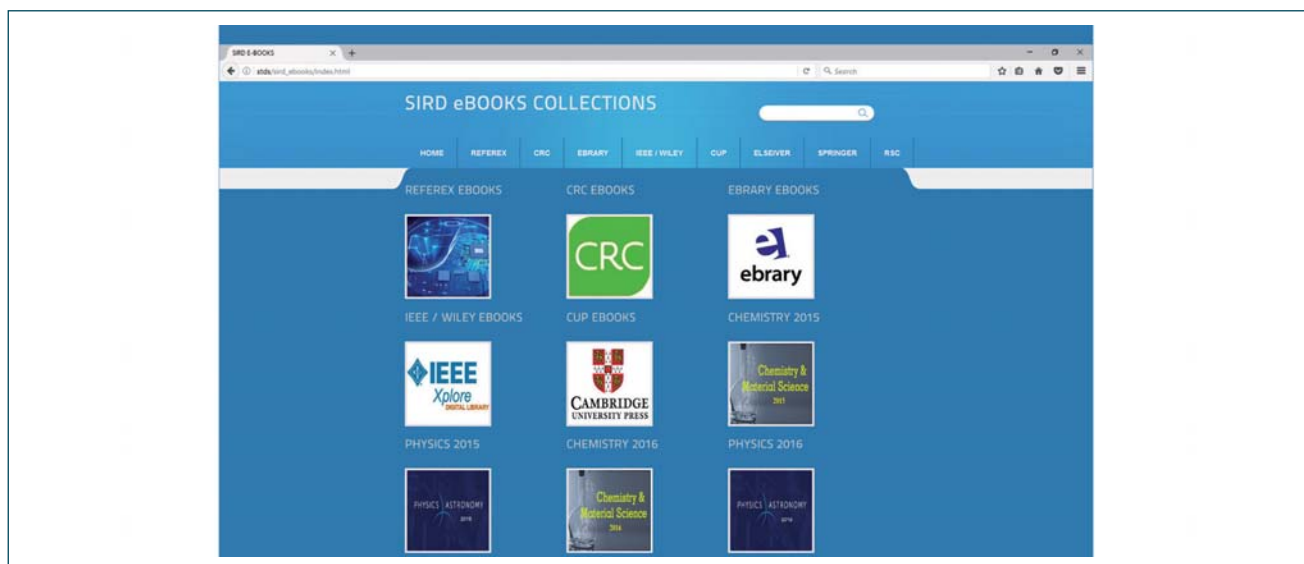


Fig. 1 e-Book access portal

V.25 Payroll Package for AERB and GSO

Automation of payroll is one of the important processes in Accounts. The payroll software package automates the steps involved in the processing of data to calculate the pay, allowances and deductions pertaining to all the employees of an organisation. A new payroll package was implemented in IGCAR since 2015. The components of payroll package are: pay and allowance module, income tax module, provident fund module. Subsequent to implementation of the package in IGCAR, requests were received from AERB and GSO to implement the payroll package at their respective Units. The project was taken up during June 2016. The package has been customized to the requirements of GSO & AERB and handed over. The PHP language and MySQL database has been used to develop the payroll package.

Payroll processing includes two types of components, i.e., entitlements and deductions. Entitlement includes the components which are paid to the employees in the form of pay and other allowances. The deductions are the components which are recovered from the entitlement amount to arrive at the net pay. Both the entitlements and deductions can be continuous in nature or as and when paid/deducted. For example, pay, dearness allowance, house rent allowance etc. are paid every month to the eligible employees. Components like arrears, library recovery, electricity bill etc. are paid or deducted as and when needed.

As there could be requirement for addition of new components, the system architecture of the payroll package has been designed in such a way that adding a new component to the payroll system does not require such additions in the program. At present the software package at IGCAR is dealing with 68 entitlement components and 101 deduction components.

Since the payroll package is already in use at IGCAR, the requirements of AERB and GSO had to be incorporated to customize the package. During the gap analysis, following points were identified where further customization was necessary.

- a) Delinking of the existing payroll package from ATOMS
- b) Incorporation of new grades and designations
- c) Addition of new payroll components

The payroll package at IGCAR is tightly integrated with the existing “Automated Workflow Management System (ATOMS)” software. The data like employee details, pay details and other change requests flow to the payroll package through other modules of the ATOMS packages. In order to develop the standalone payroll package, all the interface modules were developed and linked with the payroll package. Figure 1 shows the schematic of standalone payroll package.

Since the hierarchy of these organizations differs from IGCAR, new grades and the associated calculations were incorporated in the system. Doctors, Nurses etc are few examples of such grades for GSO.

Additional allowance and deduction components were added along with the associated calculations into the system. These include non practicing allowance, nursing allowance, uniform allowance etc. Apart from addition of these components, the printing of schedule of new components was also added.

Post development, data migration and trial run were carried out at IGCAR for two months before handing over the system to the respective Units. The payroll package is now being used at AERB and GSO.

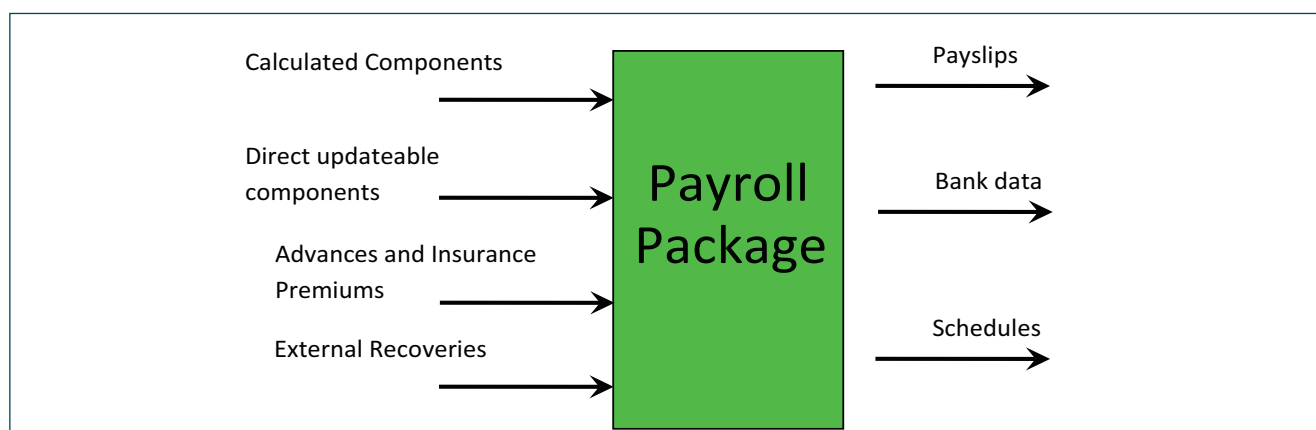
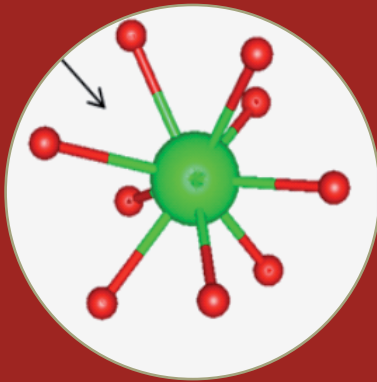


Fig. 1 Schematic of standalone payroll package: input and output



CHAPTER VI
Basic Research

VI.1 Phase Transformation in BaTe_2O_6 by *in-situ* High-Pressure X-ray Diffraction, Raman Spectroscopy and First-Principles Calculations

Tellurium-based oxides are of widespread interest due to their nonlinear dielectric and optical properties. The crystal chemistry of Te-based oxides is important to the nuclear energy industry due to their appreciable yield in fissions of U^{235} and Pu^{239} . The stability of Te-oxides is strongly dependent on the oxidation state of Te and ionic radii of counter cations present in the structure. Interestingly, the coexistence of Te^{4+} and Te^{6+} cations generates further complexity in the structures even at ambient conditions. BaTe_2O_6 (BTO) is one such mixed-valent tellurate that stabilizes in an orthorhombic ($Cmcm$) structure with an ordered arrangement of $\text{Te}(2)^{4+}$ and $\text{Te}(1)^{6+}$ (Figure 1). Corner-shared $\text{Te}(1)^{6+}\text{O}_6$ octahedra and $\text{Te}(2)^{4+}\text{O}_5$ square pyramidal polyhedra result in the formation of Te_2O_6 layers perpendicular to the b-axis of the unit cell. Ba^{2+} ions are sandwiched between these layers. Such layered arrangement of $[\text{Te}_2\text{O}_6]^{2-}$ and Ba^{2+} ions is expected to give rise to anisotropic compressibilities and may exhibit novel high-pressure (HP) phase transformations. In this article, we briefly report the pressure-induced effects in this mixed-valence tellurium compound BTO, using *in-situ* high-pressure synchrotron x-ray diffraction (XRD) and Raman spectroscopic measurements using a diamond-anvil cell (DAC). It is observed that the orthorhombic structure of the titular compound becomes unstable at high pressure and transforms into a new structure that remains stable up to 37 GPa. The experimental results on phase stability and structural transitions are corroborated by *ab initio* density functional (DFT) calculations. Single phase BaTe_2O_6 was synthesized by a solid-state reaction

method. *In situ* angle dispersive high-pressure X-ray diffraction measurements upto 16 GPa were carried out in transmission mode using a DAC at beamline-11 of Indus-2, RRCAT, Indore. Powder sample of BTO along with methanol-ethanol in 4:1 ratio as pressure transmitting medium and silver powder as a pressure calibrant were loaded into a 200- μm hole of a stainless-steel gasket in the DAC. Raman spectra of the sample in the DAC were collected upto 37 GPa using a micro-Raman spectrometer. The phase and structural parameters of the BTO sample were determined by Rietveld refinement of the observed powder XRD data. The final refined unit cell parameters were obtained as $a = 5.5710(1)$, $b = 12.7971(1)$, $c = 7.3276(1)$ Å and $V = 522.50(1)$ Å³ with $Z = 4$ at ambient pressure (Figure 2). Upon increasing pressure, all XRD patterns recorded up to 12 GPa could be refined successfully using the structural parameters of orthorhombic phase. However, beyond this pressure, appearance of new reflection peaks could not be properly accounted using the orthorhombic phase that could satisfactorily be fitted to a primitive monoclinic lattice ($P2_1/m$). The refined unit cell parameters of the monoclinic HP phase at 15.7 GPa are: $a = 5.4047(7)$, $b = 7.1847(3)$, $c = 6.5490(2)$, $\beta = 115.237(4)^\circ$ and $V = 230.035(2)$ Å³ with $Z = 2$ (Figure 3). In both phases, Te ions retain their octahedral and square pyramidal coordination. However, both polyhedra are distorted and the anion positions are split in the transformation process, leading to an increase in the co-ordination of Ba^{2+} ion from 12 to 14 in HP monoclinic phase. Anisotropic compression of lattice parameters with the effect being more along the b-axis

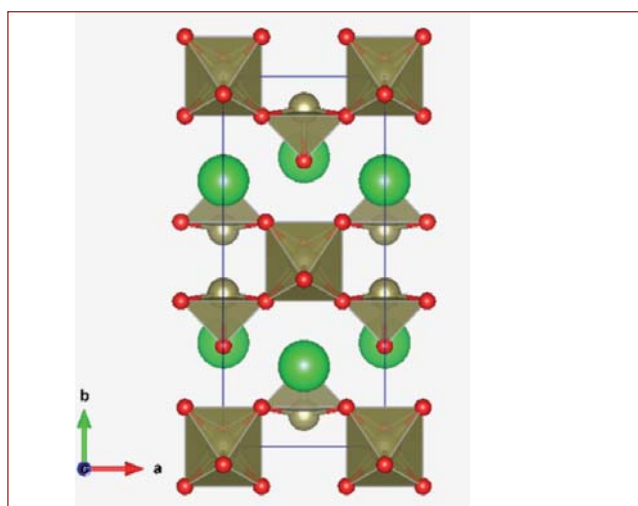


Fig. 1 Orthorhombic unit cell of BaTe_2O_6

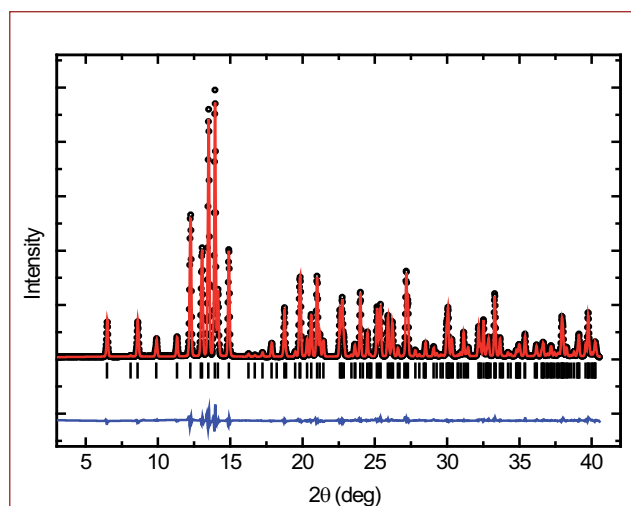


Fig. 2 X-ray diffraction pattern of BaTe_2O_6 at ambient pressure

of the ambient phase and the c-axis of the monoclinic phase are observed. It is seen that the compressibility along the b-axis reduces appreciably at the transition due to steric hindrance. The equation of state (EOS) for the ambient orthorhombic phase is obtained from an analysis of the pressure (P)-volume (V) data using the third-order Birch-Murnaghan EOS; the bulk modulus and its derivative are found to be $B_0 = 88(2)$ GPa and $B'_0 = 4.1(7)$ respectively. Only $\sim 2\%$ reduction in volume across the transition and the structural closeness of both phases (group-subgroup relation) indicate that this is a displacive phase transition. *Ab initio* DFT calculation of total energy versus unit cell volume for the orthorhombic (red curve) and the monoclinic (black curve) phases (Figure 4) indicates the transition pressure to be ~ 10 GPa, close to that observed in the XRD and Raman studies. Raman spectra of BaTe_2O_6 at high pressure was measured in a DAC upto 37 GPa and the pressure dependencies of modes were obtained (Figure 5). For the ambient orthorhombic phase, the factor group analysis predicts twenty-four Raman active modes ($7A_g + 7B_{1g} + 3B_{2g} + 7B_{3g}$). In our experiment, at ambient conditions fourteen distinct Raman bands out of the expected twenty four could be obtained. Low frequency bands $< 400 \text{ cm}^{-1}$ correspond to lattice and external modes, while those at higher wave numbers arise due to the internal vibrations of TeO_6 octahedra and TeO_5 pyramidal units. Upon increasing pressure the unique Raman bands of orthorhombic phase shows a decrease in intensity. The bands at 288 and 423 cm^{-1} do not disappear but they split into $315, 323 \text{ cm}^{-1}$ and $446, 460 \text{ cm}^{-1}$, respectively at around 9 GPa, the transition pressure. Furthermore, new characteristic Raman bands for HP monoclinic phase appear at 9.1 GPa. Mode Grüneisen parameters are calculated using the expression, $\gamma_i = \frac{B_0}{\omega_i} \frac{d\omega_i}{dP}$. Small values of Grüneisen

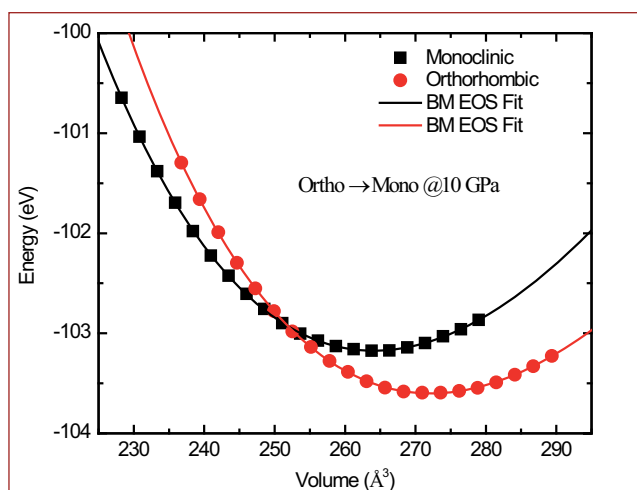


Fig. 4 Calculated total energy versus unit cell volume curves

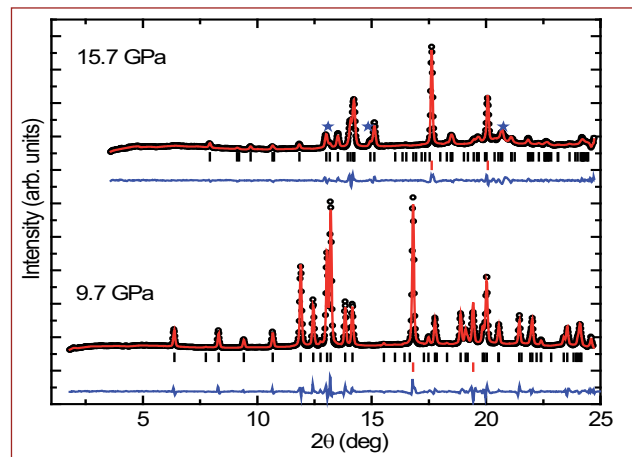


Fig. 3 Rietveld fitted patterns for orthorhombic (9.7 GPa) and monoclinic (15.7 GPa) phases

parameters for different internal modes indicate that the TeO_5 square pyramidal and TeO_6 octahedral units are less sensitive to pressure. On the other hand, large Grüneisen parameters for the low frequency lattice modes suggest that these vibrations are more sensitive to pressure, and can be easily compressed and deformed. Therefore Ba^{2+} sublattice is the first to become unstable at high pressure; consequently the Te and O ions also have to move due to the large size of the Ba^{2+} ion, and this results in a distortion in the TeO_n ($n = 5, 6$) polyhedral units to maintain the polyhedral network and the integrity of the structure. In the HP phase, the Grüneisen parameters for the internal modes are 2-3 orders of magnitudes smaller than those of the lattice modes, thus confirming the stronger bonding within the TeO_n units. Pressure-induced amorphization of the HP phase does not occur until 37 GPa. The orthorhombic structure is found to be reversible after complete release of pressure from the highest level of 37 GPa. To conclude, we have investigated the high-pressure phase transformation in BaTe_2O_6 using in situ high-pressure XRD and Raman

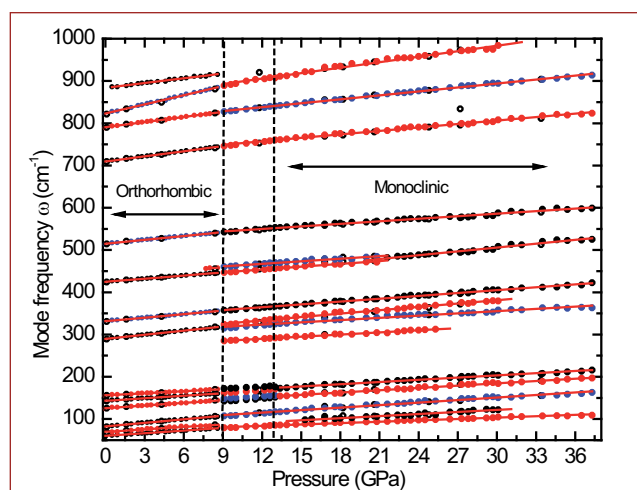


Fig. 5 Raman mode frequencies as a function of pressure

spectroscopy complemented by *ab-initio* DFT calculations. The high-pressure monoclinic phase results from slight distortions that occur in the structural arrangement of the ambient orthorhombic phase. The equation of state for the orthorhombic phase is obtained along with bulk

modulus $B \sim 88$ GPa. Phonon behavior and Grüneisen parameters are discussed for both the phases. Internal modes of TeO_n ($n = 5, 6$) polyhedra are found to be less sensitive to pressure as compared to the Ba^{2+} sublattice. BaTe_2O_6 is found to be stable until 37 GPa.

VI.2 Oscillatory Superconducting Transition Temperature in $\text{Cu}_{73}\text{Ni}_{27}/\text{Nb}$ Bilayer

The developing field of superconducting spintronics offers a plenty of exciting phenomena and the experiments probing the π phase shift are predicted to be the promising candidates as basic elements in the field on quantum computation. The basic building block for all these experiments are thin film heterostructures involving superconductivity (S) and magnetism (F). Due to proximity effect, cooper pairs penetrate into the F layer and one can study the properties of superconducting electrons under the influence of large exchange field. One of the implications of the ferromagnetic superconductors is that superconducting electron pair density may be non uniform which gives rise to non monotonic dependence of superconducting critical temperature (T_c) of S/F bilayers and the realization of π Josephson junctions in S/F/S systems. Usually these studies are performed by varying the thickness of the ferromagnetic layer in S/F bilayer and in S/F/S type Josephson junctions.

In our studies, in comparison to strong ferromagnetic material such as Ni, a relatively weak ferromagnetic material like ($\text{Cu}_{73}\text{Ni}_{27}$) was chosen and Nb was chosen for superconducting layer. We studied the superconducting properties of Nb as a function of current injection into the ($\text{Cu}_{73}\text{Ni}_{27}$)/Nb layer and magnetic field. All the films were deposited by DC/RF magnetron sputtering. Using photolithography and RF ion beam etching, $\text{Cu}_{73}\text{Ni}_{27}$ film with a thickness of 50 nm was

patterned as the bottom layer having a linewidth of 200 μm . By lift off technique, superconducting Nb layer having a thickness of 50 nm was defined over $\text{Cu}_{73}\text{Ni}_{27}$ thin film. T_c of Nb was measured using four probe geometry as a function of currents injected from the magnetic layer to the superconducting layer. Magnetotransport measurements were carried out using cryogenic measurement system for magnetic fields upto 1.6T and for temperatures down to 4 K. Figure 1 shows resistance as a function of temperature for magnetic fields varying between 0 to 1.6 T. A constant current of 20 μA was passed to the top layer Nb film and the resistance was measured as a function of magnetic field. T_c is seen to progressively decrease from 8.4 K (at 0T) to 5 K (at 1.6T).

Keeping the magnetic field constant, current is injected (I_{bias}) into the $\text{Cu}_{73}\text{Ni}_{27}/\text{Nb}$ bilayer and superconducting transition temperature, T_c is plotted as a function of I_{bias} (for 0T) in Figure 2. T_c is seen to oscillate as I_{bias} is varied up to 100 μA . This is the first time that an oscillation in T_c with current injection into the S/F bilayer has been observed. Earlier reports on T_c oscillation were observed as magnetic layer thickness was varied in S/F systems. Initial results provide evidence for coupling between superconducting and ferromagnetic layers and further progress in micro-fabrication technology will throw light on new findings in this exciting field.

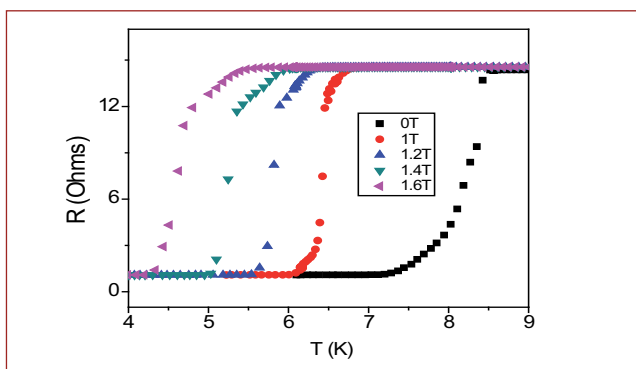


Fig. 1 Resistance versus temperature for $\text{Cu}_{73}\text{Ni}_{27}/\text{Nb}$ bilayer with magnetic field

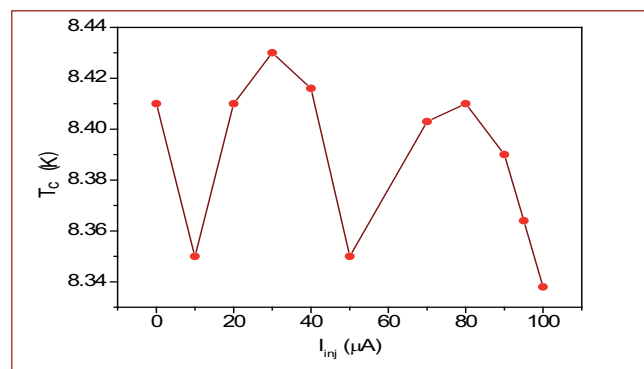


Fig. 2 Oscillation of superconducting T_c versus current injection for $\text{Cu}_{73}\text{Ni}_{27}/\text{Nb}$ bilayer

VI.3 An Innovative Method of Imaging at Sub-Diffraction Limit using Confinement of Polarized Light

Imaging a nanostructure, using the diffraction limited optical technique is a breakthrough achievement in the present century. The nanoscale imaging in the sub-wavelength limit was boosted with the application of plasmonics or by keeping it in a micro-cavity. Tightly confined light or trapped photons in between two semiconductor or dielectric media with sizes comparable to the wavelength of the confined light, increases photon density leading to the enhanced light–matter interaction, enabling a range of nonlinear applications.

In this article, the far-field spectroscopic photoluminescence (PL) imaging of a single semiconductor AlGaIn nanowire (NW) using the peak intensity of free excitonic (FE) emission in the sub-wavelength scale is reported.

The polarized PL measurements at 300K for the single AlGaIn NW (schematic, Figure 1a) are performed in two different configurations of $Z(X\bar{X})\bar{Z}$ and $Z(XY)\bar{Z}$, which are considered as parallel (π) and perpendicular (σ) polarizations, respectively. The long axis of cylindrical NWs is considered as X direction, whereas the incident and backscattered light propagation directions are measured along the Z and \bar{Z} directions, respectively. It was observed that the polarized PL peak intensity value for a single NW was higher for π -polarization, as compared to that of the σ -polarization (Figure 1b). This observation is typical in 1D semiconductor NWs and it is because of the optical confinement of polarized light within the material, due to variation of refractive index of NWs and its surrounding media. The peak observed at ~ 3.55 eV is due to the recombination of free exciton (FE). An increase in the PL intensity by one order is observed, when the separation from the nearest

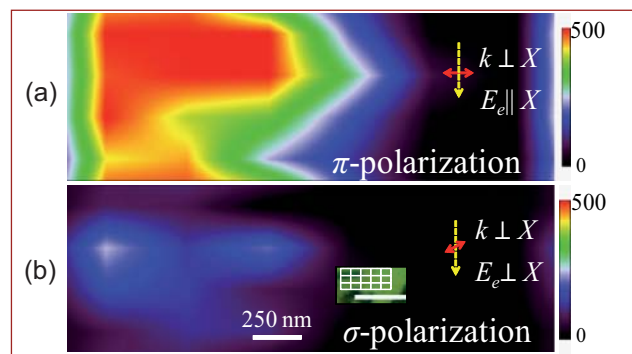


Fig. 2 (a) π - and (b) σ - polarized photoluminescence maps for a single AlGaIn NW. The optical image of a typical single NW with a schematic grid pattern used for PL imaging is shown in the inset (scale bar 3 μ m)

neighbor NW is decreased from 4 μ m (inset of Figure 1c) to 2 μ m (inset of Figure 1b). The excitation photons are confined between the NWs giving rise to long lived photon enhancing its intensity.

The PL imaging of single AlGaIn NW with diameter 100 nm, which is in the sub-diffraction limit ($\lambda/2$.N.A.) using 325 nm excitation (N.A. = 0.5 for NUV objective 40x), is carried out over an area of $3 \times 1 \mu\text{m}^2$ (Figure 2). The variation of intensity in the PL maps observed for different polarization configuration is due to difference in the interaction of electric field strength with NW.

Thus, for the first time, we have achieved spectroscopic imaging of a single NW in sub-diffraction limit. The PL emission intensity from a single NW is observed to be strongly influenced by the proximity of other NWs. In case of the proximity induced optical confinement effect, a nonzero non-equilibrium population of long lived photons is envisaged to influence the increased PL emission intensity from the single NW.

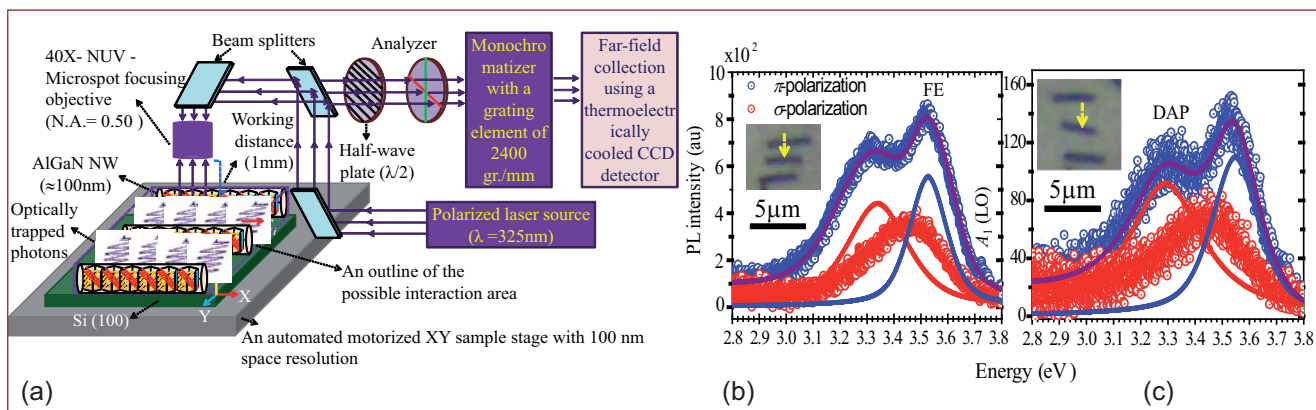


Fig. 1 (a) The schematic representation of the experimental setup for recording single NW spectra and imaging using polarized PL spectroscopy. T polarized PL spectra for π - and σ - polarization configurations of a single AlGaIn NW for the inter-NW separations of (b) 2 μ m and (c) 4 μ m. Inset shows the optical image of NWs

VI.4 Multinuclear Solid-State NMR and DFT Studies on the Lithium uptake in Strontium Chlorapatite

One of the important aspects of nuclear energy generation is reprocessing of the spent fuel and nuclear waste management. In fast breeder reactors employing metallic fuel, molten salt electro-refining method (electrolyte: 45 wt% LiCl+55 wt% KCl) of reprocessing is followed and the resulting waste contains rare earth, alkali and alkaline earth fission products in the form of chlorides. For this type of waste, ceramic matrixes act as better hosts and, in particular, apatites having the general formula $M_{10}(PO_4)_6X_2$, $M=Ca, Sr, Ba$; $X=Cl, F, OH$ are very promising candidates. In this context, it is important to understand the effect of the guest ions on the host matrix at the atomic level. Solid State NMR (SSNMR) is an ideal tool for such studies as it gives direct information about the local structure. In this work, we have taken up substitution of one of the alkali atoms, namely lithium, to study its uptake in the strontium chlorapatite (Sr-ClAp) host matrix using multinuclear SSNMR experiments and DFT calculations.

Sr-ClAp samples doped with 0-20 wt% of lithium were prepared by solid state reaction route and characterized by powder XRD technique. Analysis of the XRD patterns showed the 'a' and 'c' lattice constants decreasing with increasing dopant concentration, confirming lithium uptake into the Sr-ClAp lattice.

Figure 1 shows ^{31}P Magic Angle Spinning (MAS) NMR spectrum (spinning frequency: 12 kHz) of Sr-ClAp loaded with various amounts of lithium. Undoped Sr-ClAp shows a peak at ~ 3.6 ppm with an asymmetric lineshape, whereas, in the case of spectra of all lithium-substituted samples, this asymmetry is more pronounced. A faint feature on the lower frequency side is also observed in all the spectra. A comparison of single pulse spectrum and $^{31}P - \{^1H\}$ CP-MAS NMR spectrum of the doped sample showed no difference between the two. Based on this observation and previous studies, the low frequency component at 2.6 ppm could be attributed to unprotonated PO_x sites on the surface. The linewidths of all Li substituted samples were lower compared to plain Sr-ClAp and a general trend of decreasing linewidth with increasing Li content is also observed. The asymmetry of the main peak is attributed to the incommensurate nature of crystal lattice that leads to structural modulations. Further, the asymmetry in the lineshape is more predominant for higher lithium loading.

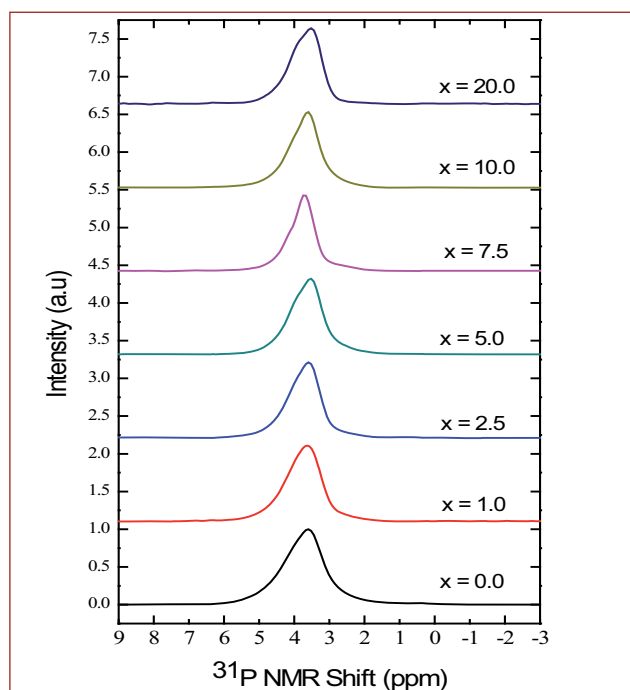


Fig. 1 Area-normalised ^{31}P MAS NMR spectra of Sr-ClAp: Li_x

In the strontium chlorapatite structure, there are two crystallographically inequivalent sites for strontium, M(I) coordinated to 9 oxygen atoms and M(II) to 6 oxygen and two chlorine atoms, as shown in Figure 2. Although the decrease of lattice parameters, as seen from the XRD data and the linewidth change observed from ^{31}P NMR spectrum upon lithium substitution indicate Li uptake into the lattice, 7Li NMR signal would give exact information about the sites Li atom occupies.

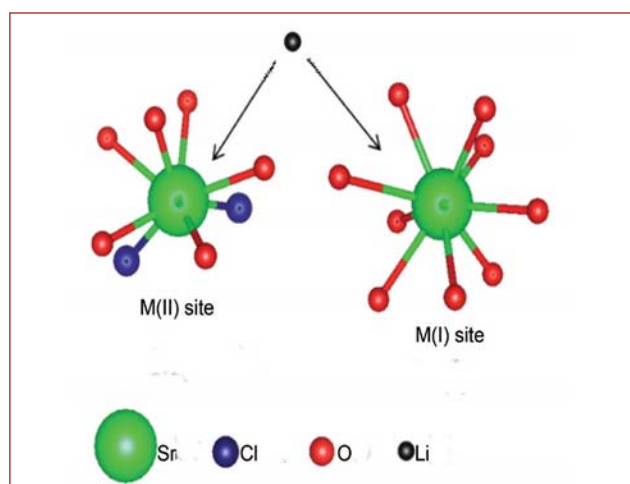


Fig. 2 Schematic showing coordination of Sr sites in Sr-ClAp

^7Li is a quadrupolar nucleus with spin 3/2 and interacts with local electric field gradients (EFG) created by the surrounding atoms. In general, strong EFG broadens the NMR line, whereas line narrowing occurs whenever the probe nuclei are mobile. Also, EFG vanishes for quadrupolar nuclei in high symmetry sites such as in cubic environments giving rise to narrow NMR lines. Figure 3 shows intensity-normalized ^7Li MAS NMR spectra (spinning frequency: 8 kHz) of Sr-ClAp with various amounts of lithium substitution. All Li substituted Sr-ClAp materials show superposition of a broad and a narrow intense peak with broad peak, centered around ~ 0.1 ppm. The narrow component shows weak sidebands indicating that the ^7Li nuclei experience negligible EFG and/or has high mobility.

A systematic analysis of these spectra has shown that Li prefers only one of the Sr sites. Further, ionic radii considerations indicate the site of preference for Li to be M(II) in strontium chlorapatites.

For simulation of NMR spectra, the structure of pure Sr-ClAp was optimized in a supercell of size $(1 \times 2 \times 1)$ with the general formula $\text{Sr}_{20}(\text{PO}_4)_{12}\text{Cl}_4$ by allowing both atomic coordinates and lattice vectors to vary. The cell parameters obtained from powder XRD data are respectively $9.859(1)$ Å and $7.206(2)$ Å for 'a' and 'c' and the variation of the values obtained from the geometry optimization are found to be within 3% of these experimental values. One strontium atom was substituted by lithium in the supercell structure which corresponds to an effective lithium doping of 5 mol%. Site-specific replacement of strontium with lithium showed that Li substitution in M(I) site results in structural change from hexagonal to orthorhombic structure, whereas, Li in M(II) site results in reduction of cell parameters by 0.1 and 0.2 % along 'a' and 'c' respectively retaining the original structure. The decrease in the calculated lattice parameters is in accordance with the experimental XRD parameters. These computational results clearly support our experimental finding that Li prefers to substitute for M(II) site. NMR simulation using CASTEP code gives absolute chemical shielding. Chemical shifts were calculated according to $\delta_{\text{iso}} = -(\sigma_{\text{iso}} - \sigma_{\text{ref}})$, where δ_{iso} is isotropic chemical shift, σ_{iso} is isotropic chemical shielding and σ_{ref} is reference chemical shielding. The reference chemical shielding for ^{31}P NMR was obtained with respect to pure Sr-ClAp (270.5 ppm). All phosphorous atoms in the pure Sr-ClAp were found to have the same chemical shift. In lithium substituted Sr-ClAp, the phosphorus chemical shift varied between 9.8 to 1.6 ppm for the three phosphorous atoms closest to lithium even though they are not directly bonded to it. This indicates that bond lengths of PO_4 groups are affected by lithium substitution at the Sr site. This is

substantiated by the experimental result (Figure 3), where we see the asymmetry getting more pronounced with lithium substitution. In other words, substitution of Li results in a distribution in the local environment around phosphorous atoms which, in turn, reflects the Li environments. The CASTEP results for ^7Li NMR chemical shift in doped Sr-ClAp is found to be 0.8 ppm for Li in M(II) site where as 0.2 ppm for Li in M(I) site. From the calculations of quadrupolar coupling constant C_Q , we get ~ 133.3 and 196.1 kHz for Li substituted Sr-ClAp in M(II) and M(I) site respectively.

In summary, the local structural aspects of lithium substituted strontium chlorapatites were investigated for the first time using ^{31}P and ^7Li NMR spectroscopy and the results compared with DFT and DFT-GIPAW calculations. The amount of lithium substitution was varied from 1 - 20 wt% in order to study its uptake into the host matrix as well as to obtain a microscopic picture of the local structural modifications to provide guidance to waste matrix applications in nuclear environment. The studies have clearly indicated the specific site preference that takes place on lithium loading in the host matrix. Both the experimental and the calculated chemical shift values indicate a distribution of the local environment around lithium ion.

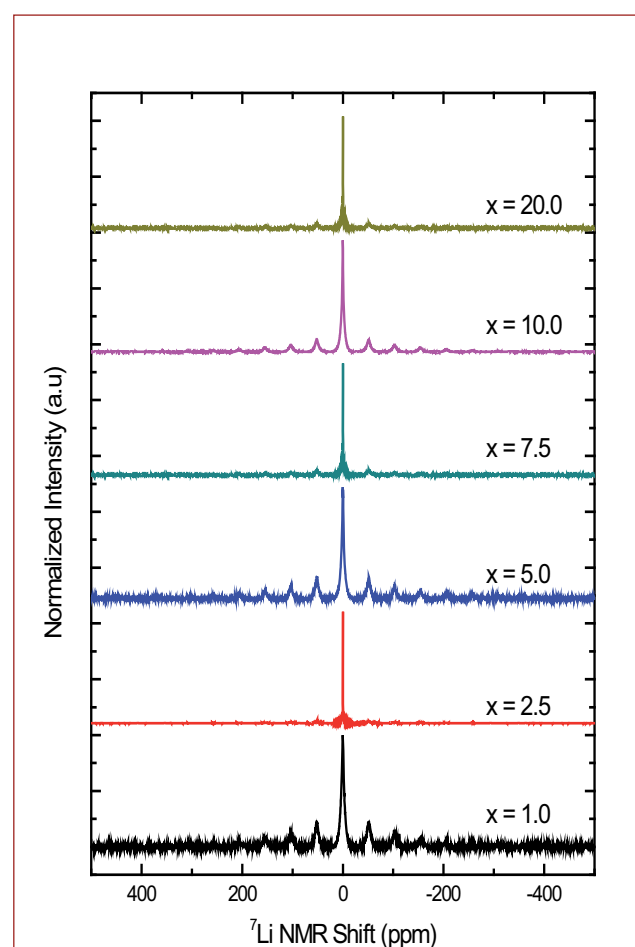


Fig. 3 ^7Li MAS NMR of Sr-ClAp: Li_x

VI.5 Development of Travelling Heater Method for Growth of Technologically Important Single Crystals for Detector Applications

Room temperature semiconductor gamma detectors based on CdZnTe (CZT) occupy an important niche between the cryogenically cooled HpGe detectors and scintillation detectors. CZT detectors exhibit a resolution of about 1% or lower for the 662 keV ^{137}Cs gamma line. These detectors find application in a number of areas of the fuel cycle, safeguards measurements and in portable devices for security applications.

A program for the development of technology for the indigenous manufacture of CZT detectors has been taken up. As part of this activity, a facility to grow CZT single crystals based on travelling heater method (THM) has been established. In THM the molten solvent (excess Te) is made to migrate through a solid source material (CZT) by the slow movement of the charge relative to the heater. The ratio of cadmium to tellurium within the solution determines its melting point, and the growth temperature is usually in the range of 850 – 950 °C.

The charge is encased in a high quality semiconductor grade fused quartz tube. In this process the dissolution of feed material occurs at the advancing (hotter) liquid-solid interface and the crystallization of the feed material occurs at the receding (cooler) liquid-solid interface. The growth rate is determined by the liquid diffusion of the constituent species through the solvent material. This method is capable of achieving stoichiometry by avoiding the Cd vacancies which normally occurs in Bridgman technique whose growth temperature is at 1100 °C. The developed THM system (Figure 1) is basically equipped with a two-zone furnace which is indigenously designed and fabricated (Figure 2). Each resistive heated zone of the furnace is independently controlled through a control circuit and the desired temperature gradient range of 10-50 °C could be achieved at 950 °C by optimizing the



Fig. 1 Travelling heater method setup

set temperature. A high precision vertical translational assembly is utilized, which could move the ampoule/furnace unit at a very slow rate of 1 mm/day. Monitoring thermocouples placed at different points inside the furnace revealed stability to be better than 0.5 °C. The THM setup has been tested for continuous operation of 30 days by performing a growth run of CZT crystal (Figure 3).



Fig. 2 Heating module

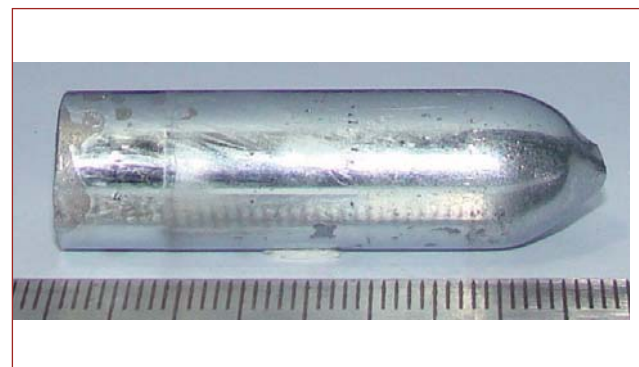


Fig. 3 CZT crystal grown using travelling heater method

VI.6 Development of Nanophase Modified Flyash Concrete as a Potential Candidate for Seawater Applications

With the prospects of continuing operation of nuclear reactors for more than 60 years, the impact of natural as well as human induced events have become a driving force for the development of modified concrete with enhanced concrete properties and durability for nuclear applications. A holistic study on 40% Ordinary Portland Cement (OPC) replaced with flyash (FA) concrete revealed that it is far superior to normal concrete for seawater applications has been demonstrated. However, studies revealed that flyash concrete suffers from higher carbonation depth and calcium leaching, low early strength and antibacterial activity. It has been reported that nano TiO_2 and nano CaCO_3 can accelerate the rate of hydration due to seeding effects and nucleation of C-S-H gel, causing enhanced strength in the early days of curing. Nano TiO_2 by virtue of its photocatalytic activity can also contribute to antibacterial activity and retard biofilm formation on concrete surface. Thus, we attempted nanophase modification of flyash concrete and the results are reported.

Four different types of concrete specimens namely flyash concrete (40% FA), flyash concrete with 2% nano TiO_2 (FAT), flyash concrete with 2% nano CaCO_3 (FAC) and flyash concrete with 1% nano TiO_2 and 1% nano CaCO_3 (FATC) were cast, cured for 28 days and exposed to seawater for a period of one year. Compressive strength analysis after curing for 7 days yielded values of 23.2, 22.4, 26.1 and 38.4 N/mm^2 for FA, FAT, FAC and FATC respectively. FATC also exhibited the highest compressive strength of $> 55 \text{ N/mm}^2$ after exposure for 365 days.

Decarbonation of concrete was monitored using a simple colorimetric method based on phenolphthaleine spraying and advanced thermogravimetric analysis. Results showed that FATC concrete exhibited the least decarbonation of CaCO_3 in the temperature range 600–730°C.

The reduction in pH on the surface and in the crushed nanophase modified concrete was found to be less (8.6–10.0) compared to the 8.2 to 8.5 in the flyash concrete. Resistance to chloride ingress assessed using rapid chloride penetrability test (RCPT) indicated that nanophase modified concrete exhibits better resistance with FATC showing the least value of < 100 Coulomb even after 365 days exposure in

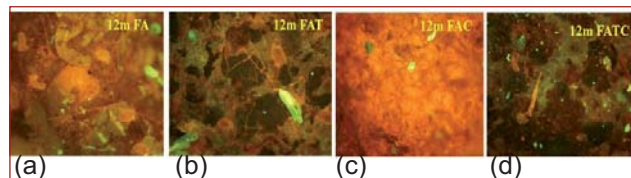


Fig. 1 Epifluorescence micrographs of biofilms on mortar surfaces (a) FA, (b) FAT, (c) FAC and (d) FATC

seawater. Half cell potential of the reinforced nanophase modified concrete enhanced and resistivity increased with increased exposure time, indicating enhanced durability in seawater. EDAX analysis indicated that calcium leaching of nanophase modified concrete was lower than that for flyash concrete.

The epifluorescence micrographs (365 days exposed samples) and thermography phase images presented in Figures 1 and 2, respectively show that titania nanoparticle addition in FAT and FATC concrete provided excellent micro and macro fouling resistance.

Minimum phase angle regions (Figure 2) indicating micro and macrofouling on mortar surfaces are depicted as blue in the phase images and it is evident that FAT and FATC surfaces have least biofouling. Comparable values of phase angle between reference (unexposed) and FATC samples implied least degradation in FATC concrete.

Thus, FATC concrete with 1% each of TiO_2 and CaCO_3 nanoparticles exhibited all the desired characteristics such as early strength, lower carbonation, calcium leaching and enhanced micro and macrofouling resistance, and emerged as a potential candidate for seawater applications.

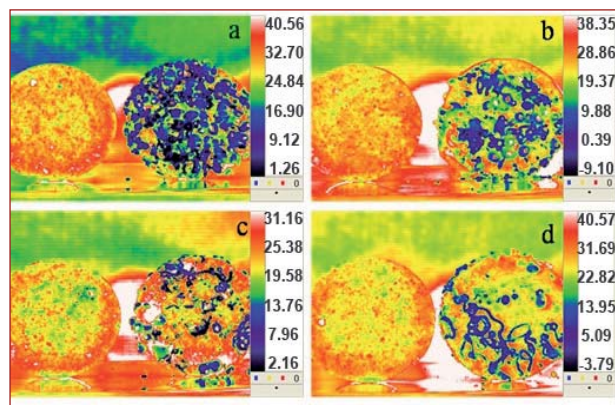


Fig. 2 Phase images at $f = 0.01 \text{ Hz}$ of reference and exposed samples (a) FA, (b) FAT, (c) FAC and (d) FATC

VI.7 Development of Metal Magnetic Memory Technique for Early Detection of Damage in Ferromagnetic Steels

Metal magnetic memory technique has gained considerable interest in the last decade for nondestructive evaluation (NDE) of early damage, micro-defects and stress state in ferromagnetic materials. In this technique, the distribution of self-magnetic leakage fields (SMLFs) induced at a stress concentration zone during mechanical loading is measured using magnetic field sensors. Compared to traditional magnetic NDE techniques, metal magnetic memory technique uses the earth's magnetic field as the magnetizing source instead of strong artificial magnets. This makes the metal magnetic memory technique a potential tool for on-line condition monitoring of engineering components. Giant magneto-resistive (GMR) sensors offer high sensitivity for low magnetic fields and high spatial resolution. This article presents development of a giant magneto-resistive sensor based metal magnetic memory technique for early detection of damage in 3 mm thick carbon steel specimens during tensile deformation.

The in-house developed metal magnetic memory imaging system consists of a giant magneto-resistive sensor, tensile specimen, XY scanner, data acquisition card and a personal computer as shown in Figure 1. The tensile specimens used in this study have the following dimensions: length 140.0 mm, width 24.0 mm and thickness 3.0 mm. The specimens are tensile loaded to pre-defined load values. After unloading and dismantling the specimens from the tensile testing machine, SMLF measurements are made by scanning the tensile specimen in steps of 0.2 mm. The sensor output is digitized using a 16-bit A/D conversion card and stored in a computer for subsequent analysis.

The SMLF images of the tensile specimens for different levels of tensile load (0, 14.7, 21.6 and 22.5 kN) are shown in Figure 2. Small magnetic stray fields of the order of $\Delta H = \pm 50$ A/m are present in the specimen before the tensile load (0 kN). After applying the tensile loads (Figures 2b to 2d), the specimens started exhibiting deformation-induced magnetization inducing SMLFs on the surface of the specimens. The intensity of the SMLF images is found to increase with increase in the tensile load. This is primarily attributed to the increase in SMLFs due to stress-induced magnetization and decrease in the effective magnetic permeability at the central region of the specimen due to the development of dislocation

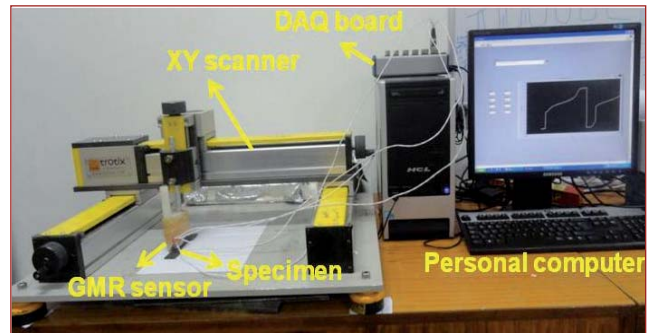


Fig. 1 In-house developed metal magnetic memory imaging system

structures. Once the reduced cross-section is plastically deformed, the specimens get irreversibly narrowed resulting in the development of necking at the gauge length region (Figure 2c). Afterwards the specimens undergo fracture (Figure 2d). The study reveals that the giant magneto-resistive based metal magnetic memory technique can be used for early detection of damage and estimation of degree of tensile deformation in ferromagnetic steels.

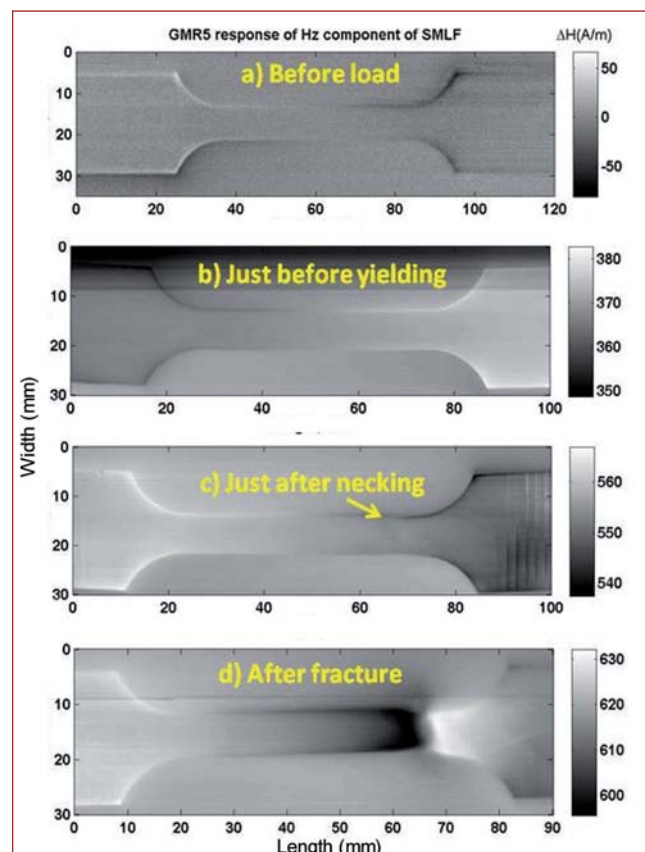


Fig. 2 SMLF images of the tensile specimens after tensile loads of (a) 0, (b) 14.7, (c) 21.6 and (d) 22.5 kN

VI.8 Development of Pulsed Eddy Current Imaging Technique for Damage Assessment in Stainless Steel

Pulsed eddy current (PEC) technique is an emerging electromagnetic non-destructive evaluation technique, for detection of flaws in thick metallic materials. PEC technique uses pulse excitation as it contains continuum of frequencies. Hence, it is possible to simultaneously interrogate different depths in a material following the *skin-effect* phenomenon. This report details the in-house development of high sensitive PEC instrument and high throughput probes for estimation of thickness and for imaging of buried flaws in thick stainless steel components. Detection of sub-surface flaws is challenging as it involves measurement of feeble secondary magnetic fields associated with the eddy currents. These fields can be made measurable by strengthening the primary field i.e. by increasing the excitation current in the coil. Further, it is beneficial to use a high sensitive pick up sensor such as Hall or GMR sensor. Working in this direction, a GMR sensor based PEC probe and PEC instrument, have been developed.

The PEC instrument (Figure 1) consists of a high current driving excitation unit and a high sensitive receiver unit. Excitation unit uses a MOSFET switching device to discharge high current momentarily in excitation coil.

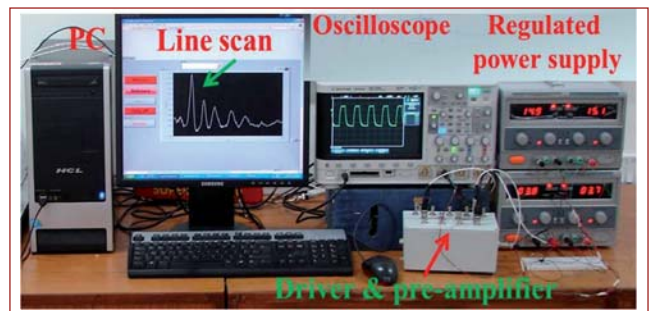


Fig. 1 Photograph of the in-house developed pulsed eddy current instrument

It is capable of driving 5 A current in the coil, and offers variable rise time pulses with a repetition frequency of 10-1000 Hz and duty cycles in the range of 20-70%. The receiver unit uses a 24-bit analog-to-digital converter card at a sampling frequency of 200 kHz. The PEC probe is connected to an XY scanner for raster scanning for imaging of flaws.

In order to evaluate the performance of the PEC instrument and probe, specimens have been fabricated with thickness variations, wedge and sub-surface flaws in 8 mm thick stainless steel plate.

Figure 2 shows the differential PEC signals for different thickness response. It also depicts the variation of the PEC signal parameters viz., peak amplitude and time to peak. As can be seen time to peak increases with thickness of the specimen.

In order to image sub-surface flaws in stainless steel plate, raster scanning has been performed. Sixty line scans have been made to cover full width of specimen with a step size of 1 mm. Figure 3 shows the PEC peak amplitude image of the specimen with sub-surface flaws.

The in-house developed PEC instrument and probe are capable of measuring the absolute thickness variation up to 1.0 mm and also able to image flaws located 6.0 mm below the surface in 8.0 mm thick stainless steel plates.

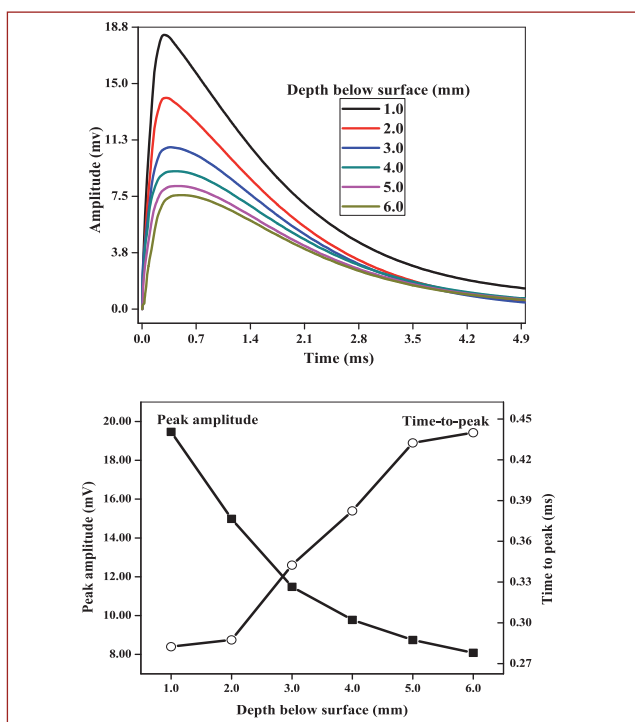


Fig. 2 Typical pulsed eddy current signals for different thickness and variation of signal parameters with thickness of the specimen

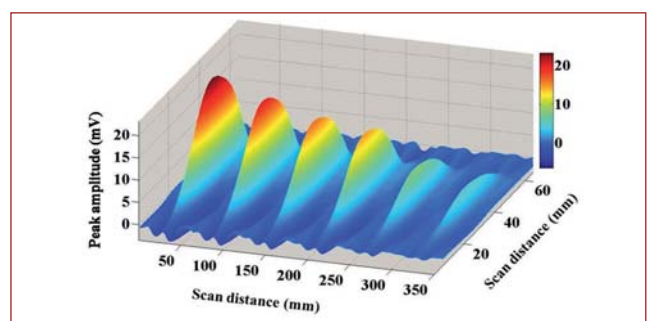


Fig. 3 Pulsed eddy current images of plate having the subsurface flaws

VI.9 Development of a non HF based Environmentally Benign Formulation for Chemical Cleaning of Modified 9Cr-1Mo Steel

During the course of operation of PFBR, oxide scale is likely to be built up inside the modified 9Cr-1Mo ferritic steel steam generator (SG) tubes due to the reaction of high temperature water and steam with the alloying elements (Fe, Cr etc.). The oxide scale deposited on the inner surface of the steam generator tubes adversely affects the heat transfer efficiency of the steam generator and leads to reduction in the wall thickness of steam generator tubes. The oxide scale may spall off after attaining a critical thickness and results in blocking of tubes. Hence, efforts are on to devise a chemical formulation which could effectively remove the oxide scale and clean the material with minimum loss of the base metal. Chemical cleaning of modified 9Cr-1Mo steel was carried out in weak sulphamic acid (H_3NSO_3) solution. The corrosion rates and thickness loss determined for modified 9Cr-1Mo steel specimens (10x10x5 mm) by weight loss measurements in 2, 5 and 10% of sulphamic acid for 4 hours are shown in Figure 1.

Addition of four different concentrations (0.5, 1, 2 and 3 mM) of the corrosion inhibitor 2-MBI (mercaptobenzimidazole) to 10% (w/v) sulphamic acid solution showed that with increase in the concentration of corrosion inhibitor from 0.5 to 3 mM, the corrosion rate decreased from 24 to 13 mpy. A drastic decrease in the corrosion rate from 364 (without inhibitor) to 24 mpy (with inhibitor) was observed with the addition of just 0.5 mM MBI. Further increase in the concentration of MBI indicated a marginal effect on the decrease in corrosion rate.

To evaluate the performance of sulphamic acid as an effective cleaning agent for steam generator

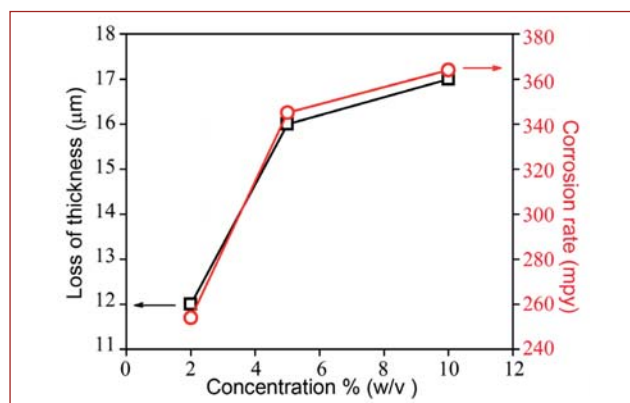


Fig. 1 Corrosion rate and thickness loss of mod. 9Cr-1Mo steel in sulphamic acid solutions

applications, the specimens were heat treated at 500°C for 2 hours. The hard oxide scale was chemically cleaned in 10% sulphamic acid with and without the addition of inhibitor. The corrosion attack on base metal was severe in sulphamic acid solution without inhibitor. The inhibitor formed a protective surface on the base metal and prevented the corrosion attack.

Corrosion rates and thickness loss determined after exposing the specimens to conventional pickling solution ($HNO_3 + HF$; solution A) as well as 10% sulphamic acid without and with 2 mM MBI inhibitor (solutions B and C, respectively) for 30 minutes are shown in Figure 2. It is evident from this figure that sulphamic acid with MBI inhibitor could be used as a suitable cleaning agent for ferritic steel in place of HNO_3 and HF mixture.

A combination of 10% (w/v) sulphamic acid and 2 mM MBI showed the best chemical cleaning effect on modified 9Cr-1Mo steel with minimum corrosion rate as well as base metal loss. This combination was used to clean the rusted modified 9Cr-1Mo steel weldment, which showed excellent cleaning effect and complete removal of the rust deposit (Figure 3).

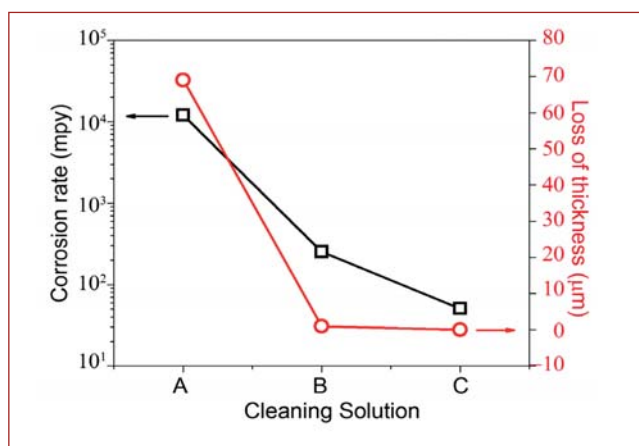


Fig. 2 Corrosion rate and thickness loss of modified 9Cr-1Mo steel in cleaning solutions A, B and C (30 minutes exposure)

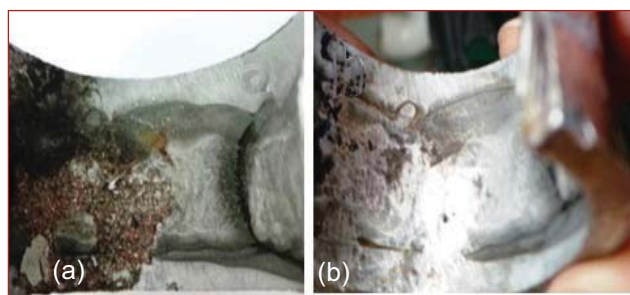


Fig. 3 Pictures of modified 9Cr-1Mo steel specimens: (a) rusted and (b) chemically cleaned weldment using inhibited 10% sulphamic acid

VI.10 Development and Standardization of Ultra Sub-size Tensile Specimen for Evaluation of Mechanical Properties

Sub-size tensile specimen of 3.0 mm gage width, 1.0 mm thickness, 12.5 mm gage length (GL) and 40 mm total length has been extensively employed for structural material irradiation and mechanical property evaluation of irradiated components. This is because, as compared to standard specimens, sub-size specimens (i) permit efficient use of costly reactor space for test irradiations (ii) experience near uniform flux and temperature across its volume (iii) simplify extraction from irradiated components and (iv) permit easy handling due to reduced activated dose.

Recently, further miniaturization of tensile specimens has been carried out with a gage width of 1.5 mm and gage length of 3.0 mm carved out from a disc sample of 10 mm diameter and 0.5 mm thick (Figure 1a). Various analytical and experimental tools have been employed towards optimizing this specimen size referred as ultra sub-size (USS) for reliable evaluation of tensile properties and results compared with that of ASTM E8 specimen (GL: 25mm) and sub-size geometry (GL: 12.5 mm) already in use.

The fillet radius between gripping and gage section of USS specimen was optimized to 1.2 mm to maintain the same stress concentration factor (≈ 1.33) as in ASTM specimen geometry. To fix a geometrical tolerance on gage width of USS specimen, the non-uniformity of stress distribution (Figure 2) and tri-axiality factor across the gage section were examined for various tolerance values using finite element analysis (FEA) and compared with results of ASTM specimen. Based on the analysis and machining capability, a tolerance of ± 0.01 mm on gage width and thickness was fixed for machining. The fabrication of USS specimen was standardized to achieve good dimensional tolerances using wire EDM technique followed by diamond grinding/polishing to remove the recast layer. A customized light weight gripping fixture (Figure 1b) with guide-ways for self alignment was developed for testing USS specimens in a universal testing machine (UTM) at ambient and elevated temperatures of upto 600°C.

As it is practically impossible to fit conventional extensometers to USS specimen, digital image correlation (DIC) method was adopted for strain measurement. In DIC method, a random speckle pattern (Figure 1c) is applied on the gage section of specimen and the image is acquired on-line by a camera during the test. By comparing the images and by tracking the

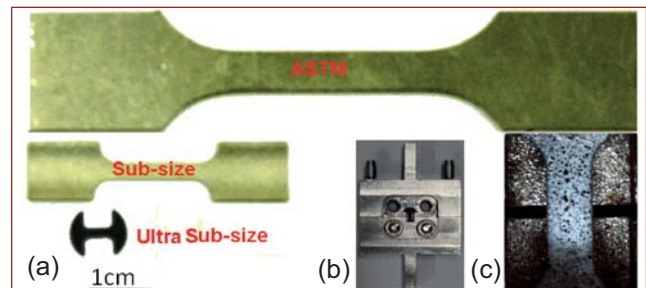


Fig. 1 (a) ASTM standard, sub-size and ultra sub-size tensile samples, (b) grips for testing ultra sub-size specimen and (c) pattern for strain measurement using digital image correlation

blocks of pixel at different instants of deformation, the surface displacement is obtained and converted into strain distribution using image processing algorithms.

Tensile tests on USS specimens on different materials (Aluminum, Copper, Carbon steel, SS316, Cr-Mo steels, Maraging steel) exhibited a scatter of about 2-5% in the tensile properties. The 0.2% proof strength and UTS from USS specimen tests were within 5-7% and 2-5% respectively of the corresponding values from sub-size/ASTM specimen results, while uniform elongation of USS specimens were within 4-6 % of the values from large size specimens.

This study suggests that tensile tests with ultra sub size specimen (1.5 mm gage width, 3.0 mm gage length and 0.5 mm thick) has the potential to provide the stress-strain data representative of bulk material and is useful not only for the nuclear industry but also for other applications like life estimation of any in-service component and for development of new and exotic materials where material availability is limited.

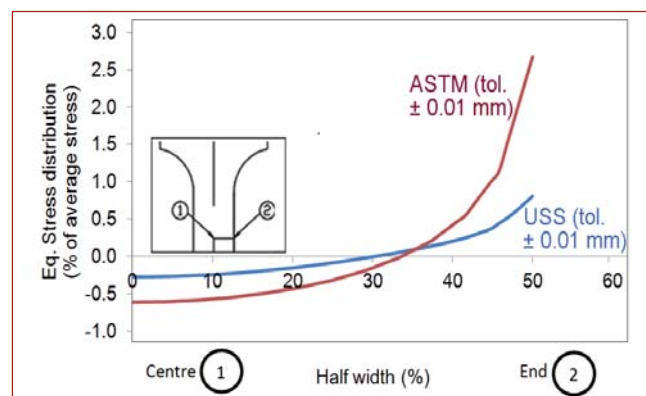


Fig. 2 Stress distribution across the half width of ultra sub-size specimen

VI.11 Development of a Dual-Irradiation Platform for Studies of Radiation Response in Fission and Fusion Reactor Materials

While using ion irradiation as a surrogate for neutron irradiation one needs to account for differences with respect to primary knock atom energies, the cascade structure, injected interstitials and the most significant being the effect of high damage rate. Ion irradiation experiments emulate the production of transmutation gases in a reactor either by pre-injection or co-implantation during damage creation. As shown from studies the mode of helium injection can cause considerable differences in void micro-structure.

Dual beam implantations of simultaneous heavy ions and helium-ion irradiations emulate better the irradiation conditions of fission and fusion candidate materials for purposes such as material screening and evaluation of basic mechanisms or model calibration. In this regard a dual beam facility which comprises of co-implantation with heavy ion beams (Fe/Ni) from the existing 1.7 MV accelerator and helium ions from an indigenously built 400 kV accelerator has been developed. The general layout of the facility is shown in Figures 1 and 2. The UHV beam line which transmits helium ions to the UHV irradiation chamber has been designed after carrying out detailed ion optics calculations in order to ensure maximum beam intensity by optimizing the parameters of beam optical components.

Electronics and instrumentation to facilitate control and monitoring of the UHV beamline and the 400kV accelerator has been designed and developed in-house.

Figure 3 shows the structure of a fiber optically linked distributed control system (DCS). Important features of

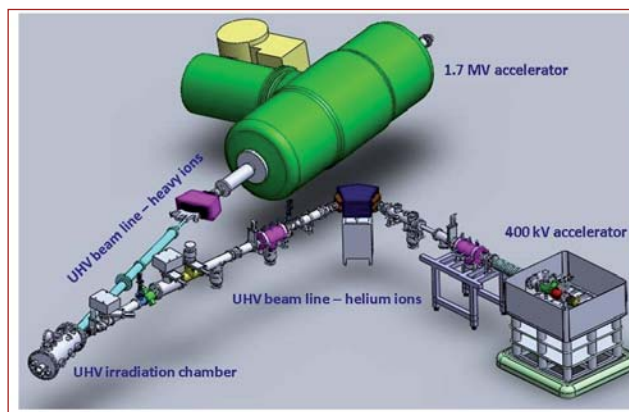


Fig. 1 A schematic of the dual beam ion irradiation facility where simultaneous heavy ion irradiation and helium injection is carried out using the 1.7 MV Tandatron and 400 kV ion accelerators

the control system include fibre optic communication for high voltage isolation, fast data rate (1.2 MBaud) and no transient pick up, modular design, high resolution, high update rate upto 32k channels/sec, rugged and reliable operation through fault-tolerant and self-correcting software and built-in diagnostics.

The dual implantation facility has been tested for its capability to perform irradiations with He/dpa ratios relevant to fission and fusion reactor conditions. This facility will help simulate synergistic effects of displacement damage and gaseous helium or hydrogen, which are important in the context of development of radiation resistant materials for fission, fusion and accelerator driven systems.

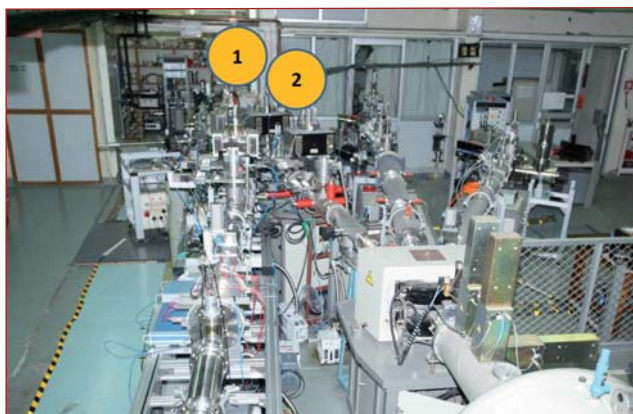


Fig. 2 Photograph showing the dual beam ion irradiation facility along with other beam lines of the 1.7 MV tandatron accelerator. '1' and '2' marked in the picture represent the helium injection and heavy ion irradiation beam lines respectively

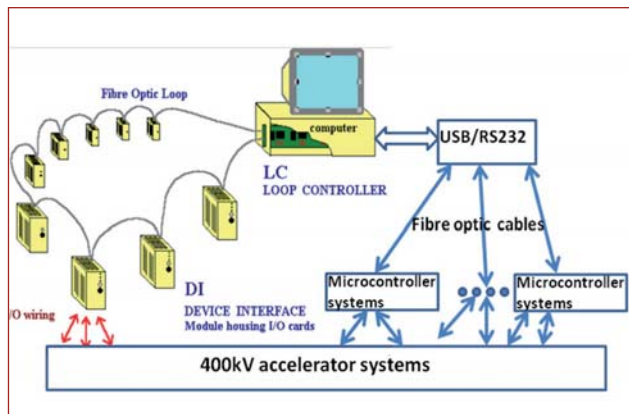


Fig. 3 Block diagram of distributed control system developed for control of the 400 kV accelerator

VI.12 Fabrication and Characterization of SiO₂ Microcantilevers

Microcantilevers (MCs) have been demonstrated to be extremely sensitive chemical, biological and environmental sensors. When operated in static bending mode, one side of the microcantilevers is coated with a thin film, which is sensitive to a specific target molecule, while the opposite surface is made passive. When target molecules interact with the sensitized surface of microcantilevers, differential surface stress is generated, resulting in a measurable mechanical deflection of the cantilever beam.

MCs are conventionally fabricated from c-Si. However, in recent times, microcantilevers made of silicon dioxide (SiO₂), are gaining importance because of larger mechanical sensitivity i.e. bending amplitude under the same condition as conventional Si microcantilevers. In the present work, SiO₂ microcantilevers of various dimensions are successfully fabricated using direct laser writer (DLW) (Figure 1a) and by anisotropic wet etching method.

Thermally grown SiO₂ (230 nm) layer on single crystalline Si was utilized for the microfabrication. Initially, a mask file with microcantilevers of different dimensions were prepared using LEdit software (Figure 1b) and loaded into DLW to transfer the pattern on photoresist coated SiO₂/Si wafer (Figure 1c). At this stage, various process optimizations such as photo resist thickness, laser exposure energy for writing, development time, pre- and post-baking temperatures etc were carried out. After successful pattern transfer on photoresist, SiO₂ was etched in buffered hydrofluoric acid (Figure 1d) and finally Si was etched in tetramethyl ammonium hydroxide solution to release the SiO₂ microcantilevers (Figure 1e). It may be noted that the thickness of the released microcantilevers is the thickness of SiO₂ layer itself i.e. ~ 230 nm.

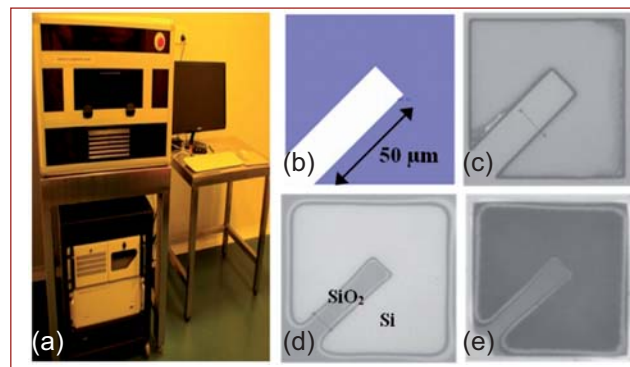


Fig. 1 (a) Direct laser writer installed inside class 1000 clean room, the optical resolution of this equipment is 0.8 μm, (b) mask file showing a typical microcantilever, (c) pattern transferred on photoresist coated SiO₂/Si wafer using direct laser writer, (d) after etching SiO₂ and (e) SiO₂ microcantilever released after etching Si

Resonance frequencies of released microcantilevers were measured using nanovibration analyzer (NVA). Wafer containing microcantilevers was glued on a piezo actuator, which was excited using a function generator. Amplitude of vibration at various frequencies was recorded using NVA and resonance frequency was estimated from the peak of frequency versus amplitude plot. A typical resonance spectrum acquired using NVA is shown in Figure 2a. Resonance frequency of the microcantilever was also estimated using finite element modeling (FEM) and is shown in Figure 2b.

It is clear from these two figures that the resonance frequency value estimated by FEM simulation is higher than the experimentally obtained value. The difference in observed resonance frequency is attributed to the presence of residual stress in released microcantilevers. Studies are underway to quantify the residual stress using micro Raman spectroscopy.

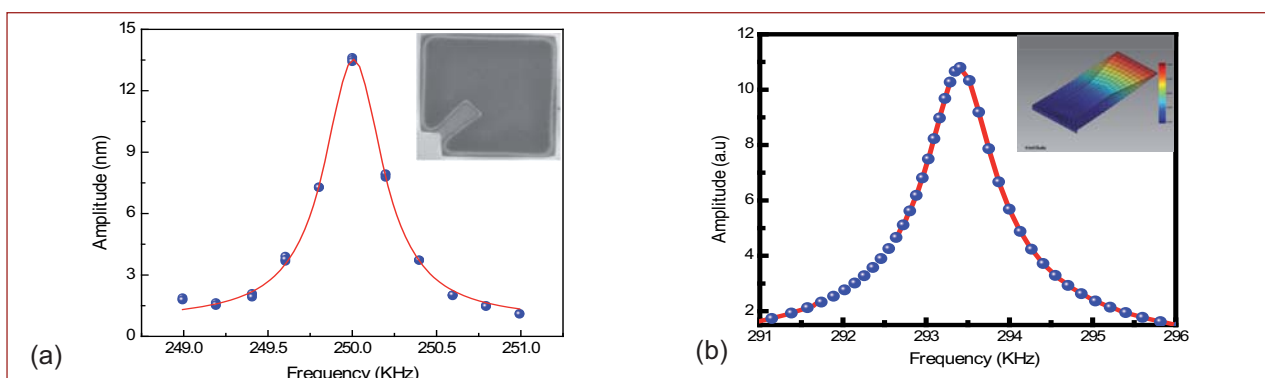


Fig. 2 Resonance spectrum of the released SiO₂ microcantilever measured using (a) nano vibration analyzer and (b) obtained from FEM simulations

VI.13 Au-DLC Nano Composite Thin Films Grown by Excimer Laser Ablation

Diamond like carbon (DLC), is a metastable form of amorphous carbon consisting of the sp^2 bonded (graphite-like) carbon clusters inserted into the sp^3 bonded (diamond like carbon) carbon matrix. Diamond like carbon films have received considerable attention from the researchers and industry due to very interesting combination of properties. Large Young's modulus and high hardness (up to 80% of the crystalline diamond hardness and modulus), low friction coefficient, high wear and corrosion resistances, biocompatibility as well as possibility to vary optical and electronic properties render diamond like carbon suitable for several applications. Properties of the diamond like carbon films can further be controlled by inserting into the diamond like carbon different chemical elements as well as compounds. Particularly, doping of diamond like carbon by metals of Group 1 such as gold, silver or copper results in some additional beneficial features such as presence of the surface plasmon resonance, antibacterial properties, haemodynamic compatibility, increased wear resistance and substantial reduction of the film residual stress while maintaining hardness that is almost unchanged. In this communication, Au nanocluster doped diamond like carbon films were synthesized and characterized using sub-nanosecond excimer laser ablation.

Coherent complex pro-nanosecond excimer laser (248 nm) was set up along with beam steering optics (Figure 1a) to obtain stable diamond like carbon

films with high sp^3 content. These films were synthesized on Si (100)/ Ti (80 nm) by ablating a graphite target sectorially covered with Au disc at various laser pulse energies (200, 300, 400, 500, 600 and 700 mJ) while maintaining other parameters like substrate to target distance (50 mm), number of shots (10,000), repetition rate (10 Hz) and vacuum (5×10^{-6} mbar) constant. The sector arrangement is shown in Figure 1b. Diamond like carbon films with highest sp^3 content of $\sim 48\%$ could be easily realized with 400 mJ of laser power. This film is designated as DLC-400.

The deconvoluted Raman spectrum of DLC-400 is shown in Figure 1c. Two different concentration of gold embedded DLC films were also grown on Si (100) / Ti (80 nm) with optimized deposition parameters by a special type of arrangement of gold foil on graphite target as shown in Figure 1c. All the specimens were characterized by Raman spectroscopy and FESEM imaging. In Figure 1c, Raman spectrum of pristine DLC specimen indicate sp^3 content in Ti bond coated silicon (in this film is 48%). The Au: DLC films synthesized under similar conditions depressed the sp^3 content to 42%. Increase in Au loading reduced the sp^3 content further. This reduction in sp^3 content possibly occurs due to the presence of catalytically active Au nano-clusters which normally promote sp^3 bond cleavage leading to graphitization. This has been confirmed by plasmon resonance motivated enhanced optical absorption. Figure 1d shows FE-SEM image of gold nanoparticles on DLC surface.

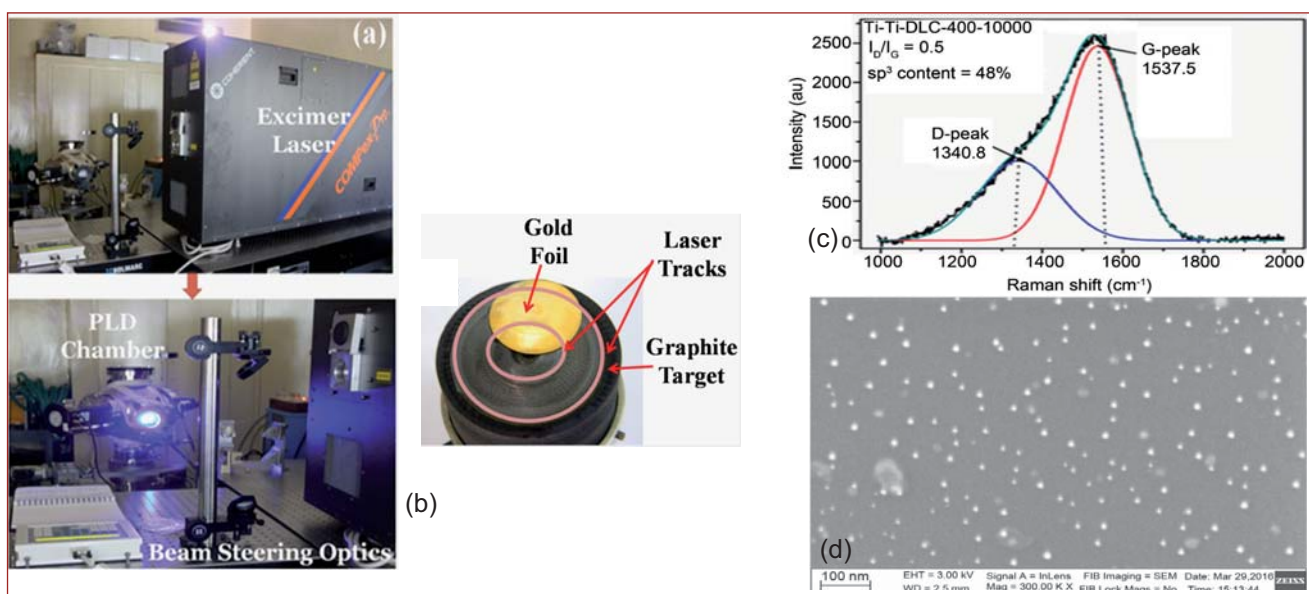


Fig. 1 (a) Photograph of excimer laser with beam steering optics and PLD chamber, (b) sector arrangement of Au-Foil on high density graphite target, (c) Raman spectrum of DLC-400 and (d) FE-SEM image of Au-DLC film

VI.14 Spin Transfer Torque in Magnetic Nanostructures: Modeling and Evaluation

The phenomenon of spin transfer torque (STT) which is the reorientation of the magnetization by spin polarized current in magnetic nanostructures is being intensively investigated in the recent years. The interest is primarily due to its potential application in the development of STT-magnetoresistive random access memories. STT in magnetic tunnel junctions (MTJs) is the interest of several research groups. While the experimental studies at the atomic scale resolution is possible in these nanostructures, the modeling has gained substantial attention as it is useful in the interpretation and understanding of experimental results as well as to probe avenues inaccessible to experiments. Thus, the modeling can be an aiding tool in the design of STT devices. The non-equilibrium Green's function (NEGF) technique is a powerful tool in the modeling of STT. Model studies of STT in different nanostructures exist in the literature. Reliable prediction of the STT requires that the formulation takes into account all the relevant material parameters as well as other external influences. A generalized formulation that addresses this issue is hence developed. The computer codes required to obtain numerical results are also developed. The formulation is used to study STT in non-collinear MTJs. A schematic diagram of the non-collinear MTJ considered in the study is shown in Figure 1. The electrodes of the MTJ are assumed to possess non-collinear magnetism as well as many body interactions. θ represents the non-collinear angle. The STT can be obtained from the spin current (J^S) at the insulator (β) - right electrode (γ) interface, which can be estimated through the NEGF formulation. Thus, the STT is given as:

$$\mathbf{T} = J^S = Tr(\mathbf{A}\sigma)$$

Where \mathbf{A} is given as

$$\mathbf{A} = -Re \int dE \left(\sum_k (\epsilon_k^{\beta\gamma} \mathbf{G}_k^{<(\beta\gamma)}(E) - \epsilon_k^{\gamma\beta} \mathbf{G}_k^{<(\gamma\beta)}(E)) \right)$$

Here the G^S are the wave vector (k) dependent Keldysh Green's function matrices that correspond to the interface layers n_β and m_γ and ϵ^S are the interlayer Bloch energy matrices. σ is the vector of Pauli spin matrices appropriately generalized to take into account the multiple layers and bands in the MTJ. A lengthy procedure is involved in the evaluation of the G^S . It can be shown that for the MTJ geometry considered in the study, the x and y components of the STT alone are active and they are referred as the parallel (T_{\parallel}) and

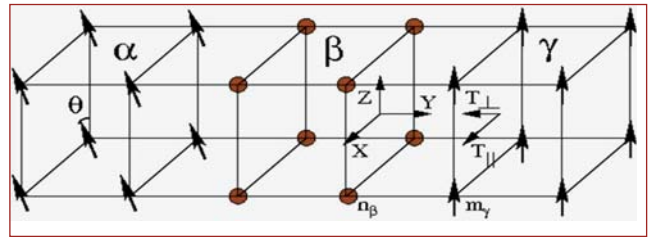


Fig. 1 Schematic diagram of the MTJ. α , γ represent the left and right electrode regions and β represent the insulating region

perpendicular (T_{\perp}) components of the STT. The STT in model MTJs with different values of layer thicknesses, exchange coupling strengths, non-collinear angles and band occupations are investigated. The STT obtained from the formulation for a MTJ with three layers at the insulating region is shown in Figure 2. As the STT is maximum for $\theta = \pi/2$, we have shown in the figure, the STT corresponding to this value of θ (ζ represents the exchange coupling strength of the electrode regions and \square represents the interfacial area of the MTJ).

It is observed that the bias dependence of the STT obtained for certain values of the band occupation agrees with the trends obtained from experimental measurements. Hence, further sophisticated calculations with the incorporation of ab-initio band structure results can lead to reliable prediction of the STT.

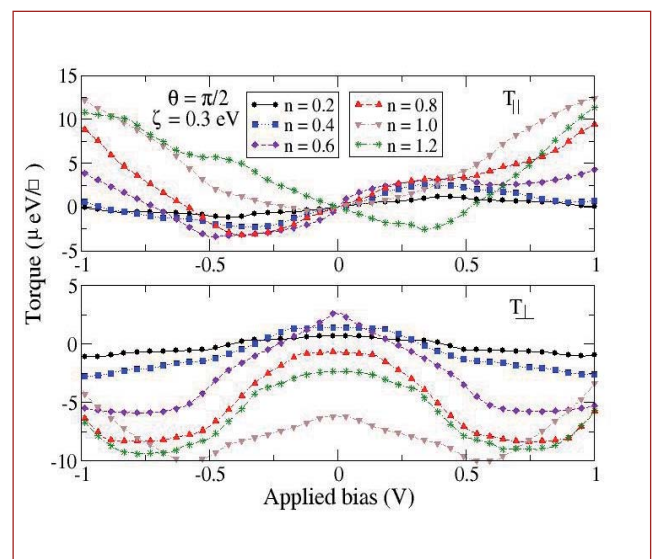


Fig. 2 The parallel and perpendicular components of the STT as a function of the applied bias for different values of the band occupation (n) of the electrodes

VI.15 Mapping Local Elastic Heterogeneities in DLC Films Grown by ECR CVD

Diamond like carbon (DLC) is an amorphous carbon network comprising of sp^2 and sp^3 bonding states. DLC is very popular because of its ability to mimic diamond in terms of optical, electrical, mechanical properties and created immense scientific interest. Owing to its exceptional properties, DLC films are potential candidate for countless applications that include protective coatings on cutting tools, memory storage devices, bio-medical devices, anti-reflection coating on infrared optical windows and Si solar cells. DLC films also find applications in micro-electromechanical systems as a structural material which is used to fabricate high frequency resonators and comb-drives for communication and sensing applications. The key parameter of DLC films is sp^3 C-C bonding which gives maximum hardness and high film density. For this purpose almost all the growth methods of DLC films adopted substrate biasing. However, high substrate bias introduces high residual stresses which limit the achievable film thickness. Nitrogen doping is found to be the right choice to achieve lower residual stresses in DLC films. It forms C-N bonds and improves their electrical conductivity, toughness, adhesion, mechanical properties and it also reduces the intrinsic compressive stresses.

In this study, DLC films were grown on Si (100) substrates using electron cyclotron resonance plasma enhanced chemical vapor deposition system. The first set of DLC films were grown at different substrate biases viz. -50, -100, -150 and -200V and these samples are labeled as B_1 , B_2 , B_3 and B_4 , respectively. The second set of DLC films were grown by allowing nitrogen at the rate of 0.5, 1 and 2.5 sccm and are labeled as $B_{2-0.5}$, B_{2-1} and $B_{2-2.5}$, respectively.

Table 1 illustrates the chemical structural details of these films obtained by Laser Raman spectroscopy and physical properties like film density and hydrogen content measured by Rutherford Backscattering Spectroscopy (RBS) and Elastic Recoil Detection Analysis (ERDA). The obtained results signify influence of substrate bias and nitrogen doping on the physical and chemical properties of DLC films.

The AFAM is one of the most powerful techniques to obtain quantitative elastic properties of thin films. The Contact Resonance Frequency (CRF) of the tip – sample assembly is an important parameter in estimating the

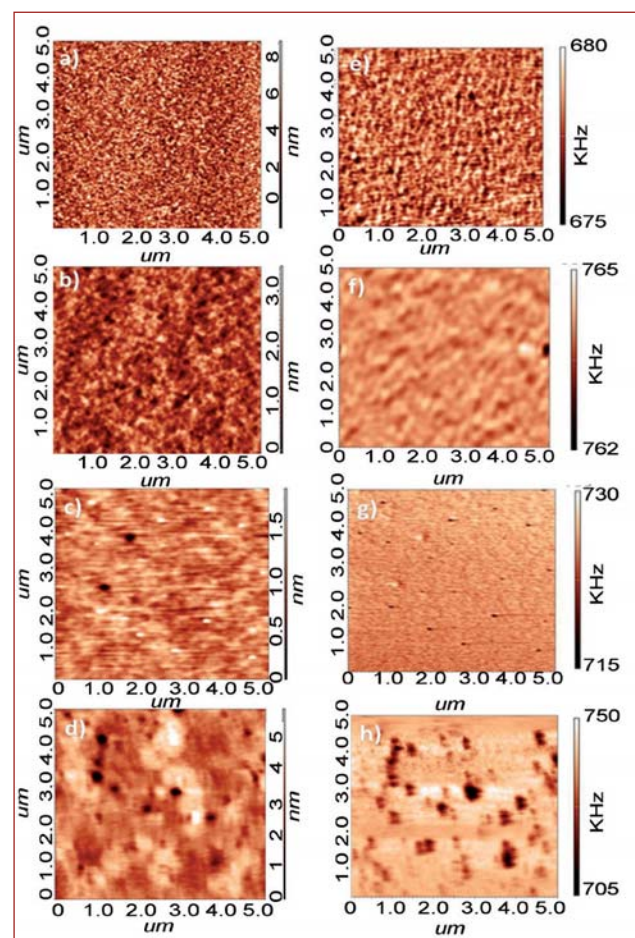


Fig. 1 Simultaneously recorded topography and CRF mapping of DLC films grown at different substrate biases of (a,e) -50, (b,f) -100, (c,g) -150 and (d,h) -200 V respectively

elastic modulus of the given material.

Figures 1a to 1d and Figures 1e to 1h show the simultaneously recorded topography and AFAM mapping of DLC films grown at different substrate biases, respectively. The topography of the films B_1 and B_2 are found to be extremely smooth with root mean square roughness of 0.5 and 0.14 nm, respectively. The film B_3 exhibits isolated clusters of about 50 nm in diameter and a few nanometers of height over an extremely smooth surface. But, the sample B_4 exhibits an inhomogeneous surface with large rms roughness of 4.5 nm. The corresponding CRF mapping of the samples B_1 and B_2 are also very smooth as shown in Figures 1e and 1f. Similarly, the film B_3 also exhibits a smooth CRF mapping but several isolated low CRF regimes are observed over the homogeneous background. In contrast, the film B_4 is highly inhomogeneous with lot of low CRF regimes.

Table 1: The growth parameters, thickness and Raman analysis of the diamond-like carbon films

Sample	Bias (V)	CH ₄ :Ar:N ₂ (sccm)	Thickness (nm)	Raman analysis		Rutherford back scattering	ERDA	Calculated Elastic modulus (GPa)
				FWHM(G) (cm ⁻¹)	I _D /I _G ratio	Density (g/cc)	Hydrogen content	
B1	-50	6:9:0	850	176	0.36	0.7	37	102
B2	-100	6:9:0	475	159	0.40	2.1	22	185
B3	-150	6:9:0	290	147	0.55	1.8	19	145
B4	-200	6:9:0	240	114	0.76	1.5	14	130
B2-0.5	-100	6:9:0.5	330	144	0.47	1.9	19	169
B2-1.0	-100	6:9:1.0	290	137	0.54	1.6	17	160
B2-2.5	-100	6:9:2.5	200	133	0.60	1.4	14	140

These regimes are found to coincide with topography mapping corresponding to the nanoclusters. Thus, we can infer that these regions possess lower elastic modulus than the matrix. This phenomenon is attributed to the graphitization of the DLC films with increase in bias.

Figures 2a to 2c and Figures 2d to 2f show the simultaneously recorded topography and CRF mapping of nitrogen doped DLC films, respectively. The doped films exhibited homogeneous topography upto a nitrogen flow rate of 1 sccm. Further increase in nitrogen concentration increases the sp² cluster size in lateral dimension and

evolves as second phase as shown in Figure 2c. The corresponding AFAM mapping of these films also reveal that these second phases have lower elastic modulus than the matrix. Thus, the increase in nitrogen concentration in DLC leads to the formation of second phase, similar to the phenomena observed with increase in applied bias. Based on the CRF mapping, statistical analysis is carried out and from average CRF of a particular film, the elastic modulus is computed. The calculated elastic modulus values are tabulated in Table 1. From these results it is evident that the bias and nitrogen doping influence the elastic modulus of DLC films.

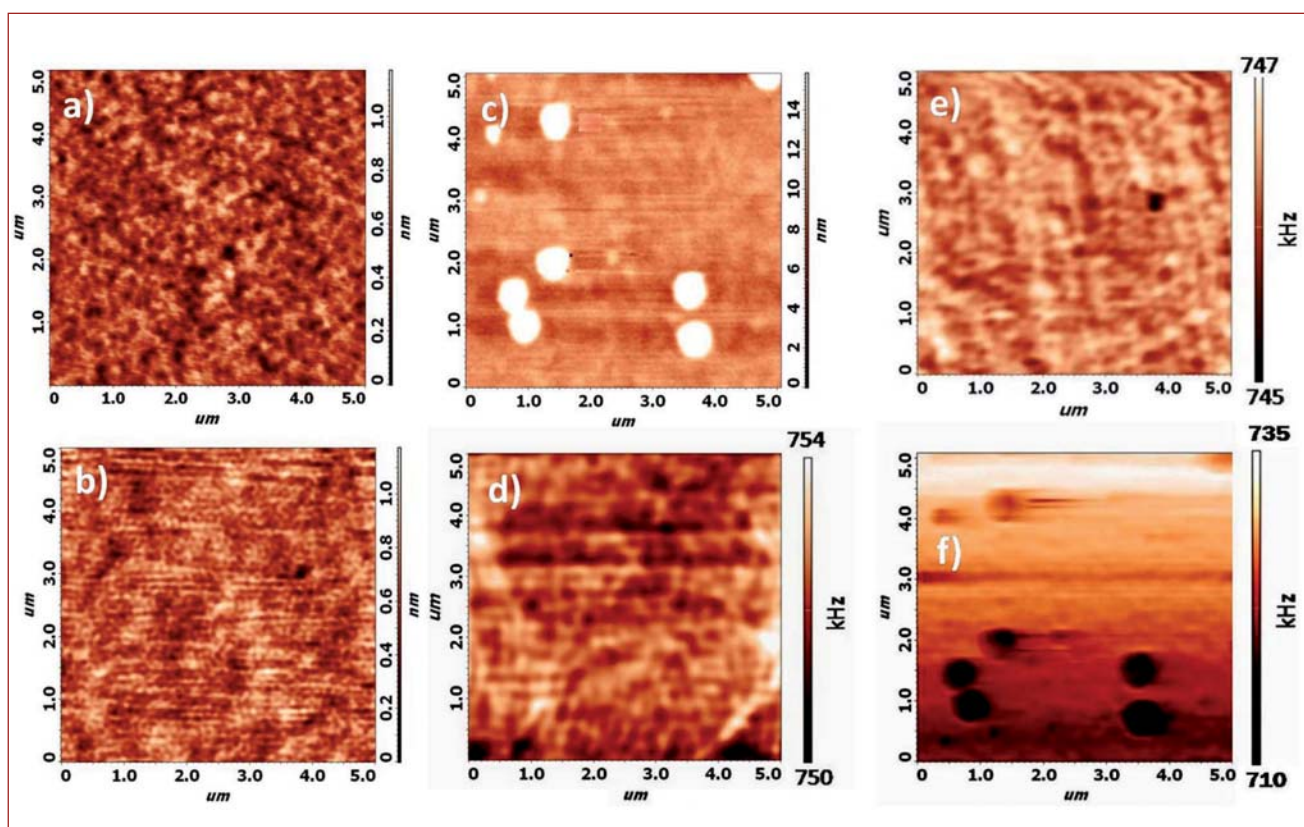


Fig. 2 Simultaneously recorded topography and CRF mapping of DLC films grown at different nitrogen flow rate of (a,d) 0.5 (b,e) 1 and (c,f) 2.5 sccm, respectively

VI.16 Acoustic Emission Technique for Monitoring Damage in Concrete under Compressive Loading

Understanding the growth of damage in concrete under different loading conditions is of considerable importance. Once damage is initiated, it can grow at a faster rate and lead to catastrophic failure of the concrete structure. Therefore, it is important to detect damage in concrete at an early stage. Acoustic emission technique is an online nondestructive testing technique that has potential to detect damage initiation, as well as growth of damage in concrete. Recently, fly ash concrete is being used for many constructions, especially bridges. Acoustic emission technique is used to monitor damage growth in plain and fly ash concrete, subjected to uniaxial compression loading. Two types of concrete (plain and with 30% fly ash) are used to produce concrete cubes (150x150x150 mm³). A piezoelectric sensor having resonant frequency at 150 kHz is used to record acoustic emission signals. Acoustic emission counts and stress with strain during compression tests of plain and fly ash concrete are shown in Figures 1a and 1b. At the beginning of the compression test, many acoustic emission signals detected are attributed to the formation of micro cracks. Reduced acoustic emission in the second stage is due to stable cracks. As long as the cracks are stable, their presence is not harmful. Upon further increase in load close to the ultimate strength sudden increase in acoustic emission counts is observed due to unstable cracking.

An attempt has been made to compare the types of cracking in both types of concrete using acoustic emission parameters viz. Relative amplitude value and average frequency as per JCMS-III B5706 code. Relationship between the relative amplitude values and average frequencies of plain and fly ash concrete is shown in Figures 2a and 2b. In both the types of concretes, average frequencies of acoustic emission

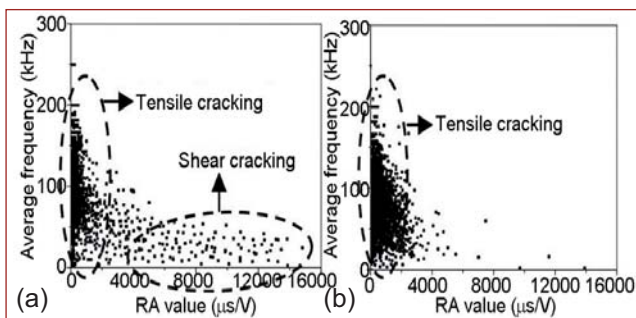


Fig. 2 Relationship between relative amplitude value versus average frequency for (a) plain and (b) fly ash concrete

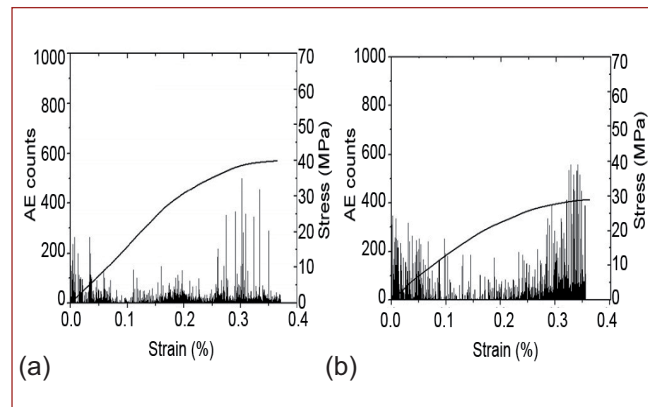


Fig. 1 Variation acoustic emission counts and stress with strain during compression tests of a) plain and b) fly ash concrete

hits are distributed up to 200 kHz. Relative amplitude value distribution is different and plain concrete is found to show higher relative amplitude value which is an indication of formation of shear cracks dominating the failure process. The studies show that plain concrete exhibits both tensile and shear cracking. Lower relative amplitude value of fly ash concrete is an indication of formation of only tensile cracks and this is due to accelerated pozzolonic reaction of fly ash and formation of more calcium silicate hydrate which fills the voids and pores. The acoustic emission results have been supported by SEM examination. SEM micrographs of the fracture surfaces of the plain concrete shows diverged multiple cracking (shown by arrows) and more localized failure regions as shown in Figure 3a. Fly ash concrete shows reduction of diverged multiple cracking (Figure 3b) as compared to plain concrete. This information on likely cracking direction is useful for deploying the acoustic emission technique for nondestructive structural health monitoring of concrete structures.

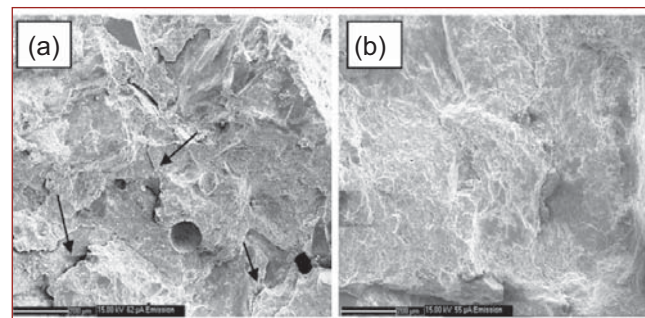


Fig. 3 SEM images of fracture surface of (a) plain and (b) fly ash concrete

VI.17 Thermodynamic Stability of Sigma (σ) and Alpha (α) Phases in $\text{Fe}_{55.4}\text{Cr}_{44.6}$ Alloy

Fe-Cr is a fundamental binary system for ferritic, ferritic-martensitic and some 300 grade austenitic stainless steels. The comprehensive understanding of Fe-Cr binary is essential for knowledge based steel development for advanced engineering applications. In such a milieu, the σ -phase formation upon prolonged exposures at high temperature and under stress, in steels having high Cr-content, is a major issue. Although there exists a wealth of literature on the metallurgy of σ -phase in Fe-Cr and related systems, there is nevertheless a paucity of reliable data on its thermal stability and thermophysical properties. In the reported study, the effect of sigma phase on thermal stability of $\text{Fe}_{55.4}\text{Cr}_{44.6}$ model alloy has been carried out.

The alloy was made by arc melting under flowing argon atmosphere and was subject to standard homogenization treatment. At room temperature, the alloy exhibited a single bcc phase (Figure 1a). The hardness (220 VHN) also corresponded to that of α -ferrite (Figure 2a). To induce σ -phase formation, the alloy was aged at 700 °C for 250 hours under vacuum. The XRD of aged alloy (Figure 1b) showed the complete conversion of bcc to the tetragonal σ -phase structure. The lattice parameter of α phase is $a_{\alpha}=0.287$ nm; while that of σ -phase is $a_{\sigma}=0.882$ nm and $c_{\sigma}=0.455$ nm. The microstructure of σ -phase (Figure 2b) showed the formation of numerous grain boundary micro-cracks due to transformation strains, and possessed a high hardness of 1088 VHN.

The high temperature stability of both α and σ phases has been investigated using dynamic calorimetry (10 °C/min scans). The DSC thermogram of α -ferrite phase (blue line in Figure 3) showed only one inflection at 558 °C which is attributed to the ferromagnetic to paramagnetic transition. No such magnetic phase change is noted for σ phase (pink line in Figure 3). The σ -phase exhibited only one phase transformation, namely that of $\sigma \rightarrow \alpha$ reverse conversion at 856 °C. Further, it is observed

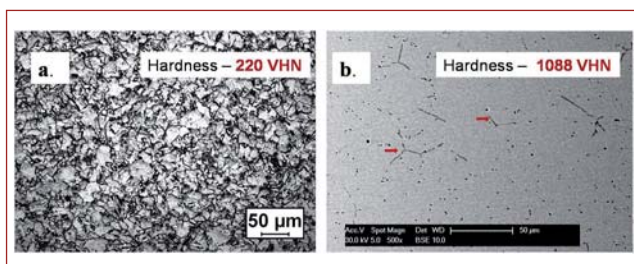


Fig. 2 Metallographic characterization of (a) alpha and (b) sigma phase

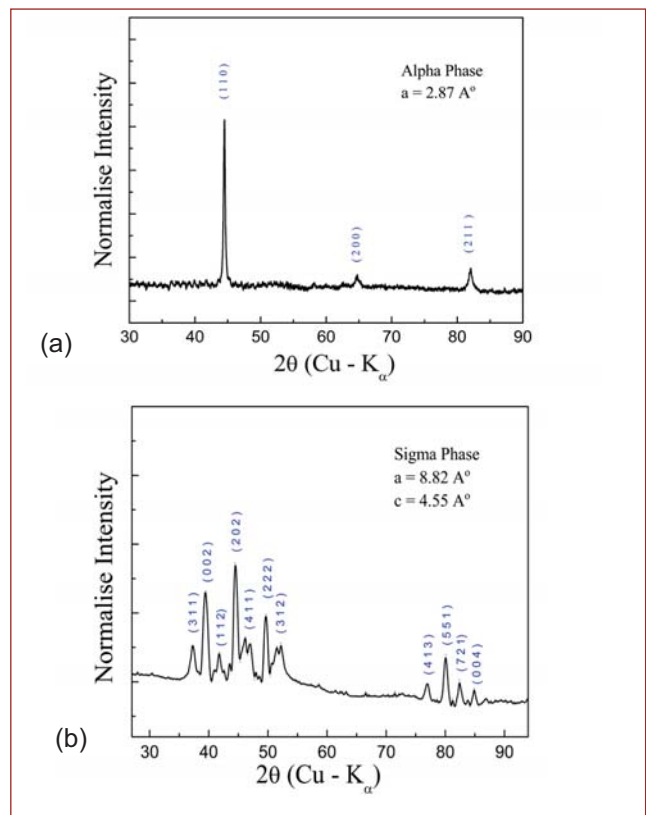


Fig. 1 XRD characterization of (a) alpha and (b) sigma phase

that the measured transformation temperature is higher than the previously reported value by about 40 °C. It is also seen that σ to α phase transformation is found to be irreversible; since the reverse transformation did not occur during cooling (Pink line in Figure 3). The average enthalpy of $\sigma \rightarrow \alpha$ phase change is estimated to be 3.6 kJ/mole, at 10 K min⁻¹ heating rate.

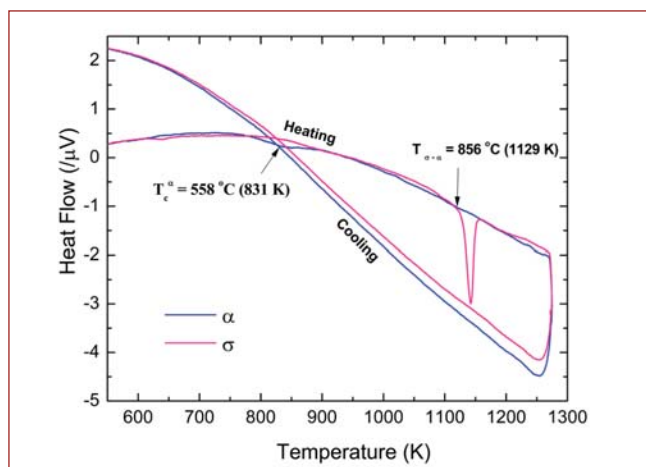


Fig. 3 DSC thermograms of alpha and sigma phases in $\text{Fe}_{55.4}\text{Cr}_{44.6}$ alloy

VI.18 Microstructural Evolution in Multiprincipal Elemental Cr-Fe-Nb-Ni-V Alloy

Multiprincipal elemental alloys commonly referred to as high entropy alloys (HEA) are a relatively new class of materials gaining large interest in recent times due to their new microstructures, excellent mechanical and corrosion properties. High entropy alloys, though typically contain five or more elements in a near equiatomic ratio, form a simple/ordered solid solution, which can be predicted empirically by considering the thermodynamic parameters like entropy and enthalpy of mixing, differences in the atomic size, valence electron concentration (VEC) and electronegativity.

The present study reports the microstructural evolution in an equiatomic high entropy Cr-Fe-Ni-Nb-V alloy consisting predominantly of bcc elements, synthesized by multiple vacuum arc melting. Analysis of XRD pattern of the as cast alloy in Figure 1, showed that the predominant phase is a hexagonal close packed (hcp) Laves phase of CrNiNb type with a lattice parameter of $a = 0.46918$ nm and $c = 0.87082$ nm. Based on the microchemistry, the alloy in as cast and aged condition (1100°C) showed a microstructure consisting of Nb rich grains (matrix) surrounded by Nb lean phase (Figure 2). TEM studies confirmed that Nb rich grains are Laves phases and the Nb lean, Cr rich phase has a fcc structure (Figure 3). The average hardness of the alloy was measured to be high about 1400 VHN, the high strength, could be due to the presence of the intermetallic Laves phase. XRD and microstructural analyses confirm that the microstructure with predominant Laves phase is stable upto 1100°C .

The observation of a predominant hcp phase is in contrast to the prediction of a bcc solid solution through empirical calculations. But a higher calculated VEC

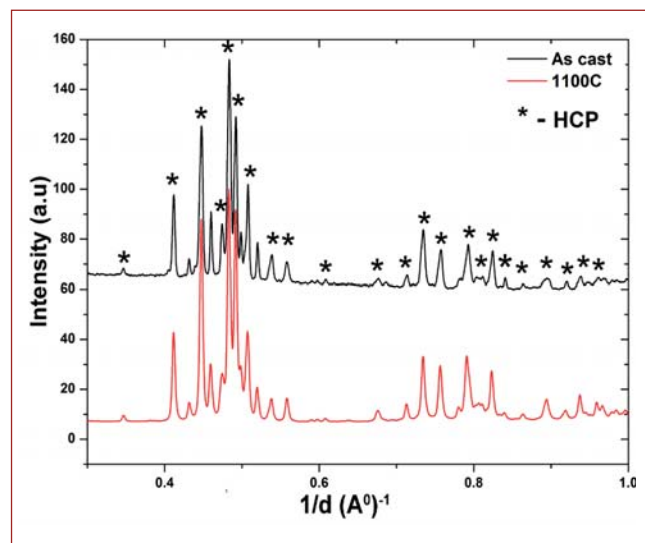


Fig. 1 XRD patterns of the Cr-Fe-Ni-Nb-V alloy in as cast condition and after aging at 1100°C showing the predominant Laves phase

value of 6.8 suggests the possibility of a small amount of intermetallic phase. It is known that the formation of intermetallic phases is strongly related to the d-electron bonding of the elements in an alloy. Hence, another parameter called average d-orbital energy level of the alloy (\overline{M}_d), a concept that generally predicts the formation of topological alloy close packed (TCP) phases in Ni, Co and Fe based superalloys was calculated, since this parameter is more suitable for alloys containing higher amount of transition elements. The \overline{M}_d value for the alloy is calculated as 1.46, which is higher than the value of 1.09 identified as the threshold for formation of TCP phases in large number of high entropy alloys containing transition elements.

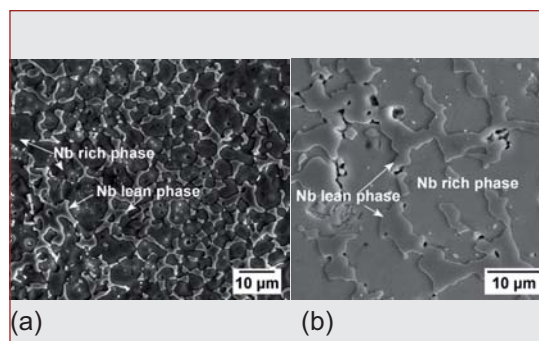


Fig. 2 SEM micrographs of Cr-Fe-Ni-Nb-V alloy in (a) as cast condition and (b) after aging at 1100°C showing the Nb rich Laves phase surrounded by Nb lean phase

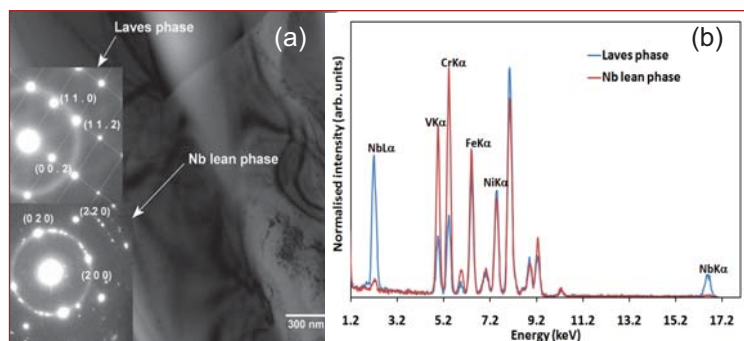


Fig. 3 (a) TEM micrograph of the as cast Cr-Fe-Ni-Nb-V alloy with insets showing the SAD patterns from Laves phase and fcc phase along $[-11.0]$ and $[100]$ zone axis respectively (b) EDX spectra showing Nb enrichment in Laves phase and Nb depletion in fcc phase respectively

VI.19 High Temperature Mass Spectrometric Studies on U-19Pu-6Zr

Vaporisation behaviour and thermochemical properties of the fuel are very essential to understand the fuel behaviour during irradiation and under transient conditions. Vaporisation studies help in understanding the nature and composition of vapour phase over the fuel and to determine its thermodynamic stability. In the present work, results of Knudsen effusion mass spectrometric studies (also known as High Temperature Mass Spectrometry) on the fuel composition proposed for Indian fast reactors are presented. The experiments were conducted using a home built Knudsen effusion mass spectrometer housed inside an argon atmosphere glove box. U-Pu-Zr alloy corresponding to the composition U-19 wt%Pu-6wt%Zr was taken in an yttria Knudsen cell fitted with yttria lid (channeled orifice 0.7 mm diameter) and this was placed in an outer cup and lid made of tantalum. A hole drilled at the bottom of the tantalum cup serves as a black body source for measuring temperature using an optical pyrometer. The tantalum cup containing the sample was heated by electrons emitted from two tungsten filaments encircling it. The vapour effusing from the Knudsen cell was ionised by electron bombardment (electron energy = 30 eV; emission current = 100 μ A) and the ions produced were mass filtered using a quadrupole mass analyser and their intensities were measured using a secondary electron multiplier operating in pulse counting mode. The temperature was measured by focusing the pyrometer into a black body hole provided at the bottom of the cup. The temperature of the sample was slowly increased in steps of 50 degree and at each temperature above 1400 K, the mass scanning was carried out looking for shutterable peaks. Pu⁺ and PuO⁺ were the ions observed in the mass spectra of the equilibrium vapour (from 1650 K onwards) over the alloy. The ion intensities of PuO⁺ vanished quickly as the sample was heated further. The ion intensities of ²³⁹Pu⁺ were measured as a function of electron energy (to obtain ionisation efficiency curve) to deduce its appearance energy. Temperature dependence measurements were carried out in the range 1661-1763 K. In a given run, the first temperature was maintained for about one hour and the constancy of ion intensities during the period ensured the chemical equilibrium inside the Knudsen cell. The temperature changes were effected in cyclic fashion to check for the reproducibility

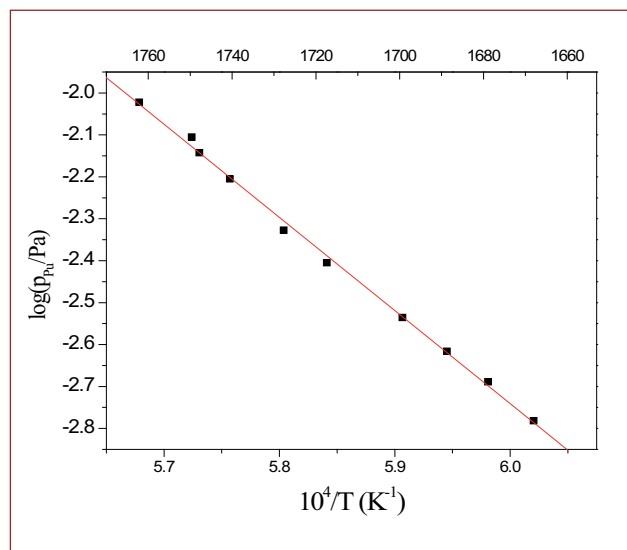


Fig. 1 A typical plot of $\log(p_{Pu}/Pa)$ versus $1/T$ (K^{-1})

of the ion intensities. Overall two runs of temperature dependence of ion intensities of ²³⁹Pu⁺ were carried out. Pressure calibration experiments were carried out by taking pure silver in an alumina liner kept inside the same yttria Knudsen cell that was used for U-Pu-Zr measurements.

From the ionisation efficiency curve of ²³⁹Pu⁺ the appearance energy was derived by linear extrapolation method. The value of 6.3 ± 0.5 eV thus deduced, agreed well with the value 6.02 eV reported in the literature. From mass, isotopic abundance and appearance energy, the neutral precursors for the ions detected in the mass spectra were ascertained to be Pu(g) and PuO(g). Relative abundance of PuO(g) was less than 4% and its ion intensity vanished quickly with increase in temperature. The mean pressure calibration constant derived from the calibration experiments with pure silver was used to convert the measured ion intensities of ²³⁹Pu⁺ to partial pressures. The data obtained correspond to the liquid alloy as the temperature range of measurements was above the liquidus temperature of the alloy. The pressure-temperature relations were obtained by least squares fitting of individual partial pressure points. A typical plot of $\log(p_{Pu}/Pa)$ versus $1/T$ (K^{-1}) is shown in Figure 1. The mean enthalpy of vaporisation of Pu(g) over the alloy was deduced to be 425.9 ± 12.8 kJ/mol at 1712 K, the middle temperature of the investigation. Partial pressure of Pu(g) over the alloy at this temperature is 4.5×10^{-3} Pa.

VI.20 Studies on Effect of Disorder in Quantum Transport Behavior of Bi_2SeTe_2 Topological Insulator

Bismuth-based chalcogenides such as Bi_2Se_3 , Bi_2Te_3 and their derivative belong to a new class of materials called Topological insulators (TI) in which two dimensional (2D) surface states (SS) exist within the band gap of a 3D bulk crystal. Interestingly, these 2D states are spin polarized, less susceptible to localization, backscattering and are more promising for application in spintronics and quantum computing. However, the 2D contribution is often masked by undesirable excess charge carriers arising on account of the unintentional defects, impurities, anti-site disorders and vacancy states in bulk. Significant efforts have been made to suppress these metallic contributions by adopting different preparation methods, doping or by growing thin films. Here we study the effect of disorder in TI.

Figure 1 shows the magneto-resistance (MR) of the pristine and annealed Bi_2SeTe_2 (BTS) sample at several fixed temperatures from 4.2 to 300 K. At 4.2 K for $B < 2.5$ T the pristine sample shows a clear cusp due to weak antilocalization (WAL) of the surface electrons. However, for $B > 2.5$ T the WAL transforms to a weak localization (WL) where MR reduces with increasing field. For $T \geq 100$ K MR gradually transform to classical B^2 dependence. In contrast, the annealed sample does not exhibit any signature of WL. For $T < 20$ K, it rather depicts a WAL cusp for $B < 10$ T and a parabolic behavior for the higher field ($B > 10$ T). The magnitude of the MR and the parabolic component decreases upon increasing the temperature upto 20 K. Interestingly, the MR measured at 40, 50 and 100 K shows a linear dependence with respect to B.

To get further insights into these features the carrier density (n) and the mobility (μ) are deduced from the resistivity and Hall measurements. Figures 2a and 2b shows the temperature dependence of these parameters. The carrier density increases by a factor of 3 upon annealing whereas the mobility decreases by one order of magnitude. The temperature evolution of these parameters shows a marked difference between the two samples. For pristine sample, n and μ show a decreasing trend initially and at $T < 100$ K, n increases with further decrease in temperature.

In the case of annealed sample they decrease monotonically upto $T \sim 100$ K with decreasing temperature and then it saturates for $T < 100$ K. The theoretical Hikami-Larkin-Nagaoka (HLN) equation describing the localization effect yields good fit to our data as shown in

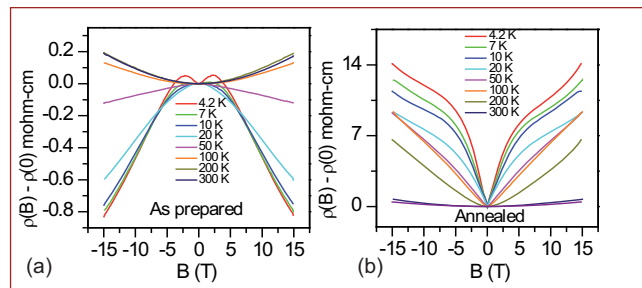


Fig. 1 Temperature dependence of magneto-resistance of (a) pristine and (b) annealed Bi_2SeTe_2 sample

Figure 2c. The phase coherence length deduced from the fits decreases with increasing temperature with two distinct power laws.

Due to the presence of quenched-in disorder in the sample, the contribution of the bulk carriers get reduced at low temperatures by localization. Therefore, transport from the surface carriers, that are immune to localization, is enhanced. The surface carriers of quantum nature coexisting with classical bulk counterpart give rise to interesting features seen in the MR. As the temperature increases the bulk carriers increases due to delocalization and thereby the transport become more classical in nature. The parallel conductance of surface and bulk channels is believed to cause the coexistence of the WAL and the WL in the pristine sample. Whereas the absence of WL and the presence of linear MR in annealed sample is due to the increase of the disorder that alters the ratio of the surface to bulk carriers. These studies show that the defects play a vital role in revealing the coexistence of surface and bulk carriers and their interactions.

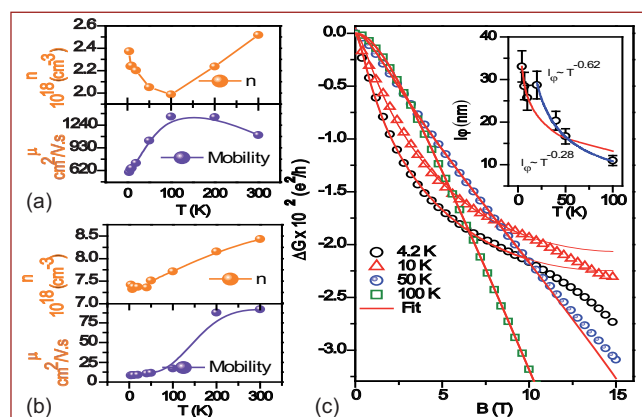


Fig. 2 (a) and (b) Temperature dependence of carrier density and mobility of pristine and annealed sample, respectively. (c) Theoretical fit for the conductance data of the annealed sample. Inset shows the evolution of the coherence length with T

VI.21 High Pressure X-Ray Diffraction and Raman Studies on Mixed Rare Earth Sesquioxide Ceramic System : $(\text{Eu}_{1-x}\text{Ho}_x)_2\text{O}_3$

Rare earth oxide ceramics have applications in nuclear reactors because of their high thermal neutron absorption coefficient. Structural stability and phase diagram of these oxides are of technological interest. Depending on their cationic radii, rare earth sesquioxides (RES) exist in three different polymorphic modifications such as type-A(hexagonal), type-B(monoclinic) and type-C(cubic). Although the cation radii increases in the sequence $C \rightarrow B \rightarrow A$, the molar volumes are observed to be decreasing in the same sequence. Considering this fact, a structural sequence of $C \rightarrow B \rightarrow A$ is expected to occur under high pressure. But the medium size RES do not obey this sequence and instead go through a direct $C \rightarrow A$ transition. The reason is not well understood.

In this study, the oxide samples of $(\text{Eu}_{1-x}\text{Ho}_x)_2\text{O}_3$ ($0 \leq x \leq 1$) are prepared by chemie douce method. Angle dispersive X-ray diffraction measurements confirmed cubic bixbyite structure with space group $Ia-3$, ensuring complete miscibility of the two components. Rietveld refinement of the diffraction data showed random distribution of the two cations in the rare earth (RE) ion sites. Raman spectroscopic measurements revealed an anomalous mode softening of a low frequency weak band around 232 cm^{-1} with decrease in Eu^{3+} content. This mode disappears for x above 0.8, which coincides with a distinct slope change observed in the RE (24d) positional coordinate. In Figure 1 the change in RE positional coordinate and the softening behavior of 232 cm^{-1} mode are shown, which indicates that the mode disappears exactly where a sharp change in the slope of $x(\text{RE}_{24d})$ versus x is seen. It is speculated that for $0.8 \leq x \leq 1$, Eu

atom is sufficiently displaced away so as not to contribute to any electrostatic interaction responsible for this mode. For $0 \leq x \leq 0.8$ the mode becomes increasingly harder, signifying larger contribution of Eu ion to the interaction.

In addition, in-house HPXRD measurements on monoclinic Eu_2O_3 obtained by heating the cubic phase at 1200°C , showed anomalous lattice compressibility for the HP hexagonal phase. This is characterized by the pronounced hardening of a axis above 15 GPa. The observed incompressible nature of the hexagonal a -axis in the pressure range 15-25 GPa is found to be compensated by doubling the compressibility along the c -axis. Further, HPXRD measurements of $(\text{Eu}_{1-x}\text{Ho}_x)_2\text{O}_3$ are carried out using INDUS-2 synchrotron facility at RRCAT. Major conclusions drawn from our investigation are summarized in Figure 2, which shows the pressure-concentration (P-X) phase diagram up to 15 GPa. The cubic, hexagonal and monoclinic phases along with their crystal structures are marked as I, II, III respectively. The region marked as IV, is the phase boundary between hexagonal and monoclinic structures. The average cationic radius is calculated from the individual ionic radii of Eu^{3+} and Ho^{3+} : $R_r = xR_{\text{Ho}^{3+}} + (1-x)R_{\text{Eu}^{3+}}$. In the region IV, the range of R_r lies within $0.9164 > R_r < 0.9220 \text{ \AA}$. Average ionic radii equivalent to or below 0.9164 \AA prefers a $C \rightarrow B$ transition whereas cationic radii equivalent to or above 0.9220 \AA prefers a transition from $C \rightarrow A$. With an increase in R_r , transition pressure was observed to decrease indicating that the cubic phase becomes increasingly unstable with an increase in R_r . Further studies are in progress to understand the possible mechanisms involved in these phase transitions.

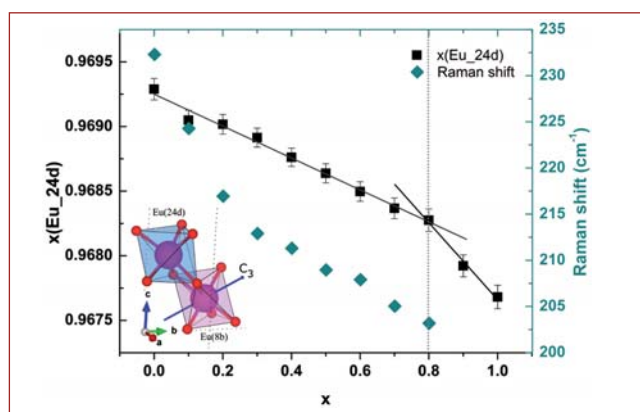


Fig. 1 Change in RE (24d) ion co-ordinate and Raman mode at 232 cm^{-1} . Solid lines represent two distinct slope changes

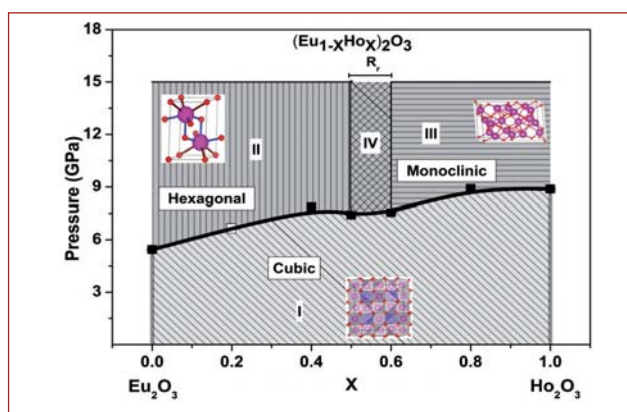


Fig. 2 Pressure Concentration phase diagram for $(\text{Eu}_{1-x}\text{Ho}_x)_2\text{O}_3$

VI.22 Development of Instrumentation for the Study of High Temperature Thermochemical Properties of Materials

Measurement of electromotive force (emf) output from an electrochemical cell without affecting the electrode equilibrium requires an electrometer whose input impedance is in the order of $10^{14} \Omega$. An indigenous electrometer is developed, along with suitable user interface software as a replacement to the expensive commercial electrometer. Special fabrication techniques are adopted to minimize errors due to surface leakage current.

The cell electromotive force varies typically from -1000 to + 1000 mV, which is amplified to a maximum of 10 V. This voltage is converted into a proportional frequency using voltage to frequency converter. In the same way, the temperature signal from K-type thermocouple is fed to an op-amp and instrumentation amplifier with suitable gain so that the maximum output is 10 V. These two signals are transmitted through RS485 line driver to data collection module.

A microcontroller based unit measures the incoming frequency from signal conditioning unit. These frequency pulses are counted for a period of 100 ms. The processor recalculates the actual EMF and temperature from the counts.

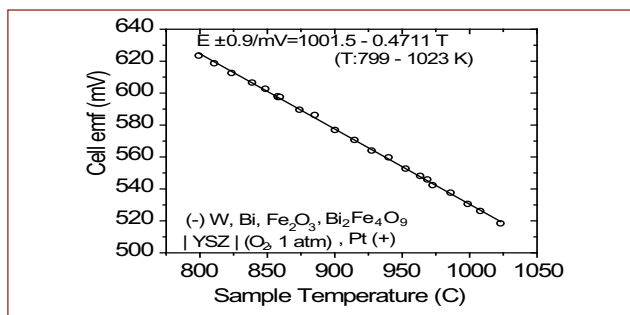


Fig. 1 Graph showing cell EMF as a function of sample temperature

A Graphical User Interface (GUI) developed to acquire the cell EMF and sample temperature, displays in the form of online graph, in gauges and text boxes. The auto scale feature is provided to get the full scale value automatically. The off-line trend of the same can be viewed by a single click as a pop-up window to view a larger data, say overnight run data. The acquired data is saved in a file for later analysis. Typical result of cell EMF is shown in Figure 1. Experiments were conducted for the study of Bi-Cr-O and Bi-Fe-O systems and the results have shown that their performance is on par with commercially available instruments.

VI.23 Studies on Lithium – Steel Chemical Interaction

Liquid lithium (Li-6) is considered for use in the third shut down system of future fast breeder reactors (FBR) as a liquid poison. In this context, identification of a suitable container material compatible with liquid lithium at reactor operation temperature (~823 K) is important.

In order to identify a compatible steel for use in liquid lithium, chemical compatibility study of steel samples such as SS 316 LN, alloy D9, 9Cr-1Mo, oxide dispersion strengthening (ODS) along with pure iron were carried out in liquid lithium at 823 K for various time durations ranging from 250 to 1000 hours. Further, in order to simulate accelerated test conditions, studies were also carried out at 973 K. After equilibrations, the sample coupons were cleaned and characterised by X-ray diffraction (XRD) and SEM/EDX. It is observed from the XRD studies that the pure austenite phase of as received sample partially transforms to ferrite phase on exposure to liquid lithium at 823 K which in turn becomes fully converted into ferrite phase at 973 K. Similar observation was also noticed in the XRD patterns of alloy D9.

Microstructures of SS 316 LN, alloy D9, 9Cr-1Mo, ODS and Fe exposed to lithium at 973 K for 1000 hours were studied and elemental analysis on the surface layer were also carried out. Typical cross sectional SEM image of SS 316 LN equilibrated at 973 K for 1000 hours is shown in Figure 1. The micrograph shows a modified layer with selective removal of material from the surface over a depth of ~ 50 μm . Similar behaviour was seen in other steel samples over depth of ~25 to 50 μm . No such microstructural changes were observed on the surface

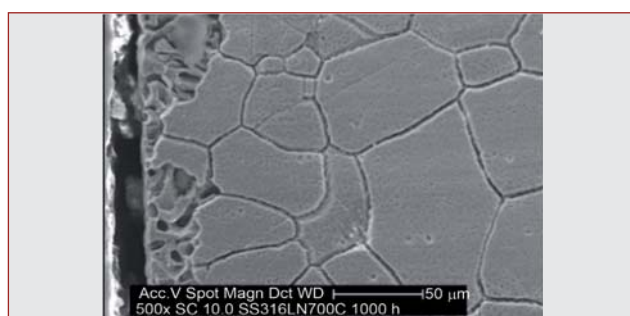


Fig. 1 SEM image of SS 316LN equilibrated at 973 K for 1000 hours

of pure Fe. Elemental analysis showed that the Ni and Cr content in the modified layer of SS 316 LN was 3 and 5 wt% against the bulk concentration of 12 and 18 wt%, respectively. However, in alloy D9 the Cr content in the modified layer was observed to be 11 wt% against bulk concentration of 15 wt%. Selective leaching of Cr was also observed in 9Cr-1Mo and ODS.

The study on chemical compatibility of steel samples such as SS 316LN, D9, 9Cr-1Mo and ODS with liquid lithium carried out at 823 and 973 K revealed significant chemical interaction of liquid lithium with all the steel samples at 973 K for a total exposure time of 1000 hours. The depth of interaction ranges between ~25 to 50 μm from the surface.

VI.24 Synchrotron Studies of fcc-Ti Phase in Magnetron Sputtered Ti/Al Multilayer Thin Films

Artificially modulated thin film multilayer architectures are used in modern technologically important areas like giant magneto resistance (GMR), X-ray reflectivity, nuclear fuel shields and sensors. The present study pertaining to Ti/Al multilayer thin films grown on glass substrates by magnetron co-sputtering technique. Elemental Ti is known to exist in two crystal structures: body centered cubic (bcc, β -Ti, A2) at high temperature (>882°C) and hexagonal close packed (hcp, α -Ti, A3) at low temperature. The first reported occurrence of fcc-Ti was in sputter deposited Ti-Al multi layer thin films by TEM and explained the formation of such metastable phase during TEM sample preparation. Earlier reports also argued that the formation of fcc-Ti was purely an artifact of TEM specimen preparation method rather than an intrinsic property of the synthesized material. However, this report unequivocally establishes the presence of fcc-Ti in the as deposited Ti/Al multilayer thin film, using glancing incidence X-ray diffraction (GIXRD) technique and high resolution synchrotron studies, which is free from the possibility of introducing impurity stabilized artifact during the sample preparation. Also the X-TEM with SAED analysis also used to identify the presence of fcc-Ti phase.

Ti / Al multilayer thin films were deposited on glass substrates in a sputtering system (MECA-2000, France) using high pure Ti (99.99%), Al (99.99%) targets and ultra pure Ar (99.999%) feed gas introduced at a flow rate of 20 sccm, at room temperature. Base pressure of 6×10^{-6} mbar and the deposition pressure of 1×10^{-2} mbar was maintained. Ti and Al layers were deposited using 300 W rf (13.56 MHz) and 400 W dc powered guns, respectively. Both single and dual RF guns were used for depositing Ti. The sequence of deposition has been Glass/ Al/ Ti /Al/...../Ti (30 layers). High resolution synchrotron studies were carried out at Elettra, Italy with an energy of 12 keV (energy resolution of 0.00005), photon flux of 10^{11} photons/sec and a wavelength of 1.0332 Å.

Figure 1 shows the GIXRD patterns of the Ti/Al thin films deposited on glass substrates using single as well as dual guns for sputtering elemental Ti. XRD peaks corresponding to hcp-Ti and fcc-Al have been identified by comparison with JCPDS of respective phases and marked in the figure as (hkl) Ti-H and (hkl) Al-F, respectively. Interestingly, in all the XRD patterns, the strongest peak is observed from (10.0) plane of hcp-Ti as against (10.1) for polycrystalline materials taking structure factor into consideration. This is indicative of preferential orientation in these films. Although conventional XRD does not provide complete information about orientation of the crystallites, it can be stated that majority of the hcp-Ti crystals are orientated such that the prismatic (10.0) Ti-H type of planes are parallel to the film or substrate surface (Type I) while second major set of hcp-Ti crystallites have their basal (00.2)Ti-H type of planes lying parallel to the substrate surface (Type II). On the other hand, Al peaks are relatively weak; one of which (111) F-Al overlaps with hcp-Ti (00.2)Ti-H while another corresponds to (220) F-Al. Both these peaks are comparable in intensity. As against the XRD pattern from the single gun case, the

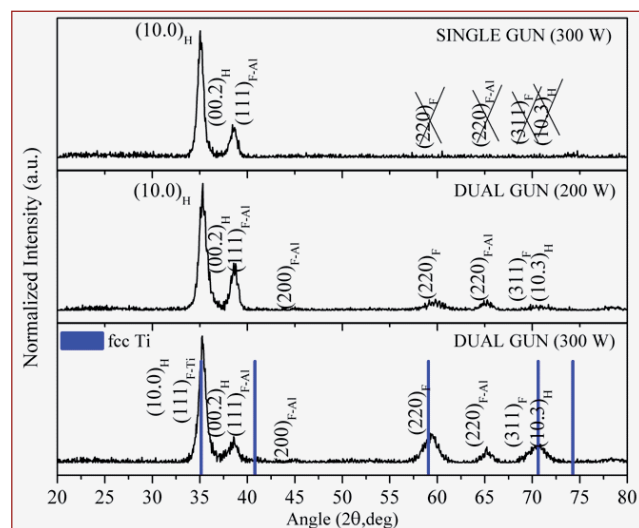


Fig. 1 GIXRD of Ti-Al multilayer thin films

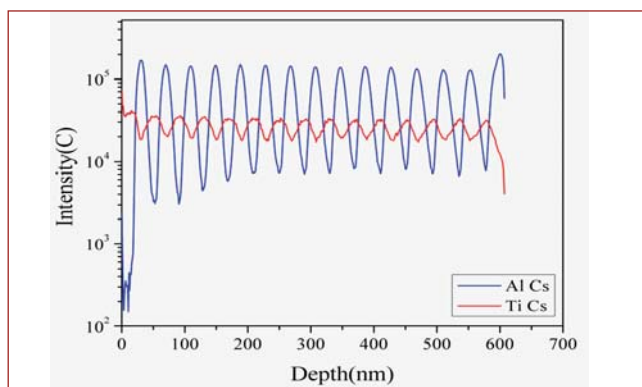


Fig. 2 SIMS of Ti-Al multilayer thin film

films deposited using dual guns for Ti, show an additional peak at 59.25° which does not match with any known reflections from hcp-Ti, bcc-Ti, fcc-Al or even their intermetallics. This peak is attributed to a metastable phase of titanium (fcc-Ti). It is also observed that as the dual rf power is increased from 200 to 300 W, the relative intensity of the XRD peak at 59.25° corresponding to the fcc-Ti phase increases. This suggests that the appearance of the fcc-Ti phase is dependent on the type of gun and power used for Ti deposition. Dual gun as well as higher power increases the Ti sputtering rate resulting in an increased deposition rate of Ti which is believed to be responsible for the presence of fcc-Ti phase. The crystallite size was calculated using the Scherrer's formula for the Ti and Al phases and found to be of the order of ~ 10 nm indicating the nanocrystalline nature of these multilayer thin films. Figure 2 shows the typical SIMS profile of Ti/Al multilayer thin film. A periodicity is visible with alternate layers of Ti and Al.

Figure 3a shows a bright field TEM image of the Ti/Al multilayers. As usual, alternate bright (Al) and dark (Ti) layers are seen. Dark field imaging was independently carried out on this region using first the diffraction spot corresponding to (220) of fcc-Ti and then (00.2) of hcp-Ti. These dark field images were coloured green (fcc-Ti) and blue (hcp-Ti), respectively and merged into one figure which is shown as Figure 3b. In this manner, the regions corresponding to fcc and hcp phases of Ti can be located. Similarly, diffraction spot corresponding to (00.2) of hcp-Ti overlaps with that from (111) of fcc-Al. As a result, certain areas in Al layers also are coloured blue or green. However, by comparing with the BF image in Figure 3a the layers of Ti and Al can easily be demarcated, since no intermixing of the layers have been observed. Hence by concentrating on the Ti layers alone, the hcp and fcc Ti phases are clearly identified. Therefore, under the dual beam deposition condition for Ti, the Ti layers are composed of a hcp-Ti and fcc-Ti, both of which are stable at room temperature.

Figure 4 shows the synchrotron GIXRD with an incident

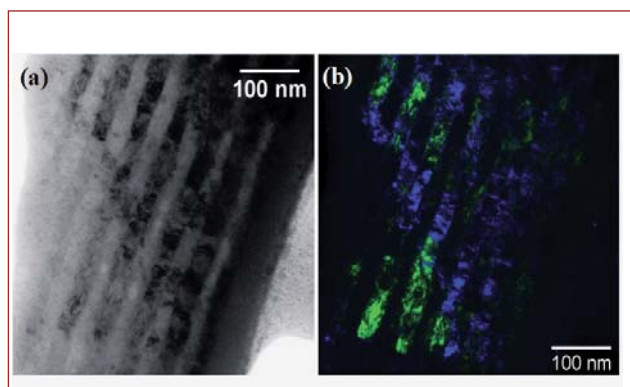


Fig. 3 X-TEM of Ti-Al multilayer thin film, (a) BF mode and (b) DF mode fcc (green) and hcp (blue) in color

angle of 0.5° and $\psi=60^\circ$ exhibited all necessary peaks for fcc-Ti phase at lower angles. This suggests that fcc-Ti phase do exist in the magnetron sputtered Ti/Al thin films. There is tendency of preferential orientation of the Ti nanocrystalline grains in these multilayer thin films under all conditions of depositions that are discussed in this article, such as the number of guns used for Ti depositions or the power used. An fcc-Ti phase, which is stable in the film at room temperature and is certainly not an artifact of TEM sample preparation as its signatures were observed in XRD as well, forms alongside the hcp-Ti phase only when more than one rf guns are used for its deposition. Ti fcc-phase can be stabilized, by the underlying fcc-Al with which it has a lattice mismatch of only about 9%. This may be understood as follows: the usual ABAB stacking of the hcp crystal structure can be faulted to ABCABC kind of crystal structure as in the case fcc lattice under the influence of Al. Recent studies showed that in Ti base Al systems, the stacking fault energy of hcp-Ti is greatly reduced by the addition of Al. Hence it is likely that during the initial stages of Ti growth when Al coverage is much higher than Ti, a fcc stacking in Ti as in Al is promoted. In short, we can say that under the joint influence of high arrival rate Ti adatoms and the Al underlayer, the fcc-Ti phase is stabilised.

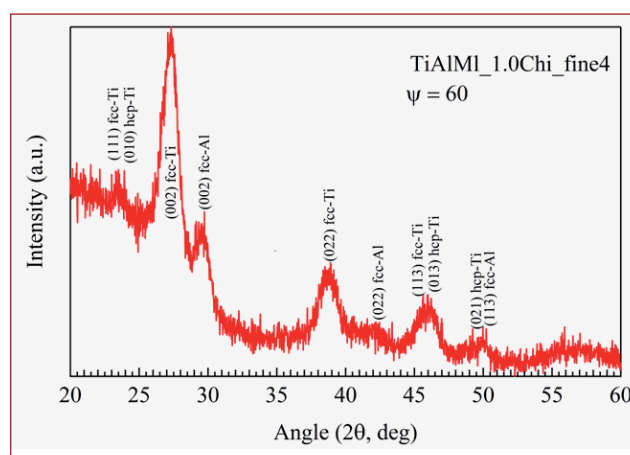


Fig. 4 Synchrotron XRD of Ti-Al multilayer thin films

VI.25 Studies on ω Phase Formation Induced by Compositional Instabilities in V-Ti Alloys

V-Ti based alloys have emerged as the potential candidate for many advanced engineering applications e.g. first wall blanket for fusion reactors, alternative energy technologies and hydrogen storage. However, the phase transformation behavior of these alloys is not completely understood and even the binary V-Ti phase diagram is still debated. The system becomes even more complicated with the addition of Cr as a ternary component. Thermodynamic calculations indicate that within a certain composition range in the V-Ti system, a prominent miscibility gap exists and the propensity for phase separation decreases with the addition of Cr in the binary system. As a result of the chemical fluctuation, the local chemistry changes which subsequently promotes the nucleation of different metastable phases. In the present context, it is worth mentioning that phase separation in an immiscible system could occur either through nucleation and growth or spinodal decomposition mechanism. Both of these phenomena have their own characteristic features. In the case of nucleation and growth, the mechanism depends on long range diffusion process and hence the formation of precipitates with fixed composition and sharp incoherent interface is expected. In contrast, spinodal decomposition is governed by the development and growth of composition fluctuation wave and is governed by short range uphill diffusion. Naturally, the interfaces between two such spinodally decomposed phases are expected to be coherent and quite diffuse. Both these mechanisms can be distinguished by studying the early stages of the phase separation and require detailed microstructural and microchemical investigations. Present work deals with the phase separation and microstructural evolution studies of binary V-Ti alloy. Alloy with a nominal composition of V-50Ti has been synthesized in a vacuum arc melting unit and subsequently heat treated as per requirement. Z-contrast and phase contrast microscopy confirmed the phase separation in both of these alloys. Energy filtered TEM (EFTEM) micrograph confirms the presence of a chemical segregation in equiatomic V-Ti alloy where the modulation length in the as-melt condition was measured as 4-5 nanometres. However, after heat treatment it is found that the fluctuation wave with modulation length ~ 18 -20 nanometres is getting stabilized in the alloy as shown in Figures 1a to 1d (For both the elements the modulation length measured is as ~ 18 -20 nanometres). The chemical segregation propagates along $\langle 111 \rangle$

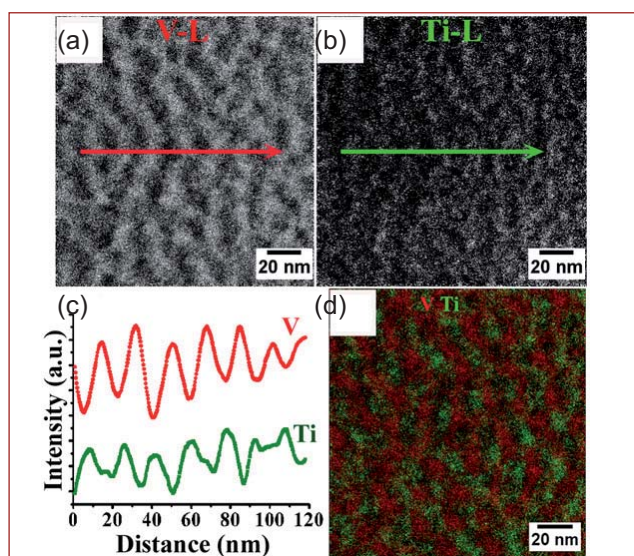


Fig. 1 (a) Vanadium EFTEM map, (b) titanium EFTEM map, (c) compositional fluctuation of V and Ti in the region shown in a and b. (d) EFTEM color composite showing the relative distribution of V and Ti in the phase separated domain of a heat treated V-50Ti alloy specimen

which is an elastically soft direction for *bcc* structured system. Moreover, the dark field imaging as well as the phase contrast microscopy along the phase separated domains confirms the presence of deformed hexagonal zones of ω phase (Figure 2). The interface between the ω and the *bcc* phase is almost coherent in nature showing a gradual change over 6-7 atomic layers for complete structural transformation. In light of the present study, it can unambiguously be stated that in the case of binary equiatomic V-Ti alloy, a phase separation reaction dominated by spinodal decomposition takes place. It can further be concluded that this phase separation in the *bcc* phase acts as a precursor for the ω precipitation.

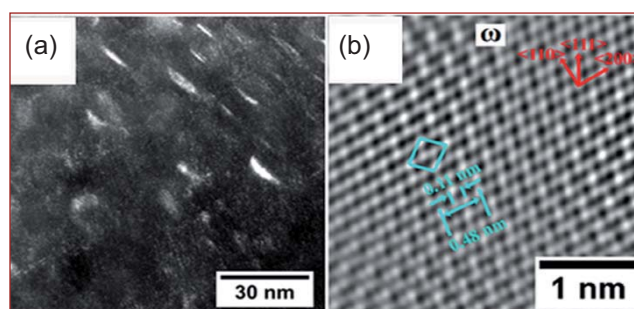


Fig. 2 (a) Dark field micrograph showing the distribution of the ω particles along one of the phase separated arms and (b) HRTEM image showing one such partially collapsed ω domain

VI.26 Probing Sulphur Speciation in Sea Water Exposed Concretes using Raman Spectroscopy

Concrete structures of nuclear reactors using sea water as coolant are continuously being exposed to harsh marine environment. This leads to extensive biochemical corrosion induced damage of these structures. Improving resistance of concrete against bio deterioration is one of the important aspects in long term reactor operations. Flyash reinforced concretes are known to possess better resistance to corrosion in view of their superior mechanical strength as compared to normal concrete. Further improvement in corrosion resistance, especially under harsh marine environments, is being brought about by selective nano phase modification of flyash concrete using nano titania and nano calcium carbonate. Related structural changes due to nanophase modification and changes on account of sea water exposure (SWE) provide important inputs in understanding concrete durability. Optical techniques like Raman and Infrared (IR) are ideally suited to study the associated micro-structural changes of nanophase modified concretes upon SWE.

The present study is aimed at following the micro-structural changes in concrete associated with prolonged SWE using Raman and IR spectroscopy. Measurements have been carried out on flyash concrete (FA), flyash concrete reinforced with calcium carbonate nanoparticles (FAC), with titania nanoparticles (FAT) and with both calcium carbonate and titania nanoparticles (FATC) on both as cast and 365 days sea water exposed samples. IR measurements revealed expected phonon features for all the four types of concrete prior to SWE. It was interesting to note that sea water exposed FAC, FAT and FATC revealed white micron sized particulates in clusters on the surface of the concrete (Figure 1). Raman measurements on these particulates showed sharp well defined intense features peaked at 153, 219 and 472 cm^{-1} indicative of presence of elemental sulphur (Figure 2). Sulphur speciation and colonisation during sea water exposure indicates the onset of bio deterioration in concrete. Presence of sulphur is attributed to the chemical oxidation of sulphides present in concrete. Sulphur oxidizing microbes (SOM) present in sea water is said to further oxidize sulphur to sulphuric acid, which is the main cause of bio deterioration of concrete.

The fact that such clusters of sulphur are absent in FA indicates that all the sulphur formed has been entirely consumed/attacked by SOM converting it to sulphuric acid. Meanwhile for the same period of exposure, the

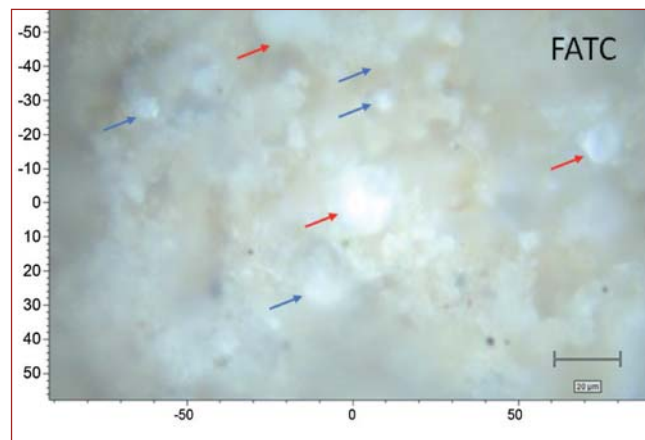


Fig. 1 Optical micrograph showing sulphur particles on sea water exposed FATC concrete. Red arrows show fully transformed sulphur particles while blue arrows point to partially transformed ones

surfaces of nanophase modified FA concrete (FAC, FAT and FATC) still show the presence of elemental sulphur, clearly implying that these surfaces are more resistant to attack by the SOM. The presence of sharp well defined satellite features at 186, 247 and 437 cm^{-1} along with main modes (Figure 2) is indicative of a structural transformation of sulphur that occurs just before the onset of bio-oxidation of sulphur to sulphate by SOM.

The present work thus provides excellent and direct evidence that nanophase modification of flyash concrete has indeed improved the resistance of the sea water exposed concrete towards microbial attack.

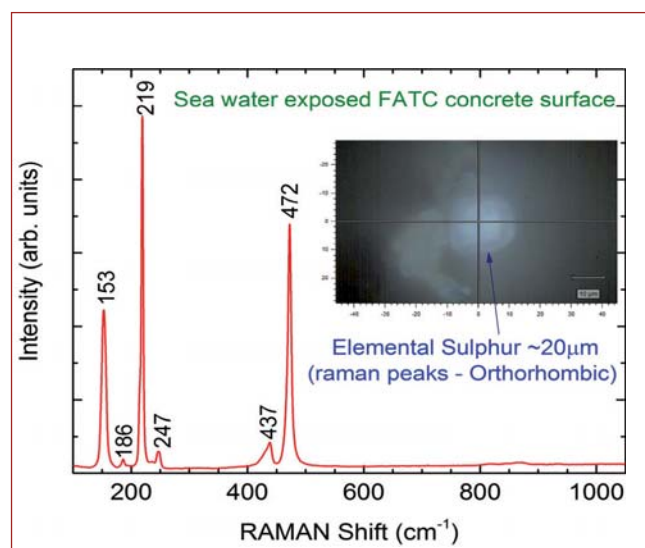


Fig. 2 Raman spectrum of sulphur particle on sea water exposed surface of FATC concrete

VI.27 Helium Aggregation in Helium Ion Irradiated Thorium Oxide

The radiation tolerance of actinide fuel materials is of primary concern for the design of nuclear reactors with long operating lifetimes. In nuclear fuel material, fission gas induced swelling is one of the major concerns. Among fission gases, helium is the lightest one and it can diffuse substantially in materials. Thorium oxide is one of the popular nuclear fuel materials which exhibit better thermo-physical properties. In literature, it is predicted that helium diffusion can occur only in the presence of Th-vacancy and it may lead to helium aggregation causing failure of the thorium oxide fuel.

In this context, it is interesting to study the behaviour of helium in the presence of vacancies. During ion irradiation, a large amount of vacancies are produced and hence, the study of helium aggregation behavior is investigated by irradiating ThO₂ with 100 keV helium ions.

The thorium oxide pellets were irradiated with 100 keV He⁺ ions upto ion fluence of 1×10¹⁷ ions/cm² and the projected range is 340 nm (from SRIM calculations). The damage at the projected range is 3.85 dpa (for the ion fluence of 1×10¹⁷ ions/cm²).

GIXRD measurements were carried out at an incident angle of 3° which probes ~184 nm. In He⁺ ion irradiated sample, additional peaks were seen (as shown in Figure 1). It is attributed to lattice expansion in ThO₂ and the expansion is found to be 1.07%. The HRTEM image of He⁺ ion irradiated ThO₂ sample shows regions with dark contrast, which are absent in the as-prepared sample (Figure 2) and magnified view of a dark region is shown in the inset. Three lines A, B and C in the inset were analyzed using intensity profiles, where Line B alone passes through the dark region. Some of the peaks in Line B are shifted (indicated by an arrow). This lattice

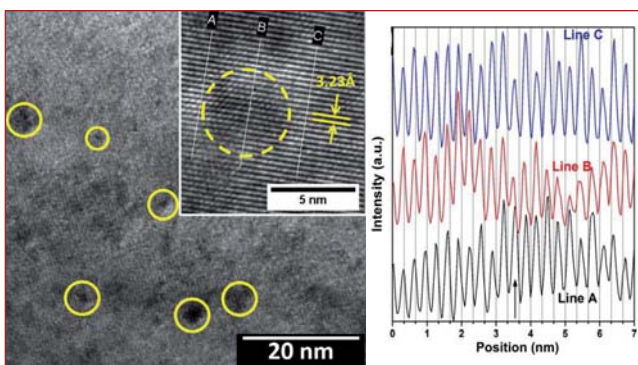


Fig. 2 The HRTEM image of He⁺ ion irradiated ThO₂ sample showing the dark patches. The line profile across lines A,B,C in the inset of HRTEM image, showing lattice expansion in marked position

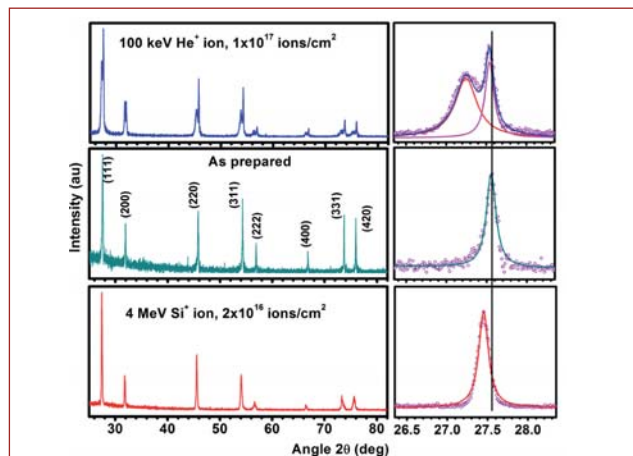


Fig. 1 The GIXRD patterns of He⁺ ion irradiated, as-prepared and Si⁺ ion irradiated thorium oxide

expansion (1.07%) could be due to either accumulation of helium and/or defect and defect clusters. The GIXRD pattern of 4 MeV Si⁺ ion irradiated ThO₂ sample (damage 3.69 dpa) shows the lattice expansion of 0.05% which is only due to defect clusters and so defect clusters does not produce the observed expansion of 1.07%.

The lattice expansion and the possibility of He aggregation were studied using DFT calculations. The He atoms are introduced in the octahedral interstitial sites (energetically favoured site) in fcc lattice of ThO₂. The total energy is calculated and given Figure 3. It is found that a lattice expansion of 1.09% is possible when the helium concentration is 33 at%. In the presence of He⁺ ion induced Th-vacancies, the barrier height for helium diffusion is 0.10 eV and it gives rise to helium atom aggregation and ordering in octahedral interstitial sites. Helium aggregation and ordering takes place in isolated nanometric regions of thorium oxide upon helium ion irradiation and it leads to the lattice expansion. The expansion is confirmed with both experiments (GIXRD and TEM) and DFT calculations.

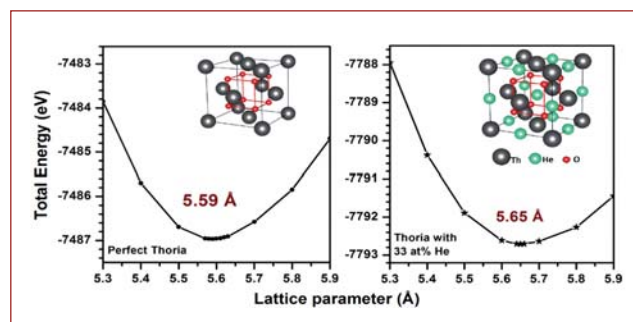


Fig. 3 The plots of total energy versus lattice parameter of perfect thorium oxide and with 33 at% helium

VI.28 Alloying of Metal Nanoparticles by Ion-beam Induced Sputtering

Ion-beam sputtering (IBS) technique has been utilized for controlled synthesis of metal alloy nanoparticles of compositions that can be tuned. Analysis of various experimental results reveals the formation of alloy metal nanoparticles. Surface-plasmon resonance (SPR) positions and observed shifts of Ag Bragg angles in X-ray diffraction pattern particularly confirm formation of Ag-Cu alloy nanoparticles on silica glass. Sputtering induced nano-alloying mechanism has been discussed and compared with thermal mixing of Ag and Cu thin films on silica glass. Compositions and sizes of alloy nanoparticles formed during IBS processing are found to greatly exceed the values of thermal mixing. Synthesizing alloy nanoparticles beyond the miscibility range is particularly important due to their interesting physical properties with many applications.

Schematic representation of the IBS experiments is shown in Figure 1. A Cu foil was placed at the centre of the Ag foil. These foils were irradiated by 100 keV Ar ion-beam with a fixed ion dose ($1 \times 10^{17} \text{ cm}^{-2}$) at normal incidence. Scanned ion-beam of area $\sim 1 \text{ cm}^2$ over targets were used to achieve required sputtering in a high vacuum chamber ($\sim 10^{-7} \text{ mbar}$). Sputtered Ag and Cu atoms were collected on silica-glass substrates kept at an angle of 45° with respect to the target foils.

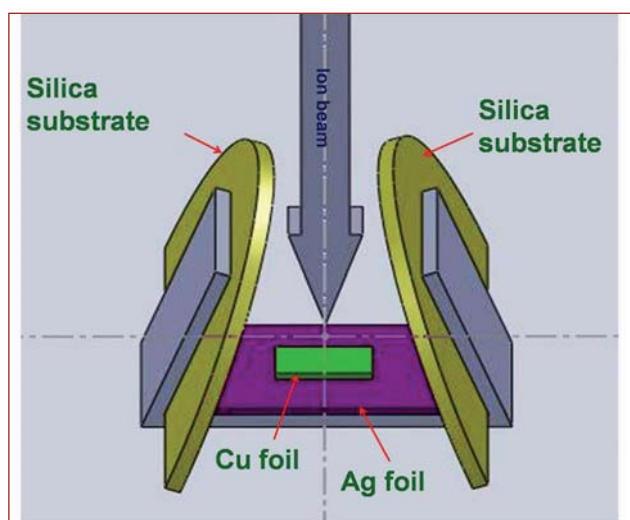


Fig. 1 Schematic representation of IBS depositions of Ag and Cu atoms on silica glass substrates

The amount of Cu and Ag atoms sputtered has been controlled by varying the area of the Cu foil. Depending on the area of Cu foils, large to small, samples prepared are named as L, M and S, respectively. For thermal mixing studies, Ag/Cu thin films of thickness 70 nm each were deposited on silica-glass substrates. Thermal annealing of these samples was carried out in vacuum ($\sim 10^{-6} \text{ mbar}$) at 400°C up to 2 hrs for the mixing to take place.

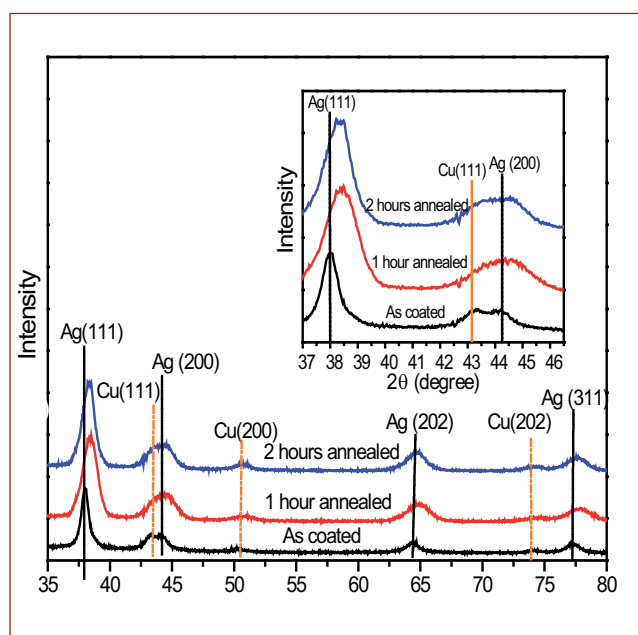


Fig. 2 XRD pattern of Ag/Cu films on silica-glass substrates, before and after thermally annealing in high vacuum at 400°C , are displayed. Shifts of Ag (111) peak on annealing are shown in the inset for better clarity

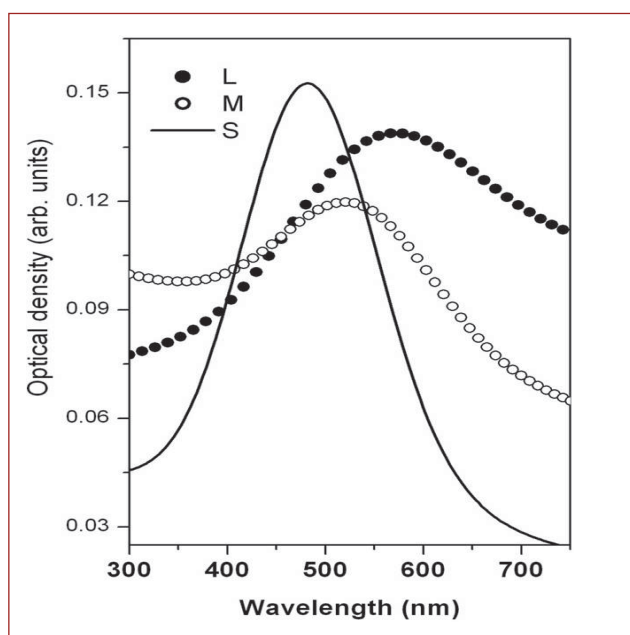


Fig. 3 Optical absorption spectra of IBS deposited Ag/Cu on silica-glass substrates. With increase of the exposure area of Cu foils to the Ar ion-beam, red shift of SPR peak has been observed

X-ray diffraction patterns of IBS deposited and thermally annealed samples have shown corresponding diffraction peaks belonging to pure Cu and Ag metals. In IBS deposited and thermally annealed samples, effect of alloying has resulted in small shifts of the diffraction peaks with respect to corresponding diffraction positions of pure metals (see Figure 2). Changes of the lattice parameters due to the nano-alloying have been calculated from the observed shifts of the diffraction peaks. Formation of the nano-alloy has been further elucidated in subsequent discussions taking clues from optical absorption and electron microscopy (TEM) studies.

During the process of alloying, smaller Cu atoms may replace a fraction of Ag atoms in the crystalline lattice structure of Ag. As a result, lattice contraction of Ag may take place. With the shrinking of lattice spacing, Bragg's law enforces the Ag diffraction peaks to shift to higher 2θ values and Cu diffraction peaks to shift to lower 2θ values. The shift has been used to determine alloy composition using Vegard's law. Sizes estimated (Debye-Scherrer's formula) for alloy nanoparticles of IBS and thermally annealed samples are enlisted in Table 1. Results show that sizes of alloy nanoparticle are increased with the increasing concentration of sputtered Cu atoms in samples S to L, respectively. Sizes estimated from XRD and TEM measurements agree extremely well. Increase in average nanoparticle sizes is likely due to faster diffusion of smaller Cu atoms with increasing Cu concentration.

Figure 3 shows the optical absorption spectra of samples S, M and L. The SPR absorption peak has been observed around 483, 520 and 572 nm for samples S, M and L, respectively. While SPR absorption position of Ag nanoparticles in a silica-glass is around 400 nm, for Cu nanoparticles the SPR absorption appears around 650 nm. As shown in Figure 3, position of the SPR peak has shifted towards higher wavelength with increasing amount of Cu-atoms in the alloy nanoparticles. The optical response for the alloy nanoparticles is thus tunable in the wavelength range of 400 to 650 nm with variations in the alloy compositions.

Rutherford backscattering spectrometry (RBS) study has been carried out to find atomic concentrations of Ag and Cu in the alloy nanoparticle samples. RBS experimental and simulated spectra are shown in Figure 4.

Quantitatively, RBS results show that for a fixed value of Ar ion fluence, total no. of sputtered atoms is of the same order. Calculated ratios of Ag:Cu in IBS samples are shown in Figure 4. This shows Cu atomic % is ~ 21, 26 and 41 in IBS samples S, M and L, respectively. Amount of Cu atoms thus increases with increasing

Table 1: XRD results of IBS deposited Ag/Cu samples and thermally mixed Ag/Cu thin films on silica-glass substrates

Sample history		Ag (111) diffraction positions ($2\theta^\circ$)	Lattice parameters (Å)	Estimated sizes of alloy nanoparticles (from XRD)
Ion-beam sputter deposited	L	39.1	3.9855	32.0 nm
	M	38.9	4.0052	23.0 nm
	S	38.8	4.0152	17.0 nm
Thermally mixed Ag/Cu thin films	As-deposited	38.0	4.0965	No alloying
	Annealed for 1 hr	38.3	4.0656	4.7 nm
	Annealed for 2 hrs	38.4	4.0554	4.8 nm

exposed area of Cu foils during the ion-beam induced sputtering.

A comparison has been made between IBS and thermal mixing of thin films for the synthesis of alloy nanoparticles. The study shows that the non-equilibrium processing is more efficient compared to thermal equilibrium synthesis. Alloy compositions and sizes of nanoparticles thus formed during IBS have been found to exceed far from the values of thermal mixing. In general, the approach followed here with an example of Ag-Cu system would enable to prepare alloy nano-systems of other poorly miscible metals as well.

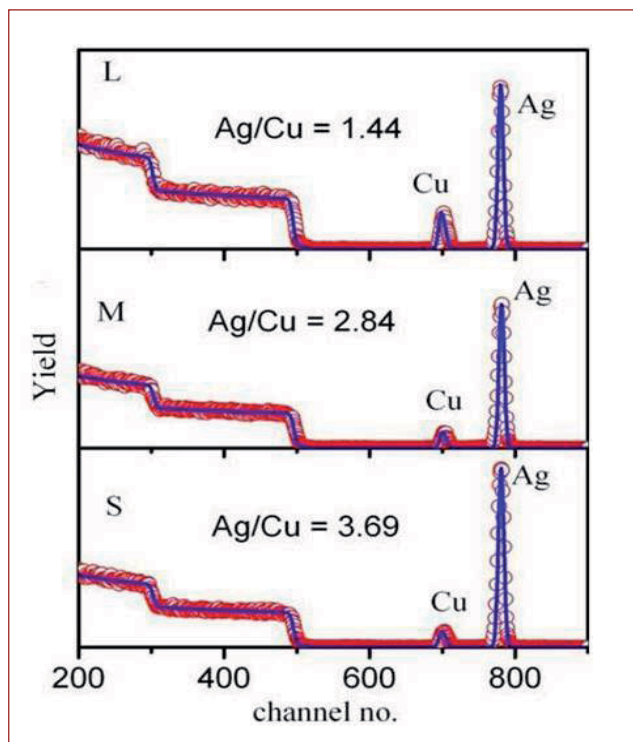


Fig. 4 RBS spectra of IBS deposited Ag/Cu on silica-glass substrates. Red symbols are data points and thick blue line is SIMNRA fitted graph

VI.29 Calibration of In-Vivo Monitoring System using Indian BOMAB Phantom and Validation using ICRP Voxel Phantom

Calibration of in-vivo monitoring systems is an important part for the estimation of internal dose. It is essential to use state of art phantoms which closely resemble the subject being counted. BOMAB phantom is the internationally accepted standard for the calibration of in-vivo monitoring systems like wholebody counters which are being used for the measurements of high energy photons (fission and activation products). The calibration factor obtained is a function of the subject's body dimension, which varies with the ethnic group. BARC has recently developed an Indian BOMAB phantom which is an approximate representation of the human subject. A realistic adult Voxel (volume element-mathematical) phantom was developed by ICRP from CT images of a deceased adult male (ICRP-AM) for dosimetry and simulation purposes. A study was carried out to compare the experimental calibration results of BOMAB phantom with that of simulation using Voxel phantom.

In this study, Shadow Shield whole body counter (SSC) was calibrated with the BOMAB phantom (Figure 1) having a specific radioactive source in the mid axis of each part of the phantom. The SSC consists of a NaI(Tl) of 10.15 cm diameter and 7.6 cm thickness. Measurements are carried out in scanning mode. The sources used were ^{133}Ba (14.5 kBq), ^{137}Cs (37 kBq) and ^{60}Co (6 kBq). The net counts were used to estimate the calibration factor. The simulation was carried out using Monte Carlo method for the SSC consisting of NaI(Tl) detector, shadow shield and the shield around the detector. The SSC model was validated using measured point source efficiencies at different energies. The scanning mode was simulated by averaging the results at 18 static locations considering the ICRP-AM of height 177 cm (Figure 2a). Around 144 organs were modeled using repeated square lattice structure. The ^{137}Cs source was distributed uniformly in 32 soft tissues throughout



Fig. 1 SSC with BOMAB phantom

the body. Pulse height spectra for 662 keV gamma emitted by ^{137}Cs (Figure 3) were simulated at all the 18 locations of the detector along the height of the phantom. In order to simulate the spectrum broadening induced by the detector, Gaussian energy broadening (GEB) parameters, obtained from the measured full width at half maximum of the full energy peak, was used. The calibration factor was estimated from the counts in the photo peak. The overall calibration factor was estimated by averaging the calibration factors at different detector locations. From Figure 3 it is observed that the maximum response is near the thigh. The simulated calibration factor is higher than the measured by 37% which is due to i) axial source distribution in BOMAB ii) Uncertainty in the calibration factor value due to the positional variation of the phantom and iii) geometry variation due to the dimensional differences between the phantom (Figures 2a and 2b). After correcting for these parameters the deviation is reduced to 10% which confirms that the BOMAB phantom with the present axial source distribution is equivalent to the realistic phantom (subject) for high energy photon measurement using SSC.

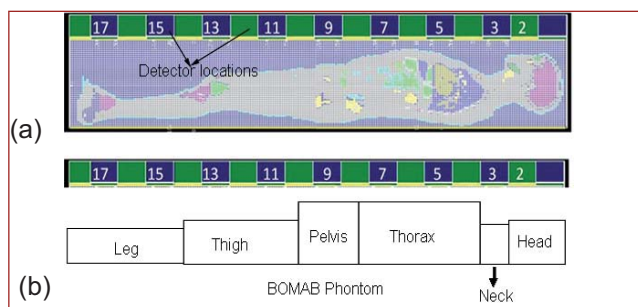


Fig. 2 (a) Modeling of the ICRP-AM phantom with 18 static detector locations and (b) schematic of the BOMAB phantom with the SSC detector locations

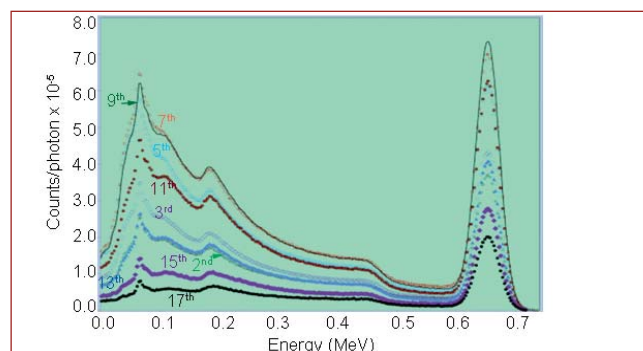


Fig. 3 ^{137}Cs spectra at different detector locations

VI.30 Gross Leak Detection in Fabricated Components Using Infrared Thermography

Infrared Thermography (IRT) is one of the advanced NDE methods that is gaining attention due to its ability to inspect non invasively large areas in short times and as it provides full field images in a non contact nature. It does not involve any hazardous radiations like radiography and hence is safer. IRT started as a condition monitoring tool in electrical and process industries. The advances in sensors, electronics and imaging devices resulted in equipments with better resolution and thermal sensitivity, leading to wider range of application such as materials characterization, tensile deformation studies, online weld monitoring, thermal diffusivity measurements, etc.

In the present study, detection and visualization of leaks in two 6th stage mixer-settler (Figure 1) were carried out during leak testing using infrared thermography. The mixer settler is a critical component used in reprocessing of nuclear fuel pins. Integrity of nozzle weld joint has to be tested for the safe and reliable operation of the component. For achieving vacuum inside the component, it is evacuated with a separate pumping system. The surface temperature variation on the component is monitored using CEDIP Silver 420 infrared camera. Before the component is evacuated a reference thermal image was acquired to record the initial temperature profile. Then the vacuum is created and thermal images were acquired. Sufficient vacuum could not be achieved in the component for investigation using Leak testing. Infrared camera was used to locate the presence of gross leak in the component. Thermal imaging clearly revealed the drop in temperature at the bottom of mixer settler indicating the failure of leak



Fig. 1 6th stage mixer settler

tightness in and around the nozzle joints. During the leak due to significant gas expansion, rapid cooling takes place around the failed weld joints leading to drop in temperature in that region. Compared to the normal temperature, the drop in temperature at the leak region is due to the expansion of the gas which is due to decrease in the frequency of the atomic collision of the gas.

The region where gross leak ($\sim 10^{-2}$) was detected a drop in temperature was recorded compared to other regions revealing the possible defects in the nozzle welds. To validate leak location and leak rate helium sniffer method was used. Figure 2 clearly reveals the region of temperature drop due to Joule-Thomson effect.

Locating gross leak areas by full field thermography testing has been successfully demonstrated for the first time in a large piping network. The study also demonstrates the novel application and extension of IRT as a reliable NDT technique to quickly detect areas of gross leaks in piping network. In the area of leak, a temperature drop is observed. Hence IRT can be used for detecting leaks in the components.

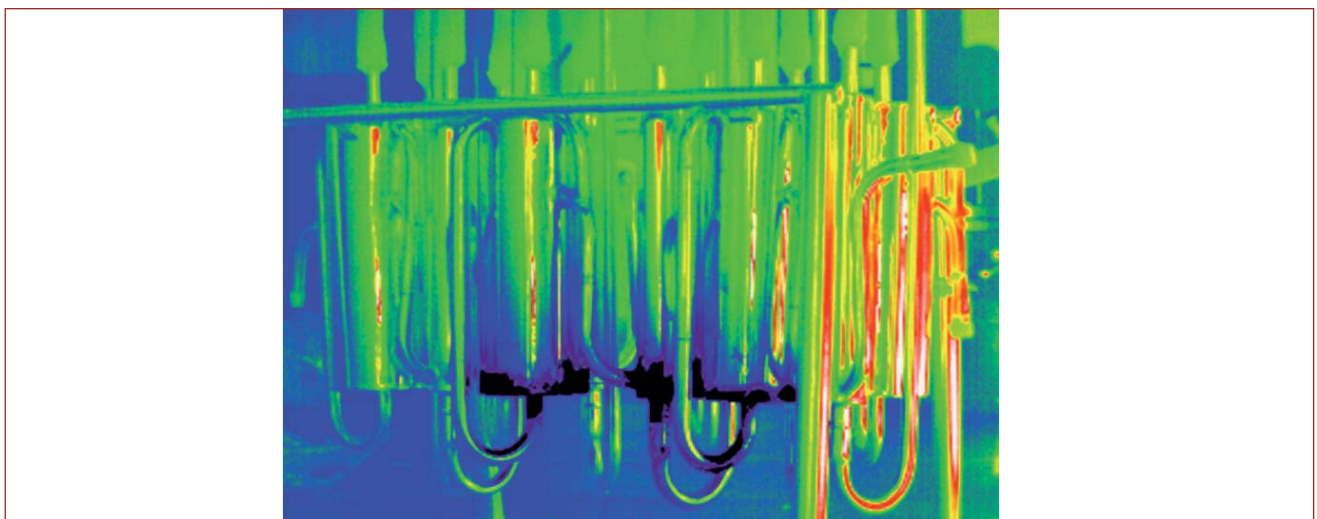


Fig. 2 Thermal images of mixer settler from both sides

VI.31 Characterization of Ultrasonic Transducers for Reliable NDT for Nuclear Critical Application

Ultrasonic non-destructive testing is one of the most widely used volumetric component examination method in material processing industry. An ultrasonic NDT measurement system is basically a linear time-shift invariant system comprising of response functions. One such response function is for the conversion of an electric pulse into a mechanical motion which generates an elastic wave. This is called direct piezoelectric effect. Piezoelectric transducers used in ultrasonic measurement systems for NDT converts electrical energy into mechanical energy (ultrasonic waves) and the converse. The transducer consists of a piezoelectric crystal of desired frequency and dimensions properly enclosed into a sealed housing. When driven by a short, high amplitude voltage pulse, this crystal converts electrical energy into mechanical motion (pulses) which can then travel as elastic waves into the adjacent material. These waves interact with the surrounding environment and the results of these interactions can be received by the same or another ultrasonic transducer and displayed as an electrical signal. Hence the evaluation of the performance of the transducers is very important in reliable measurement of the state of the material. Natural piezoelectric crystals used for fabrication of ultrasonic transducers was quartz. Progress in material science has enabled to create a lot of advanced composites and engineering materials. Examples of composite ceramic piezoelectric materials include lead zirconate titanate, barium titanate, lithium niobate, lead metaniobate etc. Among these, lead zirconate titanate is the most widely used piezoelectric material with the curie temperature of 350 °C. The excitation properties of an ultrasonic transducer is generally characterized as per the ASTM standard E1065. The parameters to be measured for

transducer characterization include, but not limited to, aperture, bandwidth, centre frequency, maximum frequency, near field length, depth of field, focal length, focal size, wave form duration, beam divergence and intensity distribution.

Generally, in the construction of the transducer, the piezoelectric crystal will be diffusion bonded to the metallic diaphragm and electrical terminals will be provided for excitation. Adhesiveness of this bond determines the transmission and emission powers of the transducers. Due to usage and ageing, the bond strength deteriorated and the performance of the transducer got affected. De-bonding serves as source of acoustic noise due to increased ringing in the signal. The de-bonding basically makes the transducer appear to be lightly damped which causes a reduction in the bandwidth and distortion in symmetry of the beam divergence (Figure 1). Hence performance of the ultrasonic transducers need to be verified over a period of time in order to ensure repeated and error less measurements. A six-axis ultrasonic C-scan system was used for evaluating the performance of the transducers and beam mapping. The transducers to be evaluated was excited by a spike pulser (JSR-300) and a pinducer (Valpey fisher make) was used as the receiver. Both the transmitter and the receiver was immersed in water for mapping the ultrasonic waves. Planar (un-focused) and focused commercial ultrasonic transducers of different frequency were taken for analysis. Both axial and cross sectional intensity distribution over a sufficiently enough area were mapped and displayed. From this intensity distribution, necessary parameters could be derived. All transducers used for ultrasonic examination are expected to have symmetric intensity distribution.

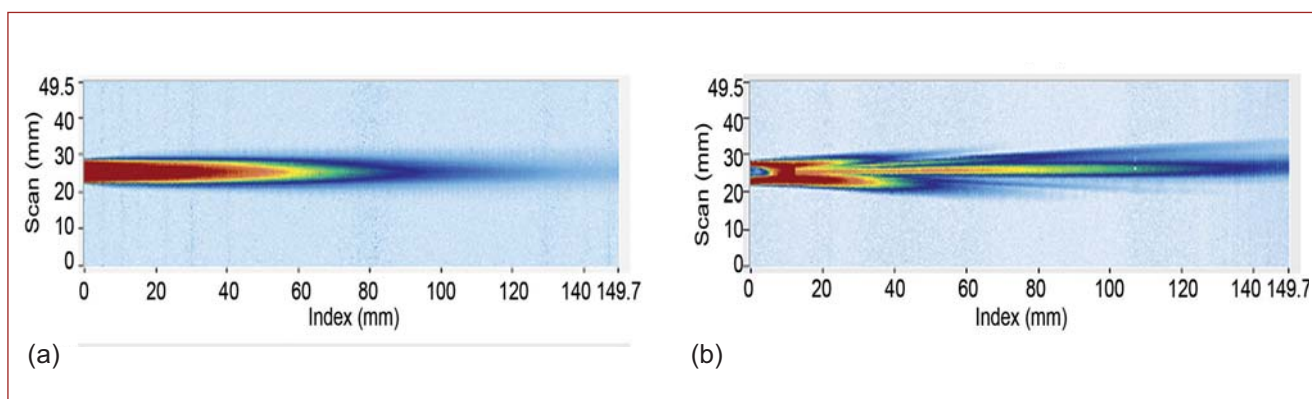


Fig. 1 (a) Symmetric and (b) asymmetric intensity distribution

VI.32 Characterization of Grain Size Variation in Austenitic Stainless Steel Using Non-Linear Ultrasonics

The properties of crystalline metallic materials are determined by their deviation from a perfect lattice periodicity which occurs due to the intrinsic crystal defects. Wide variety of applications of crystalline materials become possible due the presence of these intrinsic defects. Different types of crystal defects are distinguished by their spatial dimension and one of the largest is the grain boundary. Grain boundaries which disrupt long-range crystalline order play an important part in determining the properties of a metal. Grain boundaries in a material determines its susceptibility towards the transgranular and intergranular fractures.

A metal can approach a more stable state by reducing its grain-boundary area. There are two ways in which this may be achieved. First, boundaries may move so as to straighten out sharply curved regions and second, they may move in such a way that some crystals are caused to disappear, while others grow in size. The latter phenomenon, which results in a decrease in the total number of grains, is called grain growth. Normally, when a metal is heated at a sufficiently high temperature for a long enough time, grain growth occurs. Normal grain growth in polycrystalline material is defined as a uniform increase in the average grain size of a polycrystalline aggregate by grain boundary migration as a result of annihilation of smaller grains. During this process, the distribution of grain size remains relatively uniform. The size of the average grain is a very important structural parameter in a polycrystalline material. The smaller the grain size, the greater the hardness or flow-stress. Variation in grain size can be observed and quantitative measurements can be performed using the microscopic methods. But all microscopic examination methods are time consuming and destructive. Grain size estimation using ultrasonic examination are widely accepted as a non-destructive method whereas non-linear ultrasonic examination is an advanced technique which rely on the generation of harmonics from the grain boundaries. As the harmonics are being generated from the grain boundaries, the non-linear ultrasonic testing is superior and more accurate than conventional ultrasonic methods such as attenuation and velocity measurements and back scatter methods. In this work AISI grade SS304 has been heat treated to different temperature and soaking time in order to vary the grain size. Austenitic stainless steel, a widely used polycrystalline material, has wide applications at higher temperatures for its good mechanical properties, corrosion resistance,

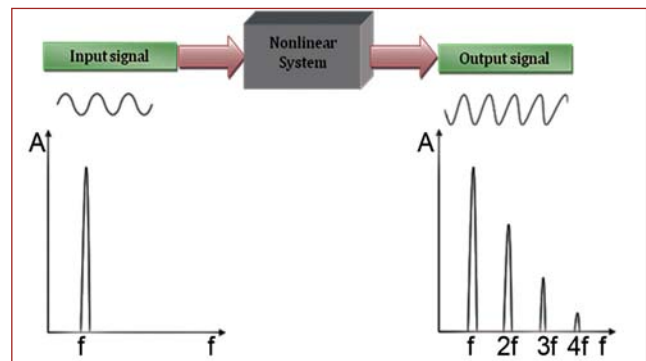


Fig. 1 Schematic of harmonic generation

formabilities and weldabilities. These superior properties make the austenitic stainless steel to be widely used in nuclear industry. Results of non-linear ultrasonic testing reveals that this technique can distinguish specimens with varying grain sizes in their order.

When a high power ultrasonic wave propagates through a material, due to the inherent lattice nonlinearity, higher harmonics are being generated. Fourier analysis of the output signal transforms time domain received signals into frequency domain. Let A_1 be the amplitude of the fundamental wave, A_2 that of the second harmonic, x the distance travelled and k the wave vector, then the nonlinearity parameter β is defined as

$$\beta = \frac{8}{k^2 x} \frac{A_2}{A_1^2}$$

Schematic of higher harmonics generation is shown in Figure 1.

Five specimens of AISI SS304 of dimension 50×50×10 mm have been prepared by heat treatment described in Table 1 to vary the grain sizes. The specimens were then subjected to machining to have a surface finish better than 1 micron. These specimens were then subjected to nonlinear ultrasonic testing with the help of a specially developed specimen holder. Optical micrographs of

Table 1: Heat treatment		
Sp. ID	Temperature (C)	Soaking time (hr)
A	As received	
B	1050	1
C	1050	2
D	1100	2
E	1150	2
F	1200	1

these specimens are shown in Figure 2a to 2f. Proper alignment of the transducers were also ensured in this holder. A high power RF tone burst modulated with a Hann window was sent through the sample using a piezoelectric transducer of 5 MHz central frequency and 6 mm crystal diameter. Another transducer with 10 MHz central frequency and of the same size placed in through-transmission mode was used as the receiver. The pulser/receiver used was RITEC RAM-5000 SNAP system; a fully computer controlled system with an operational frequency range of 50 kHz to 10 MHz. This system also allows the number of cycles to be adjusted and the phase of the signal to be inverted. Data collection was performed with care by keeping the contact pressure constant. A uniform layer of couplant was provided between the sample and the transducer. Number of cycles in the tone burst was limited to 10 to prevent overlapping of multiple echoes. Figure 3 shows a tone burst Hann modulated signal sent to the sample and its Fourier transform. On each specimens, NLU measurements were taken at ten positions and at each position, power level was varied from 40% to 90% of the maximum input power. In all the specimens, experiments were carried out in similar conditions to ensure the repeatability. Grain boundaries are interfacial defects which separates grains of different orientations and where the localized strains are high. It was observed that, as grain size increases, the nonlinearity parameter, β , decreases. Results are shown in Figure 4. The reasons for harmonic generation in this material are:

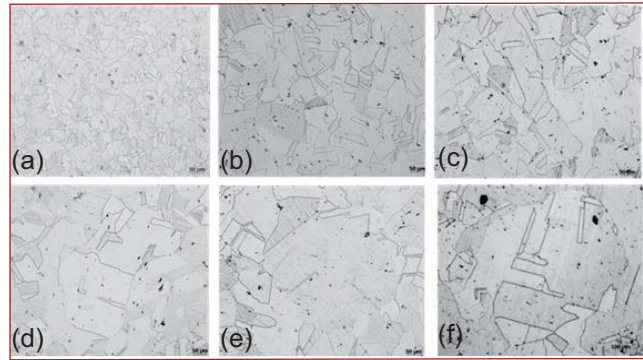


Fig. 2 Optical micrographs of the heat treated specimens (a) as received, (b) 1050°C one hour soaking, (c) 1050°C two hours soaking, (d) 1100°C two hours soaking, (e) 1100°C two hours soaking and (f) 1200°C one hour soaking

1. Atomic mismatch and localized stresses at the grain boundaries
2. Variation of crystallographic orientation of individual grains
3. Number of grain boundaries the wave interacts with in its propagation

Conventional ultrasonic testing in the linear elastic regime does not respond to these material properties and hence cannot be used as a tool to evaluate the grain size variations. Hence, quantitative evaluation of grain size variation is possible with the non-linear ultrasonic examination methods.

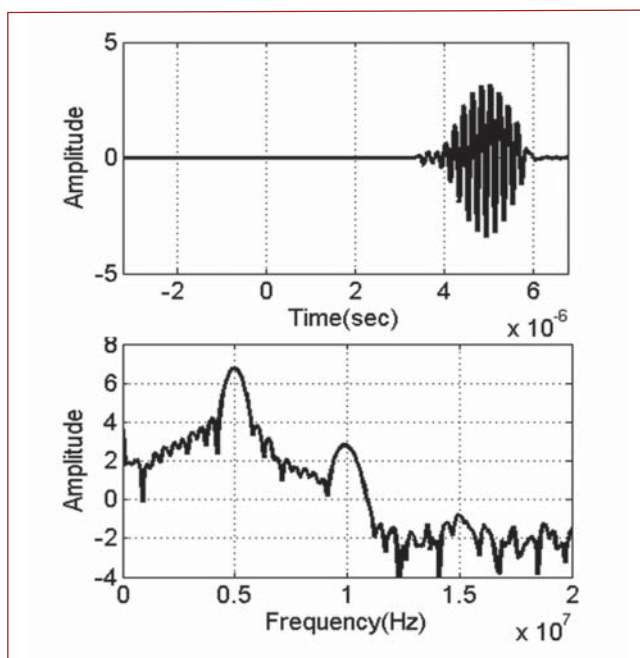


Fig. 3 Time domain and frequency domain signals

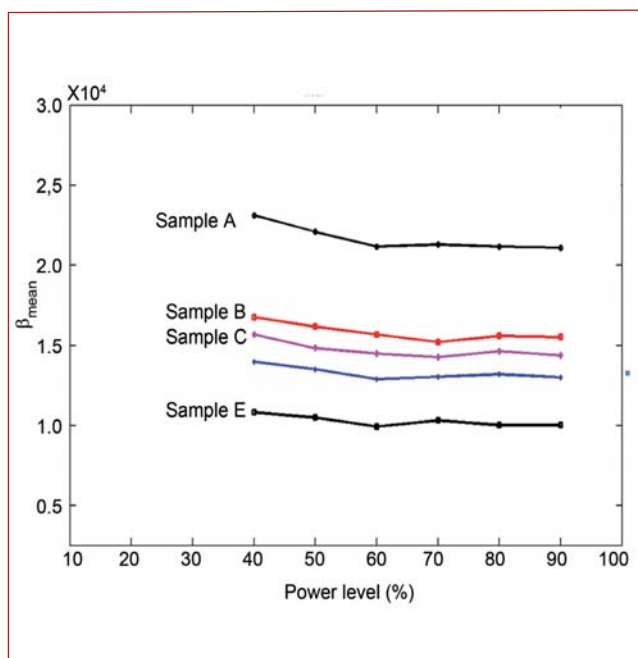


Fig. 4 Beta variation for different samples at various power levels

VI.33 CFD Simulations of Indoor Dispersion of Aerosols

In an unlikely accidental leak of radioactive aerosols within a well ventilated laboratory, it would be transported to different parts of the room by the circulation of indoor air and can also migrate to other rooms in the building through interconnections. A similar situation can arise if a toxic gas is leaked within a chemical laboratory. To ensure the safety of the operating personnel in such accidental situations, it is required to set an alarm at an optimum location so that the leak can be detected in a quick and efficient way. For a given inflow rate, the flow pattern inside the room depends on the room geometry, internal distribution of objects, location and number of inlets and outlets and the presence of air circulation sources like fan, AC, duct etc. For this, a detailed and comprehensive analysis of the migration of particles/gas in indoor environment is performed.

The method of assessment of the transport of an aerosol inside a room involves numerical simulation supported by experimental verification for different operational conditions with distributions of internal objects. As first step, a study is carried out using CFD to simulate the transport of methylene blue aerosol within a well ventilated and isolated empty room (with split AC) of dimensions 5.9 X 5.8 X 3.8 metres. The AC unit is placed on X=0 plane and it is symmetric about Y=2.9 and Z=3 planes. First the air flow is simulated using experimentally measured inlet velocity (10 m/s) and considering 9655 grids in CFD. To ensure convergence, the computation is redone with double the number of nodes. The simulated flow pattern on Y=2.9 plane (Figure 1a) shows good agreement with the experimental values. Next, 3.0×10^8 particles are released continuously in a span of 5 seconds from the point (2.95, 2.9, 1.5). To generate aerosols, atomization technique is employed

Table 1: Details of number of particles tracked by two counters located at two different points

Location (X,Y,Z) cm	Measured concentration	Simulated value
(100, 350, 65)	2.55×10^{-2}	3.21×10^{-2}
(470, 65, 86)	5.75×10^{-2}	7.18×10^{-2}

for a liquid solution of methylene blue dispersed in methanol. The size distribution is estimated using an Optical Particle Counter. The number of particles is tracked by two counters located at two different points and are given in Table 1. A time step of 0.01 sec is used to simulate dispersion. Here also, the convergence is assured by re-performing the simulation with doubling the number of nodes and reducing the time step by half. From Table 1, it can be seen that the numerical results agree reasonably with the experimental observations within ~25%. The concentration distribution of aerosol at Z=1.5 plane after 2 seconds and at Y=2.9 plane after 10 seconds from the beginning are shown in Figures 1b and 1c. In both these cases the concentration is normalized with respect to the total release. As the study is conducted in an empty room, the airflow pattern which drives the aerosols is very symmetric about Y=2.9 plane. It is seen that the point where concentration reaches the detectable limit quickly is located on the roof around the point (3.5, 2.9, 3.8). In practical situations, a room will be filled with internal objects that would modify the flow pattern. The study shows that CFD simulation technique can provide details of flow pattern and concentration distribution which inturn helps to identify any hotspot within the room. However, further simulations considering the actual situations are required to locate the optimum position for placing the alarm.

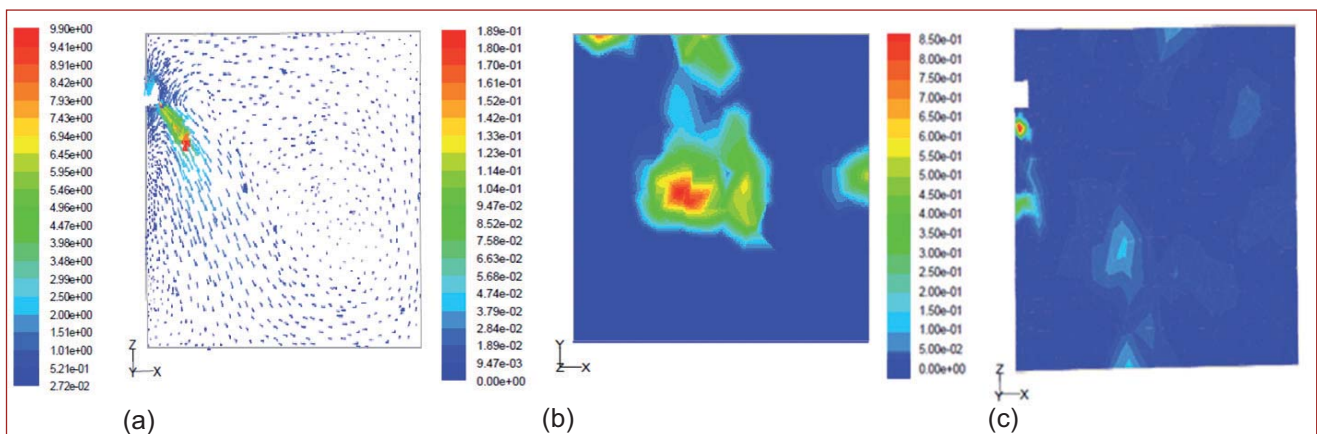


Fig. 1 (a) Airflow velocity at the Y=2.9 plane, (b) concentration at the Z=1.5 plane after 2 seconds and (c) concentration at the Z=1.5 plane after 10 seconds

VI.34 Characterization of Heavy Density Concrete for Operational Environment of Nuclear Power Plant

Concrete is used in nuclear reactor and fuel cycle facilities, to shield both gamma and neutron radiations. Various special types of concretes of density ranging from 3.6 to 4.6 g/cc (heavy density concrete) by incorporating different compositions of high 'Z' elements in normal concretes have been effectively employed to achieve less shielding thickness. As the operational environment in a fast breeder reactor subjects the heavy density concrete to temperatures just above the boiling temperature of water, its effect on physical and mechanical properties of heavy density concrete was evaluated. Four series of concrete specimens A, B, C and D were prepared with hematite aggregate. Pure hematite, a natural red rock that contains iron oxide, has a Mohs hardness between 5.5 to 6.5 and the specific gravity between 4.1 to 4.8 g/cc. Details of mix design of concrete, aimed at achieving high density are presented in Table 1.

Apart from increasing cement content, admixture in the form of super plasticizers (naphthalene based) is added to achieve a cohesive workable concrete mix which can be easily placed within reinforced concrete vault.

Three specimens each (cuboidal as well as cylindrical) were cast and cured as per BIS. The measured density of the specimens are given in Table 1. The samples were then subjected to a heat treatment, at a constant temperature of 120°C, in a thermal cyclic chamber.

To estimate the rate of weight loss, the samples were withdrawn from the thermal cyclic chamber at 1, 3, 7, 14, 28 and 56 days (Figure 1a). Non destructive tests using ultrasonic pulse velocity and Rebound hammer (RH) were adopted to understand the variations in heavy density concrete under heat treatment (Figures 1b and 1c). Ultrasonic pulse velocities were measured by a commercially available pulse meter (PROCEQ make) with an associated transducer pair. The transducer pair had a nominal frequency of 54 kHz. The transmitter and receiver were placed on opposite sides of the specimen and pulse measured in direct method. The plunger of

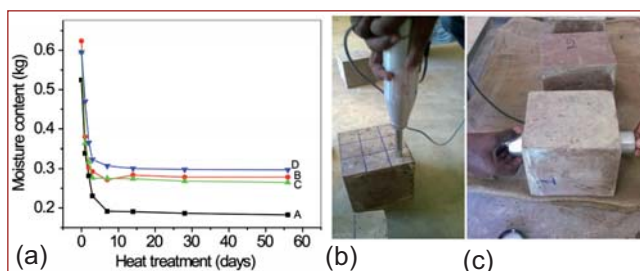


Fig. 1 (a) Moisture loss, (b) Rebound hammer test and (c) ultrasonic pulse velocity test

Specimen ID	Cement, kg/m ³	Water, Kg/m ³	Aggregate, kg/m ³			Steel shots, kg/m ³		Admixture, Kg/m ³	Measured density, g/cc
			Coarse (mm)		Fine	4mm	2 mm		
			20	12					
A	420	155.4	580	580	772	-	-	2.94	2.50
B	420	185.0	884	884	1274	-	-	5.04	3.65
C	420	176.4	740	740	1105	416	416	5.04	4.02
D	420	176.4	555	555	1075	831	675	5.04	4.29

Rebound hammer is allowed to strike perpendicularly to the surface and ten readings were taken from each tested area.

The specimens were then tested for compressive and split tensile strength as per IS 516 and IS 5816. The tests were conducted while the specimens were still hot. Figure 2 depicts the residual strength and integrity of the specimens under sustained heat treatment. Conclusions are as follows.

- Density loss in the specimens are in the range of 1-4%, with maximum in specimen A, which happens within 7 days of exposure to 120°C
- Overall it is concluded that the sustained thermal ageing at 120°C did not deteriorate the mechanical properties of concrete
- Specimen D with measured density of 4.29 g/cc showed high thermal stability as well as high strength
- Residual strength as measured from strength tests, ultrasonic pulse velocity and Rebound hammer confirms integrity of heavy density concrete under sustained temperature of 120°C.

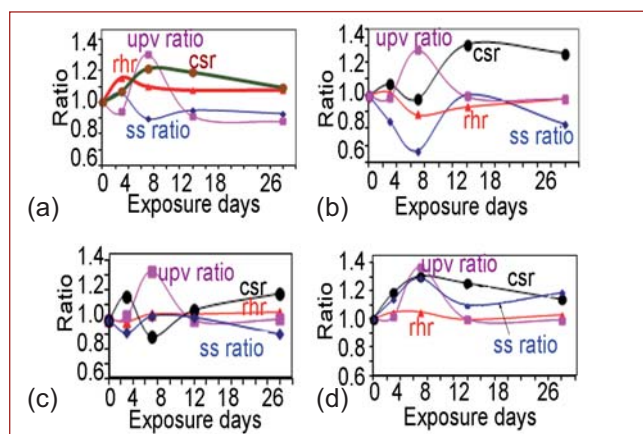


Fig. 2 Residual strength of concrete (a) A, (b) B, (c) C and (d) D with respect to unexposed specimens-(csr-compressive strength ratio, ss-split tensile strength, rhr-rebound hammer ratio, upv- ultrasonic pulse velocity)

CHAPTER VII

**Awards/Publications/News&Events/
Organisation**

Awards & Honours

Dr. U. Kamachi Mudali, Director, MC&MFCG has been conferred “Meritorious Award 2016” by National Corrosion Council of India, CECRI

Dr. M. Sai Saba, Director, RMG has been elected as an “Executive Member” for the Academy of Sciences, University of Madras, Chennai

Dr. B. K. Panigrahi, MSG has been conferred MRSI Medal 2016

Dr. Rani P. George, MMG received “Corrosion Awareness Award 2016” for Meritorious Contribution to Research and Education in Corrosion Science & Technology, from NACE International Gateway India Section

Dr. R. Divakar, MMG was conferred Fellowship of the Electron Microscope Society of India during the Annual Meeting of EMSI held during June 2-4, 2016 at IIT BHU, Varanasi.

Dr. G.K. Sharma, MMG, received “Dr. T. K. Saksena Memorial Award” for the best Ph. D. thesis titled “Ultrasonic NDE of Type 316 Austenitic Steel by Time Frequency analysis” by Ultrasonics Society of India

Dr. M. Vasudevan, MMG has been awarded “Metallurgist of the Year Award 2016” by the Steel Ministry Government of India during 54th National Metallurgist Day Awards at Indian Institute of Technology, Kanpur on November 14, 2016

DAE Awards

Department of Atomic Energy has instituted annual awards for excellence in Science, Engineering and Technology in order to identify best performers in the area of Research, Technology Development and Engineering in the constituent units (other than Public Sector Undertakings and Aided Institutions). The Young Applied Scientist, Young Engineer, Young Technologist, Homi Bhabha Science and Technology Award and Scientific and Technical Excellence Award fall under this category. Group Achievement awards for recognition of major achievements by groups have also been instituted. Life-time Achievement Award is awarded to one who has made significant impact on the DAE’s programmes. They are the icons for young scientists and engineers to emulate. The awards consist of a memento, citation and cash prize.

The recipients of the Awards from IGCAR for the year 2015 are:

Homi Bhabha Science and Technology Award	: Dr. John Philip, MMG
Scientific and Technical Excellence Award	: Dr. Divakar Ramachandran, MMG Dr. Anish Kumar, MMG
Young Applied Scientist / Technologist Award	: Shri Ranga Ramakrishna, FRTG Shri T. K. Haneef, MMG
Young Engineer Award	: Shri T. Sakthivel, MMG Shri Piyush Kumar Aggarwal, FRTG Shri Ram Kumar Maity, RDG Shri R. Dheenadhayalan, EIG
Meritorious Technical Support Award	: Shri M. Rajendran, RFG Shri A. Amalraj, MC&MFCG Shri K. Kamaludeen, RFG
Meritorious Service Award	: Shri A. Christopher, Administration Shri Sairam Ramadorai, Director’s Office

Group Achievement Awards:

Development of Nitrogen Enhanced 316LN Austenitic Stainless Steel for Primary Components of Sodium Cooled Fast Reactors.

Dr. A. K. Bhaduri, Director, IGCAR, Group Leader

Dr. U. Kamchi Mudali, Dr. K. Bhanu Sankara Rao, Dr. M. D. Mathew, Dr. K. Laha, Dr. Shaju K. Albert, Dr. B. K. Choudhary, Dr. C. Mallika, Dr. N. Parvathavarthini, Dr. R. Sandhya, Dr. P. Parameswaran, Dr. V. S. Srinivasan, Dr. M. G. Pujar, Dr. A. Nagesha, Dr. S. Ningshen, Shri G. Srinivasan, Dr. S. Ravi, Dr. Vani Shankar, Dr. G. V. Prasad Reddy, Shri J. Ganesh Kumar, Shri M. Nandagopal, Dr. Sunil Goyal, Shri J. Christopher, Ms. P. Poonguzhuli, Dr. Anita Topoo, Shri V. David Vijayanand, Shri T. Sakthivel, Shri R. Kannan, Shri Aritra Sarkar, Shri Durga Prasad Rao Palaparti, Ms. M. Divya, Shri K. Thyagarajan, Shri N. Sivaibharasi, Shri V. Ganesan, Shri Srinivas Manneppalli, Shri K. Mariappan, Ms. S. Panneerselvi, Shri A. Vinod Kumar, Shri N. S. Thampi, Shri K. Vaithyanathan, Shri S. Sakthy, Shri M. Arul, Shri M. Gandhi, Shri M. Srinivasarao, Shri M. Munivel, Ms. R. Uma Maheswari, Ms. M. Jayalakshmi, Shri M. Govindaswamy, Ms. Indira Logu, Ms. M. Esakkiammal and Ms. N. Santhi from **MMG**

Remote Replacement of Radiation Shielding Window and Resolution of Challenges during Operation at CORAL Facility

Dr. A. Ravishankar, RpG & Shri V. Vijayakumar, RpG - Group Leaders

Shri K.C. Ajoy, Shri A. Dharsekaran, Dr. B. Venkataraman, Dr. M.T. Jose, Shri V. Rajagopal, Shri R. Santhanam, Shri S. Viswanathan, Shri R. Mathiyarasu, Shri S. Baskar, Dr. S. Kalaiselvan, Shri S. Chandrasekaran, Dr. U. Madhusoodanan, Shri S. Balasundar, Dr. O. Annalakshmi, Dr. M. Manohari, Shri R. Arul, Ms. R. Akila, Shri S.M.S Murthy, Shri D. Karthikeyan, Shri N. Yuvaraj and Ms. Nitu Sinha from **HSEG**; Shri B. M. Ananda Rao, Shri E. Balu, Shri A. Palanivel, Shri G. Surendar Kumar, Shri Apurba Kumar Majumder, Shri M. D. Mohauddain Ansari, Shri K.K. Shimjith, Shri N. Divakar, Shri M. Elumalai, Shri K. Ajai Kumar, Shri S.S. Kumar Goru, Shri C. Kannan, Shri V. Venugopal, Shri N. Govindan, Shri G. Rajendran, Shri Prashant Kumar, Shri M. Dhayalan, Shri T. Sengalani, Shri S. Sengayani, Shri L.A. Leo Felix, Shri H. Humayoun, Shri Shekar Kumar, Shri Surajit Halder, Shri M. Muthukumar, Shri Kinkar Mandal, Shri Peeyush Gupta, Shri Varatharajan, Shri J. Thiyaga Senthilkumar, Shri S. Somasundaram, Shri Saju George, Shri S. Sivakumar, Shri Abdul Muqtadir, Shri M. Selvarasan, Shri R. Sajikumar, Ms. Radha Rani, Shri Vijayaraghavan, Shri K. Arasakumar, Shri D. Natarajan, Shri K. Ilanchezhian, Shri Ravi Islavath, Shri N. Balasubramanian, Shri Potta Ramjee, Shri P. Santhanadevan, Shri V. Kumara Vijayan, Shri M. Suresh, Shri A.K. Sasi, Shri S. Pandurangan, Shri P. Ramesh Kumar, Shri K.K. Vinod Kumar, Ms. C.M. Bagyalakshmi, Shri L. Yogananth, Shri J. Madhusudhana Rao, Shri M. Bhaskar, Shri Ashish Shriram Ladhe, Shri Nanhe Rajendra Manohar, Shri Harendra Kumar, Shri J. Palanivel, Shri Ramprasad Pal, Shri Ghanshyam Kumar, Shri N. Sreekumar, Shri Bonu Sanyasi Rao, Ms. N. Abirami, Shri E. Krishnamurthy, Shri M. Ananthan, Dr. R. V. Subba Rao, Dr. P. Govindhan, Shri K. Dhamodharan, Shri D. Jebaraj Mahildoss, Dr. P. Sivakumar, Dr. S. Sukumar, Shri K.S. Vijayan, Shri D. Sivakumar, Shri G. Santhosh Kumar, Shri S. Parthasarathy, Dr. M. Subha, Shri S. Ganesh, Shri Pradeep Kumar Sharma, Shri S. Pugazhendi, Shri S. Sudhagar, Shri T. Aneesh, Shri Satya Narayan Das, Shri Saptarshi Chatterjee, Shri Akhilesh K. Nair, Ms. K. Ponkamini Sasirekha, Ms. C.S. Suganya Devi, Shri K. Stanley, Shri R. Karthick, Shri Shantaram Jandhyala, Shri I. Sriharsha, Ms. D. Jayanthi, Shri K. Rajkumar, Shri S. Prakash, Ms. T. Selvi, Ms. C. Shibina, Ms. V. Varalakshmi, Ms. S. Poongudi, Ms. Bhavya S. Nair, Shri Suresh Borado, Shri A. John Deepak Lawrence, Ms. G. Preetha, Shri Saurabh Suman, Shri V. Anandha Narayanan, Shri N. Srinivasan, Shri Aravind Kumar Meena, Shri Alok Kumar Mishra, Shri B. Krishnamurthy, Shri Geo Mathews, Shri M. S. Gopikrishna, Shri P. Vijayasekaran, Shri R. Amudhu Ramesh Kumar, Shri J. W. Reuben Daniel, Shri R. N. Verma, Ms. Swatilekha Bhattacharjee, Ms. M. Swapna, Shri Padi Srinivas Reddy, Shri S. Manickam, Shri P.C. Sandheep, Shri. K. P. Desheeb, Shri M. Vinoth Kumar, Shri P. Anbazhagan, Shri R. Anbarasan, Ms. B. Uma, Ms. P. G. Sethulakshmi, Shri G. Alagesan, Shri C. U. Jayakumar, Ms. G. Maheswari, Shri. D.C. Thomson, Shri S. Pushpa Selva Kumar, Shri Pradip Paul, Shri R. Gopalakrishnan, Shri C. Murugesan, Shri S. Ramesh, Shri P. Sudalaimani, Shri G. Velu, Shri A.K. Kannan, Shri S. Suresh Babu, Shri R. Mouli, Shri K. Paramasivan, Shri K.G. Ramesh Babu, Shri E. Murthy, Shri A. Jahangeer, Shri M. V. Praveen Kumar, Shri A. Vilvanathan, Shri S. Venkatesh, Shri Satish Verma, Shri K. Damodaran, Shri V. Raja, Shri Satish Kumar Velaga, Shri V. Muralikrishnan, Shri R. Ganesan, Shri K. Sampath,

Dr. C. Mallika, Shri K. Rajan, Shri N. K. Pandey, Shri N. Krishnan, Shri R. Rajeev, Ms. Heera Balachandran, Dr. Falix Lawrence, Shri Jayendra Kumar D. Gelatar, Shri B. Lokeshwara Rao and Shri T. Dinesh from **RpG**

Testing and Qualification of HTFC in FBTR & KAMINI

Shri C. P. Nagaraj, **EIG**, Group Leader

Shri C.P. Nagaraj, Shri K. Madhusoodanan, Shri M. Sivaramakrishna, Shri Chandrakant Upadhyay, Shri N. Anand Kumar, from **EIG**. Shri G. Srinivasan, Shri K. V. Suresh Kumar, Shri S. Varatharajan, Shri A. Babu, Shri S. Sridhar, Shri G. Shanmugam, Shri K. Bhanumurthy, Shri T.V. Ravindranath, Shri M. Murugesan, Shri A. Mani, Shri K. Asokan, Shri B. Kadirappa, Ms. P. Akilandeswari, Shri Dinkar Jha, Shri B. Manoharan, Shri P. Saravanan, Shri K. G. Subramanian, Shri S. Kanagaraju, Shri K. Kamaludeen, Shri D. Vinoth, Shri V. Velu, Shri M. Jayasankar, Shri V. Rajkumar, Shri D. Jaisrinivasan, Shri A. Udaya Shankar, Shri V. Padmanaban, Shri B. Dharmiah, Shri M. Babu, Shri D. Vignesh Babu, Shri N. Kathresan, Shri M. Arumugam, Shri R. Gopal, Shri P. Maharajan, Shri C. Kannan, Shri R. Sekar, Shri N. Manimaran, Shri N. Balakrishnan, Shri D. Visweswaran, Shri M. Elumalai, Shri J. V. Srinivasan, Ms. Sheela Nambiar, Shri M. Elango, Shri J. Sasi Kumar, Dr. S. Sivakumar, Shri G. Raghukumar, Ms. E. Radha, Shri V. Sathiamoorthy from **RFG**; Shri V. Praveen Kumar, Shri Karuppasami, Shri S. Murugan, Shri D. Dileep, Shri V. Kodiarasan, Shri S. Yuvaraj, Shri E. Gothandan, Shri B. Ramalingam, Shri P. Shunmugam from **ESG**; Shri P. Ramesh, Shri Uma Shankar and Shri B. Govindaswamy from **HSEG**. Shri K. Natesan from **RDG**

Best Paper/Poster Award

Soil Structure Interaction Studies of a Nuclear Facility Structure Supported on Engineering Backfill

Shri N. Nitheesh, Shri G. Padmanaban, Ms. Sudipta Chattopadhyaya

International Conference on Advances in Civil Engineering and Sustainable Construction organised by SRM University, 30 March – 01 April, 2016

Best Paper Award

Temperature and Pressure Dependent Phase Transitions of Fast Ion Conductor β' -LiZr₂(PO₄)₃ Studied by Raman Spectroscopy

Ms. K. Kamali and Dr. T. R. Ravindran

DAE-BRNS Symposium CoMPEC (Condensed Matter Physics under Extreme Conditions) held in BARC Mumbai during April 13-16, 2016

Best Poster Award

Representing Unstructured Data Using NQSQL: Consistent Hashing Approach using MONGODB

Shri Pabbaraju Chirag Ramdas, Shri E. Soundararajan and Dr. M. Sai Baba

10th National Conference on Recent Advances in Information Technology (READIT-2016)

Indira Gandhi Centre for Atomic Research, July 13-14, 2016

Best Poster Award

Role of Quality Circles in Clean India Mission

Shri S.P. Manivannan

Quality Circle Annual Meet (QCAM) - 2016, Kalpakkam, August 29, 2016

Best Poster Award

Biofouling control of Sea Water Cooled Titanium Condenser Material Through in Situ Application of Alternate Anodic and Cathodic Potential

Shri B. Anandkumar, Dr. Rani P. George, Dr. C. Mallika and Dr. U. Kamachi Mudali

DAE-International Corrosion Conference and Expo (CORCON-2016), New Delhi, September 18 - 21, 2016

Best Poster Award

Estimation of Fatigue Life of Notched Specimens of P91 Steel by Analytical Approaches

Shri J. Veerababu, Shri Sunil Goyal, Dr. R. Sandhya and Dr. K. Laha

2nd International Conference on Fatigue, Durability and Fracture Mechanics (FatigueDurability India 2016), Institute of Structural Integrity and Failure Studies, Indian Institute of Science, Bengaluru, September 28-30, 2016

Best Paper Award

Setting up of Holographic Optical Tweezer Arrays

Shri Deepak K. Gupta

61st DAE Solid State Physics Symposium, Board of Research in Nuclear Science, DAE, December 30, 2016

Best Poster Award

High Temperature Mass Spectrometric Studies on U-19Pu-6Zr

Shri P. Manikandan, Shri V. V. Trinadh, Shri M. Prasad, Dr. T. S. Lakshmi Narasimhan, Dr. M. Joseph

6th Interdisciplinary Symposium on Materials Chemistry (ISMC-2016) at BARC, Mumbai, December 6-10, 2016

Best Paper Award

Experimental Determination of Liquidus of Fe-Zr by Spot Technique

Shri P. Ramakrishna, Shri B. Samanta, Shri S. Balakrishnan, Dr. K. Ananthasivan

6th Interdisciplinary Symposium on Materials Chemistry (ISMC-2016) at BARC, Mumbai, December 6-10, 2016

Best Paper Award

Automated Web based System for Task Force/High Level Committees

Ms. M. Kanaga, Ms. J. Jasmine Smila, Ms. Sujatha, Ms. K. Saipriya, Dr. Vidya Sundararajan and Dr. M. Sai Baba

10th National Conference on Recent Advances in Information Technology (READIT-2016)

Indira Gandhi Centre for Atomic Research, July 13-14, 2016

Best Poster Award

Information Management at MRPU: A Case Study

Ms. P. Janupriya, Shri P. P. Muralikannan, Shri Narendra Kumar Kushwaha, Dr. Vidya Sundararajan and Dr. M. Sai Baba

10th National Conference on Recent Advances in Information Technology (READIT-2016)

Indira Gandhi Centre for Atomic Research, July 13-14, 2016

Best Paper Award

Single Window Logon and Federated Gateway for Information Retrieval

Shri Renigunta Vinay Datta, Shri E. Soundararajan and Dr. M. Sai Baba

10th National Conference on Recent Advances in Information Technology (READIT-2016)

Indira Gandhi Centre for Atomic Research, July 13-14, 2016

Best Poster Award

Supercomputing cluster at IGCAR

S. Rajeswari, R. Jehadeesan and S. A. V. Satyamurty

Symposium on Emerging Trends in I&C and Computer Systems, June 23-24, 9th DAEVIE 2016, IGCAR, Kalpakkam

Best Poster Award

Review of Software Architecture for Data Communication Between Distributed Components of PFBR Full Scope Replica Operator Training Simulator Text Retrieval Models

Shri Jaideep Chakraborty, Ms. Bindu Sankar, Ms. H. Seetha, Shri Nakul Raj Sethi, Ms. T. Jayanthi and Shri K. Madhusoodanan

10th National Conference on Recent Advances in Information Technology (READIT-2016)

Indira Gandhi Centre for Atomic Research, July 13-14, 2016

Best Poster Award

Server Consolidation Algorithms using Live Migration of Virtual Machines

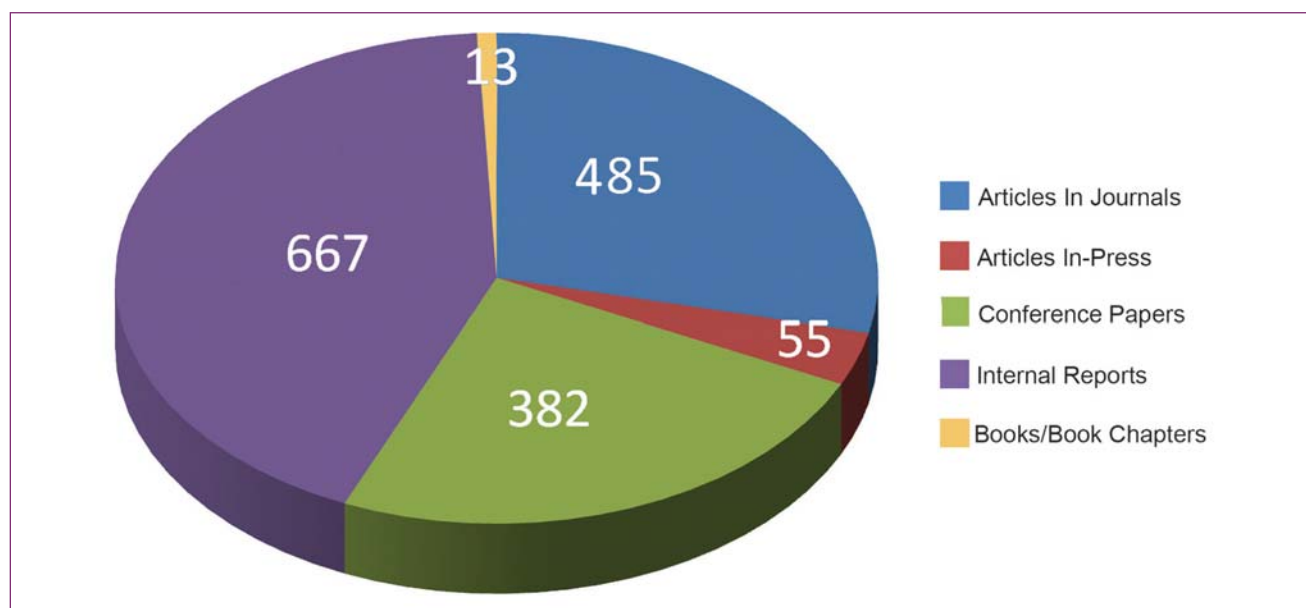
Shri Pathikrit Ghosh, Shri E. Soundararajan and Dr. M. Sai Baba

10th National Conference on Recent Advances in Information Technology (READIT-2016)

Indira Gandhi Centre for Atomic Research, July 13-14, 2016

Best Poster Award

IGCAR Publications during the Year 2016



Special Lectures and Colloquia Series

IGC Colloquium

1. "Pebbles on the Shore" by Dr. G. Srinivasan, Former Director, Reactor Operation and Maintenance Group & Reactor Design Group, IGCAR, February 25, 2016
2. "Modelling and Experimental Studies related to the Behaviour of PHWR Fuel Pins during LOCA Conditions" by Shri D.N Sah, Formerly RRF and Head, PIED, BARC, August 25, 2016
3. "Nanotechnology in the Polymers" by Prof. A.K. Bhowmick, Professor of Eminence, RTC, IIT, Kharagpur November 11, 2016
4. "Large-Scale Energy Storage using Redox Flow Batteries " by Dr. Vijay Mohan Pillai, Director, Central Electrochemical Research Institute, Karaikudi, November 23, 2016
5. " Nuclear Power from Thorium: Different Options" by Dr. Srikumar Banerjee, Homi Bhabha Chair Professor & Former Chairman, AEC, November 29, 2016

Special Lectures

1. "Molecules that Enjoy Celebrity Status", Bhatnagar Memorial Lecture by Prof.S. Chandrasekhar, Director, Indian Institute of Chemical Technology, CSIR Hyderabad, February 19, 2016
2. "Curie Therapy in the Service of Mankind: From Radium Roads to Brachytherapy Suites", Curie Memorial Lecture by Prof. Rajeev Sarin, Tata Memorial Hospital, Mumbai, March 18, 2016
3. "Programmes and Activities of Radiochemistry & Isotope Group, BARC" by Dr. K. L. Ramkumar, Former Director Radiochemistry & Isotope Group, BARC & Head Nuclear Control Planning Wing, DAE, March 31, 2016
4. "Variable Energy Cyclotron Centre - An Introduction" by Dr. Dinesh Kumar Srivastava, Director, Variable Energy Cyclotron Centre, Kolkata, May 04, 2016
5. "ERA Implemented and its impact in Indian industries", by Dr. M Surianarayan , Principal Scientist, CLRI June 08,2016
6. "Self Motivation" by Dr. M. Sai Baba, Director, Resources Management Group, IGCAR, August 05, 2016

7. "Future of Protons in Radiotherapy Photons: promises and points" by Dr. C. S. Mani , Senior Consultant, Surgical Oncologist,
"Setting up Proton Therapy Unit" by Dr. K. Ganapathy, Senior Medical Physicist,
"Clinical use of Protons" by Dr. P. Mahadev Senior Consultant Radiation Oncologist Apollo Speciality Cancer Hospital, Chennai, Curie Memorial Lecture", November 07, 2016

Seminars, Workshops and Meetings

1. 7th International conference on "Creep, Fatigue and Creep-Fatigue Interaction (CF-7) during January 19-22, 2016
2. IARP International Conference on "Radiological Safety in Workplace, Nuclear Facilities and Environment" during February 22-25, 2016
3. "DAE-BRNS Theme Meeting on Plutonium 75" during May 23-25, 2016
4. "Workshop on Web of Science", May 31, 2016
5. 9th DAE – VIE 2016 Symposium on "Emerging Trends in I & C and Computer Systems" during June 23-24, 2016
7. "10th National Conference on Recent Advances in Information Technology (READIT-2016)" during July 13-14, 2016

Nurturing Activities

1. "Science Day Celebration", February 27, 2016
2. "Radiation Awareness Program" for Vidyagyan Schools from Uttar Pradesh, April 5, 2016 & April 12, 2016
3. "Industrial Safety Workshop" during April 6-7, 2016
4. "National Technology Day Meet 2016", May 11, 2016
5. "Summer Training in Physics and Chemistry (STIPAC-2016)" from May 26 to July 3, 2016
6. "BITS Pilani Practice School" May 23 to July 16, 2016.
7. "2nd International Yoga Day", June 21, 2016
8. "Inter-School National Level Quiz Contest (NLQC-2016)" during July 28-29, 2016
9. "Electrochemistry and Corrosion Camp", August 13, 2016
10. "Quality Circle Annual Meet (QCAM-2016)", August 29, 2016
11. "AECS School Teacher's Day Celebration", September 03, 2016
12. "Metal Camp Programme" during September 22-23, 2016
13. "Prof. Brahm Prakash Memorial Material Quiz - 2016 Grand Finale" organised by IIM Kalpakkam Chapter", during September 23-24, 2016
14. Interaction Session with Dr. Srikumar Banerjee, Homi Bhabha Chair Professor & Former Chairman, AEC, November 30, 2016

Administrative Seminars / Meetings

1. "World Hindi Day Celebration", January 11, 2016
2. ATI/DAE Programme on "Pension and Retirement Benefits", February 18, 2016 & October 20, 2016
3. ATI/DAE Workshop on "Art of Writing" during February 22-24, 2016
4. "Hindi Workshop", March 30, 2016 & June 22, 2016
5. "Hindi Scientific Seminar-2016", August 03, 2016
6. "Hindi Fortnight-2016 Celebrations" during September 14-28, 2016
7. "Vigilance Awareness Week" during October 31 to November 05, 2016

Conference and Meeting Highlights

Graduation Function of the 10th Batch of Trainee Scientific Officers of BARC Training School at IGCAR July 29, 2016



Dr. A. S. Kiran Kumar, Chairman, ISRO distributing the course completion certificates to the TSO's during the graduation function

The 10th batch of thirty seven Trainee Scientific Officers from the BARC Training School at IGCAR have successfully completed their training and were graduated in a special ceremony that took place on July 29, 2016. Dr. A. S. Kiran Kumar, Chairman, Indian Space Research Organisation, Department of Space, Government of India was the Chief Guest. Dr. M. Sai Baba, Director, Resources Management Group welcomed the gathering. Dr. A.K. Bhaduri, Distinguished Scientist and Director, IGCAR delivered the presidential address. Dr. A.S. Kiran Kumar released the souvenir featuring the training school

programme during the academic year and its successful completion of ten years. Dr. Kiran Kumar gave away the prestigious 'Homi Bhabha Prizes' comprising of a medallion and books worth Rs. 5000 to the toppers from each discipline and addressed the gathering. He also gave away the course completion certificates to all the graduates passing out. A few of the Trainee Scientific Officers passing out shared their experience, gave a feedback on the academic programme and their stay at the hostel. Dr. Vidya Sundararajan, Head, Strategic Planning and Human Resource Development Division, Resources Management Group, proposed the vote of thanks.



Graduates of BARC Training School at IGCAR with Dr. A. S. Kiran Kumar, Chairman, Indian Space Research Organization, Dr. Arun Kumar Bhaduri, Director, IGCAR, and senior colleagues of the Centre and the Department

DAE BRNS Theme Meeting on Plutonium 75

May 23 – 25, 2016



Dr. Sekhar Basu, Chairman AEC and Secretary, DAE inaugurating the DAE BRNS Theme Meeting on Plutonium 75

Towards commemorating the 75th year of the discovery of Pu-239, a DAE BRNS theme meeting titled “Plutonium 75 (Pu75)” was organised during May 23 - 25, 2016 at IGCAR, Kalpakkam. The theme meeting took stock of the excitement and progress in plutonium research and the central role it plays in the Indian Nuclear Power Programme.

The theme meeting was inaugurated by Dr. Sekhar Basu, Chairman, AEC and Secretary, DAE with Dr. R. Chidambaram, Scientific Adviser to the Government of India presiding over the inaugural function. The first plenary lecture was by Dr. David L Clark, Los Alamos National Laboratory, who described details of the discovery of plutonium and the Manhattan Project with the lecture being interspersed with video recordings of Dr. Glenn T Seaborg, the discoverer of plutonium. A number of other invited talks by Indian experts as well as those from abroad on the chemistry, metallurgy and engineering aspects of plutonium, highlighted the progress in plutonium research and technology in our country and elsewhere. A poster session to enable the young researchers to highlight their work was held on the second day.

One of the highlights of the theme meeting was a special session dedicated to the pioneers in plutonium science and technology in the country. Dr. A. N. Prasad, former Director, BARC, Shri S. V. Kumar, former Vice-Chairman, AERB, Dr. D. D. Sood, former Director, Radiochemistry and

Isotope Group, BARC, Shri G. R. Balasubramanian, former Director, Reprocessing Group, IGCAR and Shri M. K. T. Nair, former Director, Waste Management Group, BARC gave a brief account of the various challenges that they had faced when they started the construction of the first reprocessing plant in the country – the Plutonium Plant at BARC, Trombay and also gave a glimpse into the various basic studies that had been conducted in the early sixties on this element at BARC. On the ultimate day after the conclusion of the meet, a special visit to the Reprocessing Facilities at Kalpakkam was arranged to enable them to interact with the current generation of scientists and engineers involved in the design and development of reprocessing facilities. The intense discussion that took place and the transfer of knowledge and advice from the pioneers immensely benefited the current generation.

On the final day of the theme meeting, Shri K. N. Vyas, Director, BARC delivered a special address and handed over prizes to the winners in the poster session. A special session to enable participants from the Indian Industry to discuss their indigenous products generated a lot of interest from the delegates.

The final session of the theme meeting was devoted to Seaborg Memorial Lecture conducted by IANCAS-SRC. Dr. David L Clark, Los Alamos National Laboratory, delivered the lecture titled “Plutonium Science for the 21st Century.”



Dr. R. Chidambaram, Principal Scientific Advisor, Government of India, delivering the Presidential address

BITS Practice School

May 23 - July 16, 2016



Dr. Arun Kumar Bhaduri, Director, IGCAR distributing certificates to the participants during the valedictory function

Fifty one students from BITS Pilani, Hyderabad and Goa campuses underwent Summer Practice School at our Centre during May 23-July 16, 2016. This programme is aimed at exposing the students to industrial and research environments, how the organizations work, to follow and maintain work ethics, study the core subjects and their applications in the organization, participate in the assignments given to them in the form of projects. Dr. S.A.V. Satya Murty, the then Director, IGCAR inaugurated the Practice School programme and interacted with the students. The students were from various disciplines like Chemical Engineering, Computer Science & Engineering, Electrical &

Electronics Engineering, Electronics & Instrumentation Engineering, Mechanical Engineering and Physics. Dr. Michael Alphonse, BITS Practice School Division, Hyderabad Campus was the programme coordinator. Students carried out challenging projects in various Groups of the Centre according to their discipline. During the period of their stay, they visited various facilities at IGCAR, BHAVINI and MAPS. As a part of the curriculum, quiz, project work presentations, group discussions, report writing and viva were done. The valedictory function was held on July 15, 2016 with Dr. Arun Kumar Bhaduri, Director, IGCAR delivering the valedictory address and distributing the certificates to the students.



Students from BITS Practice School with Dr. S. A. V. Satya Murty, former Director, IGCAR and senior colleagues of the Centre during the inaugural function

Summer Training in Physics & Chemistry (STIPAC-2016)

May 25 - July 3, 2016



Dr. S. A. V. Satya Murty, former Director, IGCAR addressing the inaugural function

The annual STIPAC programme has evolved over the years to train the pre-final physics & chemistry post graduate students across the country both in theoretical and experimental expertise available in IGCAR from 1995. The primary objective of this programme is to enthuse and encourage students to take up a career in scientific research. The programme generally held during the summer vacation for the students and runs on a theme for every two years. Experts from various institutions are also invited to address and interact with the students.

The 18th edition of this programme coincided with the International year of Light. The theme chosen was "Lasers in Physics & Chemistry". Around one hundred and fifty seven applications for Physics and eighty applications for Chemistry were received from which twenty students in each discipline were selected for STIPAC-16, based on their academic credentials quality of their write-up (Physics) and telephonic interview (Chemistry).

The training comprised about hundred hours of lectures on theory and fifty hours of experiments. Class room lectures were held in forenoons. In the afternoons, the students were encouraged to have a hands on learning experience by either doing project works or carrying out experimental works on various topics. Towards the end of the course, the students gave a presentation on the work done. Further, special lectures were organized in the evenings by inviting professors from premier institutions.

The STIPAC-16 programme was inaugurated by Dr. S. A. V. Satya Murty, the then Director, IGCAR. Dr. A. K. Bhaduri, Director, IGCAR and Dr. P. R. Vasudeva Rao former Director, IGCAR addressed the students on the valedictory day and distributed the certificates to the physics and chemistry students. Dr. P. R. Vasudeva Rao gave a special lecture on "Separations science and nuclear energy: some perspectives". Site visits to MAPS, BHAVINI and labs at IGCAR were also organized.



Dr. Arun Kumar Bhaduri, Distinguished Scientist and Director, IGCAR and senior colleagues of the Centre with the participants during the valedictory function

**9th DAE-VIE (Vision for Information Exchange) 2016
Symposium on Emerging Trends in I&C and Computer Systems
June 23-24, 2016**



Dr. R. Chidambaram, Principal Scientific Adviser to Government of India, Dr. K. Sivan, Director, Vikram Sarabhai Space Centre, Thiruvananthapuram, Dr. S. A. V. Satya Murty Director, IGCAR and other senior colleagues of the Centre during the inauguration

The “9th DAE-VIE (Vision for Information Exchange) 2016 Symposium on Emerging Trends in I&C and Computer Systems” was held at Sarabhai Auditorium, IGCAR, Kalpakkam during June 23-24, 2016. Dr. R. Chidambaram, Principal Scientific Adviser to Government of India inaugurated the symposium and released the souvenir. Dr. S. A. V. Satya Murty, Director, IGCAR and GSO delivered the presidential address. Dr. K. Sivan, Director, Vikram Sarabhai Space Centre, Thiruvananthapuram delivered the keynote talk on I&C experiences in space programme. Dr. G. Athithan, Director General (Micro Electronic Devices, Computational Systems & Cyber Systems), DRDO gave a special talk on the second day of the symposium on Cyber Security: Testing & Certification.

DAE-VIE 2016 was organized by Electronics & Instrumentation Group of IGCAR jointly with Kalpakkam chapter of Indian Nuclear Society. The conference was sponsored by Board of Research in Nuclear Sciences.

Seventeen invited talks by eminent experts (fourteen from DAE units, two from DRDO and one from IIT) in areas of I&C for FBR, PHWR, LWR, information technology, information security, indigenous microprocessor, high performance computing, cyber security and I&C security were delivered. Sixty nine contributory papers were presented as posters which were grouped in six categories namely Computer Networks & Network Security, PC-based & Embedded Systems, Security Systems, Sensors & Instrumentation, Servers & High Performance Computing and Software Tools, Techniques & Applications. Best poster in each category was selected by a jury of experts and each best poster was awarded a memento and cash prize. The symposium proceedings were published in electronic format and the e-proceedings were given to all participants in a USB flash drive. The technical programme was structured into five sessions with four talks in each session. Leading firms of I&C and computers exhibited their products and also gave technical presentation on their products. More than two hundred and fifty delegates from various units of DAE including aided institutes participated in the symposium. The entire symposium was also streamed live across the IGCAR campus network and also across all DAE units through high speed National Knowledge Network.



Dr. R. Chidambaram, Principal Scientific Advisor, Government of India, during his visit

10th National Conference on Recent Advances in Information Technology (READIT-2016) July 13-14, 2016



Dr. Sundeep Oberoi, Global Head, Enterprise Security and Risk Management, TCS, Dr. M. Sai Baba, Convener, READIT & Director, RMG, Dr. G. Amarendra, Director, MSG & MMG and Shri E. Soundararajan, SIRD during the release of souvenir at the inaugural function of READIT-2016

The 10th Biennial National Conference on Recent Advances in Information Technology (READIT) was organized in association with the Kalpakkam chapter of Madras Library Association (MALA) during July 13-14, 2016 with the theme of 'Information Access in Digital Era'. More than two hundred and sixty delegates including librarians from academic and public domain, Information Technology professionals and research scholars attended the conference.

The conference was inaugurated on July 13, 2016. Dr. M. Sai Baba, Convener, READIT and Director, RMG delivered the welcome address. The ceremony was chaired and presided over by Dr. G. Amarendra, Director, MSG and MMG, IGCAR. In his keynote lecture, he highlighted transition of libraries from static to dynamic and emphasized the need for relevant information access

Dr. Sundeep Oberoi, Global Head, Enterprise Security and Risk Management, Tata Consultancy Services in his keynote address and highlighted the issues relating in information access in digital era. A souvenir was released by the chief guest. Shri E. Soundararajan, SIRD, Organizing Secretary, READIT proposed the vote of thanks. Dr. Amarendra inaugurated the exhibition of stalls by various vendors representing information science, information technology and library science.

The conference incorporated invited talks by domain experts in information science and technology, oral/

poster presentations by research scholars and professionals. Intensive technical discussions on various aspects of information sharing, big data, cloud computing, digital content creation, infrastructure & access methods, information science in IT and semantic web for knowledge creation were presented during the conference by reputed persons from INFLIBNET, DRTC, NIT, TCS, IIT, NISCAIR, IT sectors and esteemed universities.

A special technical session was organized for the contributed presentations from research scholars and also a separate poster session for other contributed papers. The conference created a smooth forum and facilitated good interaction among the young researchers, students, professionals and well-known speakers in the area of modern digital technologies.

During the valedictory gathering, Shri V. Rajendran, welcomed the gathering. Dr. M. Sai Baba presented the conference summary and highlighted important issues relating to information sharing and access in digital era. In his valedictory address Dr. A. K. Bhaduri, Director, IGCAR highlighted the importance of relevant information access to patrons in helping their research and academic activities. He also shared some of his views on conducting the future READIT. The best paper awards were distributed to the respective authors by Dr. A. K. Bhaduri. Shri E. Soundararajan, thanked one and all, who participated, enlightened and cheered the conference.



Dr. Arun Kumar Bhaduri, Director, IGCAR and colleagues of our Centre with the participants

Report on Hindi Scientific Seminar August 03, 2016

With a view to encourage Scientists/Engineers to submit research papers in official language Hindi, a one-day Scientific Seminar on the subject "Science and Technology of Nuclear Reactors with Emphasis on Fast Reactors" was held under the auspices of OLIC, IGCAR, Kalpakkam on August 3, 2016 through Hindi medium at Sarabhai Auditorium. About 100 Scientists/Engineers of IGCAR and other DAE Units located at Kalpakkam viz., BARCF, MAPS, BHAVINI, SRI/AERB participated in this Seminar. In all, 20 research papers were presented in Hindi on various aspects relating to Nuclear Reactors like fuel fabrication, reprocessing, reactor operation and maintenance, quality assurance, project management, safety etc. The seminar was inaugurated by Dr. G. Amarendra, Director, MSG and MMG, IGCAR and Shri A. K. Vikraman Nair, Director (P&A) presided over the function. Shri B. K. Nashine, Head, DD & RSD and SED welcomed the participants and Dr. Awadhesh Mani,



Dr. G. Amarendra, Director, MSG and MMG inaugurating the seminar

Head, LTSS, CMPD conducted the programme being the convenor. Dr. A. K. Tyagi, former Head, SND and Dr. B. K. Choudhary, Head, DDNS have guided the technical sessions of the seminar. At the end, Shri S. S. Bhoopathy, AO (P) proposed the vote of thanks.

Hindi Fortnight Celebration September 14-28, 2016



A group photo of prize winners with chief guest and organising committee members

Hindi Fortnight was celebrated at IGCAR, Kalpakkam during September 14-28, 2016 with great enthusiasm. As part of this, Hindi Day function was organised on September 2, 2016 at Dr. Raja Ramanna Auditorium. Dr. Arun Kumar Bhaduri, Director, IGCAR was the Chief Guest. The programme was presided over by Shri A.K. Vikraman Nair, Director (P & A) who is also the Chairman of Official Language Implementation Committee (OLIC). The Hindi Day messages of Dr. Sekhar Basu, Chairman, AEC & Secretary, DAE

and Shri Rajnath Singh, Hon'ble Minister of Home Affairs were read out by Shri Pranay Kumar Sinha and Shri B. K. Nashine, respectively. Dr. Bhaduri and Shri Vikraman Nair addressed the gathering and spoke about the usefulness of Hindi and appealed to spread Hindi in daily activities at the Centre. Hindi Day function concluded with the vote of thanks by Dr. Awadhesh Mani, Head, LTSS, CMPD. During the Hindi Fortnight 2016, a variety of competitions namely, extempore speech, hindi calligraphy, essay writing,

hindi dictation, noting & drafting in hindi, vocabulary, poem recitation, GK Quiz and Hindi song, were conducted for the employees of the Centre which witnessed large participation. The valedictory function

of Hindi Fortnight-2016 was organised on September 28, 2016. Dr. G. Amarendra, Director, MSG & MMG gave away the prizes and consolation prizes to the winners of Hindi competitions.

Quality Circle Annual Meet (QCAM) - 2016

August 29, 2016



Dr. Arun Kumar Bhaduri and other senior colleagues of the Centre with Shri C. Mani, Former General Manager, BHEL, Trichy delivering the inaugural address

Quality circle is a small group of employees doing similar or related work who meet regularly to identify, analyze and solve work related problems usually led by a senior team member. After completing their analysis, they present their solutions to management for implementation and to improve the performance of the organization. Thus, implemented correctly, quality circles can help the organization to reduce costs, increase productivity and improve employee morale.

In IGCAR, every year Quality Circle Annual Meet (QCAM) is conducted and the QC case studies are presented by the QC teams. QCAM – 2016 was conducted on 29th August 2016 at Convention Centre and SRI Seminar Hall, Anupuram in parallel sessions. Welcome address was delivered by Shri A. Jyothish Kumar, Director, ESG, The Presidential address was delivered by Dr. Arun Kumar Bhaduri, Director, IGCAR. Inaugural Address was delivered by Shri C. Mani, Former General Manager, BHEL, Trichy and vote of thanks by Shri M. Krishnamoorthy, Head, FS, CWD.

Totally twenty three Quality Circles and delegates from all groups (about three hundred members) from IGCAR, schools from Kalpakkam and neighborhood presented QC case studies in a wide spectrum of topics covering Technical, Research and Development, Services and Education. Professional judges from BHEL Trichy and TVS, Hosur adjudged the QC case study presentations. Under the Mechanical and Manufacturing' stream, the PLUTONIUM QC, CG, bagged 'Dr Placid Rodriguez Memorial Trophy', while EXCEL QC, FRTG bagged the 'Shri M.K. Ramamurthy Memorial Trophy' for Plant Operation and Services category.

During valedictory function, the events were summed up by Shri G. Kempulraj, Head, CWD. The programme was concluded with the valedictory address and the prizes were distributed to the participants by Dr . G. Amarendra, Director, MSG & MMG and Shri G. Srinivasan, Former - Director, ROMG & RDG. Vote of thanks was proposed by Shri T. V. Maran, EIC, ZWS & member secretary, organising committee.

8th CEA-DAE Steering Committee Meeting on JHR Collaboration September 20, 2016



CEA and DAE delegates during the meeting

DAE and CEA have collaborative projects related to material irradiation in Joule Horwitz Reactor (JHR) being built by CEA France at Cadarache. JHR is funded by consortium of few nations in which India is one of the members and France being a lead member. Under this cooperation, many collaborative projects have been taken up. IGCAR is responsible for giving design of sodium loop to be erected in JHR for fast material irradiation testing. Similarly, BARC is responsible for In-Kind support for light water material testing and corrosion loop. 8th CEA-DAE Steering Committee Meeting on JHR Collaboration was held on September 20, 2016 at IGCAR, Kalpakkam for review of ongoing works in IGCAR and BARC. CEA team led by Dr. G. Bignan consisted of four experts where as DAE team consisting of twenty delegates from IGCAR & BARC was led by Dr. A.K. Bhaduri, Director IGCAR. CEA team visited RISHI sodium loop for conducting out of pile test as a prequalification test and witnessed the

ongoing experiment. A technical meeting dedicated to review, work related to RISHI loop was also held on September 20, 2016. RISHI loop will be tested in FBTR and the design will be supplied to CEA for fabrication and erection in JHR. Following ongoing collaborative projects were reviewed during the meeting.

- Development of a sample carrier for testing material at high temperature with online geometrical changes (by BARC)
- Design of a corrosion loop including development of instrumentation for studying Irradiation Assisted Stress Corrosion Cracking (DAE In-Kind contribution) (by BARC)
- Design of smart experiments for getting physical data of fuel sample (by BARC)
- Development of In-Core Sodium Loop for Irradiation of Multiple Samples at JHR (by IGCAR)

« Eminent Visitors to IGCAR »»



Delegations from Korea Atomic Energy Research Institute (KAERI) with Dr. S.A.V. Satya Murty, Director, IGCAR during their visit to the Centre

Delegations from Korea Atomic Energy Research Institute (KAERI) led by Dr. Park Won Seok, Director and Leader of the KAERI team, visited our Centre on February 02, 2016. During their visit, they visited Fast Breeder Test Reactor, Fast Reactor Technology Group, Sodium Safety related Experimental Facilities and 100 tonne Shake Table.



Delegation from Idaho National Laboratory with Dr. A. K. Bhaduri, Director, IGCAR and senior colleagues of the Centre

Delegation from Idaho National Laboratory led by Dr. Sarah Lennon, Director, Office of Bilateral Cooperation, Office of Nuclear Energy, DOE visited our Centre on February 16, 2016. During their visit, they visited Fast Breeder Test Reactor, KAMINI, Radio Metallurgy Laboratory, Fast Reactor Technology Group, Sodium Safety related Experimental Facilities and 100 Tonne Shake Table.



Shri G Srinivasan during the IGC Colloquium

Shri G Srinivasan, former Director, Reactor Operation and Maintenance Group and Reactor Design Group delivered IGC Colloquium on the topic “Pebbles on the Shore” on February 25, 2016.



Shri Vinod Kumar Thakral, IAS, Member Finance, Atomic Energy, Space & Earth Commission with Dr. Arun Kumar Bhaduri, Director IGCAR and senior colleagues during his visit

Shri Vinod Kumar Thakral, IAS, Member Finance, Atomic Energy, Space & Earth Commission visited our Centre on 19 April 2016. During his visit, he visited, the construction site of Fast Reactor Fuel Cycle Facility, Fast Breeder Test Reactor, KAMINI and Hot Cell Facility.



Delegations from United States Nuclear Regulatory Commission led by Dr. Stephen Burns with Dr. A.K. Bhaduri, Director, IGCAR and senior colleagues of the Centre

A delegation from United States Nuclear Regulatory Commission led by Dr. Stephen Burns, Chairman, US Nuclear Regulatory Commission visited the Centre on November 9, 2016. The delegation visited the Fast Breeder Test Reactor, KAMINI, Radio Metallurgy Laboratory, facilities in Fast Reactor Technology Group and Reactor Design Group.



Prof. A. K. Bhowmik, Professor of Eminence, RTC, IIT Kharagpur during the IGC Colloquium

Prof. A. K. Bhowmik, Professor of Eminence, RTC, IIT Kharagpur and former Director, IIT, Patna delivered IGC Colloquium on the topic “Nanotechnology in the Field of Polymers” on November 11, 2016



Prof. Vijayamohan K Pillai, Director, CECRI delivering the IGC Colloquium

Prof. Vijayamohan K Pillai, Director, Central Electrochemical Research Institute delivered IGC Colloquium on the topic “Large-scale Energy Storage using Redox Flow Batteries” on November 23, 2016



Dr. Srikumar Banerjee, Homi Bhabha Chair Professor, DAE & Former Chairman, AEC during the IGC Colloquium

Dr. Srikumar Banerjee, Homi Bhabha Chair Professor, DAE & Former Chairman, AEC delivered IGC Colloquium on the topic “Nuclear Power from Thorium - Different Options” on November 29, 2016

IGC COUNCIL

Chairman

Dr. Arun Kumar Bhaduri

Distinguished Scientist & Director, IGCAR



Dr. Arun Kumar Bhaduri, obtained his Ph.D. in Metallurgical Engineering from the Indian Institute of Technology, Kharagpur and joined Department of Atomic Energy in 1983. He has been with the Metallurgy and Materials Group of Indira Gandhi Centre for Atomic Research, Kalpakkam since 1984, until he took over as Director, IGCAR. He is also a Senior Professor, Homi Bhabha National Institute. He received Research Fellowship from Alexander von Humboldt Foundation, Germany in 1994 for a 2-year post-doctoral research at University of Stuttgart, Germany. He anchored the development of materials and their fabrication technologies for the Indian programmes on sodium-cooled fast reactors, fusion reactors and advanced ultra supercritical thermal power plant. He specialises in the field of materials joining, and has to his credit more than 200 journal publications, 300 conference presentations and 2 international patents. He is a fellow of Indian National Academy of Engineering, Indian Institute of Metals and Indian Institute of Welding. He is a recipient of the Metallurgist of the Year Award during National Metallurgists' Day (2003), Homi Bhabha Science & Technology Award (2002), Indian Nuclear Society Medal Award (2002), VASVIK Award (2005), DAE Group Achievement Awards (ten times) during 2006-2015 with four of them as Group Leader, IIW-India Golden Jubilee Welding Ratna Award (2016) by Indian Institute of Welding, Carl von Bach Commemorative Medal (2016) by MPA University of Stuttgart, Germany, Placid Rodriguez Memorial Lecture Award (2016) by Indian Institute of Metals, Chennai & Kalpakkam Chapters.

Members



Shri K. N. Vyas is a Mechanical Engineering graduate from MS University, Vadodara. After completion of the training in the 22nd Batch of the BARC Training School in 1979, he joined Fuel Design & Development Section of Reactor Engineering Division of BARC. Shri Vyas has worked for design & analysis of nuclear reactor fuels. He was also responsible for design & development of a novel fuel for strategic applications. He has worked extensively in thermal hydraulics and stress analysis of critical reactor core components. Shri Vyas, as an engineer, has played a key role for completion of strategic projects. Shri Vyas has also participated in design & analysis of the Test Blanket Module planned to be installed in ITER, France. Shri Vyas has been conferred several awards, which include Indian Nuclear Society Outstanding Service Award 2011, Homi Bhabha Science and Technology Award 2006, DAE Awards in the years 2007, 2008, 2012 and 2013. He is also a Fellow of the Indian National Academy of Engineers.



Dr. G. Amarendra is the Director, Materials Science Group (MSG) and Metallurgy & Materials Group (MMG), IGCAR. He obtained his M.Sc (Physics) degree from Sardar Patel University, Gujarat in 1980, passed out from the 24th batch of BARC Training School. He then joined the Materials Science Program at IGCAR, Kalpakkam in 1981, then known as Reactor Research Centre. He obtained his Ph.D degree from University of Madras in 1991 and carried out post-doctoral work at Brandeis University, Boston during 1993-94. He was instrumental in indigenous design and development of an unique variable low energy positron beam in 1995, which enabled non-destructive depth-profiling of defects at surfaces and interfaces of materials. His broad areas of research are defect studies in materials, radiation damage studies of structural materials, nuclear spectroscopy, thin films and nanomaterials. Dr. Amarendra is a Senior Professor of Homi Bhabha National Institute, Mumbai and chairman of standing committee of

physical science of HBNI at IGCAR. He had guided five Ph.D students and has over 200 journal and conference publications and two edited books. He is a member of scientific council of RRCAT and UGC-DAE CSR. He is a recipient of INSA Young Scientist Award (1991), IPA S.N.Seshadri Memorial Award (1996), Kalpakkam Science & Technology Award (1996), DAE Homi Bhabha Science & Technology Award (2006) and MRSI Medal Award (2013).



Shri Amitava Roy is a Distinguished Scientist and Chief Executive of Nuclear Recycle Board of Bhabha Atomic Research Centre. He is an M.Tech in Chemical Engineering from I.I.T., Mumbai. After graduation from 25th Batch of BARC Training School, he joined BARC in the year 1982. He served the organization in various capacities and has about 34 years of experience in design, construction, commissioning and operation of thermal reactor fuel cycle facilities, which are vital for the nuclear energy program of the country



Shri Awadesh Narain Verma is the present Chairman & Chief Executive, Heavy Water Board. Shri A.N. Verma, Outstanding Scientist, after completing B.Tech.(Chemical Engineering) from HBTI, Kanpur in 1979 joined 24th Batch of BARC Training School. After completion of training he was deputed to HWP(Kota) in August 1981 for taking up commissioning activities of first indigenous Heavy Water Plant based on Hydrogen Sulphide-Water Exchange process. He was actively involved in commissioning and trouble shooting of the plant during 1980s and later was involved in the normal operation of the plant. On getting the plant stabilized, he worked for taking up the re-optimization of process parameters and looking for various avenues of energy conservation to make the heavy water production cost competitive. By implementing various energy conservation measures, he was able to reduce specific energy consumption by 35% and received National Energy Conservation Award from Ministry of Power, Government of India in 2001 & 2002. He also received Rajasthan Energy Conservation Award-2010 from Chief Minister, Rajasthan for excellent contribution in energy saving at HWP, Kota. Subsequently, he took up the job of improving the quality of heavy water to enable its export to other countries. During his tenure, heavy water was exported in sufficient quantities to United States in three occasions. He was elevated to the post of General Manager in 2008 and took the charge of entire activities of Heavy Water Plant, Kota. Under his leadership, Heavy Water Plant(Kota) achieved highest ever production in Financial Year 2008-09 i.e., 132% of maximum achievable capacity. He is the recipient of 'DAE Group Achievement Award-2014' for Indigenous Development of Compressor shaft of high pressure Nitrogen Compressor at HWP, Kota and DAE Group Achievement Award-2015 for "Development of Sodium Sulphide Crystallizer Unit at HWP(Kota)".



Shri A. Jyothish Kumar, is an Outstanding Scientist & Director of Engineering Services Group. He is from the 29th Batch of Training School and joined IGCAR in 1986. He graduated in Electrical Engineering from Kerala University. He was working in FBTR during the initial 18 years and contributed significantly towards the commissioning and operation of Fast Breeder Test Reactor. He was actively involved in the commissioning of Turbine Generator set and solved many of the technical issues. He contributed significantly in the area of energy auditing and implemented various measures in the area of energy conservation.

He had initiated various measures towards life extension of various substation equipments, which includes online monitoring system. The introduction of state of art safety features with the introduction of numerical relays enhanced the safety of operating and maintenance personnel. The augmentation of electrical infrastructure including capacity addition was initiated considering the load growth for the next 15 years. He was instrumental in the introduction of grid connected solar system and focus is for the utilization of alternate energy sources & DC power supply. He took a lead role and coordinated the construction, installation, testing & commissioning of state of art 2 MIGD desalination plant. He is leading infrastructure development planning in the Centre.



Shri G. Kalyanakrishnan, Distinguished Scientist, Chairman & Chief Executive, Nuclear Fuel Complex (NFC) joined the 24th batch of BARC Training School after obtaining bachelor's degree in Chemical Engineering from the-then Regional Engineering College, Warangal in 1980. On successful completion of the training, Shri Kalyanakrishnan was posted to Heavy Water Plant at Kota, Rajasthan. He has vast experience in erection & commissioning and operation of Heavy Water Plants. He has made several pioneering contributions in streamlining various activities/operations of the Heavy Water Plants, which all have led to the improved performance of these plants. He was also involved in the quality assurance, maintenance and technical services at various Heavy Water Plants. He has immensely contributed in the successful commissioning of Zirconium Complex (ZC – a Unit of NFC) at Pazhayakalay, Tuticorin, Tamil Nadu and in achieving its nameplate capacity of 250 Metric Tonnes in the shortest time. As Deputy Chief Executive (Fuels & ZC), NFC, he has ably demonstrated outstanding performance in NFC's achievement of world record production of 1252 and 1503 Metric Tonnes of fuel assemblies during 2014-15 and 2015-16 respectively. He has also played a key role in the supply of reactor components for the Prototype Fast Breeder Reactor (PFBR). Shri Kalyanakrishnan is a Member of the Indian Institute of Chemical Engineers (IChE). Shri Kalyanakrishnan was conferred with the DAE S & T Excellence Award for establishment of the Zirconium Complex.



Dr. U. Kamachi Mudali, Director of Materials Chemistry and Metal Fuel Cycle Group joined IGCAR, Kalpakkam in 1984 after completing M.Tech. from IIT Bombay. His current interest includes study of materials chemistry related to fuel, coolant, sensors, structural and others required for fast reactors and associated fuel reprocessing, and establishing metal fuel fabrication and its reprocessing technology. He is a Fellow of ASM International, USA; NACE International, USA; Asia Pacific Academy of Materials; Indian National Academy of Engineering; Indian Institute of Metals; Academy of Sciences, Chennai; Institution of Engineers (India), and a Honorary Fellow of Electrochemical Society of India, IISc., Bangalore. Dr. Mudali is a well known materials and corrosion specialist and has made excellent contributions towards development of advanced corrosion resistant materials and coating technologies for FBR and associated reprocessing applications, in addition to R&D of FBR reprocessing materials, processes, modelling and equipments. He has published 390 papers in journals, co-edited 14 books/proceedings, and holds a h-index of 31. He has guided/coordinated project works of 158 students for their UG, PG and PhD degrees. He is a Senior Professor at Homi Bhabha National Institute, Chairman of standing committee in Chemical Sciences of HBNI at Kalpakkam, and an adjunct Professor at PSG Institute of Advanced Studies, Coimbatore. He has been recognized with awards including: Homi Bhabha Science and Technology Award from DAE; Indian Nuclear Society Medal; VASVIK Award; GD Birla Gold Medal Award; National Metallurgists Day Award from Ministry of Steel, GOI and IIM; Excellence and Meritorious Awards in Corrosion from NACE India, NCCI, Karaikudi and ECSI, Bangalore; Best Scientist Award from TNSCST, Chennai; Vocational Excellence Award, Chennai; Distinguished Faculty Award from HBNI, Mumbai; Outstanding and Distinguished Professional Achievement Award from ASM Chennai Chapter; and, AICTE-INAE Distinguished Visiting Professorship. He has been a Visiting Scientist at leading laboratories and institutions in Germany, Japan, UK, France, Israel, Bulgaria etc. Dr. Mudali is Associate Editor of Journal of Electrochemical Society of India, Key Reader of Metallurgical and Materials Transactions-A, and a Member of Editorial Board of seven international journals.



Dr. Kallol Roy, an Outstanding Scientist, is B.Tech in Electrical Engineering from NIT-Calicut; M.Tech in Electronics Design from CEDT-Indian Institute of Science; Ph.D in Fault Diagnostics – Systems & Controls from IIT, Bombay and Post Doctorate in Computer Process Control from University of Alberta, Canada. He is from the 28th Batch of BARC Training School. Dr. Kallol Roy's field of specialisation includes Total Maintenance Management of Reactors, Upgrading and Retrofit of C&I and Computer Based Systems, EMI / EMC Studies and Modelling in Plants, Fault Diagnostics of Systems and Equipment Reactor Safety, Surveillance & Tech-Specs. Analysis (CRP with IAEA) using Bayesian Estimation techniques, Safety and Security aspects of Computer based Systems. He was also a Professor of HBNI. Dr. Kallol Roy took charge as Chairman & Managing Director, BHAVINI on 31st March 2016.



Shri K Madhusoodanan is an Outstanding Scientist and Director of Electronics and Instrumentation Group. He is from 25th batch of BARC Training School and joined IGCAR in 1982. He graduated in Electrical Engineering from NIT, Calicut. His initial contributions include installation and commissioning of Instrumentation and Control (I&C) systems of Fast Breeder Test Reactor. He was responsible for design, procurement and installation of I&C systems of Boron Enrichment Facility and Steam Generator Test Facility (SGTF) at Kalpakkam. Subsequently, he was responsible for design of I&C systems of Prototype Fast Breeder Reactor (PFBR). He had been the Convener of Task Force formed by BHAVINI for co-ordinating the fabrication and supply of I&C systems of PFBR including the Distributed Control Systems. Presently, he is actively involved in co-ordinating the commissioning activities of I&C systems of PFBR, and guiding the developmental activities of I&C systems for future FBRs with a thrust on indigenisation. He has published around 30 papers in national and international journal and seminars. He is a member of Indian Nuclear Society and a Fellow of Institution of Engineers (India).



Shri Y.S. Mayya obtained his B.Tech. in Electronics & Communication Engineering in 1979. He is a product of 1980 batch of the BARC Training School. As a Scientific Officer in BARC, he has been engaged in design and development of Automation and Control systems for Nuclear facilities, accelerators, telescopes and strategic systems of DAE, DRDO and ISRO for more than three decades. He pioneered the development and deployment of the real-time networks and distributed systems in nuclear facilities. Some of his important contributions in the area of computer controlled servo systems include Giant Metre-wave Radio telescope (GMRT) in India, Stabilized Antenna platform for the TEJAS Light Combat Aircraft's Multi-Mode Radar, Stabilization & tracking system for airborne Radars, Antenna Control Servo System for the 32-metre Deep Space Network antenna for the Chandrayaan-1 mission and Telescope Control Servo System for the 21 meter MACE telescope being erected in Ladakh India. He led the Indian team in the development of software systems for the magnet test facilities of Large Hadron Collider (LHC) project at CERN, Geneva. Shri. Mayya was the Chairman & Managing Director of Electronics Corporation Of India Ltd, Hyderabad during 2009- 2012. While at ECIL, he was responsible for directing the operations of company in the area of strategic electronics for nuclear, defence, aerospace and security sectors and steered its steady growth. He piloted many projects of national importance such as Integrated Security Systems of CWG-2010 Delhi, COMINT and Electronic Warfare systems, C4I systems, Antenna for Chandrayaan-I and C&I systems for Nuclear facilities. During the period 2013-16 he held various positions in BARC including Project Director of Global Centre for Nuclear Energy Partnership (GCNEP) project of DAE and Director of Electronics & Instrumentation Group of BARC. He has published around 30 papers in national and international conferences. He is the recipient of DAE Technical Excellence award.



Shri U.C. Muktibodh is a Mechanical Engineering graduate from GS Institute of Technology & Science, Indore, Madhya Pradesh. He joined the 24th batch of BARC Training School in 1980. After completion of one year training in Nuclear Science and Engineering, he joined Reactor Process Group of erstwhile Power Project Engineering Division. During his career spanning 35 years, Shri Muktibodh has contributed significantly in design, development, engineering, procurement and commissioning of many Nuclear Systems and Balance of Plant Systems for 220, 540 and 700 MWe PHWRs. He spearheaded the overall Design, Development and Engineering of 700 MWe PHWRs having many advanced safety features.

He has also contributed towards generation of design and safety codes and guides for AERB and IAEA and also served in many AERB committees for Project Design Safety Review, Plant Safety Review & Qualification of Operation Personnel and Internal Safety Review Committee of NPCIL. He was conferred NPCIL Technical Excellence Award and number of group achievement awards in recognition of his outstanding contributions to indigenous Nuclear Power Programme. He is a Distinguished Scientist of the Department of Atomic Energy and Director (Technical) and on the Board of Directors of NPCIL. He is also a member of Board of Directors of Anushakti Vidyut Nigam Ltd. a joint venture between NPCIL and NTPC.



Shri S. Paramasivam graduated as a Mechanical Engineer from Madras Institute of Technology in the year 1981 and joined BARC in the 25th batch of Training School. After successful completion of training, he was posted at Heavy Water Board Head Office, Mumbai and was associated in mechanical project activities for Heavy Water Plant (Manuguru). In the year 1986, he was transferred to HWP (Manuguru), where he was involved in erection and commissioning activities pertaining to exchange units. He was promoted as Deputy Maintenance Manager (Mechanical) in the year 1998 and as head of Mechanical Maintenance Section in the year 2003. He was posted to HWP (Tuticorin) as Maintenance

Manager in the year 2005 and promoted as Officer On Special Duty in the year 2008, subsequently as General Manager of Heavy Water Plant, Tuticorin. In July, 2013, he was appointed as Regional Director, MRP, DPS, Chennai.



Dr. Prasad A. Naik, Director, Raja Ramanna Centre for Advanced Technology, Indore, did his M.Sc. (Physics) from IIT, Bombay in 1981. He joined Laser Section of BARC in 1982. He got his Ph.D. degree from University of Mumbai for his work carried out at BARC on "X-ray diagnostics of laser produced plasmas". He moved to Raja Ramanna Centre for Advanced Technology, Indore in 1990 and has been working there since then. Dr. Naik's areas of expertise include : high power lasers, ultra-short pulse ultra-high intensity lasers, X-ray spectroscopy of highly charged ions, laser-matter interaction physics etc. He was concurrently heading "Laser Plasma

Division" and "Indus Synchrotrons Utilization Division" at RRCAT, before he took over as Director, RRCAT on September 1, 2016.



Shri P. Puthiyavinayagam is an Outstanding Scientist & Director of Reactor Design Group. He is from 26th Batch of BARC Training School and joined IGCAR in 1983. He is a Mechanical Engineering graduate from Madurai Kamaraj University in 1982 and obtained his M.Tech from IIT, Madras in 1992. Since beginning, he has been involved in the design of PFBR. He has over 30 years of experience in the field of Fast Breeder Nuclear Reactor Technology. He is a specialist in FBR core design and played a key and significant role in the design, development and technology of manufacture for the fuel and other core assemblies for PFBR. He headed the task force on Future FBR – Economy and

recommended measures for cost competitiveness in future FBRs. Also he guided his team in evolving the challenging core design for future FBRs with high performance parameters. One of his notable contribution is

towards the successful demonstration of high burnup in the unique plutonium-rich carbide fuel through rigorous analysis and modeling. He served as India's Representative in the Technical Working Group on Fast Reactors in the IAEA during 2011-2015. He participated as an international faculty in the IAEA-ICTP International School Program on 'Physics and Technology of Fast Reactors' during 2009 and FJOH summer school in 2016. He is a Recipient of DAE 'Scientific & Technical Excellence Award' in 2009 and several Group Awards. Currently, he is responsible for the design of 600 MWe FBR1&2 and 100 MWt Metal Fuelled Test Reactor. He holds additional responsibilities as the Chairman of Fuel Specification Committee, Vice-Chairman of IGCAR Safety Committee on Research Reactors, Member in PFBR-PDSC etc. He has published over 100 technical papers in International and National Conferences. He has delivered many lectures in Academic Institutions as a part of Nuclear Energy Awareness program.



Dr. A. Ravishankar, Mechanical Engineer from 25th batch of BARC training school, joined the Department in 1981. He is presently Project Director, Fast Reactor Fuel Cycle Facility and Director Reprocessing Group. Under his leadership, many Hot cell systems, High-end equipment and Remote handling systems required for COmpact facility for Reprocessing of Advanced fuels in Lead shielded cells (CORAL) and Demonstration Fast Reactor fuel Reprocessing Plant (DFRP), have been successfully developed. Some of his important achievements include development of special purpose machines like multi fuel pin chopper, electrolytic dissolver, centrifugal extractor, high speed centrifuge, Laser based fuel sub-assembly dismantling system, various versions of Master slave manipulators, robotic sampling system etc. Some of these developments are import substitutes. He has made outstanding contribution to the design, construction and commissioning of CORAL for reprocessing of irradiated FBTR fuel. He played a vital role in the operation of CORAL and successfully processed many campaigns including fuel irradiated up to 155 GWD/T burn-up, which is a first of its kind in the world. He has incorporated many novel features in the design of CORAL facility so that development of new process and R&D related activities can also be taken up in the future. He was involved in the design and development of equipment for Thorium fuel reprocessing participating in the Thorium fuel reprocessing campaigns and successfully recovered U²³³. Currently he is responsible for construction and commissioning of FRFCF and also DFRP. He has over 150 classified reports, 65 technical presentations and publications to his credit. He has been conferred INS – Gold medal by Indian Nuclear Society in 2001, NOCIL award for Excellence in Design/Development of process Plant and Equipment for the year 2005, DAE group award in the year 2006, 2011, 2012 & 2016 and DAE-Homi Bhabha Science and Technology award in 2010 and INS Outstanding Service Award in 2014. He is a Fellow of the Indian National Academy of Engineering.



Shri P. Selvaraj, Outstanding Scientist and Director of Fast Reactor Technology Group, IGCAR is a graduate in Mechanical Engineering and completed B.E. (Mech. Engg.) degree with 3rd Rank from Annamalai University, Chidambaram in 1982 and joined BARC training school in the same year. He is a Homi Bhabha Award winner in Training School in the year 1983. After successful completion of the training, he was posted in IGCAR, Kalpakkam. He has also obtained M. Tech (Heat Transfer & Thermal Power) Degree from IIT Madras. He has over 33 years of experience in the area of Thermal Hydraulics of Fast Reactors. Presently he is responsible for design, construction, commissioning, operation and maintenance of high temperature experimental sodium facilities and conducting experiments for PFBR and future FBRs. He has made substantial contributions towards thermal hydraulic analysis of FBTR, PFBR and FBR 1 & 2. He has contributed significantly for the development of simulator for PFBR. He has played a key role in getting construction clearance for PFBR from Safety committee by clearing the queries related to PFBR Thermal Hydraulics. He has more than 180 publications in national and international journals and Conferences. He is a member of Indian Nuclear Society and Indian Society for Heat and Mass Transfer.



Dr. M. Sai Baba, Outstanding Scientist and Director, Resources Management Group, IGCAR, Kalpakkam, is from 24th batch of BARC Training School and joined IGCAR in 1981. He did his masters degree in Chemistry from Andhra University, and obtained Doctoral degree from University of Madras on mass spectrometric studies on Fullerenes. His research interests are mainly in the area of high temperature chemistry and mass spectrometry. He has carried out postdoctoral work at Texas A&M University, USA and at Research Centre, Juelich, Germany. He has worked as guest scientist at Research Centre, Juelich, Germany. He has co-authored more than 160 publications in journals and presentations in symposia and conferences. He has authored chapters in four books and edited six books. He is a Member of several professional bodies. After having been a researcher in chemistry for 25 years, Dr. Sai Baba moved to the management front to take up a new assignment related to strategic planning and setting up the BARC Training School at IGCAR in 2006. As the Director of the Resources Management Group which comprises of the Scientific Information Resource Division, Strategic Planning & Human Resources Development Division including BARC Training School at IGCAR, Kalpakkam, he is associated with the activities of Scientific Information Resource Division, which caters to providing information resources in the conventional and digital forms to suit the varied needs of researchers in all disciplines including the large student community pursuing their Post-graduate and Doctoral programmes. Dr. M. Sai Baba is a member of the Board of Studies, Library Sciences of University of Madras, Chennai. He is a fellow and executive member of Tamil Nadu Academy of Sciences. He is a Senior Professor of Homi Bhabha National Institute and Adjunct professor of PSG College of Technology and Amrita University. Dr. M. Sai Baba is heading the Training School at IGCAR that provides orientation training to young officers joining the Department. His mentoring and motivation has helped quite a number of students to settle down in their assignments successfully. As the coordinating Dean and Dean of Student Affairs, he plays an important role in the activities of the Homi Bhabha National Institute at IGCAR.



Shri K.V. Suresh Kumar is a Chemical engineer from the 29th batch of BARC Training School. He joined FBTR Operation Division as a trainee engineer in 1986 and participated in the initial commissioning of Steam Generator, steam & water system, Turbo-Generator and condenser cooling water systems. Parallely, he got licensed to operate FBTR as Junior Shift Engineer first and then as Senior Shift Engineer. After holding the positions of Engineer in Charge (Operation), Operation Superintendent, Head Reactor Operation Division, Reactor Superintendent and later as AD (O&M), He took over as Director, Reactor Facilities Group in 2016



Dr. B. Venkatraman, post graduate in physics and doctorate from University of Madras is from the 27th batch of BARC Training School and joined IGCAR in 1984. He has specialised in the areas of Non-Destructive Evaluation, Radiation sciences, its applications and quality assurance. He has been primarily responsible for establishing the conventional, digital X-ray, neutron radiography and thermal imaging facilities at IGCAR. He has developed many NDE procedures and techniques such as microfocal radiography for steam generator of Fast reactor, X-and neutron radiography for highly irradiated fuel pins, neutron radiography of pyro-devices, NDE of tail rotor blades of defence helicopters, to name a few. All these have been successfully implemented in the Centre and in other industries. He is certified in American Society for NDT Level-III in X-ray and gamma radiography, penetrant testing, Visual testing and Neutron radiography. He is a Senior Professor of Homi Bhabha National Institute. He has over 300 publications in Journals and Conferences including two articles in Encyclopedia of Material Science, two monographs, three books and is the series editor for the NDT handbooks published by National Certification Board, ISNT. He is the recipient of Homi Bhabha Science and Technology Award 2007 for Individual Excellence (highest award of the Department of Atomic Energy for individual scientific excellence). DAE Group Achievement Awards in 2008, 2010, 2011, 2012, IIW-Sharp Tools Award 2011, INS Gold Medal 2005, International Recognition Award 2013, ISNT-NDT Man of the Year Award (R & D) 2001, D & H Schereon Award, 1993 and has won more than 10 best paper awards. He is presently the Director, Health, Safety and Environment Group at IGCAR, Kalpakkam and is also serving as Director, Medical Group, GSO.



Organisation and Activities of Various Groups



Dr. A.K. Bhaduri
Director, IGCAR



Electronics, Instrumentation Group



Shri K. Madhusoodanan
Director, EIG



Shri R. Jehadeesan
Head, CD



Dr. D. Thirugnanamurthy
Head, EID



Shri A. Venkatesan
Head, ICD



Ms. T. Jayanthi
Head, RTSD



Shri G. Prabhakara Rao
Head, SISD

The Electronics, Instrumentation Group is actively involved in the development of Instrumentation & Control for fast reactor, fuel cycle technologies and related projects of DAE. Towards this the I&C systems are designed with safety and availability of the reactor as the guiding requirements through redundant systems and also keeping in mind that the simplicity of design and maintainability. A judicious combination of hardwired and computer based I&C systems, state-of-the-art design, manufacturing processes and testing were employed in the design of I&C systems. The systems developed include safety critical, safety related and non safety I&C systems. The prototype systems were qualified after rigorous environmental, EMI/EMC and seismic testing. The application software developed was subjected to thorough Verification & Validation procedures. The group is also responsible for providing state-of-the-art high performance computing facility with advanced application software to meet the computing requirements of FBR design & basic research, data communication facility including internet, email, campus network, Anunet, video conferencing, national knowledge network, and development of PFBR operator training simulator, 3D Models and plant walkthrough, computational intelligence based systems for reactor applications, wireless sensor based systems, knowledge management solution for the organization, and various application software based on user requirements. R&D activities in the areas of innovative instrumentation using pulsating sensors, Wireless Sensor Networks for use in future reactors, computational intelligence, knowledge management etc. are in progress. State-of-the-art computational facilities with a total processing power of about 30 tera FLOPS and data communication facilities are being provided. To take care of the security challenges the security electronics systems are constantly deployed and upgraded. Currently indigenous I & C components are being developed for import substitution to minimize the cost of the future FBRs with improved safety.

Engineering Services Group



Shri A. Jyothish Kumar
Director, ESG



Shri B. Harikrishnan
AD, CEG & Head, CMMWD



Shri C. Chandran
Head, AC&VSD



Shri G. Kempulraj
Head, CWD



Shri K. P. Kesavan Nair
Head, ESD



Shri H. R. Sridhara
Head, ASED



Shri N. Suresh
Head, CED

The Engineering Services Group is responsible for providing quality services and activities pertaining to Civil engineering, Electrical Engineering, Voice Communication Systems, Air-conditioning and Ventilation Systems, Material Handling Equipments and Central Workshop activities. The group also coordinates the BSNL requirements of the Centre. The group has a mandate to establish additional infrastructure requirements so as to meet Design, R&D and operational objectives of IGCAR which includes the backend fuel cycle. The group has expert teams with capability to design, engineer and execute systems under their jurisdiction. Aesthetically designed buildings & structures, reliable power supply, potable water, quality-air and other services including services from Central Workshop are being extended to other units of DAE located at Kalpakkam. The group is also involved in the horticulture development and maintenance of roads and drainage system. The nature of work involves interaction with several State and Central Government Organisations. The group is responsible for providing reliable air-conditioning and ventilation services to various radioactive laboratories and R&D facilities of the Centre. It was ensured that all developments are carried out in harmony with environment.

Fast Reactor Fuel Cycle Facility



Dr A. Ravishankar
Project Director



Shri B. Anandapadmanaban
AD, QA



Shri. B.M. Ananda Rao
AD, DFE



Shri C. Sudhakar
Head, B&PD

Fast Reactor Fuel Cycle Facility is entrusted with the work of planning, designing, constructing and commissioning the Fast Reactor Fuel Cycle Facility to close the fuel cycle of PFBR. FRFCF is a multi unit project involving BARC, IGCAR and NFC. IGCAR is piloting the construction of FRFCF. The Group continuously interacts with the participating groups from different units of DAE. Having completed the initial part of its mandate of coordinating the activities related to design of the facility, obtaining regulatory and statutory approvals of the project, preparation of the detailed project report, processing and obtaining financial sanction and developing all the infrastructure of the project, the group is currently engaged in the later part of its mandate, namely, the construction and commissioning of FRFCF. Construction of several infrastructural buildings is nearing completion and civil construction activity has commenced for four of the five radiological plants in the nuclear island. Successful commissioning of FRFCF is an essential step for embarking on construction of second stage nuclear power plants based on plutonium fuel that would pave the way for achieving energy security for the nation.

Fast Reactor Technology Group



Shri P. Selvaraj
Director, FRTG



Dr. B. K. Nashine
AD, SFG



Dr. V. Prakash
AD, CDHG



Shri B. Babu
Head, DDRSD



Shri G. Padmakumar
Head, SEHD

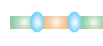
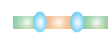


Dr. D. Ponraju
Head, SED



Shri I.B. Noushad
Head, SGTFD

Fast Reactor Technology Group (FRTG) has the mandate of development and testing of reactor components of FBRs. The group is responsible for the engineering development and testing in air, water and sodium of many components of PFBR. Design validation of critical components of FBRs are achieved through experiments in sodium and in water using full scale/scaled down models. FRTG has acquired expertise in the development of sensors and devices for sodium application, such as- EM flow meters, level probes, leak detectors, cold traps and electromagnetic pumps. Expertise has been developed in sodium handling and in the design, construction, commissioning and operation of high temperature sodium systems. The major sodium test facilities of FRTG include 5.5 MWt Steam Generator Test Facility (SGTF) for testing the model steam generators of FBRs, SADHANA loop for experimentally demonstrating natural convection based safety grade decay heat removal system of FBRs, Large Component Test Rig (LCTR) for testing critical full scale FBR components, In Sodium Test facility (INSOT) for creep and fatigue testing of advanced materials and Sodium Water Reaction Test (SOWART) facility to study self wastage and impingement wastage of SG tubes. Recent achievements of FRTG towards PFBR include qualification and testing of reactor components like Inclined Fuel Transfer Machine (IFTM), Transfer Arm(TA), under sodium ultrasonic scanner, design, fabrication and qualification of extended spark plug type leak detector, in-sodium calibration of permanent magnet flow meters and sodium testing of RADAR level probes, in-situ regeneration of cold trap and experiments on gas bubbles detection in sodium. FRTG is also involved in the developmental efforts towards improving the economics and enhancing the safety of future FBRs. The fabrication of integrated cold trap for in-vessel purification, development of model sweep arm scanner, integrated testing of Stroke Limiting Device with CSRDM, development of in-sodium pressure measurement device, high temperature ultrasonic transducer and ex-vessel level probe for sodium applications are some of the activities that are pursued for future FBRs. Major activities currently being pursued in FRTG include development of SONAR device for subassembly vibration measurement, conduct of high temperature tribology and thermal striping experiments for evaluating FBR component materials and design. Fabrication and erection of sodium test facilities namely Sodium Facility for Component Testing in Engineering Hall-I and Sodium Technology Complex are in progress. In Engineering Hall-IV, fabrication and erection of 5/8 scale sector model for hydraulic studies and facility for conducting FIV tests on seven subassembly cluster are completed.


Health, Safety & Environment Group



Dr. B. Venkatraman
Director, HSEG



Shri B. Anandapadmanaban
Head, QAD



Dr. R. Baskaran
Head, RSD



Dr. K.K. Satpathy
Head, EnSD

The Health, Safety & Environment Group comprises of Environmental Safety Division, Quality Assurance Division and Radiological Safety Division. The Health, Safety & Environment Group is actively involved in health physics, radiation safety services, radiological and environmental impact assessment studies, quality control and quality assurance services, biodiversity studies, coastal water and air quality and industrial and fire safety related services for fast reactor and fuel cycle technologies and related projects of DAE. The Group organizes public awareness programmes on radiation safety and nuclear energy in addition to training and awareness programmes on industrial, radiation and fire safety to occupational workers. The Radiological Safety Division of the Group is responsible for radiological protection and surveillance of all active plants and also occupational workers of our Centre. It also has focussed R&D activities in the areas of atmospheric dispersion and modelling, sodium aerosol science and technology, luminescence dosimetry, radiation safety through modelling & simulation and societal applications of ionising and non ionising radiations. Environment and Safety Division apart from its services to meet the mandatory requirements of MoEF and AERB has active R&D activities in the areas of studies on coastal water quality, plankton diversity, fish diversity, floral diversity, crab diversity, benthic organism diversity, sea sediment characterization, ground & surface water quality, ambient air quality, lake ecology, bio-remediation, toxicity assessment and chlorination and its byproduct. Quality Assurance Division (QAD) is primarily responsible for catering to the quality assurance, inspection, non-destructive testing (NDT) and quality audit activities of all the Groups of our Centre including FRFCF. QAD establishes and implements an effective quality management system for the mechanical works of Demonstration Fuel Reprocessing Plant (DFRP), cater to the inspection and NDT requirements of the various Divisions and Groups in our Centre, ensure conformance to in-house/national/international codes, standards and specifications during procurement fabrication, construction and erection (mechanical) for the R&D projects carried out by the various groups of our Centre. It also provides its expertise to other DAE units at Kalpakkam and also for strategic sectors.


Materials Chemistry & Metal Fuel Cycle Group




Dr. U. Kamachi Mudali
Director, MCMFCG



Dr. S. Anthonysamy
AD, DFMF



Dr. M. Joseph
AD, FChG



Dr. R. Sridharan
AD, MCG



Dr. K. Ananthasivan
Head, FChD



Dr. V. Jayaraman
Head, MCD



Shri B. Muralidharan
Head, PPED



Shri P. Muralidaran
PE, Process



Dr. B. Prabhakara Reddy
Head, PMPD



Shri R.R. Ramanarayanan
Head, CFD

Materials Chemistry and Metal Fuel Cycle Group comprises of three subgroups, Materials Chemistry Group (Materials Chemistry Division & Chemical Facilities Division), Fuel Chemistry Group, (Fuel Chemistry Division & Pyrochemical and Materials Processing Division), Demonstration Facility for Metal Fuel (Process) and Pyro Process Engineering Division. The major mandate of the group is to develop advanced fuel fabrication methods, advanced methods of reprocessing and addressing the chemistry and engineering problems associated with aqueous and pyro reprocessing; to carry out post irradiation studies such as dissolution of fuel, measurement of burn up, recovery of minor actinides; to provide expert analytical services to various programmes in the Centre and other DAE units and to develop new analytical techniques; to carry out basic chemical studies to fine tune the R&D capabilities and be in a state of readiness to undertake challenging investigations for furthering the Department's goal.

The materials chemistry related activities include sodium chemistry, chemistry of un-irradiated as well as irradiated fuels, development of fuel cycle, development of alternate solvents and extractants for the separation of actinides and lanthanides, process for minor actinide partitioning, high temperature chemistry, technology development for production elemental boron from enriched boric acid, production of radioisotopes for societal applications, development of molten salt electrolytic process, analytical chemistry and spectroscopy. Recent achievements include demonstration of remote operation of a electrorefiner for processing unirradiated U-Zr alloy in hot cells, measurement of the solidus and liquidus temperatures as well as vapour pressure of U-Pu-Zr fuel, commissioning of a glove box facility for measuring the viscosity of Pu containing broths, insights on third phase formation in trialkyl phosphate – actinide system using Small Angle Neutron Scattering technique, development of task specific ionic liquids and development of tin oxide based sensors for monitoring trace levels of hydrogen in argon cover gas plenum of FBTR.

Pyro Process Engineering Division is involved in carrying out erection, testing and commissioning of Pyro Process R&D Facility (PPRDF-1), PPRDF-2 and pursue R&D in PPRDF-1 & 2 for development of engineering scale systems for demonstration of Pyro processing in large scale. This involves development of suitable remote handling components required for hot cell operations and modeling & analysis of pyro process systems and performing experiments using already established Ambient Temperature Electro Refiner (ATER).


Materials Science Group



Dr. G. Amarendra
Director, MSG



Dr. B. K. Panigrahi
AD, ANG & Head, MPD



Dr. N. V. Chandra Shekar
Head, CMPD



Dr. Sitaram Dash
Head, SND

The Materials Science Group (MSG) has the mandate of pursuing high quality basic research on topical problems in Materials Science relevant to fast reactors. Among three divisions of MSG, the Accelerator and Nanoscience Group (ANG) consists of Materials Physics Division (MPD) and Surface and Nanoscience Division (SND). The MPD focuses on studies on ion beam simulation of radiation damage using a 1.7 MV tandem accelerator, materials synthesis and modification and manipulation of materials using ion beams, studies on defects using Positron Annihilation Spectroscopy and computer simulation of material properties. Several nuclear techniques such as Time Differential Perturbed Angular Correlation (TDPAC), Auger Electron Spectroscopy, Mossbauer Spectroscopy etc. have been used for the study of condensed matter, while positron beam set-up is used for depth resolved studies of defects. There is also an active section working on computational studies of materials using a variety of simulation and ab-initio codes. There is also intense effort towards nucleating quantum metrology based research studies. The SND focuses on the study of monolithic and multilayered thin films and nanostructures using a variety of techniques such as Secondary Ion Mass Spectrometry, nanomechanical testing and Scanning Probe Microscopy. Also, development of novel nanomaterials for advanced sensor applications is being carried out. Research activities relating to sensors based micromachined cantilevers and MEMS are also being pursued. Condensed Matter Physics Division (CMPD) pursues several theme based research programs. One of them being the investigation of structure and physical properties of materials under extreme conditions such as high pressures, low temperatures, high temperatures and high magnetic fields. Further, over the years various facilities for the synthesis of condensed matter powders and single crystals have been established in the division including Laser Heated Diamond Anvil Cell facility for synthesis of novel materials under high pressures and high temperatures. The systems being focused on encompass superconductors, strongly correlated systems, multiferroics, frustrated systems, f-electron based compounds, glasses and super hard transition metal borides Dynamic Light Scattering and Confocal Microscopy are utilized for studies on soft condensed matter. SQUID based systems for Magneto-Cardiography (MCG) and Magneto-Encephalography (MEG) have been successfully designed, assembled, standardized and used for clinical studies. Further, SQUID based measuring systems such as high field SQUID magnetometer, SQUID VSM, SQUID based set-up for Non-Destructive Evaluation (NDE) have been developed and successfully commissioned.

Metallurgy and Materials Group



Dr. G. Amarendra
Director, MMG



Shri Jojo Joseph
Head, PIED



Dr. K. Laha
Head, MMD



Dr. C. Mallika
Head, CSTD



Dr. S. Murugan
Head, RIRD



Dr. B. Puma Chandra Rao
Head, NDED



Dr. Shaju K. Albert
Head, MTD



Dr. Saroja Saibaba
Head, PMD

The Metallurgy and Materials Group (MMG) has been nurturing a vibrant research and development programme to provide active support to a variety of materials related issues of Sodium Cooled Fast Reactors and associated closed fuel cycle technologies. MMG has made major strides towards the successful development of three generations of nuclear structural materials aimed at withstanding demanding operating and environmental conditions. A few notable among them include: 316 LN steels, swelling-resistant austenitic and high Cr-based ferritic steels, especially the oxide dispersion strengthened (ODS) steels for Fast Reactors core components. In addition, MMG has also pioneered the design, fabrication and in-pile testing of irradiation capsules. Extensive post-irradiation examination facilities have been effectively utilized for obtaining extremely valuable data on in-pile performance of various fuels, structural and shielding materials. In an allied perspective, the group has immensely contributed towards developing a spectrum of nuclear application specific non-destructive evaluation (NDE) techniques for inspecting and qualifying large sized and intricate reactor components. MMG has also made immense contributions towards the development of advanced welding techniques for joining special materials, with tight control over process parameters and ensuring component integrity, automated and robotic systems for remote inspection of critical nuclear engineering components as well as for post-irradiation examination facilities. The extensive facilities for evaluation of mechanical properties of FBR materials include innovative small specimen testing techniques and evaluation of mechanical properties in dynamic sodium environment. On the theoretical front, robust modelling protocols for predicting high temperature phase stability, thermophysical properties, deformation behavior and mechanical properties of materials under various loading conditions etc. are also being pursued. MMG houses truly sprawling and state of the art materials characterization facilities that have been put into adroit use for catering to materials developmental issues of not only fission and fusion nuclear reactors, but also for the advanced ultra super critical (AUSC) power plant programme. MMG is also involved in the development of an array of novel application specific or functional materials such as ferroseals for sodium pumps, ferroboration for meeting the requirement of economical and alternate neutron shield material, iron based soft magnetic alloy for control rod applications and corrosion resistant materials and coatings for aqueous and pyrochemical reprocessing applications. The corrosion control and prevention activities include estimation of corrosion behavior of structural materials and concrete structures for long term uninterrupted service of reactor systems and reprocessing plants. Due to its focused and balanced research and developmental efforts, MMG also supports HBNI academic programmes at the Centre in terms of various students pursuing M.Tech and doctoral degrees. Thus, the group sustains synergistic academic, research and technological developmental activities seamlessly.


Reactor Design Group




Shri P. Puthiyavinayagam
Director, RDG



Shri S. Raghupathy
AD, NSDG



Dr. K. Velusamy
AD, NSAG



Ms. S. Usha
AD, PPG



Shri S. Athmalingam
Head, RCD



Dr. K. Devan
Head, RND



Shri S. Jalaldeen
Head, SMD



Dr. A. John Arul
Head, RSDD



Shri N. Kasinathan
Head, THD



Shri N. Theivarajan
Head, PPCD



Ms. R. Vijayashree
Head, CH&MD

The Reactor Design Group (RDG) is responsible for the design, analysis, safety assessment and technology development of Sodium Cooled Fast Reactors (SFR). The group is responsible for providing the technical expertise & support to the 500 MWe Prototype Fast Breeder Reactor (PFBR), design & development of future 600 MWe oxide fuelled FBRs, metal fuel pin design & development, design of metallic fuelled test reactor and theoretical & experimental R&D in the area of structural mechanics & thermal hydraulics. The group is responsible for getting safety clearance from AERB for design related activities of PFBR. The group comprises Nuclear Systems Design Group (NSDG), Nuclear Systems Analysis Group (NSAG) and Power Plant Group (PPG). The domains and systems covered by RDG are: Reactor core physics and engineering, reactor assembly systems & components, shutdown mechanisms, sodium circuit systems & components, component handling systems, plant services, plant layout and electrical power systems. The group also executes R&D in the domain of structural mechanics, thermal hydraulics and plant dynamics, involving national and international institutions. It also provides analytical support to FBTR for the continued up gradation of its core performance parameters and core plant dynamics & safety analysis. The responsibility of the group includes developing human resource of high caliber for the design and analysis of SFRs in the country. The group has completed the conceptual design of FBR1&2, to be located at Kalpkkam and is currently engaged in the detailed design activities. In parallel, it is involved in evolving the design of 100 MWt metal fuel test reactor and it has conceptualized the reactor systems. These apart, it has a modern design office with many advanced modeling and analysis softwares, a structural mechanics laboratory having state-of-the-art facilities for carrying out tests on large components, high temperature structural integrity and a structural dynamics laboratory for carrying out seismic tests on components with large sized shake tables. It is extending its experimental facilities to other DAE units also to cater to other reactor programs. This group has specific expertise in the domain of reactor physics in fast neutron spectrum, design of mechanisms operating in sodium, mechanical design and analysis of components as per the American (ASME) and French (RCC-MR) design codes, thermal hydraulics of liquid metal, plant dynamics etc.

Reactor Facilities Group



Shri K. V. Suresh Kumar
Director, RFG



Shri A. Babu
AD, OMG



Shri S. Varatharajan
AD, TTG



Shri M.S. Chandrasekar
Head, THRDD



Shri K. Dinesh
Head, TSD



Shri G. Shanmugam
Head, ROD



Shri S. Sridhar
Head, RMD

The Reactor Facilities Group (RFG) is responsible for safe operation of Fast Breeder Test Reactor (FBTR) and KAMINI Reactor within the limits given in technical specification documents. The group also takes part in the operational safety review of PFBR Project. The Training section of the group is responsible for training the O&M staff of PFBR and future FBRs besides training O&M staff of FBTR and KAMINI. Progressive modifications in FBTR to increase its availability and for gaining newer experience in operation, utilizing the reactor for irradiation of advanced fuels and materials for fast reactors and conducting safety related experiments form a major part of RFG's activities. RFG is also responsible for fabrication and safe storage of fuel and blanket subassemblies required for PFBR.

Reprocessing Group



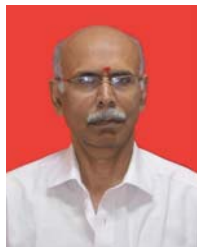
Dr. A. Ravishankar
Director, RpG



Shri B. M. Anandarao
AD, HCSPG



Shri B. Krishnamurthy
Head, RPMD



Shri N. K. Pandey
Head, RRDD



Shri K. Rajan
Head, RPDCD



Shri Shekhar Kumar
Head, RPOD



Dr. R. V. Subba Rao
Head, PRCD

Reprocessing Group of IGCAR is responsible for various activities pertaining to fast reactor fuel reprocessing technology such as the design, construction and operation of the fast reactor fuel reprocessing plants and associated R&D activities. CORAL (Compact facility for Reprocessing Advanced fuels in Lead cells) a pilot plant facility, commissioned in 2003, continues to operate successfully, processing the mixed carbide spent fuel from FBTR. Recently, a very challenging operation of in-situ replacement of Radiation Shielding Window (RSW)

at CORAL was carried out with very low dose expenditure. The facility continues to serve as a test bed and has provided valuable feedback for the design and construction of future reprocessing plants. Construction of Demonstration fast reactor fuel reprocessing plant (DFRP) is nearing completion and commissioning activities have started. Water runs of major process systems are completed and gearing up for taking up chemical runs. The group is also carrying out the design activities of the Fuel Reprocessing Plant of Fast Reactor Fuel Cycle Facility, which is a commercial scale reprocessing plant. In addition the group also lends its expertise in procurement of long delivery items such as the optical glass slabs for radiation shielding windows, various types of master slave manipulators, lead bricks etc. Concurrently focused R&D is being pursued in equipment development, alternate processes and aqueous processing of metallic fuel.

Resources Management Group



Dr. M. Sai Baba
Director, RMG



Ms. S. Rajeswari
Head, SIRD



Dr. Vidya Sundararajan
Head, SPHRDD

Resources Management Group comprises of the Scientific Information Resource Division and the Strategic Planning and Human Resource Development Division. The mandate of the Group is towards planning and management of resources like financial (budget), human and scientific information resources in the Centre. This significant activities of the Group include: Strategic planning and human resource management, conducting the academic programmes of BARC Training school at IGCAR, formulating and monitoring capital projects towards budget planning and management including providing necessary reports and proposals to DAE, automation and integration of activities pertaining to administration, accounts, stores, budget and procurement on a single platform, coordinating the visits of important dignitaries and delegations to the Centre, formulating and facilitating collaborations and MOU including patents, providing information resources through conventional library and the library on the desktop by digital networking with special emphasis to cater to the needs of students and young scholars and publishing important documents of the Centre like IGC Newsletter, Annual Report, preparation of annual reports and plan related documents.

This group also coordinates the facilitation of undergraduate and post graduate projects by students from various academic institutions, internships of students pursuing M.Tech. in Nuclear Engineering, summer schools of Harish Chandra Research Institute and BITS, and industrial visits of students from institutions on a continuous basis

Technical Co-ordination & Quality Control Division



Shri R. V. Subba Rao
Head, TC&QCD

Technical Co-ordination & Quality Control Division is primarily responsible for quality control and manufacturing process development of several critical equipments for IGCAR manufactured in the Western Region of the Country. It provides technical co-ordination services for the Centre with BARC as well as the Headquarters of DAE. TC&QCD also participates in a number of R&D activities which are being carried out at BARC towards meeting the mandate of IGCAR, PFBR and FRFCF. Presently it is also engaged in the inspection of Glove Boxes & Fume Hoods, Lead shielding bricks and components being fabricated in bulk quantity for FRFCF and High Temperature Electro Refiner and salt purification system for Metallic Fuel Reprocessing activity. Apart from the Quality Assurance and Technical Coordination works, the Division also provides logistics support for all the Liaison works of the Centre at Mumbai and carrying Public Awareness activities in the neighbourhood villages as well as across the State to take forward the public outreach programmes of the Centre.

Madras Regional Purchase Unit



Shri S. Paramasivam
RD, MRPU

Material Management activities for IGCAR, GSO, BARCF & HWP(T) are taken care of by Madras Regional Purchase Unit (MRPU) which comes under Directorate of Purchase & Stores of Department of Atomic Energy. Procurement and payment to suppliers are carried out at Chennai and inventory and accounting are carried out by Central Stores at Kalpakkam. MRPU was the first DAE unit to introduce e-tendering and more than 75% of files were processed by e-tendering mode in the e-tender portal www.tenderwizard.com/DAE. During the year 2015, MRPU processed about 3481 indents with an estimated cost of 500 Crores and released about 3290 purchase orders worth 285 Crores.

Administration & Accounts



Shri A. K. Vikraman Nair
Director (P&A)



Shri Sai Kannan
DCA, Officiating as IFA



Shri S. S. Boopathy
AO (P), IGCAR



Shri K. R. Sethuraman
AO (R&SR)

LIST OF IMPORTANT ABBREVIATIONS

AC&VSD	Air Conditioning and Ventilation System Division	MSG	Materials Science Group
AERB	Atomic Energy Regulatory Board	MTD	Materials Technology Division
A&SED	Architecture & Structural Engineering Division	NDED	Non-Destructive Evaluation Division
BARC	Bhabha Atomic Research Centre	NFC	Nuclear Fuel Complex
BARCF	Bhabha Atomic Research Centre Facilities	NICB	Nuclear Island Connected Building
BHAVINI	Bharatiya Nabhiya Vidyut Nigam Limited	NPCIL	Nuclear Power Corporation of India Ltd.
BPD	Budget & Procurement Division	NSAG	Nuclear Systems Analysis Group
CD	Computer Division	NSDG	Nuclear Systems Design Group
CDHG	Components Development & Hydraulics Group	PFBR	Prototype Fast Breeder Reactor
CED	Civil Engineering Division	PHWR	Pressurized Heavy Water Reactor
CEG	Civil Engineering Group	PIED	Post Irradiation Examination Division
CERMON	Continuous Environmental Radiation Monitoring Network	PMD	Physical Metallurgy Division
CFD	Chemical Facilities Division	PPCD	Power Plant Control Division
CH&MD	Components Handling & Mechanism Division	PPED	Pyro Process Engineering Division
CMPD	Condensed Matter Physics Division	PPG	Power Plant Group
C&MWD	Contracts & Major Works Division	PRCD	Process & Radio Chemistry Division
CORAL	Compact facility for Reprocessing Advanced fuels in Lead cell	QAD	Quality Assurance Division
CSTD	Corrosion Science & Technology Division	RCD	Reactor Components Division
CWD	Central Workshop Division	RDG	Reactor Design Group
DDRSD	Device Development and Rig Services Division	RFG	Reactor Facilities Group
DFE	Design and Field Engineering	RIRD	Remote Handling, Irradiation Experiments and Robotics Division
DFMFF	Demonstration Facility for Metallic Fuel Fabrication	RMD	Reactor Maintenance Division
DFRP	Demonstration Fuel Reprocessing Plant	RMG	Resources Management Group
EID	Electronics and Instrumentation Division	RND	Reactor Neutronics Division
EIG	Electronics and Instrumentation Group	ROD	Reactor Operation Division
EnSD	Environmental & Safety Division	RMD	Reactor Maintenance Division
ESD	Electrical Services Division	RPDCD	Reprocessing Plant Design & Commissioning Division
ESG	Engineering Services Group	RpMD	Reprocessing Maintenance Division
FBR	Fast Breeder Reactor	RpG	Reprocessing Group
FBTR	Fast Breeder Test Reactor	RPOD	Reprocessing Plant Operations Division
FChD	Fuel Chemistry Division	RpOG	Reprocessing Operation Group
FChG	Fuel Chemistry Group	RRDD	Reprocessing Research and Development Division
FRFCF	Fast Reactor Fuel Cycle Facility	RSD	Radiological Safety Division
FRPD	Fuel Reprocessing Process Division	RSDD	Reactor Shielding and Data Division
FRTG	Fast Reactor Technology Group	RTSD	Real Time Systems Division
HCSPG	Hot Cell Systems and Project Group	SED	Safety Engineering Division
HSCPG	Hot Cell Systems and Project Group	SE&HD	Sodium Experiments & Hydraulics Division
HSEG	Health, Safety & Environment Group	SFG	Sodium Facility Group
GSO	General Services Organisation	SGTFD	Steam Generator Test Facility Division
IAEA	International Atomic Energy Agency	SIRD	Scientific Information and Resource Division
IIT	Indian Institute of Technology	SMD	Structural Mechanics Division
IMSc	Institute of Mathematical Sciences	SND	Surface and Nanoscience Division
I&CD	Instrumentation & Control Division	SOWART	Sodium Water Reaction Test facility
MAPS	Madras Atomic Power Station	SP&HRDD	Strategic Planning & Human Resource Development Division
MCD	Materials Chemistry Division	TC&QCD	Technical Coordination & Quality Control Division
MCMFCG	Materials Chemistry & Metal Fuel Cycle Group	THD	Thermal Hydraulics Division
MMD	Mechanical Metallurgy Division	THRDD	Training & Human Resource Development Division
MMG	Metallurgy and Materials Group	TSD	Technical Services Division
MPD	Materials Physics Division	TTG	Technical & Training Group
MRPU	Madras Regional Purchase Unit		

INDIRA GANDHI CENTRE FOR ATOMIC RESEARCH

Dr. Arun Kumar Bhaduri
Director, IGCAR

IGC Council

IGC Scientific Committee
[IGSC]

Director's Advisory
Committee [DAC]

Shri K. Madhusoodanan
Director
Electronics & Instrumentation Group

Dr. G. Amarendra
Director
Metallurgy & Materials Group

Shri A. Jyothish Kumar
Director
Engineering Services Group

Dr. G. Amarendra
Director
Materials Science Group

Shri P. Selvaraj
Director
Fast Reactor Technology Group

Shri P. Puthiyavinayagam
Director
Reactor Design Group

Dr. B. Venkatraman
Director
Health, Safety & Environment Group

Shri K. V. Suresh Kumar
Director
Reactor Facilities Group

Dr. U. Kamachi Mudali
Director
Materials Chemistry & Metal Fuel Cycle Group

Dr. A. Ravisankar
Director, Reprocessing Group
& Project Director
Fast Reactor Fuel Cycle Facility

Shri R.V. Subba Rao
Head
Technical Co-Ordination & Quality Control Division
(Stationed at BARC, Mumbai)

Dr. M. Sai Baba
Director
Resources Management Group

Shri K. Sai Kannan
DCA, Officiating as IFA

Shri A. K. Vikraman Nair
Director (P&A)
Administration

as on 31-12-2016

Groups / Divisions / Heads

Electronics & Instrumentation Group

Shri K. Madhusoodanan
Director

Shri R. Jehadeesan
Computer Division

Dr. D. Thirugnanamurthy
Electronics & Instrumentation Division

Shri A. Venkatesan
Instrumentation & Control Division

Ms. T. Jayanthi
Real Time Systems Division

Shri G. Prabhakara Rao
Security and Innovative Sensors
Division

Engineering Services Group

Shri A. Jyothish Kumar
Director

Shri C. Chandran
Air-Conditioning & Ventilation
System Division

Shri G. Kempulraj
Central Workshop Division

Shri K. P. Kesavan Nair
Electrical Services Division

Shri B. Harikrishnan
Associate Director
Civil Engineering Group

Shri H. R. Sridhara
Architecture & Structural
Engineering Division

Shri N. Suresh
Civil Engineering Division

Shri B. Harikrishnan
Contracts & Major Works Division

Fast Reactor Technology Group

Shri P. Selvaraj
Director

Dr. B. K. Nashine
Associate Director
Sodium Facility Group

Dr. V. Prakash
Associate Director
Components Development &
Hydraulics Group

Shri B. Babu
Device Development &
Rig Services Division

Dr. D. Ponraju
Safety Engineering Division

Shri G. Padmakumar
Sodium Experiments &
Hydraulics Division

Shri I. B. Noushad
Steam Generator Test Facility
Division

Groups / Divisions / Heads

Health, Safety & Environment Group

Dr. B. Venkatraman
Director

Dr. K. K. Satpathy
Environmental & Safety Division

Shri B. Anandapadmanaban
Quality Assurance Division

Dr. R. Baskaran
Radiological Safety Division

Materials Science Group

Dr. G. Amarendra
Director

Dr. B. K. Panigrahi
Associate Director
Accelerator and Nanoscience Group

Dr. B. K. Panigrahi
Materials Physics Division

Dr. Sitaram Dash
Surface & Nanoscience Division

Dr. N. V. Chandra Shekar
Condensed Matter Physics Division

Materials Chemistry & Metal Fuel Cycle Group

Dr. U. Kamachi Mudali
Director

Dr. S. Anthonysamy
Associate Director, Demonstration Facility
for Metal Fuel Group

Shri P. Muralidaran
Project Engineer, Process

Dr. M. Joseph
Associate Director
Fuel Chemistry Group

Dr. K. Ananthasivan
Fuel Chemistry Division

Dr. B. Prabhakara Reddy
Pyro-chemical & Materials
Processing Division

Dr. R. Sridharan
Associate Director
Materials Chemistry Group

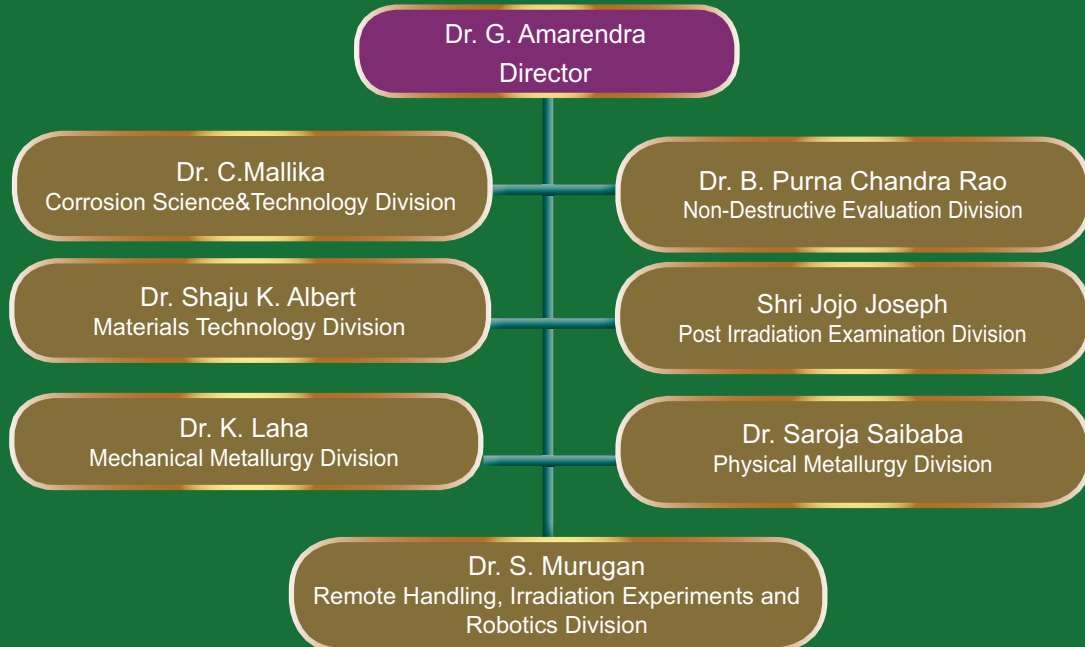
Shri R. R. Ramanarayanan
Chemical Facilities Division

Dr. V. Jayaraman
Materials Chemistry Division

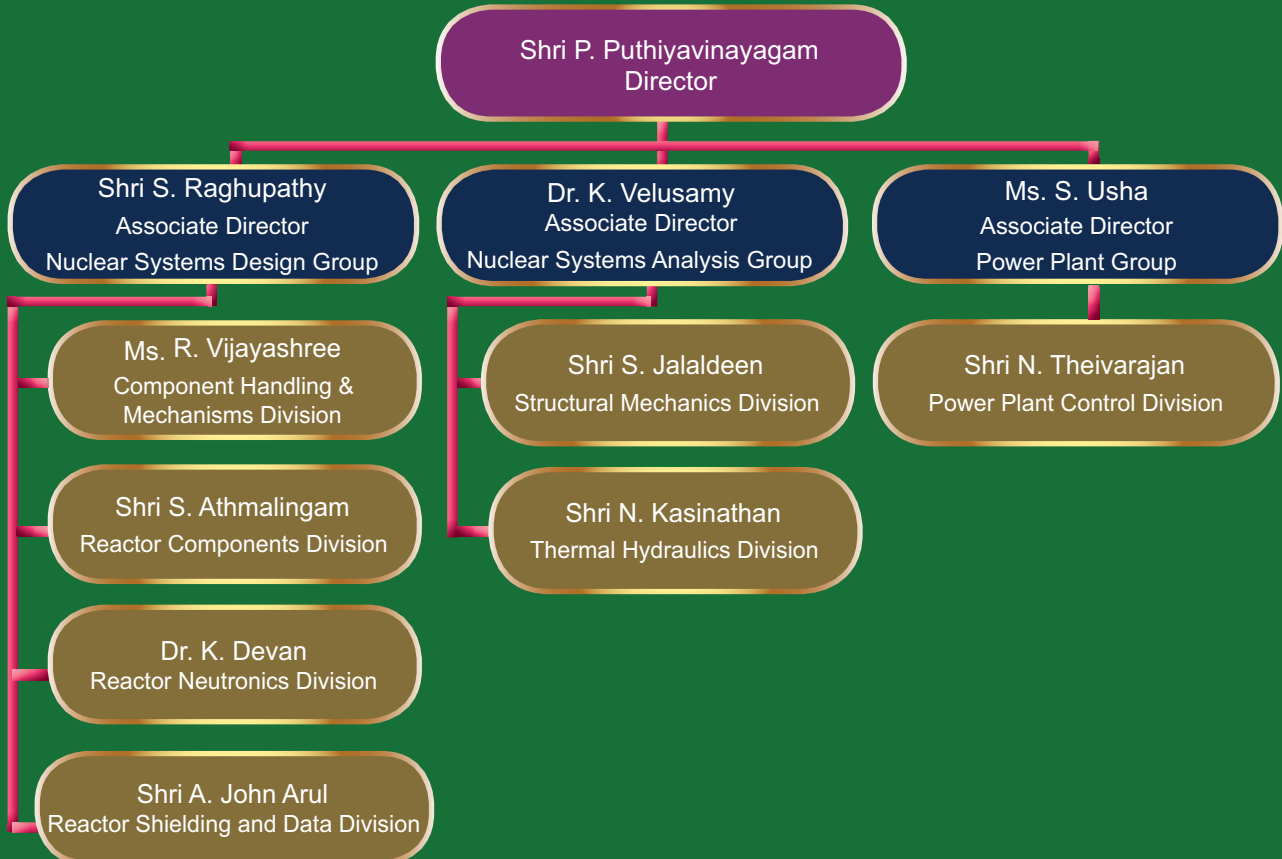
Shri B. Muralidharan
Pyro Process Engineering Division

Groups / Divisions / Heads

Metallurgy & Materials Group

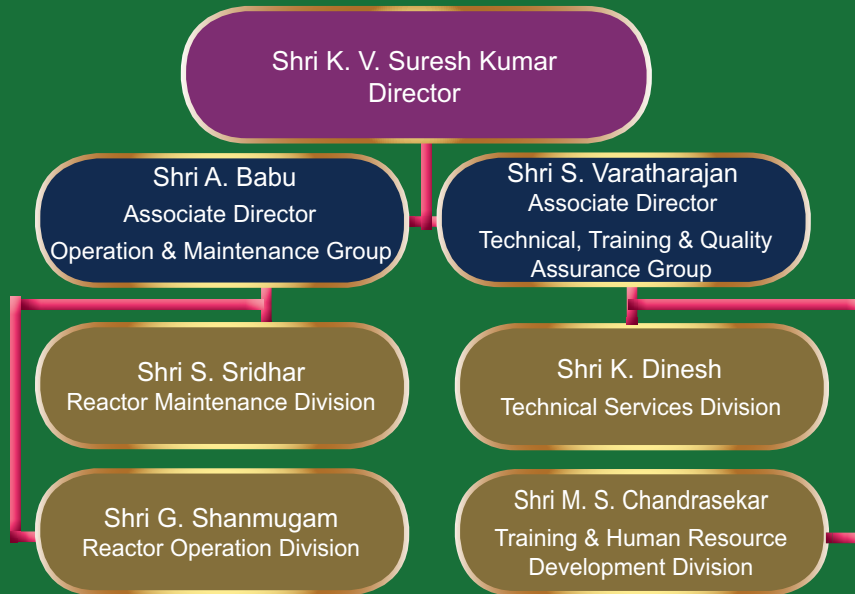


Reactor Design Group

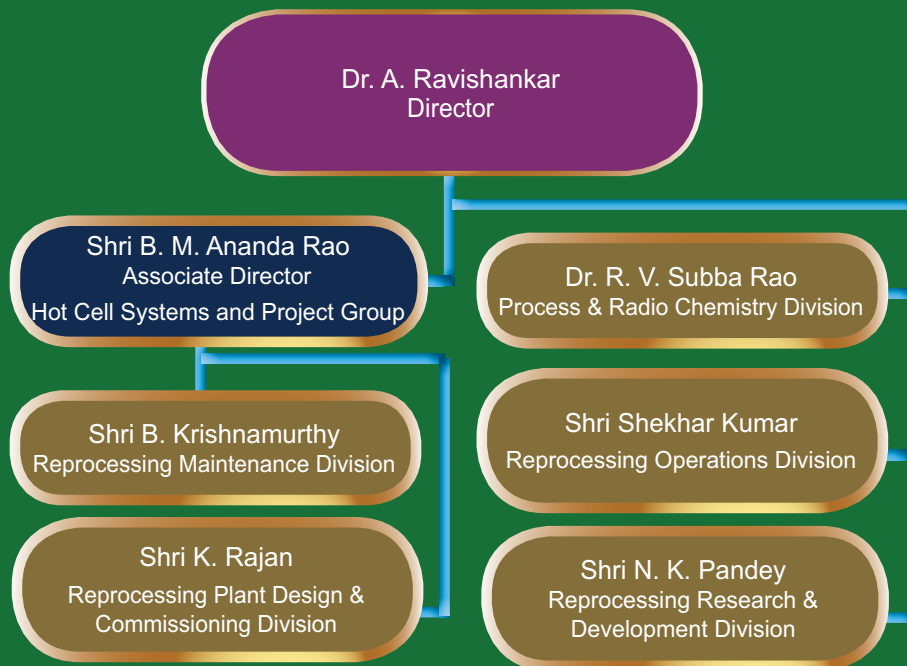


Groups / Divisions / Heads

Reactor Facilities Group

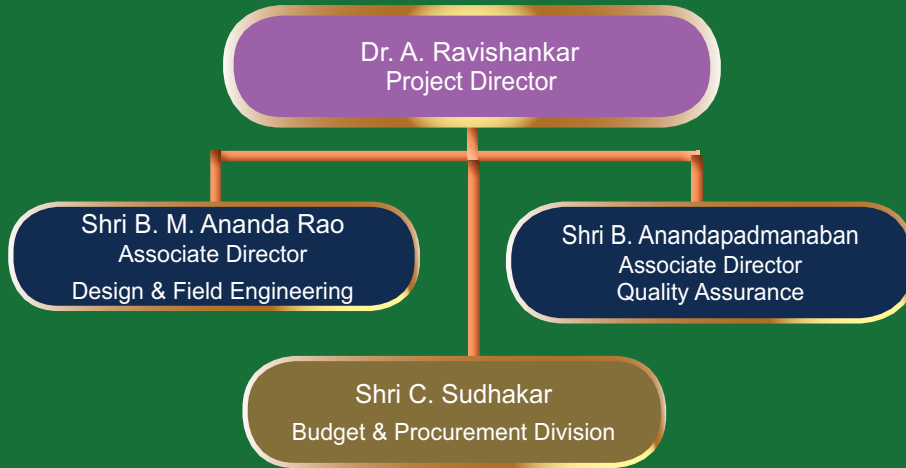


Reprocessing Group

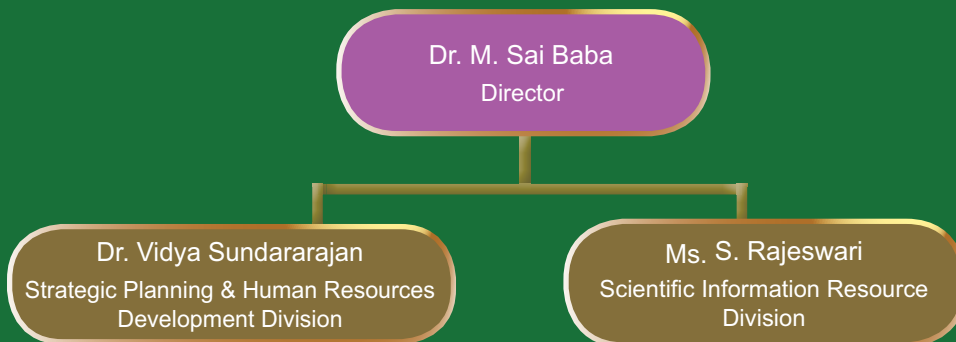


Groups / Divisions / Heads

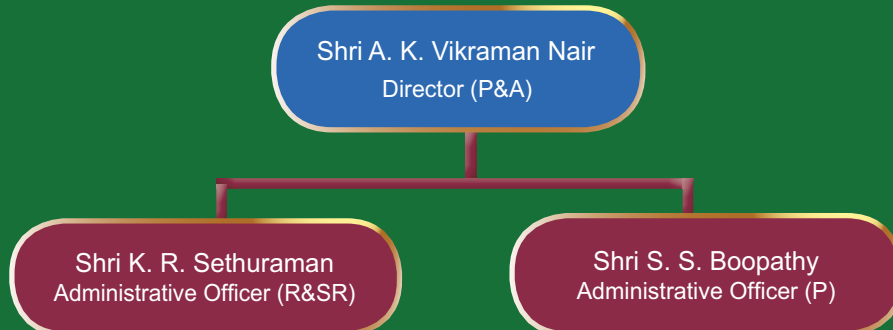
Fast Reactor Fuel Cycle Facility



Resources Management Group

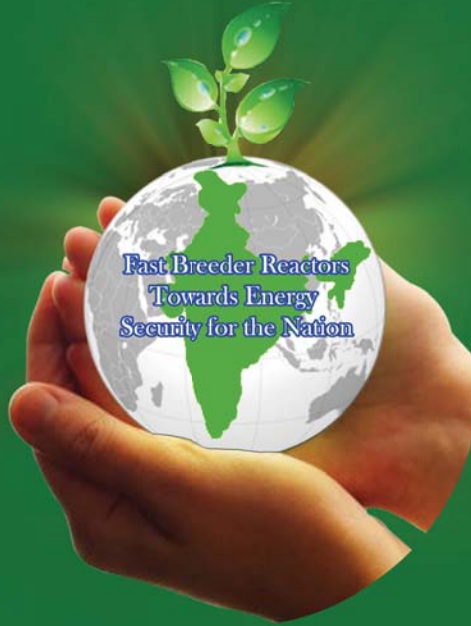


Administration



Accounts





Resources Management Group, IGCAR, Kalpakkam - 603 102